

Fumihiko Kimura  
Kenichiro Horio  
*Editors*

# Towards Synthesis of Micro-/Nano-systems

The 11<sup>th</sup> International Conference  
on Precision Engineering (ICPE)  
August 16 – 18, 2006, Tokyo, Japan

Organized by JSPE (Japan Society for Precision Engineering)  
Co-organized by ASPE (American Society for Precision Engineering)  
euspen (European Society for Precision Engineering and Nanotechnology)

JSPE Publication Series No.5

 Springer



# Towards Synthesis of Micro-/Nano-systems

---

Fumihiko Kimura and Kenichiro Horio (Eds.)

---

# **Towards Synthesis of Micro-/Nano-systems**

**The 11th International Conference on Precision Engineering (ICPE)  
August 16–18, 2006, Tokyo, Japan**

**Organized by JSPE (Japan Society for Precision Engineering)**

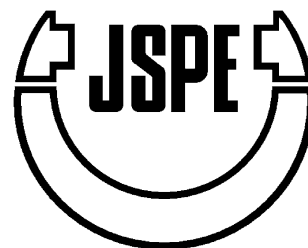
**Co-organized by ASPE (American Society for Precision Engineering),**

**euspem (European Society for Precision Engineering and Nanotechnology)**

**JSPE Publication Series No.5**

With 641 Figures

 Springer



Fumihiko Kimura, Dr. Eng.  
Department of Precision Machinery Engineering  
School of Engineering  
The University of Tokyo  
Tokyo 113-8656  
Japan

Kenichiro Horio, Dr. Eng.  
Mechanical Engineering Department  
School of Engineering  
Saitama University  
Saitama 338-8570  
Japan

British Library Cataloguing in Publication Data  
International Conference on Production/Precision  
Engineering (11th : 2006 : Tokyo, Japan) Towards synthesis of micro-/nano-systems : proceedings of  
the 11th International Conference on Precision Engineering  
1. Production engineering - Congresses 2. Microtechnology -  
Congresses 3. Nanotechnology - Congresses  
I. Title II. Kimura, F. (Fumihiko), 1945- III. Horio,  
Kenichiro  
620'.0045  
ISBN-13: 9781846285585  
ISBN-10: 1846285585

Library of Congress Control Number: 2006929601

ISBN-10: 1-84628-558-5 e-ISBN 1-84628-559-3 Printed on acid-free paper  
ISBN-13: 978-1-84628-558-5

© Springer-Verlag London Limited 2007

MATLAB® and Simulink® are registered trademarks of The MathWorks, Inc., 3 Apple Hill Drive, Natick, MA 01760-2098, USA.  
<http://www.mathworks.com>

The software disk accompanying this book and all material contained on it is supplied without any warranty of any kind. The publisher accepts no liability for personal injury incurred through use or misuse of the disk.

Apart from any fair dealing for the purposes of research or private study, or criticism or review, as permitted under the Copyright, Designs and Patents Act 1988, this publication may only be reproduced, stored or transmitted, in any form or by any means, with the prior permission in writing of the publishers, or in the case of reprographic reproduction in accordance with the terms of licences issued by the Copyright Licensing Agency. Enquiries concerning reproduction outside those terms should be sent to the publishers.

The use of registered names, trademarks, etc. in this publication does not imply, even in the absence of a specific statement, that such names are exempt from the relevant laws and regulations and therefore free for general use.

The publisher makes no representation, express or implied, with regard to the accuracy of the information contained in this book and cannot accept any legal responsibility or liability for any errors or omissions that may be made.

Printed in Germany

9 8 7 6 5 4 3 2 1

Springer Science+Business Media  
[springer.com](http://springer.com)

# Preface

At the beginning of 21st century, manufacturing industry is facing new challenges due to globalization and environmental sustainability. In accordance with the progress of micro/nano technology, precision engineering is considered to be one of the core engineering to cope with severe requirements of new product and system developments. From basic research to practical applications, it becomes gradually important how to synthesize and how to design micro-/nano-systems based on advanced precision process technology. For contributing to these emerging developments, this book is edited as a collection of all the papers presented at the 11<sup>th</sup> International Conference on Precision Engineering, ICPE, where industrial papers as well as high-quality scientific papers are solicited for discussing front-edge technology and forecasting future trends.

The ICPE has been consecutively held as one of the major international conferences organized by the Japan Society for Precision Engineering, JSPE. The 11<sup>th</sup> ICPE takes place in Tokyo from August 16 to August 18, 2006. This conference is a second collaborative meeting organized jointly by the three major societies for precision and production engineering: Japan Society for Precision Engineering, JSPE, American Society for Precision Engineering, ASPE, and European Society for Precision Engineering and Nanotechnology, euspen. It is sponsored by the International Academy for Production Engineering, CIRP. The general aim of these consecutive conferences is to promote research and development activities in precision and

production engineering, and to discuss the advanced technologies of the related fields.

This proceedings book of the Conference includes 3 keynote papers and 71 contributed papers, which consist of 52 full papers and 19 short papers. Keynote papers address important topics in the field of precision engineering from academic and industrial perspectives. Contributed papers cover many aspects of recent issues of micro/nano technology, and discuss following topics areas: precision systems and their design, measurement technology, actuator and precision mechanisms, control and sensing technology, machine tools, micro/nano manipulation, plasma process, laser process, polishing/grinding, and integrated processes. These papers are good basis for capturing the current status and future trends of production and precision engineering, and they will stimulate further research and development in micro/nano technology and systems.

I would like to express my deep appreciation to all the contributors of this book, especially to the authors of the keynote papers, which give special inspiration to the future of the micro/nano technology. I also would like to extend my sincere appreciation to the members of the Organizing Committee and the International Program Committee for their considerable efforts in organizing the Conference and in making this book available in its present form.

I expect this book is a valuable source of knowledge for researchers, engineers and students in their future research and development activity.



*Fumihiko Kimura*  
*Chairman of the Organizing Committee*  
*11<sup>th</sup> ICPE*

Tokyo, Japan, August 2006

# Table of Contents

Preface .....	v
Organization .....	xiii
<b>Keynote Papers</b>	
<b>Merging Technologies for Optics</b> .....	1
E. Brinksmeier, O. Riemer, R. Gläbe	
<b>Fast Tool Servos: Advances in Precision, Acceleration, and Bandwidth</b> .....	11
D.L. Trumper, X. Lu	
<b>Microsystem Technologies for Automotive Applications</b> .....	21
Y. Ueno, N. Kawahara	
<b>Full Papers</b>	
<b>[A1 Design]</b>	
<b>System Concept and Innovative Component Design for Ultra-Precision Assembly Processes</b> .....	29
A. Schubert, R. Neugebauer, B. Schulz	
<b>Development of a Design Tool for Machine Tools Combining Conceptual Design Support and Detail Design Method</b> .....	35
N. Mishima	
<b>Precision Contouring Control of Multi-Axis Feed Drive Systems</b> .....	41
N. Uchiyama, S. Sano, S. Takagi, K. Yamazaki	
<b>Areal Gear Flank Description as a Requirement for Optical Gear Metrology</b> .....	47
G. Goch, A. Günther	
<b>[A2 System]</b>	
<b>Detecting Perturbation Occurrence during Walking</b> .....	53
Y. Hagane, W. Yu, R. Katoh, T. Katane, M. Sekine, T. Tamura, O. Saitou	
<b>Supporting the Reuse of Parts Based on Operation Histories of Products and Preference of Consumers</b> .....	59
N. Fukuda, H. Hiraoka, T. Ihara	
<b>Multi-objective Reactive Scheduling Based on Genetic Algorithm</b> .....	65
Y. Tanimizu, T. Miyamae, T. Sakaguchi, K. Iwamura, N. Sugimura	
<b>[A3 Measurement]</b>	
<b>Ultraprecision Wide-angle Profile Measurement with Air-bearing Cylinder Slant Probes</b> .....	71
S. Moriyasu	
<b>Development of a Laser-Guided Deep-Hole Measuring System: Autocollimation System</b> .....	77
A. Katsuki, H. Murakami, H. Onikura, T. Sajima	
<b>Development of an Optical Measuring Device for Rotation Accuracy of Micro-Spindle - Application to Measurements of a High-Speed Spindle -</b> .....	83
K. Fujimaki, K. Mitsui	
<b>Laser Interferometric Measurement of Involute Profile by Rolling of Artifact</b> .....	89
F. Takeoka, M. Komori, A. Kubo, H. Fujio, S. Taniyama, T. Ito, T. Takatsuji, S. Osawa	
<b>[A4 Actuator]</b>	
<b>Study on Manufacturing Method to Reduce Cogging Torque of Motor with Separate Core</b> .....	95
H. Akita, Y. Nakahara, T. Yoshioka, T. Miyoshi	

<b>A High Power and Precision Ultrasonic Linear Motor with Lateral Flexible Supports</b> .....	101
H. Lee, W. Kim, C. Yun, H. Cha, C. Kang, S. Lee	
<b>A Precise Motion Measurement of a Miniature Robot Driven by the Deformation of Piezoelectric Actuators</b> .....	107
A. Torii, A. Shimada, K. Doki, A. Ueda	
<b>Development of IVUS (Intra-Vascular Ultrasound) Driven by Ultrasonic Micromotor -Principle of Drive and Detection Methods-</b> .....	113
T. Wada, A. Nakajima, T. Moriya, Y. Furukawa	
<b>[A5 Precise mechanism]</b>	
<b>Development of Membrane Driven Micropump -Principle of Microbubble Driving Mechanism and Prototype-</b> .....	117
M. Yamada, Y. Furukawa, K. Morishima	
<b>A 3-DOF Rotational Precision Positioning Stage using Spring-mounted PZT Actuators</b> .....	121
Y. Liu, G. Lee	
<b>Active Damping of a Wafer Loading Robot using Piezoceramic Actuators</b> .....	127
B. Pletner, G. Zvonar, Y. Kayama, T. Kamiyama, M. Iwagawa, S. Bhola, G.R. Kessenich	
<b>[A6 Control/Sensing]</b>	
<b>Visual Feedback Control of a Micro Lathe</b> .....	133
H. Ojima, K. Saito, L. Zhou, J. Shimizu, H. Eda	
<b>An 8-Axis Robot Based Rough Cutting System for Surface Sculpturing</b> .....	139
J. Zhu, R. Tanaka, T. Tanaka, Y. Saito	
<b>A New Position Surveying System for the Underground Pipes Using Two Rotary Encoders</b> .....	145
T. Hamano, M. Ono, S. Kato	
<b>[A7 Machine tools]</b>	
<b>Measurement of Cutting Torque by Speed Increasing Spindle</b> .....	151
M. Yamanaka, S. Miyamura, K. Inoue	
<b>Diamond Turning using Water Drive Spindle</b> .....	157
Y. Nakao, Y. Sagesaka	
<b>Development and Evaluation of a High-Precision Machining Center with Friction-Less Drives</b> .....	163
D. Kono, A. Matsubara, S. Ibaraki, H. Otsubo, M. Tsuboi, I. Oshita	
<b>Machining Feature-Driven 5-Axis CNC Machine Tools</b> .....	169
S. Mitsui, F. Tanaka, T. Kishinami	
<b>[B1 Micro structure]</b>	
<b>Selective Anodising Technologies for Obtaining Translucent Micro Structures</b> .....	175
H.N. Hansen, P. Møller, C. Jarnov, J.Staun, J.P. Prichystal	
<b>Development of Rectangular Microblasting Nozzle</b> .....	181
M. Sugimoto, T. Shakouchi	
<b>Thick SU-8 Mask for Micro Channeling of Glass by using Micro Abrasive Jet Machining</b> .....	187
A.S. Saragih, J.H. Lee, T.J. Ko, H.S. Kim	
<b>Fabrication of Self-assembled Microstructure using Controlled Liquid Spreading on Textured Surface</b> .....	191
A.Kaneko, N. Moronuki, M. Mogi, Y. Yamamura	
<b>[B2 Micro/Nano manipulation]</b>	
<b>Improving Performance of Direct Photosynthetic/Metabolic Micro Bio Fuel Cell (DPBFC) by Gene Manipulation of Bacteria</b> .....	197
A. Furuya, T. Moriuchi, M. Yoshida, M. Ota, K. Morishima, Y. Furukawa	

<b>Nanometer Deflection Control of AFM Probe by Irradiating Polarized Laser and its Application to Nano-Structuring Process</b> .....	203
D. Mezaki, K. Chuma, A. Kakuta, Y. Furukawa	
<b>Investigation on Fabricating 3D Structures Using Inkjet Printing Technology</b> .....	209
M. Ibrahim, T. Otsubo, H. Narahara, H. Koresawa, H. Suzuki	
<b>Miniaturization of Dot Pattern by Metal Forming for Direct Marking of 2D Barcode Symbols</b> .....	215
H. Ike	
<b>[B3 Plasma process]</b>	
<b>Plasma Etching Based Processes for the Fabrication of Micro Structured Linear Guide</b> .....	221
A. Phataralaoha, S. Buttgenbach	
<b>Ultraprecision Finishing of Photomask Substrate by Utilizing Atmospheric Pressure Plasma</b> .....	227
K. Yamamura, A. Fujiwara, K. Ueno, Y. Sano, M. Shibahara, K. Endo, Y. Mori	
<b>Development of Ultra Precision Finishing Method for Quartz Crystal Wafer Utilizing Atmospheric Pressure Plasma</b> .....	233
M. Shibahara, Y. Yamamoto, K. Yamamura, Y. Sano, K. Endo, Y. Mori	
<b>Sub-nanometer Smoothing of Diamond-turned Metal Surfaces using Ion Beams</b> .....	239
F. Frost, H. Takino, R. Fechner, A. Schindler, N. Ohi, K. Nomura	
<b>[B4 Laser process]</b>	
<b>Laser Machining of Cobalt Cemented Tungsten Carbides</b> .....	243
B. Karpuschewski, E. Wolf, M. Krause	
<b>Study of Thermal Deformation of a Base Sheet Caused by Laser Cutting</b> .....	249
M. Nunobiki, K. Okuda, T. Yoshida, S. Kita	
<b>Laser Welding of Transparent Resin Plates</b> .....	255
S. Hayakawa, T. Miura, T. Nakamura, F. Itoigawa, T. Hasegawa	
<b>Fabrication of Carbon Nanotube Reinforced Hydroxyapatite Coating on Stainless Steel 316L by Laser Surface Treatment</b> .....	261
C.T. Kwok	
<b>[B5 Polishing/Finishing]</b>	
<b>Novel Abrasive-free Planarization of Si and SiC using Catalyst</b> .....	267
H. Hara, Y. Sano, H. Mimura, K. Arima, A. Kubota, K. Yagi, J. Murata, K. Yamauchi	
<b>Polishing of Single Crystal SiC with the LHA Pad</b> .....	271
M. Sato, K. Okuda	
<b>A Computational Study on Slurry Flow between a Wafer and CMP Pad with Grooves</b> .....	277
K. Nagayama, H. Morishita, K. Kimura, K. Tanaka	
<b>[B6 Integrated process]</b>	
<b>Multilevel Computer Generated Hologram on a Curved Surface for High Power CO2 Laser Beam Shaping</b> .....	281
H. Hagino, C.S. Park, H. Kikuta, K. Iwata	
<b>Milling-Combined Laser Metal Sintering System and Production of Injection Molds with Sophisticated Functions</b> .....	285
S. Abe, Y. Higashi, I. Fuwa, N. Yoshida, T. Yoneyama	
<b>Development of Optical Elements with ELID-grinding and MRF Synergistic Finishing Process</b> .....	291
W. Lin, H. Ohmori, Y. Uehara, Y. Watanabe, T. Suzuki, S. Yin	
<b>Fabrication of Ultraprecisely Figured Mirror for Nano Focusing Hard-x-ray</b> .....	295
H. Yumoto, H. Mimura, S. Matsuyama, S. Handa, K. Yamamura, Y. Sano, K. Endo, Y. Mori, M. Yabashi, Y. Nishino, K. Tamasaku, T. Ishikawa, K. Yamauchi	



<b>[B7 Grinding]</b>	
<b>Surfaces Formation of Precision ELID Grinding Rock Minerals</b> .....	301
J. Shen, W. Lin, H. Ohmori, X. Xu	
<b>Dressing of Coarse-Grained Diamond Wheels for Ductile Machining of Brittle Materials</b> .....	305
D. Grimme, K. Rickens, Q. Zhao, C. Heinzl	
<b>Study on Subsurface Damage Generated in Ground Si Wafer</b> .....	309
B.S. Hosseini, L. Zhou, T. Tsuruga, J. Shimizu, H. Eda, S. Kamiya, H. Iwase	
<b>Fabrication of High-quality Surfaces on Precise Lens Mold Materials by a new ELID Grinding Wheel</b> .....	315
T. Saito, K. Katahira, H. Ohmori, J. Komotori, M. Mizutani, A. Nemoto	

## Short Papers

<b>[Design]</b>	
<b>A GA-based Optimization of Compliant Micro-manipulator</b> .....	319
G.B. Madhab	
<b>Path Control Scheme for Vision Guided Micro Manipulation System</b> .....	321
H. Asano, Z. Qiu, L. Zhou, H. Ojima, J. Shimizu, T. Ishikawa, H. Eda	
<b>Machined Surface Analysis for 5-axis Machine Tools</b> .....	323
M. Yamada, F. Tanaka, T. Kondo, T. Kishinami	

<b>[System]</b>	
<b>A New Approach Manufacturing Cell Scheduling based on Skill-based Manufacturing Integrated to Genetic Algorithm</b> .....	325
B. Suksawat, H. Hiraoka, T. Ihara	
<b>Slide-bending Formation of Thin Metal Sheet by Using an Industrial Robot</b> .....	327
H. Harada, Y.Z. Sun, Y. Marumo, T. Matsuno, L. Ruan	

<b>[Machine]</b>	
<b>High Accuracy and High Capacity Motor Cooling System Using Phase Change of Refrigerant for Semiconductor Lithography Apparatus</b> .....	329
A.K.T. Poon, F. Nishimatsu, M. Totsu, L. Kho, G. Keswani	
<b>Development of the Earthworm Robot using a Shape Memory Alloy</b> .....	331
T. Saito, T. Kagiwada, H. Harada, Y. Kawamura	
<b>Improvement of Propulsion Mechanism based on the Inertial Force</b> .....	333
H. Yoshikawa, T. Kagiwada, H. Harada, M. Mimura	

<b>[Measurement]</b>	
<b>A High-order Spline Filter for Surface Roughness Measurement</b> .....	335
M. Numada, T. Nomura, K. Yanagi, K. Kamiya, H. Tashiro	
<b>Surface Structure of Monocrystalline Silicon Anisotropically Etched with the Help of Microwaves</b> .....	337
T. Krah, S. Büttgenbach	

<b>[Novel Process]</b>	
<b>Development of an Ultra-Thin 100 Micron Diametrical Coaxial Cable using a Coating Technique</b> .....	339
H. Miyagawa, H. Ishihara, S. Kobayashi, K. Hira, Y. Horibe, Y. Suzuki	
<b>Study on Si Wafer Cooling by Low Pressure Argon Gas in Vacuum Environment</b> .....	341
S. Udagawa, S. Takahashi, D. Nakamura, K. Maeno	

<b>[Process]</b>	
<b>Research on Development of Advanced Analyzer Components with Ultraprecision .....</b>	<b>343</b>
H. Ohmori, K. Katahira, W. Lin, Y. Uehara, Y. Watanabe, A. Nakao, F. Yatagai, M. Iwaki, M. Mizutani	
<b>Effects of Wear of Single Crystal Diamond Tool with Large Nose Radius on Work Hardening and Residual Stress .....</b>	<b>345</b>
E. Kondo, R. Iwamoto, I. Tanaka, N. Kawagoishi	
<b>Experimental Analysis And Optimization of Cutting Parameters for End Milling Aluminium Alloy ...</b>	<b>347</b>
N. Ahmad, R. Wakabayashi, T. Tanaka, Y. Saito	
<b>Study on the ELID Grinding Forces of Ceramics and Steels .....</b>	<b>349</b>
J. Guo, H. Ohmori, Y. Uehara, Y. Watanabe, M. Asami	
<b>Grinding of C/C-SiC Composite in Dry Method .....</b>	<b>351</b>
T. Tashiro, J. Fujiwara, Y. Takenaka	
<b>Micromachining Characteristics of Sapphire Surface with Fifth Harmonic Nd:YAG Lasers .....</b>	<b>353</b>
T. Noji, K. Nakamura, H. Horisawa, N. Yasunaga	
<b>Development of an Automatic Scraping Machine with Recognition for Bearing of Scraped Surfaces - Construction of Automatic Scraping Machine - .....</b>	<b>355</b>
H. Tsutsumi, R. Yamada, A. Kyusojin, T. Nakamura	

# Organization

## Organizing Committee

### Chairman

- F.Kimura (The University of Tokyo, Japan)

### Executive Secretary

- H.Suzuki (The University of Tokyo, Japan)

- T.Aoyama (Keio University, Japan)
- H.Hiraoka (Chuo University, Japan)
- K.Horio (Saitama University, Japan)
- I.Inasaki (Keio University, Japan)
- K.Mori (AIST, Japan)
- T.Moriwaki (Kobe University, Japan)
- T.Obikawa (Tokyo Institute of Technology, Japan)
- H.Ohmori (RIKEN, Japan)
- S.Takata (Waseda University, Japan)
- H.Tokura (Tokyo Institute of Technology, Japan)

## International Program Committee

### Chairman

- K.Horio (Saitama University, Japan)

- Y.Altintas (The University of British Columbia, Canada)
- H.Aoyama (The University of Electro-Communications, Japan)
- T.Aoyama (Keio University, Japan)
- E.Brinksmeier (University of Bremen, Germany)
- G.Byrne (University College Dublin, Ireland)
- J.Corbett (Cranfield University, UK)
- D.A.Dornfeld (University of California, USA)
- H.Hiraoka (Chuo University, Japan)
- R.J.Hocken (University of North Carolina, USA)
- F.Klocke (T.H. Aachen, Germany)
- F.-L.Krause (TU Berlin, Germany)
- J.Lee (University of Cincinnati)
- D.A.Lucca (Oklahoma State University, USA)
- T.Masuzawa (The University of Tokyo, Japan)
- N.Mohri (The University of Tokyo, Japan)
- L.Monostori (Hungarian Academy of Science, Hungary)
- K.Mori (AIST, Japan)
- T.Moriwaki (Kobe University, Japan)
- T.Obikawa (Tokyo Institute of Technology, Japan)
- H.Ohmori (RIKEN, Japan)
- M.Rahman (National University of Singapore, Singapore)
- Y.Saito (Tokyo Institute of Technology, Japan)
- S.Shimizu (Sophia University, Japan)
- M.Shpitalni (Technion, Israel)
- H.Suzuki (The University of Tokyo, Japan)
- S.Takata (Waseda University, Japan)
- H.K.Toenshoff (University of Hannover, Germany)
- H.Tokura (Tokyo Institute of Technology, Japan)
- D.L.Trumper (Massachusetts Institute of Technology, USA)
- E.Uhlmann (T.U. Berlin, Germany)
- H.van Brussel (K.U.Leuven, Belgium)
- F.van Houten (University of Twente, the Netherlands)
- R.Wertheim (ISCAR, Israel)
- E.Westkaemper (University of Stuttgart, Germany)
- G.X.Zhang (Tianjin University, China)

## Conference Secretariat

The Japan Society for Precision Engineering  
Kudan-Seiwa Building, 1-5-9 Kudan-kita, Chiyoda-ku, Tokyo 102-0073 JAPAN  
Phone +81-3-5226-5191 Fax +81-3-5226-5192 E-mail icpe11@jspe.or.jp Web <http://www.icpe11.jspe.or.jp>

---

# Merging Technologies for Optics

Ekkard Brinksmeier, Oltmann Riemer, Ralf Gläbe  
Laboratory for Precision Machining, University of Bremen, Germany

Keywords: Precision Optics, Process Chains, Molded Optics

## Abstract

The market for optical and optoelectronic components is a rapidly growing global market. The development of new manufacturing technologies for the fabrication of optics enables the fabrication of optical components with nanometer roughness and submicron form accuracy for mass markets like digital cameras, video projectors and automotive applications, even for low cost applications with short product life cycles. Therefore, the process chain for fabricating optical high quality mass products has to be deterministic flexible as well as in order to suppress cost intensive and time consuming iterations within the manufacturing chain. This paper introduces several approaches to take up this challenge.

## 1 Introduction

Optics and optoelectronics are an ever growing global market. The global market for optoelectronics grew from 1997 to 2004 from 139 billion USD up to 236 billion USD turnover [1]. Mass products like DVD, camera phones, are the drivers for such growing turnover.

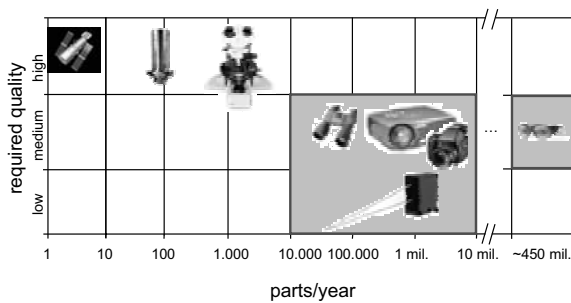


**Fig. 1.** Applications like video projectors or digital cameras require low to medium quality complex optical components. They have to be fabricated by replication to meet the demands of mass market products. [after Zeiss, VKE, Spectaris]

Optics and optonics are key technologies for high volume consumer products, that are getting faster, smaller, a higher functionality and even more easy to handle and cheaper (cf.

Fig 1.). The driver for innovation is the need for increasing precision of optical parts and the integration of several functions within one component.

For meeting these market needs, optical components for mass products have to be fabricated in replication processes. The process for making optical components of plastics or glasses by replication requires: a broad knowledge in optical design, mold making, coatings, the replication processes itself and advanced measuring techniques as well as the ability to merge all these disciplines to a powerful, effective, fast and economic process chain for mass production.

The Frost & Sullivan report "Machine Vision Systems" gives a broad view on the technologies of the next decade. It is reported that the drivers for important innovations of the coming decade are the manufacturing technologies (discussed in [2]). This leads to the idea, that the improvement of manufacturing processes for replicated optics are the keys to innovations in optics. Moreover, those innovations are the drivers to new degrees of freedom in optical design.

Yamamoto divides the innovations in manufacturing processes for optical components into four groups [3]:

- integration of functions
- providing the productivity of the machining process
- improving of the quality of machined components
- improving of the quality of the machining process

The integration of several functions in one component will be a challenge for the optical design. It suffers, however, from the limitations of the mold manufacturing and the replication process. Furthermore, intelligent combinations could lead to new functionalities and, therefore, to new degrees of freedom in optical design. An example is the diffractive structure on an aspherical lens for decreasing aberration of an optical system. After having succeeded in this innovative step as well as secondly having found an appropriate manufacturing technology for machining such parts, the productivity of the machining process has to be improved for reducing the costs per piece. In the third step the machining process has to be developed to higher quality, so the machined products could be used for similar applications in a broader spectrum of usage e.g. at shorter wavelengths. Finally, the manufacturing process has to be

improved to a flexible module in a lean production system. This final step is the driver for a mass production of high quality optical products.

However, there are several limitations in a process chain for the replication of plastic and glass components. Replicating plastic parts will be done by injection molding at temperatures less than 200°C, so temperature sensitive mold materials like electroless nickel are appropriate. The advantage of this material in contrast to steel materials and ceramic is its excellent machinability by diamond milling or turning.

If higher hardness or temperature stability is demanded steel could be an alternative mold material. The machining process suffers, however, from tool wear when diamond turning or milling are applied. This is caused by chemical interaction between the steel workpiece and the carbon of the diamond tool [4]. As an advantage, diamond turning and milling operations do not require subsequent polishing processes, however they are applicable only to a small selection of mold materials useful for molding of plastics. The improvement of grinding, polishing and diamond machining processes to higher flexibility, higher precision and a larger spectrum of machinable mold materials is therefore an important goal for current research activities.

The relatively low viscosity of plastic at replication temperature will provide the possibility to integrate mechanical interfaces for mounting and assembly of the lens or haptic components. Nevertheless, the most important advantage of replication of plastic in contrast to glass is the short cycle time and the low wear of the mold, so that hundreds of thousands parts can be manufactured using a single mold. However, the optical quality of plastic lenses is strictly limited by deviations of the geometry and invariance of the plastic density and consequently the variation of refraction. Moreover, the range of plastics optical properties like refraction index or aberrations of the optical system is limited too, which results in limitations in optical design using plastic lenses.

In contrast to plastics, glass optics are showing a much smaller tendency to irregular deformation under invariant thermal, chemical and mechanical environmental conditions like deviations in temperature or moisture. So, the replication of glass is a key technology for fabricating high performance optical products e.g. for projection lenses. However, molding of glass needs precision molds with high temperature stability, even if new innovative glass materials with softening point not much higher than 400°C are applied. Therefore, glass molds should be made of hard and brittle materials like ceramics that require grinding and polishing in contrast to diamond machinable ductile metals like electroless nickel.

During the replication process the mold material will suffer from tribological stress. Hard coatings with tailored mechanical, chemical and thermal properties may help to overcome those limitations for enlarging the parameter window for the replication process and the spectrum of replicated materials. Finally, measuring techniques have to move closer to the replication process to reduce time consumptive handling operations.

Each process step from design over mold making to the replicated part comprises its own limitations and restrictions e.g. form deviations when machining or shrinkage of the

replicated part when it cools down. An exact knowledge about the deviations in roughness and geometry of the mold and replicated part is necessary for geometry compensation in an earlier stage of production. This is the first step to a deterministic process chain and presupposes a holistic view to the complete chain. This procedure will take all limitations of each process step into account will merge the process chain to an advanced and powerful instrument for fulfilling the current and coming industrial needs.

## 2 Applications

There are a large number of products that are drivers for the development of innovative and more precise optical components. Their applications lie in the field of mass markets, so the applied optical components have to be fabricated by replication.

Tab. 1 shows typical applications utilizing replicated optics. The range of the size of the optical components and optic material varies. Each application has its own needs and limits in relation to the process chain. Moreover, there are many technologies needed for fabricating replicated optics - almost different if molding optical glass or plastic components. The technologies in a typical process chain are optical design, fabrication of the mold, possibly using a hard coating for wear reduction and better relief of the replicated part, replication process and finally metrology and quality management. Nevertheless, the required accuracy and complexity of shape will increase in future as discussed above.

**Table 1.** Markets and applications for replicated optical parts

<b>Markets</b>	<b>Applications</b>
Automotive	Headlights Head-Up-Displays
Life science	Optics for endoscopes Head-Mounted-Displays
Display equipment	Video projectors Flat displays
Optical I/O equipment	Fiber optics
Measuring / Sensing	Optical sensors
Storage	CD / DVD / HD-DVD
Cameras / Mobile phone cameras	Digital optics

## 3 Design and layout of process chains

The process chain for an economic mass production of complex optical elements resulting from this concept is shown in Fig. 2. The process chain comprises all aspects of

production ranging from the design phase to mold fabrication, replication and performance tests of the final products. It can only be realized by qualified measuring and testing. Quality chain management is of overall importance, since it guarantees a holistic view of the complete process chain assuring an effective interaction between the individual process steps.

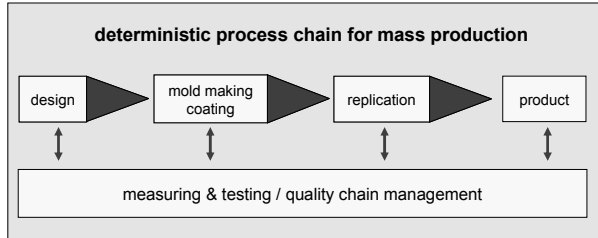


**Fig. 2.** Deterministic process chain for the replication of high precision optical components

The following chapter will give an overview on current research activities for meeting these challenges. Moreover, it will be shown, that an optimized process chain for fabricating precision optical components has to consider the interaction between mold design, mold making and replication.

**Table 2.** Requirements, limitations, challenges, and interactions between mold design, mold making and replication process.

mold design process	mold making process	replication process
geometry and dimension - flat - (a)spherical - free-form - superimposed structures	machining process - dynamic stiffness and temperature stability of machine tool - cutting tools - number of axis	replication temperature molded material - rheology / viscosity
roughness	machining process - diam. machining - grinding - polishing	rheology mold material - corrosion resistance - mold life
optical material - glass - plastic	mold material - molding temp.	replication process - injection mold. - inj. embossing - hot pressing
accuracy	machining accuracy mold material - creep tendency	

In the mold design process several boundary conditions will be determined for the mold making and replication process.

After planning the design of an optical surface, the mechanical interface, the material to be molded and the mold machining process are almost determined too. Moreover, the spacial dimensions do also affect the replication process, because of the temperature dependent shrinkage of plastic when injection molding large, thin parts like mirrors for head-up-displays. Another issue is the required accuracy of the optical component that leads to the choice of the replication process and the mold material selection. The latter is of interest for the long-term dimensional stability of the mold which requires the use of ceramic mold inserts instead of steel for hot pressing of glass. Moreover, for plastic replication processes the step from conventional injection molding to injection embossing (embossing utilizes an additional compression of the replicated part during the cooling process) can be used for increasing the form accuracy.

The replication of glass is carried out at higher temperatures than injection molding of plastic, even if lowTg glasses (softening point at temperatures between approx. 400 and 500°C) are used. Therefore, the spectrum of mold materials differs for molding glass and plastic.

More aspects of interaction between design, mold making and replication process are shown in Tab. 2. It can be seen, that a close interaction - or merging - between the three disciplines is evident for taking the specific advantages and limitations into account.

### 3.1 Design

Design in a deterministic process chain must not only focus on optical design but has to consider also inherent strategies for predicting and compensating process dependent deformations of the mold insert and the replicated part. For developing such strategies calculating tools for optical design and simulation of injection molding (discussed in chapter 3.6) are needed as well as suitable measuring techniques.

A basic requirement for the comparison of designed and simulated geometries with the produced results like the deformation of glass in a hot pressing procedure or the filling procedure of a plastic forming process is to use a uniform surface data description. State of the art mathematical descriptions are Non-Uniform Rational Basic Splines (NURBS). Due to their ability to describe any type of surface, especially those without analytical function behind, and the small amount of required data, this type of data is ideal for the use in optical applications.

The designed surface data can be further used as reference data for the entire process chain - for comparison of measured interferometric data of the mold as well as of the replicated plastic part.

In Fig. 3 the simulated topography of a designed optical surface described by NURBS is shown. This topography is calculated by an optical calculation program. The data can be directly used for calculating the NC-program for machining the mold insert. The calculation of the tools trajectory has to take the machining process, the tool geometry and its position in the machine tool into account. Calculating the trajectory could be done off-line (before machining), nevertheless, the calculation will take some time, because of

the small distance between the nodes to be programmed needed for nanometer precision. This leads to a large amount of data. Moreover, processing of these data is difficult for most numerical machine controls, because of the large data volume and the necessary fast data processing. The consequent step is to use the NURBS surface data for on-line controlling of the machine tool so there is no need to store and provide the data, however, a fast computer system for calculating the data is necessary. Applying this technique to a diamond turning operation a Fast-Tool-System can be used for the control of the tool's motion parallel to the spindle axis [5].

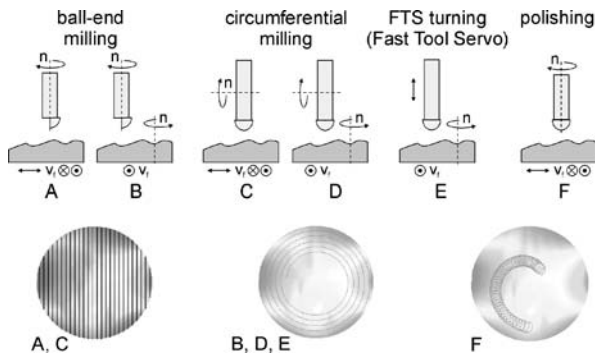


**Fig. 3.** Simulated, topography of a calculated optical surface (color/gray shade indicates the height in Z direction) and referenced trajectory for the respective machining technology [source: LFM-Bremen]

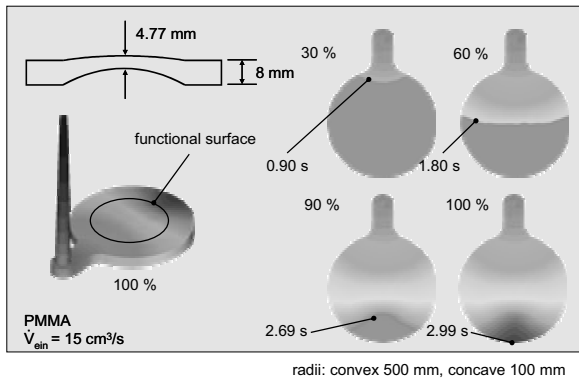


**Fig. 4.** Simulation of mold filling [source: IKV-Aachen]

Another design aspect is the design of the injection mold. The injection mold has to hold the mold insert in a fixed position, it has to provide the molding temperature and it has to maintain all its functions precisely under the mechanical and thermal load during the injection process. It was found out, that an important aspect for getting plastic parts with low form deviation is the need for a constant and symmetrical pressure distribution during the filling and cooling phase of the molding process. However, during replication any component of the injection mold will affect the geometry of the replicated part more or less. E.g. the clamping torque of the screw for fixing the insert will influence the form deviation considerably [6]. It was proven

that molding is a multivariable process, where the form of the replicated part is nearly impossible to predict precisely. However, a simulation program for calculating the filling process can support the design process for the injection mold, mold insert and filling parameters under consideration of the lens geometry, size and thickness as well as the position and size of the sprue (Fig. 4) [7].

However, the simulation has not yet the ability to predict the filling process and the following cooling/shrinking process precisely cause of the noted multivariable situation. Therefore, the geometry of the replicated optical component and its density distribution as a consequence of the locally distributed cooling gradients has to be measured after replication. For achieving high precision plastic parts, the form deviations have to be removed by correcting the mold in a couple of iteration steps. However, simulation techniques and a broad knowledge about the replication process will definitely reduce the number of iteration steps.

### 3.2 Mold making

There is a large number of machining processes available for making mold inserts made of steel or ceramic material [8]. The processes differ in the spectrum of machinable geometry, material, removal rate, achievable form accuracy and roughness. Diamond machining is a state-of-the-art machining technology with various opportunities for further process improvements that makes this technology more flexible. The spectrum of machinable geometries by grinding or polishing is limited in contrast to diamond machining, but harder materials like ceramics are better machinable by abrasive processes.

#### Diamond machining

The largest spectrum of geometries is machinable by diamond turning and milling. The processes are adaptable to continuous and structured surfaces as well. The machining of structured surfaces can be done by circumferential or ball end milling. For machining structures like prisms or spherical lens arrays, diamond tools with high form and angular accuracy are necessary. Moreover, the tools have to be in an accurate position within the tool holder and in relative position within the coordinate system of the machine tool.

To prevent geometrical deviations when machining micro structures, the diamond tool has to be positioned in the machine tool with respect to its coordinate system. Besides a geometrical error of the cutting edge ( $\Delta\epsilon$ ) a profiled diamond tool exhibits three degrees of freedom inside the tool fixture (Fig. 5): tilt error  $\kappa$  (kappa) in the Y-Z-plane of the tool, tilt errors  $\xi$  (ksi) in the X-Y-plane of the tool, and tilt error  $\psi$  (psi) in the X-Z-plane of the tool. These tilt errors lead to a misalignment of the tool which has to be avoided for the manufacturing of defined microstructures. Whereas the errors a, b and d Fig. 5 will lead to deviations in the including angle of the V-groove, the misalignment Fig. 5c will lead to an angular tilt between the adjacent V-grooves. For tool alignment a tool holder is necessary that offers six degrees of freedom for tool positioning at micrometer scale. The design must be capable to be used at spindle speeds up to several thousands rpm [13]. Customized scratch traces and

reversal tests as well as the machining of witness samples have to be performed for exact positioning of the tool is the tool holder. Fig. 6 shows an example of a manual 2-axis tool holder as preliminary work for a 5-axis piezo-electric driven tool holder that can be dynamically (re)positioned during the machining process. The two axes can be used to compensate for the tools radius and angular deviations of  $\varepsilon$  and  $\zeta$  by alignment of  $\Psi$ .

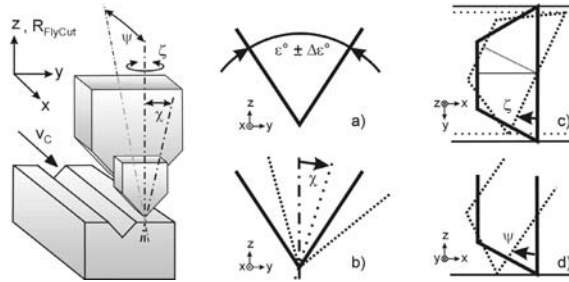


**Fig. 5.** Degrees of freedom for positioning the diamond tool in a circumferential milling process (left) and in ball end milling (right)

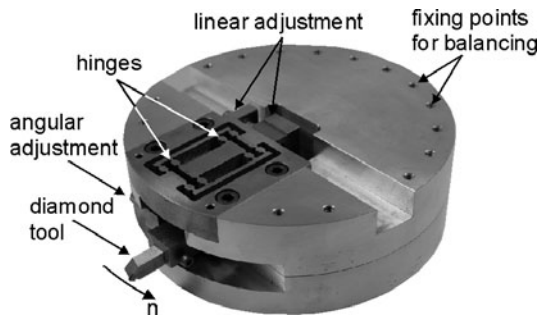
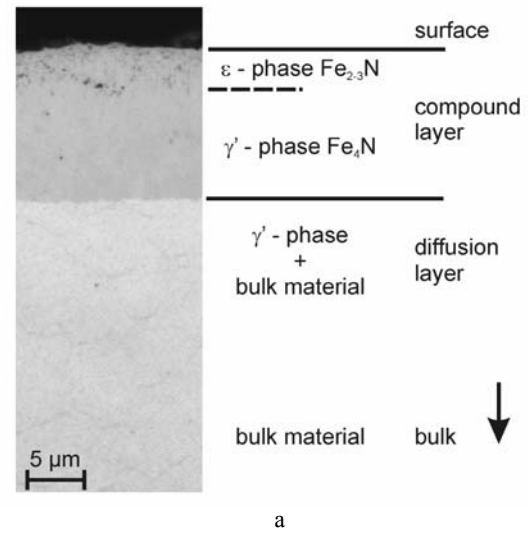
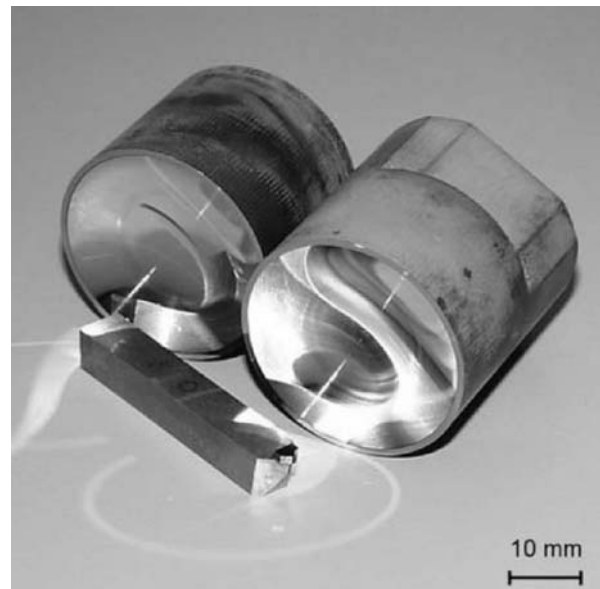


**Fig. 6.** Study on a manual tool holder for 2-axis positioning of V-shaped monocrystalline diamond tools used in circumferential diamond milling (diameter 150 mm) [source: LFM-Bremen]

In the following new possibilities for the diamond machining of steel molds shall be addressed. Due to the catastrophic tool wear when diamond turning steel, the spectrum of machinable materials is so far limited. Thus, the amorphous electroless nickel coating is the only diamond machinable hard material (approx. 550V). This is state of the art for making mold inserts for injection molding, but this material suffers from its low hardness and low temperature stability above approx. 200°C, e.g. for hot pressing of glass. Mold materials with sufficient properties are - up to now - machinable by grinding and polishing only, therefore, structured surfaces or cavities with small radii are almost not machinable. However, two alternative processes seem to beat this limitation. The ultrasonic assisted diamond turning introduced by Moriwaki [9] and revisited by Brinksmeier [10] and the thermo-chemical modification of the mold material by a new nitriding process [11].



a



b

**Fig. 7.** Cross section and dominant phases of steel after thermo-chemical treatment; b diamond turned aspheric high alloyed tool steel molds (1200HV)

The basic idea of the new method is to avoid chemical reactions between the carbon of the diamond tool and the iron of the workpiece by establishing a chemical bond between the iron and another chemical element. A propriety thermo-chemical process for altering the chemical composition of the subsurface zone of the workpiece was developed and succeeded in reducing diamond tool wear by more than two orders of magnitude (cf. Fig. 7a). The surface roughness obtained in single point diamond turning of carbon steel was better than 10nm Ra. Similar results were obtained with sintered high alloyed tool steel with a Vickers hardness of approx. 1200HV. Fig. 7b shows two aspherical hard steel molds diamond turned with one diamond tool.



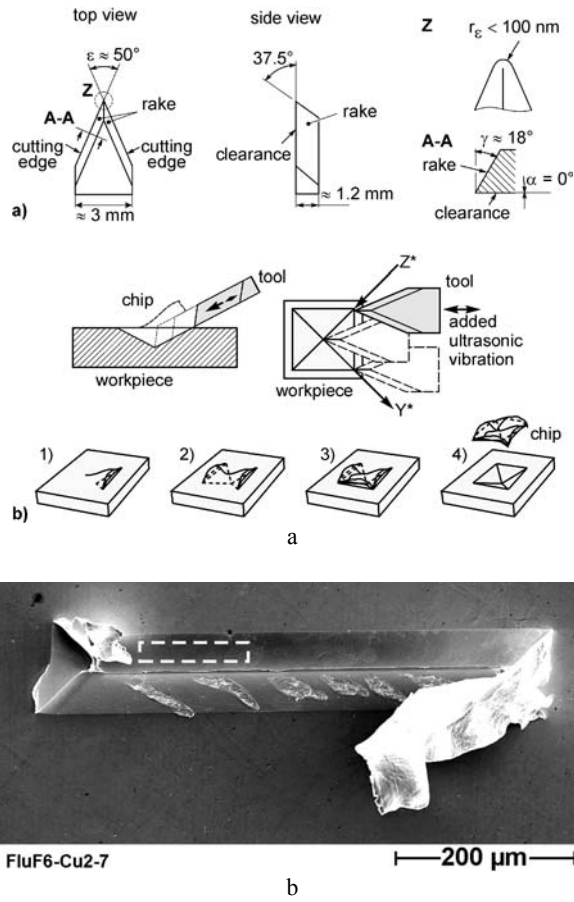


**Fig. 8.** Geometry of the monocrystalline diamond tool and tool motion and cutting process for micro cutting of a four sided pyramidal micro cavity; b SEM image of a four-sided V-groove ( $80 \mu\text{m} \times 500 \mu\text{m}$ ) machined in OFHC-copper by diamond micro chiseling

Another challenge in mold making is the direct diamond machining of micro cavities. The spectrum of machinable structures by diamond turning and milling is inherently limited by the tool geometry and its intrinsic kinematic. Whereas the machining of retro-reflective triple structures is state of the art in diamond cutting the machining of a more efficient retro-reflective cube corner array cannot be machined because of the need to generate a 3-fold pyramidal cavity. A machining technology that offers the ability to machine sharply ended discontinuous structures in a range between  $50$  to  $500 \mu\text{m}$  will be a key technology for new applications. With this technology available new optical functions can be implemented in complex optical components leading to a new degree of freedom in optical design.

For meeting this challenge a novel cutting process, diamond micro chiselling, is being developed. This process enables the generation of discontinuous structures like V-shaped grooves with defined endings and perpendicular bends. The applied tool is similar to a V-shaped diamond tool and the cutting procedure for a 4-sided pyramidal cavity will take at least 4 individual cuts (cf. Fig 8a). Fig. 8b shows a sharply ended V-shaped groove as first result of this

investigation. Roughness of approximately  $S_a = 4 \text{ nm}$  (measured in the indicated area of Fig. 8b) is realizable using this process [14].

### Precision Grinding

Precision grinding technologies have to be developed in order to get optical or near optical surface quality when machining steel or ceramic mold materials. A key technology is the electrolytic in-process-dressing (ELID) and shaping technology for the metallic bonded diamond grinding wheels for maintaining its sharpness and form accuracy even for machining of hard materials in (near) optical quality [15][22]. Another strategy for sharpening and shaping diamond grinding wheels is electrical discharge machining (EDM) that also allows integrating small shaped profiles to the grinding wheel in order to machine structured molds in near optical quality in ceramic materials like tungsten carbide WC or silicon nitride  $\text{Si}_3\text{N}_4$ .

### Polishing

In some cases the surface quality of precision molds with structured elements super imposed onto envelope surfaces like plane, spherical, aspheric as well as free formed surfaces is not sufficient for optical applications. Therefore, deterministic polishing processes to improve surface roughness of structured surfaces are necessary. However, since polishing of aspheres, free-forms and structures is a point polishing process, the challenge of the polishing process is to maintain the form accuracy during the polishing process. Several approaches for point polishing of optical components are known. For fast polishing of free-form surfaces Klocke et al. introduced an adaptive polishing head [16][17].

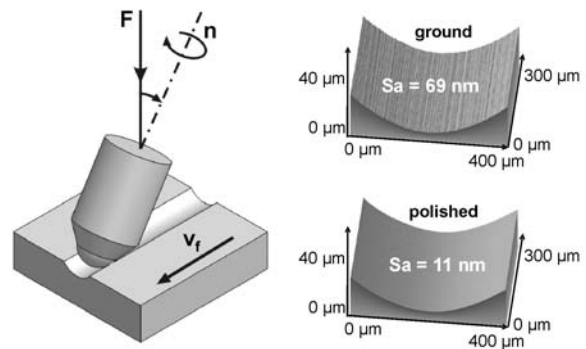


**Fig. 9.** Structure polishing process for polishing a cylindrical groove using a plastic polishing pad and (right) white light interferometric images of a cylindrical groove in tungsten carbide after grinding and additional structure polishing [source LFM-Bremen]

Besides the continuous optics, structured optics with V-shaped or cylindrical grooves with structure size less than  $1 \text{ mm}$  are increasingly required. These kinds of structures cannot be polished using state of the art polishing technology. A new structure polishing technology to meeting these demands has been introduced in [12]. By using conical pin

type tools or conical polishing pads cylindrical and V-shaped grooves with structure size less than 1 mm could be polished after grinding (cf. Fig 9). The goal is, to decrease surface roughness without loss of form accuracy.

The process chain for making steel or ceramic molds is to grind and polish them after premachining as described above. A future target is to substitute one of the used processes - grinding or polishing. However, when substituting the polishing process, the grinding process has to produce nanometer roughness. In the other case polishing has to have a much higher removal rate and to produce a deterministic form accuracy. It was found, that the grinding process can indeed substitute polishing when machining steel molds. The fabrication of polished steel and ceramic molds are almost below one micrometer with aspherical or free-form shapes. Therefore, the necessary step to a deterministic polishing process needs a fundamental knowledge about mechanical and chemical interaction between workpiece and tool during the polishing process. Basic research is underway to in describe and model the surface and contour generation when grinding and polishing [18][19].

Polishing of steel or ceramics is still a process that bases on the experience of the operator of the polishing machine tool. A kind of 'polishing process feeling' is necessary for finding optimal process parameters. Moreover, the demands on the form accuracy of polished steel and ceramic molds are almost below one micrometer with aspherical or free-form shapes. Therefore, the necessary step to a deterministic polishing process needs a fundamental knowledge about mechanical and chemical interaction between workpiece and tool during the polishing process. Basic research is underway to in describe and model the surface and contour generation when grinding and polishing [18][19].

### 3.4 Hard coatings

Hard coatings are essential as interfacing layers for the relief of the molded part from the mold and may considerably increase mold life. They will be used in two different ways: (1) a coating that will be placed on the mold after the mold surface has been completely machined and (2) a coating that is machined itself by the final finishing process. An example for the latter type is diamond machinable electroless nickel commonly used for machining of mold inserts for plastic forming.

Innovative coatings which are diamond machinable and also wear resistant in molding processes are deposited by magnetron sputtering with a thickness of at least 20  $\mu\text{m}$ . The coating properties considered to be necessary include high adhesion, low stress, small grain size, moderate hardness, and sufficient oxidation resistance [20]. Sol-gel-layers can be micro-structured by diamond turning or milling prior to hardening were presented in [21]. The coatings consists of metals of organic sol systems for the deposition of machinable  $\text{Al}_2\text{O}_3$  and  $\text{ZrO}_2$ -coatings which show plastic like properties in a pre-ceramic state. Deposition techniques like dip-coating and spin-coating or the electrophoretic aided sol-gel deposition are applied to steel molds. Finally, a thermal treatment with temperatures up to 700°C is applied in order to achieve maximum hardness for the sol-gel-coatings. The deposited coatings have to be characterised regarding film thickness, density, porosity, (ultra micro) hardness, adhesion and phase composition.

### 3.5 Replication

Replication techniques are particularly suited for large volume production and possess a great potential for improving the quality of molded optical elements.

The machining technology for injection molding has to optimize by analyzing process behavior of different optical plastics materials, machine technology, processing and process control. Besides the analysis of the injection molding process, it is important to investigate the influence of the injection compression and injection embossing technology .

For glass molding of (structured) optical components hot pressing of glass is the technology that could be used for replicating high precision parts. The goal is to extend the potential of this technology. A new approach is the implementation of a concept with separates the heating of mold and glass material [24]. The aim is to avoid sticking of glass to the mold and to achieve shorter process times by improving the heating and cooling management.

### 3.6 Measuring techniques and quality chain management

For describing the geometrical condition of the mold insert as well as the replicated part micro- and macro-geometrical properties have to be determined.

An important issue is the integration of measuring equipment into the machining process, since there is a great demand of in-process and in-situ measuring techniques regarding the optimisation of process chains.

A new approach to characterise the functional properties of lenses, mirrors, replication tools and molds at micro scale combines two laser optical measuring principles to measure local and integral features of continuous and structured surfaces. The method of double scattering by speckle pattern illumination characterises the integral measure surface roughness in the range of  $R_a < 100 \text{ nm}$ . A modified measuring arrangement based on the principle of angle resolved scattering (ARS) analyses local defects (e.g. scratches, cracks, chips) and structure deviations. Scattered light techniques are generally parametric and fast and therefore show in-process capabilities for micro-form and micro-structure measurement [25].

For measuring the form deviation of a mold with optical aspheric or free-form surface in production machines using interferometry the vertical measurement range of the interferometer has to be extended. Another more flexible way is the use of multiple wavelength interferometry [26]. In the end, such a system could be used for the online quality control of production processes of injection molding or pressing forms with continuous surfaces.

As an innovative non destructive near surface zone analysis photo thermal techniques are applied yielding information about hardness(-profiles), layer thickness, adhesion defects, flaws like cracks and pores, and residual stress of tools and replicated objects in near surface zones from a depth of few micrometer down to 1mm below the surface [27].

Especially for determining the properties of the hard coatings presented above an extensive study of the near surface mechanical nature of these coatings has to be performed as high resolution surface and subsurface analysis

by using nano indentation and nano scratching technique [28]. Measured information about the mechanical state of the surface layer concerning its processing conditions can be used to create the surfaces and their resulting mechanical state. E.g. elastic modulus E and hardness H, of the molds, coatings and final glass/polymer optical components can be determined for characterizing its mechanical properties.

#### 4 Merging Technologies

The manufacture of optics in high volume requires process chains including optical design, mold making and replication as well as measuring techniques. Any applied technology within a process chain has its advantages and limits. And for making a powerful process chain, it is necessary to take all advantages and limits of each process step into account. Moreover, it is important to transfer the applied processes to deterministic processes, so, the result of a process step should be known in advance. This information can be used as data for a knowledge base for planning process chains with less time consumptive and, therefore, expensive iteration steps. Precise physical or empirical models as well as simulation tools have to be taken into account to reach this goal. Additionally, qualified metrology including surface and subsurface inspection as well as figure evaluation plays a vital role.

Nevertheless, a holistic view of the complete process chain is required. Quality chain management is of overall importance since it guarantees an effective interaction between the individual process steps. Therefore, closed process chains comprising all aspects of production will open the possibility to produce high precision complex optical elements as mass-product articles for many optical applications.

Deterministic process chains have their foundation in merging technologies by separate process steps which means, that anybody in a process chain will act with the knowledge, what anybody else in the chain needs for his step and vice versa. An example is a NURBS based common description of the geometry from the optics design, the simulated shape, the shape to be machined for fabricating the mold insert, the measured shape of the insert to the shape of the replicated part. Converting errors or miscommunication can be avoided using a common data description.

The quality chain management has to organize the connections and the process steps - or in other words - it has to spread the filtered common knowledge to all individual processes. So, any process step of the chain will get sufficient data, in order to eliminate process time for unneeded specifications of the finished part.

The connections are represented by requirements to following or preceding process steps as shown in Fig. 10. The requirements could be the designed form and roughness, maximum size or weigh of a part, predicted (simulated or measured) shrinkage or anything else what is necessary to guarantee an unobstructed and fast procedure of the process chain. Moreover, the information could also show organizing or logistic character like a date of delivery. This schematic view of a process chain is easy to convert to a web-based computer application. So, it can be used for planning, for

performing and for evaluating process chains in the large group of the process chain participants, especially, if not all process steps are carried out at the same location [29].

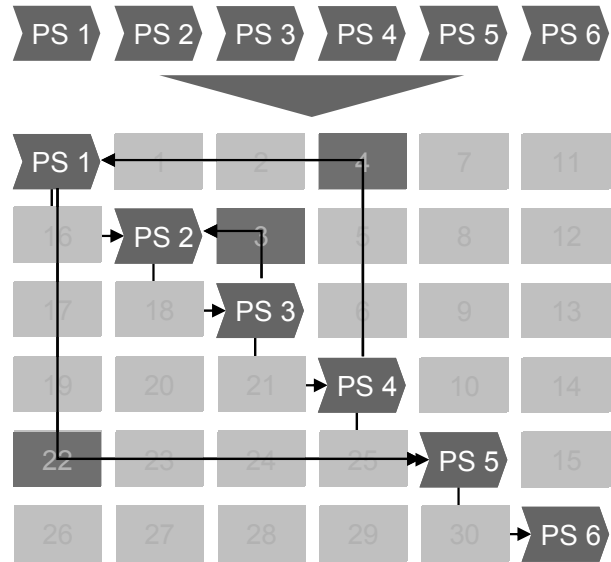


Fig. 10. Each process step (PS) in a process chain (PS1...PS6) has requirements to following or precede process steps [source: IPT-Aachen]

#### 5 Conclusion

The mass production of high precision molds with aspheric, structured or free-form shape is still a great challenge, whereas, the number of optics, its complexity and its quality needed increases year by year. Innovative fast, precise and deterministic machining and measuring technologies are required to meet this challenge and the integration of measuring techniques is required. Moreover, a holistic view over the entire process chain is necessary to transfer a conventional optics fabrication into a powerful and effective process chain.

## Acknowledgements

The research work associated with merging technologies is funded by the German Research Foundation (DFG) within the Transregional Collaborative Research Center SFB/TR4 "Process Chains for the Replication of Complex Optical Elements".

## References

- [1] Bergh AA, (2006) Commercial Applications of Optoelectronics. *Photonics Spectra*, 2:54-61
- [2] Fischer AL, (2006) Multifaceted Innovation Drives - Machine Vision Industry. *Photonics Spectra* 4:36
- [3] Yamamoto H, (2004) Manufacturing Process Innovation in the Precision Industry. *Proceedings of the 11th IMEC Conference* :223-230
- [4] Evans CJ, Paul E, Mangamelli A, McGlaufflin ML, (1996) Chemical aspects of tool wear in single point diamond turning. *Precision Engineering* 18/1:4-19
- [5] Brinksmeier E, Autschbach L, Weck M, Winterschladen M, (2004) Closed Loop Manufacturing of Optical Molds using an Integrated Simulation Interface. *Proceedings of the euspen International Conference- Glasgow, Scotland (UK)* :215-217
- [6] Schmitt R, Dörner D, Michaeli W, Forster J, (2005) Interferometrische Formprüfung in der Spritzgießmaschine. *QZ* 50/9:72-74
- [7] Michaeli W, Koch M, Rettmeier G, Forster J, (2004) Spritzgießsonderverfahren II. *IKV-Kolloquium Aachen Germany*: 1-20
- [8] Taylan A, Lilly B, Yen YC, (2001) Manufacturing of Dies and Molds. *Annals of the CIRP* 50/2:405-424
- [9] Moriwaki T, Shamoto E, (1999) Ultraprecision Diamond Cutting of Hardened Steel by Applying Elliptical Vibration Cutting. *Annals of the CIRP* 48/1:441-444
- [10] Brinksmeier E, Gläbe R, (2001) Advances in Precision Machining of Steel. *Annals of the CIRP*, 50/1:385-388
- [11] Brinksmeier E, Dong J, Gläbe R, (2004) Diamond Turning of Steel Molds for Optical Applications. *Proceedings of the 4th International Conference of the euspen, Glasgow (UK)*:155-156
- [12] Gessenharter A, Autschbach L, Grimme D, Riemer O, Brinksmeier E, (2005) Ultraprecision Machining and Polishing of Structured Molds. *Annals of the WGP, Production Engineering XI/1*:11-14
- [13] Brinksmeier E, Riemer O, Gläbe R, Autschbach L, (2005) Micro-Structured Precision Moulds. *Lamdamap 7th International Conference - Cranfield UK*: 354-361
- [14] Flucke C, Gläbe R, Brinksmeier E, (2006) Diamond Micro Chiseling of Micro Structured Moulds. *International euspen Conference in Baden*: tpb
- [15] Brinksmeier E, Preuß W, Rickens K, Grimme D, (2005) Dynamic Behavior of ELID-processes. *Proc. of euspen International Conference, Montpellier France*:569-572
- [16] Weck M, Wenzel C, (2004) Adaptable 5-axes polishing machine- head. *Annals of the WGP*:95-98
- [17] De Chiffre L, Kunzmann H, Peggs GN, Lucca DA, (2003) Surfaces in Precision Engineering, Microengineering and Nanotechnology. *Annals of the CIRP* 52/2: 561-577
- [18] Evans CJ, Paul E, Dornfeld D, Lucca DA, Byrne G, Tricard M, Klocke F, Dambon O, Mullany BA, (2003) Material Removal Mechanisms in Lapping and Polishing. *Annals of the CIRP* 52/2:611-633
- [19] Dambon O, (2006) Das Polieren von Stahl für den Werkzeug- und Formenbau. *PhD Thesis, RWTH-Aachen, Shaker*
- [20] Gießelbach M, Stock HR, Zoch HW, (2005) Neue Titan-Nickel-Nitrid-Schichten zur Abformung optischer Bauteile. *Werkstoffe und werkstofftechnische Anwendungen: Neue Materialien und Verfahren in der Beschichtungstechnik, TU Chemnitz* 22:286
- [21] Datchary W, Mehner A, Zoch HW, Lucca DA, Klopffstein MJ, Ghisleni R, Grimme D, Brinksmeier E, (2005) High Precision Diamond Machining of Hybrid Sol-Gel Coatings. *Journal of Sol-Gel Science and Technology*, 35:245-251
- [22] Webster J, Tricar M, (2004) Innovations in Abrasive Products for Precision Grinding. *Annals of the CIRP* 53/2:597-601
- [23] Kordonski WI, Shorey AB, Tricard T, (2006) Magnetorheological Jet (MR Jet) Finishing Technology. *Transactions of the ASME - Journal of Fluids Engineering* 128:20-26
- [24] Klocke F, Pongs G, (2004) Precision Glass Molding of Optical Components. *Annals of the WGP* :21-25
- [25] Goch G, Prekel H, Patzelt S, Faravashi M, (2005) Precise Alignment of Workpieces Using Speckle Patterns as Optical Fingerprint. *Annals of the CIRP* 54/1:523-526
- [26] Weck M, Pfeifer T, Brecher C, Schmitt R, Dörner D, Winterschladen M, (2005) Approach to a Machine-Integrated Measurement and Simulation Tool for the Manufacturing of ultra precise Surfaces. *Annals of the WGP* 12/1:133-136
- [27] Prekel H, Liu H, Wang L, Goch G, (2003) Zerstörungsfreie Randzonenanalyse von Freiformflächen und strukturierten Oberflächen. in Goch G, Heeg FJ, Hirsch BE, Müller DH, Scholz-Reiter B: *Technik-, Organisations- und Kompetenzgestaltung aus interdisziplinärer Sicht. Bremer Schriften zu Betriebstechnik und Arbeitswissenschaft* 44:213-215.
- [28] Datchary W, Mehner A, Zoch HW, Lucca DA, Klopffstein MJ, Ghisleni R, Grimme D, Brinksmeier E, (2005) High Precision Diamond Machining of Hybrid Sol-Gel Coatings. *Journal of Sol-Gel Science and Technology* 35:245-251
- [29] Schmitt R, Vinke J, (2005) Standortübergreifend verkettete, Produktionsprozessketten mit Workflow-Werkzeug steuern. *QZ*, 50/8:43-45

---

## Fast Tool Servos: Advances in Precision, Acceleration, and Bandwidth

Trumper, David L.<sup>1</sup>, Lu, Xiaodong<sup>2</sup>

<sup>1</sup>Massachusetts Institute of Technology, <sup>2</sup>University of British Columbia, <sup>3</sup>

Keywords: Fast tool servo, diamond turning, precision, mechatronics, electromagnetic actuator

### Abstract

Fast tool servos can be used in conjunction with diamond turning machines to produce precision contoured surfaces. This paper presents an overview of fast tool servo (FTS) technology and applications. A literature review groups the FTS devices by operating principle and performance. A new class of FTS is described in detail which uses a flux-steering actuator to achieve unprecedented performance levels. This Ultra-Fast Tool Servo (UFTS) has 30  $\mu\text{m}$  stroke, 23 kHz closed-loop bandwidth, acceleration of 5000  $\text{m}/\text{sec}^2$ , and positioning noise of 2.1 nm RMS while cutting.

### 1 Introduction

This paper focuses on recent developments in fast tool servo technology which is used in conjunction with diamond turning to produce contoured surfaces on parts. A fast tool servo (FTS) is capable of rapidly and accurately positioning the cutting tool in a lathe manufacturing operation such that the cut surface can include features which are not symmetric with respect to part rotation. Typically, the cutting tool is a single crystal diamond such that optical quality surfaces can be produced. However, in cases where optical finish is not required, then conventional cutting tools such as cubic boron nitride, tungsten carbide, or steel can be used in conjunction with a fast tool servo. Examples of manufactured parts which might include such contoured surfaces include: eyeglass lenses and molds, molds for contact lenses, oval pistons for automotive engines, films for brightness enhancement and controlled reflectivity, sinewave ring mirrors used in CO<sub>2</sub>-laser resonators, fusion experiment targets, two-dimensional planar encoders, as well as in micro-optical devices such as Fresnel lenses, multi-focal lenses and micro-lens arrays. In-depth perspective and reviews of the applications and production of such surfaces are given in [5] and [10].

A schematic representation of the shape of parts which might be cut with a lathe and fast tool servo is shown in Figure 1. This part shows the surface of a 0 $\times$ 4 diopter toric surface for an eyeglass lens of about 60 mm diameter. To cut this part, the tool must move in synchronization with the part rotation through a stroke of about 4mm in the  $z$  direction (height).

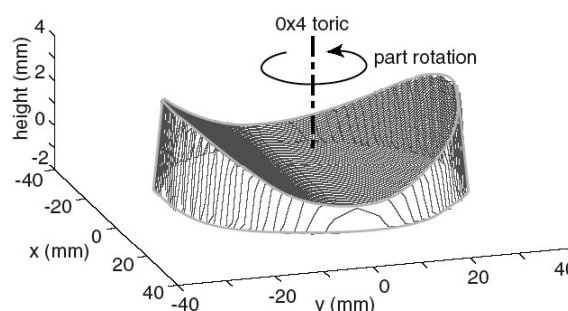


Figure 1: Surface of a part which might be cut with a fast tool servo.

In order to accurately cut such parts, the tool must move with high precision despite the high acceleration and high frequencies associated with the surface trajectory. In the lens surface shown above, the tool oscillation frequency will have a fundamental of twice the spindle rotation frequency, and harmonic content out to a significant multiple of the spindle rotation frequency. For example, if the spindle rotates at 3000 rpm (50 Hz), the first fundamental of the part shape will be at 100 Hz, and there will be significant harmonics in the trajectory to 1 kHz. Meanwhile, in order to obtain optical quality surfaces, the tool trajectory must be accurate to the order of 10 nanometers.

This simultaneous requirement for precision and high dynamic performance makes the fast tool servo area quite demanding. This need for precision and fast dynamics places fast tool servos at the intersection of precision engineering and mechatronics. Similar multiple-domain demands exist in other systems such as semiconductor lithography machines, hard disk and optical drives, and galvo drives for mirror scanners. Thus fast tool servo technology can adapt techniques from these fields as well as serve as a source of ideas for cross-fertilization.

The need for high bandwidth is clear on the basis of part throughput. In order to achieve sufficient productivity, the part spindle needs to be rotated rapidly, on the order of 1000-10,000 rpm. The bandwidth requirement for a fast tool servo is then set by the number of spatial harmonics required per revolution. The acceleration requirement for a fast tool servo is set by the amplitude and frequency of these harmonics. Both of these are demanding limitations. For example, in the eyeglass example, controllable motion is required out to 500-1000 Hz. This allows on the order of 5

to 10 spatial harmonics in a cut with a spindle speed on the order of 1000-3000 rpm. A stroke of 20-30 mm is required to cut typical eyeglass part shapes. Suppose that a harmonic of the trajectory is specified as  $z(t) = A \sin \omega t$ . Then the acceleration associated with this trajectory is  $a(t) \equiv \ddot{z}(t) = A\omega^2 \sin \omega t$ . For the eyeglass example, let  $A = 0.01m$ , and  $\omega = 2\pi 25$  (1500 rpm). Then the maximum acceleration on such a cut is  $a_m = A\omega^2$ ; in this case  $a_m = 2.47 \times 10^2 \text{ m/sec}^2$ . This is 25 times the acceleration of gravity (25 Gs). This is quite challenging for a long-stroke device.

The short-stroke application is even more demanding in terms of bandwidth and acceleration. For example, suppose we need to cut 720 cycles of a sine wave with an amplitude of  $A = 1 \mu\text{m}$  on the surface of a part which is rotating at 1500 rpm. The fundamental frequency of the cut is then  $\omega = 720 \cdot 2\pi 25 = 1.13 \times 10^5 \text{ rad/sec}$  (18 kHz). This is a very high frequency of operation for an electromechanical device. Even worse in some sense is the required acceleration. Here  $a_m = A\omega^2 = 1.28 \times 10^4 \text{ m/sec}^2$  (1300 Gs).

In summary, fast tool servo design provides a very challenging environment for precision engineering and mechatronic design.

## 2 Prior Art Fast Tool Servos

A significant amount of research effort has been devoted to FTS design over the years. There are many FTSs reported in the literature using a variety of actuating mechanisms and configurations, depending on the application needs. The articles cited above [5] and [10] and the theses [20] [32] [24] have significant literature reviews. Some key prior art is summarized below.

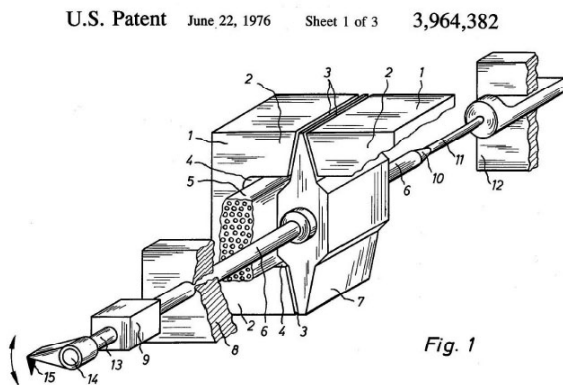


**Figure 2:** Electromagnetically-driven engraver head from U.S. Patent 3,964,382.

The earliest prior art relevant to fast tool servos appears to be from the field of electric engravers, which are used to produce the precise patterns of fine pits which define the inking pattern of rotogravure plates used in printing. A survey of this technical area is given in [32]. As an example, the image shown in Figure 2 is taken from the patent [2].

Here the diamond cutting tool 15 is attached to an arm which is mounted on the near end of the slender shaft 13. The shaft is contoured (feature 11) so as to establish a given resonant frequency. The actuator consists of fixed core 1 and coils 5 which direct magnetic fields so as to apply a torque to the wedge-shaped rotor 7, and thereby drive the resonance of the engraving tool/arm on the shaft. A required source of biasing magnetic field is not shown in this figure.

A key distinction of the devices used for electric engraving is that these are operated at a frequency coinciding with a mechanical resonance. This is possible because the pits on a rotogravure plate have constant spacing; the amplitude of the resonant motion is controlled with an actuator on the engraving head in order to set the pit depth which controls printed ink quantity. Typical resonance frequencies for electric engraving heads are in the range of 3-10 kHz. In comparison, fast tool servos are required to follow arbitrary trajectories with a wide range of frequencies, and thus cannot take advantage of resonant operation. This requirement places quite stringent demands upon mechanical structure, actuators, sensors, and controllers for FTSs which makes them distinct from the electric engraver application.

The actuation principles for FTSs can be divided into the following main categories: hydraulic, piezoelectric, magnetostrictive, Lorentz force (including linear and rotary), shear-stress electromagnetic, and normal-stress electromagnetic. These devices can also be categorized according to their operating range, or stroke. We define short-stroke as less than 100  $\mu\text{m}$ , intermediate as between 100  $\mu\text{m}$  and 1mm, and long-stroke as above 1 mm.

### 2.1 Hydraulic FTS

Hydraulic devices are less common in the literature, but some good work has been done in this area. Hydraulic long-stroke FTSs have been studied for non-round piston turning in for example [41] along with repetitive control algorithms for following error reduction [21] [17]. A short-stroke hydraulic FTS with 180  $\mu\text{m}$  stroke and 10 Hz bandwidth is presented in [40].

### 2.2 Piezoelectric FTS

Most short-stroke FTSs and similar micro-positioning devices are based on piezoelectric stacks [37], which have the advantage of quick response, high acceleration, accurate micro positioning, and high stiffness (usually greater than 50 N/ $\mu\text{m}$  in the typical sizes used).

Piezoelectric ceramic materials can produce up to 0.1% normal strain, readily achieve bandwidth on the order of several kHz, and are capable of nanometer resolution positioning. Further, piezo actuators are open-loop stable, and thus in principle easy to control.

However, piezoelectrically actuated FTSs also have disadvantages. First, with an attached payload mass, the resonant frequency of the system is reduced over that of the actuator alone. This problem is particularly acute when motion-amplifying mechanisms are used to increase travel,

since such mechanisms reflect the actuator stiffness as the amplification ratio squared, and thus the resonant frequency falls linearly with the amplification ratio. Since the resonant modes of a piezo-driven system tend to be lightly damped, this imposes significant limits on the achievable closed-loop bandwidth of such devices. Another problem is that the internal structural resonance modes of the piezo stack limit the working frequency range, because operation near internal resonances can cause local tensile failure of the PZT ceramics. It is also somewhat difficult to design coupling structures which guide the FTS in the desired direction of actuation and provide sufficient lateral stiffness, but do not impose unacceptable side loads or moments on the piezo actuator.

A further limit to dynamic performance are mechanical and electrical energy losses in the material when undergoing deformation. Such hysteresis not only degrades the tracking performance, but also imposes a thermal limit due to the energy loss which is converted into heat. The allowable stroke for a piezo actuator therefore reduces significantly at high frequencies. In some cases liquid cooling must be used to achieve acceptable performance. Finally, the high-voltage/high-current amplifiers required to drive a piezo actuator at high frequencies and large stroke are bulky and expensive as compared to conventional motor drive amplifiers which can be used with the electromagnetic devices.

Nonetheless, piezoelectric actuated FTSs have seen significant research contributions. In this class of actuators, we can cite the following contributions from the literature: Kouno published the design for a piezoelectric fast tool servo of 6.5  $\mu\text{m}$  stroke, 10 nm resolution, 70 Hz bandwidth and 300 N/ $\mu\text{m}$  stiffness [22]. The piezoelectric stack consists of 18 rings, each of which is 25 mm OD, 15 mm ID, and 1 mm thick.

Patterson and Magrab designed a fast tool servo for diamond turning with 2.5  $\mu\text{m}$  stroke, 660 Hz bandwidth (-3dB), and 1.3 nm dynamic repeatability at Lawrence Livermore National Laboratory [35]. A PZT stack of 6 mm diameter and 12.5 mm length provided stiffness sufficient to place the resonance above 1 kHz when supporting the maximum FTS body weight of 450 gm. The moving portion of the FTS consisted of a cylindrical shell supported by two diaphragm flexures fixed to a cylindrical support.

Faulter and Dow developed an FTS of 20  $\mu\text{m}$  stroke and 2 kHz open-loop bandwidth using a hollow piezoelectric actuator (25 mm OD and 18 mm long) [12, 8, 13]. The resonance frequency was approximately 10 kHz. However, at 1 kHz this FTS has a maximum stroke of 5  $\mu\text{m}$  and could not work continuously because of internal heat generated by losses inside the piezoelectric actuators. Based on similar concepts, Jared developed a piezoelectric FTS of 11.4  $\mu\text{m}$  stroke and 200 Hz bandwidth for inertial confinement fusion targets [19].

Okazaki developed a fast tool servo with 5  $\mu\text{m}$  stroke, 470 Hz bandwidth, and 5 nm resolution [33]. Later, Okazaki developed an improved fast tool servo with 15  $\mu\text{m}$  stroke, 2.5 kHz bandwidth, 2 N maximum cutting force, and 2 nm resolution [34]. A stacked ring piezoelectric actuator of 25 mm OD, 14 mm ID and 19 mm length was fixed inside a stainless steel cylinder, with a size of 53 mm in diameter and 112 mm length. The primary resonance frequency was at 10

kHz. However, at 1 kHz continuous operation the effective stroke is only several micrometers.

Hara designed an FTS of 3.7  $\mu\text{m}$  stroke and 2 kHz flat frequency response in open loop [18]. Rasmussen and Tsao described a system for asymmetric turning, by using a piezoelectric actuator to drive a tool through a lever assembly [36]. The FTS had 50  $\mu\text{m}$  stroke and 200 Hz bandwidth.

Falter and Youden designed a device that is commercially available on a machine for contact lens generation. This fast tool servo has 400  $\mu\text{m}$  stroke at DC and 600 Hz bandwidth. It uses a T lever to achieve 14:1 mechanical motion amplification [11]. A pair of PZT stacks against the horizontal part of the T lever provides push and pull motion.

Cuttino developed an FTS of 100  $\mu\text{m}$  stroke and 100 Hz bandwidth [6]. In order to obtain the 100  $\mu\text{m}$  stroke against the preloaded rod, the PZT stack was 13 cm long and had an open-loop stiffness of around 70 N/ $\mu\text{m}$ . As a result, the natural frequency of the piezoelectric system was 250 Hz.

Altintas presented a piezo tool actuator of 370 N/ $\mu\text{m}$  stiffness, 36  $\mu\text{m}$  stroke, 50 Hz bandwidth for holding or 300 Hz bandwidth for dynamic contour machining, and 10 nm positioning during finish hard turning [1].

In summary, although piezoelectric actuators have significant applicability in practice, they appear to be limited to about 1 kHz operating frequency and become more difficult to apply as the bandwidth and acceleration requirements are increased.

### 2.3 Magnetostrictive FTS

As a dual to piezoelectric materials that respond with strain to an applied electric field, magnetostrictive materials strain under an applied magnetic field. This actuation principle provides another option for FTS devices.

There are some research efforts on such devices in the literature. Eda developed a giant magnetostriction actuator with a stroke of 2  $\mu\text{m}$  [9], but no frequency response of this device was reported. Liu *et al* developed a magnetostrictively-actuated tool holder of 50  $\mu\text{m}$  stroke to investigate vibration abatement in turning processes [23]. The actuator had a resonance frequency at 1.5 kHz, but no closed loop bandwidth specification was reported for this device.

A common magnetostrictive material is called Terfenol, but it also has hysteresis and heating problems [23]. It is claimed that magnetostrictive materials have higher maximum strain and are less temperature dependent, in comparison to piezoelectric materials. However, their performance as reported in the literature appears to fall significantly behind that achieved by piezoelectric devices, and we do not view these as competitive with piezoelectric devices or the short-stroke electromagnetic devices discussed below.

### 2.4 Lorentz Force FTS

Another broad class of actuators employ the Lorentz force  $\mathbf{J} \times \mathbf{B}$ . Herein we use this term broadly to include permanent magnet rotary and linear motors, even in the cases where the

motor coils are housed in slots which mean that the force on the motor is not primarily due to the Lorentz force. However, since slots can be approximately modeled as bringing the slot currents to the surface of a smooth air-gap machine, this inclusion is reasonable. Said another way, this class then includes true Lorentz machines such as voice coil actuators, as well as slotted iron-core machines such as most DC brushless linear and rotary motors.

An advantage of this type of actuator is that it can have much longer stroke than those of the piezoelectric FTSs. However, the maximum steady-state acceleration is limited by the heat generated in the coil, the method by which the coil is cooled, and by the achievable magnetic flux density. Basic electromagnetic and thermal calculations indicate [20], and the literature confirms, that the steady-state acceleration of these devices is limited to about 100 Gs.

Within the class of Lorentz actuated fast tool servos, Douglass used a voice-coil-motor driven slide for a fast tool servo [7], which had a stroke of 500  $\mu\text{m}$  and 100 Hz bandwidth. Wang described a voice-coil-based actuator to achieve 0.4 mm stroke and 0.1  $\mu\text{m}$  resolution [42].

Weck *et al* developed a hybrid long stroke fast tool servo, which integrated a piezoelectric system and a linear motor [43]. The piezoelectric system has a stroke of 40  $\mu\text{m}$  at 1 kHz bandwidth, and the linear motor has a stroke of 2 mm at 40 Hz. The piezoelectric translator had a maximum force of 2400 N, a stiffness of 50 N/ $\mu\text{m}$  and a resonance frequency with the loaded mass close to 2 kHz. The peak thrust force was 900 N with a time constant of 5 ms. The power loss of the linear motor and the piezoelectric translator was dissipated by a water-cooling system. Temperature stabilization was guaranteed by Peltier elements, which control the heat dissipation to the cooling media. A compensation of these forces to reduce excitation of the supporting machine was achieved by the use of a balance mass.

Greene and Shinstock developed a linear voice coil based fast tool servo [14]. This FTS had a 100 Hz bandwidth and 6 mm stroke. Because of the low mass of the actuator-tool assembly and the low bandwidth, the dynamic stiffness at 15 Hz was so low that it was considered not feasible for FTS application due to chatter instability.

Todd and Cuttino built a long-range traction-type FTS for diamond turning applications [39]. The tool shuttle was driven by a rotary motor through a steel ribbon. The achieved performance was 1 mm stroke at 20 Hz.

Ludwick and Trumper used a commercial brushless motor to develop a rotary fast tool servo with a bandwidth of 200 Hz, 50 G peak acceleration, micrometer resolution, and a stroke of 3 cm [20] [29]. This machine was designed for the production of plastic spectacle lenses, with shapes such as shown in Figure 1. Because of the fast tool servo's balanced rotary design, reaction forces are essentially cancelled, and only reaction torques are transmitted to the supporting machine base. A picture of this machine is given in Figure 3.

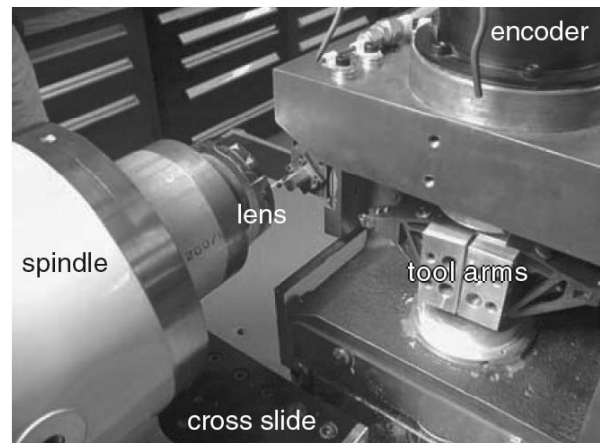


**Fig. 3.** Picture of rotary fast tool servo based diamond turning machine for production of eyeglass lenses.

An advantage of this design is that the rotary axis can carry two or more tools which can be rotated into position, for example, for roughing and finishing operations that use two different types of tools. The axis in the photo uses two tool arms which respectively carry a polycrystalline diamond tool for roughing and a single-crystal diamond tool for finishing. A cross-section of the machine is shown in Figure 4.

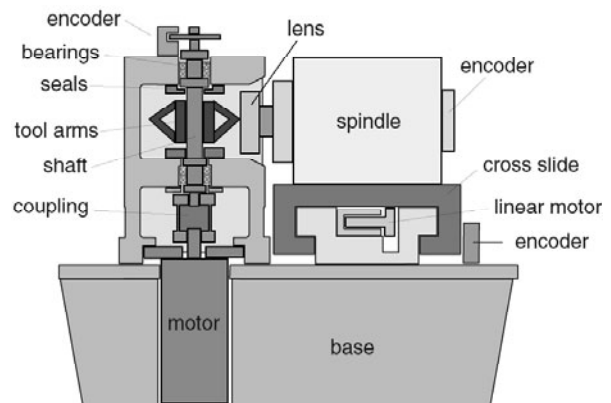


**Fig. 4.** Cross-section of rotary fast tool servo based diamond turning machine for production of eyeglass lenses.

Adapting the rotary fast tool servo concept to the short-stroke domain, Montesanti designed a rotary FTS using a commercial moving magnet motor (galvanometer) to achieve 50  $\mu\text{m}$  stroke, 20 Gs tool acceleration, and 2 kHz bandwidth [30]. Here the rotary axis is supported on flexures rather than the rolling element bearings used in the long-stroke eyeglass fast tool servo [29]. This device is the first of two which Montesanti designed for use in the fabrication of contoured surfaces for laser fusion targets; the second device is discussed in the following section.



## 2.5 Normal-Stress Electromagnetically-Driven FTS

As opposed to shear stress actuation in moving-coil or moving-magnet motors, normal-stress solenoid-type actuators can also be used for FTSs, because normal-stress motors potentially have higher force density and thus possibly higher acceleration than shear-stress motors. Very few people have looked at variable reluctance actuation for FTSs, probably because of the difficulty of controlling these devices in the presence of inherent nonlinearities.

Stancil, Gutierrez and Ro developed a normal-stress fast tool servo with a stroke of  $800\ \mu\text{m}$  [38]. The achieved bandwidth was 100 Hz, and the tracking performance at 30 Hz was problematic [15]. Later a sliding mode control algorithm was applied, and the tracking performance of FTS at its resonance frequency 200 Hz was improved [16].

As a first design effort towards a short-stroke high-bandwidth FTS, we studied an electromagnetically actuated FTS with  $50\ \mu\text{m}$  stroke, 160 G acceleration to frequencies of 3 kHz, 10 kHz bandwidth, and 1.4 nm resolution [25, 27]. In this variable reluctance FTS, opposing solenoids provide push and pull forces to a steel armature which is attached to a carbon fiber tube which serves as the structural backbone of the moving system. The diamond tool is installed at the other end of the carbon fiber tube. The whole moving system is suspended by a front flexure and a rear flexure. These flexures constrain five degrees of freedom of the moving system while allowing only motion in the axial direction of the carbon tube. The motion of the armature is measured by the capacitance probe which passes through the center of the rear solenoid.

However, the solenoid-type actuators used in this device are highly nonlinear, because the actuating force is proportional to current squared and inversely proportional to air gap squared. This nonlinear behavior will introduce significant errors in high frequency operation. Flux biasing can be used to eliminate this nonlinearity [31, 26].

Following ideas for a rotary axis flux-biased short-stroke FTS, Montesanti designed a hybrid rotary/linear fast tool servo with a stroke of  $70\ \mu\text{m}$  and 10 kHz closed-loop bandwidth [31, 32]. This fast tool servo achieves 400 G acceleration at 5 kHz and 870 G acceleration at a mechanical resonance frequency of 10 kHz. A picture of this device on the diamond turning machine is shown in Figure 5.

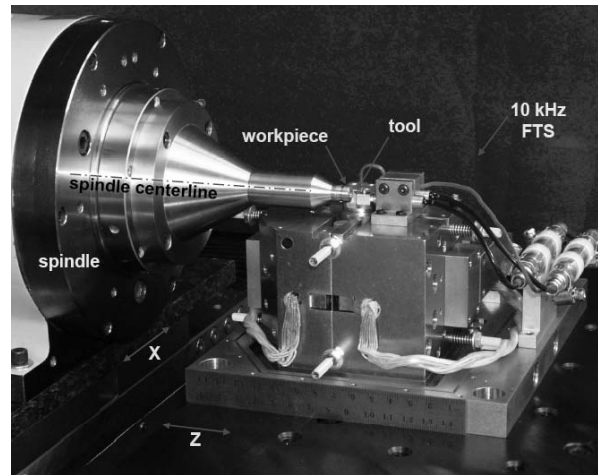


**Fig. 5.** Montesanti's 10 kHz fast tool servo [32] mounted on the diamond turning machine. A 15 cm ruler is included in the figure to provide a scale.

Section 3 of this paper gives details of our new fast tool servo which uses a flux-steering actuator to achieve  $30\ \mu\text{m}$  stroke and 23 kHz closed-loop bandwidth [26, 28], and with experimentally-demonstrated acceleration of 500 G, as well as positioning noise of 2.1 nm RMS while cutting. A picture of this FTS is shown in Figure 6.

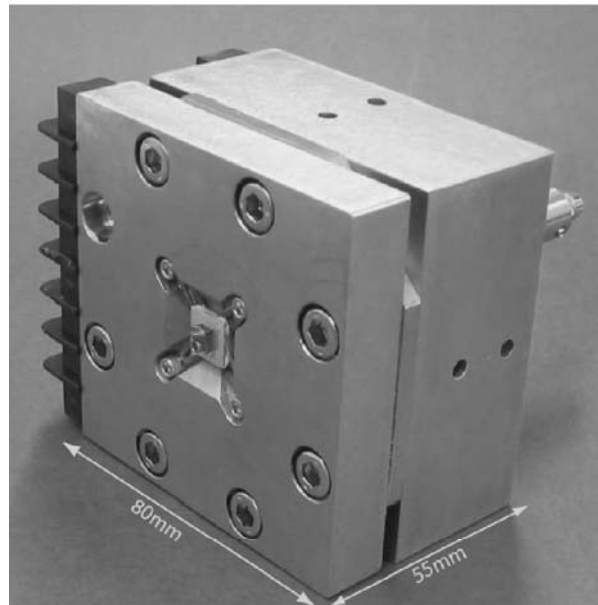


**Fig. 6.** Front view of 10 kHz fast tool servo [26, 28]. The diamond tool and front flexures are visible at the center of the near face of the device. The back end of the capacitance probe can be seen at the right side of the figure.

## 2.6 Performance Comparison

It is instructive to study the relative performance of a representative set of FTSs. Key performance metrics for a

fast tool servo are its low-frequency stroke, small-signal bandwidth, maximum acceleration, and positioning noise level. Unfortunately, most of the literature references don't report acceleration limits or the achievable travel as a function of frequency, but only report travel and small-signal bandwidth. Using this reported data, we have constructed a plot of low-frequency (DC) stroke versus small signal bandwidth as shown in Figure 7.

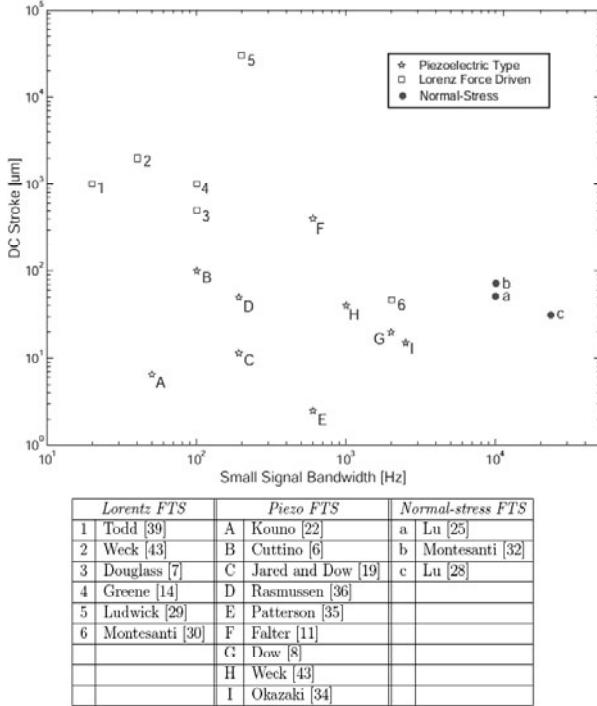


Fig. 7. Performance comparison of representative fast tool servos. Numbers refer to references listed in the table.

In this figure we have also grouped the devices according to their operating principles. Lorenz actuated FTSs are shown as squares, piezoelectric devices are shown as stars, and the new class of normal-stress devices are shown as dots. The numbers and letters next to these symbols key them to the references shown in the table below.

In the plot of Figure 7, a possible metric of quality is the product of stroke times bandwidth. Contours of this metric are then hyperbolas in the plot axes. The further out on these level sets a device is the better its performance in this sense. It can be observed that Lorenz FTSs generally have larger strokes but lower bandwidth than piezoelectric FTSs. Of the Lorenz devices, number 5, which is Ludwick's eyeglass manufacturing machine [20] [29] has the largest stroke-bandwidth product. The rotary fast tool servo of Montesanti [30] has the highest bandwidth of the Lorenz devices. The piezoelectric devices generally have strokes in the range 10-100 µm, and bandwidth in the range 100 Hz-2 kHz. Finally, the three short-stroke normal-stress electromagnetic devices (a,b,c) demonstrate a new performance class, greatly exceeding the bandwidth of any other reported device. These devices establish new design principles for fast tool servos.

### 3 Flux-steering Ultra-Fast Tool Servo

This section describes some of the design features of the flux-steering linear fast tool servo we have designed, shown as point c in Figure 7. A picture of this device is shown in Figure 6. We refer to it herein as the Ultra-Fast Tool Servo (UFTS). In cross-section, the UFTS appears as shown in Figure 8.

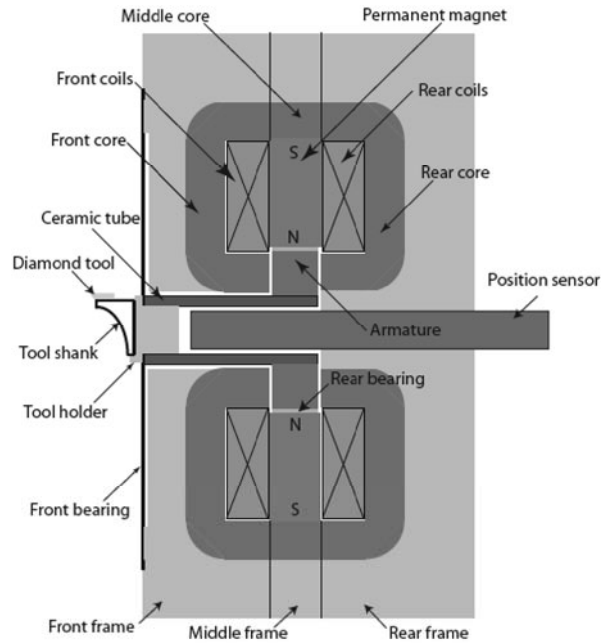
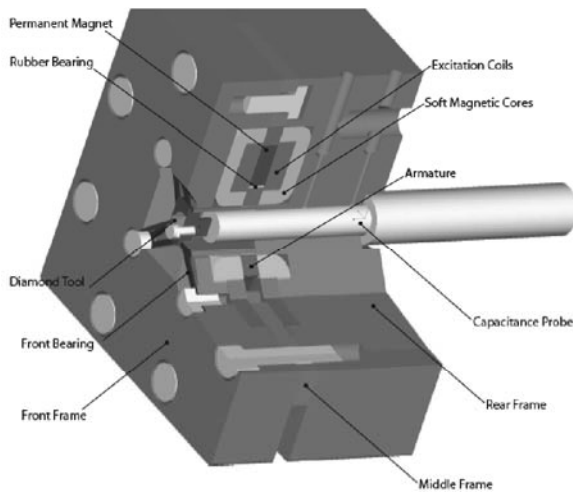


Fig. 8. Cross-section of Ultra-Fast Tool Servo.

As shown in the figure, the motion of the armature is transferred to the tool holder by a segment of aluminum oxide ceramic tube. The moving assembly is suspended by a spring steel flexure bearing in the front and a rubber pad bearing in the back. Consequently, the diamond tool moves primarily along the axial direction of the ceramic tube and the other five degrees of freedom are fully constrained. The air gap  $X_0$  is set at 100 µm to easily ensure 50 µm stroke. In this schematic design, the stator cores are split into three parts: the front core, the middle core, and the rear core to simplify manufacturing and fabrication. All frames (including the front frame, the middle frame, and the rear frame) are made of Type 304 non-magnetic stainless steel to provide good structural stiffness. The permanent magnets in the UFTS are Ne-Fe-B permanent magnets of 1.2 T remanence, which are rated up to 120° C operation. A capacitance probe (ADE 5501 active probe) of 100 kHz bandwidth directly measures the tool holder motion from behind. Therefore, the tool can be controlled accurately, in spite of structural length variations induced by thermal expansion or cutting/inertial forces. Figure 9 shows a detailed cutaway view of the UFTS.



**Fig. 9.** Cutaway model of the ultra-fast tool servo.

Figure 10 gives an overall view of the flux-carrying components in the actuator: the armature core, the front core, the middle cores, permanent magnets, and the rear core.

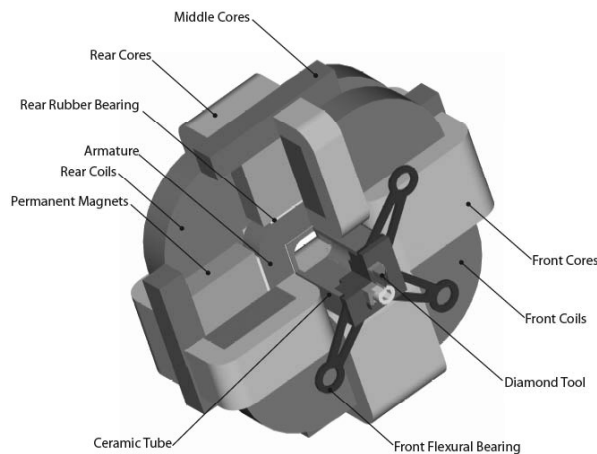


**Fig. 10.** 3-D Magnetic Path of the Ni-Fe based UFTS.

The key assembly of the UFTS is the moving assembly as shown in Figure 11a, which includes an armature made of soft magnetic materials, a structural backbone made of ceramic materials, a flexural front bearing, and a rear bearing made of four rubber pads interposed between the armature and the permanent magnets. The moving assembly has a total mass of about 11 gm.

The rubber bearings used in the UFTS are believed to be novel in the field of precision engineering, and grew out of Barton's thesis work [4] [3]. These bearings contribute stiffness and damping to the actuated mechanism. They also occupy a far smaller region in the actuator than the conventional steel flexural bearings at the front of the actuator, and do not interact with the actuator magnetic fields. The dynamical model shown in Figure 11b indicates how the cutting force loads are distributed to the bearings. Because of the ratio of  $L_1$  to  $L_2$ , the tool tip stiffness is dominated by the steel flexures, which relaxes requirements on the rubber bearings.

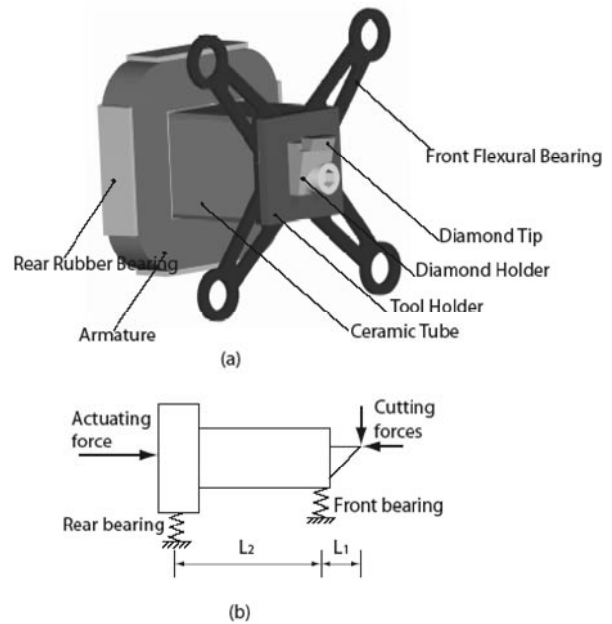


**Fig. 11.** Moving Assembly. (a) Structure of the moving assembly. (b) Simplified dynamical model.

### 3.1 Ultra-Fast Motor

The design motivation for this ultra-fast tool servo derives from the following simple observation about magnetic pressure and the possible acceleration capabilities of magnetically-actuated fast tool servos. The magnetic pressure on the air gap of a normal stress actuator is given by  $P_m = B^2 / 2\mu_0$ . Assuming a flux density of  $B = 1.5$  T, which is below the saturation of many soft magnetic materials, a normal stress actuator can generate a pressure of about  $9 \times 10^5$  Pa. If we can apply this pressure to an armature iron disk of 3 mm thickness, then the resulting acceleration will be 4000 G! This large potential acceleration capability is the motivation for pursuing the work reported here. Based on this analysis, we predicted that normal-stress actuators can be used to drive a FTS with unprecedented acceleration and bandwidth performance. This potential has been well-realized in the UFTS.

### 3.2 Fast Tool Servo Control

The compensated loop transmission without adaptive feedforward controllers (AFC) achieves a crossover frequency of 10 kHz with 30 degree phase margin as shown in Figure 12. For large signal response, this actuator has demonstrated 500 G acceleration at 10 kHz open-loop operation.

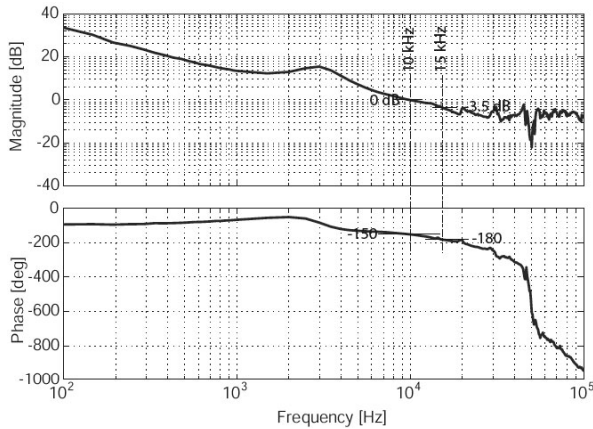


**Fig. 12.** The measured negative loop transmission of the compensated UFTS without AFC control.

We have also developed a new method for AFC controller implementation/design. By putting the AFC controllers in parallel with the integrator, as shown in Figure 13, we can design the conventional motion controller ( $C_b(s)$  and  $K_I/s$ ) and AFC controllers in one consistent loop. The effectiveness of the designed AFC controllers has been demonstrated experimentally by tracking a 16  $\mu\text{m}$  p-v sine wave at 3 kHz, with a resulting tracking error of only 2.1 nm RMS.

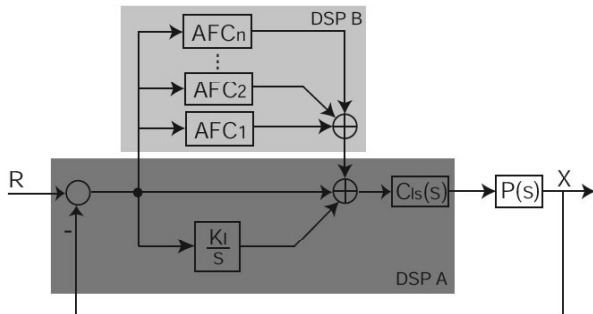


**Fig. 13.** The controller structure for the SM2-based UFTS. The controller is composed of three parts: a loop-shaping controller  $C_b(s)$ , PI term  $1+K_I/s$  and adaptive feed-forward controller AFC(s).

### 3.3 Experimental Results

We have integrated the UFTS with a commercial diamond turning machine. Both 1-D and 2-D sinusoidal surfaces have been cut on aluminum and copper parts with an azimuthal period of  $0.5^\circ$  at 500 RPM, and a corresponding UFTS working frequency of 6 kHz. No chatter was observed for cutting at depths from 0.5  $\mu\text{m}$  to 30  $\mu\text{m}$ . Figure 14 shows an interferometric microscope image of a machined 2-D surface which indicates the contoured optical-quality surfaces which can be produced with the UFTS. These experimental results confirm that electromagnetically-driven FTSS with flux steering actuators are a promising new technology for diamond turning contoured surfaces.

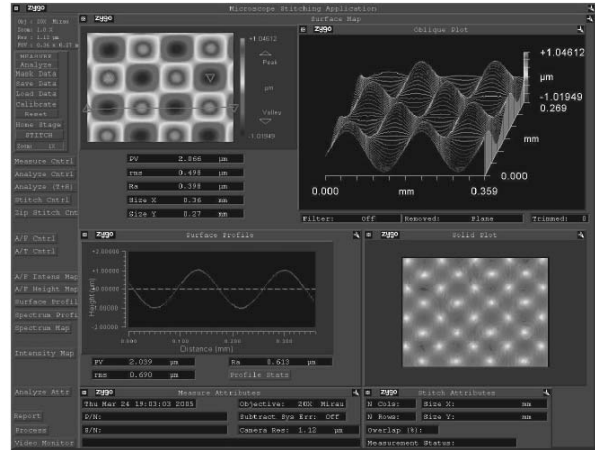


**Fig. 14.** Surface metrology for diamond turned 2-D surface on an OFHC copper workpiece.

### 4 References

- [1] Y. Altintas and A. Woronko. A piezo tool actuator for precision turning of hardened shafts. *Annals of the CIRP*, 51(1), 2002.
- [2] Walter Baar, Herbert Koehler, and Walter Muecke. Engraving device for a printing from engraving machine. *US Patent 3964382*, June 1976.
- [3] A.E. Barton. *Rubber bearings for precision positioning systems*. MS thesis, M.I.T., Department of Mechanical Engineering, September 2005.
- [4] A.E. Barton and D. L. Trumper. Rubber bearings and their applicability in precision machines. *Proceedings from ASPE 2005 Annual Meeting*, October 2005.
- [5] E. Brinksmeier and W. Preuss. Complex surfaces - applications and generation by diamond machining. *Proceedings of the ASPE 1997 Annual Meeting*, 1997.
- [6] J. F. Cuttino. Performance optimization of a fast tool servo for single-point diamond. *IEEE/ASME Trans. on Mechatronics*, 4(2), June 1999.
- [7] S. Douglass. *A machining system for turning non-axis-symmetric surfaces*. PhD dissertation, the University of Tennessee, Knoxville, 1983.
- [8] T. A. Dow, M. H. Miller, and P.J. Falter. Application of a fast tool servo for diamond turning of nonrotationally symmetric surfaces. *Precision Engineering*, 13(4), 1991.
- [9] H. Eda. Ultra-precise machine tool equipped with a giant magnetostriction actuator - development of new materials and their application. *CIRP annals*, 41(1), 1992.
- [10] Chris J. Evans and James B. Bryan. "structured", "textured" or "engineered" surfaces. *CIRP annals*, 48(2), 1999.
- [11] K. J. Falter and David H. Youden. The characterization and testing of a long stroke fast tool servo. *International Progress in Precision Engineering: Proceedings of 8th International Precision Engineering Seminar*, 1995.

- [12] P. Falter and T. Dow. A diamond-turning apparatus for fabrication of non-rotationally symmetric surface generation. *Proceedings of the International Congress for Ultraprecision Technology, Aachen*, pages 187-201, 1988.
- [13] H. G. M. Moorefield. Generation of rotationally asymmetric optical surfaces using a fast tool servo. *Proc. of ASPE 1995 annual meeting*.
- [14] W. Greene and D. Shinstock. Design of a linear voice coil actuator for fast tool servo applications. *Proc. of ASPE 1997 annual meeting*.
- [15] H. M. Gutierrez and P. I. Ro. Parametric modeling and control of a long-range actuator using magnetic servo-levitation. *IEEE Tran. on Magnetics*, 34(5), 1998.
- [16] H. M. Gutierrez and P. I. Ro. Sliding-mode control of a nonlinear-input system: application to a magnetically levitated fast tool servo. *IEEE Tran. on Industrial Electronics*, 45(6), 1998.
- [17] R. D. Hanson and T.-C. Tsao. Periodic sampling interval repetitive control and its application to variable spindle speed non-circular turning process. *ASME Journal of Dynamic Systems, Measurement and Control*, Vol. 122, pages 560-566, September 2000.
- [18] Y. Hara, S. Motonishi, K. Yoshida, and N. Ikawa. A new micro-cutting device with high stiffness and resolution. *Annals of the CIRP*, 39(1), 1990.
- [19] B. Jared. Fabrication of surface perturbation on inertial confinement fusion targets. *Proc. of ASPE 1996 annual meeting*.
- [20] Stephen Joseph Ludwick Jr. *A Rotary Fast Tool Servo for Diamond Turning of Asymmetric Optics*. PhD dissertation, M.I.T., Department of Mechanical Engineering, June 1999.
- [21] D. H. Kim and T.-C. Tsao. Robust performance control of electrohydraulic actuators for electronic cam motion generation. *IEEE Transactions on Control Systems Technology*, Vol. 8, pages 220-227, March 2000.
- [22] E. Kouno. A fast response piezoelectric actuator for servo correction of systematic errors in precision machining. *Annals of the CIRP*, 33(1):369-372, 1984.
- [23] D. Liu. Surface texture improvement in the turning process via application of a magnetostrictively actuated tool holder. *ASME Journal of DSCMC*, 120, 1998.
- [24] Xiaodong Lu. *Electromagnetically-Driven Ultra-Fast Tool Servos for Diamond Turning*. PhD dissertation, M.I.T., Department of Mechanical Engineering, September 2005.
- [25] Xiaodong Lu and David L. Trumper. Electromagnetically driven fast tool servo. *Proceedings from ASPE 2003 Annual Meeting*, pages 103-106, 2003.
- [26] Xiaodong Lu and David L. Trumper. Electromagnetically driven ultrafast tool servo. *Proceedings from ASPE 2004 Annual Meeting*, pages 269-272, 2004.
- [27] Xiaodong Lu and David L. Trumper. High bandwidth fast tool servo control. *American Control Conference 2004*, June 2004.
- [28] Xiaodong Lu and David L. Trumper. Ultra fast tool servos for diamond turning. *Annals of the CIRP*, 54(1):2005.
- [29] S. Ludwick and D. L. Trumper. Design of a rotary fast tool servo for ophthalmic lens fabrication. *Precision Engineering*, 23(4):253-259, 1999.
- [30] R. C. Montesanti and D. L. Trumper. High bandwidth short stroke rotary fast tool servo. *Proceedings from ASPE 2003 Annual Meeting*, pages 115-118, 2003.
- [31] R. C. Montesanti and D. L. Trumper. A 10 kHz short-stroke rotary fast tool servo. *Proceedings from ASPE 2004 Annual Meeting*, October 2004.
- [32] Richard Montesanti. *High Bandwidth Rotary Fast Tool Servos and a Hybrid Rotary/Linear Electromagnetic Actuator*. PhD dissertation, M.I.T., Department of Mechanical Engineering, September 2005.
- [33] Y. Okazaki. A micro-positioning tool post using a piezoelectric actuator for diamond turning machines. *Precision Engineering*, 12(3), 1990.
- [34] Yuichi Okazaki. Fast tool servo system and its application to three dimensional fine surface figures. *Proc. of ASPE 1998 annual meeting*.
- [35] S. R. Patterson and E. B. Magrab. The design and testing of a fast tool servo for diamond turning. *Precision Engineering*, 7(3):123-128, 1985.
- [36] J. D. Rasmussen. Dynamic variable depth of cut machining using piezoelectric actuators. *International Journal of Machine Tools and Manufacture*, 34(3):379-392, 1994.
- [37] P. Schellekens. Design for precision: Current status and trends. *Annals of the CIRP*, 47(2):557-586, 1998.
- [38] B. Stancil, H. Gutierrez, and P. Ro. Design of a long range fast tool servo system using magnetic servo levitation. *Proceedings from ASPE 1995 Annual Meeting*, pages 301-304, 1995.
- [39] M. W. Todd and J. F. Cuttino. Development of a long range, traction drive fast tool servo for diamond turning applications. *Proc. of ASPE 1997 annual meeting*.
- [40] H. Tran and D. DeBra. Design of a fast short-stroke hydraulic actuator. *Annals of the CIRP*, 43(1):469-472, 1994.
- [41] T.-C. Tsao and M. Tomizuka. Robust adaptive and repetitive digital tracking control and application to a hydraulic servo for noncircular machining. *ASME Journal of Dynamic Systems, Measurement, and Control*, Vol. 116:1, pages 24-32, February 2000.
- [42] X. Wang. Experimental research on the linear motor micro-feed devices with high frequency response, long travel and high accuracy. *Annals of the CIRP*, 40(1):379-382, 1991.
- [43] M. H. Weck. A new hybrid concept for a long stroke fast tool servo system. *Proc. of ASPE 1995 annual meeting*, 1995.

---

## Microsystem Technologies for Automotive Applications

Yoshiki UENO and Nobuaki KAWAHARA  
Research Laboratories, DENSO CORPORATION

microsystem, MEMS, sensors, engine control, safe systems, ITS, fabrication technology, DRIE, AHS, internet ITS

### Abstract

Within the automotive industry, micro-electro-mechanical-systems (MEMS) technology has contributed to the improved performance, reliability and lower-cost sensors that support basic automobile functions, including driving, turning, and stopping. Future goals of the automobile industry must target the development of environmentally friendly cars that are capable of obtaining higher gas mileage, are safer, and more comfortable. Also, these cars should be capable of the reception and transmission of necessary information. At this time the automotive industry is currently focusing its R&D on ultra-low emission vehicles and intelligent transport systems (ITS). MEMS technology is expected to play an extremely important role in this future direction of R&D in the automotive field, particularly in achieving higher levels of safety. The integration of MEMS technology in various devices is essential so that the system maintains a high level of reliability and mass productivity. This paper discusses how MEMS technologies are used in current vehicles and will have been used in the future vehicles.

### 1 Background of MEMS in the Automotive Industry

MEMS has made major progress over the past years, due to advancement in miniature machining techniques, drastic improvement in performance due to miniaturization, and realization of new functions which could only be attained by miniaturization. With progress in electronics, MEMS sensors have replaced mechanical sensors in many applications. MEMS sensors have the following advantages:

- (1) Deterioration-free and durable for a long period
- (2) Low cost (Suitable for mass production)
- (3) Small in size, and easy for installation
- (4) Good dynamic characteristics  
(High response and sensitivity)
- (5) Superior impact resistance
- (6) Low power consumption
- (7) Self-diagnosis function

Due to these overwhelming merits, use of MEMS sensors has been naturally increasing in scale. Those sensors permit sophisticated control, contributing to the improvement in the basic performance of various kinds of equipment. MEMS sensors are commonly made by silicon, which is better than mechanical sensors, due not only to the superior physical properties of semiconductor silicon but also to their compactness and light weight (essential requirements for automotive parts), in addition to their high environmental resistance and reliability.

**Table 1.** Physical Properties of Silicon and Iron

	Si	Fe
Density( $\text{g} \cdot \text{cm}^{-3}$ )	2.33	7.86
Young's Modulus(GPa)	190(111) 130(100)	210
Melt point( $^{\circ}\text{C}$ )	1412	1534
Specific heat( $\text{J} \cdot \text{g}^{-1} \cdot \text{K}^{-1}$ )	0.76	0.64
Thermal expansion coefficient ( $\times 10^{-6} \text{K}^{-1}$ )	2.6	11.8
Heat conduction ( $\text{W} \cdot \text{m}^{-1} \cdot \text{K}^{-1}$ )	168	48

Table 1 compares the physical properties of iron and silicon as the substrate material of MEMS sensors. Silicon is equivalent to steel in its physical properties, is precisely machined into desired shape by semiconductor processes, has various effects for converting change in physical properties to electrical signals (piezo-resistance effect, photoelectric effect, Hall effect, etc.), and enables integration in electrical circuits.

### 2 Practical MEMS Applications in Automotive Sensors

The survey by the Japan Electronics and Information Technology Industries Association (JEITA)<sup>1)</sup> reveals that approximately 310 million automotive sensors were

**Table 2.** Automotive Sensors

Application Measurement	Drive, stop and turn	Safety, Conformity & Environment	Information/Communication
Temperature	Water temp. sensor, Intake air temp. sensor Exhaust temp. sensor	Oil temperature sensor Room temperature sensor, Air temperature sensor Refrigerant temp. sensor	
Pressure	<b>Intake air pressure</b> <b>Fuel tank pressure</b> <b>Atmospheric pressure</b> <b>Combustion pressure</b>	<b>Air-conditioner coolant pressure sensor</b> <b>Brake pressure sensor</b>	
Acceleration		<b>Acceleration sensor for Air bag,</b> <b>ABS, VSC</b>	
Position/Angle	Throttle sensor <b>Steering angle sensor</b>	<b>Car height sensor</b>	
Rotation	<b>Cam angle sensor</b> <b>Crank-angle sensor</b> <b>Vehicle speed sensor</b>	<b>Wheel-speed sensor</b>	
Flow	<b>Airflow sensor</b>		
Level	Fuel sensor Engine oil sensor	Brake oil sensor	
Vibration	Knock sensor		
Gas	O2 sensor, A/F sensor	Smoke sensor, CO sensor Humidity sensor	
Light/Electromagnetic wave		<b>Solar sensor</b> <b>Auto-light sensor</b> Clearance sonar	<b>Laser radar</b> <b>Millimeter wave radar</b> <b>Satellite communication antenna</b> <b>Infrared camera</b> <b>Car recognition camera</b> <b>Other cameras</b>
Other		<b>Gyroscope</b>	Geomagnetic sensor, Magnetic nail

produced in Japan during 2002, and approximately 10.26 million motor vehicles in the same year.

This means that on average about 30 sensors are installed in each vehicle. Although it is difficult to obtain accurate figures since the specific number of sensors installed per vehicle differs according to vehicle model, a recent luxury car contains some 100 sensors of about 70 types<sup>2)</sup>.

Table 2 lists typical automotive sensors used in current vehicles. As for the controlling basic vehicle functions of “drive,” “turn” and “stop”, they are the largest in number, of which many are of the semiconductor/MEMS type. The detection objects are temperature, pressure, acceleration, position/angle, rotation, flow, liquid level, vibration and gas. The number of MEMS sensors is increasing due to the advantages mentioned above. In the table, the bold-faced type is MEMS sensor.

**2.1 Pressure sensor**

Figure 1(a) and 1(b) show the structure and principle of the sensing element of pressure that use the piezo-resistance effect (phenomenon in which solid material changes in electrical resistivity as it is deformed), respectively. The pressure sensor is characterized by a thin-wall structure called a diaphragm. In the figure, the center part of the silicon substrate is thinner than surrounding part, which is deformed according to the applied pressure. The diaphragm is produced by etching part of a silicon wafer using a unique

single-wafer etching<sup>3)</sup>. Piezo-resistors are formed in a bridge configuration on this diaphragm, so that when the diaphragm is deformed by the application of pressure, the sensor can detect the pressure in terms of change in resistance.

**Bold face: MEMS sensors**

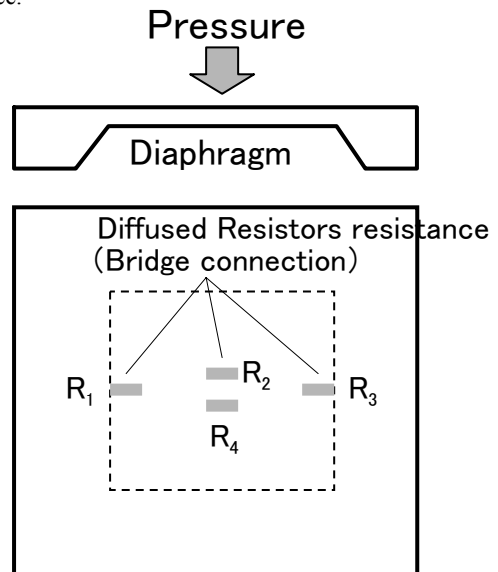


**Fig. 1(a).** Structure of Pressure Sensor

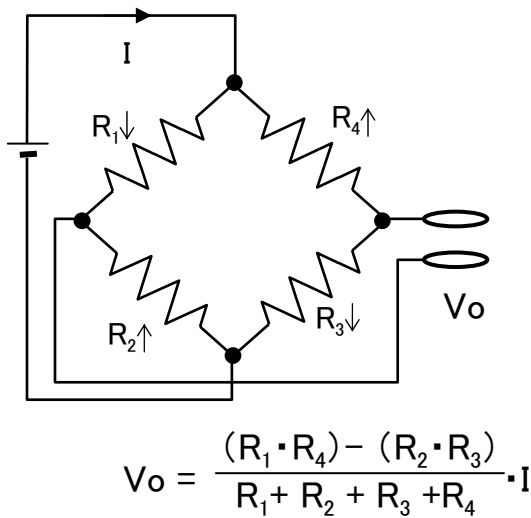


Fig. 1(b). Principle of Pressure Sensor

Piezo-resistance pressure sensors have been commercialized handling a wide range of pressure (a factor of 40,000 in the pressure range), from 5 kPa for gasoline vapor pressure sensors that detect a trace leakage from gasoline pipe to 200 MPa for common-rail pressure sensors that detect fuel pressure in the diesel-engine common-rail system<sup>4</sup>. Therefore, many different type of pressure sensors are used in current vehicles, which have different size and thickness of the diaphragm. A pressure sensor is used for engine control as well. Specifically, intake air volume is calculated based on the engine-intake-manifold pressure and temperature (density) measured by a pressure sensor and temperature sensor, respectively, to optimally control the volume of fuel injection into the engine. In this application, if the ratio of fuel/air is high, carbon mono-oxide and hydro carbon complex are increased in the exhaust gas, if low, NOx which is not good for environment is increased. So to say, the pressure sensor contributes to ensuring cleaner exhaust gases and enhanced engine output.

The technology employed to form the diaphragm of pressure sensors is MEMS bulk micromachining or anisotropic etching, which uses the phenomenon in which the silicon single crystal etching rate differs with the crystal orientation. Anisotropic etching uses potassium hydroxide (KOH) as etchant. The etching condition has been established and compiled in a database. Simulation technology has also been developed for this application. Figure 2 shows the calculated shapes of etched silicon diaphragms<sup>3</sup>. We used a silicon (110) substrate on which an octagonal diaphragm can be formed. An octagonal diaphragm permits thermal stress distribution well balanced with the piezo-resistive gauges, making it possible to minimize distortion of a sensor's offset-voltage temperature characteristic.

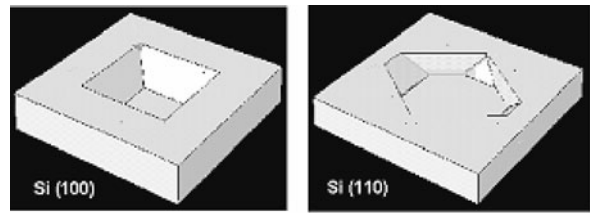


Fig. 2. Calculated Diaphragm Shape of Si(100) and Si(110)

### 2.2 Accelerometer

An accelerometer, or acceleration sensor, used in airbag systems etc. comprises micro beams and inertial mass formed by etching part of a silicon substrate, and piezo-resistors formed as strain gauges on the beams, showed in figure 3.

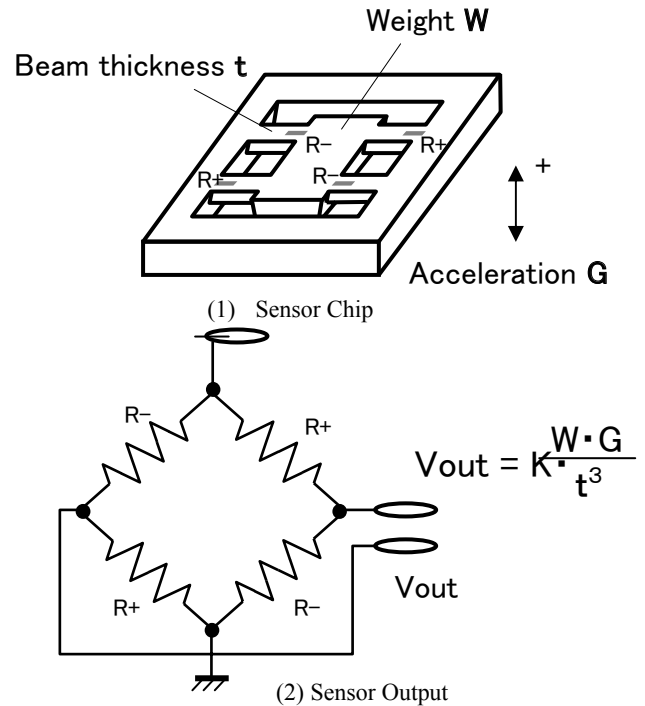


Fig. 3. Structure and Principle of Accelerometer

When acceleration is applied, the beams are bent, causing the resistance of piezo-resistors to change so that the sensor can measure the acceleration. With progress in silicon-substrate micromachining technology, sensor chips have been significantly reduced in size and costs. The overall volume of an accelerometer has been reduced to one-fiftieth, and the price to one-tenth, compared with the product in the early '90s. This has made it possible to install airbag systems in almost all vehicles, from luxury cars to light vehicles. As the most advanced accelerometer, a capacitance type sensor (an electrostatic sensor capable of



detecting acceleration in terms of change in static capacitance) has been developed for practical application. The capacitance type sensor is far smaller in size than the strain-gauge-type sensor, and is highly functional with the self-diagnosis function incorporated. The sensor has micro comb structure and consists of two different electrodes; static electrode and movable electrode. When acceleration is applied, the distance of them is changed and the capacitance is also changed. In the self-diagnosis function, when a voltage is applied to the two electrodes, the gap between them is changed by electrostatic force, and the capacitance is also change and detected. This diagnosis is done whenever the engine is started. Applications of an acceleration sensor are not limited to airbag systems. It is also used in vehicle motion control systems, such as the Antilock Braking System (ABS), which prevents wheels from locking up based on the deceleration and rotation of wheels during braking. The ABS contributes significantly to vehicle safety, and has been installed in almost all vehicles, including low-price compact vehicles.

### 3 Future Direction of Automotive Industry

One hundred years have passed since the birth of the modern automobile. While the automobile has provided us with great convenience, one cannot deny the problems it has left: environmental pollution from fuel emissions in addition to an increase in the number of deaths and injuries due to traffic accidents. Accordingly, future methods of manufacturing cars must target environmentally friendly cars that obtain higher gas mileage ratings and safer cars capable of, if not preventing accidents, a reduction of the injurious effects of accidents on passengers and pedestrians. In the early twentieth century, the basic functions of the automobile were to run, turn, and stop. Recently, in addition to those basic functions, automobiles have a new function: communication. Advances in electronic technology have contributed to this new function. Through various media, such as satellites, cellular phones, and broadcasts, we have the ability to drive safer and more comfortably. We call this "Telematics," which is derived from the words Telecommunication and Informatics. Automotive Telematics includes the transmission of information to and from vehicles with advanced telecommunication technologies. In the future, the world is scheduled to evolve into ITS (Intelligent Transport Systems) by DSRC (Dedicated Short-Range Communications) between roads and vehicles as well as between vehicles. ITS is based on the principle that humans, roads and vehicles mutually interact and cooperate through the sharing of information and cooperate mutual as shown in figure 4. New systems, such as AHS (Advanced cruise-assist Highway System), ASV (Advanced Safety Vehicle), HMI (Human Machine Interface) as well as others are key technologies in the realization of this principle. After the realization of these technologies a new relationship between humans, roads and vehicles will be created.

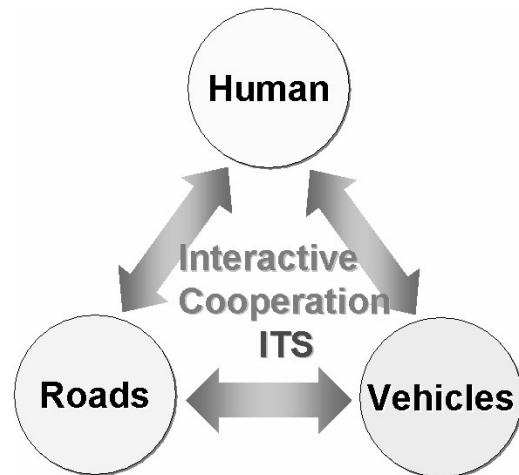


Fig. 4. Basic Concept of ITS

Automotive manufacturing technologies for the future must be aimed at creating vehicles which are fuel-efficient and environmentally friendly, as well as safe, i.e., collision-free or minimal in impact to pedestrians and vehicle occupants in the unfortunate event of a collision. Also important is to incorporate into vehicles advanced information and communication technologies that are coordinated with road infrastructure systems, with the aim of ensuring efficient vehicle traffic and creating safer and more comfortable vehicles in which drivers can share necessary information with other people anywhere and anytime. In future, vehicles are expected to evolve along the three vectors of ecology, safety and comfort<sup>5)</sup>. It is therefore necessary to develop and manufacture vehicles and automotive systems to comply with these vectors. Of the three vectors, safety should be given the highest importance since it relates to human lives. MEMS technology is expected to play an immense role in realizing the automotive safety.

### 4 Concept of Advanced Driving Assistance

From this viewpoint, the automotive industry has been implementing research and development with focus on the Intelligent Transport Systems (ITS). Typical one is the development of Advanced Cruise-assist Highway Systems (AHS) in which the Ministry of Land, Infrastructure and Transport has taken the initiative in Japan. Through the AHS, the Ministry intends to provide seven basic services which are considered necessary for realizing a safe motorized society in future<sup>6)</sup>. The seven services are proposed to provide support for: (1) prevention of collisions with forward obstacles, (2) prevention of overshooting on a curve, (3) prevention of lane drift, (4) prevention of crossing collisions, (5) prevention of right-turn collisions, (6) prevention of collisions with pedestrians on a crossing, and (7) road surface information for maintaining an appropriate headway distance etc. The support services of items (1) through (3) are being realized by a radar system<sup>7)</sup> and lane

keep system by camera, which have already been installed in some vehicles.

At present, however, these systems are costly and affordable only on some luxury cars. It is necessary to further reduce the size and cost of these systems through the use of MEMS technology. If these systems are to follow the same course of evolution as automotive sensors, the reduction in size and cost will make the systems and the safety secured by them affordable on general-class vehicles as well. For this reason, a high expectation is placed on MEMS technology. Recently, many MEMS sensors have come to be adopted for more advanced vehicle motion control systems, such as the Vehicle Stability Control (VSC) system which prevents the vehicle from exceeding the limit for friction between road surface and tire when turning<sup>8)</sup>. In the system, several sensors, two accelerometers, speed sensors and a gyroscope are used for detecting vehicle dynamics. This system will be improved onto a more sophisticated system which controls complicated vehicle dynamics and realize safer driving.

The other support service of item (4) –(7) cannot be realized by on-vehicle equipment alone. Coordination with infrastructure systems is indispensable. In the U.S., development of a system that supports driver's decisions at intersections is under way in a project led by the University of California<sup>9)</sup>. A device installed at each intersection identifies vehicles approaching the intersection and advises each vehicle's driver whether he/she may make a left turn (right turn in Japan). Safety-related support for pedestrians and vehicles at intersections is highly desired for the future. One of the effective and promising measures for such support is a wearable human-machine interface (HMI) device manufactured by micromachining technology. The HMI device would be embedded in a tag, which is to be worn by vulnerable road users, i.e., pedestrians. A sensor installed at each intersection would detect the tag information and inform vehicle drivers of the presence of pedestrians. The tag should be manufactured extremely small in size using MEMS technology, and desirably be integral with, say, elderly certificates, security labels on bicycles, name tags worn by elementary-school children, etc. In those tags, a self power supply system by Power-MEMS is much desirable than batteries. At each intersection, an appropriate infrastructure system would inform vehicle drivers of approaching pedestrians and bicycles, to help the drivers avoid recognition mistakes and resultant unfortunate collisions.

Many possibilities can be imagined when contemplating the contributions of MEMS technology to the needs of advanced driving assistant systems. Many MEMS technologies, such as a micro sensor, a micro actuator, an optical-MEMS, a RF-MEMS, Power-MEMS and an auditory-MEMS are currently in the research stage and are regarded as promising technologies for these systems. It is not an overstatement that advanced driving assistant systems are realizable with integration of various MEMS technologies. Here, the word "integration" does not mean the simple gathering of device functions. Instead, it means the creation of new standard of production ability, and robustness.

## 5 MEMS Technology as Fabrication Technology

Manufacturing for the 21st century is recycling-oriented. In this regard, MEMS, which can save resources and energy, plays an extremely significant role in the resource-recycling and resource-saving society. Since MEMS is essentially based on silicon micromachining techniques, development and progress of micromachining techniques are indispensable for further advances in MEMS technology. At present, our attention is focused on the deep reactive ion etching (DRIE) process as a promising micromachining technique. This process offers a deep etching ( more than 100  $\mu$  m), a highly vertical accuracy, and a high etching rate ( more than 1  $\mu$  m/min.) without crystal orientation dependence. This excellent character realizes state-of-the-art 3-Dimensional MEMS devices built in Si substrate<sup>10,11)</sup>.

In some micro accelerometers operated by electrostatic force, the key component of comb-structure is fabricated on Si substrate by the DRIE. In this case, if the trench between the comb-structured electrodes becomes narrower and deeper, in other words higher in aspect ratio, a capacitance between the electrodes becomes higher. This increase makes the accelerometer more sensible<sup>12)</sup>. Furthermore, the DRIE requires a smaller chip area to produce the same mass portion of an acceleration sensor than with the conventional micromachining process, which result lower cost and higher sensitivity. In this DRIE process, only the bottom part of the trench is possibly etched and the sidewall of the trench is protected through etching. We have proposed a new DRIE process to obtain higher aspect ratio of deep trench. In the process, we use SiO<sub>2</sub> layer for protection because a binding energy between Silicon and Oxygen (106kcal/mol) is higher than that between Carbon and Carbon (85kcal/mol) in the polymeric film which is used in conventional DRIE process. In addition, an etching rate of SiO<sub>2</sub> in the SF<sub>6</sub> plasma is about 1/100 to that of Si. Therefore, if a SiO<sub>2</sub> layer with sufficient thickness can be formed only on the trench sidewall, it would suppress lateral etching completely during the etching after the formation of it. A new etching process is shown in Figure 5. In this process, the DRIE process and SiO<sub>2</sub> layer formation are carried out alternately. The oxidation process is done by Oxygen (O<sub>2</sub>) plasma irradiation<sup>13)</sup>. In this process, oxidation and the DRIE process can be carried out in the same etching chamber only by switching the introducing gases. A repetition of the O<sub>2</sub> plasma irradiation can be expected much less than that of passivation step in the conventional DRIE process because of high etching durability of SiO<sub>2</sub> layer. In this process, the substrate was firstly covered by 10nm thickness of the polymeric film by the passivation step of the DRIE process. Then the O<sub>2</sub> plasma is irradiated on the substrate. Before and after the O<sub>2</sub> plasma irradiation, the substrate surface was analyzed by XPS measurement. Before the irradiation, bond peaks such as C-C, C-Fx are obtained. That means the polymeric film is formed on the Si surface. However, after the O<sub>2</sub> plasma irradiation, those peaks are decreased, and Si-O bond is obtained in Si<sub>2</sub>p peak.

That means the polymeric film is decomposed into gas phase by the O<sub>2</sub> plasma and the exposed Si surface is oxidized by it. Therefore even if the sidewall of the trench is

covered by the polymeric film, it can be oxidized and removed through the plasma oxidization. The O<sub>2</sub> plasma irradiation can oxidize the surface of the trench which makes a strong protection layer on the sidewall. In addition, it can remove the polymeric film on the deep trench bottom and realize an excellent vertical trench profile. Products manufactured using our DRIE process provide an aspect ratio of 5 (15 μm/3 μm) in the production level, and an

aspect ratio of 80 (80 μm/1 μm) or higher in the research level. Figure. 6 shows an example of electrostatic comb actuator fabricated by our DRIE process. Needless to say, as MEMS technology is based on fabrication technologies, further researches not only on etching technology but also on other MEMS technologies; release process, packaging, coating, dicing, and etc., will have been being carrying out.

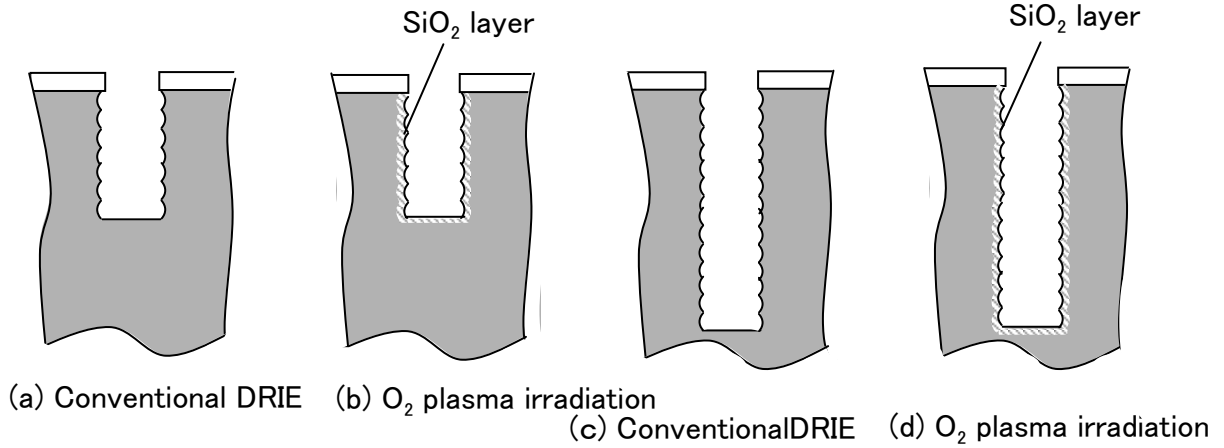


Fig. 5. New Etching Process

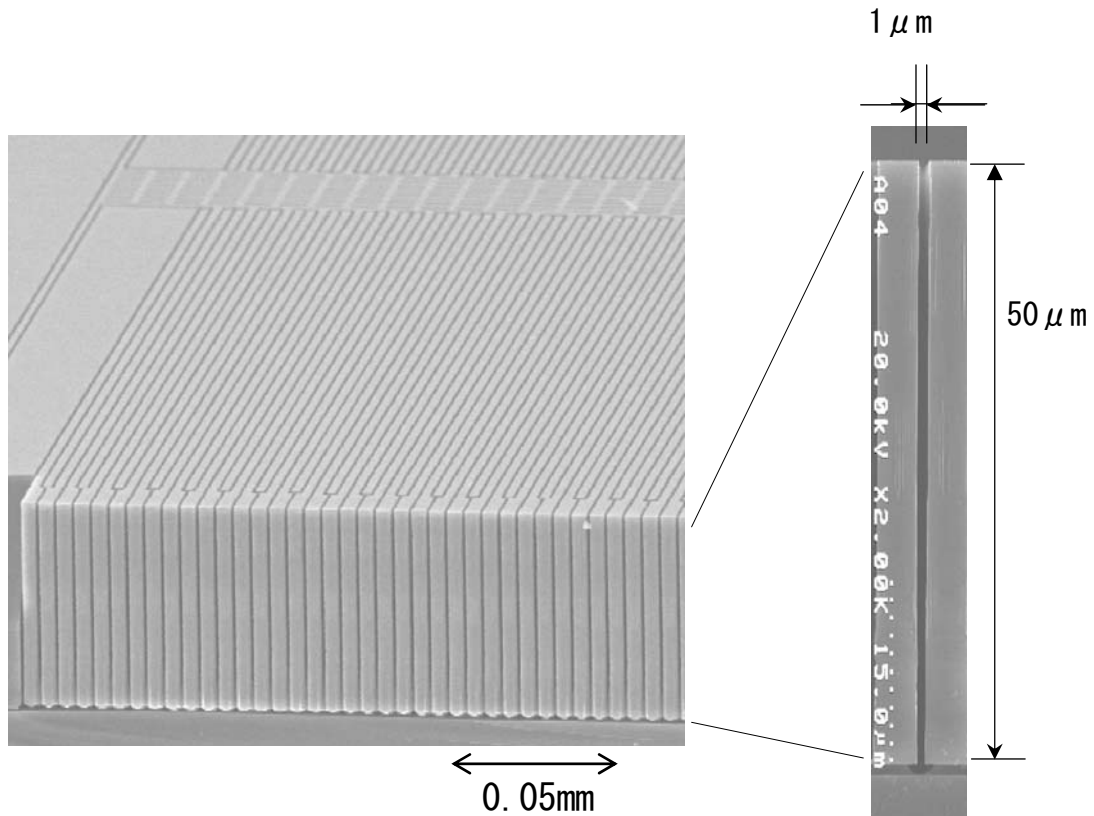


Fig. 6. Example of Etched Micro Structure

## 6 Conclusion

The above paragraphs describe some practical automotive application examples of MEMS sensors, and the evolutionary trend of MEMS technology for the future. MEMS is highly regarded as a key technology with potential to meet the requirements of the coming “ITS-based society” and “ubiquitous information network society” and to create new systems with new functions. MEMS technology is expected to play an extremely important role in the future direction of R&D in the automotive industry, particularly in achieving new levels of safety. In performing this role, the degree of integration of MEMS devices is essential so that these systems maintain a high level of reliability and mass productivity. However, MEMS is basically a manufacturing technology. For further progress in this technology, therefore, it is vital and indispensable to develop a wide variety of core technologies, which is time-consuming. To this end, we believe it necessary to carry out joint technical development through collaborations among industry, academia and government, and between companies.

## 7 References

- [1] Report of Sensor Production X VII , the Japan Electronics and Information Technology Industries Association (JEITA), (2004) p.72
- [2] Touma FUJIKAWA, “MEMS for Automotive Electronics Systems”, Proceedings of the 10th International Micromachine/Nanotech Symposium, Tokyo, Japan, November 11, p.14, (2004)
- [3] Y.Suzuki, M.Imai, T.Mizuno and I.Yokomori, “Evolution of Automotive Semiconductor Pressure Sensors”, DENSO Technical Review, Vol.6, No.1, 2001, p.96-100
- [4] J. Marek, and et.al : “Sensors for Automotive Technology”, p.314, WILEY VCH(2003)
- [5] Kunihiko Hara, “Micromachine Strategy in Automotive Industry”, Proceeding of the 8th World Micromachine Summit, Maastricht, The Netherlands.
- [6] ITARDA URL;  
[http://www.itarda.or.jp/info33/info33\\_1.htm#part1](http://www.itarda.or.jp/info33/info33_1.htm#part1)
- [7] K.Osugi, K.Miyauchi, N.Furui and H.Miyakoshi, ”Development of the Scanning Laser Radar for ACC system”, DENSO Technical Review, Vol.6, No.1, 2001, p.43-48
- [8] TOYOTA MOTOR CORPORATION, URL;  
<http://www.toyota.co.jp/jp/tech/safety/active/vsc.html>
- [9] Steven Shladover, California PATH Program, “Intersection Decision Support”, Proceeding of the IVI National Meeting and Demonstration, June 24-26, 2003, Washington DC, URL: <http://www-path.eecs.berkeley.edu/>
- [10] F.Larmer, A.Schip, K.Funk, M.Offenberg, BOSCH DEEP SILLICON ETCHING:IMPROVING UNIFORMITY AND ETCH RATE FOR ADVANCED MEMS APPLICATIONS, Technical Digest MEMS’99, Florida,USA,1999, pp211-216,
- [11] K.Kuhl, S.Vogel, U.Schaber, R.Schafflik,B.Hillerich, Advanced silicon trenchetching in MEMS applications, Part of the SPIE Conference on Micromachining and Microfabrication Process Technology IV , California, September, 1998, pp.97-105,
- [12] R. Yeh, S. Hollar, and K. S. J. Pister, SINGLE MASK, LARGE FORCE, AND LARGE DISPLACEMENT ELECTROSTATIC LINEAR INCHWORM MOTORS, Technical Digest MEMS2001, Interlaken, Switzerland,2001, pp.260-264,
- [13] J. Ohara, K. Kano, Y. Takeuchi, IEEJ Transaction on Sensors and Micromachines, Vol.123, No.12, 2003, p.541

---

# System Concept and Innovative Component Design for Ultra-Precision Assembly Processes

A. Schubert<sup>1</sup>, R. Neugebauer<sup>1</sup>, B. Schulz<sup>1</sup>

<sup>1</sup>Fraunhofer Institute for Machine Tools and Forming Technology (IWU), Chemnitz, Germany

Keywords: Precision Engineering, Assembly System, Precision Gripper, Alignment error compensation

## Abstract

In this article technical requirements and trends in development of high-precision micromachining and assembly systems are discussed. As a current example of research activities on the field of ultra-precision assembly it is shown the solution of a micro-assembly system for passive alignment of electric-optical modules in optical circuit boards. The realized system concept and a method of innovative component design will be introduced in this paper.

## 1 Introduction

Present trend to highest precision micro-machining and assembly systems bases on continuous miniaturization and functional integration of products. Application areas with enormous market growth are automotive, optoelectronics, biomedicine, micro-chemistry and consumer goods. Microelectronics needs mechanical interfaces, electrical and optical connections with smaller geometries, structures and tolerances down to nano-meters, as shown in fig. 1 [1].

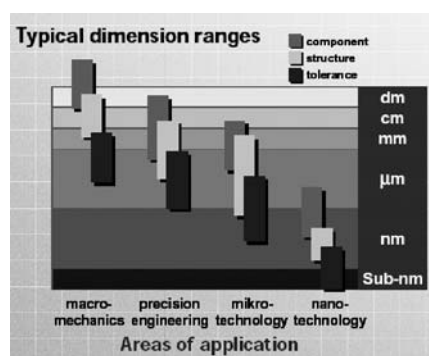


Fig. 1: Typical dimension ranges [1]

State of the art is determined by expensive serial processing steps of micro parts, which tends to future multiprocessing machines with fast parallel processing units, highest position repeatability and integrated quality control.

A key-problem in micro-manufacturing and assembling is the accurate position assignment between micro-tool, micro-gripper and work-piece surface or geometry outline. The processing of complex geometries on a high level of accuracy and within multiple set-up is not satisfactorily solved today. This is not only a question of machine-accuracy and measuring resolution, but also of process set-up, high-precision alignment methods and additional precise calibration equipment.

## 2 Problems and Trends in Development

Precision problems in production systems arise with the integration and calibration of 3D-sensors and measuring components, micro-actuators, micro-manipulators and clean surfaces in a small workspace. Gravitational and inertial forces lose its influence on handling processes. Mechanical deformations, thermal elongation in micrometer range and typical micro-effects, like adhesion, surface tension, slip-stick, capillary force and electrostatic attraction become more important to affect the micromachining and assembly processes. New design ideas and processing strategies for reducing or compensating these influences are necessary.

Today's leading high-precision processing and assembling machines accomplish a positioning accuracy below 1  $\mu\text{m}$ , using a special structural design similar to a measuring device, integrated high-resolution measuring systems and numeric control correction functions. Dominating errors in processing or assembling are coming more from mechanical interfaces between tool-holders and spindle or between a gripper unit and a positioning axis.

The development of recent high-precision micromachining and assembly systems bases on new methodology and construction principles with mechatronic design and modeling tools for modular plug-in units.

At the second period of the nineties at Fraunhofer IWU Chemnitz, Germany, started scientific investigations on micro-technologies. Main fields are micro-forming (high-speed-forming and hot-embossing), micro-cutting (milling and drilling), ECM-technology and the development of dedicated micro fabrication equipment.

One important research project was the development and testing of a high-precision guiding system for a laser ablation on large PCBs with "macro-dimensions" (630x530  $\text{mm}^2$ )

and micro-tolerances at  $\pm 2 \mu\text{m}$ . The problem was solved with a granite-based guiding machine with aerostatic high-precision ( $\pm 1 \mu\text{m}$ ) axes in combination with a new developed correction control unit (DE 101 57 983) using a high-resolution HEIDENHAIN glass-scale and an image processing system for optical alignment.

In 2003 a new 5axis freeform milling machine KUGLER Micromaster MM3 has been established at the IWU laboratory for precision die and prototype manufacturing. It operates with an positioning accuracy of 0.5 micrometers.

In the last years, the development of high-precision assembly solutions and innovative component design became more and more important. There is a growing demand for complete process chains, beginning with the manufacturing technology of the single micro-components to the point of high-precision assembly on today's market.

### 3. System Concept for an Ultra-Precision Assembly Process

#### 3.1 The Assembly Task and Strategy

Optical circuit boards provide an essential technology for future computer and server techniques. Vertical-Cavity-Surface-Emitting-Laser (VCSEL) represents a latterly established class of semiconductor-lasers designed for transmission sections from centimeter- to meter-ranges. For transforming the light signal into an electric signal Positive-Intrinsic-Negative-Diodes (PIN) are employed [2].

Today these components are mounted and adjusted predominantly manually under special laboratory conditions. The technical challenge is to develop new methods and assembling components for high-precision and reproducible packaging in an automated assembling process. This is an important step to reduce the fabrication costs drastically and to smooth the way from a pure laboratory method to an industrial solution concept. The assembly scheme is illustrated in the following graphic (fig. 2).

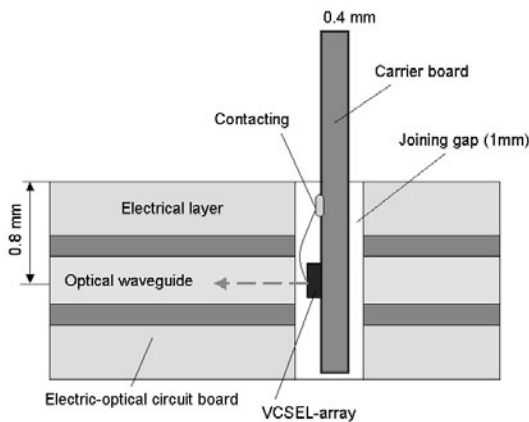


Fig. 2: Assembly scheme (direct light-coupling principle)

A key problem in assembly is the accurate alignment of the light emitting or detecting modules in front of the parallel arranged wave-guides (see fig. 3) inside the circuit board. Conventional machines of surface assembly do not achieve the claimed accuracy and are not able to operate in the vertical Z-direction.

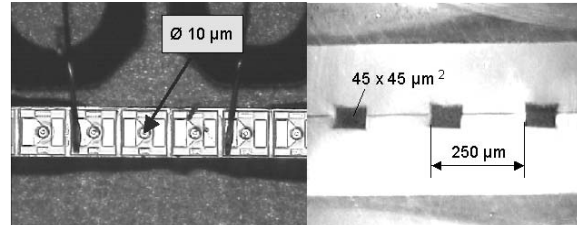


Fig. 3: VCSEL (left) and a polished micro graph section of the optofoil (right)

The mounted components are in passive state. That means, there is no active feedback from the optical transmission section. The highly sensitive components have to be gripped and taken in a safe and reproducible way to the accurate assembly position in a milled joining gap. The hot-embossed buried waveguides for the first application feature a cross section of  $45 \times 45 \mu\text{m}^2$  (see fig. 3). The VCSEL surface has a diameter of  $10 \mu\text{m}$ . The pitch between the 12 single waveguides is  $250 \mu\text{m}$ . The surfaces of the detecting side (PIN) are approximately  $70 \mu\text{m}$  in diameter.

Because of the parallel alignment of the waveguides, angle errors in the light coupling plane are evaluated more critical of their influence on light-transmission than positioning errors in vertical or horizontal direction. The tolerance in vertical and horizontal direction is taken as  $\pm 2 \mu\text{m}$ .

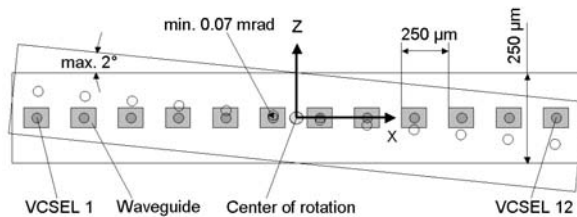


Fig. 4: The problem of accurate angle correction

The outer VCSELs (in this case number 1 and 12, see fig. 4) should be able to launch the complete optical output into the wave guide. The outcome of this is a narrow angle tolerance with  $\pm 0.05$  degree. The possible defective angle positions and the geometrical dimension of the semiconductor chip requires smallest increments of  $0.07 \text{ mrad}$  for aligning the accurate angle position in the light coupling plane. The major technical challenge is arising thereby, that the center of rotation for correcting the angle is on the gripped component and that the center of the axis of rotation is mechanically not available (component 1 immerses into component 2 during assembly process).

The assembly strategy provides a multi-stage catching and adjusting of the emitter and detecting modules with following measurement and correction of the current position. Milled alignment targets in the die are being used for their replication by embossing in the optofoils. These visible alignment targets mark the location of the 12 parallel wave-guides in the optofoil. A gripper integrated camera measures these alignment targets for the chip position arrangement relatively to the waveguides. A second frontal measuring camera determines the tilt angle of the VCSEL or PIN windows on the chip by means of feature extraction and image recognition at the two ends of the array. The automatic assembly process uses image recognition for 2D-measurements and laser triangulation on the micro parts with micrometer accuracy. A new developed position correction control system is embedded in the motion control of the assembly system. It calculates the correction data from the detected image processing data in reference to deposited CAD-coordinates. An essential advantage of the image processing system is the possibility to detect VCSEL as well as PIN surfaces in a directly way. So the influence of imprecise mechanical edges on positioning is being minimized. The passive assembly strategy contains the main following steps:

- Measuring of the optical alignment targets of wave-guides inside the multilayer-board
- Detecting the current Z-coordinates at these positions with the help of a laser-triangulation sensor
- Pre-alignment of emitter or receiver board before gripping
- Measurement of the VCSEL- or PIN-position and angle position during the gripping process with the help of a high-resolution measuring camera
- High-precision angle adjustment in the light coupling plane using a tilt-gripper
- Correction of the vertical and horizontal position in the light coupling plane
- Positioning of the passive emitter- or receiver board relative to the waveguides after coordinate transformations
- Index matching and fixing of the electric-optical modules in the assembly position
- Opening and moving away the gripper-unit after hardening without mechanical contact

### 3.2 State of the Art

Surface assembly systems, presenting on today's market are not able to countersink accurately defined components in vertical direction. There exist no packaged VCSEL-arrays with guiding structures. Furthermore, there are no useable positioning facilities like V-grooves [2].

Now, there is a current german BMBF Project NegIT [3]. This project deals with the manufacture of circuit boards with embedded polymer optical waveguides. As part of this project, a design of an optical coupling in the daughter card and board backplane interfaces was developed. This NegIT-

Pin called element exists only for first laboratory tests, it is not available on the market now.

Commercial available 6-axis-roboter accomplish a repeatability of  $\pm 50 \mu\text{m}$ , particulate as well  $\pm 20 \mu\text{m}$ . A good repeatability near  $1 \mu\text{m}$  enables the "Autoplace 411" by SYSMELEC. Other cartesian or portal robots with a similar accuracy are offered by SPI and LPKF. A precision gripper with integrated tilt function is not available for this devices on the market [4].

A technical implementation of a tilt movement is known from goniometers. Such precision components are offered e.g., by NEWPORT ([www.newport.com](http://www.newport.com)). Goniometers rotate an object about a point located over the center of the top platform. The rotation point is unobstructed by the goniometer itself. These components are usually designed with sliding or rolling bearings in a compact configuration. Still existing eccentricity errors and the slip-stick effect are influencing the positioning accuracy. The design does not include central-free optical path for image measuring optics. The heaviness of goniometers is not usable for precision gripper units.

Solid state hinges are more adapted for superfine precision motions because of its friction-free functioning and zero backlash. General properties and design considerations for "Flexural Bearings" are discussed and exemplified in "Precision Machine Design" [5] in an extensive way. Therein are also discussed problems of kinematic coupling design. This is important for the design of a contact zone e.g., between an actuator and a flexural structure.

### 3.3 System Concept

The master concept of the precision assembly system is based on a 4-axis positioning system, similar to a measuring device, that guides the modular gripper unit.

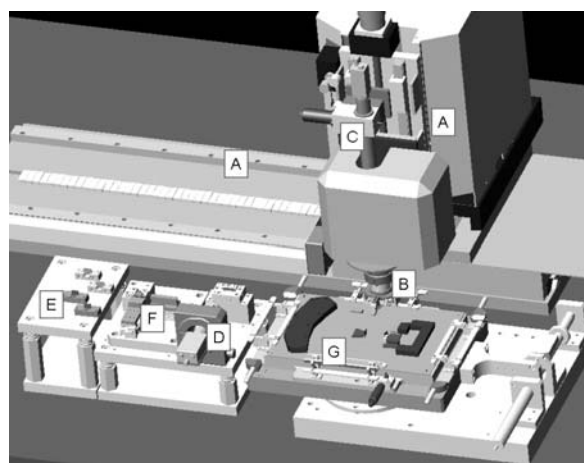


Fig. 5: Main components of the assembly system

Fig. 5 shows by means of the CAD-model the main components like the precision-axes (A), the gripper (B), the integrated camera (C) and the second, fixed measuring camera (D). In front of the assembly system, magazines for

the modules (E), the fine alignment station (F) and the circuit board chuck (G) are arranged.

The working space is defined as follows: X 800 mm, Y 150 mm, Z1-carriage (for gripper) 50 mm, Z2-carriage (for camera) 30 mm, 360°-rotation axis on Z1 (with gripper admission). The system allows a position repeatability of 0.5  $\mu\text{m}$  / axis, alternatively 12 arcsec in the rotation axis. The absolute accuracy in positioning over all axes is  $\pm 2 \mu\text{m}$ .

For the object measurement and the integration of the vision components in the assembly system, a new developed software-tool GPP VISION MICROHANDLING was implemented in the motion control of the positioning system.

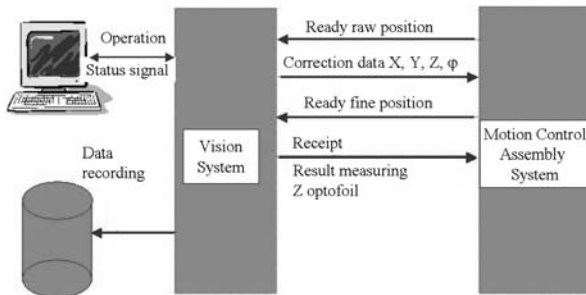


Fig. 6: System concept GPP VISION MICROHANDLING (simplified scheme)

This general system concept was realized with a first demonstrator at the testing facilities at Fraunhofer IWU in Chemnitz. The following picture gives an impression from the testing period.

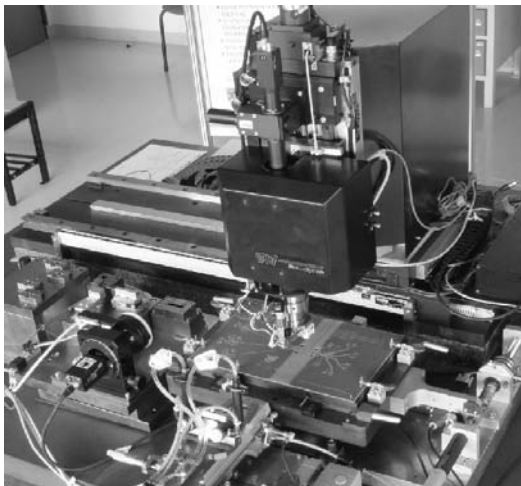


Fig. 7: Demonstrator of the micro assembly system

In front of the system a new dispensing station with 3 precision-axes is placed. It enables the finally fixing and index matching in an automated way. So it completes the process chain of assembling. This is an important premise to increase the operating speed and therewith the product acceptance of such a future machine system too.

### 3.4 The High-Precision Tilt-Gripper

The key component for this ambitious micro-assembly task is a new developed precision gripper with an integrated tilt-function. The modular designed gripper unit is connected with the positioning system via a special designed mechanical interface (see fig. 8).

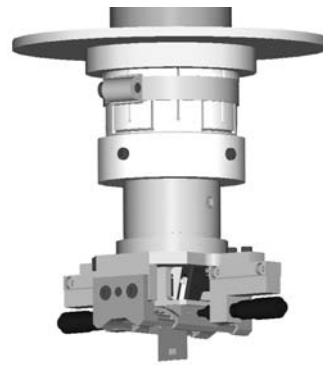


Fig. 8: CAD-model of the tilt-gripper unit

The gripper unit consists of two micro finger grippers, which are adjusted in a V-shape to keep the center free for a camera view (see fig. 9). These grippers in a first version are manipulated by shape-memory alloy actuators and in a second version with the help of a pneumatic actuator.



Fig. 9: The gripper unit with the two micro-finger grippers

Besides very small steps till 0.07 mrad, the angle adjustment should execute absolutely free of backlash. A sliding bearing cannot be used for transmitting minimal movements due to the slip-stick effect. A rolling bearing solution is not included either, because of existing backlash and manufacturing difficulties. Starting from the initial kinematic scheme, a tilt element similar to a tube section only can be used. The design idea was a pipe segment shaped tilt element, where solid state hinges are mounted in pairs radiating around the axis of rotation (see fig. 10). This symmetrical arrangement of solid state joints effects the circular movement without additional guide elements. An actuating force initially effects bending deformation and a contingent of torsion momentum on the individual solid state



hinges. The individual movements together produce the tilted movement at the gripper unit [6].

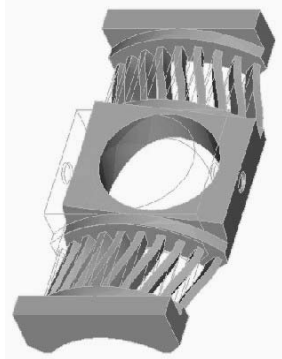


Fig. 10: FEM-deformation plot of the tilt principle [6]

A technical risk of this principle could be a feasible drifting of the rotation point during angle correction. In a first step, a simplified model was deflected to calculate the flexural strength, the bending stress and the torsional stress of a variety of materials (plastics and steel) and cross sections to discover a suitable cross section for the individual joint. The following initial FEM analysis showed, that the material POM (= polyoxymethylene) has the most favorable proportion between potential displacement and appeared stress. A right-angle cross-section with 1.2 mm x 3 mm and a joint length of 13 mm was determined as a convenient dimension of the joints. These geometrical dimensions allow 9 pairs of solid state joints at the pipe shaped segment.

Based on this calculations the precision gripper unit design was finished and a prototype (shown in fig. 11) of the tilt-module was manufactured for following experimental work. For actuating the tilt-module, differential-micrometer screws (actuating from both directions) were used in the earlier period of the test program [6].



Fig. 11: POM-made tilt-module with gripper unit

Meanwhile, a mini-servo drive working with the Harmonic Drive® principle enables a high resolution positioning in an automated assembly procedure. In combination with a special eccentric wheel the mini-servo drive is able to pivot the tilt-module in both directions with 80.000 single steps if needed.



Fig. 12: Tilt-gripper with HarmonicDrive® mini-servo in assembling position

#### 4. Results of Testing

The transmission behavior of the tilt-module was analyzed with the help of FEM and predominantly on experimental way. A FE-model gives results for mechanical strength and kinematics analysis. A separate test stand for measuring the tilt characteristics was built. Instead of the VCSEL or PIN a glass plate with chrome markers was clamped into the tilt-module. The chrome marker positions were measured in x- and y-direction using a CCD-camera with a high resolution lens (resolution 1 micron). A second glass plate was positioned on the top of the tilt-module. The tilt angle was measured with an autocollimator (resolution 30 arcsec), using the optical reflections from this second glass plate.

The FEM simulations were made with a slightly simplified 3D-model of the tilt-module, using ProE/ProMechanica. The following diagram in fig. 13 shows both simulation and experimental results in a angle range from 0 to 60 arcmin. The coherency between tilt angle and actuator force is linear. The stiffness of the tilt-module is about 0.1 N per micron. In the complete tilt angle range from -120 to 120 arcmin a maximum actuator force of 84 N was measured. The required actuator path was determined with 840 micrometers [6].

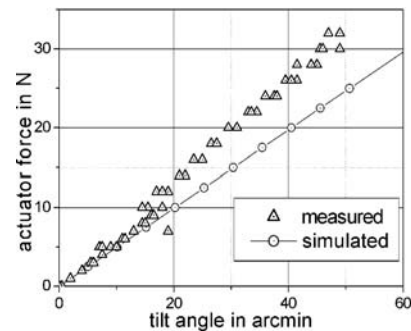


Fig. 13: Measurement results and simulation by comparison

Based on the described system concept a first test stand was built up at Fraunhofer IWU in Chemnitz to demonstrate the micro-assembly process. In several equated experimental series complete assembly-flows were proven and altogether 10 samples of the electric-optical circuit board could be finished successfully (fig. 14) [7]. The following high-frequency tests of the assembled electric-optical circuit boards in laboratories at the Technical University Dresden resulted light transmission performances with a data-rate of 2.5 Gigabits per second and over 50% of the injected laser-activity could be received at the detector side. The experimental work took place under conditions similar to real production (not in special clean-room, other machines in the neighborhood). The surrounding temperature was controlled at 20°C ( $\pm 1$ K).

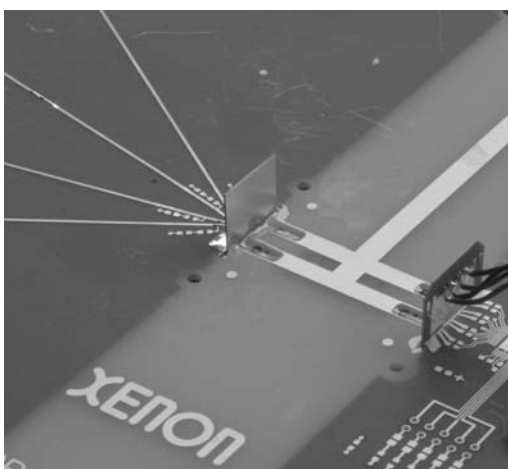


Fig. 14: Mounted emitter and receiver module in the optical circuit board

The assembling accuracy (including dispensing and hardening) could be verified with 5 micrometers. The accuracy of positioning the VCSEL- or PIN-modules was demonstrated with  $\pm 2 \mu\text{m}$ . The targeted precise solution in angle adjustment was solved with a repeatability of  $\pm 0.003^\circ$  over a travel range of  $\pm 2^\circ$ . Angle tolerances in a range of  $\pm 0.05^\circ$  have been adjusted during various assembling trials. So the closely assembling requirements were accomplished.

## 5. Summary and Outlook

This paper describes the system concept and innovative component design for passive alignment of electric-optical modules in optical circuit boards. The key component is a new developed precision gripper unit with the implemented possibility to correct the angle position of a gripped part.

For assembling highly sensitive electric-optical modules succeeded the step from a pure laboratory method to a controllable automated machine system. The methodology of accurate positioning and angle adjustment is applicable to future modular machining and assembling systems with similar highly precise handling tasks e.g., desktop machine centers. There are conceivabilities for scaling the tilt-module

for a wide application area. Future fields of interest and research activities are 3D-measurements and micro actuation of micro assembled objects with sub-micrometer repeatability and the design of flexible, modular assembly systems.

The goal of a just running German integrated project (MIMS) [7] is the targeted investigation of assembly integrated multi-sensor three-dimensional measurement for increasing reliability and productivity in high accuracy micro-assembly processes. The combination of vision systems, laser triangulation sensor and machine-axis measurement with an intelligent correction control unit should allow for capturing the precise position of objects with 6 DOF close to the micro-assembly process. The novel precision gripper unit with the integrated tilt-function has central significance for achieving this goal. It facilitates the local position correction directly in the working space of a micro-assembly system, following the 3D-measuring.

## 6. References

- [1] *van de Venn, H.-W.*: Microassembly – Current development trends and new assembly paradigms, [http://www.microsolutions.fhso.ch/pdf/mechrob\\_van\\_de\\_venn.pdf](http://www.microsolutions.fhso.ch/pdf/mechrob_van_de_venn.pdf), 2004
- [2] *Schmieder, K.*: Aspekte der Aufbau- und Verbindungstechnik elektro-optischer Verdrahtungsträger. Dissertation TU Dresden 2002, In: Themenreihe Elektronik-Technologie in Forschung und Praxis, Vol. 10, *Sauer, W.; Wolter, K.-J.* (Eds.), Verlag Dr. Markus A. Detert, Templin, 2003
- [3] *Schröder, H.; Bauer, J.; Ebling, F.; Franke, M.; Beier, A.; Demmer, P.; Süllau, W.; Kostelnik, J.; Mödinger, R.; Pfeiffer, K.; Ostrzinski, U.; Griese, E.*: Waveguide and packaging technology for optical backplanes and hybrid electrical-optical circuit boards. Speech manuscript, Photonics West 2006, 21<sup>st</sup>–26<sup>th</sup> Jan. 2006, San Jose, USA,
- [4] *Hesselbach, J.; Raatz, A. (eds.)*: mikroPRO Untersuchung zum Internationalen Stand der Mikroproduktionstechnik. In: Schriftenreihe des Instituts für Werkzeugmaschinen und Fertigungstechnik der TU Braunschweig, Vulkan Verlag, 2002
- [5] *Slocum, Alexander H.*: Precision Machine Design. Society of Manufacturing Engineers, Dearborn, Michigan, 1992
- [6] *Neugebauer, R.; Schubert, A.; Koriath, H.-J.; Schulz, B.* Friction-Free TCP-Kinematic for Tilt Micro Manipulator. In Proceedings of the 3<sup>rd</sup> euspen Conference, Aachen, 2003, pp. 77-80
- [7] *Schulz, B.; Koriath, H.-J.; Freitag, H.*: Highest Precision Micromachining and Assembly Systems. In Proceedings of 8<sup>th</sup> CIRP International Workshop on Modeling of Machining Operations, May 10-11, 2005, Chemnitz, pp. 603-610

---

## Development of a Design Tool for Machine Tools Combining Conceptual Design Support and Detail Design Method

Nozomu Mishima, Advanced Manufacturing Research Institute, AIST, 1-2 Namiki, Tsukuba, Ibaraki, 305-8564 JAPAN T: +81-29-861-7227 F: +81-29-861-7201 Email: n-mishima@aist.go.jp

### 1 Backgrounds

Machine tool design has been a rather experience-based procedure. However, the products machined by those machine tools tend to have more varieties and quantity deviation. In response to the situation, not only the products design, but also the machine tools design should have efficiencies. For that purpose, a design tool which can review machine tools design in its early stage whether the design is appropriate or not, will be helpful. The design tool does not need to be too accurate in predicting machine tool performance. But it should review machine tool design without prototyping or precise modeling. In order to support machine tool design, the author proposed a design tool [1]-[3] combines the form-shaping theory [4] of machine tools and the Taguchi method [5]. Originally, the form-shaping theory assumes that the structural components of the machine tool are rigid objects. However, deformation of the machine tool structures such as deformation caused by static force or heat affect the machine tool performance significantly. The proposed design tool offers a simplified method to consider those deformations of machine tool structure, combining with component errors which are also critical for machine tool performances. By this extension, the design tool can clarify which error factors of machine tools have considerable effect on the performance. By doing this, it can support systematic design of machine tools.

### 2 Design evaluation method

A machine tool structure can be thought of as a chain of directly linked rigid components extending from the product through the cutting tool. An orthogonal coordinate system  $S_i$  corresponding to element  $i$  ( $i = 0$  to  $k$ ) is defined. The translation from  $S_i$  to  $S_{i+1}$  is represented by a coordinate transformation. Form-shaping theory represents these respective coordinate transformations by homogeneous transformation matrices [7];  $A_i$ . In an ordinary machine tool,  $A_i$  is represented by a parallel translation along the  $x$ ,  $y$  or  $z$  axes or rotation around the axes. Each of these six coordinate transformations is assigned a distinguishing number, with

movement parallel to the  $x$ -axis being 1, and so on. When the homogeneous transformation matrices  $A_i$  are represented by the transformations  $j_i$ , ( $= 1$  to 6), and the amount of each motion is represented by  $l_i$ , we define  $A(i)(j_i)(l_i)$  as the expression of the matrices. Vector  $\vec{r}_0$  represents the relative displacement between the product and the tool, and the tool shape vector  $\vec{r}_t$  is also defined. The relation between  $\vec{r}_0$  and  $\vec{r}_t$  is as given by equation (1), and  $\vec{r}_0$  is the definition of the form-shaping function that expresses the cutting motions of the machine tool. The theory that expresses cutting motions mathematically is called form-shaping theory. Actual machine tools have imperfect alignment, and experience thermal deformation, wear, and many other sources of error. In order to describe actual cutting motions, one must take these errors into account. Such errors may for convenience's sake be treated as errors in transformations between elements. I defined another homogeneous transformation matrix  $A_{ei}$  (eq. (2)) to generally represent transformation error between elements. By inserting the error component matrix  $A_{ei}$  between  $A(i)(j_i)(l_i)$  and  $A(i+1)(j_{i+1})(l_{i+1})$  into equation (1), the form-shaping function including errors,  $\vec{r}_{e0}$  is written as equation (3). The form-shaping error function  $\Delta \vec{r}_0$ , expressing the error as a quantitative deviation from the target value, is defined as the difference between the form-shaping function with and without errors, as equation (4). The form-shaping error function  $\Delta \vec{r}_0$  is a 4 dimensional vector which has error lengths in the  $x$ ,  $y$ ,  $z$  directions for the first three elements. The last element of  $\Delta \vec{r}_0$  is 0, because  $\Delta \vec{r}_0$  is defined as the difference between  $\vec{r}_0$  and  $\vec{r}_{e0}$ .

$$\vec{r}_0 = A(0)(j_0)(l_0) \cdot \cdot A(i)(j_i)(l_i) \cdot A(i+1)(j_{i+1})(l_{i+1}) \cdot \cdot A(k-1)(j_{k-1})(l_{k-1}) \vec{r}_t \quad (1)$$

$$A_{\varepsilon_i} = \begin{bmatrix} 1 & -\gamma_i & \beta_i & \delta_{xi} \\ \gamma_i & 1 & -\alpha_i & \delta_{yi} \\ -\beta_i & \alpha_i & 1 & \delta_{zi} \\ 0 & 0 & 0 & 1 \end{bmatrix} \quad (2)$$

$$\begin{aligned} \vec{r}_{\varepsilon_0} &= A(0)(j_0)(l_0)A_{\varepsilon_0} \cdots A(i)(j_i)(l_i)A_{\varepsilon_i} \\ &A(i+1)(j_{i+1})(l_{i+1})A_{\varepsilon_{i+1}} \cdots \\ &A(k-1)(j_{k-1})(l_{k-1})A_{\varepsilon_{k-1}} \cdot \vec{r}_t \end{aligned} \quad (3)$$

$$\Delta \vec{r}_0 = \vec{r}_{\varepsilon_0} - \vec{r}_0 \quad (4)$$

To achieve a machining tolerance that is stable under a variety of machining conditions, a method is needed to obtain a design that is robust with respect to unknown local errors. The Taguchi method is widely used in the field of quality engineering, and provides an environment for robust design. This study uses the Taguchi method to evaluate the dimensional effect imposed on machining errors by the machine structure, when local errors are unknown. Analysis was performed by applying the method to the form-shaping error function. The Taguchi method allows us to calculate combinations of values of control factors to optimize an evaluation function, when given noise factors fluctuate within given ranges. In this study, the primary objective is to determine the effect on machining performance of structural design, when some local errors exist in the various components of the machine tool. Therefore, it is appropriate to use the design parameters and product dimensions as control factors and the local errors as noise factors. We define  $\Delta x$ ,  $\Delta y$ ,  $\Delta z$  as the magnitudes of the errors in each direction. In other words,  $\Delta x$ ,  $\Delta y$ ,  $\Delta z$  are the first 3 elements of the form-shaping error function defined by equation (4). Then  $(\Delta x^2 + \Delta y^2 + \Delta z^2)^{1/2}$  is used as the evaluation function and the quantity that indicates machine performance. As the Taguchi method presents, orthogonal arrays are applied to the defined control and noise factors. When the value of the evaluation function at  $i$ th trial is expressed as equation (5) and the number of trials is “ $n$ ”, the average of the function is given by equation (6). And with  $V$  being the variance of the function, the SN ratio, which indicates the robustness of machine performance to the noise factors, is expressed by equation (7).

$$f_{ei} = (\Delta x^2 + \Delta y^2 + \Delta z^2)^{1/2} \quad (5)$$

$$f_{em} = \sum_{i=1}^n f_{ei} / n \quad (6)$$

$$Sn = -10 \log(V + f_{em}) \quad (7)$$

### 3 Consideration of structural deformations

Although the original form-shaping theory does not handle structural deformations, those have significant effects on machine tool performance. Therefore, most CAE tools try to calculate the deformations. However, CAE tools are not very efficient in handling component errors such as straightness errors of slides, etc. Since they based on a modeling of macroscopic shape of the machine structure, it is difficult to simulate errors caused by meso/microscopic behaviors of components, such as repetitive deviation of ball slides caused by slight differences of ball diameter, and so on. Of course it can be possible, but focusing on meso/microscopic behaviors results enormous effort in simulating overall machine structure. And it is not a practical choice in design review of machine tools in its early design stage. Because of that, the paper proposed a method to combine form-shaping theory with calculation of structural deformation based on FEM. Considered structural deformations are categorized and shown below.

- (1) Deformation caused by static force.
  - a) Deformation caused by machine weight
  - b) Deformation caused by cutting force
- (2) Thermal deformation.
  - a) Thermal deformation of a tool caused by cutting heat.
  - b) Thermal deformation of a spindle caused by heat generation at the motor/bearing.
  - c) Thermal deformation caused by external heat sources

To take these error factors into account, a relatively simple machine tool structure was assumed and deformation of each component caused by abovementioned error sources was calculated. Not only the structural deformation, but also component errors such as eccentricity of bearings or straightness errors of slides should be considered. Component errors are also important for overall machine performance. As it was mentioned, to calculate component errors would not be easy. So, the paper assumed component errors by using guaranteed value in component catalogs. Sum total of the calculated structural deformation and component errors are equivalent to the geometric errors of the machine tool element that can be written generally by equation (2) in the previous section.

### 4 Design options

In creating a new design concept, there are many possible structures that have different sequences of motion axes. The issue is how to apply the proposed design evaluation method to create a design concept for a machine tool. The performance of several designs can be compared by introducing some assumptions into the Taguchi method. By assuming that every design concept has the same control factors, noise factors and their ranges of variation, the results calculated by the Taguchi method are expected to show the rank order of the designs directly. By means of this extension, a machine tool designer can determine the best design concepts for machine tools from several listed designs. Tracking the components from the workpiece to the cutting

tool, it is possible to categorize machine tool structures by the number of components that appear before the machine tool base. It is common to represent translational motions along the  $X$ ,  $Y$  and  $Z$  axes as 1, 2 and 3, and rotational motions around the  $X$ ,  $Y$  and  $Z$  axes as 4, 5 and 6. Using this convention, milling machines that have three translational motions and one spindle rotation can be categorized into 4 major structural types, by the distribution of DOF. Those 4 are shown in Fig. 1. (a) –(d). Type 12036 is frequently seen in small/medium size drilling machines. Type 20136 is called a column-traverse type machine and is often used for relatively large products such as automobile parts, because it does not require extra space for table movement. Type 01236 is sometimes seen in a manufacturing system called “transfer line,” while type 12306 is rarely seen in actual machine tools. A significant question is which of the four commonest types has the best theoretical performance. To isolate the effect of machine tool structure, common design parameters and noise factors were defined. Tables 1 and 2 show the defined noise and control factors.

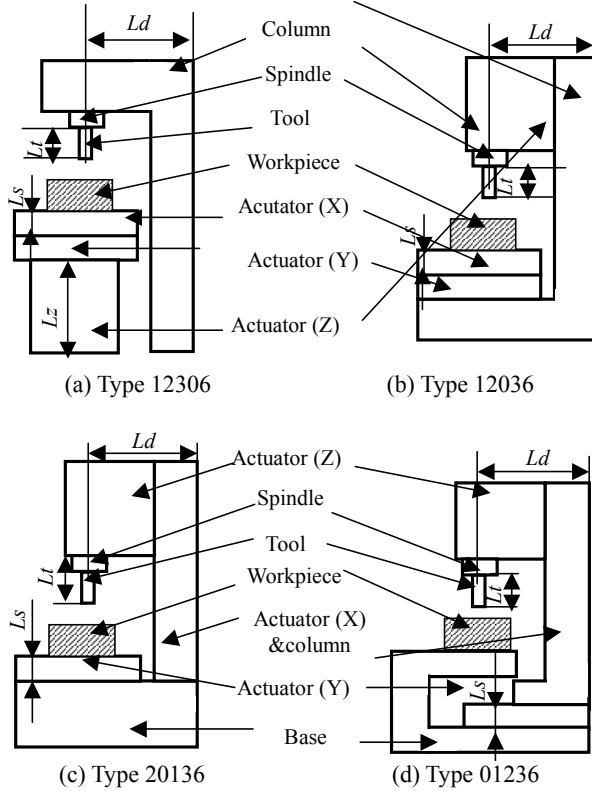


Fig.1 Design options of milling machines

Table 1 Control factors

Factor name	Variable
Workpiece size	$W_s$
Bearing diameter	$Db$
Rotational speed	$N$
Tool length	$L_t$
Spindle - column distance	$L_d$
Thickness of the linear actuators	$L_s$

Table 2 Noise factors

Name of the factor	Variable
Rotational errors of the horizontal guide ways	$\alpha_1$
	$\beta_1$
	$\gamma_1$
Axial error of the horizontal guide ways	$\delta_{x1}$
Straightness error of the horizontal guide ways (H)	$\delta_{y1}$
Straightness error of horizontal guide ways (V)	$\delta_{z1}$
Rotational errors of the vertical guide way	$\alpha_3$
	$\beta_3$
	$\gamma_3$
Straightness error of the vertical guide way (H)	$\delta_{x3}$
Straightness error of the vertical guide way (V)	$\delta_{y3}$
Axial error of the vertical guide way	$\delta_{z3}$
Rotational errors of the spindle	$\alpha_4$
Eccentricity of the spindle	$\delta_{x4}$
Expansion of the spindle	$\delta_{z4}$

These factors were defined in four machine tool types to clarify the effect of machine tool structure on machine performance. The six control factors,  $W_s$ ,  $Db$ ,  $N$ ,  $L_t$ ,  $L_d$  and  $L_s$  from Table 1 were considered to be independent control factors. At the same time,  $L_d$  was selected to represent the overall size of the machine tool. An L25 array was used for the control factors, and an L16 array for 15 noise factors shown in Table 2. Each form-shaping error function ( $\Delta \vec{V}_0$  for the design shown in Fig. 1) can be expressed using the parameters defined in Tables 1 and 2. Equations (8) – (11) are the form shaping error functions of milling machines corresponding to the design candidates shown in Fig. 1(a) - (d). A designer needs to compare these four equations to evaluate the performance difference of the designs with the same control and noise factors.

$$\begin{bmatrix} \Delta x \\ \Delta y \\ \Delta z \\ 0 \end{bmatrix} = \begin{bmatrix} \delta_{x1} + \delta_{y1} + \delta_{x3} + \delta_{x4} - \beta_4 \cdot L_t + \beta_3 \cdot (L_z + 2L_s) \\ + \alpha_1(2L_s + h) + \beta_1(L_s + h) - \gamma_1 \cdot d \\ \delta_{x1} + \delta_{y1} + \delta_{y3} + \delta_{x4} - \alpha_3 \cdot (L_z + 2L_s) \\ - \beta_1 \cdot (2L_s + h) - \alpha_1 \cdot (L_s + h) \\ 2\delta_{z1} + \delta_{z3} - \delta_{z4} + \alpha_1 \cdot d \\ 0 \end{bmatrix} \quad (8)$$

$$\begin{bmatrix} \Delta x \\ \Delta y \\ \Delta z \\ 0 \end{bmatrix} = \begin{bmatrix} \delta_{x1} + \delta_{y1} + \delta_{x3} + \delta_{x4} - (\beta_3 + \beta_4) \cdot L_t \\ + \alpha_1(2L_s + h) + \beta_1(L_s + h) - \gamma_1 \cdot d \\ \delta_{x1} + \delta_{y1} + \delta_{y3} + \delta_{x4} - (\alpha_3 + \alpha_4) \cdot L_t \\ - \beta_1 \cdot (2L_s + h) - \alpha_1 \cdot (L_s + h) \\ 2\delta_{z1} + \delta_{z3} - \delta_{z4} + \alpha_3 \cdot L_d + \alpha_1 \cdot d \\ 0 \end{bmatrix} \quad (9)$$

$$\begin{bmatrix} \Delta x \\ \Delta y \\ \Delta z \\ 0 \end{bmatrix} = \begin{bmatrix} \delta_{x1} + \delta_{y1} + \delta_{x3} + \delta_{x4} - (\beta_3 + \beta_4) \cdot Lt \\ + (\alpha_1 + \beta_1)(Ls + h) - (\gamma_1 + \gamma_3) \cdot Ld \\ \delta_{x1} + \delta_{y1} + \delta_{y3} + \delta_{x4} - (\alpha_3 + \alpha_4) \cdot Lt \\ - (\alpha_1 + \beta_1)(Ls + h) + \gamma_1 \cdot w \\ 2\delta_{z1} + \delta_{z3} - \delta_{z4} + (\alpha_1 + \alpha_3)Ld - \alpha_1 \cdot w \\ 0 \end{bmatrix} \quad (10)$$

$$\begin{bmatrix} \Delta x \\ \Delta y \\ \Delta z \\ 0 \end{bmatrix} = \begin{bmatrix} \delta_{x1} + \delta_{y1} + \delta_{x3} + \delta_{x4} - (\beta_3 + \beta_4) \cdot Lt + \alpha_1(2Ls + h) \\ + \beta_1(Ls + h) - (\gamma_1 + \gamma_3) \cdot Ld - 2\gamma_1 \cdot d \\ \delta_{x1} + \delta_{y1} + \delta_{y3} + \delta_{x4} + (\alpha_3 + \alpha_4) \cdot Lt \\ - \beta_1(2Ls + h) - \alpha_1(Ls + h) + \gamma_1 \cdot w \\ 2\delta_{z1} + \delta_{z3} - \delta_{z4} + (\alpha_1 + \alpha_3)Ld - \beta_1 \cdot w \\ 0 \end{bmatrix} \quad (11)$$

### 5 Design review of machine tools

The same ranges of noise factors and design parameters were estimated roughly, and substituted into the four forming error functions shown in the previous section. In the calculation, the scale effects of the noise factors were also considered. For example, the “expansion of the spindle” is likely to be smaller, when the machine tool size is small. Fig. 2 shows comparisons of the theoretical performance. According to the figure, when the design parameters vary within the defined ranges, the lines marking the positioning error of type 12036 are always the lowest, and those of type 12306 are the highest. Among the 6 control factors, “*Ld*,” which represents the spindle-column distance, is the most critical parameter affecting machine performance. The figure shows that type 12036 has better theoretical performance than types 12306 and 01236. Based on these results, type 12036 was selected as the “best” design for a milling machine from the 4 options shown in fig. 1. Next fig.3 shows the more detailed analysis of the effect of machine tool size which is represented by “*Ld*”. The horizontal axis of the figure shows that the “*Ld*” divided by that of the standard machine tools. The sizes of the machine tools were assumed to be changed proportionally.

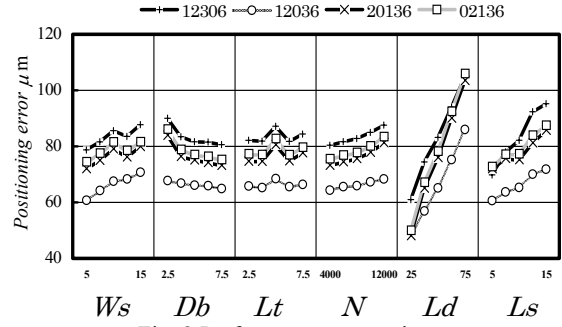


Fig. 2 Performance comparisons

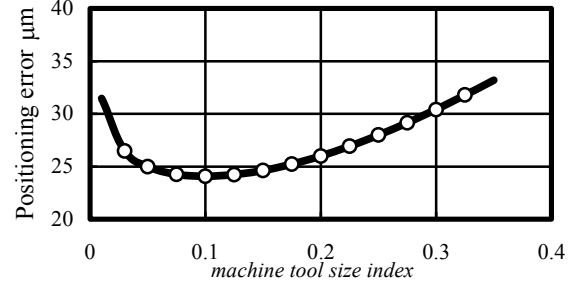


Fig.3 Effect machine tools size

According to fig.3, it can be said that, considering only the theoretical positioning errors, a machine tool that is 1/10 of the standard machine tool has the smallest error. Although there are many other design constraints and requirements for machine tools, a miniature machine tool having 1/10 size of the standard machine tool has a better theoretical performance. Especially, for micro mechanical fabrication which is getting practical and important in recent micro device productions, miniature machine tools are possible options for design. Actually some miniature machine tools have been developed and showed practical capability for machining. [8]-[11]

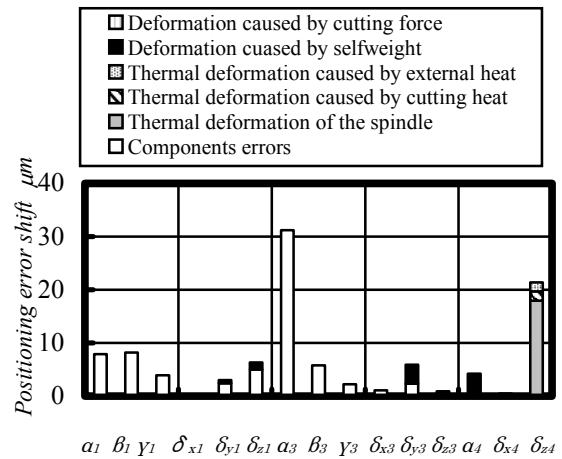


Fig.4 Contributions of error sources (standard)

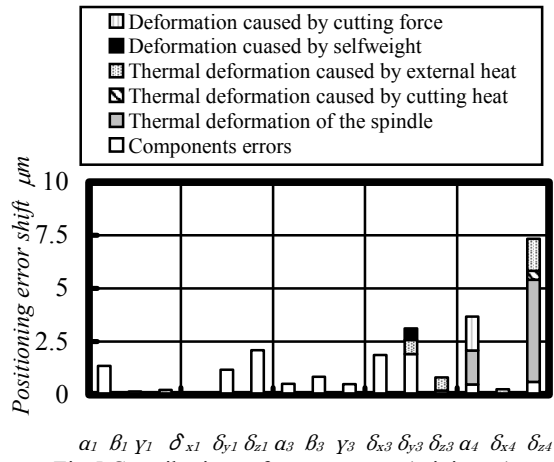


Fig.5 Contributions of error sources (miniature)

Fig.2 suggests which design parameter and fig. 4 and 5 indicate which error factors have large influence on the overall error amount. To calculate the error contributions shown in fig.4 and 5, noise factors defined in the table 2 were changed accordingly to the assigned range of each factors. The each bar shows the difference of the overall error amount when the corresponding noise factors take the lowest and highest value. The information suggests us to determine which design parameters should be designed carefully to obtain higher machining tolerance. And it also clarifies which machine components should have tight tolerance to improve the machine performance. From fig.2, following design suggestions about design parameters can be derived.

- 1) The most critical design parameters was the distance of the spindle from the slide.
- 2) The thickness of the slides and the product size had the next largest influence.
- 3) The diameter of the spindle and the rotational speed has relatively smaller impacts.
- 4) The length of the tool has no evident influence on the machine performance.

From fig.4 and 5, design review concerning error factors is possible. By comparing two figures, it is also possible to obtain design guidelines corresponding to the sizes of machine tools, such as, “when a machine tool designer designs a miniature machine tool, it these components and these error sources should be improved”, etc. Following descriptions are some of the results of the design review.

- 1) Rotational errors of the vertical guide way have the largest influence on the performance of the standard machine tool.
- 2) Rotational errors of the horizontal guide ways have relatively large impacts.
- 3) Thermal expansion of the spindle plays an important role both for the standard machine tool and the miniature machine. It has to be improved to obtain high accuracy.
- 4) For miniature machine tools, rotational errors of the vertical guide ways are not very important. Straightness

errors of slides are relatively important.

5) External heat sources are more critical for miniature machine tools than for standard machine tools.

6) Structural deformations caused by machine weight are negligible for the miniature machine tool.

## 6 Examination of the method

As calculated in the previous section, type 12036 was predicted to have the best performance among the 4 major types. And a miniature machine tools having 1/10 size of the standard machine is predicted to be the suitable size for micro mechanical fabrication. The best way to examine this result is to make milling machines actually and compare their positioning accuracies. However, producing milling machines of practical size would need too much time and budget, so miniature milling machines were prototyped based on the theoretical results. Fig. 6 show a schematic view of the miniature milling machine designed as an experimental model for the design evaluation tool. The machine has a 57.5 mm column-spindle distance. Positioning errors of the model were measured for comparison with the predicted results. At the same time, the prototyped miniature milling machine was used in the Microfactory project [6] and proved to have practical machining capability. Fig. 7 shows the actual miniature milling machine designed in Fig. 6. The machine size being approximately 12 x 12 x 10 cm, it was able to perform end-milling up to 2 mm in depth, and surface milling of an area up to 4 x 4 mm. DC servo motors were used for the linear and rotational motions. Fig.8 is the results of comparison of the measured errors and calculated errors for the miniature mill shown in fig.6. The figure shows that the measured errors are not very different from the calculated value. The fact leads us to conclude that the proposing design tool have sufficient accuracy for the usage in the conceptual design stage of machine tool.

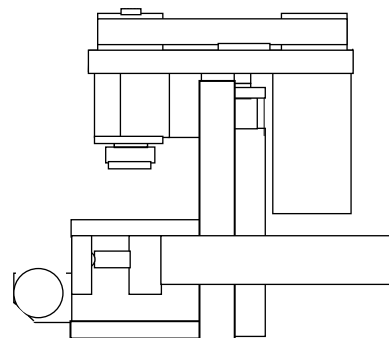


Fig. 6 Miniature mill design (type 12036)

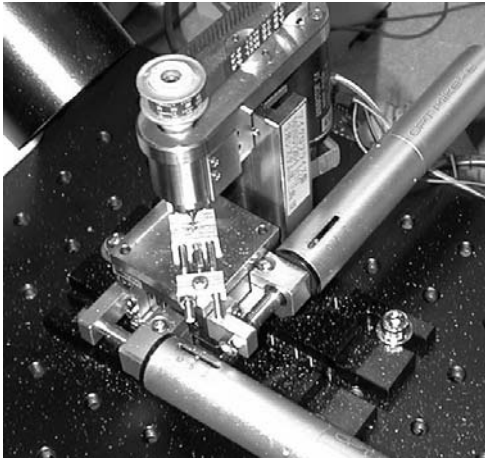


Fig. 7 Prototyped experimental model

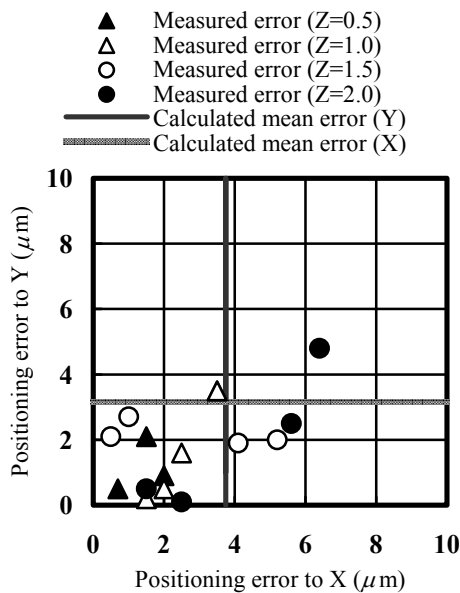


Fig.8 Comparison of measured and calculated errors

## 7 Conclusions

The proposed design evaluation tool was effective in identifying the critical design parameters and error factors of a machine tool. By combining a method which is suitable for determining which factors are significant for overall machine performance, and a method which can calculate structural deformation more precisely, it was possible to obtain guidelines for conceptual design of machine tools, without design experience and detailed calculation.

As the results of the design review, machine tool size which was represented by spindle-column distance had an important effect on machine performance. Therefore, designing a machine tool in a proper size is a good strategy for obtaining better performances by less cost. As for error sources, geometric errors of components, especially straightness errors of linear slides had significant influences

on machine performance. Thermal expansion of the main spindle was also a critical source of error. The results led us to conclude that, in designing a precise miniature machine tool, these errors should be minimized or eliminated.

Calculated and measured errors of a miniature milling machine which was originally developed for the microfactory, were compared to prove the effectiveness of the design tool. The results showed a good match and proved that the design method was effective enough for conceptual design of machine tools.

## References

- [1] Mishima, N. and Ishii K., Robustness Evaluation of a Miniaturized Machine Tool, Proc. of ASME/DETC99. Las Vegas, Sept. 1999.
- [2] Mishima, N., Ashida, K., Tanikawa, T. and Maekawa, H., Design of a Microfactory, Proc. of ASME/DETC 2002, Montreal, Canada, Sept. 2002.
- [3] Mishima, N., Design of a Miniature Manufacturing System for Micro-fabrication, Proc. of 10th Annual Conference for Concurrent Engineering, Madeira, Portugal, July 2003, pp.1129-1135.
- [4] Reshtov, D.N. and Portman, V.T., Accuracy of Machine Tools, ASME Press, New York, (1988).
- [5] Taguchi, G. and Konishi, S., Quality Engineering Series, ASI Press. (1994).
- [6] Okazaki, Y., Mishima, N and Ashida, K., Microfactory -Concept, History and Developments-, Journal of Manufacturing Science and Engineering, Trans. ASME, Vol.126, pp.837-844, Nov. 2004.
- [7] Paul, R.P., Robot Manipulators, THE MIT press, Cambridge (1981).
- [8] Kitahara, T., Ishikawa, Y., Terada, K., Nakajima, N., and Furuta, K., Development of Micro-lathe, Journal of Mechanical Eng. Lab., Vol. 50, No. 5 (1996), pp. 117-123.
- [9] Okazaki, Y. and Kitahara, T, Micro-lathe to Machine Micro-parts, Proc. of ASPE 15th Annual Meeting, Phoenix, USA, Oct. 2000, pp.575-578.
- [10] Iijima, D. et. al., A Super Small CNC Precision Lathe for Microfactories, Proc. of 3<sup>rd</sup> International Workshop on Microfactories, Shanghai, China, Oct. 2004, pp./37-40.
- [11] Volger, M. et. al., Miniaturized machine tools for CNC based micro/meso scale machining of 3D features, Proc. of 3<sup>rd</sup> International Workshop on Microfactories, Shanghai, China, Oct. 2004, pp-45-48.



---

# Precision Contouring Control of Multi-Axis Feed Drive Systems

Naoki Uchiyama<sup>1</sup>, Shigenori Sano<sup>1</sup>, Shoji Takagi<sup>1</sup>, Kazuo Yamazaki<sup>2</sup>

<sup>1</sup>Toyohashi University of Technology, Japan, <sup>2</sup>University of California, Davis, USA

Keywords: Feed Drive System, Machine Tool, Contouring Control

## Abstract

In order to improve the contouring accuracy in machine tool control, using the contour errors, which is defined as tracking error component orthogonal to desired contour curves, as feedback signals is known to be effective. This paper presents a new contouring control method for multi-axis feed drive systems. The method is applicable to any smooth contour curves and achieves better control performance with small control input variance compared to the conventional methods. The effectiveness of the proposed method is demonstrated by experimental results with the circular and non-circular contour curves.

## 1 Introduction

Feed drive systems are used in most of machine tool systems, and positional errors are generally defined with respect to each axis of the feed drive systems (tracking errors) in their control systems. From the viewpoint of machining, however, error components orthogonal to desired contour curves are rather important than the errors with respect to the feed drive axes. The orthogonal error components to the contour curves are called contour errors.

There have been many researches focusing on the reduction of the contour errors. Koren proposed a cross-coupling controller that uses the contour errors as feedback signals [1]. Kulkarni and Srinivasan developed an optimal cross-coupled controller based on a linear quadratic regulator (LQR) [2]. Chiu and Tomizuka presented a controller based on the technique of integrator backstepping, though implicit representation of the contour curve is needed for the controller design [3]. McNab and Tsao formulated the contour tracking as a receding horizon LQ problem with variable state weighting matrices. They proved the stability for linear trajectory case [4].

Since both the contour errors and the tracking errors are used to calculate control inputs in these methods, there may be degradation of contour tracking performance. Considering both the tracking and the contour errors simultaneously brings some difficulties in adjusting controller parameters.

In order to overcome this problem, Lo and Chung proposed a contouring control method based on a coordinate transformation for biaxial feed drive systems [5], in which tracking errors are transformed into the errors with orthogonal and tangential components to the desired contour

curves. They proved the stability of their method only for straight-line trajectory motion. Since, in their method, two decoupled single-input single-output systems with respect to the orthogonal and tangential directions are obtained, controllers for both directions can be designed independently, and hence controller parameters are adjusted rather easier. Their method, however, is effective only for the case that the mismatch of the dynamics of both feed drive axes is enough small. The case is practically impossible since one-axial feed drive system reposes on the other in most of biaxial feed drive systems.

In this paper, we propose a new contouring control method based on a complete coordinate transformation of the tracking errors. The proposed method allows the feed drive systems to have the dynamics mismatch between each axis. And also, the stability of control systems is guaranteed to any smooth contour curves. The effectiveness of the proposed method is demonstrated by experimental results with circular and non-circular contour curves.

## 2 Problem Formulation

### 2.1 Definition of Contour Errors

In this paper, we consider the 3 dimensional case as shown in Fig. 1, where the curve  $c$  is the desired contour of a point of the feed drive system. The symbol  $\Sigma_w$  is a fixed coordinate frame whose axes correspond to the feed drive axes. The symbol  $r = [r_1 \ r_2 \ r_3]^T$  is a desired position of the feed drive system at time  $t$ , and defined with respect to  $\Sigma_w$ . The actual position of the feed drive system is assumed at  $x = [x_1 \ x_2 \ x_3]^T$ . We further define a local coordinate frame  $\Sigma_l$  whose origin is at  $r$  and three axes are  $l_i$  ( $i=1,2,3$ ) in the figure. The axis  $l_1$  is in the tangential direction of  $c$  at  $r$ . The direction of  $l_2$  is perpendicular to  $l_1$  and in the tangential plane of the machined surface at  $r$ . The direction of  $l_3$  is perpendicular to both  $l_1$  and  $l_2$  as shown in Fig. 1.

The tracking error vector  $e_w$ , which consists of tracking errors of each feed drive axis, is defined as follows:

$$e_w = [e_{w1} \ e_{w2} \ e_{w3}]^T = r - x. \quad (2.1)$$

This error vector can be transformed into that with respect to  $\Sigma_i$  as follows:

$$e_i = [e_{i1} \ e_{i2} \ e_{i3}]^T = R^T e_w, \quad (2.2)$$

where  $R$  is a  $3 \times 3$  rotation matrix that transforms a position with respect to  $\Sigma_i$  into that to  $\Sigma_w$ .

From the viewpoint of machining, error components orthogonal to the desired contour curve are rather important than the tacking errors of feed drive axes. Hence we propose a controller design that allows us to adjust the control performance with respect to three axes of  $\Sigma_i$  independently each other. In the design, we can set the controller gain for reducing the error along  $l_1$  to smaller value than that for the other axes from the reason that the tangential error component to the contour curve is less important than the orthogonal ones. It also should be noted that the error components  $e_{i2}$  and  $e_{i3}$  are just approximate values of contour errors, because even if they are reduced to zero by some controllers, the position  $\hat{x}$  in Fig. 1 moved from  $x$  is not still on the curve  $c$ . It is, however, difficult to calculate actual contour errors online because we need to solve nonlinear equations if the contour curve is not a simple one. For this reason, the control objective of the proposed system is to reduce the error components  $e_{i2}$  and  $e_{i3}$ . They may be good approximations of contour errors if the error component  $e_{i1}$  is small.

## 2.2 Plant Dynamics

In this paper, we consider the feed drive system driven by servo motor systems, which are commonly used as industrial applications. The feed drive dynamics is generally represented by the following decoupled second order system:

$$\begin{aligned} M\ddot{x} + C\dot{x} &= F, \\ M &= \text{diag}\{M_i\}, C = \text{diag}\{C_i\}, i=1,2,3, \\ F &= [F_1 \ F_2 \ F_3]^T, \end{aligned} \quad (2.3)$$

where  $M_i (> 0)$ ,  $C_i (\geq 0)$  and  $F_i$  are the mass of load, the viscous friction coefficient and the driving force on the  $i$  th drive axis, respectively. The symbol  $\text{diag}\{A_i\}$  is a diagonal matrix with the element  $A_i$  at the  $i$  th row. Nonlinear frictions such as Coulomb frictions are not explicitly considered in this dynamics.

The dynamics of the motors for driving the feed drive systems is described as follows:

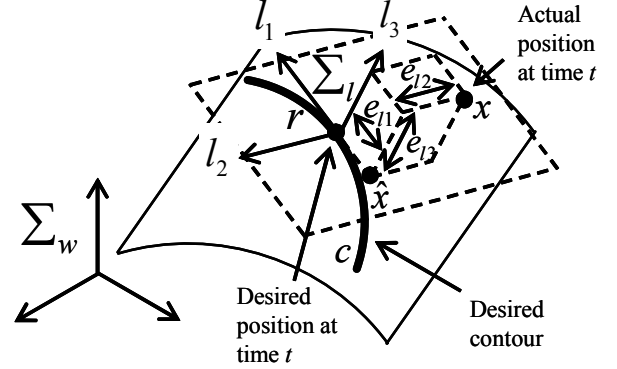


Fig. 1. Definition of tracking errors

$$\begin{aligned} J\ddot{\theta} + D\dot{\theta} + \tau &= KV, \\ J &= \text{diag}\{J_i\}, \quad D = \text{diag}\{D_i\}, \\ K &= \text{diag}\{K_i\}, \quad i=1,2,3, \\ \tau &= [\tau_1 \ \tau_2 \ \tau_3]^T, \quad V = [V_1 \ V_2 \ V_3]^T, \end{aligned} \quad (2.4)$$

where  $J_i (> 0)$ ,  $D_i (\geq 0)$ ,  $K_i (> 0)$ ,  $\tau_i$  and  $V_i$  are the motor inertia, the motor viscous friction coefficient, the torque-voltage conversion ratio, the torque for driving the feed drive system Eq. (2.3) and the motor input voltage of the  $i$  th axis, respectively.

The relation among the force  $F_i$ , torque  $\tau_i$ , position  $x_i$ , angle  $\theta_i$  and pitch of the ball screw  $P_i$  are represented as follows:

$$F_i = \frac{2\pi\tau_i}{P_i}, \quad x_i = \frac{P_i\theta_i}{2\pi}. \quad (2.5)$$

## 3 Controller Design

We assume the followings on the controller design:

- The desired trajectory  $r_i$ , and its derivatives  $\dot{r}_i$  and  $\ddot{r}_i$  are available.
- The rotation matrix  $R$ , and its derivatives  $\dot{R}$  and  $\ddot{R}$  are available.
- The position of the feed drive system  $x$  and its derivative  $\dot{x}$  are measurable.
- The plant parameters  $M, C, J, D, K$  and  $P_i$ 's are all available.

Since the matrix  $R$  is a function of the desired trajectory, we can calculate it and its derivatives beforehand. Hence the second assumption is not a strict one.

We propose the following control:

$$\begin{aligned}
 V &= H \left\{ \ddot{x} - R(-K_{vl}\dot{e}_l - K_{pl}e_l - \ddot{R}^T e_w - 2\dot{R}^T \dot{e}_w) \right\} + E\dot{x}, \\
 H &= \text{diag} \left\{ \frac{M_i + J_i(2\pi/P_i)^2}{2\pi K_i/P_i} \right\}, \\
 E &= \text{diag} \left\{ \frac{C_i + D_i(2\pi/P_i)^2}{2\pi K_i/P_i} \right\},
 \end{aligned} \quad (3.1)$$

where  $K_{vl}$  and  $K_{pl}$  are the so-called velocity and position feedback gain matrices, and we assume that they are also the diagonal matrices with all positive elements. Considering Eqs. (2.1)-(2.5) and (3.1), we have the following relation:

$$HR(\ddot{e}_l + K_{vl}\dot{e}_l + K_{pl}e_l) = 0. \quad (3.2)$$

Since  $H$  and  $R$  are nonsingular matrices, we have

$$\ddot{e}_l + K_{vl}\dot{e}_l + K_{pl}e_l = 0. \quad (3.3)$$

From the above equation, it is concluded that by appropriately assigning the feedback gain matrices  $K_{vl}$  and  $K_{pl}$  in Eq. (3.1), we can achieve  $e_l \rightarrow 0$  as  $t \rightarrow \infty$ . And also we can independently adjust the error convergence speed along each axis of  $\Sigma_l$  in Fig. 1 since the matrices  $K_{vl}$  and  $K_{pl}$  are both diagonal. Setting the feedback gains with respect to  $e_{l2}$  and  $e_{l3}$  larger than that for  $e_{l1}$ , we may reduce the contour errors faster than the tracking error tangential to the desired contour curve.

In order to comparatively see the effectiveness of the proposed design, we consider the following non-contouring control using the error signals on  $\Sigma_w$ :

$$V = H(\ddot{x} + K_{vw}\dot{e}_w + K_{pw}e_w) + E\dot{x}, \quad (3.4)$$

where  $K_{vw}$  and  $K_{pw}$  are the  $3 \times 3$  velocity and position feedback gain matrices on  $\Sigma_w$ . The matrices are assumed also to be diagonal with positive elements. Then we can have the following error dynamics on  $\Sigma_w$ :

$$\ddot{e}_w + K_{vw}\dot{e}_w + K_{pw}e_w = 0. \quad (3.5)$$

Both in Eqs. (3.3) and (3.5), we can have decoupled systems and assign control system poles to any places on the complex plane. For simplifying the analysis, we consider the case that the desired contour is a straight-line (i.e.,  $\dot{R} = \ddot{R} = 0$ ) and some gains are increased for reducing the contour errors. It is possible to assign greater values only to the second and third diagonal elements in  $K_{vl}$  and  $K_{pl}$  in Eq. (3.3) from the reason that they directly relate to the contour errors. This assignment is not possible in Eq. (3.5), because the relation between the controller gains and their effect to the contour

errors is not obvious. The dynamics Eq. (3.3) can be transformed into the following one on  $\Sigma_w$  with Eq. (2.2):

$$\ddot{e}_w + RK_{vl}R^T\dot{e}_w + RK_{pl}R^Te_w = 0. \quad (3.6)$$

Note that only the feedback gain matrices are different in Eqs. (3.5) and (3.6). Assuming that the first diagonal elements of  $K_{vl}$  and  $K_{pl}$ , which relates only to  $e_{l1}$ , are set smaller than the others in  $K_{vl}$ ,  $K_{pl}$ ,  $K_{vw}$  and  $K_{pw}$ , we can make the Frobenius norms of  $RK_{vl}R^T$  and  $RK_{pl}R^T$  in Eq. (3.6) smaller than those of  $K_{vw}$  and  $K_{pw}$  in Eq. (3.5). This means that the proposed design may achieve the similar contouring control performance with smaller feedback gains on  $\Sigma_w$ , which may provide a wider stability margin.

## 4 Experiment

We have designed both the control systems in Eqs. (3.3) and (3.5) for an X-Y table, which is driven by DC servo motors and ball screw drives as shown in Fig. 2, and experimentally compared the control performances. All the 3-dimensional vectors and matrices used in the previous sections are reduced to 2-dimensional ones in the following design. The 2-dimensional definitions of error signals are shown in Fig. 3, where the contour error is  $e_{l2}$ . In the 2 dimensional case, the matrix  $R$  in Eq. (2.2) is

$$R = \begin{bmatrix} \cos \theta & -\sin \theta \\ \sin \theta & \cos \theta \end{bmatrix}. \quad (4.1)$$

The nominal parameter values of the X-Y table are shown in Table 1. The position of the X-Y table is measured by linear scales attached to each drive axis, and the sensor resolution is  $0.1[\mu\text{m}]$ . The velocities of each drive axis are computed by the backward difference operation of the position measurements.

In the experiment, the circular contour curve as shown in Fig. 4 (a) is employed, namely,

$$r_1 = L_c \cos \omega t, \quad r_2 = L_c \sin \omega t, \quad (4.2)$$

where  $L_c = 3[\text{mm}]$ ,  $\omega = 2\pi/5[\text{rad/s}]$ . The control time  $T$  is  $10[\text{s}]$ . The actual contour error  $e_c$  can be calculated as follows:

$$e_c = \sqrt{x_1^2 + x_2^2} - L_c. \quad (4.3)$$

The closed loop poles of the dynamics for  $e_{l1}$  are set to  $q_{l1} = -30[1/\text{s}]$  as repeated poles, while those for  $e_{l2}$  are changed from  $q_{l2} = -30$  to  $-70$  by  $-20[1/\text{s}]$  as also the repeated poles. Namely the following feedback gain matrices are used for the error dynamics Eq. (3.3).

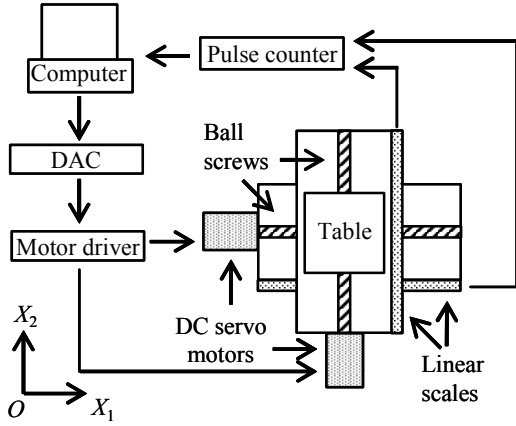


Fig. 2. Experimental system

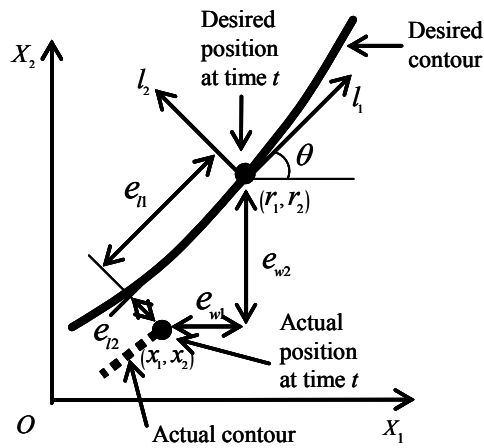


Fig. 3. Definition of errors for the experimental system

$$K_{vi} = [-2q_{i1} \quad -2q_{i2}]^T, \quad K_{pi} = [q_{i1}^2 \quad q_{i2}^2]^T. \quad (4.4)$$

On the other hand, in the experiment with the system Eq. (3.5), both the poles for the dynamics of  $e_{w1}$  and  $e_{w2}$  are changed from  $q_{w1} = q_{w2} = -30$  to  $-70$  by  $-20$  [1/s], and hence the following feedback gain matrices are used:

$$K_{vw} = [-2q_{w1} \quad -2q_{w2}]^T, \quad K_{pw} = [q_{w1}^2 \quad q_{w2}^2]^T. \quad (4.5)$$

As mentioned above, only in the proposed method, we can increase the controller gain for reducing the contour error as in Eq. (4.4), because the relation between the controller gain and the size of the contour error is obvious. Since the relation is not obvious in Eq. (3.5), we need to increase the controller gains for reducing tracking errors in both feed drive axes as in Eq. (4.5).

The experimental results are shown in Fig. 5, where (a)-(c) and (d)-(f) are the results by the conventional and the

Table 1. Parameter Values

Parameters	Values
$P_1$ & $P_2$	0.005 [m]
$M_1(P_1/2\pi)^2$ : load inertia moment of axis 1	1.30 [kgm <sup>2</sup> ]
$M_2(P_2/2\pi)^2$ : load inertia moment of axis 2	0.77 [kgm <sup>2</sup> ]
$C_1$ & $C_2$	0 [Ns/m]
$J_1$ & $J_2$	0.05 [Kgm <sup>2</sup> ]
$D_1$ & $D_2$	0.31 [Nm/(rad/s)]
$K_1$ & $K_2$	1.42 [Nm/V]

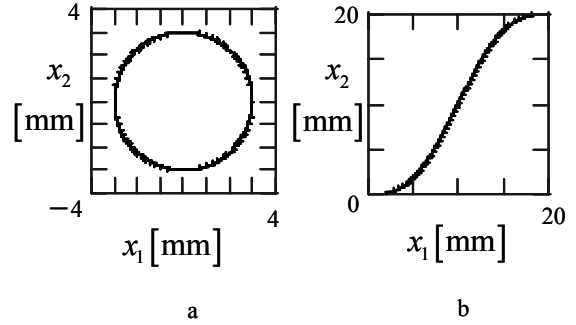


Fig. 4. Desired contour curves used in experiments

proposed methods, respectively.

Comparing the results (a) and (d), and (b) and (e), respectively, we can see that almost the same contour error and control input profiles are obtained. However comparing the results (c) and (f), we can confirm that the control input variance for the system Eq. (3.3) is much smaller than that for Eq. (3.5), and as a result, the size of the contour error in (c) is greater than that in (b) and (f).

The stability of the control system with the proposed methods is guaranteed for any contour curve, though this is not possible in some existent methods. In order to verify the effectiveness to non-linear and non-circular contour curves, we have also applied both the control systems to the following trajectory:

$$r_1 = L_n \frac{t}{T}, \quad r_2 = L_n \left\{ \frac{t}{T} - \frac{1}{2\pi} \sin\left(\frac{2\pi t}{T}\right) \right\}, \quad (4.6)$$

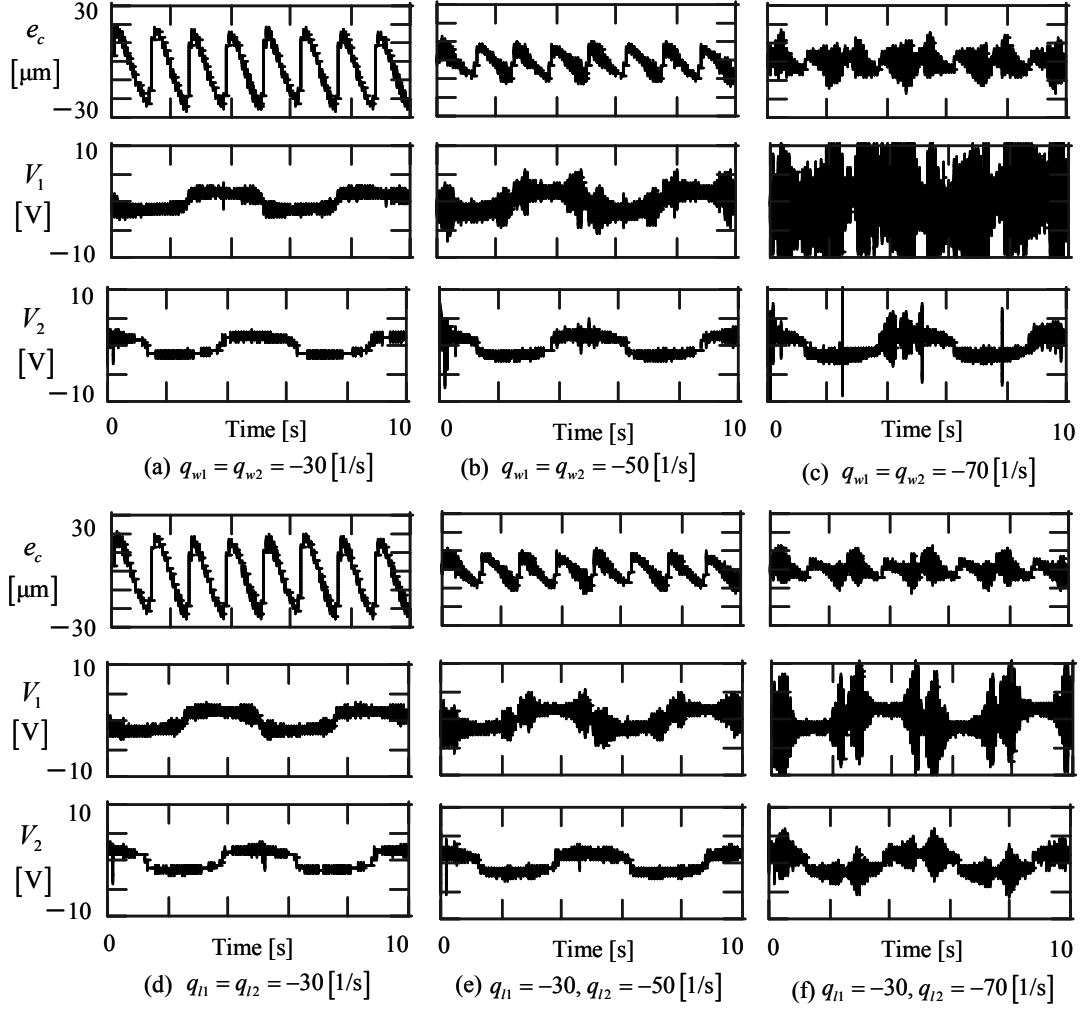


Fig. 5. Experimental results (Circular trajectory case, (a)-(c): Conventional, (d)-(f): Proposed)

where  $L_n = 20$  [mm] and  $T = 10$  [s]. The desired contour curve is shown in Fig. 4 (b). The actual contour error size is calculated by solving the following minimization problem:

$$|e_c| = \min_i \left\{ (r_1 - x_1)^2 + (r_2 - x_2)^2 \right\}. \quad (4.7)$$

The control results are shown in Fig. 6, where (a)-(c) and (d)-(f) are the results by the conventional and the proposed methods, respectively. Comparing (b) and (e), we can see that the variance of the control inputs is greater in (b). Also in the result (c), the variance of the control inputs is much greater than that in (f), and as a result, the size of the contour error in (c) is also greater than those in (b) and (f). From these experimental results, we can conclude that the

proposed method achieves the better control performance with smaller controller gain, because we can adjust the controller gain for reducing the contour error independently from the tracking error tangential to the contour curve.

## 5 Conclusions

We have proposed a new contouring method for multi-axis feed drive systems. The advantages are that the method can be applied to any smooth contour curve and the stability of the control systems is guaranteed if the plant dynamics is known. We have experimentally confirmed the effectiveness of the proposed method by comparisons with the conventional controllers. The proposed method achieves the

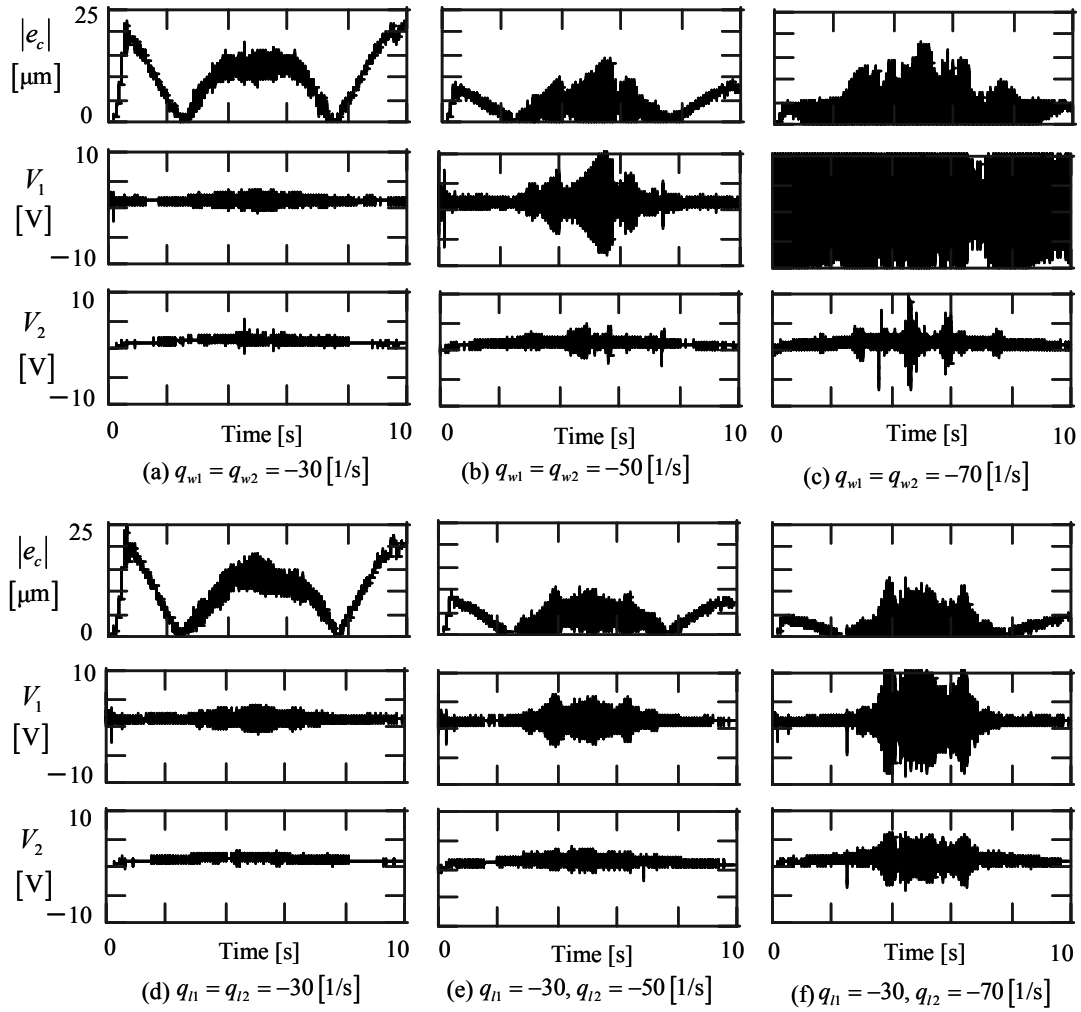


**Fig. 6.** Experimental results (Non-circular trajectory case, (a)-(c): Conventional, (d)-(f): Proposed)

better control performance with small control input variance because only the controller gains for reducing the contour errors can be increased.

In the current controller design, nonlinear frictions such as Coulomb frictions are not explicitly considered. Adding a nonlinear friction compensator to the proposed controller is expected to achieve the further better control performance. Furthermore, it is also expected to develop robust contouring controllers with respect to plant modeling errors.

## References

- [1] Koren, Y. (1980) Cross-coupled biaxial control for manufacturing systems, *ASME Journal of Dynamic Systems, Measurement, and Control*. 102:265–272.
- [2] Kulkarni, P. K., and Srinivasan, K. (1989) Optimal contouring control of multi-axis feed drive servomechanism, *ASME Journal of Engineering for Industry*. 111:140–148.
- [3] Chiu, G. T.-G., and Tomizuka, M. (1998) Coordinate position control of multi-axis mechanical systems, *ASME Journal of Dynamic Systems, Measurement, and Control*. 120:389–393.
- [4] McNab, R. J., and Tsao, T.-C. (2000) Receding time horizon linear quadratic optimal control, *ASME Journal of Dynamic Systems, Measurement, and Control*. 122:375–381.
- [5] Lo, C. C., and Chung, C.-Y. (1999) Tangential contouring controller for biaxial motion control, *ASME Journal of Dynamic Systems, Measurement, and Control*. 121:126–129.

---

# Areal Gear Flank Description as a Requirement for Optical Gear Metrology

Goch, Gert<sup>1</sup>, Günther, Anke<sup>2</sup>

<sup>1</sup>University of Bremen – BIBA, <sup>2</sup>Hexagon Metrology GmbH (Leitz)

Keywords: Areal Flank Modelling, Alignment, Optical Gear Measurement

## Abstract

Gear drive designers are confronted with increasing demands concerning lifetime, power transmission and noise emission, whereas the size and weight of gear drives is constantly reduced. Thus, the measurement of gears and gear tools is of decisive importance for gear production. This paper summarizes new modelling and measuring principles, enabling an areal description and an optical inspection of gears.

## 1 Introduction

The gear measurement inspection of today refers to a description of the nominal gear geometry, which is limited to only a few prescribed tracks across the flank (profile, lead) or singular points (pitch). Its origin dates back to the 30's of the past century, where only a "mechanical control" of conventional gear measuring devices could generate the required probing path along a nominal involute curve or a lead screw.

The technology at NC-measuring devices is opposed to this historical probing and evaluation along prescribed section lines. The correct evaluation of measured flanks either requires ideally mounted gears or a numerical alignment prior to flank probing. Otherwise the standardized profile and helix (lead) lines cannot be probed exactly. These requirements can only partially be fulfilled by specialised gear measuring devices with adapted mechanical alignment or by CMMs. Thus, errors inevitably occur during evaluation.

Moreover, new optical measuring devices like fringe projection or holographic systems can obtain several 10 000 points per flank within a few seconds, all containing valuable information about the actual gear flank. An evaluation strictly following the valid standards of gear metrology has to ignore the major part of this information.

Additionally, modern gear drives require more and more complex flank modifications (lead, crowning, twist, tip and root relief, k-charts, protuberance etc.), leading to a confusing increase of evaluation rules, conditions and exceptions.

Obviously, all three trends and difficulties explained before point out into the same direction: future gear metrology should enable an areal description, measurement and evaluation of (preferably all) gear flanks. It should also avoid time-consuming gear alignment prior to measurement. Instead, it is possible to fit all measured points according to the given nominal surface using a previously published numerical alignment algorithm. The self-contained mathematical sur-

face description of all tooth flanks offers a versatile, reliable and even more precise assessment of profile, helix and pitch deviations. This contribution gives a survey about the theoretical approaches, a series of simulations, evaluations and results.

## 2 Areal description and inspection of gear flanks

### 2.1 Areal mathematical description of involute gear flanks

The basic numerical equations describing the nominal surface of involute gears are known since about 70 years [1, 2]. Due to some manufacturing requirements, several approaches were published already in the 70's and 80's aiming at a complete mathematical description of gear flanks. But, due to restrictions in terms of calculation times, computer memory and computer hardware costs, these approaches were based on simple mathematical functions (polynoms, splines, etc.) and a low point density.

Today the continuing dramatically change in available computational resources offers new options in gear metrology and quality control for gear manufacturing processes [3-10]. They include the complete 3D-model of the whole gear, i. e. the gear body (shaft, wheel) and all gear flanks. The basic mathematical equation is a 3-dimensional extension of an involute function, shown in Figure 2.1. A point  $P$  is given in cartesian coordinates by

$$\begin{aligned}x &= r \cdot (\cos(\xi + \Lambda) + \xi \cdot \sin(\xi + \Lambda)) \\y &= r \cdot (\sin(\xi + \Lambda) - \xi \cdot \cos(\xi + \Lambda))\end{aligned}\quad (2-1)$$

with

$$\xi = \alpha + \text{inv } \alpha = \tan \alpha \quad (2-2)$$

$r$ : base radius,  $\alpha$ : pressure angle,  $\xi$ : roll angle,  $\beta$ : helix angle

The quantity  $\Lambda$  determines the origin of the involute at the base diameter. For helical gears, these intersection points follow a conventional screw.

$$\Delta\Lambda = \Lambda(z_2) - \Lambda(z_1) = \frac{(z_2 - z_1) \cdot \tan \beta}{r} \quad (2-3)$$

A pair of one left and right flanks differ by  $\Delta\Lambda = 2\eta_b$ , where  $\eta_b$  is the tooth space half angle at base diameter.

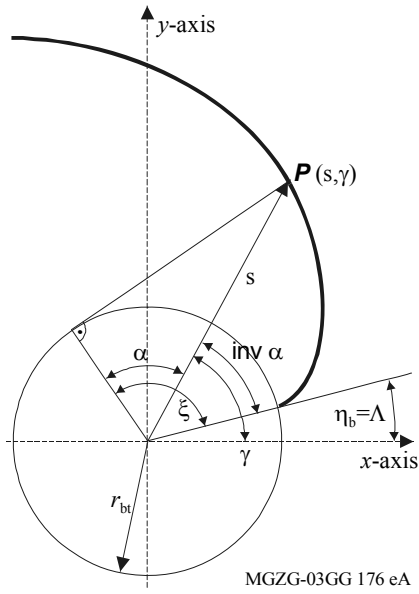


Fig. 2.1. Gear involute [3]

Thus, the 3D description of an involute flank without modifications is generated by a conventional involute function “screwed” along one helix line (Figure 2.2).

For further calculations, a certain intersection point of involute profile and lead screw is assumed at  $(x, y, z) = (r, \Lambda, 0)$ . Then equation (2-3) changes to

$$\Lambda = \eta_b + z \cdot \tan(\beta) / r \quad (2-4)$$

where lead and profile is limited by

$$0 \leq z \leq b; \quad b : \text{gear width}$$

$$\xi_{\min} \leq \xi \leq \xi_{\max}$$

This approach must be extended by introducing the flank modifications common for modern involute gears. The amount of modification is assumed as symmetrical for left and right flank. Profile inclination and profile crowning depicted in Figure 2.3 and described by equation (2-5) are linearly superimposed to the involute equations (2-1). In the same way, other profile modifications like protuberance, tip and root relief, k-charts, etc. may be added to the mathematical profile description. This still 2-dimensional involute

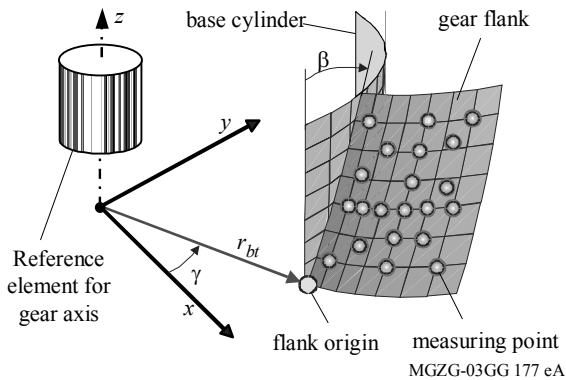
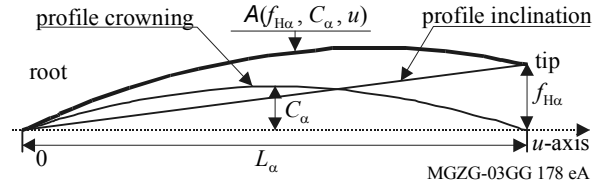


Fig. 2.2. 3D-model of a helical gear flank [10].



$C_\alpha$ : Profile crowning,  $f_{Ha}$ : Profile inclination,  $L_\alpha$ : Profile evaluation length

Fig. 2.3. Profile modifications [3, 5]

profile may end up in a rather complex function of 10 to 15 gear parameters.

$$A(f_{Ha}, C_\alpha, u) = \frac{-4 \cdot C_\alpha}{L_\alpha^2} \cdot u^2 + \frac{4 \cdot C_\alpha + f_{Ha}}{L_\alpha} \cdot u \quad (2-5)$$

The coordinate  $u$  in Figure 2.3 and equation (2-5) is a curved coordinate, determining the position of a nominal point along the profile and extending from root to tip.

Superposition of regular involute and profile correction  $A$  is performed in the normal direction, i.e. corresponding points of the two curves (2-1) and (2-5) can be calculated along the  $u$ -coordinate by the intersection of the normal vector  $\mathbf{n}_{Evol}$  at one specific profile point  $\mathbf{P}_s$  with the profile correction function  $A$ . The unit normal direction vector  $\mathbf{n}_{Evol}$ , expressed in cartesian coordinates, is given by

$$\mathbf{n}_{Evol}(\mathbf{P}_s) = \begin{pmatrix} + \sin(\xi_s + A) / |\mathbf{n}_{Evol}| \\ - \cos(\xi_s + A) / |\mathbf{n}_{Evol}| \\ r \cdot \tan(\beta) / (r_t \cdot |\mathbf{n}_{Evol}|) \end{pmatrix} \quad (2-6)$$

$$\text{with } |\mathbf{n}_{Evol}| = \sqrt{1 + (r \cdot \tan(\beta) / r_t)^2} \quad (2-7)$$

$r_t$ : pitch radius

Again, an areal gear flank description can be obtained by screwing this modified profile, consisting of equations (2-1) to (2-7) and given at a certain height ( $z$ -axis), along one helix line as depicted in Figure 2.2.

In order to include also lead modifications, a similar correction function is linearly superimposed to the conventional screw line. Here, different angles and signs for lead inclination of left and right flank may be foreseen [3, 5]. Equation (2-8) describes this modification along a  $v$ -axis, which is also a curved coordinate along the lead screw line on the base cylinder.

$$B(C_\beta, v) = \frac{-4 \cdot C_\beta}{L_\beta^2} \cdot v^2 + \frac{4 \cdot C_\beta}{L_\beta} \cdot v \quad (2-8)$$

All these calculations end up with complex areal descriptions of gear flanks, given in cartesian coordinates by equation (2-9). [3, 5] alternatively present a gear flank description in cylinder coordinates. Within these equations,  $\mathbf{n}_{Evol}$  gives the normal direction at a certain unmodified flank point  $(\xi_s, \Lambda, z_s)$ , crossing the modified profile at  $(x_k, y_k, z_k)$ .

Cartesian coordinates:

$$x_k = r \cdot (\cos(\xi_s + \Lambda) + \xi_s \cdot \sin(\xi_s + \Lambda)) + (A(f_{Ha}, C_\alpha, \xi_s) + B(C_\beta, z_s)) \cdot \sin(\xi_s + \Lambda) / |\mathbf{n}_{Evol}| \quad (2-9)$$



$$y_k = r \cdot (\sin(\xi_s + \Lambda) - \xi_s \cdot \cos(\xi_s + \Lambda)) - (A(f_{H\alpha}, C_\alpha, \xi_s) + B(C_\beta, z_s)) \cdot \cos(\xi_s + \Lambda) / |n_{Evol}|$$

$$z_k = z_s + (A(f_{H\alpha}, C_\alpha, \xi_s) + B(C_\beta, z_s)) \cdot r \cdot \tan \beta' / (r_t |n_{Evol}|)$$

with :

$$\Lambda = f(\eta_b, \beta, f_{H\beta}, z_s)$$

$$= \eta_b + z_s \cdot \underbrace{\left( \tan \beta / r_t + \frac{f_{H\beta} \cdot |n_{Evol}|}{b \cdot r} \right)}_{\tan \beta' / r_t}$$

The new options of areal gear flank descriptions (mainly restricted to involute gears and worms) are summarized in [3-11].

## 2.2 Areal mathematical description of bevel gears

Also for bevel gears, an areal mathematical description of gear flanks would substantially improve the inspection procedure, the measuring uncertainty and thus the production of bevel gear sets.

The current industry approach for presentation of nominal bevel gear data and inspection results uses the cutter geometry and the theoretical machine motions to describe the tooth surface. Consequently, all inspection data are referenced from that surface.

A transfer of the approach described in section 2.1 to bevel gears, was partially realised in industry [12-15]. They propose the conjugate reference system as an alternative to the machine settings reference system. This approach uses a theoretically perfect gear as reference for gear inspection and the surface conjugate to the theoretically perfect gear as reference for pinion inspections. The reasons for proposing this system are outlined in [11]. [15] provides further information regarding the two approaches and discusses the advantages of each in more detail. [12] records the conjugate approach as an alternative presentation method for bevel CMM inspection data. [14] describes the reasoning for using the conjugate system for engineering analysis.

## 3 Areal measurement

### 3.1 General aspects

The 3-dimensional description of involute gear flanks and their geometric relationship, given by the pitch (angular distance between equal sided flanks) and the tooth thickness (distance between left and right flanks) results in a complete 3-dimensional nominal description of the whole gear workpiece. As described in section 2.1, this areal description is able to reflect all kinds of geometric modifications without any simplifications or neglects. It also includes the relationship of gear flanks to the gear body and possibly, in cases of a layshaft, the geometric relationship between two and more gears, mounted on one shaft.

The totality of all nominal points contains information about the desired functionality of the gear wheel. It also reflects the intended result of the manufacturing processes.

On the other hand, all actual flank points, obtained by measurement of a real gear workpiece, contain valuable information reflecting both, the probable functional behavior of the workpiece and the actual state of the manufacturing process. Conventional gear metrology is restricted to a few prescribed section lines (profile, lead) and singular points (pitch). The historical reasons for this standardized measurement were outlined in section 1. But, at least for nominal/actual points situated at the centre of a gear flank and belonging to the tooth contact area, an equal importance concerning their functionality and production process assessment can be assumed. Thus, such restrictions can be regarded as fully historical, but still important, since all national and international gear metrology standards are based on these restrictions.

This leads to a major demand for all future gear metrology, using an areal description of gear flanks:

- a) All measurement results must be directly comparable to standardized conventional (2-dimensional) gear deviations and parameters.
- b) Even though the areal gear flank description offers completely new aligning principles of the actual gear with respect to the nominal gear, all conventional aligning procedures must still be available. Otherwise, direct comparisons of measuring results according to demand a) are not possible.

As long as the measurement procedures obtain data sets of high lateral density, demand a) can easily be fulfilled. For example, optical probing methods like stripe pattern projections or interferometric measurements register several 10 000 points up to more than 200 000 points per flank within a few seconds. This point density is high enough to generate the standardized section lines by filtering out subsets of the measured data, representing the section lines with a sufficient accuracy.

### 3.2 Areal measurements using optical instruments

Tactile gear metrology using GMIs or CMMs has reached a state-of-the-art, where significant further improvements in terms of accuracy and velocity are hardly expected. On the other hand, increasing demands in functionality and production efficiency require faster inspections, preferably close to the production line, at an enhanced information content and (at least) equal accuracy level. The study [21] states that various optical measurements (Figure 3.1) offer the potential to fulfil all these demands. Especially methods based on the triangulation principle promise a good feasibility concerning accessibility of gear flanks, speed and accuracy, whereas interferometric measurements are supposed to fail, mainly due to a minor accessibility [21, 22]. Namely stripe pattern projection gives access to both, a high and complete information content (areal recording of a whole flank at once) and a sufficient accuracy (coded light approach [4, 23-26, 32, 33] and phase shift procedure [24, 27-29]).

Figure 3.2 illustrates the triangulation principle and the basic set-up, where a well-defined black and white pattern (mostly parallel stripes) illuminates the curved measuring object. A camera (CCD or CMOS) observes the projected pattern at a defined (and previously verified) triangulation angle, extracting

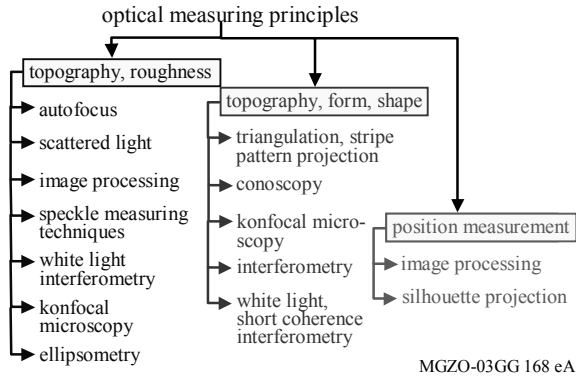


Fig. 3.1. Scope of optical measuring methods available for gear metrology

the object’s 3D-surface coordinates from the distortion of the recorded pattern, caused by the sculptured surface. The main advantages of this measuring principle are

- simple and fast implementation,
- stripe density and phase shift adaptable to the measuring problem,
- measuring area from mm<sup>2</sup> to m<sup>2</sup>,
- depth resolution down to 1/10.000 of diagonal of measuring area possible,
- improved cameras and image processing directly applicable

One major difficulty occurs on evaluating the registered pattern, caused by the so-called “order problem” [23, 24, 33]: one certain camera pixel cannot identify the number (order) of an observed stripe period, leading to an ambiguity in the detected distance  $d$  between the inspected surface point and the corresponding camera pixel (Figure 3.2).

An elegant procedure labelled “coded light approach” avoids this problem [24], where a series of pattern (e.g. 8) with varying period lengths illuminate the (static) object surface. Thus, each pixel “sees” a sequence of dark and light spot intensities, transformed into a binary code. Moreover, phase shifting of the “finest” stripe pattern further increases the depth resolution of this measuring principle. [30] reports another method for identifying the order of a certain stripe by varying the pattern.

Another problem arises from the complex shape of gear flanks (namely bevel gears), where a large portion of illumination rays do not hit the detector or the perceived camera spot at the triangulation angle. Therefore, effects like multi-

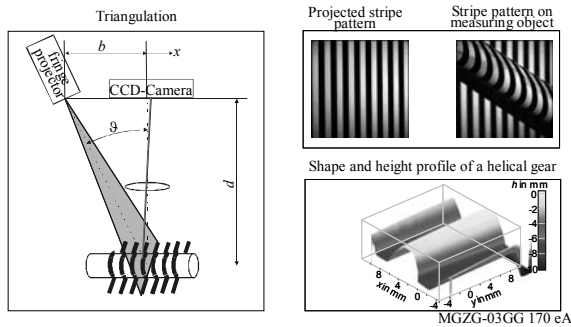


Fig. 3.2. Geometry measurement using fringe projection.

ple scattering, “blooming” or distant light noise lead to invalid coordinate values [31]. CMOS cameras significantly reduce problems caused by exceeding reflected light intensities. Problems due to ray tracing can be avoided by superimposing several evaluated data sets, obtained at different angular positions of the flank.

Instead of triangulation principle also a conoscopy sensor was investigated in [21]. As explained in [11] today these sensors are not under inspection in gear metrology.

[4, 11] summarize the main advantages and disadvantages of both the tactile and optical measurement of gears.

## 4 Evaluation of measured areal gear data

### 4.1 Distance definitions

Provided the gear alignment is given and all measured points have been transformed to the workpiece-related coordinate system using the transformation  $T$ , all transformed measured points (labelled actual points) are in the “vicinity” of their corresponding nominal points. The phrase “in the vicinity” characterizes a spatial distance. It should be small enough to clearly define, which nominal point corresponds to a certain actual point.

Then, the deviation  $d_i$  determines the distance between this pair of points no.  $i$ . Three options are explained in [3, 5, 6] to express the distance mathematically:

- the Euclidean distance,
- the projected distance (Figure 4.1),
- the plumb line distance from the actual point, crossing the nominal surface perpendicularly (Figure 4.2).

The Euclidean distance is given by equation (4-1). The projected distance in equation (4-2) and the plumb line distance in equation (4-3) require the knowledge of the normal unit vector  $\underline{n}_s = \underline{n}_{Evol}$  (equation (2-6), (2-7)).

They thus more sensitively reflect the influences of any alignment/surface changes on the compound dislocation of the whole actual surface. The projected distance  $d_{proj}$  is simply the scalar product of Euclidean distance and unit normal vector.

$$d_{Euklid} = P_i - P_s \quad (4-1)$$

$$|d_{Euklid}| = \sqrt{(x_i - x_s)^2 + (y_i - y_s)^2 + (z_i - z_s)^2}$$

$$|d_{proj}| = d_{Euklid} \cdot \underline{n}_{Evol} \quad (4-2)$$

$$P_i = P_s + d_{lot} \quad (4-3)$$

$$= P_s + |d_{lot}| \cdot \underline{n}_{Evol} = P_s + \frac{d_{lot}}{|\underline{n}_{Evol}|} \cdot \underline{n}_{Evol}$$

$$d_{plumb} = \frac{r}{|\underline{n}_{Evol}|} \cdot \left( \sqrt{\frac{s_i^2}{r^2} - 1} - \text{atan} \left( \sqrt{\frac{s_i^2}{r^2} - 1} \right) \right) \quad (4-4)$$

$$\left( -\gamma_i + \eta_b + z_i \cdot \tan(\beta) / r_t \right)$$

The plumb line distance  $d_{plumb}$  according to equation (4-3) is more difficult to evaluate, since the point  $P_s$ , where the

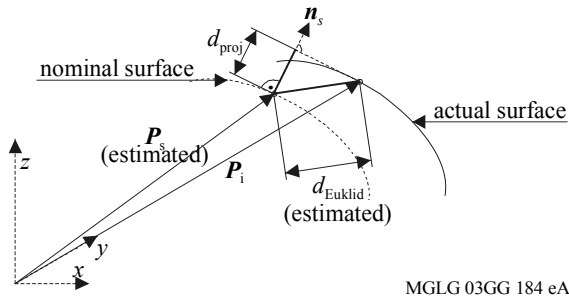


**Fig. 4.1.** Projected distance  $d_{proj}$  [3, 6].

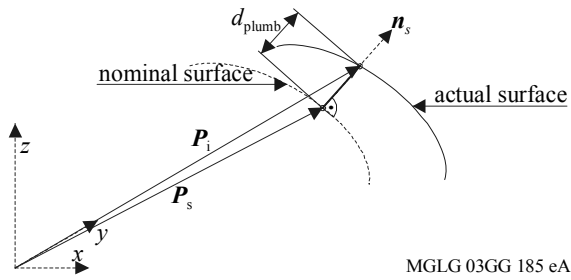


**Fig. 4.2.** Plumb line distance  $d_{plumb}$  between a measured point  $P_i$  and the root point (intersection point) at  $P_s$  [3, 6]

plumb line crosses the (modified) involute profile, is initially unknown (Figure 4.2).

For the non-modified gear flank the distance  $d_{plumb}$  was derived analytically in [6, 7]. Apart from the nominal gear parameters,  $d_{plumb}$  in equation (4-4) fortunately depends on the actual coordinates  $s_i$ ,  $\gamma_i$  and  $z_i$  (in cylindrical coordinates). Thus, a search or calculation of the corresponding nominal point coordinates is not necessary, which saves a large portion of the formerly required calculation time.

Now the major advantage of adding the modifications A and B in section 2.1 perpendicularly to the involute profile occurs: as explained in [6, 7], the distance  $d_{plumb}$  between an actual point  $P_i$  and the modified nominal surface is very accurately given by subtracting the modifications A+B from the distance  $d_{plumb}$  of equation (4-4). [6, 7] gives more details of the approach explained here.

#### 4.2 Deviation Function Method

The calculation of distance and deviation between nominal and actual points with respect to all the distance definitions in equations (4-1), (4-2) and (4-4) require the knowledge of the transformed actual point  $P_i$ . On the other hand, any alignment by a coordinate transformation  $T$  leading to the transformed measured points and minimizing an objective function assumes that all the distances  $d_i$  are already known, i.e. the mapping of the cloud of measured points to their corresponding nominal points was already realized. A convenient and transferable method guiding an exit out of this dilemma is the deviation function method, explained in detail in [17, 18, 20]. The main idea behind this approach is to perform the numerical alignment and the nominal-actual

comparison in one step, i.e. to define an approximation problem, where all the independent variables (workpiece-related deviation parameters) plus the 6 degrees of freedom for alignment are calculated during one iteration procedure. Therefore, the distance  $d_i$  must be expressed as a function of all these independent variables. For basic geometric elements like a circle, plane, sphere or cylinder, this leads to comparably simple functions. They usually depend on less than ten independent variables, including the transformation parameters. For an involute gear, the number of independent variables regularly exceeds 10 per flank for all the standardized profile, lead and pitch deviation parameters including the modification functions A and B of equations (2-5) and (2-8).

Based on the plumb line distance definition of Figure 4.2, this deviation function can be expressed by equation (4-3), where the quantity  $d_{plumb}$  must be replaced by expression (4-4) and  $\underline{u}_{Evol}$  by expression (2-6) and (2-7). Within these detailed mathematical expressions, the coordinates  $s_i$ ,  $\gamma_i$ ,  $z_i$  and the involute parameters  $\xi_s$ ,  $\Lambda$  themselves must be expressed as functions of the six alignment parameters. This requires a rather complex analytical deviation function, representing the major challenge for this approximation approach. Once the deviation function is known, the procedure follows standardized steps easy to perform [11, 17-20]. First, the objective function comprising all the (detailed) deviations  $d_i$  is partially derived to all the independent variables. This leads to a linearized equation system of all unknown independent variables, which are iteratively approximated. In the end, this leads to a self-contained measurement and evaluation of both, the complete set of all gear deviation parameters for all measured flanks plus the alignment of the whole gear with respect to the workpiece body. Moreover, this approach offers to define different alignment parameters for the gear wheel itself and the workpiece body. This option enables to separate deviations induced e.g. by shrinkage, hardening and residual stress deformation from those caused by the gear manufacturing process itself.

If optical probing methods or high speed scanning devices are applied for measurement, several thousand measuring points up to more than 1 million points are incorporated into the approximation procedure. Therefore, the results will be very stable in statistical terms and are less affected by local measuring errors (“outliers”). But, due to the large amount of independent variables, the convergence of the approximation procedure may cause difficulties. By providing good starting values for the iteration loop and by including significance and verification tests within the algorithms, these problems can be reduced to a reasonable minimum.

[3] and [7] report results obtained by simulations, indicating a sufficient convergence behavior and accuracy of the implemented algorithms. Results of [9] based on both simulations and experiments support these findings even though the theoretical approach differs from the one reported here.

## 5 Summary

Gear metrology following the current state-of-the-art represents a key technology for the production of modern gear

drives. Further improvements aiming at a reduction of weight, noise and manufacturing costs as well as the production of very small (< 2 mm) and very large (up to 16 m) gears require new approaches concerning the mathematical flank description, areal probing and evaluation methods. Therefore, areal research efforts will be necessary, carried out with new measuring devices and verified using new calibration methods.

## 7 References

- [1] Niemann, G., Winter, H., 1989, *Maschinenelemente*, Vol. 1-3, Springer-Verlag, Berlin.
- [2] Roth, K., 1989, *Zahnradtechnik*, Vol. 1 and 2, Springer-Verlag, Berlin.
- [3] Goch, G., Günther, A., 2002, Future Gear Metrology, Superficial Description and Inspection of Flanks, in: *International Conference on Gears Vol. 2*, VDI-Berichte 1665, p. 751-768.
- [4] Goch, G., 2002, *Optische Messung von Zahnrädern*, VDI-Berichte 1673, p. 171-194.
- [5] Günther, A., 1996, *Flächenhafte Beschreibung und Ausrichtung von Zylinderrädern mit Evolventenprofil*, Diploma Thesis, University Ulm-Germany.
- [6] Günther, A., Peters, J., Goch, G., 2000, Numerische Ausrichtung und Korrigierte Auswertung von Zylinderrädern mit Evolventenprofil auf der Basis einer Flächenhaften Beschreibung. *Proceedings XIV. Meßtechnisches Symposium des Arbeitskreises der Hochschullehrer für Meßtechnik*, AHMT, Wien, S. 1-12.
- [7] Günther, A., Peters, J., Goch, G., 2001, Flächenhafte numerische Beschreibung, Ausrichtung und Auswertung von Zylinderrädern. *Technisches Messen* 68, p. 160-165.
- [8] Lotze, W., 1996, Neue Wege und Systeme für die wirtschaftliche 3D-Verzahnungsprüfung. *VDI Bericht Nr. 1230*, *International Conference On Gears*, p. 1021-1030.
- [9] Lotze, W., 2002, Flächenhafte Auswertung von Zahnflanken. *VDI-Berichte 1673*, p. 195-206.
- [10] Lotze, W., Härtig, F., 2001, 3D gear measurement by CMM. *Laser Metrology and Machine Performance "Lambdamap"* in Birmingham, UK, p. 333. ISBN 1-85312-890-2.
- [11] Goch, G., 2003, *Gear Metrology*. *Annals of the CIRP Vol. 52/II*, p. 659-695.
- [12] ANSI/AGMA 2009-B01, 1998/2001, *Bevel Gear Classification, Tolerances, and Measuring Methods*, American National Standard.
- [13] Brown, R.E., *Feature-Based Definition of Bevel Gears*. AGMA 95FTM11.
- [14] Chambers, R. O., Brown, R. E., 1987, *Coordinate Measurement of Bevel Gear Teeth*. SAE Technical Paper Series 871645. *International Off-Highway & Powerplant Congress & Exposition*. Milwaukee, Wisconsin September 14-17, 1987.
- [15] Takeda, R., Wang, Z., Kubo, A., Asano, S., Kato, S., 2002, Performance Analysis of Hypoid Gears by Tooth Flank Form Management, *Gear Technology*, part 7/8, p. 26-30.
- [16] N. N., 1999, PRIMAR Mx 4, Mahr GmbH, Göttingen, Germany.
- [17] Goch, G., 1982, *Theorie und Prüfung gekrümmter Werkstückoberflächen in der Koordinatenmesstechnik*, PhD-Thesis, Universität der Bundeswehr, Hamburg.
- [18] Goch, G., 1990, Efficient Multi-Purpose Algorithm for Approximation- and Alignment-Problems in Coordinate Measurement Techniques. *Annals of the CIRP Vol. 39/I*, p. 553-556.
- [19] Goch, G., Peters, R.-D., Schubert, F., 1980, Beschreibung gekrümmter Oberflächen in der Mehrkoordinaten-Messtechnik. *VDI-Berichte Nr. 378*, p. 85-91.
- [20] Goch, G., Tschudi, U., 1992, A Universal Algorithm for the Alignment of Sculptured Surfaces. *Annals of the CIRP Vol. 41/I*, p. 597-600.
- [21] Goch, G., Steiner, R., Schmitz, B., Patzelt, S., 2003, *Optische Messtechnik - Einsatzmöglichkeiten und Grenzen in der Antriebstechnik*, Abschlussbericht, Forschungsvereinigung Antriebstechnik e.V., Forschungsvorhaben Nr. T 423, FVA-Forschungsreporte, Frankfurt a.M.
- [22] Forschungsvereinigung Antriebstechnik E.V., 1992, *Forschungsvorhaben Nr. 207 Studie, Optische Verfahren für die Zahnradmessung*, Final report No. 374.
- [23] Hof, A., Hanßen, A., 1992, *Messung von Funktionsflächen mit Streifenprojektion*. Manuskript zum Vortrag beim 5. Ulmer Industriekolloquium.
- [24] Malz, R., 1995, *Photogrammetrische Verfahren zur Kalibrierung und Positionsbestimmung optischer 3D-Sensoren mit Matrixkamera und kodierter Streifenprojektion*, *Proceedings zum Symposium Bildverarbeitung '95*, 29. November - 1. Dezember 1995, an der Technischen Akademie Esslingen.
- [25] Peters, J., Goch, G., Günther, A., 2000, *Helical Gear Measurement Using Structured Light*. *Proceedings of the XVI IMEKO World Congress*, Wien, p. 227-230.
- [26] Peters, J., Patzelt, S., Horn, F., Goch, G., 2001, *Calibration Techniques for Fringe Projectors*. *SPIE Proceedings Vol. 4398*, *Optical Measurement Systems for Industrial Inspection II*, Application in Industrial Design. München, p. 207-215.
- [27] Lu, Guowen, Wu, Shudong, Palmer, Nicholas, Liu, Hongyu, *Application of Phase Shift Optical Triangulation to Precision Gear Gauging*. *SPIE Vol. 3520*, p. 52-63.
- [28] N. N., *Optische 3D Messung von Zahnflanken*. Personal information from G. Frankowski, 21.09.2001.
- [29] Sciammarella, F., 2001, *Optical Technique for Gear Contouring*. AGMA 01FTMS1. Alexandria (VA), USA.
- [30] Denkena, B., Tönshoff, H. K., 2002, *Fast Inspection of larger sized curved surfaces by stripe projection*, *Annals of CIRP 51/1*.
- [31] Hüser-Teuchert, D., Trapet, E., Garces, A., Torres-Leza, F., Pfeifer, T., Scharsich, P., *Performance test procedures for optical coordinate measuring probes final project report, Part 2 "Proposal of user performed test procedures"*. European Commission, bcr information, Hannover. ISSN 1018-5593.
- [32] Goch, G., 1997, *Berührungsloses Messen der Maß- und Formabweichungen gekrümmter Oberflächen*. Patentanmeldung DE Z, Az. 197 18 494.4
- [33] Hanßen, A., Hof, A., 1991, *Verfahren und Vorrichtung zur Vermessung von Objekten, insbesondere Zahnrädern, mittels projizierter Streifenmuster*. Patentanmeldung 91059P.

---

## Detecting Perturbation Occurrence during Walking

Yoko Hagane<sup>1</sup>, Wenwei Yu<sup>1</sup>, Ryu Katoh<sup>2</sup>, Tamotu Katane<sup>1</sup>, Masaki Sekine<sup>1</sup>, Toshiyo Tamura<sup>1</sup>, Osami Saitou<sup>1</sup>  
<sup>1</sup>Chiba University, <sup>2</sup>University of Tokyo

### Abstract

This research aims at the development and verification of a system that can detect the occurrence of perturbation during walking for walking-assist as soon as possible by from output signals of an artificial sensor system fitted on users' body. In this research, a back-propagation based artificial neural network (ANN) model was employed to build pattern recognition unit that can deal with the individual variation and time-varying characteristics. Results showed that the occurrence could be detected from four channels within 87.5ms, which could be considered as short enough for walking assist systems to response to the perturbation.

### 1 Introduction

It is very difficult for most walking-impaired people to cope with obstacles and uneven ground, and other perturbation during walking, because their afferent, efferent pathways and musculoskeletal functions were both impaired to a certain extent. As a result, the perturbation during walking becomes one of the serious risk factors for falling-down of the walking-impaired people. Thus, assist systems for the real-world environment walking, should be able to appropriately deal with the perturbation. However, most walking assist systems reported, including robotics systems [1] and those using Functional Electrical Stimulation (FES) [2] couldn't deal with the perturbation, because the research work has not taken into consideration the perturbation like uneven terrain and slip, which frequently occur in daily-life walking.

A prerequisite for building a walking assist system for daily-life is that, the perturbation could be detected after its occurrence within a period short enough for balance recovery by means of certain assistive technology, such as Functional Electrical Stimulation or robotics power assists. That is, a right triggering signal and a suitable power assist could form so called artificial reflex to help the balance recovery in the case of perturbation occurrence during walking.

Little has been done on the automatic detection of perturbation during walking. There have been research efforts to study the role of reflexes during human walking [3][4]. In [5] the role of afferent information during animal walking has been studied using a simulation model. It showed that virtual reflexes triggered by afferent information

could improve walking stability. However, the onset of the the virtual reflexes was not sufficiently studied because the simulator "knows" the right timing to trigger the reflexes. In another research [6], a "vestibulospinal" reflex was coupled to its control mechanism of a robot dog. Since the reflex is a posture-related one, a simple threshold mechanism is enough to process gyro sensor data to trigger the reflex.

This research aims at the development and verification of a system that can detect the occurrence of perturbation during walking as soon as possible by an artificial sensor system fitted on users' body and an Artificial-Neural-Network based pattern recognition system.

### 2 Method

Since responses to perturbation during walking are the results of the interaction between human neuro-musculo-skeletal system and walking environment, they might be entangled sequences of body sway and muscle activation. So that, the motion sensors that can reflect fast body motion, and sensors that can directly reflect muscle activation, should be employed. However, there has been no such measuring data available in the research field, nor research results indicating sensor combination that could result in effective detection of perturbation occurrence.

In this study, an experiment was performed to acquire the data concerning responses to the slip perturbation occurrence during walking. Then, Davis Information Criterion [7] was employed to analyze effective feature vectors for slip perturbation occurrence detection. Finally, an Artificial-Neural-Network based pattern recognition system was built to detect the occurrence. In this study, the analyzation and detection were conducted in an off-line manner.

## 2.1 Measurement of perturbation occurrence during walking

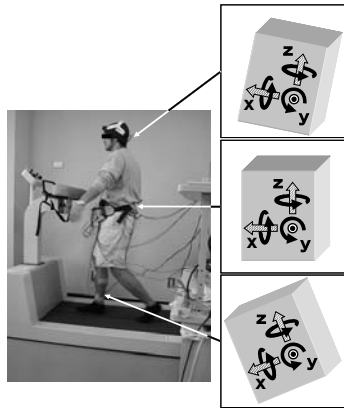


**Fig.1.1.** Fittings and sensitivity axial direction of each sensor

### A. Subject

10 male subjects, with age  $24.8 \pm SD5.1$ , height  $176.9 \pm SD5.7$ cm, weight  $68.2 \pm SD5.9$  kg and with no previous history of musculoskeletal or neurological disease, participated in the experiments. The subjects signed their written informed consent and were asked to report their dominant lower limbs prior to the experimental procedures. Besides, a pre-test (see *Procedures* for details) for safety-assurance was conducted for all subjects.

### B. Equipment

8 Dry-type EMG surface differential electrodes (Model DE-2.3, DELSYS) were fitted on the skin surface above the belly of the following muscles: gluteus medius, rectus femoris, vastus lateralis, vastus medialis, semitendinosus, tibialis anterior, gastrocnemius medialis, gastrocnemius lateralis. Three 3-Axis accelerometers+gyro sensors (GYROCUBE/3A, O-navi) were fitted on the head, waist and ankle (Fig. 1.1). Two A/D cards (DAQ3024, NI) were used to collect all the sensor data, at a 1.6 kHz sampling rate. The EMG signals were amplified to 2000 times, by the pre-amp equipped in the surface EMG electrodes, and a hand-made EMG amplifier.

Perturbation to gait was realized by a split-belt (PW-21, HITACHI), for which the speed of each belt could be independently and accurately controlled from 0-3km/hr., within 270ms (200ms for PC split-belt machine communication and 70ms for speed change), which could be treated as a constant delay to control signal. The real speed was monitored using a rotary-encoder (RP-721 ONOSOKKI). A slip perturbation could be generated by slowing down one side at the moment of heel-strike.

### C. Procedures

A pre-test was first applied to the subjects. In the pre-test, all subjects experienced the perturbation weaker than that would occur in the experiment, that is, the speed down from 2km/h→1km/hr, and 3km/h→1km/hr. The subjects were asked to describe their feeling, and they can decide to quit or continue the experiment. Or if the experimenters recognized

that one subject is not suitable for the experiment, by observing the subject's movement and behavior, they could suggest a quit to the subject.

After all the sensors were fitted to the specified places of subjects' dominant lower limbs, each subject was asked to walk on the split-belt at a speed of 3 km/hr. The gait of the subject was monitored using x-axis accelerometer fitted to the ankle of the subject. Concretely, the heel strike was detected according to the method described in [8], which decides heel strike by comparing the peak of x-axis of accelerometer fitting to the ankle with a preset threshold (Fig. 2). After the gait reaches a steady state, that is, the heel strike to heel strike interval tends to be similar, the perturbation, a speed down (3 km/hr→0.5km/hr) would be given to the belt of the dominant side of the subject, at the moment of heel strike of the dominant lower limb. 10 perturbations would be given to a subject in one trial. Then the perturbation would be given to another side of the same subject for 10 times in another trial. That is, for each subject, 2 trials, corresponding to left and right sides, would be conducted. There was a rest for at least 10 minutes between each two trials.

## 2.2 Extraction and selection of feature vectors

In consideration of convenience of use in everyday life and rapidity of processing, the minimum feature vector of the artificial sensor system necessary and sufficient for the detection of perturbation occurrence should be determined. To choose the feature vectors, the Davis's cluster separation measure [7] was employed as an index to make difference between normal walking and perturbed walking. Davis's cluster separation measure could be expressed in equation (1.1)

$$f_{cc} = (u_1 + u_2) / |c_1 - c_2| \quad (1.1)$$

Where  $u$  and  $c$  are standard deviation and average of one cluster, respectively, 1 denotes of the data cluster of normal walking, and 2 denotes the data cluster of perturbed walking. The raw and Short Time Fourier Transformed (STFT) accelerometers+gyro data from head, hip and ankle were used. The Davis's cluster separation measure was calculated for each walking cycle (from heel-strike to heel-strike). The sensors and the moments with lower Davis's cluster separation measure value would be considered as the candidates for the features.

## 2.3 Discrimination of the perturbation occurrence from normal walking

Responses to perturbation is varying with individuals and time, therefore information processing should be able to adapt to the changes. Also because, in future, the detection of the perturbation is expected to perform in an on-line manner, an back-propagation based Artificial-Neural-Network [9], which is characterized by its learning facility, was used for pattern recognition. The inputs of the ANN include the features from the sensors fitted on foot, waist, head. The neuron number of middle layer is 10, and that of output layer

is 1. Training was performed for each 40 strides using the data from all nine subjects, and test was performed using the data of unused 5 strides from nine subjects. If the output of the network doesn't agree with the walking condition of the test sample (that is normal or perturbed), the data set of the subject with recognition errors would be excluded from the training data set and added to test data set, and the training would be performed again for the remaining training data set. In addition, for the data set with at least one recognition error, another training and test would be performed for this individual subject.

### 3 Results

The raw data of Z-axis of accelerometers fitted on head is shown in Fig.1.2, and Davis's cluster separation measure value of the sensor is shown in Fig.1.3.

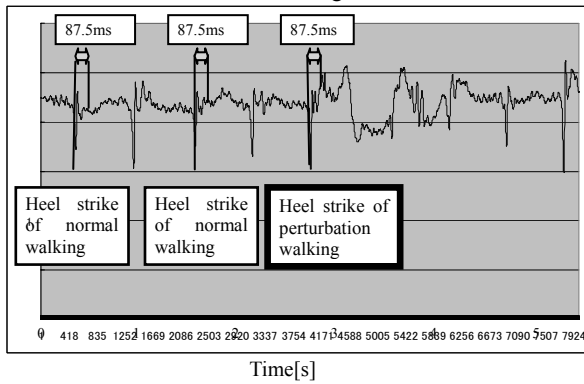


Fig.1.2. Raw data of Z-axis of accelerometers fitted on head

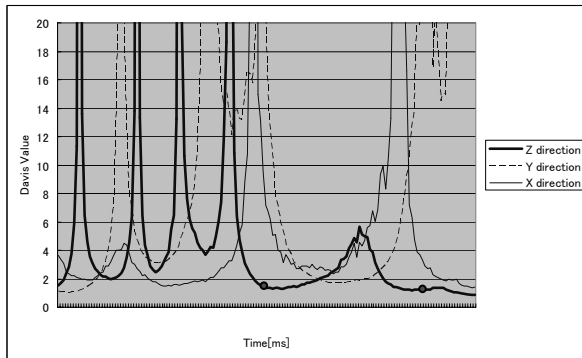


Fig.1.3. Davis's cluster separation value for Z-axis of accelerometers fitted on head

According to these results, the feature candidates could be chosen. If the Davis's cluster separation value is lower, it might contain more information for discriminating perturbation occurrence from normal walking. The index value for all subjects is calculated by summing and averaging the index values of all subjects. The feature candidates are listed in Table.1.1 with their index values.

Moreover, the test results when combining 3 or 4 feature candidates into sensor groups and taking the respective feature vectors as the input of the ANN are shown in

Table.1.2. The values of those feature vectors in both normal walking and perturbed walking are also shown in Fig.1.4. The horizontal axis denotes the feature candidate number, and the vertical axis shows the input value and the output value (calculation result).

Furthermore, learning curves are shown for in Fig.1.5. The vertical axis stands for the number of mis-recognition.

Table 1.1 Feature candidates and Davis's cluster separation value

Feature candidates				
	sensor	Wave pattern	Time(heel strike+)	Davis's value
1	acceleration X-axis of ankle	original	0ms	0.893
2	angular velocity Z-axis of ankle	original	0ms	0.519
3	acceleration Z-axis of hip	original	15ms	3.92
4	angular velocity Z-axis of hip	STFT	40ms	5.27
5	angular velocity Z-axis of hip	original	40ms	6.87
6	acceleration Z-axis of head	original	50ms	2.78
7	acceleration Z-axis of head	original	87.5ms	1.47

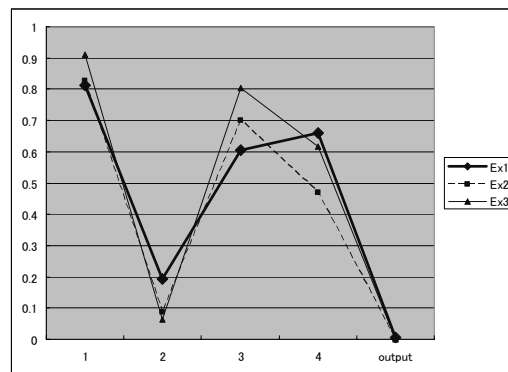
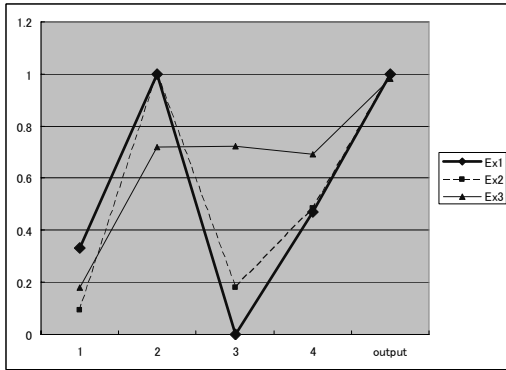
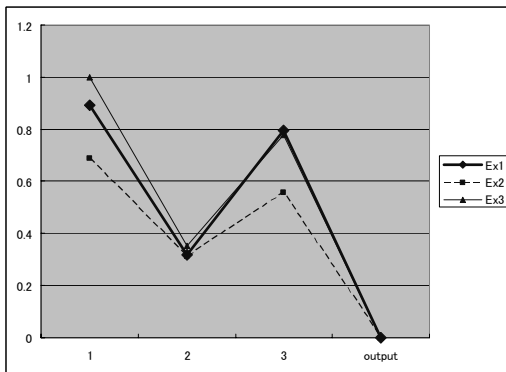


Fig.1.4.1 Feature vectors for sensor group A in the case of normal walking



**Fig.1.4.2** Feature vectors for sensor group A in the case of perturbation occurrence



**Fig.1.4.3** Feature vectors for sensor group E in the case of normal walking

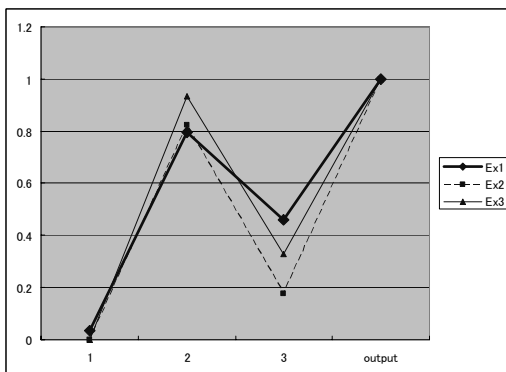


**Fig.1.4.4** Feature vectors for sensor group E in the case of perturbation occurrence

**Fig.1.4.** Feature vectors for sensor group a and e in the case of normal walking and perturbation occurrence

**Table 1.2** Judgment by ANN

Group	feature vector	success rate (Training for all 9)	success rate (Training by oneself)
A	1,2,4,7	45/45	-
B	1,2,7	83/85	5/5
C	1,2,5,7	82/85	5/5
D	1,2,3,6	137/141	9/10
E	1,2,6	137/141	10/10

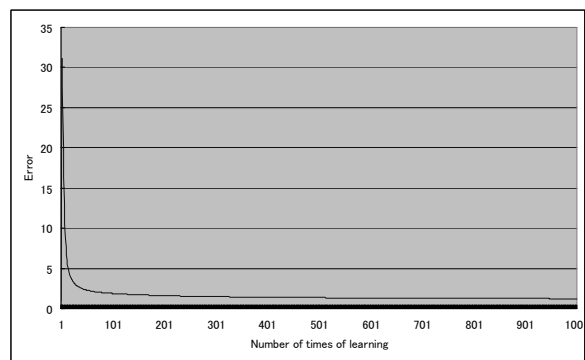


**Fig.1.5.1** Learning curve for data set for all 9 subjects

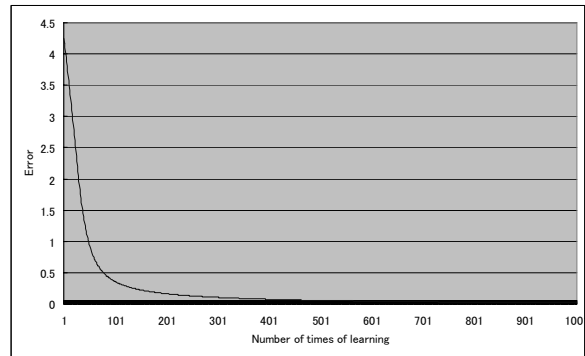


**Fig.1.5.2** Learning curve for data set of one individual subject with at least one mis-recognition in the first learning trial

## 4 Discussion

From table 1.1 and 1.2, it is clear that feature 1 and 2 are basic features for perturbation detection. They are from X-axis acceleration of and Z-axis angular velocity of ankle. Those two features could be related to the physical motion caused by the slip before the neuro-control mechanism begins to response. But these two features might be slip perturbation dependent.

The sensor groups containing feature 4,5,7 are the important



ones other than feature 1 and 2, reflecting the reflexive response of hip and head. The success rate of the test is high when these features were included in the feature vectors. However, feature 4 needs more computation for Short time fourier transform, and feature 7 needs 87.5ms after the heel-strike moment.

Sensor group e(1,2,6) could result in fast detection, however 4 samples from 2 subjects were failed.

## 5 Conclusion

In this study, by using ANN whose input were the selected feature vectors from an artificial sensor system containing accelerometers+gyro on hip, hip and ankle, and EMG, the possibility of detecting perturbation occurrence during walking was shown

We suppose that, the feature vectors selected by Davis's cluster separation measure are slip-perturbation dependent.

However, in order to realize an on-line perturbation detection, it is necessary to consider specialty (early detection) and generality (robust and could coped with other perturbation).

## 6 Acknowledgement

This work was supported in part by the Ministry of Education, Science, Sports and Culture, Grant-in-Aid for Scientific Research (B), 2005, No. 16300178

## 7 References

[1] Hiroaki Kawamoto, Shigehiro Kanbe, Yoshiyuki Sankai:  
"Power Assist Method for HAL-3 Estimating Operator's

Intension Based on Motion Information", Proc. of 12th IEEE Workshop on Robot and Human Interactive Communication (ROMAN 2003), 2003

- [2] W. Yu, H. Yamaguchi, H. Yokoi, M. Maruishi, Y. Mano & Y. Kakazu: "EMG automatic switch for FES control for hemiplegics using artificial neural network", *Robotics and Autonomous Systems*, Vol.40, pp.213-224 (2002)
- [3] E.P. Zehr & R.B. Stein: "What functions do reflexes serve during human locomotion?", Elsevier Science Ltd : *Progress in Neurobiology*, Vol.58, pp185-205 (1999)
- [4] J.J. Eng, D.A. Winter & A.E. Patla: Strategies for recovery from a trip in early and late swing during human walking, *Exp. Brain Res.*, Vol.102, pp.339-349 (1994)
- [5] A. Porchazka, S. Yakovenko, Locomotor control: from spring-like reactions of muscles to neural prediction. In: *The Somatosensory System: Deciphering The Brain's Own Body Image*. ed. Nelson, R.J. Boca Raton, CRC Press, 141-181 (2001)
- [6] Yasuhiro Fukuoka, Hiroshi Kimura and Avis H. Cohen, Adaptive Dynamic Walking of a Quadruped Robot on Irregular Terrain based on Biological Concepts, *International Journal of Robotics Research*, Vol.22, No.3-4, pp.187-202 (2003)
- [7] D.L. Davis and D.W. Bouldin: "A cluster separation measure" *IEEE Transactions on Pattern Analysis and Machine Intelligence*. vol PAMI-1, no.2 pp224-227(1979)
- [8] K. Aminian, K. Reza Khanlou, E. De Andres, C. Fritsch, P. -F. Leyvraz and P. Robert: "Temporal feature estimation during walking using miniature accelerometers: an analysis of gait improvement after hip arthroplasty", *Medical & Biological Engineering & Computing*, Vol.37, pp.686-691 (1999)
- [9] Simon Haykin "Neural networks, A comprehensive foundation"(1999)

---

# Supporting the Reuse of Parts Based on Operation Histories of Products and Preference of Consumers

Naoto Fukuda<sup>1</sup>, Hiroyuki Hiraoka<sup>1</sup>, Tohru Ihara<sup>1</sup>  
<sup>1</sup> Chuo University

Keywords: re-use, network agent, operation history, simulation

## Abstract

For the effective re-use of parts, each re-usable part is required to be under appropriate management throughout their life cycle. A hindrance to the circulation of re-used parts is behavior of users. The flow of re-used parts around the user is uncontrollable and unpredictable. Authors are proposing “Part agent system” that is the combination of network agent called “Part agent” and radio frequency identification chip RFID. This paper discusses the mechanisms how Part agents use the operation history of the parts and the user's preference on maintenance of the parts to support their effective reuse.

## 1 Introduction

To achieve the effective re-use of parts, authors are proposing a system that is the combination of network agent and RFID where the network agent is assigned to a particular part and is programmed to follow their real counter-part wherever it goes. We call this agent a "Part agent" [1][6].

Behavior of users is a hindrance to the circulation of re-used parts. The flow of re-used parts around the user is uncontrollable and unpredictable in spite of the great effort of the manufacturer. The cause of such instability may include user's inability to manage all the parts in his products as well as his inaccessibility to the correct information on maintenance.

The purpose of our proposal of Part agent is to give users appropriate advices on the re-use of parts and to promote the circulation of the re-used parts. In previous work [2], it has been shown by simulation of Part agents that advices can be generated in consideration to user's preference and operation histories of products. However, it is revealed that the retrieval of operation history of a part is difficult when it is a reused part. It is also understood that some means are required to provide users with the information of part. In this paper, we discuss the mechanism how Part agents retrieve the operation history of the part and how they provide information to the owner of part.

First, the concept of Part agent is described in section 2. In section 3, how the operation history and user's preference is used in maintenance is discussed. Proposed mechanisms

are discussed in sections 4 and 5 how Part agents retrieve the operation history and how the information is provided to users. Preliminary results of the prototype system for these mechanisms are shown in section 6. Section 7 summarizes the paper.

## 2 Life Cycle Support of Products Using Network Agent

We are proposing Part agent system that manages the life cycle of mechanical parts by using network agent and RFID. The system is to manage all the information on the individual part throughout its life cycle on the assumption that network environment is available ubiquitously.

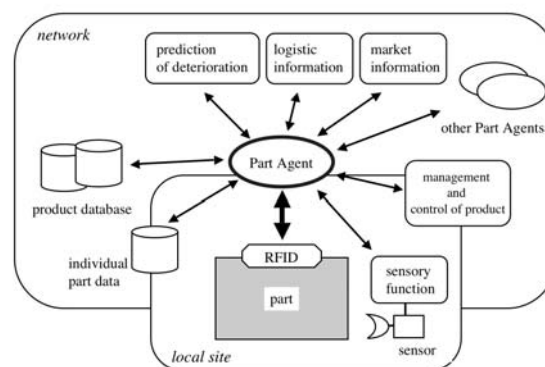


Fig. 1.1. Conceptual Scheme of Part Agent

### 2.1 Concept of Part Agent

The concept of Part agent is shown in Fig. 1.1. In our scheme, Part agent has the following functions.

(a) It follows the corresponding part through the network. Part agent uses Radio Frequency Identification (RFID) [5] attached to the part as the key to find and to identify its corresponding part.

(b) It gets the design information of part from the product database in the network, provided by the manufacturer.

(c) It manages the current information of the corresponding individual part, including assembly configuration, historical records, deterioration level, environmental status, etc. that may be stored in databases in the network, in the local site or in RFID.

(d) It may activate the sensors in the local site and gets the information of part such as applied load and wear, and environmental information around the part such as temperature.

(e) It uses the application in the network to decide the action of the part. We assume applications are available that provide Part agents the information such as prediction of deterioration, logistic information and market information. Part agent uses the information as well as the current status for its decision.

(f) Based on the decision, it requests the operator or function that controls the product to take the necessary action.

Combining these functions, Part agent autonomously and intelligently supports the life cycle of the part. Based on this concept, we are currently developing functions using network agents and RFIDs to realize Part agent system.

## 2.2 Part Agents to Support User's Activity [2]

As described previously, user's behavior is a hindrance to the circulation-oriented society. Part agent is applied to provide users with advices on maintenance of parts, which will promote the circulation of re-used parts.

We have performed simulation where Part agents give users advice on replacement of the part. Advice is created with the following factors in consideration.

- Current and predicted deterioration
- Availability of the alternative part in market
- Cost required for the replacement
- Logistic cost to transfer the part to and from the maintenance site,
- Predicted operation cost
- Environmental load

In this simulation, the models for deterioration, logistic cost and operation cost are linear to the duration of operation. The model of environmental load is constant except for production and disposal. Though the models are simple, the re-use of parts achieves less environmental load when the factor of environmental load is large.

We have added the function to this system that allows user's preference on maintenance to the simulation. Following kinds of users are assumed that are;

- Users who cares only about the current deterioration of the part,
- Users who cares about the current deterioration of the part and the deterioration of the replacement part in market,
- Users who cares about the trade-in price of the part and the price of replacement part in market,

- Users who cares about all the characteristics, i.e., the current deterioration of the part, its trade-in price, the deterioration and price of the replacement,

Result of the simulation shows that the users who only cares about the current deterioration of the part, in other words, who will not accept Part agents advice pay more than other type of users.

The simulation showed that, if several types of users with different preference in maintenance exist, Part agent will promote effective circulation of re-used parts by providing appropriate advice to users.

## 3 Maintenance Using Operation Histories of Products and Preference of Consumers

Maintenance of products is provided depending on the characteristics of product, maintenance cost and owner's strategy on maintenance. In some cases, mechanical parts are repaired only after their breakdown. In other cases, diagnosis is performed periodically and parts are replaced when symptoms such as large deterioration are detected on the diagnosis. More advanced maintenance may predict the process of deterioration based on the operation history of the part, such as monitored motor revolutions against time.

We have implemented a prototype system for Part agent. In the system, three types of maintenance are provided as shown in Fig. 1.2. Type (a) is the corrective maintenance where parts are repaired only after their breakage. Type (b) and (c) are the preventive maintenance. For (b), the degradation of part is measured by sensors or calculated based on the operation data. Failure is predicted if the cumulative value reaches the threshold and the part is replaced. For type (c), in addition to these values, the operation history is used to determine if the part should be replaced or not.

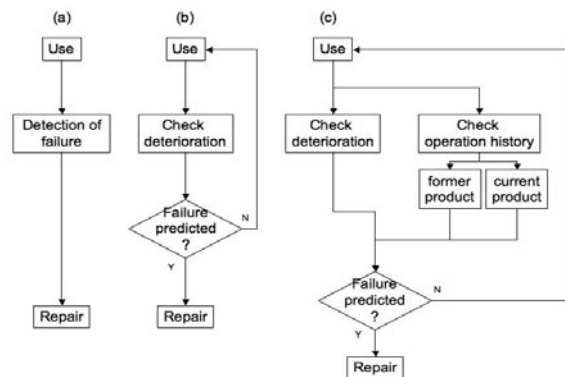


Fig. 1.2. Options of Maintenance; (a) Corrective Maintenance, (b) Preventive Maintenance Based on Accumulated Data on Deterioration and (c) Preventive Maintenance Based on Operation History.

When the part is a reused one, its operation history must be collected not only from the current product data but also from the former product that the part once belonged. Details

of proposed mechanism for collecting the operation history is described in the next section.

Parts or products that are re-used through used parts market such as cars or small computers have difficulty in reducing total environmental burden of their whole life cycle. For manufacturers, it is difficult to predict the behavior of their customers that affects the quality and quantity of take-back parts. Such information is a requisite to perform efficient and effective circulation oriented production.

For users of products, it is not easy to behave truly in favor of the environment, as it is difficult to give adequate maintenance to every goods they are using. Users may not know the precise deterioration level of their products or the available options of the maintenance. It is also difficult to decide what is good for environment, as they do not have a measure to evaluate the greenness of a specific option. Furthermore, users may want an option on their own strategy. Some users may prefer new version of products, and others may prefer to use it longer.

We consider that the behavior of users is essential element to reduce the environmental burden of total life cycle of products and that it is important to provide adequate assistance to the users. Mechanism to provide the owner of the part with its information is discussed in section 5

## 4 Using Operation Histories of Products

Use of the operation history is an important element to realize an advanced maintenance system. However it also brings out an issue when we consider the re-use of parts.

Usually, operation history is recorded for the product and not for each part to avoid redundancy. When a failed part is taken back and repaired to be re-used in a different product, its operation history in the former product will be lost.

### 4.1 Requirement of Operation History

If the maintenance can be achieved with simple values such as accumulated duration of usage, operation history is not required. Operation history is required when the diagnosis criteria are changing and a single value to be monitored cannot be determined beforehand.

When a phenomenon that leads to the failure of part is found, new diagnosis criterion will be established and the operation history of each part should be analyzed according to the new criterion. We consider that recalls of vehicles may be fallen into this type. The current recall is performed for all the possible vehicles due to the lack of traceability of operation history. If the function to check the operation history on site, unnecessary recalling will be avoided.

Operation history is also required for complex cases where multiple diagnosis criteria are combined.

### 4.2 Retrieval of Operation History

For Part agent to retrieve operation history, the following procedure shown in **Fig. 1.3** is developed for the prototype system.

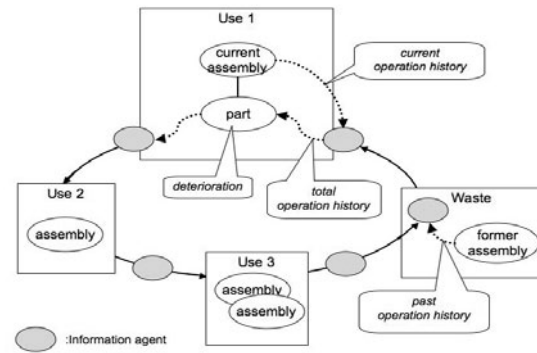


**Fig. 1.3.** Retrieving the Operation History.

When diagnosis requires the operation history of a part, the part agent creates an information agent to find the former and current assembly that contains the part. The information agent visits every candidate sites and checks if the designated assembly exists in the site. If it finds the assembly, the required operation history is obtained. The information agent goes back to the site of the original Part agent with the retrieved information on the operation history.

For assemblies disassembled, the part agents representing the assembly should be kept for some period in order to provide operation history in response to the request from its former parts that are re-used. Special site shown as Waste in the figure is established for that purpose.

### 4.3 Technical and Social Issues

Retrieving the operation history contains both technical and social issues.

In the above procedure every sites are checked to find the former assembly. However, it may not be feasible to check all possible sites. We need a robust mechanism to trace the former assembly, especially when we cannot rely on the manufacturer of the part for that role.

When an assembly is taken back for maintenance, it may be reused with new alternative part installed for the failed part, but it may be discarded. The information of operation history of those discarded assembly should be kept somehow. Our solution in the prototype system is to establish the Waste site shown above, but an issue still remains who manages such a site in real world.

When a part is reused, the owner of the current assembly that contains the part may be different from the owner of the former assembly that contained the part in the past. It is difficult to determine who is the owner of the operation history of a part that is recorded in the former assembly.

There exist privacy issue [4] for the retrieval of operation history. Users may not accept the idea that the operation history of his or her product is transferred to the other person. Careful management is also required for keeping information of discarded assemblies.

Security is another big issue for not only managing the operation history but also for Part agent system itself. Mechanism that assures the valid motion of agents should be developed. Effective encrypting of the information of agents or RFIDs is also required to avoid the stealing.

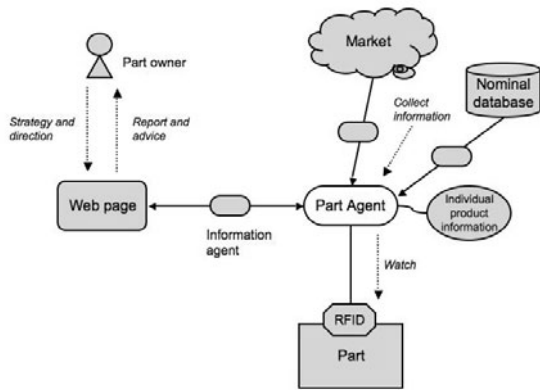


Fig. 1.4. Communication of Part Owner with Part Agent.

### 5 Consumer's Preferences

As described above, one of the problems for consumers is that they cannot perform the maintenance on his parts according to his preference.

Preliminary results of previous research [2] suggest that when consumers have various preferences in maintenance, the adequate support of their preference promotes the effective reuse of parts.

Method is required for users to communicate easily with Part agent. For that purpose, we are developing web-based communication between users and part agent as shown in Fig. 1.4. Part agent sends subordinate information agent to the web site. Report and advice from Part agent is provided via web page to the user. Inversely, user can send the preference of maintenance strategy or the direction to the Part agent through this mechanism.

### 6 Usage of Operation History in Prototype System

Prototype system for Part agent is developed with function using the operation history in maintenance.

### 6.1 Prototype Part Agent System

Prototype Part agent system is developed based on agent function of CORBA system Voyager [3]. The developed system has ability to communicate RFIDs but it is not used in the following simulation where only Part agents moves in the system. The supposed product is a vacuum cleaner, an assembly with five components that are a motor, a body, a hose, a nozzle and a filter.

Fig. 1.5 shows the display of the system. Windows in the figure shows, from top left in clockwise,

- Production site that produces Part agents,
- Assembly site that assembles 5 components in one assembly,
- Two Use sites where the products are operated,
- Maintenance site that disassembles assembly and send re-usable parts back into assembly site, and
- Waste site that keeps disassembled assembly information.

### 6.2 Results on Use of Operation History

Simulation is performed based on the following assumptions. Part is assumed to deteriorate by the turns of motor that turns 600 revolutions per minute. Duration of operation is defined randomly from 5 to 20 minutes. For each operation of cleaner, each part is deteriorated. The level of deterioration is represented with a single integer value. The level of deterioration for each part increases 2 to 6 in one operation. The rate of deterioration depends on the kind of part. When the level of deterioration reaches 200 the part breaks down. For each operation whose duration is more than 15 minutes, motor is assumed to receive additional damage. Furthermore, part breaks down accidentally with the probability of once per 30 operations.

Two kinds of maintenance are assumed; corrective maintenance that is performed after the detection of breakage and preventive maintenance that is performed based on the prediction. Cost of maintenance is assumed respectively 1000 for the former and 100 for the latter.

Prediction is made based on the deterioration level of the part derived from the cumulative turns of motor. Different threshold value is assigned for each kind of part to send the part to maintenance.

For motors, additional prediction may be performed

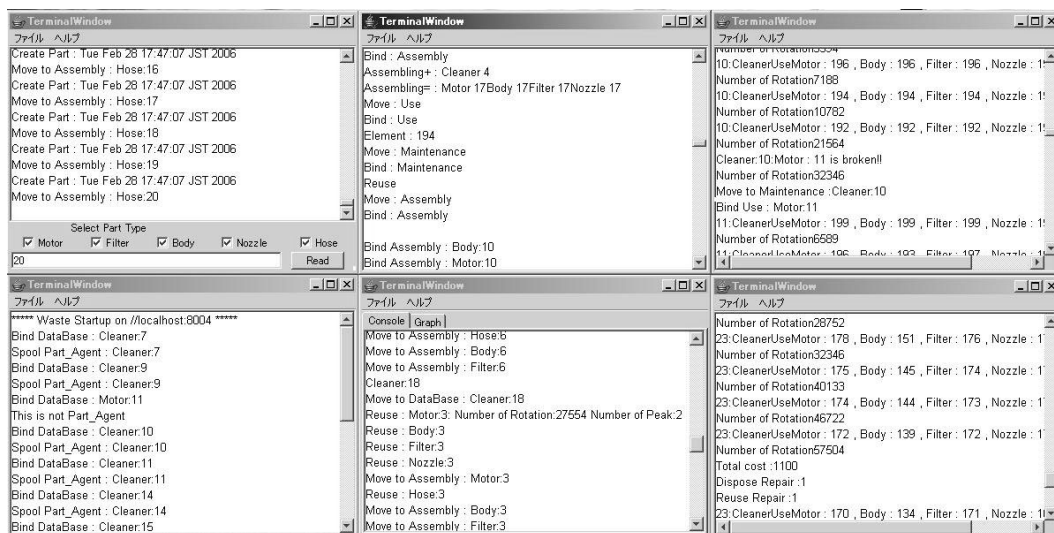


Fig. 1.5. Display of Part Agent System.

based on the number of damages caused by the operation with long period. This damage information is stored only in assembly and, although it is a single value, is supposed to be operation history in this simulation. If the maintenance requires this information, Part agent should send a subordinate information agent to find the assembly that contains the part now and one that contained the part previously.

Three types of maintenance are performed for comparison. Type A is the case where corrective maintenance is applied to all the parts. Type B is the case where predictive maintenance is applied for all the parts whenever possible. If the cumulative turns of motor exceeds 100,000 under this type of maintenance, the agent suggests repair of the assembly. Type C is the case where the operation history is checked for motors in addition to the predictive maintenance based on cumulative turns of motor. If the cumulative turns of motor exceeds 100,000 under this type of maintenance, the agent sends information agent and suggests repair of the assembly based on the historical damage information acquired by the information agent.

30 sets of vacuum cleaner are manufactured in the simulation. Part agent system as well as the mechanism searching the former assembly to obtain the operation history works well. Maintenance using the operation history is successfully performed.

The result of simulation is shown in **Figs. 1.6** and **1.7**. **Fig. 1.6** shows the cumulative cost of maintenance against the number of operations of cleaner. The difference between corrective maintenance and preventive maintenance is due to the difference of their cost. Effect of use of the operation history can be seen.

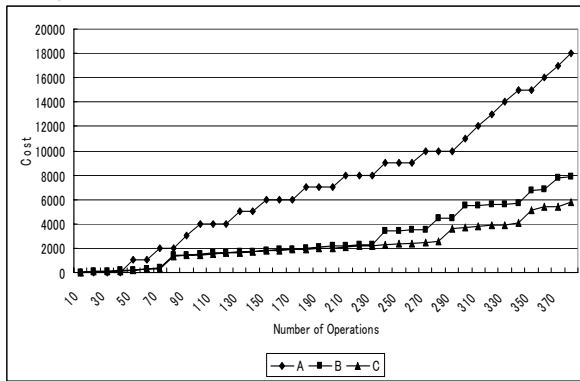


**Fig. 1.6.** Comparison of Maintenance Cost.

**Fig. 1.7** shows the number of maintenance actions. Even if the preventive maintenance is performed, corrective maintenance is also required due to the randomness of failure and unpredictable cause of deterioration. Examining the operation history reduces the number of corrective maintenance.

Though the result shows the effectiveness of the scheme, it is not fully persuasive because the simulation is based on a simple model. We should further research the applicability and effectiveness of the method.

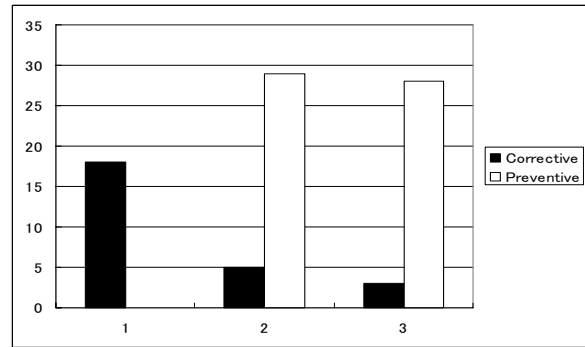


**Fig. 1.7.** Comparison of maintenance actions.

## 7 Conclusion

To achieve the effective re-use of parts, Part agent system is proposed that helps the users on maintenance of the part. In this paper, two functions of the system are focused. The mechanism is proposed to obtain the operation history stored in the former assembly that contained the part previously and web-based communication mechanism between user and Part agent is proposed. Preliminary result of simulation on retrieval of the operation history is reported. Related remaining issues are also discussed.

## Acknowledgement

This research is partly supported by IMS/PROMISE Project and Chuo University Joint Research Grant.

## References

- [1] Hiraoka H, et al., Network Agents for Life Cycle Support of Mechanical Parts, Proc. of EcoDesign2003, pp. 39-40, IEEE Computer Society, 2003.
- [2] Hiraoka H, Iwanami N, Network Agent's Advice for Promoting the Reuse of Mechanical Parts, Proc. of EcoDesign2005, 2005.
- [3] Voyager homepage, Recursion Software, Inc., <http://www.recursionsw.com/products/voyager/voyager.asp>.
- [4] Ohkubo M, Suzuki K, Kinoshita S, RFID Privacy Issues and Technical Challenges, Communications of the ACM, Vol.44, No.9, pp. 66-71, 2005.
- [5] Borriello G, RFID: Tagging the World, Communications of the ACM, Vol.44, No.9, pp. 34-37, 2005.
- [6] Suzuki M, Sakaguchi K, Hiraoka H, Life Cycle Support of Mechanical Product Using Network Agent, Initiatives of Precision Engineering at the Beginning of a Millennium (ed. Inasaki I), Kluwer Academic Publishers, pp. 912-916, 2001.
- [7] Hiraoka H, Ihara T, Workpiece-Centered Distributed System in the Shop Floors for Machining and Assembly, Advancement of Intelligent Production (ed. Usui E), Elsevier Science B.V., pp. 87-92, 1994.

---

# Multi-objective Reactive Scheduling Based on Genetic Algorithm

Yoshitaka TANIMIZU<sup>1</sup>, Tsuyoshi MIYAMAE<sup>1</sup>, Tatsuhiko SAKAGUCHI<sup>2</sup>, Koji IWAMURA<sup>1</sup>, Nobuhiro SUGIMURA<sup>1</sup>  
<sup>1</sup>Osaka Prefecture University, <sup>2</sup>Kobe University

Keywords: Reactive scheduling, Genetic algorithm, Crossover, Tardiness, Flow time, Multi-objective

## Abstract

A genetic algorithm based reactive scheduling method was proposed in the previous research, in order to modify and improve a disturbed initial production schedule without suspending the progress of manufacturing process. This paper proposes a new crossover method to improve the performance of the reactive scheduling method for total tardiness minimization problems and total flow time minimization problems. A multi-objective reactive scheduling method is also proposed based on the reactive scheduling method improved in this research. A prototype of multi-objective reactive scheduling system is developed and applied to computational experiments for job-shop type scheduling problems.

## 1 Introduction

It is assumed, in the traditional scheduling researches, that manufacturing environments are stable and controllable. However, unscheduled disruptions, such as delays of manufacturing operations, inputs of additional jobs and failures in manufacturing equipment, often occur in the agile manufacturing systems. If the disruptions occur during the progress of manufacturing process, the initial production schedule is disturbed and the manufacturing system cannot satisfy the predetermined constraints on the make-span and the due dates. Therefore, a systematic scheduling method is required to modify the disturbed initial production schedule to cope with the unforeseen disruptions in the agile manufacturing systems.

Several scheduling methods have been proposed to cope with the disruptions in the manufacturing systems. The proposed methods are basically classified into two types. They are, real-time scheduling and reactive scheduling. Most of the existing researches on the real-time scheduling use the heuristic rules, such as FCFS, SPT and MWKR, to select the next job to be manufactured, when manufacturing equipment finishes its present job in the manufacturing system [1]-[2]. There are still some remaining problems in the existing real-time scheduling methods from the viewpoint of the optimization of the production schedules. The reactive scheduling method modifies the predetermined initial production schedule, when unscheduled disruptions occur in the manufacturing system [3]. The existing reactive

scheduling methods are not enough to generate optimal production schedules during the progress of manufacturing process.

The previous research proposed a Genetic Algorithm (GA) based reactive scheduling method [4]. The proposed reactive scheduling method can modify and improve the disturbed initial production schedule without interrupting the manufacturing processes, when unscheduled disruptions occur in the manufacturing system and the production schedule cannot satisfy the given due-date of products.

This paper deals with a new crossover method to improve the performance of the GA based reactive scheduling method for the total tardiness minimization problems and the total flow time minimization problems. The multi-objective reactive scheduling method is also proposed based on the reactive scheduling method improved in this research. A prototype of reactive scheduling system is developed and applied to the multi-objective reactive scheduling problem of the total tardiness minimization and the total flow time minimization.

## 2 Reactive Scheduling Method Using GA

### 2.1 Reactive Scheduling Concept

The reactive scheduling process is activated, only when unscheduled disruptions occur during the manufacturing process. It is necessary to consider the progress of manufacturing process in the reactive scheduling process.

It is assumed in this research that the reactive scheduling process improves the disturbed production schedule, without suspending the progress of manufacturing process. Figure 1 shows the whole reactive scheduling process proposed in this research. The reactive scheduling process is activated at the present time  $T_1$ , only when some unscheduled disruptions occur and the predetermined production schedule does not satisfy the given constraint. It is assumed that the reactive scheduling process takes computation time  $dt$  to generate new feasible schedule. Therefore, the schedules of the operations starting before  $(T_1 + dt)$  cannot be modified through the reactive scheduling process.

A modified production schedule is applied to the manufacturing system, if the modified production schedule is

better than the current production schedule. When the newly generated production schedule does not satisfy the given constraint, the reactive scheduling process is activated continuously until new production schedule satisfies the given constraints, or until all the manufacturing operations have already started.

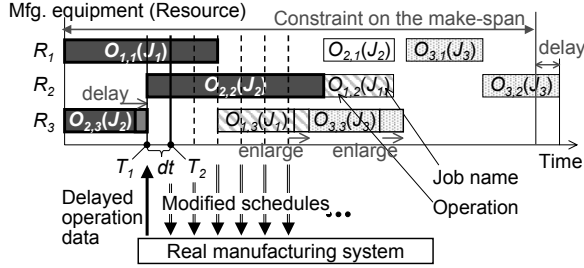


Fig. 1. Reactive scheduling process

## 2.2 Basic Reactive Scheduling Method Using GA

The proposed reactive scheduling method uses GA to improve the disturbed initial production schedule [4]. The GA is a probabilistic search technique based on the evolution mechanism [5]. The algorithms start with a population of parent individuals from which offspring are generated. Each individual has a chromosome, and it is evaluated based on a fitness value.

A production schedule is represented as a chromosome in the GA based scheduling method. The genes in the chromosome represent the job names of the operations to be completed. The job names are allocated to an array in the order of the execution sequence of the operations, as shown in Figure 2. This array of the job names represents the chromosome of the first individual. Other individuals in the initial population are randomly created by changing the positions of the genes of the first individual. The number of the individuals in the initial population equals to the population size  $s$ .

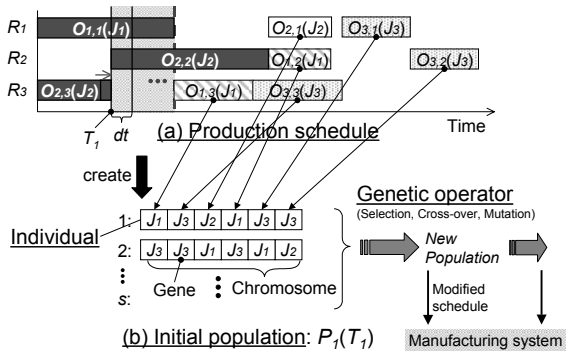


Fig. 2. Generation of initial population using GA

A fitness value, such as the value of make-span, total tardiness and total flow time, is evaluated for each individual. Based on the fitness value, genetic operators, such as selection, crossover and mutation, are applied to the

individuals, in order to create new individuals representing the modified production schedules. The current schedule of the manufacturing system is replaced by the new schedule. If the improved schedule does not satisfy the constraint on the make-span, the genetic operators are applied to the individuals. The reactive scheduling processes are repeated until new production schedule satisfies the given constraints, or until all the manufacturing operations have already started.

## 3 Advanced Crossover Method

A new crossover method is proposed, in this research, to generate suitable individuals faster than the basic reactive scheduling method using the conventional crossover method. The conventional crossover method exchanges all the genes between two crossover points, which are randomly selected in two parent individuals, and generates two offspring individuals. The new crossover method exchanges genes of two individuals in consideration of the dominance and recessiveness of genes from the viewpoint of the objective functions, such as the total tardiness and the total flow time.

### 3.1 Evaluation of Genes for Tardiness Minimization

The total tardiness of jobs is calculated by using the following equation.

$$\sum_{i=1}^n \max(0, C_i - dd_i) \quad (1)$$

Where,

$C_i$ : completion time, which represents maximum value of the finishing time of the job  $J_i$ .

$dd_i$ : due date of the job  $J_i$ .

$n$ : total number of jobs.

When the  $k$ -th gene is decoded to the  $h$ -th operation of job  $J_i$ , the lower bound of the finishing time of the operation is estimated for the  $k$ -th gene of the individual by using the following equation.

$$Lb_k = \left( f_i^{(h)} + \sum_{s=h+1}^n pt_i^{(s)} \right) - dd_i \quad (2)$$

where,

$f_i^{(h)}$ : finishing time of the  $h$ -th operation of the job  $J_i$ .

$pt_i^{(s)}$ : processing time of the remaining operations of the job  $J_i$ .

If the value of  $Lb_k$  is more than 0, it is impossible for the job  $J_i$  to finish the remaining operations by its due date. Therefore, the evaluation value for the recessiveness of genes is defined for the tardiness minimization problem as the following equation.



$$RC_k = \begin{cases} 0 & (Lb_k \leq 0) \\ 1 & (Lb_k > 0) \end{cases} \quad (3)$$

### 3.2 Evaluation of Genes for Flow Time Minimization

The total flow time of jobs is defined by the following equation.

$$\sum_{i=1}^m (ft_i^{(n)} - st_i^{(1)}) \quad (4)$$

Where,

$ft_i^{(n)}$ : finishing time of the last operation of the job  $J_i$ .  
 $st_i^{(1)}$ : starting time of the first operation of the job  $J_i$ .

The waiting time of the  $h$ -th operation of the job  $J_i$  is defined by the following equation.

$$wt_i^{(h)} = st_i^{(h)} - ft_i^{(h-1)} \quad (5)$$

Where,

$st_i^{(h)}$ : starting time of the  $h$ -th operation of the job  $J_i$ .  
 $ft_i^{(h-1)}$ : finishing time of the  $(h-1)$ -th operation of the job  $J_i$ .

The decrease of the waiting time makes the flow time of the job short in the production schedule. Therefore, the waiting time of each operation is compared with the average waiting time of operations for all the jobs, in order to evaluate the recessiveness of gene in the individual. When the  $k$ -th gene is decoded to the  $h$ -th operation of job  $J_i$ , the evaluation value for the recessiveness of genes is defined as the following equation for flow time minimization problems,

$$RC_k = \begin{cases} 0 & (wt_i^{(h)} \leq wt_{ave}) \\ 1 & (wt_i^{(h)} > wt_{ave}) \end{cases} \quad (6)$$

Where,

$wt_{ave}$ : average waiting time of operations of all the jobs.

### 3.3 Exchange of Genes in Crossover Process

Two crossover points are randomly selected in two parent individuals. The individuals exchange the genes between the crossover points with each other. The advanced crossover method proposed in this research changes only the recessive genes, which have the evaluation value of 0. The rest of genes are inherited to offspring individuals as the dominant genes, which have the evaluation value of 1.

The genes whose job names are same as the job name of the allele are searched from the front of the former crossover point as the candidate of the gene to be exchanged, since the jobs allocated former in the individual are executed earlier than the ones allocated latter. The position of the gene is exchanged with the one of the genes selected from the candidate, as shown in Fig. 3.

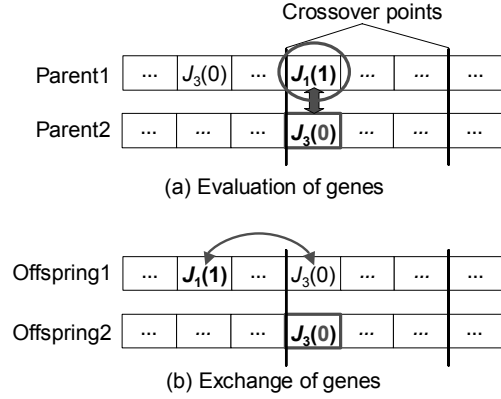


Fig. 3. Crossover process

## 4 Multi-objective Reactive Scheduling

### 4.1 Advanced Crossover for Multi-objective Problem

More than one objective function is simultaneously considered in the multi-objective scheduling problems. The combination of the evaluation values for recessiveness of gene is discussed in this section for the multi-objective reactive scheduling problems.

If  $p$  kinds of objective functions are considered in the reactive scheduling problems, each gene has  $p$  evaluation values for recessiveness of gene. The advanced crossover method changes the recessive genes, which have more than one evaluation value of 1, and inherits the dominant genes, which have all the evaluation value of 0, to offspring individuals.

In case of the combination of the total tardiness and the total flow time, the genes whose job names are same as the job name of the allele are searched from the front of the former crossover point as the candidate of the gene to be exchanged. The position of the gene is exchanged with the one of the genes selected from the candidate.

### 4.2 Multi-objective Reactive Scheduling Process

The multi-objective reactive scheduling processes consist of the following five steps.

*Step 1: Setting up of present time  $T_i$*

The present time  $T_i (i=1, 2, \dots)$  is set up.

*Step 2: Estimation of computation time  $dt$*

The computation time  $dt$  is the time in which GA creates a new generation of the populations representing the modified production schedules. The time  $dt$  is estimated based on the time needed to generate a new population in the GA based initial production scheduling process, and it is modified based on the time for creating the modified production schedules through Step 3 to Step 5.

*Step 3: Creation of initial population*

Two cases are considered in the creation of the initial population constituted of the individuals.

*Step 3-1: First activation of the reactive scheduling process*

In case of the first activation of the reactive scheduling process at time  $T_1$ , the reactive scheduling system has only the initial production schedule. Therefore, the reactive scheduling process generates the initial population based on the initial production schedule as shown in Figure 2. The first individual is generated by allocating the job names of the operations starting after  $(T_1 + dt)$  to an array. Other individuals in the initial population are randomly created by changing the positions of the job names of the first individual.

*Step 3-2: Second or later activations of the reactive scheduling process*

In case of the second or later activations of the reactive scheduling process at time  $T_2$  or later, the reactive scheduling process can inherit the population created in the previous reactive scheduling process. In other words, the last population of the previous reactive scheduling process can be the initial population. Two cases are considered for the inheritance process of the population as shown in the followings.

*Case-A: No operations start between  $T_i$  and  $(T_i + dt)$*

If no operations start between  $T_i$  and  $(T_i + dt)$ , all the individuals of the last population of the previous reactive scheduling process are inherited to a new reactive scheduling process between  $T_i$  and  $(T_i + dt)$ .

*Case-B: Some operations start between  $T_i$  and  $(T_i + dt)$*

If some operations start between  $T_i$  and  $(T_i + dt)$ , the production schedules of these operations should be fixed. Therefore, a new reactive scheduling process can inherit only the individuals, which are consistent with the schedules of the fixed operations, from the last population created in the previous reactive scheduling process. The other individuals are deleted, and new individuals are randomly created from the inherited ones.

*Step 4: Creation of next population*

All the individuals in the population created in Step 3 are evaluated, and applied the genetic operators, such as selection, crossover and mutation, in order to create new individuals of the next population.

*Step 4-1: Pareto rankings*

The pareto ranking method proposed by Goldberg [6] is used to provide the rank for the individuals in the population. All non-dominated individuals have same rank, which represents equal probability of being selected. Non-dominated individuals in the population are firstly assigned rank 1 in the ranking process. Then, the individuals having rank 1 are removed from a set of candidates of individuals. The ranking method gives rank 2 to non-dominated individuals in the remaining individuals and removes them from the candidates. This ranking process is repeated, until all the individuals in the population are assigned the rank.

*Step 4-2: Application of selection operator*

Based on the rank, the selection operator is applied to the individuals of the population created in Step 3. All of the individual having rank 1 are selected and inherited to the next population.

*Step 4-3: Application of crossover operator*

The crossover operator is applied to the individuals, in order to create new individuals. Based on the rank, two individuals are selected by using the roulette selection. Two crossover points are randomly selected in the individuals. If the gene between the crossover points in an individual has more than one evaluation value of 1, the position of gene is changed with the one of gene whose job name is same as the job name of the allele in the other individual. The rest of genes are inherited to offspring individuals in the next population.

*Step 4-4: Application of mutation operator*

The mutation operator inverts the positions of genes between two points selected randomly in the individual.

*Step 5: Evaluation of modified production schedule*

*Step 5-1: Selection of most suitable production schedule*

The most suitable production schedule is selected in the new individuals created in Step 4, in order to exchange it for the current production schedule. The value of each objective function is firstly normalized by using the following equation. This equation makes it lie between 0 and 1.

$$Of'_p = \frac{Of_p - \min Of_p}{\max Of_p - \min Of_p} \quad (7)$$

Where,

$Of'_p$  : normalized value of the objective function  $f_p$ .

$Of_p$  : value of the objective function  $f_p$ .

$\min Of_p$  : minimum value of the objective function  $f_p$ .

$\max Of_p$  : maximum value of the objective function  $f_p$ .

All the normalized objective functions are secondly combined as an integrated objective function by using the following equation. Each individual is provided with an integrated objective function as a criterion for the selection of the most suitable production schedule in the new individuals.

$$OF = \sum_{p=1}^r w_p Of'_p \quad (8)$$

$$\sum_{p=1}^r w_p = 1 \quad (9)$$

Where,

$w_p$  : weight for the objective function  $f_p$ .

*Step 5-2: Exchange of current production schedule*

If the most suitable production schedule in the new individuals makes one of the objective functions, such as the

total tardiness and total flow time, shorter than the one of the current production schedule, the new production schedule is substituted for the current production schedule. If all the objective functions of the new production schedule are shorter than the constraint on the objective functions, the reactive scheduling process is terminated.

All the steps from Step 1 to Step 5 are repeated, until the created production schedule satisfies the given constraint on all the objective functions or all the manufacturing operations have started in the manufacturing system.

### 5 Computational Experiments for Multi-objective Scheduling Problems

A prototype of multi-objective reactive scheduling system has been implemented and applied to the computational experiments for job-shop type scheduling problems. The experimental results of the new reactive scheduling method with the advanced crossover method were compared with the ones of the previous reactive scheduling method with the conventional crossover method. Numbers of jobs, manufacturing equipment and operations considered in the experiments were 50, 10 and 500, respectively. Parameters of GA, such as population size, crossover rate and mutation rate, were 30, 0.8 and 0.2, respectively. These parameter values were estimated based on preliminary case studies of job-shop type production scheduling problems.

Operations were randomly selected and their processing time was enlarged to less than five times. The prototype system automatically started reactive scheduling, in order to modify the disturbed production schedule. Figures 4 and 5 show experimental results of the previous reactive scheduling method and the new reactive scheduling method. The horizontal axis shows the time for reactive scheduling process and manufacturing process. The vertical axis shows the total tardiness and the total flow time of the modified production schedule in Figs. 4 and 5, respectively. These figures show that the new reactive scheduling method improves the disturbed production schedule faster than the previous method from the viewpoint of the minimization of the total tardiness and the total flow time.

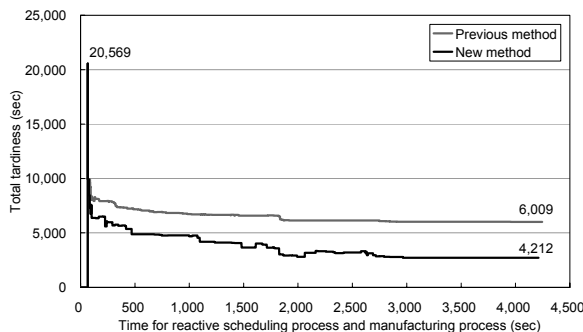


Fig. 4. Experimental results of total tardiness

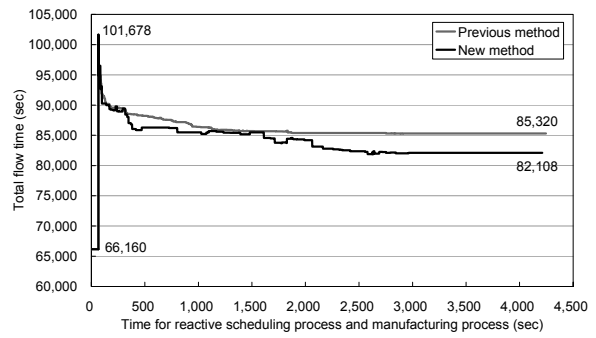


Fig. 5. Experimental results of total flow time

Ten cases of computational experiments were carried out based on the same initial production schedule. Different operations were randomly selected on each experiment and their processing time was enlarged. Figure 6 summarizes experimental results of the previous reactive scheduling method and the new reactive scheduling method. The vertical axis shows the decrease rate of the increased total tardiness and the decrease rate of the increased total flow time. This figure shows that the new reactive scheduling method improves the disturbed production schedule better than the previous method from the viewpoint of the minimization of the total tardiness and the total flow time.

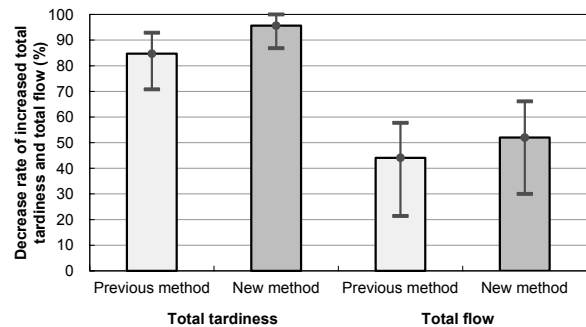


Fig. 6. Ten cases of experimental results

Figures 7 and 8 show the variations of individuals of all the populations generated in the previous reactive scheduling method and the new reactive scheduling method, respectively. The horizontal axis shows the total tardiness. The vertical axis shows the total flow time. Through the analysis of the variations of individuals, the new reactive scheduling method generates more various individuals for searching feasible production schedules than the previous reactive scheduling method.

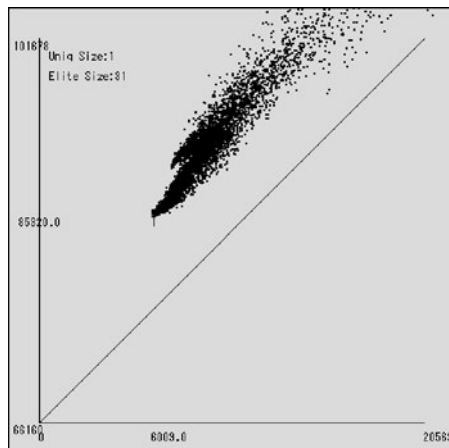


Fig. 7. Variations of individuals in previous method

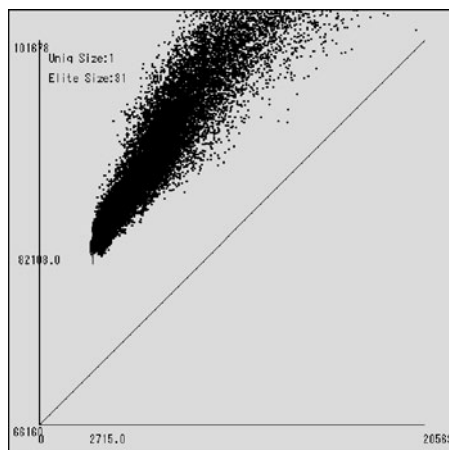


Fig. 8. Variations of individuals in new method

## 6 Conclusions

This paper proposed a new crossover method to improve the performance of the GA based reactive scheduling method for the total tardiness minimization problems and the total flow time minimization problems. The new crossover method exchanges genes of two individuals in consideration of the dominance and the recessiveness of genes, in order to improve the production schedule faster than the conventional method. The multi-objective reactive scheduling method was also proposed based on the improved reactive scheduling method in this research. The combination of the evaluation value for recessiveness of genes was discussed for the multi-objective reactive scheduling problems of the total tardiness minimization and the total flow time minimization. A prototype of multi-objective reactive scheduling system was developed and applied to the multi-objective reactive scheduling problems for the total tardiness minimization and the total flow time minimization. The experimental results have shown that the new reactive scheduling method is

superior to the previous reactive scheduling method from the viewpoint of the minimization of the total tardiness and the total flow time.

## 7 References

- [1] Shin H, Kuroda M, (1996) An autonomous job shop scheduling system under dynamic production environment considering machine breakdowns. *Advances in production management systems*, Chapman & Hall: 399-410
- [2] Sugimura N, Tanimizu Y, Iwamura K, (2004) A study on real-time scheduling for holonic manufacturing system. *CIRP journal of manufacturing systems*, 33, 5: 467-475
- [3] Smith SF, (1995) *Reactive scheduling systems*. Intelligent scheduling systems, Kluwer academic: 155-192
- [4] Tanimizu Y, Sugimura N, (2002) A study on reactive scheduling based on genetic algorithm. *Proc. of the 35th CIRP international seminar on manufacturing systems*: 219-224
- [5] Hollanad JH, (1975) *Adaptation in natural and artificial systems*. University of Michigan press
- [6] Goldberg DE, (1989) *Genetic algorithm in search, optimization and machine learning*. Addison Wesley, Reading, Massachusetts

# Ultraprecision Wide-angle Profile Measurement with Air-bearing Cylinder Slant Probes

Sei MORIYASU

RIKEN Institute, Advanced Development & Supporting Centre, Rapid Engineering Team

Keywords: Profile measurement, Probe, Optics, Air-bearing cylinder, Slant probe, On-machine measurement, 3D-CMM

## Abstract

This chapter introduces a newly-developed profile measuring method with air-bearing cylinder slant probes to measure the profile in the wide range of angles with high accuracy. The air-bearing cylinder can be moved by electric-pneumatic regulator accurately with low friction. Since the measuring force can be controlled in a very low value, high measuring accuracy can be obtained. And the combination of multiple measurements by using slant probes enables to achieve high measuring accuracy in the points with steep angles. The air-bearing cylinder slant probe can be also applied to general 3D-CMM to improve the measuring accuracy.

## 1 Introduction

Demands for CCD camera lens of cellular phones or pick-up lens for CD or DVD players have been increasing in these days. Some of these lens profile have steep angle of over 70 degrees to achieve high quality and multi-functions. In many cases, it is very difficult not only to machine lens or lens molds with steep angle, but also to measure the profile with high repeatability and accuracy.

In this chapter, a new profile measuring method with an air-bearing cylinder slant probe or probes is introduced to achieve high repeatability and accuracy in the profile measurement of the surface with steep angles.

## 2 Difficulties with Wide-Angle Profile Measurement

### 2.1 Probe Structure

Fig. 1 shows the schematic view of the profile measuring probe for ultraprecision optics with an air-bearing cylinder. The air-bearing cylinder has large stiffness in the radial direction and much small stiffness in the axial direction, and it can be moved in the axial direction with no friction by air pressure. By controlling the air pressure in a low value with the high resolution electro-pneumatic regulator, the measuring force can be controlled precisely in about 100mgf or lower. Gravity cancel port is used when the probe is installed

vertically or slantly in the vertical direction to cancel the gravity force to the probe shaft.

The tip of the probe shaft has a sphere ball which is contacted with the surface of the measured object. The movement of the probe shaft can be measured with the displacement sensor attached to the opposite side of the probe shaft.

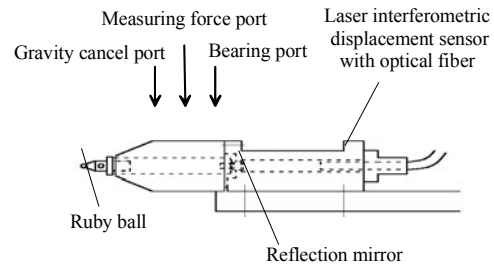


Fig. 1. Schematic view of a profile measuring probe

### 2.1 Kinematic Analysis

Fig. 2 shows the kinematic model of the profile measuring probe when the tilt surface whose angle is  $\phi$  is measured with the measuring force  $F_y$ . The tip sphere ball of the probe whose radius is  $r$  is contact with the surface of the measured object. The probe shaft is supported by two air bearings, whose lengths are  $l_1$  and  $l_2$ , and the lengths between the center of the tip ball of the probe and the endface of the air bearings are  $a$  and  $b$ .

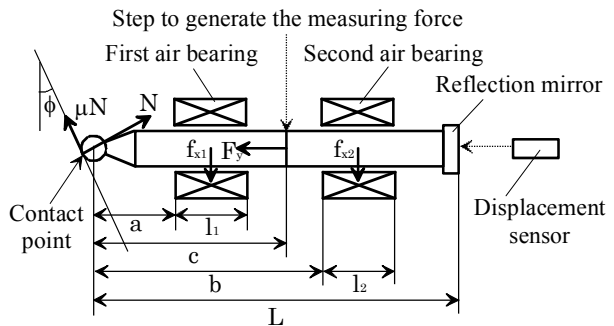
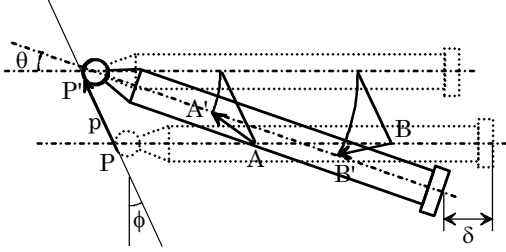


Fig. 2. Kinematic model of the profile measuring probe

During the measurement, the probe shaft is affected by the normal drag  $N$  and friction force  $\mu N$  from the measured object, so the probe shaft is tilted and slipped.

Assuming that the probe shaft is slipped between the length of  $p$  along the tangential line from the contact point  $P$  to  $P'$  and tilted in the angle of  $\theta$ , the cross points  $A$ ,  $B$  between the probe shaft and the first and second airbearings move to  $A'$ ,  $B'$  shown in **Fig. 3**. The probe shaft is balancing during the measurement among the forces  $N$ ,  $\mu N$ ,  $F_y$  and thrust forces at the air bearings,  $f_{x1}$ ,  $f_{x2}$ . The case that no change in acceleration (constant velocity) during the measurement is discussed.



**Fig. 3.** Slip and tilt model of the probe shaft

First the forces and moments generated at the air bearings are calculated. Assuming that the forces only in the radial direction are generated, the spring constants of the first and second air bearings along X axis,  $k_{x1}$ ,  $k_{x2}$ , are expressed as follows:

$$k_{x1} = \rho_1 l_1 \quad (1)$$

$$k_{x2} = \rho_2 l_2 \quad (2)$$

where  $\rho_1$  and  $\rho_2$  are the spring constant per unit length of the first and second air bearings.

Assuming that the forces in X direction and the moments around the center of the probe tip ball affected at the air bearings are  $f_{x1}$ ,  $f_{x2}$ , and  $M_1$ ,  $M_2$  respectively, the following equations can be expressed by using the equation (1) and (2).

$$\begin{aligned} f_{x1} &= \int_a^{a+l_1} \rho_1 (p \cos \phi - y \sin \theta) dy \\ &= k_{x1} \left[ p \cos \phi - \left( a + \frac{l_1}{2} \right) \sin \theta \right] \end{aligned} \quad (3)$$

$$\begin{aligned} f_{x2} &= \int_b^{b+l_2} \rho_2 (p \cos \phi - y \sin \theta) dy \\ &= k_{x2} \left[ p \cos \phi - \left( b + \frac{l_2}{2} \right) \sin \theta \right] \end{aligned} \quad (4)$$

$$\begin{aligned} M_1 &= \int_a^{a+l_1} \rho_1 (p \cos \phi - y \sin \theta) y dy \\ &= k_{x1} \left[ p \cos \phi \left( a + \frac{l_1}{2} \right) - \left( a^2 + a l_1 + \frac{l_1^2}{3} \right) \sin \theta \right] \end{aligned} \quad (5)$$

$$\begin{aligned} M_2 &= \int_b^{b+l_2} \rho_2 (p \cos \phi - y \sin \theta) y dy \\ &= k_{x2} \left[ p \cos \phi \left( b + \frac{l_2}{2} \right) - \left( b^2 + b l_2 + \frac{l_2^2}{3} \right) \sin \theta \right] \end{aligned} \quad (6)$$

Here the equations of motion are following,

$$0 = -f_{x1} - f_{x2} + N \sin \phi + \mu N \cos \phi \quad (7)$$

$$0 = F_y - N \cos \phi + \mu N \sin \phi \quad (8)$$

$$0 = M_1 + M_2 + r \cdot \mu N + c \cdot F_y \sin \theta \quad (9)$$

The normal drag  $N$  is solved from the equation (8);

$$N = \frac{F_y}{\cos \phi - \mu \sin \phi} \quad (10)$$

Under the approximation that the stiffness of the air bearings in the axial direction is ignorable to that in the radial direction, the tilt angle  $\theta$  and the slip length  $p$  are expressed from the equations (3) to (10) as follows;

$$\theta = \frac{\{A(\sin \phi + \mu \cos \phi) + \mu(k_{x1} + k_{x2})r\}F_y}{\{(k_{x1} + k_{x2})B - A^2\}(\cos \phi - \mu \sin \phi)} \quad (11)$$

$$p = \frac{\{B(\sin \phi + \mu \cos \phi) + \mu A r\}F_y}{\{(k_{x1} + k_{x2})B - A^2\}(\cos \phi - \mu \sin \phi) \cos \phi} \quad (12)$$

where some parameters are replaced as follows;

$$A \equiv k_{x1} \left( a + \frac{l_1}{2} \right) + k_{x2} \left( b + \frac{l_2}{2} \right) \quad (13)$$

$$B \equiv k_{x1} \left( a^2 + a l_1 + \frac{l_1^2}{3} \right) + k_{x2} \left( b^2 + b l_2 + \frac{l_2^2}{3} \right) \quad (14)$$

When the same two air bearings are used, the spring constants  $k_{x1}$ ,  $k_{x2}$  and lengths  $l_1$ ,  $l_2$  are the same  $k_x$  and  $l$  respectively. The equations (11), (12) can be simplified;

$$\theta = C \cdot \xi \cdot \Phi \quad (15)$$

$$p = D \cdot \xi \cdot \frac{\Phi}{\cos \phi} \cdot a \quad (16)$$

where some parameters are replaced as follows;

$$C \equiv \frac{\left(\frac{b}{a}\right) + \left(\frac{l}{a}\right) + 1}{\left\{\left(\frac{b}{a}\right) - 1\right\}^2 + \frac{1}{3}\left(\frac{l}{a}\right)^2} \quad (17)$$

$$D \equiv \frac{\left(\frac{b}{a}\right)^2 + 1 + \left\{\left(\frac{b}{a}\right) + 1\right\}\left(\frac{l}{a}\right) + \frac{2}{3}\left(\frac{l}{a}\right)^2}{\left\{\left(\frac{b}{a}\right) - 1\right\}^2 + \frac{1}{3}\left(\frac{l}{a}\right)^2} \quad (18)$$

$$\xi \equiv \frac{F_y}{k_x a} \quad (19)$$

$$\Phi \equiv \frac{\sin \phi + \mu \cos \phi}{\cos \phi - \mu \sin \phi} \quad (20)$$

The measurement error  $\delta$  in the normal axis caused by the tilt and slip of the probe shaft is expressed as follows;

$$\begin{aligned} \delta &= p \sin \phi + L(1 - \cos \theta) \\ &\approx \left[ D \tan \phi \cdot \Phi \cdot \xi + \frac{1}{2} \left(\frac{L}{a}\right) (C \cdot \xi \cdot \Phi)^2 \right] \cdot a \end{aligned} \quad (21)$$

In the equation (21), the first term is the error caused by the tilt of the probe shaft and the second term is the error caused by the slip of the probe shaft. Since the probe is designed as the stiffness of the air bearings bigger and the measuring force smaller to achieve high accuracy, the absolute value of  $\xi$  is thought to be much smaller than 1. When the tilt angle of the measured object  $\phi$  is relatively big, the measurement error  $d$  is mainly caused by the tilt of the probe shaft. The equation (21) is simplified as follows;

$$\begin{aligned} \delta &\approx D \tan \phi \cdot \Phi \cdot \xi \cdot a \\ &= D \cdot \xi \cdot a \cdot \tan \phi \cdot \Phi \\ &\equiv k_1 \cdot \tan \phi \frac{\sin \phi + \mu \cos \phi}{\cos \phi - \mu \sin \phi} \end{aligned} \quad (22)$$

When the measured surface is ideally smooth and the friction force is almost zero ( $\mu = 0$ ), the equation (22) is simplified as follows;

$$\delta = k_1 \cdot \tan^2 \phi \quad (23)$$

When the measurement error at the measured surface angle  $\phi$  of 45 degree is defined  $\delta_{45}$ ,

$$k_1 = \frac{\delta_{45}}{\tan^2 45^\circ} = \delta_{45} \quad (24)$$

The equation (23) can be expressed as follows;

$$\delta = \delta_{45} \cdot \tan^2 \phi \quad (25)$$

The measurement error  $\delta$  caused by the tilt of the probe shaft increases in proportion to  $(\tan \phi)^2$ , and has very big value in the steep surface near 90 degree.

From the equations of (19) and (22), the relation between the measuring force  $F_y$  and the measured surface angle  $\phi$  can be expressed as follows;

$$\begin{aligned} F_y &= k_x a \cdot \xi = \frac{k_x \cdot \delta}{D \tan \phi \cdot \Phi} \\ &\equiv k_2 \cdot \frac{\cos \phi - \mu \sin \phi}{\tan \phi (\sin \phi + \mu \cos \phi)} \end{aligned} \quad (26)$$

In the same way at the discussion of the measurement error  $\delta$ , when the measured surface is ideally smooth and the measuring force at the measured surface angle  $\phi$  of 45 degree is defined  $F_{45}$ , the equation (26) can be expressed as follows;

$$F_y = \frac{F_{45}}{\tan^2 \phi} \quad (27)$$

The measuring force  $F_y$ , with which the measurement error  $\delta$  is less than the desirable measurement accuracy, is in proportion to  $(\tan \phi)^{-2}$ , and must be controlled almost zero in the steep surface near 90 degree.

## 2.2 Maximum Scanning Speed Analysis

To conduct a profile measurement successfully, the probe shaft must be always contact with the surface of the measured object. Too fast scanning leads the probe tip to jumping from the surface of the measured object, and it is impossible to measure accurately along the surface profile. The following discussion is the analysis of the maximum scanning speed in which the profile measurement can be successfully conducted along the surface of the measured object.

Assuming that the measured surface is ideal periodic sine wave surface shown in **Fig. 4**, whose amplitude is  $A$ , angular frequency is  $\omega$ , wave length is  $d$ , the mass of the probe shaft is  $m$ , the measuring force is  $F_y$ , and the acceralation of the probe shaft in the amplitude direction is  $a$ , the equation of the motion is as follows;

$$ma = F_y \quad (28)$$

On the other hand, the position  $y$  in the amplitude direction on the measured surface can be expressed as follows;

$$y = A \sin \omega t \quad (29)$$

$$\frac{d^2 y}{dt^2} = -A\omega^2 \sin \omega \quad (30)$$

Here it is necessary that the acceleration of the probe shaft  $a$  is always more than the maximum acceleration of the measured object to keep the probe tip contact with the measured surface.

$$\left| \frac{d^2 y}{dt^2} \right|_{\max} = A\omega^2 \leq a = \frac{F_y}{m} \quad (31)$$

In case of satisfying the equation, the maximum angle frequency  $\omega_{\max} = 2\pi f_{\max}$  ( $f_{\max}$ : maximum scanning frequency), the following equation is satisfied;

$$A = \frac{F_y}{4\pi^2 m} \cdot \frac{1}{f_{\max}^2} \quad (32)$$

The maximum scanning speed  $v_{\max}$  can be expressed with the measuring data pitch  $d$  as follows;

$$v_{\max} = f_{\max} \cdot d = \frac{d}{2\pi} \cdot \sqrt{\frac{F_y}{mA}} \quad (33)$$

To improve the maximum scanning speed, it is necessary to make the measuring force  $F_y$  bigger or the mass of the probe shaft lighter. It is impossible in the conventional way to keep the measuring force  $F_y$  bigger in the measurement of a steep angle to maintain high measuring accuracy. So it is necessary to achieve high measuring accuracy to keep the mass of the probe shaft  $m$  lighter and shortly design the probe smaller and lighter. This means that it is necessary to use special micro machining method or special light material to design and manufacture the probe or to make a high-resolution controlling unit to keep the measuring force extremely light. It is so complicated that the cost of the total measuring system becomes up.

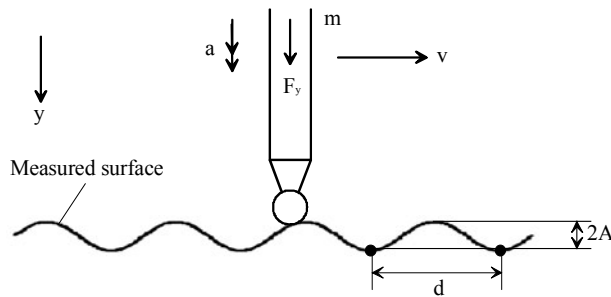


**Fig. 4.** Profile measurement of the ideal periodic sine wave surface

## 2.3 Conventional Improvements

Some improvements for the wide-angle profile measurement have been proposed as follows, but no way is the radical solution.

- Controlling the relative angle between measuring object and probe with the rotational table and calculate the profile.
- Controlling the measuring force as the normal force of the measured object is kept constant.
- Scanning only along the downward path.

## 3 Wide-angle Profile Measurement with Slant Probes

### 3.1 Concepts and Procedures

In the conventional measurement of axis-symmetrical aspherical shape, a probe is attached parallel to the axis of the measured object. In the slant probe measurement, a probe or several probes are attached with an angle of the axis, for example, 30 degree to 90 degree. The area which is measured with one probe is limited within the area which can be measured good, for example, from -45 degree to 45 degree or from -60 degree to 60 degree. In the whole surface measurement, the probe is detached and attached again in the different angle or several probes which are attached in the different angle from the beginning of the measurement are used. The whole surface profile are evaluated by connecting the multiple measured data with different angles.

**Fig. 5** shows the advantage of the slant probe measurement compared with the conventional measurement. In the slant probe measurement, it is possible to achieve high accuracy in the profile measurement of a steep surface in a poor accuracy in the conventional way, for example, 60 degree to 75 degree or a steeper surface which cannot be measured by the conventional way, for example, 75 degree to 90 degree and over 90 degree. In the conventional way, it is necessary to control the measuring force in a small value according to the increase of the surface angle to achieve high measuring accuracy. In the slant probe measurement, it is not necessary to control the measuring force in a low value to achieve high measuring accuracy in the measurement of a steep angle surface. This makes the free room for the design of the probe.

It is also possible to increase the measuring force  $F_y$  to improve the maximum scanning speed  $v_{\max}$ , so it is not necessary to use a compact and light-weight probe and high-resolution controlling unit of the measuring force. This contributes the total cost down.



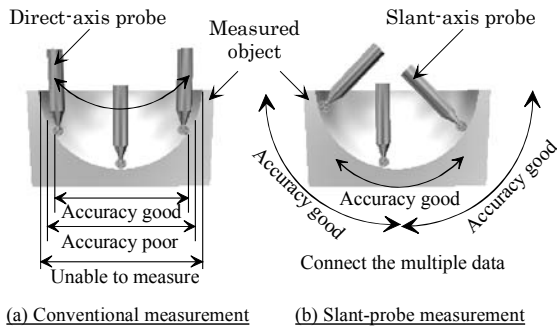


**Fig. 5.** Advantage of the slant probe measurement compared with the conventional measurement

### 3.2 Single Slant Probe Measurement

Single slant probe system is the simplest hardware set-up, in which several measurements are conducted with the probe attached angles changed, and the total profile is evaluated by connecting the multiple measured data.

However, it is necessary in each measurement to evaluate the initial probe attached angle in high accuracy and to conduct the centering procedure to search the center point of the measured object, so it is troublesome.

A system, in which a rotational stage is used to change the probe attached angle automatically in high accuracy, is useful, but it causes to the total cost up. Even if an automatic rotational stage is used, the reevaluation and recentering procedures are necessary when the positioning accuracy is not high enough.

### 3.3 Multi-probe Measurement

By using multiple probes, measurement procedures can be much simplified, because the reevaluation is conducted only when the probe is attached at the first time, and the centering is conducted only when the measured object is attached. When you want to measure the profile of wide-angle optics, for example, it is possible to measure the whole surface from the angle of  $-90$  degree to  $90$  degree by installing three measuring probes in the angle of  $-45$  degree,  $0$  degree and  $45$  degree, and each probe measurement is conducted from the angle of  $-45$  degree to  $45$  degree. The area where multiple measurements are overlapped can be used to check if the measurement process is good, or to connect data by the root mean square method when the initial probe attached angle could not be evaluated accurate enough. The number of probes, attached angles and measuring area, etc. should be decided according to the maximum angle of the measured object and the characteristics of the probes. **Fig. 6** shows the example of installing two probes in the angle of  $0$  degree and  $45$  degree.

### 3.4 On-machine Measurement

When an axis-symmetrical aspherical shape is measured on the machine, the axis of the measured object is precisely equal to the axis of the spindle because the measured object

is machined by rotating the workpiece spindle. So the three dimensional profile measurement can be conducted by using only one slant probe and the rotational angle positioning table (C axis).

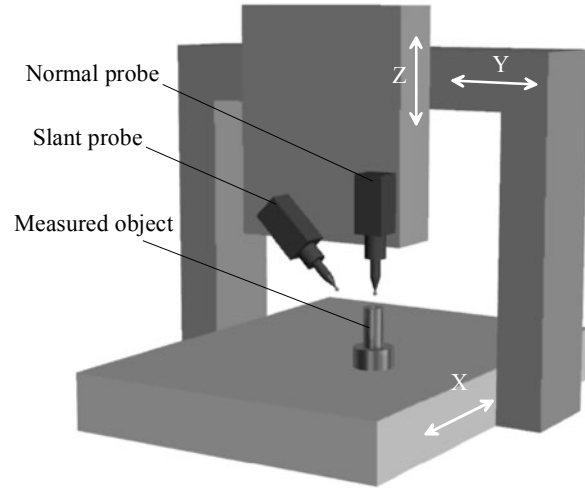


**Fig. 6.** An example of slant probe system with two probes in the angle of  $0$  degree and  $45$  degree

### 3.5 Application of Air-bearing Cylinder Probe to 3D-CMM

Slant probes have not been used in the conventional profile measurement for ultraprecision optics. On the other hand, the slant probe measurement with a touch probe is popular in the 3D-CMM, but the air-bearing cylinder probe whose measuring force can be precisely controlled by the air pressure has not been used in the 3D-CMM yet. To improve the measuring accuracy of 3D-CMM, the usage of the air-bearing cylinder probe instead of a touch probe is much effective. **Fig. 7** shows the samples of the probe head proposed for the higher-accuracy 3D-CMM with air-bearing cylinders.

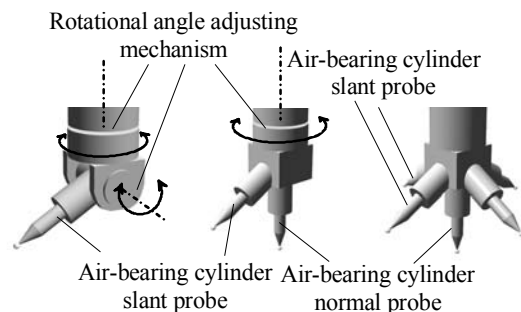


**Fig. 7.** Examples of the probe heads proposed for the higher-accuracy 3D-CMM with air-bearing cylinders

## 4 Experiments

### 4.1 Experimental Set-up and Procedures

A profile measurement with a slant probe was conducted on the lens cutting and grinding machine. Fig. 8 shows the schematic view of the experimental set-up. The machine had three linear stages (X-Y-Z axes) whose positioning resolution was 10nm. A profile measuring probe was attached in the angle of 45 degree to the Z axis in the X-Z plane on the machine. The measuring force of the probe was controlled in a low value of about 100mgf(0.98mN) by the electro-pnumatic regulator. A measured object whose shape was a sphere was attached on the workpiece spindle with the vacuum chuck. Profile measurements were conducted by sending NC data from PC to the NC controller to control the relative position between the measured object and the probe tip.

The centering procedure was conducted at the point with the angle of 0 degree to Z axis to adjust the tip ball of the probe with the center of the measured object. A profile measurement was conducted at the surface tilt angle from -50 degree to 50 degree with the 45-degree slant probe. This means the measurement from -5 degree to 95 degree against Z axis. Measured data was fitted to the ideal shape of sphere by the least mean square method and the profile error was calculated.

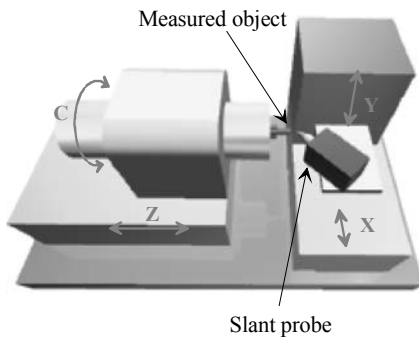


Fig. 8. Schematic view of the experimental set-up

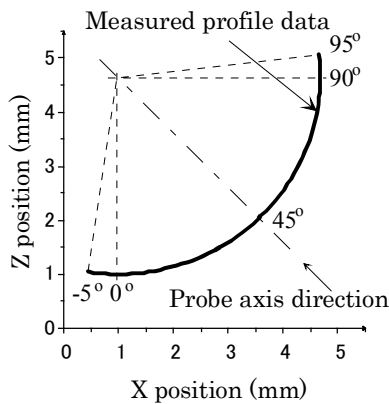


Fig. 9. Measured profile data with a slant probe

### 4.2 Experimental Results

Fig. 9 shows the measured profile data. Steep surface which is difficult or impossible to be measured by the conventional method with a pararell probe could be measured successfully.

Fig. 10 shows the profile error deviated from the sphere shape along the axis perpendicular to the probe shaft (-45 degree), because the measured data in the area near 90 degree can not be well fitted by calculating along X axis and the measured data in the area near 0 degree also can not be well fitted by calculating along Z axis.

## 5 Conclusion

In this chapter, a new profile measuring method by using air-bearing cylinder slant probes was introduced. This makes it possible to measure the profile with a steep angle in a good accuracy. It is expected that this measuring method is applied for the profile measurement of micro lenses or lens molds for CCD camera or DVD players, and the air-bearing cylinder probes make it possible to improve the measuring accuracy with 3D-CMM.

## 6 References

- Moriyasu S., Morita S., Yamagata Y., Ohmori H., Lin W., Kato J., Yamaguchi I., (2001) Development of on-machine profile measuring system with contact-type probe. Initiatives of Precision Engineering at the Beginning of a Millenium:594-598
- [1] Wills-Moren W.J., Modjarrad H., Read R.F.J., (1982) Some aspects of the design and development of a large high precision CNC diamond turning machine. Annals of the CIRP 31, 1:409-414

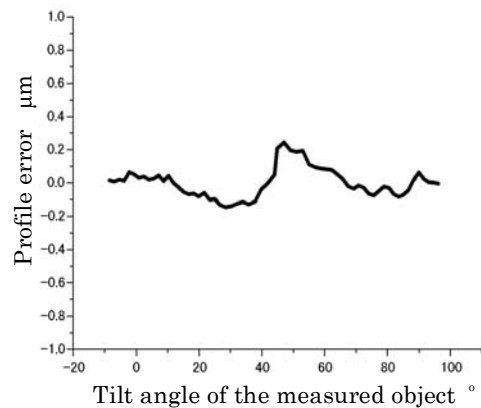


Fig. 10. Profile error calculated from the measured data

# Development of a Laser-Guided Deep-Hole Measuring System: Autocollimation System

A.Katsuki<sup>1</sup>, H.Murakami<sup>2</sup>, H.Onikura<sup>1</sup>, T.Sajima<sup>1</sup>

<sup>1</sup> Kyushu University, <sup>2</sup> Fukuoka Industrial Technology Center

Keywords: Deep hole, Laser, Autocollimation principle, Measurement, Roundness, Spherical aberration

## Abstract

It is very difficult to precisely measure the shape of a deep hole when the ratio of length to diameter ( $L/D$ ) is large. Until now, each accuracy have measured by each measuring device. To evaluate the accuracy of such a deep hole, the autocollimation principle is applied to a measuring system. The measuring system consists of a measuring unit, an actuator unit and a laser diode. The measuring unit is installed in the front end of the actuator unit. In this study, we examine the performance of the measuring unit by measuring the roundness of holes.

## 1 Introduction

Axial hole deviation in deep hole boring results in degradation of quality and a decrease in the yield rate of the products. In order to solve such problems, a 110-mm-diameter prototype laser-guided deep-hole boring tool is developed to prevent hole deviation; the attitude of this tool is controlled by piezoelectric actuators[1]. However, the evaluation of the hole after the boring process is problematic. Similarly, it is very difficult to precisely measure the shape of a deep hole when the ratio of length to diameter ( $L/D$ ) is large, e.g., a shaft of a jet engine, cylinder for plastic injection molding, cylinder liner of an engine of a large ship,

a cannon, etc. To date, the accuracy of a deep hole is determined by using measurement devices that can measure only one parameter. For example, the diameter, roundness, and straightness of a deep hole are measured by using a cylinder gage, a roundness tester, and an autocollimator, respectively.

To evaluate the accuracy of such a deep hole, the autocollimation principle is applied to a measuring system [2]. Figure 1 shows a measuring apparatus, i.e., the measuring system. This system consists of a measuring unit, an actuator unit, which controls the probe position and its inclination, and a laser diode. The laser diode is set at the back end of the actuator unit and is used to detect the position and inclination of the probe. The measuring unit is installed in the front end of the actuator unit, which is guided by the laser. The accuracy of the hole is measured by scanning the hole wall spirally. In this study, we examine the performance of the measuring unit by measuring the roundness of holes.

## 2 Measuring principle

Figures 2 and 3 show the measurement principle and the measuring unit, respectively.

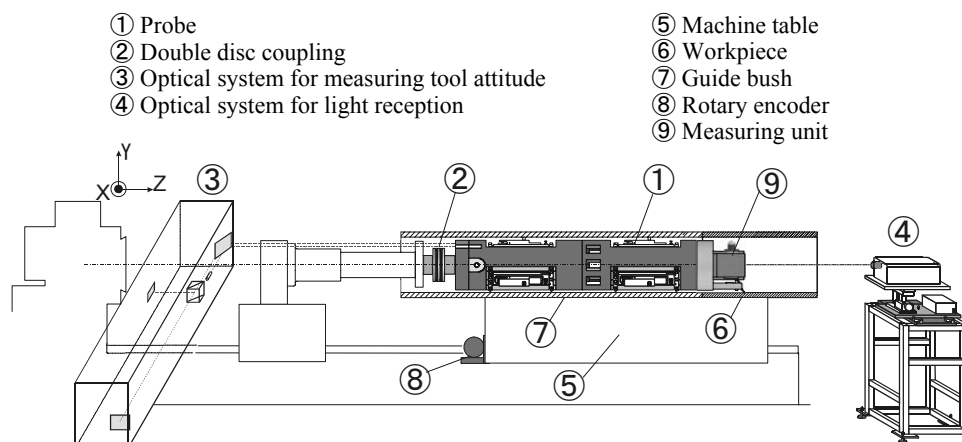


Fig. 1. Measuring apparatus

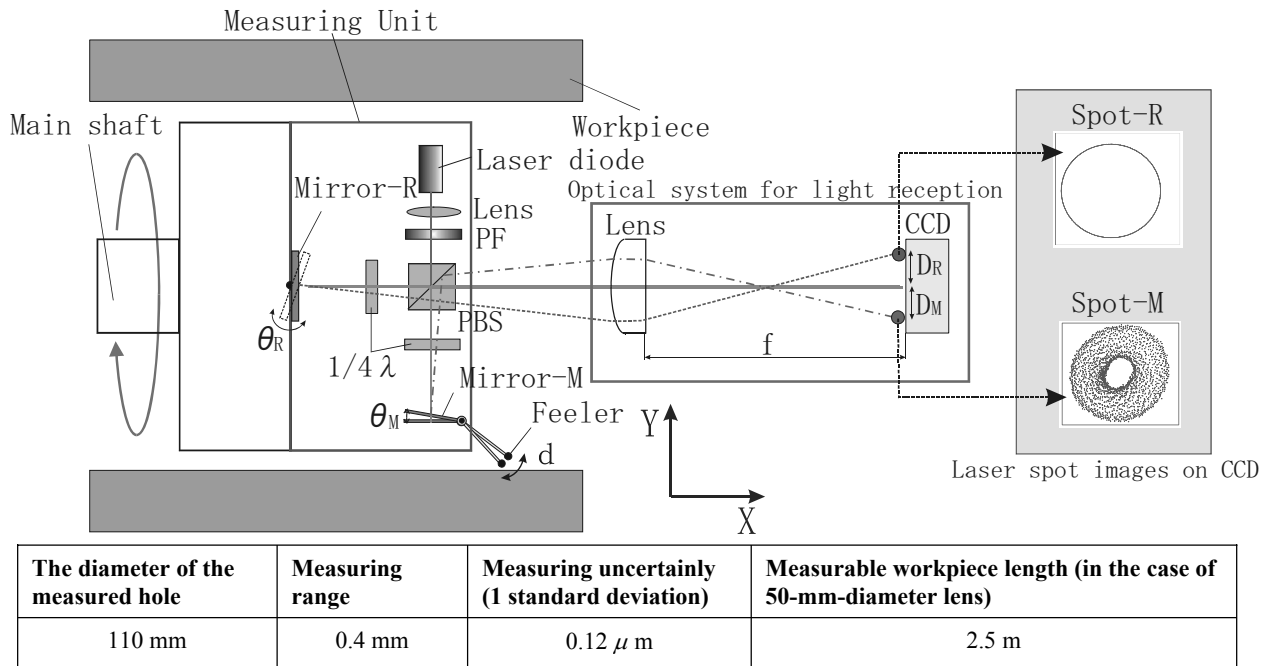


Fig. 2. Measurement principle of the topography of the hole wall

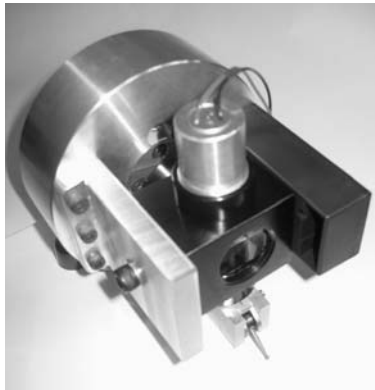


Fig. 3. Measuring unit

### 2.1 Measuring unit

The measuring unit detects the displacement of a feeler on the basis of the autocollimation principle (Fig.2). Mirror-M is used to measure the hole wall and is connected to the feeler. Mirror-R is used to detect the rotating angle of the main spindle and is installed on its rotation axis. After the laser beam is radiated to the polarizing beam splitter, it is divided into the transmitting and reflecting laser beams. These divided laser beams pass through the 1/4 wave plates, and reach Mirror-M and Mirror-R. They are then reflected toward the 1/4 wave plate. The beams passing through the 1/4 wave plate then reach the polarizing beam splitter and are reflected toward the measuring unit (X-direction).

### 2.2 Optical system for light reception

The optical system for light reception comprises a lens (plano-convex lens, focal distance  $f = 100\text{mm}$ ) and a CCD camera (CS5110, teli) and receives the laser beam irradiated from the measuring unit. The CCD images of the laser beams reflected in the Mirror-M and Mirror-R are defined as Spot-M and Spot-R, respectively. The ratio of incoming light at Spots-M and R is maintained at approximately 6:4 by adjusting the two 1/4 wave plates. The region with more than 100 gray level of the laser spot images on the CCD is labeled. Thus, there are two labeled regions, namely, Spot-M, where the luminance value is high, and Spot-R, where the luminance value is low. The two coordinates  $(x, y)$  of Spots-M and -R on the CCD are obtained by calculating the center of gravity of the labeled regions. Spots-M and -R on the CCD are displaced in the optical system for light reception when there is a tilting of the axis of the laser beam irradiated from the measuring unit. In other words, the tilting of Mirror-M causes the displacement of Spot-M on the CCD when the feeler of the measuring unit scans the hole wall and displaces due to its forms (by  $d$ ) (Fig.2). Consequently, the position of the wall surface is obtained. In a similar manner, a slight tilting of Mirror-R causes the displacement of Spot-R when the main spindle rotates. Consequently, the rotation angle and the inclination of the measuring unit can be obtained.

$f$  is the focal distance of the lens.  $D_M$  and  $D_R$  are the distance between the focus (the center in CCD) and the image points of the laser beams on the focuses of the Mirror-M and Mirror-R, respectively.  $\theta_M$  and  $\theta_R$  are the tilting angles of Mirror-M and Mirror-R, respectively.  $D_M$  and  $D_R$  can be expressed as follows:

$$D_M = 2f\theta_M, D_R = 2f\theta_R.$$

$$(1) \quad \theta_a = \theta_0 - \beta, \quad \theta_b = \sin^{-1}(n_0 \sin \theta_a / n_1) \quad (8)$$

### 2.3 Correction of spherical aberration

Since a plano-convex lens is used, the optical system for light reception is accompanied by an aberration. Spherical aberration is a phenomenon in which the ray that passes through the circumference of the lens and the ray that passes through the near center of the lens do not coincide at a point on the optic axis for the ray emitted from a point on the axis[3]. It is necessary to correct spherical aberration because it greatly influences the measurement accuracy. In this study, we use ray tracing to correct the spherical aberration of the lens.

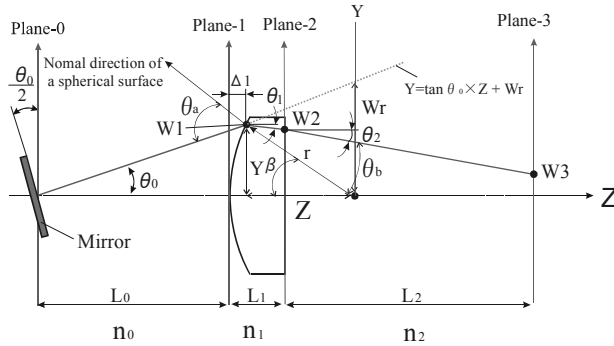


Fig. 4. Ray tracing of the optical system for light reception

Figure 4 shows the ray tracing of the optical system for light reception. Plane-0, plane-1, plane-2, and plane-3 correspond to Mirror-M and Mirror-R, the spherical tip of the plano-convex lens, the plane of the plano-convex lens, and the CCD image surface, respectively. The angle between the rotating axis and the laser beam axis is defined as  $\theta_0$ . The spot coordinate of the CCD is defined as  $W3$ . The following equations hold.

$$Wr = (L_0 + r) \tan \theta_0 \quad (2)$$

$$Z = (-\tan \theta_0 \cdot Wr - \sqrt{\tan^2 \theta_0 \cdot Wr^2 - (1 + \tan^2 \theta_0)(Wr^2 - r^2)}) / (1 + \tan^2 \theta_0) \quad (3)$$

$$\Delta 1 = r + Z \quad (4)$$

$$W1 = (L_0 + \Delta 1) \tan \theta_0 \quad (5)$$

$$W2 = W1 + (L1 - \Delta 1) \tan \theta_1 \quad (6)$$

$$\beta = \sin^{-1}(-W1/r) \quad (7)$$

$$\theta_1 = \beta + \sin^{-1}(n_0 \sin \theta_a / n_1) \quad (9)$$

$$\theta_2 = \sin^{-1}(n_1 \sin \theta_1 / n_2) \quad (10)$$

$$W3 = W2 + L_2 \tan \theta_2 \quad (11)$$

$$f(\theta_0) = -W3 + (L_0 + \Delta 1) \tan \theta_0 + (L1 - \Delta 1) \tan \theta_1 + L_2 \tan \theta_2 \quad (12)$$

where  $r$  is the radius of curvature of the lens;  $L_0, L_1$ , and  $L_2$  are the distances between plane-0 and plane-1, plane-1 and plane-2, and plane-2 and plane-3;  $Z$  is the distance from the center of curvature in the optic axis direction;  $n_0, n_1$ , and  $n_2$  are the refractive indices of the target planes;  $W_1, W_2, W_3$ , and  $W_r$  are the beam heights of the target planes;  $\theta_1$  and  $\theta_2$  are the tilt angles for the optic axis;  $\beta$  is the angle between the normal line drawn on the object curved surface and the optic axis;  $\theta_a$  is the angle of incidence;  $\theta_b$  is the angle of refraction; and  $\Delta 1$  is the offset from the top of a curved surface.

Thus, the tilting angles of Mirror-M and Mirror-R can be evaluated using Eq.12. The evaluation function  $f(\theta_0)$  can be calculated by using the quasi-newton method[4]. The displacement of the feeler  $d$  is then calculated based on the tilting angles of Mirror-M and Mirror-R.

### 2.4 Roundness error

The roundness error is measured as follows. Using the relative distance between the sequences of points (Spot-M) and those acquired by measuring a ring gage for the calibration of the 110-mm-diameter, we calculate the tilting angle of Mirror-M. Consequently, the displacement of the feeler can be obtained using Eq.(1).

## 3 Experimental method and result

### 3.1 Spherical aberration correction

The effect of spherical aberration is determined by measuring the aberration during a change in the optical axis inclination. Subsequently, the spherical aberration on the CCD is compared before and after the correction.

Figures 5 a and 5 b show the schematic diagram of the experimental apparatus and its photograph, respectively. The laser is installed in the main spindle of the NC machine tool (BN8, MAKINO). The laser is rotated at  $\theta = 0.1^\circ$  pitch

angle. The laser spot image on the CCD is recorded, and the spherical aberration  $\Delta h$  is evaluated. The distance  $d$  between the laser and the optical system for light reception is 800 mm.

Figure 6 shows the comparison between the spherical aberrations on the CCD before and after the correction. The horizontal axis shows the optic axis inclination of the laser, while the vertical axis shows the spherical aberration on the CCD from the theoretical focal position to the actual focal position. As shown in Fig. 6, the maximum spherical aberration on the CCD is 0.233 and 0.005 mm before and after the correction, respectively, according to Eq.12. The displacement of 0.005mm on the CCD corresponds to that of  $0.87 \mu\text{m}$  the feeler. These results show that the spherical aberration can be reduced by the calibration in which the ray tracing is used.

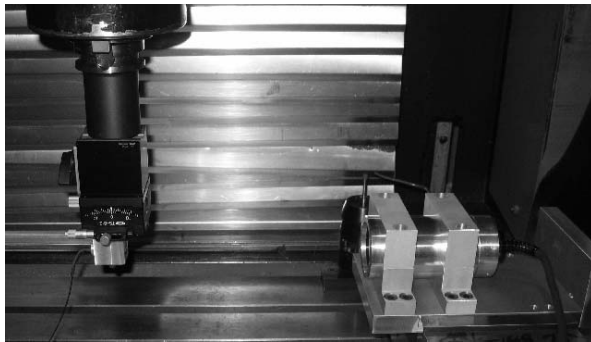
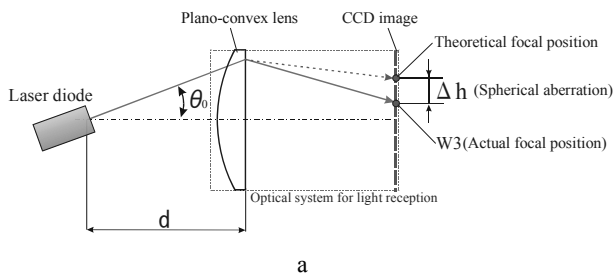


**Fig. 5.** Experimental apparatus for the measurement of the spherical aberration error: a. schematic diagram and b. photograph of the experimental apparatus.

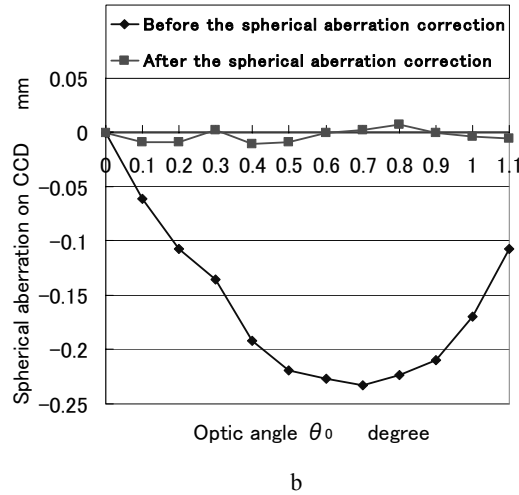
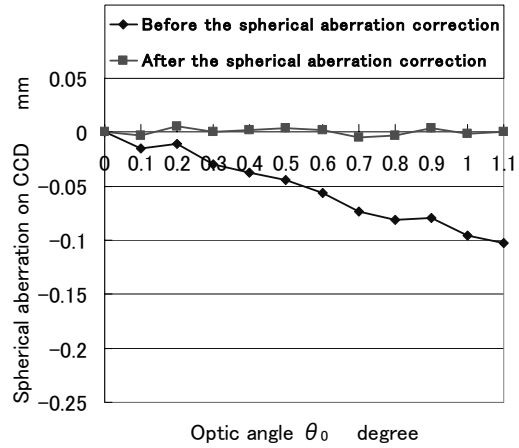


**Fig. 6.** Comparison between the spherical aberration on the CCD before and after the correction: a.  $d = 200$  mm and b.  $d = 800$  mm.

### 3.2 Roundness

The experiment is carried out by using basic apparatus for evaluating the accuracy of the roundness measurement. Figure 7 shows the basic experimental apparatus. The measuring unit is installed in the spindle that is fixed in the bearing holder. The spindle is coupled to a servo motor through a coupling.

The workpiece with a 110-mm-diameter hole is machined for roundness measurement by using a wire cut discharge processing machine (AQ325L, Sodik). A total of 163 waves with a 0.1 mm amplitude are machined on the circumference of the hole. The hole is measured at a rotation speed of  $0.75 \text{ min}^{-1}$  and a sampling frequency of 25.6 Hz. The cutoff filter is not used.

Figures 8 a and 8 b show the roundness of the workpiece measured by using the roundness tester (TALYROND252, Rank Taylor Hobson) and the measuring unit, respectively. The shapes and values determined using both the tools are very similar. However, Fig. 8 b shows that the measured roundness is slightly oval-shaped. This is because the center of the workpiece deviates from the rotation axis of the measuring unit.

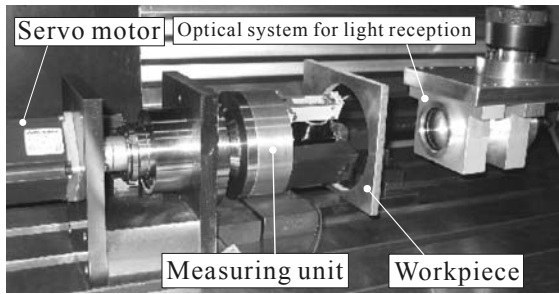


Fig. 7. Basic experimental apparatus

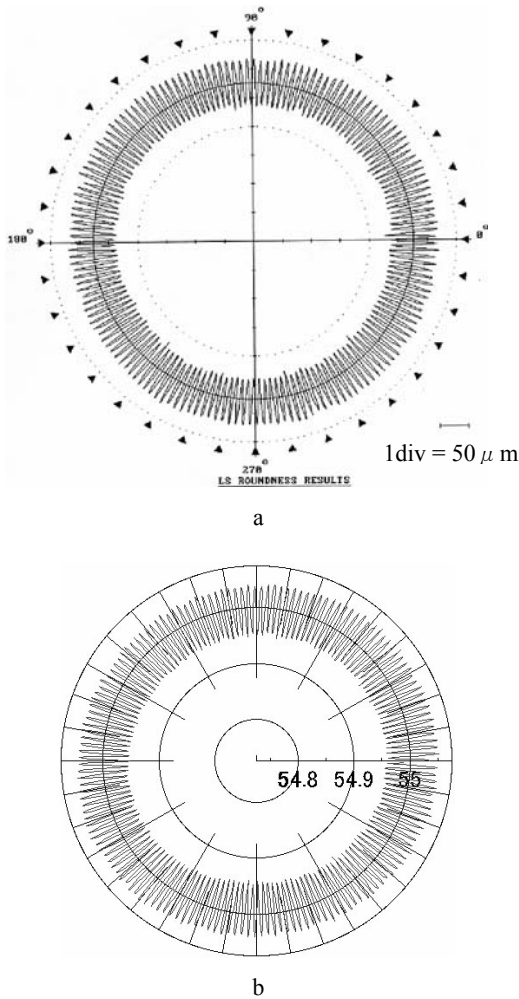


Fig. 8. Comparison of the roundness profiles by using the roundness tester and the measuring unit

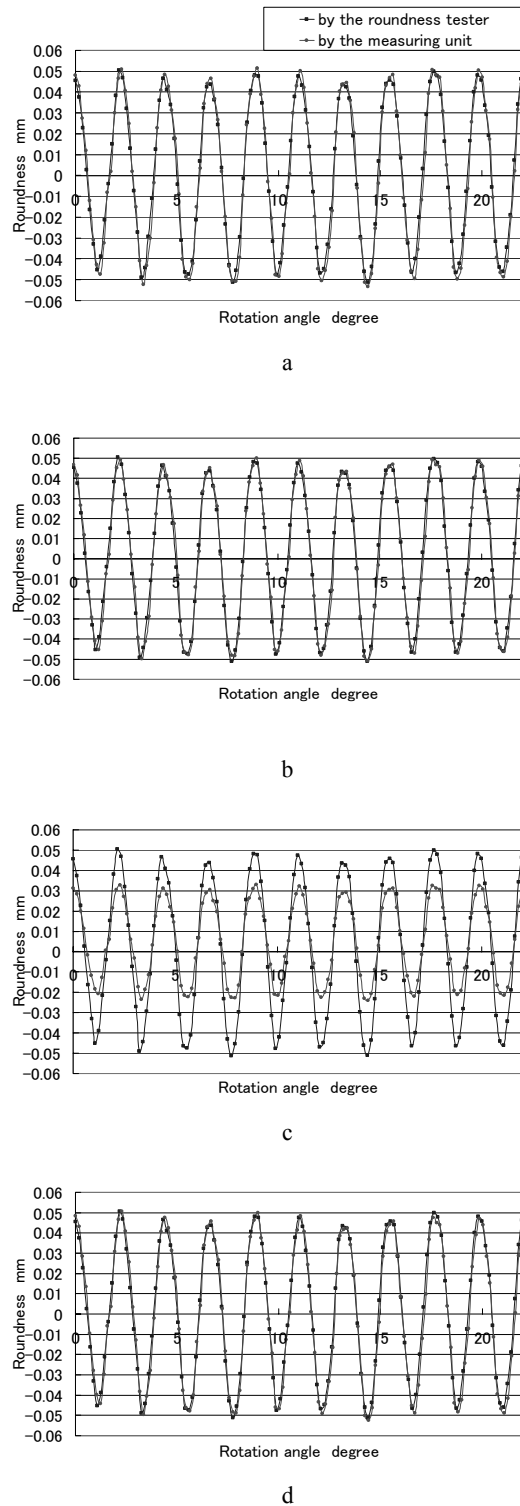


Fig. 9. Comparison between the waveforms of the roundness profiles determined using the roundness tester and the measuring unit: a. before correction ( $d = 200$  mm), b. after correction ( $d = 200$  mm), c. before correction ( $d = 800$  mm), d. after correction ( $d = 800$  mm).

Figure 9 shows the comparison between the waveforms of the roundness profiles determined by using the roundness tester and the measuring unit. Figures 9 a and 9 b show waveforms before and after the correction, respectively, when  $d$  is 200 mm. Figures 9 c and 9 d show waveforms before and after the correction, respectively, when  $d$  is 800 mm. As shown in Fig. 9, the effect of the spherical aberration is small when  $d = 200$  mm; however, the effect is large when  $d = 800$  mm. Figures 9 b and 9 d show that the roundness wave after the correction determined by the measuring unit is very similar to that determined by the roundness tester. Due to a difference in the sampling points (2000 in the roundness tester and 2048 in the measuring unit), the shapes of the waves differ slightly at their top. Thus, we confirmed the effect of the spherical aberration correction.

#### 4 Conclusions

The autocollimation principle is applied to the measuring system to determine the accuracy of a deep hole. The determination of accuracy is improved by correcting the spherical aberration of the optical system for light reception using ray tracing. The improvement is evaluated by measuring the roundness of the hole.

The following results are obtained.

1. The spherical aberration on the CCD decreases to less than 0.005 mm by the calibration method of the aberration using ray tracing. The displacement of 0.005mm on the CCD corresponds to that of 0.87  $\mu\text{m}$  of the feeler.
2. The roundness measured by using the measuring unit shows good agreement with that measured by using the roundness tester. Based on the comparison between the waveforms of the roundness profiles determined by using the roundness tester and the measuring unit, the effect of the spherical aberration correction is clarified.

In future studies, the correction of the spherical aberration by using lens (aspherical lens, etc.) and combination lens with a small spherical aberration is essential in order to improve the accuracy. From now on, straightness and cylindricity are measured on basic experimental apparatus. The systematic errors, which occur when the measuring unit is used on the measuring apparatus, are then examined.

#### 5 Acknowledgements

Mr.PARK Hyun Koo and Mr.ZHEN Ji Guo, an graduate students are appreciated for their cooperation.

#### 6 References

- [1] A.Katsuki, H.Onikura, T.Sajima, H.K.Park, J.G.Zhen, H.Murakami, (2005) Development of a practical high-performance laser-guided deep-hole boring tool: boring of steel workpieces. Proceedings of ASPE 2005 Annual Conference Blood 56:926–930
- [2] A.Katsuki, H.Murakami, H.Onikura, T.Sajima, (2005) Development of a laser-guided deep-hole measuring system: autocollimation system. Proceeding of JSPE Semestrial Conference 1273–1274
- [3] T.Kishikawa, (2002) Optics guide book. Optronics 83–89
- [4] H.Matsumoto, (1997) Numerical calculation method. 18–19



# Development of an Optical Measuring Device for Rotation Accuracy of Micro-Spindle - Application to Measurements of a High-Speed Spindle -

Kengo Fujimaki, Kimiyuki Mitsui  
Keio University

Keywords: Micro-spindle, Rotation accuracy, Run-out, Optical measuring method

## Abstract

It is very difficult to measure the rotation accuracy of miniaturized spindles running at high-speed with a common measuring method which uses capacitive displacement sensors. Therefore the authors have proposed a new optical measuring method using a small reflection sphere as a measurement target. In this paper, the basic principle of the optical measuring method, the configuration of the measuring device and some of the measurement data are shown.

## 1 Introduction

The measurement of the spindle rotation accuracy is very important to verify the machining accuracy. Some measuring methods for the rotation accuracy of spindles have been proposed [1]-[14], but a measuring method for micro-spindles, which are miniaturized spindles, has not yet been established. A common measuring method uses capacitive displacement sensors and a master target, which is a high-precision ball or cylinder. However, the target attached to a micro-spindle must be small to avoid an unbalance of the spindle. In addition, capacitive displacement sensors have limitations in the applicable radius of the target [15] and are not suitable for measuring the displacement of a small target at ultra-high speed. One of the authors has developed an optical measuring method based on Holster's method [16], which evaluates the rotation accuracy by the movement of a reflected light beam from a concave mirror attached to the spindle end [17]. However, it is difficult to obtain a small and precise target and to attach it accurately to a spindle. Therefore, we have proposed a measuring method using a reflection sphere as the measurement target. For reference's sake, a similar system has been proposed for a dimensional position measurement of the CMM (coordinate measuring machine), and so on [18]. To be precise, the run-out of the spindle axis is composed of three components, which are the radial motion, the axial motion and the angular motion [19]. In this study, the measurement of the run-out composed of the radial motion and the angular motion at a point has been targeted.

In this paper, first we describe the principle of the optical measuring method and the configuration of the trial device. Then, we show some of the results of measurements with a small steel ball and a high-speed, high-precision spindle.

## 2 Measurement Principle

Figure 1 shows the optical layout of the measurement system. A target sphere is attached to the spindle end. First, the collimated laser beam goes through a beam splitter and an objective lens, and then it is reflected on the surface of the target sphere. The reflected beam goes through the lens again and is reflected by the beam splitter. Finally, it enters a quadrant photo diode (QPD). The QPD consists of four photo cells and can sense the parallel displacement of an optical spot by the difference between the outputs of each photo cell. The outputs  $V_x$  and  $V_y$  of the QPD in the directions  $X$  and  $Y$  are shown as follows with the outputs  $S_1, S_2, S_3, S_4$  of the photo cells.

$$V_x = \frac{S_1 - S_2 - S_3 + S_4}{S_1 + S_2 + S_3 + S_4} \quad (2.1)$$

$$V_y = \frac{S_1 + S_2 - S_3 - S_4}{S_1 + S_2 + S_3 + S_4} \quad (2.2)$$

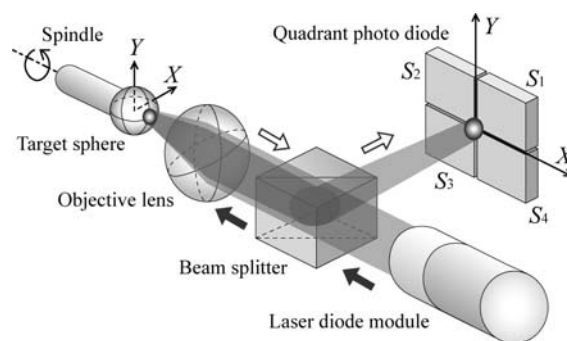


Fig. 1. Optical layout of the measurement system

Figure 2 shows an example of the relationship between the displacement  $\epsilon_x$  of the target sphere in direction  $X$  and the output  $V_x$ . It is found that this curve is non-linear, but it can be regarded as a linear curve near  $\epsilon_x = 0 \mu\text{m}$ . Therefore, the run-out of the spindle is expressed as the output divided by the measurement sensitivity  $K$ , which is the slope of the characteristic curve near  $\epsilon_x = 0 \mu\text{m}$ .

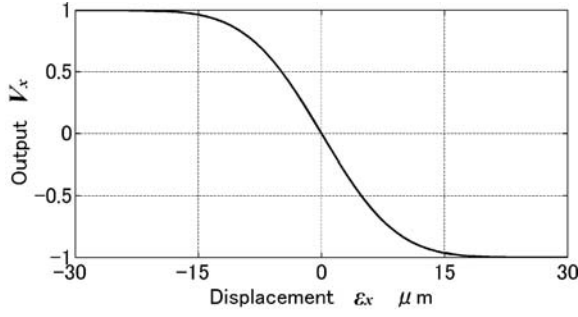


Fig. 2. An example of a characteristic curve of the output

In this measuring method, the resolution and the response speed is very high because the QPD is used as a position detector of the optical spot. And, a small sphere can be targeted because the laser beam is condensed by the objective lens. Therefore, this measuring method is suitable for evaluating the rotation accuracy of micro-spindles.

### 3 Analysis of the Basic Characteristics

Here, the analysis of the basic characteristics of this measurement system is described. It is assumed that the movement of the optical spot on the QPD follows a parallel displacement in proportion with the displacement of the target sphere.

The displacement rate  $k$  is given by the following equation.

$$k = \frac{\text{displacement of optical spot on QPD}}{\text{displacement of target sphere}} \quad (3.1)$$

Figure 3 shows the light intensity distribution on the QPD. This is a Gaussian distribution with radius  $r$  when the displacement of the target sphere in the direction  $X$  is  $\epsilon_x$ . The light intensity distribution  $I$  is

$$I(x, y) = I_0 \exp\left(-\frac{2}{r^2} \left\{ (x - k\epsilon_x)^2 + y^2 \right\}\right) \quad (3.2)$$

Here, the peak  $I_0$  of the light intensity distribution is expressed as the following, where  $P$  is the light power.

$$I_0 = \frac{2P}{\pi r^2} \quad (3.3)$$

In addition, the light power  $P$  is

$$P = S_1 + S_2 + S_3 + S_4 \quad (3.4)$$

The output  $V_x$  of the QPD in the direction  $X$  is derived as the following with the above equations.

$$\begin{aligned} V_x &= \frac{S_1 - S_2 - S_3 + S_4}{S_1 + S_2 + S_3 + S_4} \\ &= \frac{2 \int_{-\infty}^{\infty} \int_0^{\infty} I(x, y) dx dy - P}{P} \\ &= \frac{2}{r} \sqrt{\frac{2}{\pi}} \int_0^{\infty} \exp\left(-2 \frac{(x - k\epsilon_x)^2}{r^2}\right) dx - 1 \end{aligned} \quad (3.5)$$

Therefore, the differentiation of  $V_x$  with respect to  $\epsilon_x$  is

$$\frac{dV_x}{d\epsilon_x} = 2\sqrt{\frac{2}{\pi}} \frac{k}{r} \exp\left(-2 \left(\frac{k\epsilon_x}{r}\right)^2\right) \quad (3.6)$$

Because this is constant at  $|k\epsilon_x| \ll r$ , the measurement sensitivity  $K$  is expressed with the radius  $r$  of the optical spot on the QPD and the displacement rate  $k$ .

$$K = 2\sqrt{\frac{2}{\pi}} \frac{k}{r} \quad (3.7)$$

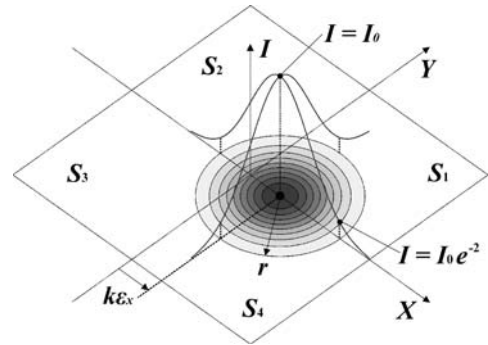


Fig. 3. Light intensity distribution on the QPD

Figure 4 shows the characteristic curve of the QPD in the direction  $X$ , which is computed by the numerical integration in Equation (3.5). The reason that this curve inverts in comparison with Figure 2 is that an optical spot on the QPD normally moves in a direction opposite to the target sphere.

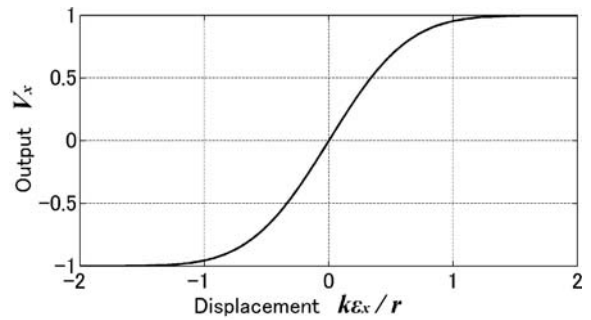


Fig. 4. Characteristic curve of the output in the direction  $X$  on the QPD

The values  $r$  and  $k$  are derived as follows by geometric optics theories with five parameters, which are the radius  $R$  of a target sphere, the focal distance  $f$  of an objective lens, the beam radius  $r_0$  of a light source, the distance  $L_s$  between a QPD and an objective lens, and the distance  $L_t$  between an objective lens and the center of a target sphere. At  $\varepsilon_x \ll R$ ,

$$k = \frac{2}{fR} \{ (L_s - f)(L_t - R) - fL_s \} \quad (3.8)$$

$$r = \left| r_0 - 2(L_t - f) \left\{ (L_s/f - 1)(x_B - L_t) + L_s \right\} \frac{\{ (f^2 + r_0^2)x_B - r_0^2(L_t - f) \}}{2r_0^2(L_t - f)x_B - 2r_0^2(L_t - f)^2 + f^2R^2} \right| \quad (3.9)$$

Here,  $x_B$  is

$$x_B = \frac{r_0^2(L_t - f) + \sqrt{(f^2 + r_0^2)f^2R^2 - f^2r_0^2(L_t - f)^2}}{f^2 + r_0^2} \quad (3.10)$$

#### 4 Validation Testing

The configuration of the optical measuring device is shown in Figure 5. This is almost the same layout as in Figure 1. The outputs from the photo cells of a QPD are faint current signals and must be converted to voltage signals by trans-impedance amplifiers before being sampled by the A/D converter. Therefore, the QPD and amplifier ICs are placed on one circuit board because the outputs are susceptible to electric noises between the QPD and the amplifiers. The response frequency is about 1 MHz after considering the specifications of these electronic components. Calculations of Equations (2.1) and (2.2) are done on a PC.

In this paper, a high-speed, high-precision spindle is used as the measuring object in order to validate the measuring results of this trial device; this method is compared with the conventional method, which uses a high-precision master ball and two capacitive displacement sensors.

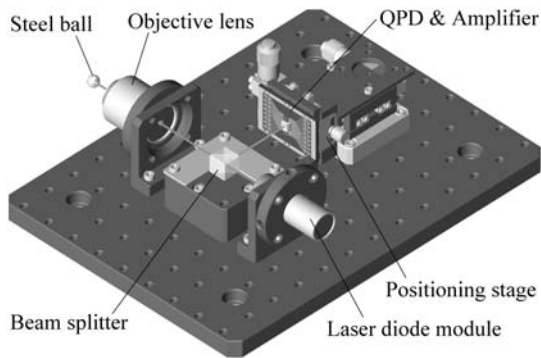


Fig. 5. Configuration of the optical measuring device

Figure 6 shows the simultaneous measurement method in the optical measuring device and the capacitive displacement sensors. The measurement sensitivity  $K$  of the optical measuring device is  $-0.20 \mu\text{m}^{-1}$ , and the resolution is about 3 nm. In addition, the steel ball has a diameter of 11.90 mm, the spindle speed is 2447 rpm and the sampling frequency of the A/D converter is 1 MHz. The resolution of the capacitive displacement sensor is 3 nm and the response frequency is 40 kHz.

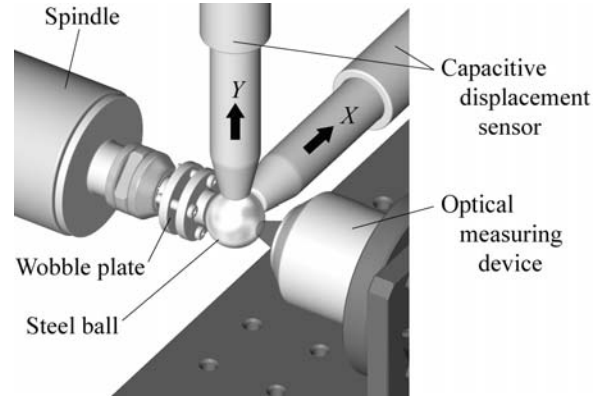


Fig. 6. Simultaneous measurement in the optical measuring device and the capacitive displacement sensors

Figure 7 shows the results of the run-out in the directions  $X$  and  $Y$ , simultaneously measured by the optical measuring device and the capacitive displacement sensors. Figure 8 shows the trajectories of the center of the steel ball. The frequency components above 30 upr (undulations per revolution) in these results have been cut off. Considering that the results measured by the capacitive displacement sensors could have errors of about  $0.08 \mu\text{m}$ , which is the sphericity of the steel ball, the result of the optical measuring device is in excellent agreement with the result of the capacitive sensors. The differences between these results are about  $0.1\text{-}0.2 \mu\text{m}$  at a maximum. Therefore, the accuracy of the optical measuring device is at least on a sub-micrometer order.

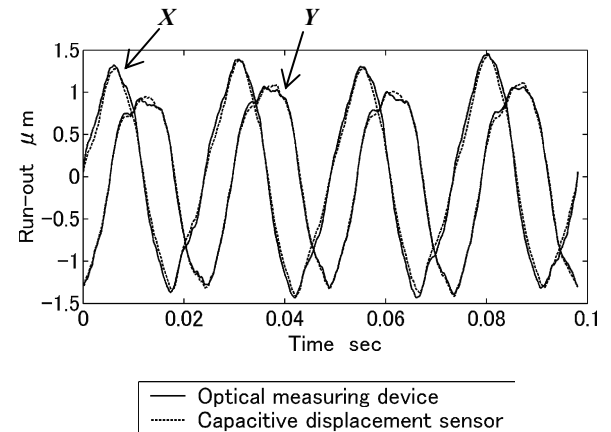
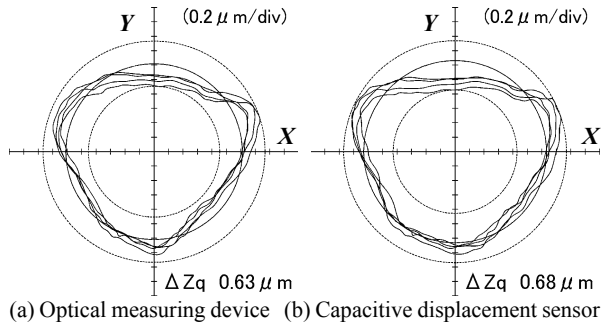


Fig. 7. Comparison of the measurement results of the run-out (4 revolutions)



**Fig. 8.** Measurement results of the run-out (Lissajous display, 4 revolutions)

### 5 Measurement of a High-speed Spindle

The validation of the optical measuring device mentioned above was made by measuring the spindle running at about 2000 rpm. Here, the optical measuring device is applied to the spindle running at a much higher speed.

A small steel ball of diameter 3 mm is attached to the collet chuck of the high-speed, high-precision spindle (Figure 9). This condition is almost the same as that for the measurement of the micro-spindle. The characteristic curve of the output with respect to the displacement  $\epsilon_x$  of the spindle in the direction  $X$  is shown in Figure 10, and the measurement sensitivity is  $-0.11 \mu\text{m}^{-1}$ . The resolution evaluated by the bit number and the input range of the A/D converter is about 7 nm.

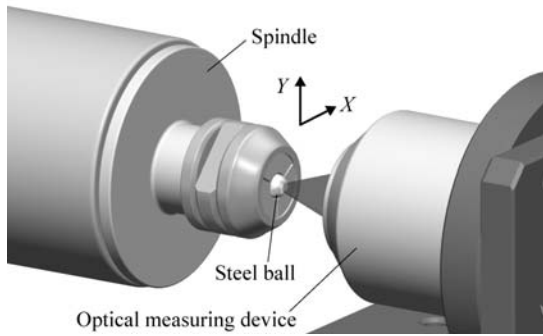


**Fig. 9.** Measurement using a small steel ball

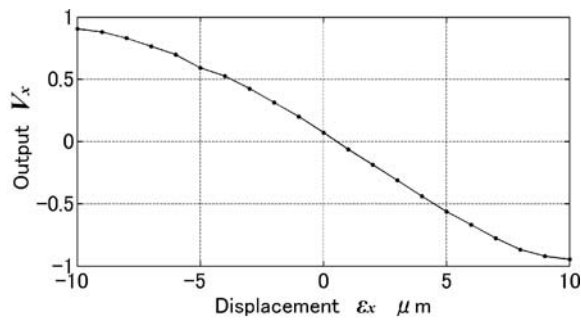


**Fig. 10.** Characteristic curve of the output

Figure 11 shows the measurement results of the run-out at a rotational speed of about 5000-30000 rpm in increments of about 5000 rpm, where the cut-off frequency is 30 upr. Because the validity of the optical measuring device at a low rotational speed has been verified and the response speed is enough, it can be regarded that this optical measuring device can measure the rotation accuracy of a high-speed, high-precision spindle attached to a small steel ball, which is almost the same in measurement conditions as those for a micro-spindle. Here, because a wobble plate is not used, unlike in the above validation testing, the eccentricity of the steel ball has widened.

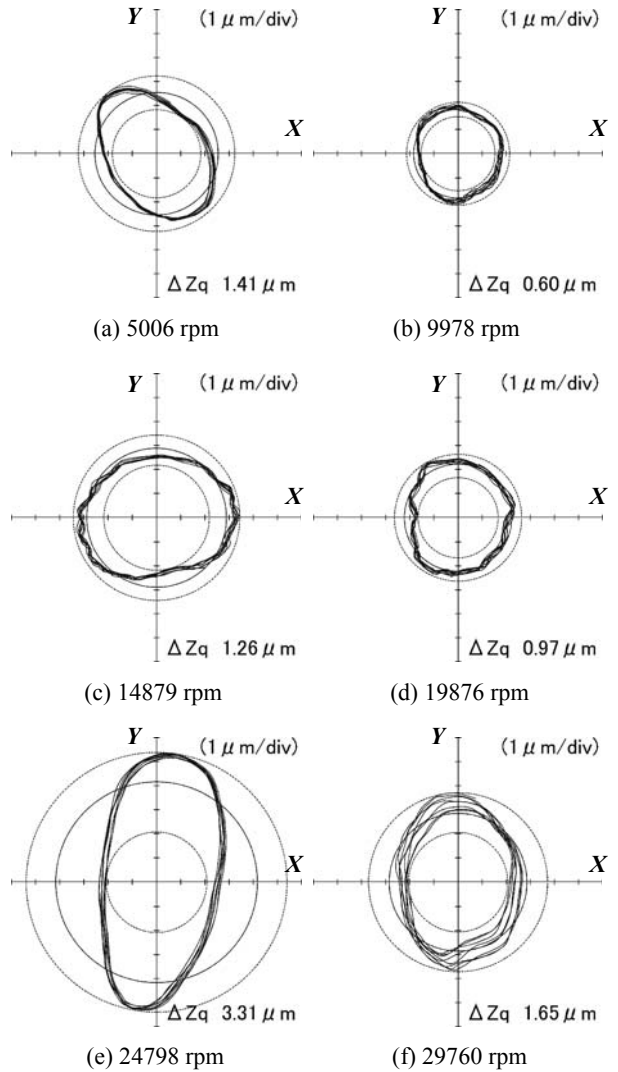


**Fig. 11.** Measurement results of the run-out (Lissajous display, 8 revolutions)

The results of the measurement of the vibration of the spindle holder by the capacitive displacement sensors (Figure 12) are shown in Figure 13. From these results, it is found that the spindle vibrates mechanically at high rotational speeds, and this is the reason that some of the results in Figure 11

show elliptical trajectories. Therefore, the holding method of the spindle should be reconsidered in future work in order to measure the pure run-out of the spindle running at a high rotational speed.

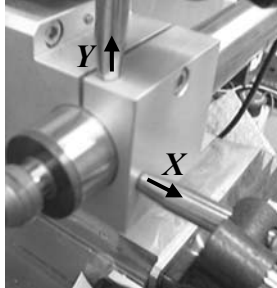


**Fig. 12.** Measurement of the vibration of the spindle holder by the capacitive displacement sensors

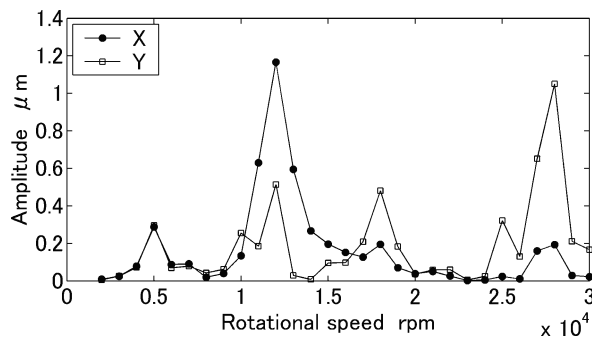


**Fig. 13.** Vibration of the spindle holder with respect to the rotational speeds

## 6 Conclusions

In this paper, the principle of the measurement method for the rotation accuracy of micro-spindles has been described, and the results of the analysis and experiments have been shown. The results are summarized as follows.

1. With the analysis of the light intensity distribution, it was derived that the characteristic curve of the output in this optical measuring method is determined by the displacement rate and the radius of an optical spot on the QPD.
2. It was shown that the displacement rate and the radius of an optical spot on a QPD can be expressed by five parameters of the optical system.
3. By integrating the QPD and high-speed amplifier ICs into one circuit board, the reduction of noises and the high-speed response of output signals were realized.
4. The validity of the optical measuring device was verified by the simultaneous measurement with capacitive displacement sensors. The accuracy of this trial device was at least on the order of sub-micrometers.

5. By applying the optical measuring device to a high-speed, high-precision spindle attached to a small steel ball, which is almost the same in measurement conditions as those for a micro-spindle, it was shown that the optical measuring device can measure the rotation accuracy of a micro-spindle.

## 7 References

- [1] R. R. Donaldson : A Simple Method for Separating Spindle Error from Test Ball Roundness Error, *Ann. CIRP*, Vol.21, No.1 (1972) pp.125-126.
- [2] K. Mitsui : Development of a New Measuring Method for Spindle Rotation Accuracy by Three Points Method, *Proc. Int. Mach. Tool Des. Res. Conf.*, Vol.23rd, (1983) pp.115-121.
- [3] P. D. Chapman : A Capacitance based Ultra-precision Spindle Error Analyser, *Prec. Eng.*, Vol.7, No.3 (1985) pp.129-137.
- [4] H. Shinno, K. Mitsui, Y. Tatsue, N. Tanaka, T. Omino and T. Tabata : A New Method for Evaluating Error Motion of Ultra-Precision Spindle, *Ann. CIRP*, Vol.36, No.1 (1987) pp.381-384.
- [5] N. Ozawa, Y. Okazaki, Y. Kitamura, T. Kohno and K. Mitsui : A New Measuring Method for Spindle Error Motion Using a Cube-corner Prism and Laser Interferometers, *Proc. of the 28th International MATADOR Conf.*, (1990) pp.515-521.
- [6] G. X. Zhang and R. K. Wang : Four-Point Method of Roundness and Spindle Error Measurements, *Ann. CIRP*, Vol.42, No.1 (1993) pp.593-596.
- [7] G. X. Zhang, Y. H. Zhang, S. M. Yang and Z. Li : A Multipoint Method for Spindle Error Motion Measurement, *Ann. CIRP*, Vol.46, No.1 (1997) pp.441-445.
- [8] E. Marsh, R. Grejda : Experiences with the Master Axis Method for Measuring Spindle Error Motions, *Prec. Eng.*, Vol.24, No.1 (2000) pp.50-57.
- [9] W. Gao, S. Kiyono, E. Satoh : Precision Measurement of Multi-Degree-of-Freedom Spindle Errors Using Two-Dimensional Slope Sensors, *Ann. CIRP*, Vol.51, No.1 (2002) pp.447-450.
- [10] H. J. Ahn, S. Heon, D. C. Han : Error Analysis of the Cylindrical Capacitive Sensor for Active Magnetic Bearing Spindles, *Trans. ASME J. Dyn. Syst. Meas. Control*, Vol.122, No.1 (2000) pp.102-107.
- [11] C. H. Liu, W. Y. Jywe and H. W. Lee : Development of a simple test device for spindle error measurement using a position sensitive detector, *Meas. Sci. Technol.*, Vol.15, No.9 (2004) pp.1733-1741.
- [12] W. Y. Jywe and C. J. Chen : The development of a high-speed spindle measurement system using a laser diode and a quadrants sensor, *Int. J. of Mach. Tools Manuf.*, Vol.45, No.10 (2005) pp.1162-1170.
- [13] C. H. Liu, W. Y. Jywe, Y. S. Lin and S. C. Tzeng : Development of a novel optical measurement system for the error verification of a rotating spindle, *Opt. Eng.*, vol.44, No.9 (2005) pp.097003.1-097003.6.

- [14] E. Okuyama, K. Mitsui : A Circular Profile Measurement Method Using Software Techniques, Key Eng. Mater., Vol.295/296, (2005) pp.265-270.
- [15] R. R. Vallance, E. R. Marsh, P. T. Smith : Effects of Spherical Targets on Capacitive Displacement Measurements, Trans. ASME J. Manuf. Sci. Eng., Vol.126, No.4 (2004) pp.822-829.
- [16] P. L. Holster, J. A. H. M. Jacobs and B. Sastra : Measuring the Radial Error of Precision Air Bearings, Philips Tech. Rev., Vol.41, No.11/12 (1983/1984), pp.334-337.
- [17] K. Mitsui, Ji Ling, Y. Hashimoto, K. Nunome and K. Hibi : Development of an Optical Measuring Method for Radial Spindle Error. Proc. of the 7th Int. Precision Engineering Seminar, (1993) pp.506-517.
- [18] K. Takamasu and T. Kasahara : Three Dimensional Position Measurement of Spherical Target Using Optical Collimator, VDI Ber., No.761 (1989) pp.87-92.
- [19] J. Bryan, R. W. Clouser, E. Holoand : Spindle Accuracy, Amer. Machinist, No.4 (1967) pp.149-164.

---

## Laser Interferometric Measurement of Involute Profile by Rolling of Artifact

Fumi TAKEOKA<sup>1</sup>, Masaharu KOMORI<sup>1</sup>, Aizoh KUBO<sup>1</sup>, Hiroshige FUJIO<sup>1</sup>, Shigeaki TANIYAMA<sup>1</sup>, Takehiro ITO<sup>1</sup>, Toshiyuki TAKATSUJI<sup>2</sup> and Sonko OSAWA<sup>2</sup>  
<sup>1</sup>Kyoto University, <sup>2</sup>AIST

Keywords: Gear, Involute, Measurement, Laser interferometer, Artifact

### Abstract

The vibration of gear is one of the serious problems for vehicles. The characteristics of vibration are influenced by tooth flank form of sub micron meter order and therefore strict quality control of tooth flank form is demanded. However, involute artifact, which is used to calibrate the measuring machine of tooth flank form of gear, must be measured with extreme precision. In this report, the method to measure the profile of involute artifact by laser interferometer is proposed. Fundamental research is carried out and it is confirmed that highly precise measurement is possible.

### 1 Introduction

Reduction of vibration / noise is one of the serious problems for involute spur and helical gears, which are used for drive train of vehicles such as automobiles. Gear tooth flank form of submicron meter order largely influences gear vibration and noise of gears, and therefore high-level quality control of tooth flank form is needed to realize excellent performance.

Tooth profile of involute gear in mass production is usually measured by a tooth profile measuring machine. For inspection and calibration of the measuring machine, involute artifact is usually used. Then the involute artifact is calibrated with a special tooth profile measuring machine which is adjusted more precisely. However the accuracy of the measuring machine is claimed to be from 1  $\mu\text{m}$  to several  $\mu\text{m}$ , and it cannot achieve measurement of involute artifact at the submicron meter accuracy. In addition, it is the problem that this calibration system is usually not traceable to national standard and measured value is not guaranteed. Therefore highly precise and traceable measuring technology of involute artifact is required.<sup>[1]</sup>

In this research, highly precise measuring method of involute artifact is proposed. The geometric feature of involute curve is utilized in this method. Laser interference displacement measurement is used, in which laser is irradiated to the surface of measured object directly. In this report, the measuring device is proposed, the investigation of the fundamental performance of it is carried out, and the possibility of highly precise measurement is examined.

### 2 Fundamentals of measurement

#### 2.1 Characteristic of involute curve and measurement principle

Bold line in fig.1 shows the base circle and involute curve which is defined by the base circle, where base circle contacts on line AB. Suppose that the base circle and involute curve roll as one body on line AB to the left direction in fig.1 without slip between base circle and line AB and then get to the position shown by the broken line in fig.1. During this rolling movement, the involute curve and line AB always intersect perpendicularly at point P, which is the characteristic point of the involute curve. Conversely, if this curve is not a true involute curve, in other words, it has form deviation from involute curve, the position of crossing point P changes. The displacement of the crossing point P in the direction of line AB means profile form deviation. Tooth profile deviation curve is expressed by the graph with profile form deviation on the y-axis and rolling length of the base circle on x. Therefore, tooth profile deviation curve can be known by measuring the displacement of the crossing point P while measuring the rolling length of the base circle. In this research, rolling length of base circle and the displacement of crossing point P is measured by laser interferometry as shown in the right side in fig.1. The principle of measuring method by rolling involute artifact is developed by Dr.W.Beyer of PTB and it was used for inspection of involute artifact.<sup>[2]</sup> In PTB, displacement was

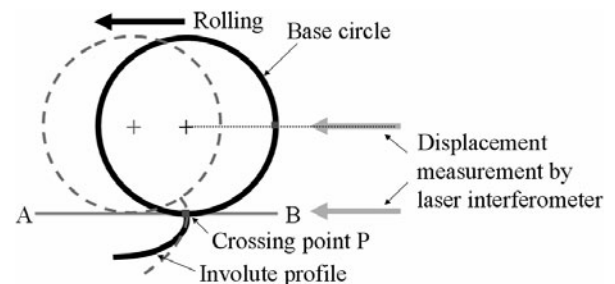


Fig.1 Measurement principle of involute artifact



Fig. 2. Involute artifact with base cylinder

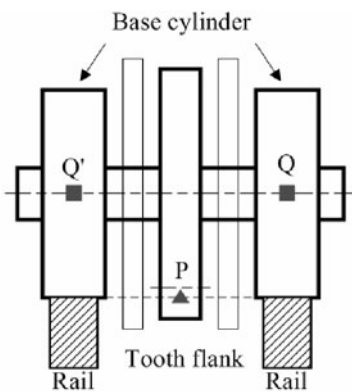


Fig. 3. Measured points of involute artifact

measured by contact stylus. In this research, non-contact measurement by laser interferometry is incorporated, which makes it easier to guarantee the traceability. This kind of non-contact tooth profile measurement has never been reported.

## 2.2 Involute artifact

Involute artifact, being used in all the experiments, is shown in fig.2. It consists of the involute-form tooth flank section and two base cylinders which correspond to base circle of the involute tooth flank. The base cylinders are installed on the both sides of the tooth flank section. There are disks between the base cylinder and the tooth flank to protect tooth flank. Tooth flank is produced so that base circle radius of its involute curve is 57.5 mm and is polished as mirror surface. The middle area of the circumferential surface of base cylinder is polished and the radius of polished part is smaller than the radius of base circle. The rolling length of the base cylinder is measured by irradiating laser to the polished area. The designed radius of non-mirror surface area of base cylinder is identical with base circle radius (57.5 mm). Radius and roundness of non-polished part of the base cylinder was measured by coordinate measuring machine (Leitz PMM12106) and roundness measuring machine (Kosaka laboratory corporation roncornder EC3400). The radius is 57.5010 mm and roundness is 77 nm on the left

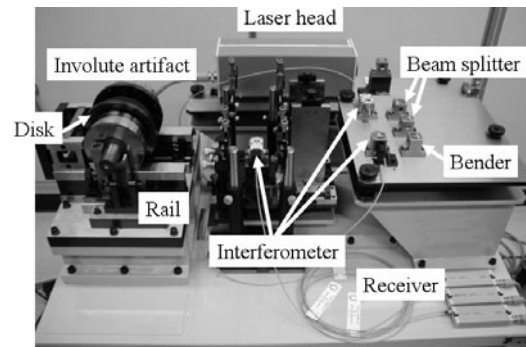


Fig.4 Setup for involute measurement

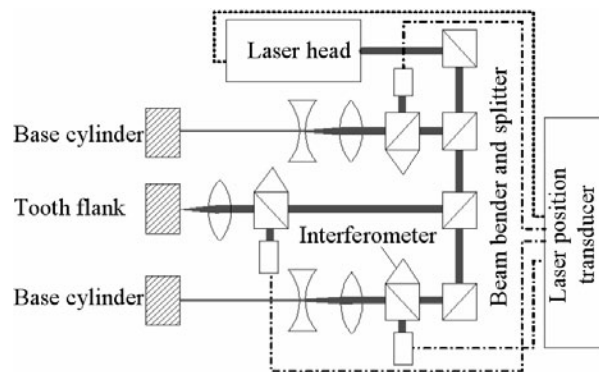


Fig.5 Optical configuration for measurement

base cylinder in fig.2 and 57.5008 mm and 82 nm at base cylinder on the right side under 20 degrees C.

## 3 Measuring device and method

### 3.1 Measuring device

Fig.3 shows measured points of involute artifact and fig. 4 shows a photo of the measuring device. As shown in fig.3 and fig.4, involute artifact is set on the rail and the displacement is measured at the points Q, Q' on two base cylinders and at the point P on tooth flank. The top surface of the rail corresponds to the line AB in fig.1. The outline of optical system of measurement is shown in fig.5. The collimated beam from laser head (beam diameter is about 3 mm) is bent by a beam bender. Then it is divided into 3 beams equally by beamsplitters and they are irradiated to involute artifact. 2 beams are irradiated to the mirror surface area of base cylinders (point Q and Q' in fig.3). They pass convex lens and concave lens, and become parallel light laser whose diameter is about 1 mm. If large diameter laser beam is irradiated to the cylindrical surface, reflected light diffuses to circumferential direction and enough light intensity for laser interferometry cannot be obtained. Therefore the diameter of laser beam is reduced. The height of central beam is lowered by two beam benders. The convex lens is installed to focus the beam on the point P of the tooth flank (c.f. fig.3), and the beam is irradiated to tooth



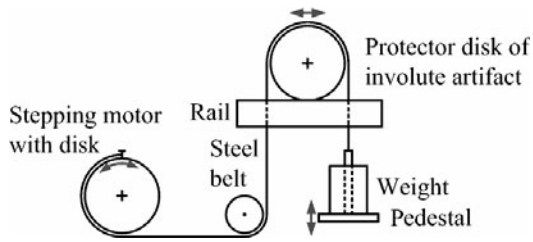


Fig.6 Wound-belt driving system for involute artifact

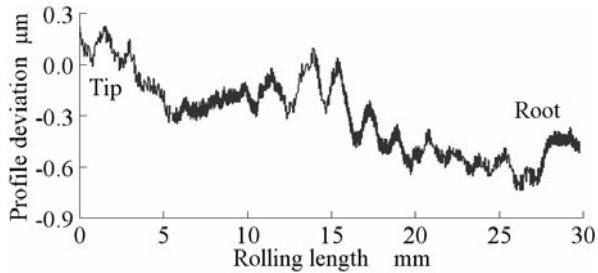


Fig.7 Measured profile deviation curve driven by motor driving system

flank. The measurement spot diameter of the beam is about 6  $\mu\text{m}$ . Displacement of tooth flank is measured by acquiring reflected light through the interferometer. Focus beam is used in order to make a spot diameter small enough, which is needed to measure the detailed form of tooth flank. Laser position transducer processes the input signal with the pulse converter, when measurement resolution is 1/4 of wave length of the laser (about 158 nm). The output pulse from the pulse converter, whose resolution is enlarged (about 10 nm), is added up in the position counter and is output as position data. Output data are taken in the computer through GP-IB interface.

The laser interference measuring system in this experiment is HP5507B Laser Position Transducer System (HP5517C Laser Head, HP10507A Single Beam Interferometer, HP10700A 33% Beam Splitter and the HP10701A 50% Beam Splitter, HP10710A Beam Bender) of the Hewlett-Packard corporation. The lens to change the beam diameter is biconvex lens for base cylinder (focal length is about 150 mm), the biconcave lens for base cylinder (focal length is about 50 mm) and biconvex lens for tooth flank (focal length is about 50 mm).

### 3.2 Processing of measured data

It is desirable to acquire the displacement data of two base cylinders and tooth flank simultaneously but in this device it is impossible to acquire all data at the same time. Then data are taken in the order of Q, P, Q', Q, P, ... at about 0.015s of sampling interval. The measured data of each point P, Q and Q' are interpolated based on measurement time. In the profile deviation measurement, the data of point P is the most important, and therefore displacement of the point Q and Q' at the data acquisition time of point P is calculated by linear interpolation. The average of displacement of point Q and Q' is regarded as rolling length of involute artifact.

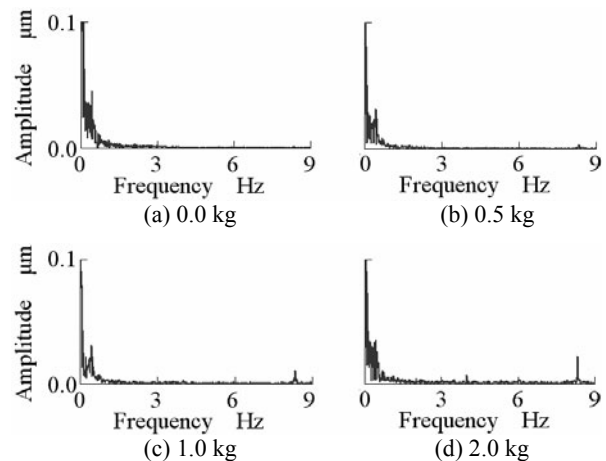


Fig.8 Result of Fourier transformation of measured profile deviation curve under different weight conditions

## 4 Measurement by driving system of involute artifact

Involute artifact is rolled automatically by motor. Outline of the driving system is shown in fig.6. It referred to PTB driving system in principle. The steel belt is fixed to winding disk (diameter 145 mm) of stepping motor and is hung on the protector disk (diameter 145 mm, the black disk in fig.2) of involute artifact set on the rail. At the end of the steel belt, pedestal (200 g) and the weight (1 kg) are equipped. Steel belt is wound and released by rotating stepping motor and involute artifact rolls on the rail according to the rotation of motor. The involute artifact rolls  $0.0072^\circ$  in 1 pulse as well as the rotation of stepping motor for belt winding disk and the protector disk of involute artifact has the same diameter. Motor driving frequency is 100 Hz in the experiment.

The profile form of the middle area of tooth width is measured. The result is shown in fig.7. The number of points is 1115. The whole tooth flank between tip and root can be measured. In the profile deviation curve, minute uneven form is observed, which is considered as the grinding mark. This result means that it is possible to measure detailed form of involute artifact by this method. Standard deviation of the total profile error<sup>[3]</sup> of 10 measurements is 25.5 nm.

## 5 Influence of driving conditions of involute artifact

### 5.1 Influence of weight size

5 repetitive measurements are carried out under 4 different weight conditions (c.f. fig.6), which is 0.0 kg (only pedestal), 0.5 kg, 1.0 kg and 2.0 kg. Standard deviation of each measured total profile errors is 12 nm, 18 nm, 22 nm and 38 nm. It means that the repeatability deteriorates as the weight

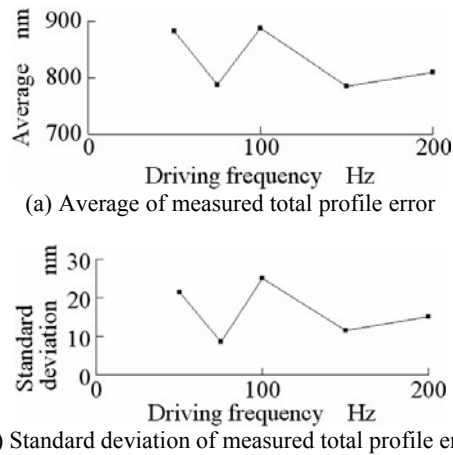


**Fig.9** Average and standard deviation of total profile error under different driving frequency

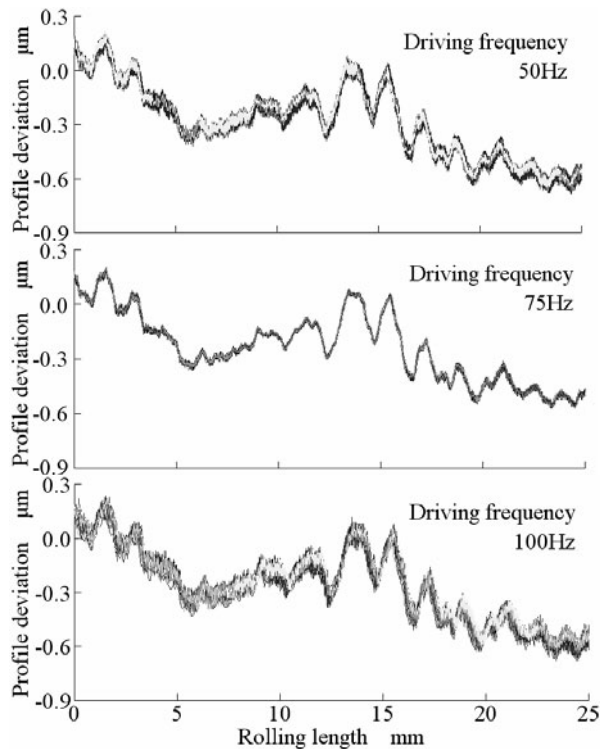


**Fig.10** Profile deviation curves of 10 measurements under different motor driving frequency

increases. Fig.8 shows the result of Fourier transformation of tooth profile deviation expressed as a function of time. The peak near 8.5 Hz becomes outstanding under large weight conditions. It is one of the reason of repeatability deterioration. In addition, it was observed the weight swings by the motion of belt, which influences the motion of involute artifact and its influence is larger under large weight condition. Those above might be reasons of repeatability deterioration under large weight. However, light weight causes the loss of stability of the motion of involute artifact.

Therefore, weight should be adjusted to the appropriate state in the measurement.

## 5.2 Influence of motor driving frequency

Profile curve of involute artifact is measured 10 times under different driving frequency of stepping motor. Average and standard deviation of measured total profile errors are shown in fig.9 and measured profile deviation curves at motor driving frequency of 50, 75 and 100 Hz are shown in fig.10. At frequency of 50 Hz and 100 Hz, high-frequency fluctuation can be observed in tooth profile curve and repeatability gets worse. The result indicates that natural frequency of driving system is about 100 Hz and therefore resonance occurs at driving frequency of 50 and 100 Hz. It is necessary to avoid motor driving frequency close to natural frequency.

## 6 Conclusion

The measuring method of tooth profile of involute artifact which is used for inspection and calibration of the tooth profile measuring machine was proposed, where geometric feature of involute curve and direct interferometry are used. The measurement device based on this principle was constructed and it is confirmed that minute form can be measured by this device. The influence of weight and motor driving frequency on measured profile is clarified.

## 7 Acknowledgements

I would like to thank Tetsuya NONAKA for his support. This research was funded by Grant-in-Aid for Creative Scientific Research (B).

## 8 References

- [1] Takeda,R., Oguma,T., (2003) Recent technology of gear tooth measurement: precision engineering periodical. 69(3): 345-348
- [2] H.Mintrop and W.Beyer, (1961) Untersuchungen uber die Verwendbarkeit Von,, Angenaherten Evolventennormalen" zum Kalibrieren Von Evolventenprufgeraten: PTB-MITTEILUNGEN (Reprinted). 71(4): 255
- [3] (1995) Cylindrical gears -- ISO system of accuracy -- Part 1: Definitions and allowable values of deviations relevant to corresponding flanks of gear teeth. ISO 1328-1.
- [4] Takeoka,F., Komori,M., Kubo,A., Fujio,H., Taniyama,S., Okamura,D., Ito,T., Takatsuji,T. and Osawa,S.: Precise Measurement of Involute Profile by Laser Interferometer (1<sup>st</sup> Report) - Measuring Device and Evaluation of Basic Performance -: Journal of the Japan Society of Precision Engineering. (Under contributing)

- [5] Komori,M., Kubo,A., Fujio,H., Taniyama,S., Okamura,D., Ito,T. and Takahashi,M.,(2004) Precise Measurement of Involute Profile by Laser Interferometer: 2004 Japan Society of Precision Engineering Conference. M50
- [6] Komori,M., Ito,T., Takeoka,F., Kubo,A., Takatsuji,T. and Osawa,S., (2004) Precise Measurement of Involute Profile by Laser Interferometer (2nd Report)
- [7] Takeoka,F., Komori,M., Kubo,A., Takatsuji,T. and Osawa,S., (2006) Precise Measurement of Involute Profile by Laser Interferometer (3rd Report) - Development of Non-Slip Driving System -: 2006 Japan Society of Precision Engineering Conference. (Before publication)
- Influence of measurement conditions -:2004 Japan Society of Precision Engineering Conference. L34.

# Study on Manufacturing Method to Reduce Cogging Torque of Motor with Separate Core

Hiroyuki Akita<sup>1</sup>, Yuji Nakahara<sup>2</sup>, Takashi Yoshioka<sup>3</sup>, Takashi Miyoshi<sup>4</sup>  
Mitsubishi Electric Corporation<sup>1,2,3</sup>, Osaka University<sup>4</sup>

Keywords: motor, torque ripple, core precision, circularity, separate core, manufacturing method, level difference

## Abstract

This paper presents a new manufacturing and estimating method of motors to achieve low torque ripple. We have developed the manufacturing method to increase the coil fill factor of motors by using separate core. That caused high efficiency of motor, however, the core precision tends to be bad in the case of separate core and that causes large torque ripple. In this paper we declared the relationship between core precision and torque ripple. And a new evaluation method which predicts torque ripple more precisely than the evaluation method from the circularity of inner core has been established.

## 1 Introduction

With the brushless DC motors coming into increased use in recent years due to high efficiency requirements, the concentrated winding coil structure has become popular. The authors have studied on the manufacturing method(1) applying separate cores for a concentrated winding motor in order to reduce the coil resistance for higher efficiency. A brushless DC motor is expected to have higher accuracy rotation, lower vibration and noise, which can be achieved by reducing cogging torque. The separate core, however, is more likely to cause machining errors than the unit core, and even a slight machining error may lead to unbalanced magnetic flux distribution at the time of motor rotation, resulting in increased cogging torque. The inner diameter shape largely influences the cogging torque, but the effect of the slight error as per region of the inner diameter shape on the cogging torque is not clear yet.

In this paper, therefore, the occurrence mechanism of cogging torque attributed to the machining error is analyzed, and an evaluation method for the inner diameter shape in order to prevent cogging torque during manufacturing process of the stator is studied.

## 2. Motor structure and cogging torque

Fig. 1 shows the structure of an 8-pole, 12-slot machine to be used in the research. The stator uses a separate core per magnetic pole tooth, and the rotor uses ring-shaped sintered neodymium magnet. The coil, which is not illustrated in the figure, is wound around each magnetic pole tooth of the

stator. The torque pulsation caused by one turn of rotor rotation with no current passed through the coil is called the cogging torque. It is known that for each turn of rotor rotation the component with 8-cycle pulsation and the component with 16-cycle pulsation are caused by the stator machining error, while the component with 24-cycle pulsation is caused by combination of the number of poles and the number of slots(2). This paper especially aims at reducing the 8-cycle component which is largely affected by the inner diameter shape of the stator. The 8-cycle component is called  $2f$  component, with  $f$  indicating the basic wave frequency of armature current.

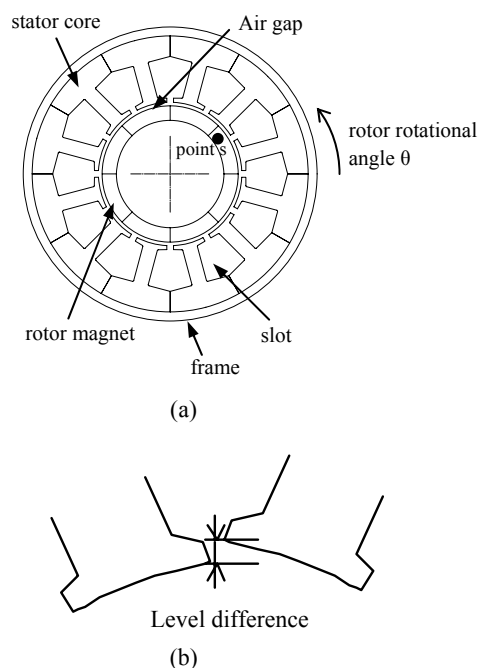


Fig. 1. Motor structure

### 3. Relation between circularity of stator inner diameter and cogging torque

Fig. 2 shows the measurement results of circularity and cogging torque 2f component for 20 sample stators used in the experiment in terms of the ratio of the stator inner diameter and the rated torque respectively. The correlation coefficient of circularity with cogging torque 2f component is low at 0.48, so that the circularity is considered inappropriate as an evaluation index to estimate the cogging torque 2f component.

The reason why the circularity cannot be used for evaluation of cogging torque 2f component lies in the fact that the circularity is a figure that merely expresses the size of configurational error and does not reflect the shape or position of the error. Especially in the case of the separate core shown in Fig. 1(a), the neighboring magnetic pole teeth have their ends radially deviated causing level difference in the inner circumference, as shown in Fig. 1(b), so that the core tends to have larger cogging torque 2f component than the stator with lenient configurational change in general. Thus, in consideration that the sharp change in inner diameter shape inflicts a large effect on the cogging torque 2f component, study is carried out on the relationship between change in the inner diameter shape and the cogging torque 2f component.

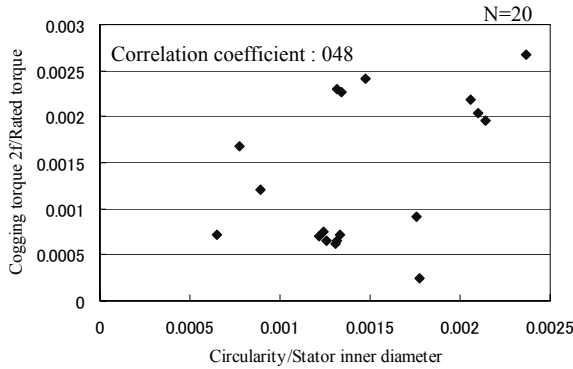


Fig. 2. Relation between circularity and cogging torque

### 4. Introduction of evaluation index taking account of the effect of change in inner diameter shape

If a point  $s$  is taken in the polar coordinates of rotor, and when this point  $s$  reaches the position of rotational angle  $q$  against the stator as the rotor rotates, a torque  $T(s, q)$  is generated at the point  $s$  due to the change in magnetic energy  $E(s, q)$ , and can be expressed as equation (1).

If a point  $s$  is taken in the polar coordinates of rotor, and when this point  $s$  reaches the position of rotational angle  $q$  against the stator as the rotor rotates, a torque  $T(s, q)$  is generated at the point  $s$  due to the change in magnetic energy  $E(s, q)$ , and can be expressed as equation (1).

$$T(s, \theta) = \frac{\partial E(s, \theta)}{\partial \theta} \quad (1)$$

The magnetic energy  $E(s, q)$  is directly proportional to the square of the product of rotor magnetomotive force  $F(s)$  and magnet permeance including magnetoresistance, and can be expressed as equation (2).

$$E(s, \theta) \propto \{F(s)\}^2 \{P(s, \theta)\}^2 \quad (2)$$

Torque  $T_0(q)$  can be obtained by substituting equation (2) into equation (1), and integrating for  $s$  over one cycle of rotor.  $A(s, q)$  is defined as in equation (3) which is a component of torque  $T(s, q)$ .

$$A(s, \theta) = \frac{\partial \{P(s, \theta)\}^2}{\partial \theta} \quad (3)$$

Torque  $T(s, q)$  is a function of  $A(s, q)$  and magnetomotive force  $F(s)$ . Here, permeance  $P(s, q)$  is both a function of an air gap between the stator and the rotor and a function of the stator inner diameter accuracy. Hence,  $A(s, q)$  is a function of the change in stator inner diameter as point  $s$  rotates in the stator, and it is also a function of change in stator inner diameter in  $q$  direction. In the present model, since the magnet has 8 poles, if the rotor has ideal shape without any configurational error or any characteristic difference of the magnet, the same magnetomotive force should appear at every 45 degrees. As mentioned previously, torque  $T_0(q)$  at the rotational angle  $q$  is the  $T(s, q)$  integrated over one cycle of the rotor. Here, the integration is carried out after taking the scalar sum of  $A(s, q)$  per 45 degrees in order to visually grasp the stator inner diameter accuracy and the effect of cogging torque 2f component.

Fig. 3 shows the inner diameter shape measured as a distance from a standard circle using a sample with level difference between the magnetic pole teeth. Fig. 4 shows the result of  $A(s, q)$  calculated from measured inner diameters for each division A1 ~ A8 in Fig. 3, and expressed as a curve, which we call "A curve". Here, the inner diameter shape of the stator is supposed to be same in the direction of the stator length, with the 45 deg division expressed in 360 deg as one cycle of the magnet. Next, the scalar sum for each A curve phase is calculated and expressed as A0 curve in polar coordinates in Fig. 5, where the vector sum of the curves is one cyclic component of A0 curve and is expressed in the figure as Y vector, with the size and phase indicated by the arrow mark.

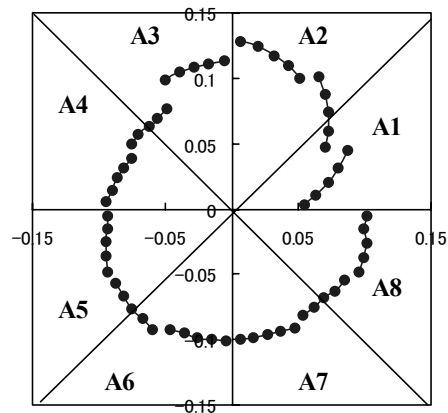


Fig. 3.. Measured inner diameter shape

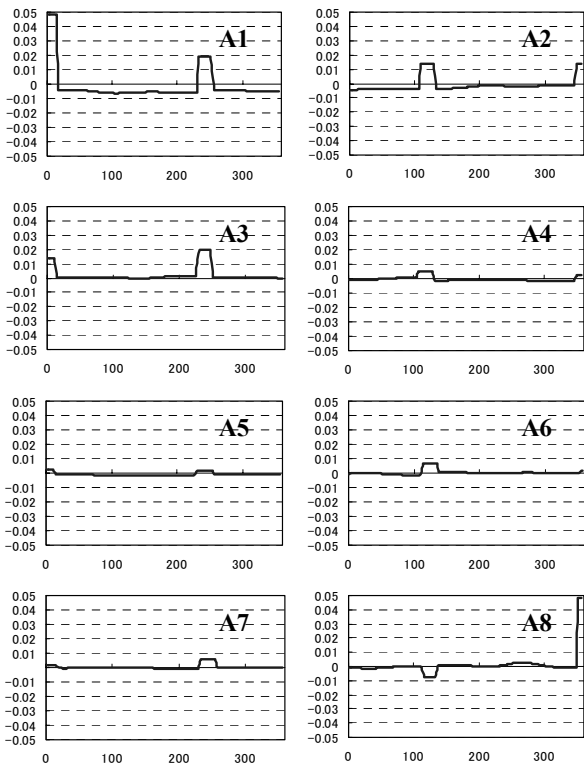


Fig. 4. A curve occurring between each magnet and stator

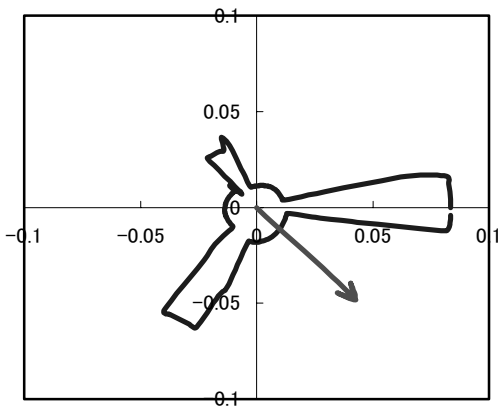


Fig. 5. A0 curve and Y vector

The sample shown in Fig. 2 is arranged by using the size of Y vector, which we call “Y value”, and shown in Fig. 6, indicating a high correlation coefficient 0.96 between the Y value and the cogging torque 2f component. Thus, it can be deduced that the Y value can be used as an indicator to estimate the cogging torque 2f component.

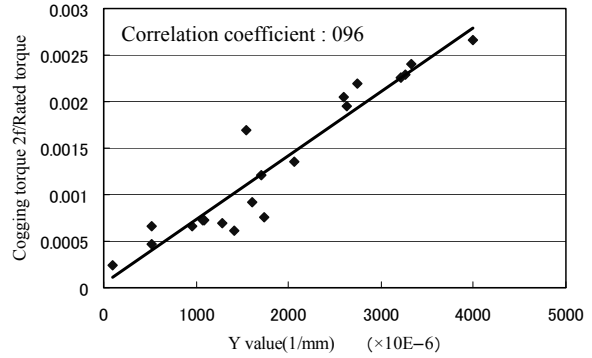


Fig. 6. Relation between Y value and cogging torque 2f component

Further, since Fig. 5 is a visual expression of the cause of the Y vector occurrence, it can be learned that the value of A ( $s, \theta$ ) near 0 degrees and 240 degrees, which we call “A value”, inflicts effect on the size of Y vector. Fig. 4 indicates that the A value near 0 degrees largely depends on A1 curve, and the A value near 240 degrees depends on A1 and A3 curves. Further, Fig. 3 indicates that the aforesaid values are influenced by the level difference in the separate sections No. 1, No. 2 and No. 5, and thus the region inflicting effect on cogging torque 2f component can be identified.

Although the level difference is attributed to the configurational error due to the mold accuracy and the assembly error due to the tool accuracy, the cogging torque 2f component can obviously be restrained by reflecting the cause clearly indicated by A curve in manufacturing process. On the other hand, it is possible to reduce the cogging torque 2f component by changing the level difference shape after assembling.

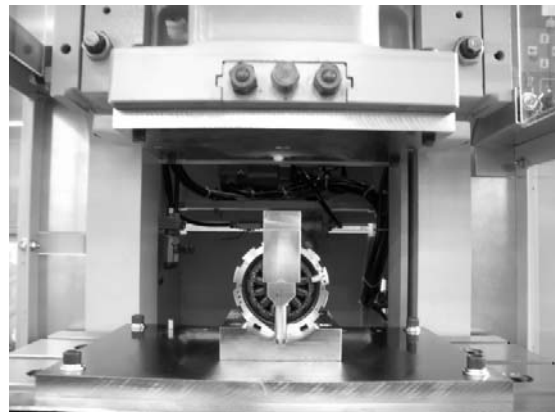


Fig. 7. Experimental equipment

### 5. Experimental verification 1

Here, in order to verify the supposition in previous chapter, the change in the cogging torque  $2f$  component caused by the change in level difference between magnetic pole teeth will be examined. Fig. 7 shows the photograph of the experimental equipment, where the stator has its outer periphery fixed by the frame before being pressed. The stator composed by core press-fitted into motor frame is located on the pedestal with its outer circumference supported by cylindrical tool, and is subjected to deformation through pressing by a punch installed to the sub-press. The punch touches the inner periphery of the magnetic pole tooth before causing plastic deformation of the magnetic pole tooth end as shown in Fig. 8. As the stator is supported by cylindrical tool, the deformations at places other than motor frame and core end are of ignorable levels. Once the magnetic pole tooth undergoes plastic deformation, a change is seen in the level difference with the neighboring magnetic pole tooth. The plastic deformation is controlled by the push-in rate of the sub-press from the position the punch touches the core. Fig. 9 shows a graph indicating the measured push-in rate of the sub-press and deformation of magnetic pole tooth. The linear relation between the two suggests that the level difference can be controlled by the push-in rate.

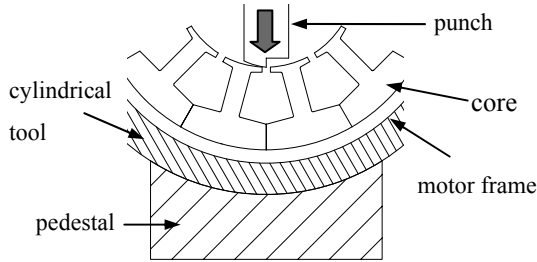


Fig. 8. Punch shape

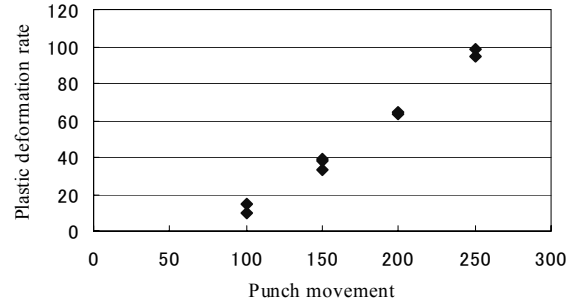


Fig. 9. Relation between push-in rate of sub-press and deformation of magnetic pole tooth

We describe the result of the change in level difference of the 2 samples with large level difference between magnetic pole teeth at 0 degrees, which is similar to the sample shown in Fig. 3.

First of all, Fig. 10 shows the changes in inner diameter shape, A0 curve and Y vector when one of the samples was pressed to plastic deformation gradually in 3 steps in the direction of reducing the level difference at 0 degrees position. The cogging torque  $2f$  component was measured at each step of deformation. The measurement result of inner diameter shape in Fig. 10 indicates that the level difference gradually decreases as the plastic deformation is applied. Further, this also leads the A0 curve near 0 degrees to decrease and Y vector to become smaller. Fig. 11 shows the change in the level difference and Y vector, and Fig. 12 the change in the Y value and the cogging torque  $2f$  component. As the level difference decreases, the Y value becomes smaller, leading to the reduction in the cogging torque  $2f$  component. In other words, the cogging torque  $2f$  component can be reduced by making the Y value smaller by slight deformation of the level difference through pressing. Thus, the supposition was verified through active application of deformation.

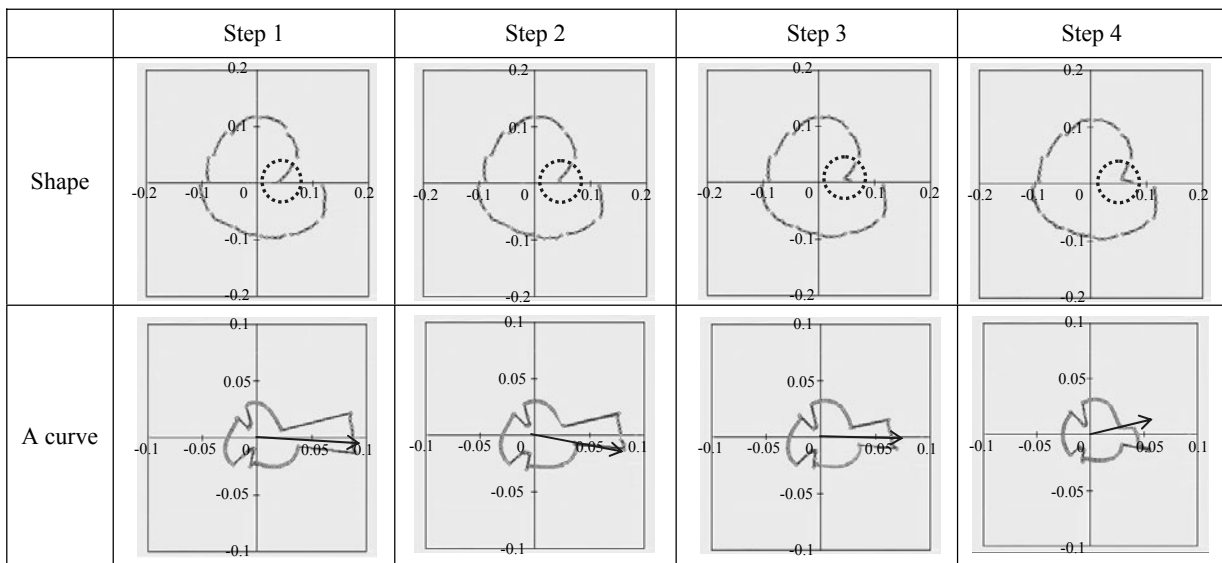


Fig. 10. Changes in inner diameter (top), A curve and Y vector (bottom) through pressing

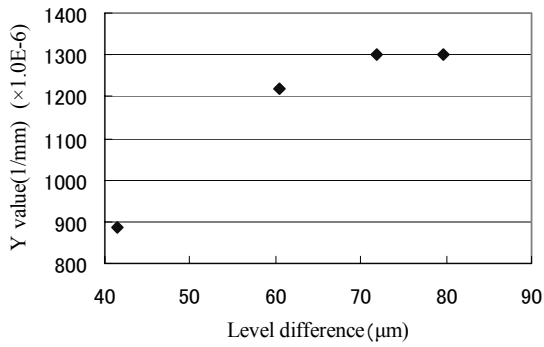


Fig. 11. Changes in level difference and Y value through pressing

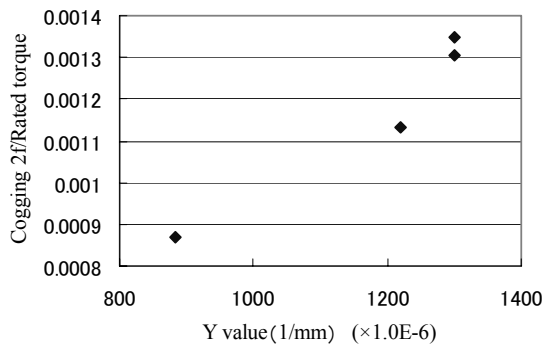


Fig. 12. Changes in Y value and cogging torque 2f component through pressing

## 6. Experimental verification 2

By applying the supposition the experiment was conducted for eliminating the level difference by creating a new level difference. Fig. 13 shows the changes in the inner diameter shape, A0 curve and Y vector when another sample, with level difference at 0 degrees position, is pressed to plastic deformation gradually near 90 degrees to form a level difference, indicating clearly that the level difference near 90 degrees increases as the plastic deformation proceeds. The level difference at 0 degrees was made to opposite direction to the level difference at 90 degrees, with the level difference at 0 degrees showing clockwise inward change while the one at 90 degrees showing clockwise outward change. The value of A0 curve near 0 degrees was found to decrease as the level difference increases by machining, and so was the case with Y vector. Fig. 14 shows the changes in the level difference and Y vector while Fig. 15 the changes in the Y value and the cogging torque 2f component, indicating the Y value getting smaller as the level difference increases and subsequently the cogging torque 2f component getting reduced. In other words, by creating a level difference against an existing level difference at a different position using a press, the A value can be nullified and the Y value decreased, leading to the reduction in the cogging torque 2f component. According to the experimental result in previous chapter, the circularity can be improved by reducing the level difference through machining. According to the experimental result in this chapter, however, the cogging torque 2f component decreases in spite of the circularity getting deteriorated because of the newly made the level difference. This suggests that the cogging torque 2f component depends not on the circularity but on the inner diameter shape, and that its size is determined by the combined effect of the respective regions. And this can be regarded as one of the grounds to verify the supposition of this paper. According to the supposition, therefore, the

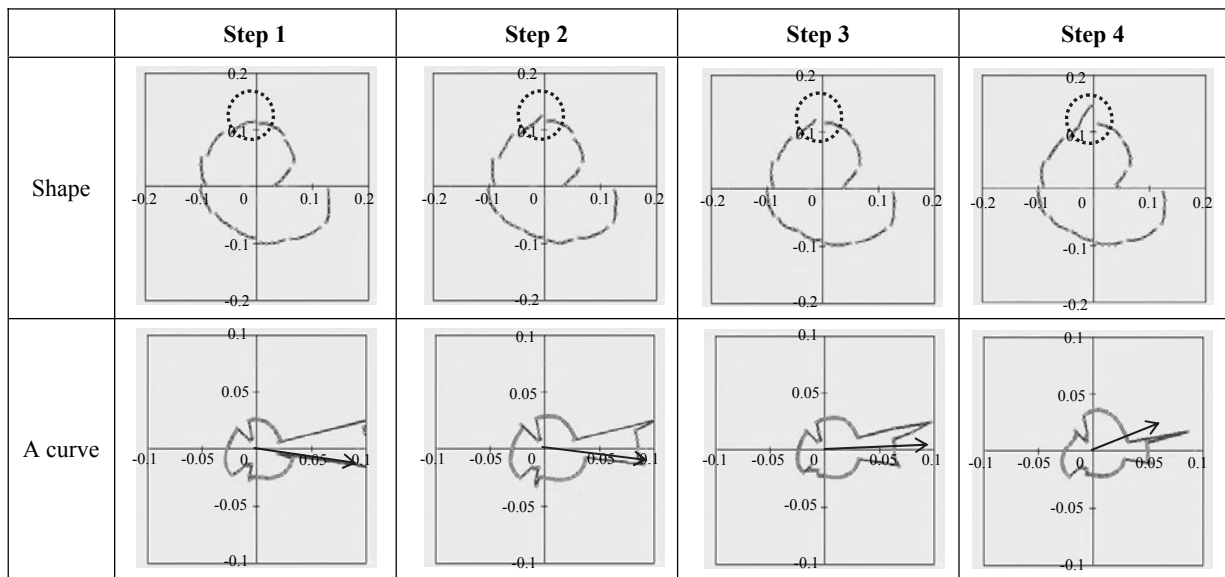
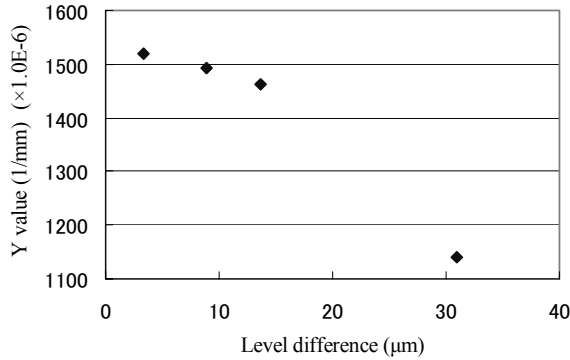


Fig. 13. Changes in inner diameter (top), A curve and Y vector (bottom) through pressing



minute control of the inner diameter shape as well as the due attention to the circularity of the inner diameter is required to reduce the cogging torque 2f component. The fact that the superposition leads to the reduction of the cogging torque 2f component further suggests that the cogging torque 2f component caused by items other than configurational errors such as stress distribution, distribution of machining deterioration, etc. could be nullified by adding new level difference.



**Fig. 14.** Changes in level difference and Y value through pressing

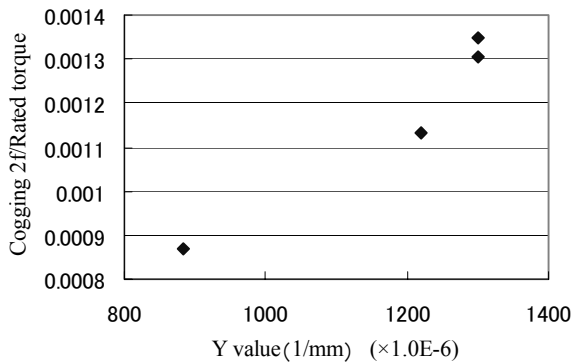


**Fig. 15.** Changes in Y value and cogging torque 2f component through pressing

## 7. Conclusions

The following points can be deduced from the study of the effect of the stator inner diameter shape on the cogging torque 2f component.

1. If Y vector is defined as an index of the magnetic effect of the stator inner diameter, a high correlation is found to exist between Y value and cogging torque 2f component.
2. The analysis of A curve can lead to identification of the region causing Y vector occurrence.
3. From the experiment showing the level difference reduced through post-machining, it is learned that the cogging torque 2f component can be reduce by reducing Y vector.
4. From the experiment showing addition of new level difference through post-machining, it is learned that the cogging torque 2f component can be reduced by reducing Y vector in spite of the deterioration of circularity.
5. In order to reduce the cogging torque 2f component, fine control of the inner diameter shape as well as the circularity is required.
6. From the two experiments showing creation of level difference, it is learned that the Y vector is an index to evaluate the cogging torque 2f component, and that the A curve can be used for cause analysis and measures for reducing the cogging torque 2f component.

## References

- [1] Akita, et al.: A New Core; IEEE Industry APPLICATIONS Magazine, Nov./Dec. 2005 vol.11, No.6 p38-43 (2005)
- [2] Goto, et al.: Elucidation of DC motor cogging torque and new method at reducing the cogging torque; IEE Journal B, Vol. 103-B, p711 (1983)

---

## A High Power and Precision Ultrasonic Linear Motor with Lateral Flexible Supports

Hyeon-Min Lee<sup>1</sup>, Wan-Soo Kim<sup>1</sup>, Cheol-Ho Yun<sup>2</sup>, Hyen-Rok Cha<sup>2</sup>, Chang-Sung Kang<sup>2</sup>, Sun-Kyu Lee<sup>1</sup>  
<sup>1</sup>Gwang-Ju Institute of Science and Technology, <sup>2</sup>Korea Institute of Industrial Technology

Keywords: Ultra sonic actuator, BLT type transducer, holding mechanism, contact stiffness

### Abstract

New holding mechanism of the ultrasonic linear motor for the high power driving in this paper is proposed to improve the positioning accuracy following with the previous studies. Through the previous holding mechanism using a resonance system with the stepped horns, a remarkable operating stability and controllability at high-power driving were achieved. However, when higher power is demanded, big noise in supporting parts of a resonance system is generated and these parts can be damaged and worn due to the discordance of resonance frequencies between a transducer and supporting horns. Moreover, the coupling problem of two vibration components remains due to the undesirable longitudinal factor in the 2nd mode of bending vibration. At first, this study proposes a new design of ultrasonic motor with multiple support points in a single vibrator in order to provide high stiffness support, and discusses about the coupling effect. A maximum driving force over 75N and the positioning accuracy of 100nm were achieved through this mechanism. Moreover the motor efficiency, the thrust force and the velocity were achieved 32%, 52N and 0.27 m/s respectively. Secondly, a new analytical model is proposed to be matched with real system. In this paper, by introducing the contact stiffness, the main reason of the discrepancy between the actual and the analytical system is discussed through FEA.

### 1 Introduction

Nowadays, great attention has been shown to the question of ultrasonic linear motor for accomplishing the high positioning accuracy and high driving force in the semiconductor and optical industry. Especially comparing with many kinds of magnetic linear motors[1-3], Ultrasonic linear motors have many advantages about simple structure, quick response, ability to maintain position without energy consumption, and electromagnetic immunity[6]. Through these characteristics of ultrasonic motor, the complicated problems about precise positioning over long strokes and holding position at any point can be clearly solved[7-10] Commercial ultrasonic linear motors have small output force, and have been used only as drivers for small x-y stage. As a point of this present situation, a bolt clamped Langevin type

transducer (BLT) proposed has attracted a fair amount of attention to accomplish large vibration amplitude and large mechanical force. The authors have already succeeded in the development of high power ultrasonic linear motor with the capability of over 100 N mechanical output force and 0.5 m/s no-load velocity [4-5].

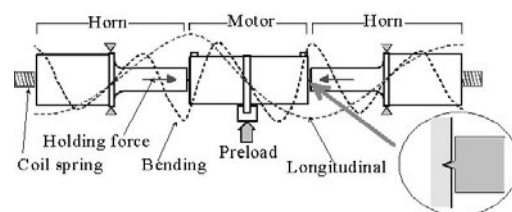


Fig. 1. Previous support mechanism using the resonance of stepped horns.

Problems of the one point holding system[4] such as long settling time, big residual vibration, and poor positioning characteristics were improved by using a resonance system with stepped horns[5](Fig. 1). Additionally, the contact surface which became irregular by a slight shift in the orientation of the vibrator could be improved using a resonance system. However, other problems not to solve have remained in previous systems until now. When higher power is demanded, there is loud noise in supporting parts of the resonance system and these parts could be damaged and worn due to the discordance of a resonance frequency between an actuator and supporting horns. Also the coupling problem of two vibration modes remains due to using a half wavelength.

To overcome these problems of previous system [4-5], this research proposes a new holding mechanism with high stiffness support as a point of this problem about the unstable operation. This new holding mechanism can be explained concretely that a new motor was designed with three supporting points in one vibrator for high stiffness, stable operation, and stable driving resonance frequency. Additionally, this research discusses the achievement of 100 nm positioning accuracy and the solution about the coupling effect by using a new holding mechanism.

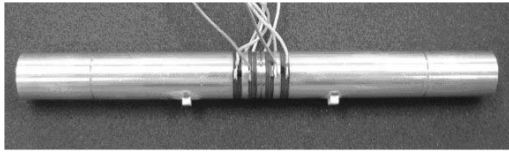


Fig. 2. New ultrasonic motor with three supporting points

## 2 Motor configuration and Operating Principle

Figure 2 shows the configuration of new ultrasonic linear motor which consists of a bolt-clamped Langevin-type longitudinal and bending hybrid transducer. To resolve the stability and the coupling problem due to using a half wave length and the discordance of a resonance frequency in higher driving power[4-5], the transducer was designed 3 times longer than the previous transducer for an ultrasonic linear motor (See Fig. 2)[4-5]. As a result, the vibrator was developed into using the 3rd longitudinal and 6th bending modes, and three nodes to support were common to the two vibrations(See Fig. 3). In Fig. 4, the vibrator is 20 mm in diameter and 241 mm in length. The stator has two types of piezoelectric elements (PZTs) to excite the two vibrations, which are sandwiched by aluminum blocks with a bolt. The dimensions of the PZTs are outer diameter of 20 mm, inner diameter of 10 mm and thickness of 2 mm. Two alumina ceramic tips were bonded on the transducer as frictional driving components.

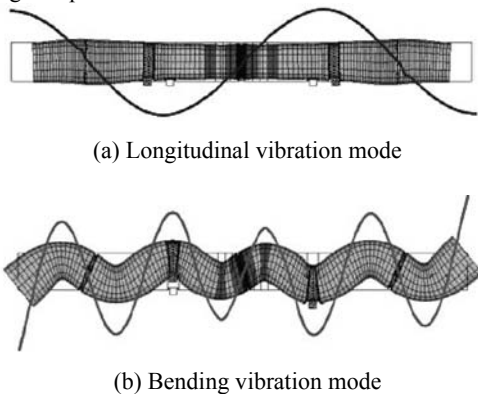


Fig. 3. Vibration modes of the stator calculated by FEM

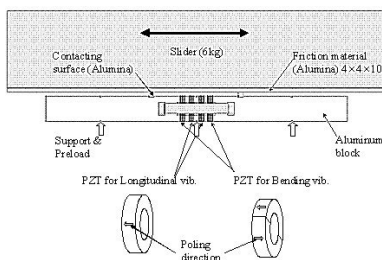


Fig. 4. Basic configuration of the motor

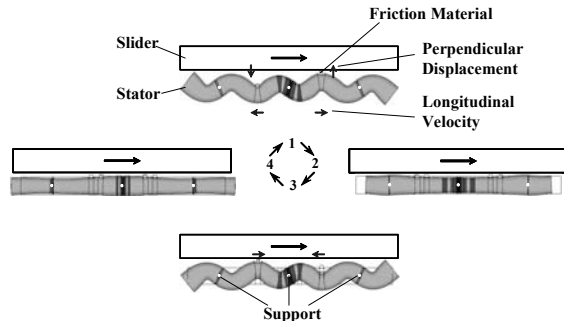


Fig. 5. Operation sequence of the BLT

The operating process shown in Fig. 5 is realized when the two modes are simultaneously stimulated with the phase difference of 90 degree in order to have the elliptic locus on the tips of the vibrator. These elliptical motions are provided by the longitudinal and bending modes of the BLT. The tips of the BLT have a horizontal displacement factor due to the longitudinal motion and a vertical displacement due to the bending motion. That is, the longitudinal vibration generates the mechanical driving force and the bending vibration controls the frictional force. In Fig. 5, since the contact between the vibrator and the slider occurs only at process 1 and process 3, the elliptic motion of the vibrator tips results in the driving force to one direction. The locus at one tip of the BLT is delayed by 180 degree compared to that of the other tip. Therefore one of the two tips in contacting and driving the slider with anti-phase. And also when the phase is changed to 180 degree, the slider can be driven to the opposite direction. The vibrator is pressed against the slider by means of the proper support mechanisms and drives the slider in one direction with frictional force in the contact points.

## 3 Motor Design

### 3.1 Problems of a resonance system with stepped horns

This resonance system with stepped horns in Fig.1 was developed to reduce a big residual vibration and long settling time of one point holding mechanism[5]. Through the resonance system, the positioning characteristics could be improved and also the damage of contact surface in one point supporting could be reduced. However, this resonance system is not enough in higher driving power due to the discordance of a resonance frequency between an actuator and supporting horns. Loud noise can be generated in these points also. And the coupling problem was serious in previous system. The length of previous motor was short due to using a half wavelength with the 1<sup>st</sup> longitudinal and the 2<sup>nd</sup> bending vibration modes. Figure 6 shows the coupling problem that the 2<sup>nd</sup> bending vibration mode to excite the

vertical way motion has including longitudinal factor. This longitudinal factor opposite to moving direction was a serious obstructive component about the positioning characteristics.

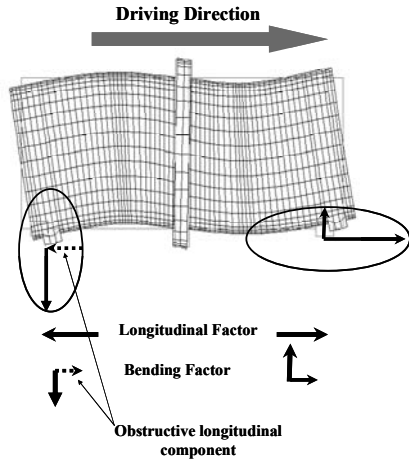


Fig. 6. Coupling effect in a resonance system

### 3.2 High stiffness support mechanism

To remove the coupling effect due to using a half wavelength, the transducer which is 3 times longer than previous transducers has been adopted with the 3rd longitudinal and the 6th bending vibration modes. However, the length of transducer should be decided including the tuning of driving resonance frequency. Usual BLT has a high mechanical quality factor, to obtain a large vibration amplitude and mechanical output, so the longitudinal resonance frequency should be tuned to the bending one. So this actuator was estimated by using the FEM simulation for the actuator design before making.

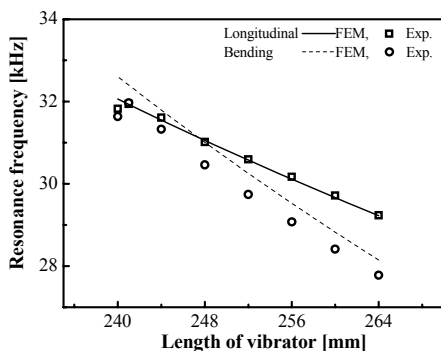
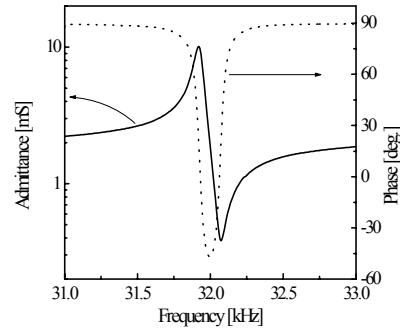
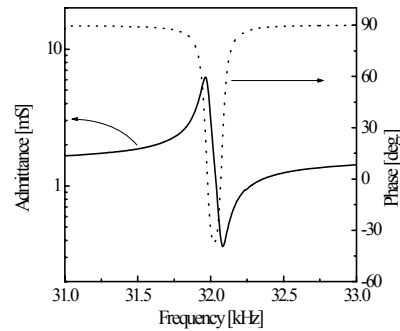


Fig. 7. Tuning the resonance frequencies by length of vibrator



(a). Longitudinal mode.



(b) Bending mode

Fig. 8. Admittance characteristics at each vibration modes

Figure 3 shows the result of 3D FEM simulation through the control of vibrator's length. From the result of simulation the resonance frequencies were same as 31.3 kHz at 248 mm in vibrator length in Fig. 7. But the vibrator's length of a trial product was made longer than the result of simulation for including the manufacturing errors. After making, the resonance frequencies were tuned by the control of length in manufacturing process. Figure 8 shows the admittance characteristics of each vibration mode from the Impedance Analyzer (HP 4294A, 1 V<sub>rms</sub>). The resonance frequencies of each vibration mode could be decided about 31.94 kHz in 241 mm vibrator length. Additionally, according to using long wavelength in the long vibrator, the ceramic tips for friction driving component can have only pure vertical way motion in the 6<sup>th</sup> bending mode shape. (See Fig. 3)

This paper adopted an idea about three supporting points in one vibrator for a high stiffness supporting mechanism proposed in this paper. So for using this idea these holding points should be common nodes of the longitudinal and bending vibration mode not to generate any displacements. Each vibration mode at the resonance frequency of motor was measured by using the Laser Doppler Vibrometer. This result of measurement is showed in Fig. 9. As designed, the three holding points in one vibrator were the common nodes of the two vibration modes.

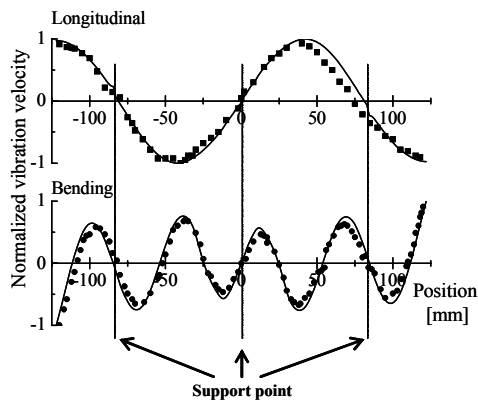


Fig. 9. Vibration distribution along the axis

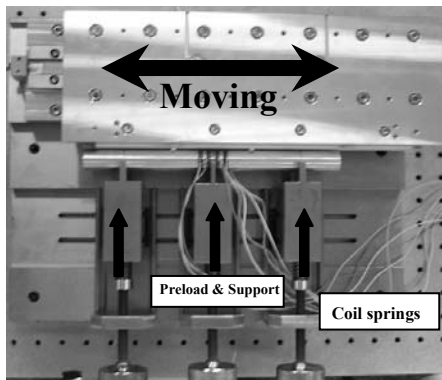


Fig. 10. Total system configuration

The friction driving force in BLT motor should be constant about the inertial force that is from moving and stopping motion of stage. Supporting parts have an important role to keep the constant friction force. So although an actuator has the capability of high driving force and high velocity, that actuator cannot be put practical use if not to solve this supporting problem. In this research, the supporting part was designed for reducing the vibration effect by supporting. Especially, three parts between supporting part and actuator was manufactured 1mm slit state. And this system can keep constantly driving friction force by using coil-springs to control the preload. Figure 10 shows the total system configuration and slit state supporting parts

#### 4 Motor Characteristics

As the genuine experiment for achieving the stable operation was done, the longitudinal mode voltage of a driving component was increased in the constant bending mode voltage. This means a friction component was constant. The

bending mode voltage of a friction component was  $V_{bending}=21 V_{op}$  which will be amplified by using the external cables in series. Figure.11 shows a result about increasing the longitudinal voltage of a driving component.

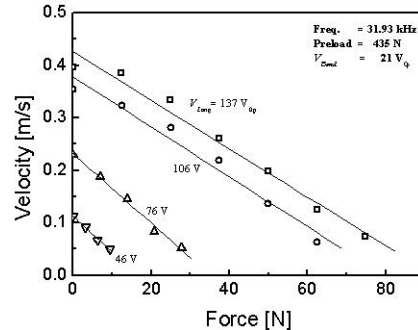


Fig. 11. Process result about increasing the longitudinal mode voltage

As the preload was increased to 435 N, the maximum velocity could be achieved over 0.4 m/s. Figure 12 shows this result. However although the driving condition was same, the moving characteristics about each direction was different. The reason of difference can be supposed by the difference of preload at each supporting part, the discordance of two driving resonance frequencies, and so on.

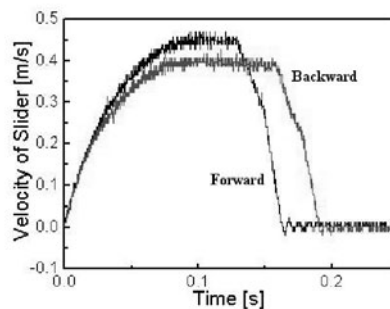


Fig. 13. Characteristics of velocity and load & Efficiency

Using the driving frequency of 31.93 kHz,  $V_{Long}=21 V_{op}$  and  $V_{bending}=21 V_{op}$ , the maximum driving force and the maximum moving velocity were achieved 75 N, 0.4 m/s and the efficiency that is the ratio between the input electric power and mechanical output force was also achieved 32% when the maximum driving force was 75 N and the maximum velocity was 0.4 m/s. (See Fig. 13)

#### 5 PID Feedback Control System

The positioning characteristics were tested in PID feedback control system about the high stiffness supporting mechanism. Figure 14 shows the basic configuration for the PID feedback control system. The control system uses an optical linear encoder to detect the position of the sliding

plate with a resolution of 50 nm. The position signal from the optical linear encoder is fed back to a PID controller through the motion board (NI PCI7304). The amplitudes of the voltages applied to the bending and longitudinal PZTs of the motor are controlled through amplitude modulations (AM) of the function generator.

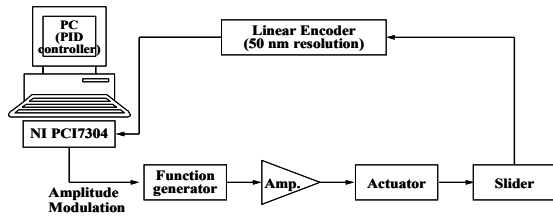
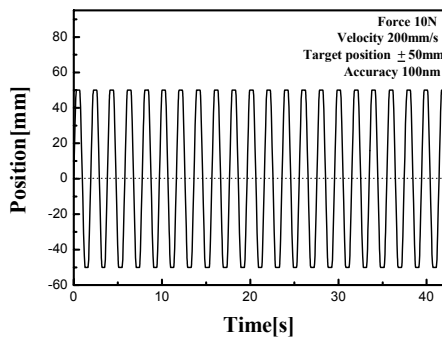
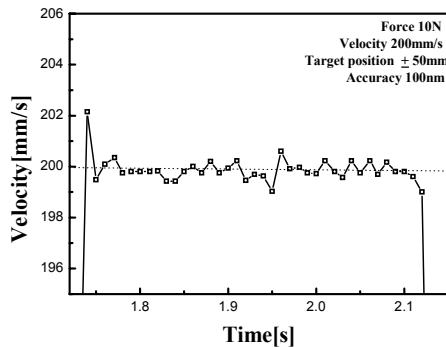


Fig. 14. Basic configuration of the PID feedback control system



(a) Continuous driving motion with 100 nm positioning accuracy.

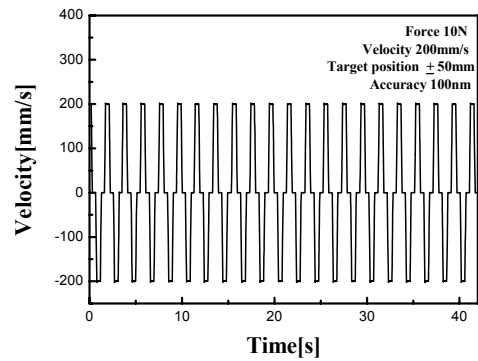


(b) 100 nm positioning accuracy

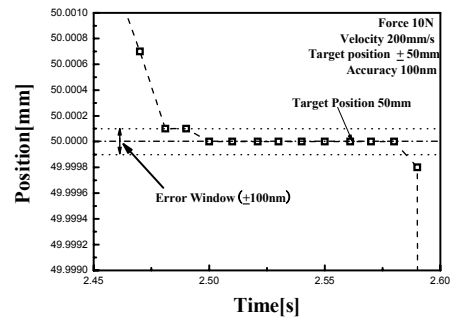
Fig. 15. Result of 100nm positioning accuracy

In order to test the performance of the proposed control system, a cycle test was carried out. After getting the 10 stable position data within error window from the encoder, the target position is changed to the opposite direction. So the stage is moved coming and going continuously with

given position accuracy. And also tuning method of each PID gain used the sustained oscillations method in the Ziegler-Nichols rules [11]. The experimental approaches to the tuning of PID controller in the Ziegler-Nichols rules are usually used when the moving stage is so complicated that its mathematical model cannot be easily obtained. Figure 15 shows the result of 100 nm positioning accuracy with the PID feedback control. The mass of the slider was 6 kg; the driving force was 10 N; the velocity was 200 mm/s; the target position was  $\pm 50$  mm from the reset position. We also confirmed that the speed fluctuation of the steady state velocity zone was less than 0.5% of the programmed velocity in Fig. 16



(a) Continuous steady state velocity control



(b) Steady state velocity control in 1 mm/s

Fig. 16. Steady state velocity control

## 6 Contact stiffness

In practical use of ultrasonic actuators, the matching of two modes driving at a resonance frequency is an essential factor. The stiffness of each part is the most important factor about the change of the resonance frequency because the mass of each part in this system is constant. Moreover, the parts which the stiffness can be changed easily in this system are specially the friction driving parts between the moving stage and the actuator. In this system, there are two stiffness which are structure stiffness and contact stiffness. However, contact stiffness between moving stage and actuator can be

easily changed. The contact stiffness changed by supporting preload affects two driving resonance frequency of transducer. The contact stiffness is difficult to find by theoretical method. Based on this, resonance frequencies of motor were calculated by FEA.

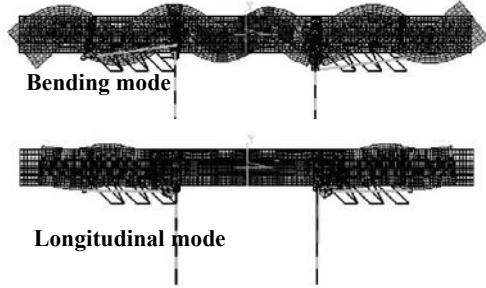
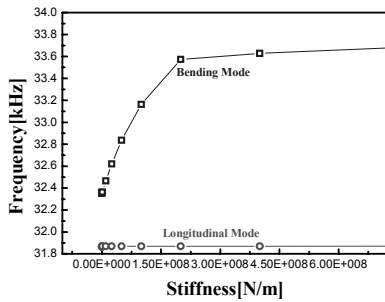
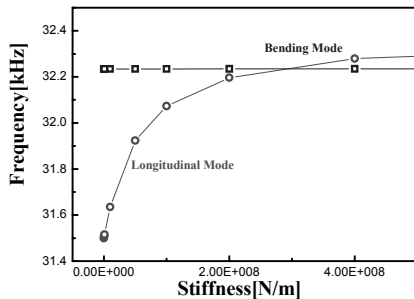


Fig. 17. Contact stiffness modeling with actuator



(a) Normal direction contact stiffness



(b) Tangential direction contact stiffness

Fig. 18. Changing resonance frequency by contact stiffness

Fig. 18 shows the result of FEA, contact stiffnesses of each direction affect certain mode resonance frequency independently. Finally, it could be found that value of normal contact stiffness is  $1.0 \times 10^7$  N/m and tangential stiffness is  $4.0 \times 10^8$  N/m to have the matched resonance

frequency 32.3 kHz. And this value close to measured value 32.10 kHz, that is the stable driving resonance frequency can be realized by the preload modulation

## 7 Conclusion

The This research proposed new high stiffness support mechanism which has three common vibration nodes in one vibrator. This mechanism became simpler than the previous resonance system by the removal of two supporting horns. And the previous coupling problem and the positioning characteristics could be improved by using the long wavelength and a high stiffness supporting mechanism in high power driving. The three points can firmly hold the motor, and also no effect the two vibration modes could be verified by experiments. Through this new mechanism, the driving resonance frequency could be used stably. In conclusion, the maximum mechanical output force was achieved 75 N and the no-load velocity was also 0.45 m/s with a 20 mm diameter motor. Incorporating the present motor into a PID feedback control system, we could achieve in positioning the 6-kg-stage at speed of 200 mm/s with the accuracy of 100 nm and the steady state velocity control in the range of 1 mm/s. And contact stiffness which is changed by supporting preload affect resonance frequency. The stable driving resonance frequency can be realized by the preload modulation.

## 8 References

D. Howe, (2000)Sensors & Actuat. Blood 81: 268  
 [1] Y. Tomita, K. Makino, d M. Sugimine, (1996) Ann. CIRP. Blood: 45: 359.  
 [2] H. Yajima, H. Wakiwaka, K. Minegishi, N. Fujiwara,  
 [3] K. Tamura, (2000)Sensors & Actuat. Blood 81:281  
 [4] Cheol-Ho Yun, Takaaki Ishii, Kentaro Nakamura, Sadayuki Ueha, (2001) A high power ultrasonic linear motor using a longitudinal and bending hybrid bolt-clamped Langevin type transducer. J. Appl. Phys. Vol. 40:3773  
 [5] Cheol-Ho Yun, Takaaki Ishii, Kentaro Nakamura, Sadayuki Ueha (2002) Jpn. J. Appl. Phys. Vol. 41: 3261  
 [6] T. Hemsel, J. Wallaschek, (2000): IEEE Ultrasonics Symp. 663  
 [7] Y. Tomikawa, T. Ogasawara, T. Takano, (1989) Ferroelectrics Vol. 91:163  
 [8] M. Kurosawa, H. Yamada, S. Ueha, (1988) Proc. 9th Symp. Ultrasonics, Sendai, Jpn. J. Appl. Phys. Vol. 28-1:158  
 [9] B. Zhai, S-P. Lim, K-H. Lee, S. Dong, P. Lu, (2000) Sensors & Actuat. Vol. 86:154  
 [10] J. Zumeris, (1995) U. S. Patent 5453653  
 [11] Katsuhiko Ogatata, (2002) Modern control engineering, fourth edition

---

# A Precise Motion Measurement of a Miniature Robot Driven by the Deformation of Piezoelectric Actuators

Akihiro Torii, Atsushi Shimada, Kae Doki, Akiteru Ueda  
Aichi Institute of Technology

Keywords: miniature robot, piezoelectric actuator.

## Abstract

We measure the motion of a miniature robot and the trajectories of three legs. The robot consists of three stacked-type piezoelectric actuators connected in an equilateral triangle. The three legs, which support the main body of the robot, are fixed at every vertex of the triangle. The input waveforms applied to the piezos are rectangle and sinusoidal waveforms. We discuss the motion of the miniature robot and the trajectories of the legs under the conditions that the miniature robot can rotate or not.

## 1 Introduction

The motion of a miniature robot driven by the deformation of piezoelectric actuators (piezos) is described. The size of the robot is approximately one cubic inch. The miniature robot is designed for a precise motion stage, which consists of three stacked-type piezos connecting in an equilateral triangle. Three legs, which support the main body of the robot, are fixed at every vertex of the triangle. The deformation of the piezos thrusts the legs of the miniature robot. By repeating the deformations of the piezos, the miniature robot realizes the linear and rotational displacement in a plane surface [1]. However, the miniature robot sometimes did not follow the control waveforms. By using control waveforms of the counter clockwise (CCW) direction, the miniature robot rotated in the clockwise (CW) direction, and by using control waveforms of the CW direction, the miniature robot rotated in the CCW direction.

In our previous work, the motions of three legs of the miniature robot were measured. When the miniature robot was operated by rectangle waveforms, the legs moves incrementally. In this paper, first, the motion of the miniature robot is measured by changing the input waveforms and frequencies. The input waveforms applied to the piezos are rectangle and sinusoidal waveforms. The direction of the rotational displacement is described. Next, the motion of the legs is measured. We discuss the motion of the miniature robot and the trajectories of the legs under the conditions that the miniature robot can rotate or not.

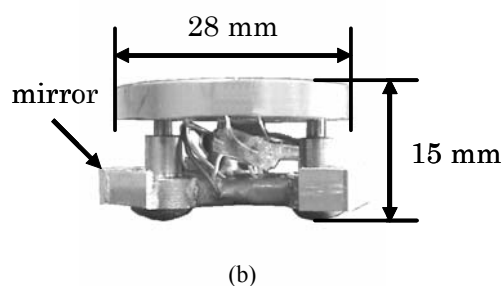
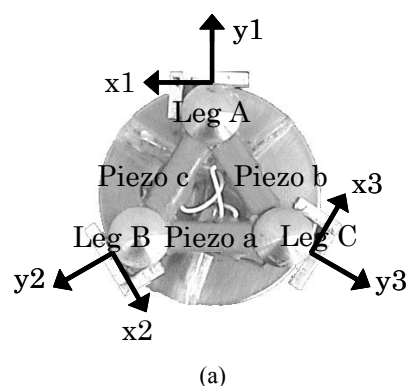


**Fig. 1** The miniature robot's photograph. (a) Bottom view of a miniature robot. (b) Side view of a miniature robot.

## 2 Miniature Robot

Fig. 1(a) shows the bottom view of the miniature robot and Fig. 1(b) shows the side view of the miniature robot. The miniature robot is 28 mm in diameter, 15 mm in height, and weights 27 g. In Fig. 1(a), we represent the piezos as Piezo a, b, c and represent three legs as Leg A, B, C. The miniature robot consists of three stacked-type piezos connecting in an equilateral triangle. The size of the piezos is 2\*3\*10 mm (NEC TOKIN AE0203D08). When a voltage is applied to



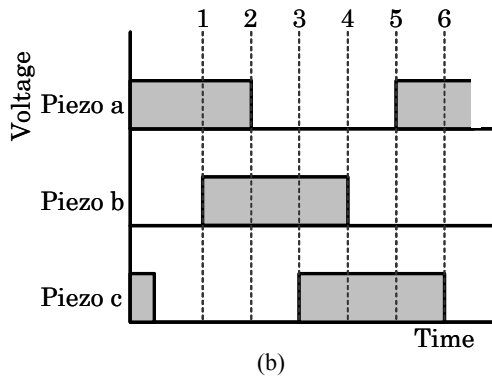
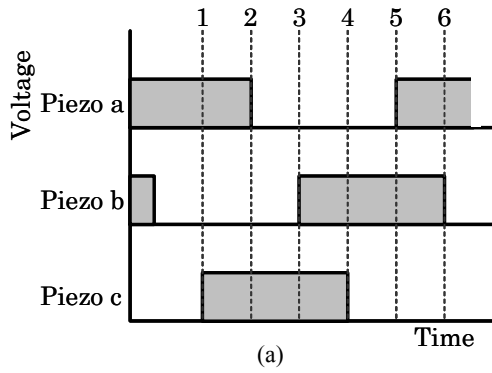


**Fig. 2** The control waveforms which rotate the miniature robot. (a) In the CCW direction. (b) In the CW direction.

the piezos, it deforms  $0.06 \mu\text{m}/\text{V}$ . Three legs, which support the body of the miniature robot, are fixed at every vertex of the triangle. Three legs has mirrors for a measurement. A thin wire supplies power to the piezos. We define  $x_1, y_1, x_2, y_2, x_3, y_3$  as the local coordinate of the legs. The miniature robot has a circular plate on the piezos. The circular plate will carry optical components and work tools.

### 3 Principle

The miniature robot moves by the deformation of the piezos, and the deformation pushes or pulls the legs which supports the miniature robot. The miniature robot does not have clamp mechanism such as an electromagnet. Therefore, the counterforce occurs, and the legs moves as the piezos deform.

Control waveforms are shown in Fig. 2. The waveforms in the CCW direction (Fig. 2(a)) and those in the CW direction (Fig. 2(b)) are different in phases. Fig. 3 shows a model as the robot rotates in the CCW direction. A period of the rotational displacement consists of six steps. In Fig. 3, Piezo c, Piezo b and Piezo a extend at point 1, 3, and 5, and Piezo a, Piezo c and Piezo b contract at point 2, 4, and 6. The principle of the rotational displacement is as follows. At point 1 in Fig. 3, Leg A moves by the expansion of Piezo c. At point 2, Leg C moves by the contract of Piezo a. From point 3 to point 6 is the similar principle. By repeating these six steps, the miniature robot rotates in the CCW direction.

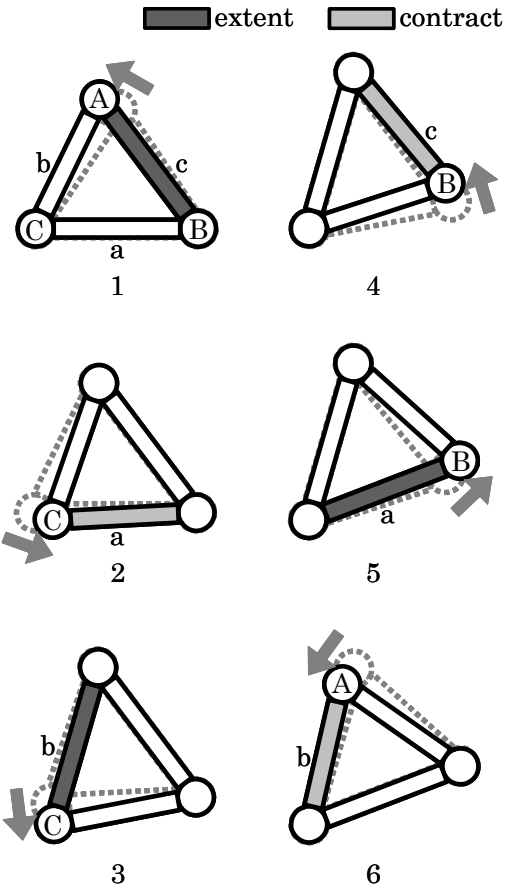


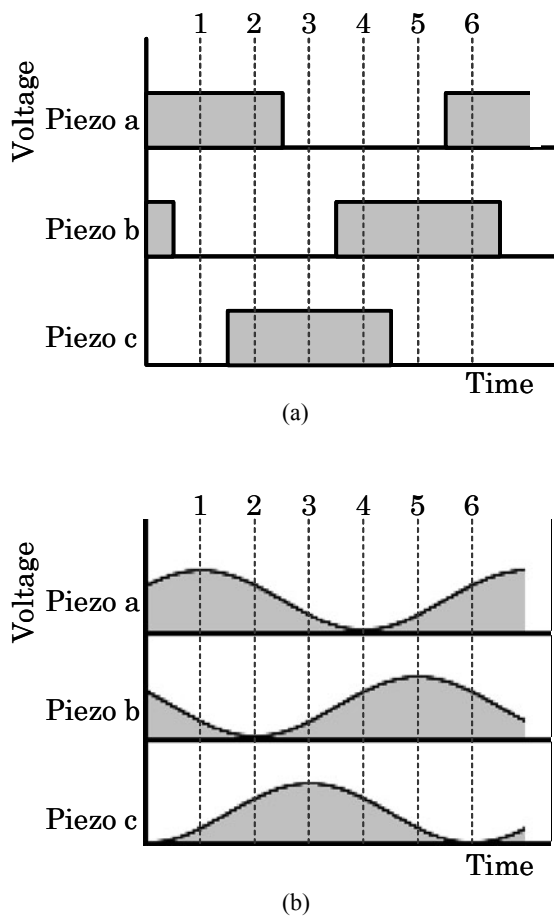
**Fig. 3** The motion mechanism in the CCW direction.

The CW directional rotation is realized by replacing the signal to Piezo b with that to Piezo c (Fig. 2(b)).

### 4 Experiments

The miniature robot is moved by the deformation of the piezos. Fig. 4 shows control waveforms which have the miniature robot rotate in the CCW direction. In our experiment, the signal in the CCW direction is used. The control waveforms are rectangle and sinusoidal waveforms. The sinusoidal waveform is the fundamental component of the rectangle waveform. The vertical axis denotes voltage and horizontal axis denotes time. The minimum voltage of the control waveforms is 0 V, and the voltage dose not take a negative value. The control waveforms in Fig. 4(a) are three-phase rectangle waveform. The control waveforms in Fig. 4(b) are three-phase sinusoidal waveform. The amplitude of the voltage is 100 V and input frequencies are from 100 Hz to 1000 Hz.

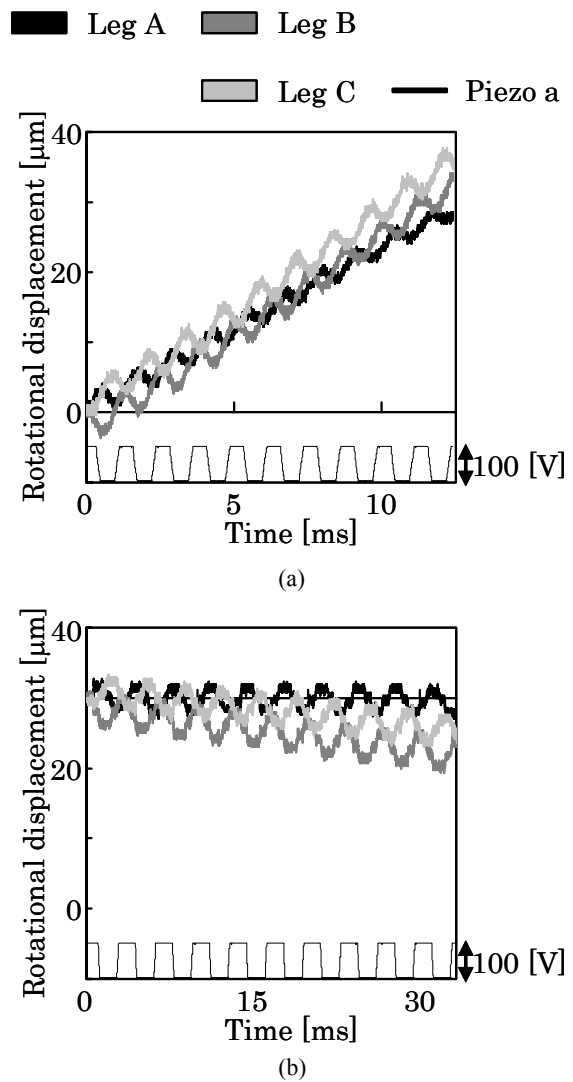
The rotational displacement of the miniature robot is measured by the liner displacement in  $x_1, x_2, x_3$  directions. The motion of the miniature robot, which moves on a glass, is measured by optical displacement sensors. We change the



**Fig. 4** The control waveforms which rotate the miniature robot in the CCW direction. (a) Rectangle waveform. (b) Sinusoidal waveform.

input frequency and repeat the measurement. We investigate the relationship between the conditions that the miniature robot can rotate or not.

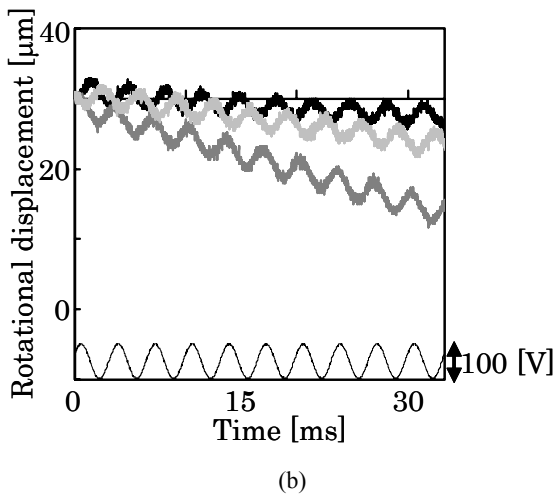
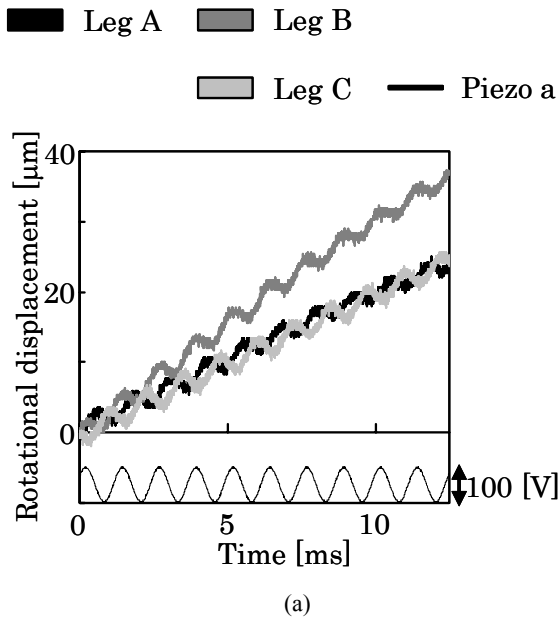
Then, we invert the miniature robot in order not to add a load to its three legs which are measured. The motions in the local axis of three legs are measured. The x-axis and y-axis are orthogonal axes. Measured results are processed by a personal computer.



**Fig. 5** The rotational displacement of the miniature robot. The control waveform is rectangle, and the direction is the CCW direction. The frequency is (a) 800 Hz and (b) 300 Hz.

**Table 1** Experimental conditions. Waveform, frequency, and direction.

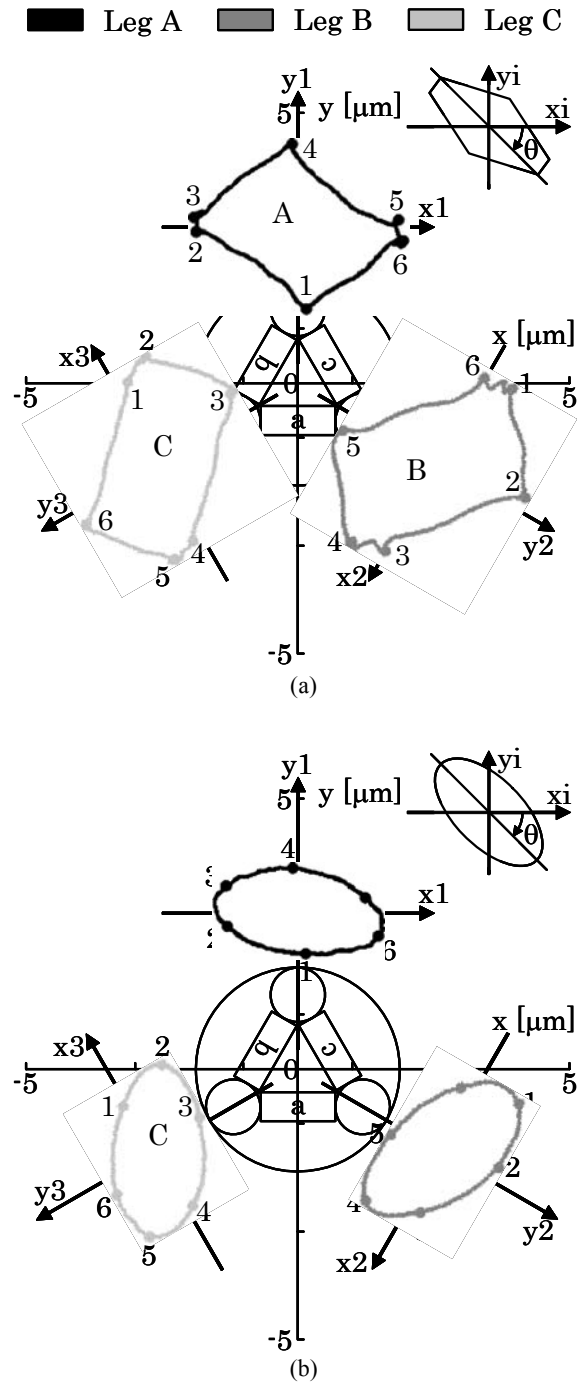
Figures	Waveform	Freq.	Direction
5(a), 7(a), 8(a)	rectangle	800 Hz	CCW
5(b), 8(b)	rectangle	300 Hz	CCW
6(a), 7(b), 9(a)	sinusoidal	800 Hz	CCW
6(b), 9(b)	sinusoidal	300 Hz	CCW



**Fig. 6** The rotational displacement of the miniature robot. The control waveform is sinusoidal, and the direction is the CCW direction. The frequency is (a) 800 Hz and (b) 300 Hz.

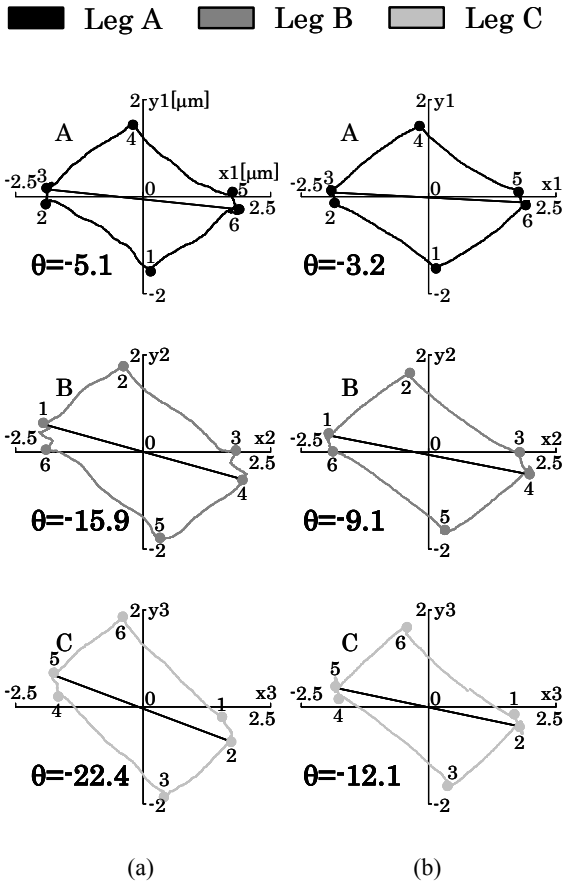
### 5 Experimental Results

Table 1 summarized experiment conditions. We applied various input signals to the piezos. Fig. 5 and Fig. 6 show the rotational displacement of the miniature robot. Fig. 5(a) is obtained when the control waveform is rectangle, the frequency is 800 Hz, and the direction is the CCW direction. Fig. 5(b) is obtained when the control waveform is rectangle, the frequency is 300 Hz, and the direction is the CCW direction. Fig. 6(a) is obtained when the control waveform is sinusoidal, the frequency is 800 Hz, and the direction is the CCW direction. Fig. 6(b) is obtained when the control



**Fig. 7** Three legs' trajectories in the local  $xy$  plane and the long axis angle  $\theta$ . The frequency is 800 Hz. The direction is the CCW direction. (a) The control waveform is rectangle. (b) The control waveform is sinusoidal.

waveform is sinusoidal, the frequency is 300 Hz, and the direction is the CCW direction. The vertical axis is a rotational displacement and horizontal axis is a time. The rotational displacement of Leg A, Leg B and Leg C and the



**Fig. 8** Three legs' trajectories in the local xy plane and the long axis angle  $\theta$ . The control waveform is rectangle. The direction is the CCW direction. The frequency is (a) 800 Hz and (b) 300 Hz.

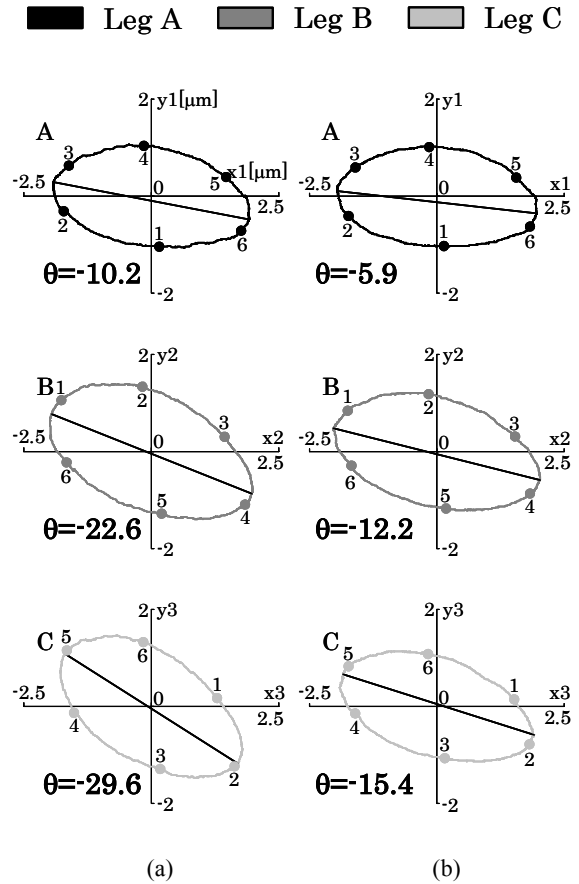


**Fig. 9** Three legs' trajectories in the local xy plane and the long axis angle  $\theta$ . The control waveform is sinusoidal. The direction is the CCW direction. The frequency is (a) 800 Hz and (b) 300 Hz.

input voltage applied to Piezo a are indicated in Fig. 5 and Fig. 6. Fig. 5 and Fig. 6 show 10 periods of the control waveforms. The rotational displacements of three legs synchronize with the input voltage.

In Fig. 5 and Fig. 6, the miniature robot can rotate properly in the CCW direction when the rotational displacement of three legs are positive. The miniature robot rotates in the wrong direction, i.e. the CW direction when the rotational displacement of three legs are negative. In Fig. 5(a), the miniature robot can rotate properly because the rotational displacement of three legs are positive. In Fig. 5(b), the miniature robot rotates in the wrong direction because the rotational displacement of three legs are negative. Fig. 6(a) shows that the miniature robot can rotate properly and Fig. 6(b) shows the miniature robot rotates in the wrong direction. Therefore when the input frequency is 800 Hz, the miniature robot can rotate properly, and when the input frequency is 300 Hz, the miniature robot rotates in the wrong direction.

Fig. 7 shows the miniature robot and three legs' trajectories indicated in the local xy plane. The coordinates in Fig. 7 are introduced in Fig. 1(a). The horizontal and

vertical axis denote the local coordinate  $x_i$  and  $y_i$  ( $i=1, 2, 3$ ) of the legs. Numbers in Fig. 7(a) correspond to those in Fig. 4(a) and numbers in Fig. 7(b) correspond to those in Fig. 4(b). In Fig. 7(a), the control waveform is rectangle, the frequency 800 Hz, and the direction is the CCW direction. The three legs' trajectories are similar to hexagonal trajectories in the CCW direction. In Fig. 7(b), the control waveform is sinusoidal, the frequency 800 Hz, and the direction is the CCW direction. The three legs' trajectories are similar to ellipse trajectories in the CCW direction. In Fig. 7(a) and Fig. 7(b),  $\theta$  is long axis angle. The long axis of the hexagonal trajectories is defined as the maximum distance between the vertexes. The angles differ by changing frequency. We investigate the relationship between the angle and the motion of the miniature robot.

Fig. 8 and Fig. 9 show the three legs' trajectories. In Fig. 8(a), the trajectories are obtained by using Fig. 7(a). When the control waveform is rectangle, the frequency is 300 Hz, and the direction is the CCW direction, Fig. 8(b) is obtained. In Fig. 9(a), the trajectories are obtained by using Fig. 7(b). Fig. 9(b) is obtained when the control waveform is sinusoidal, the frequency is 300 Hz, and the direction is the

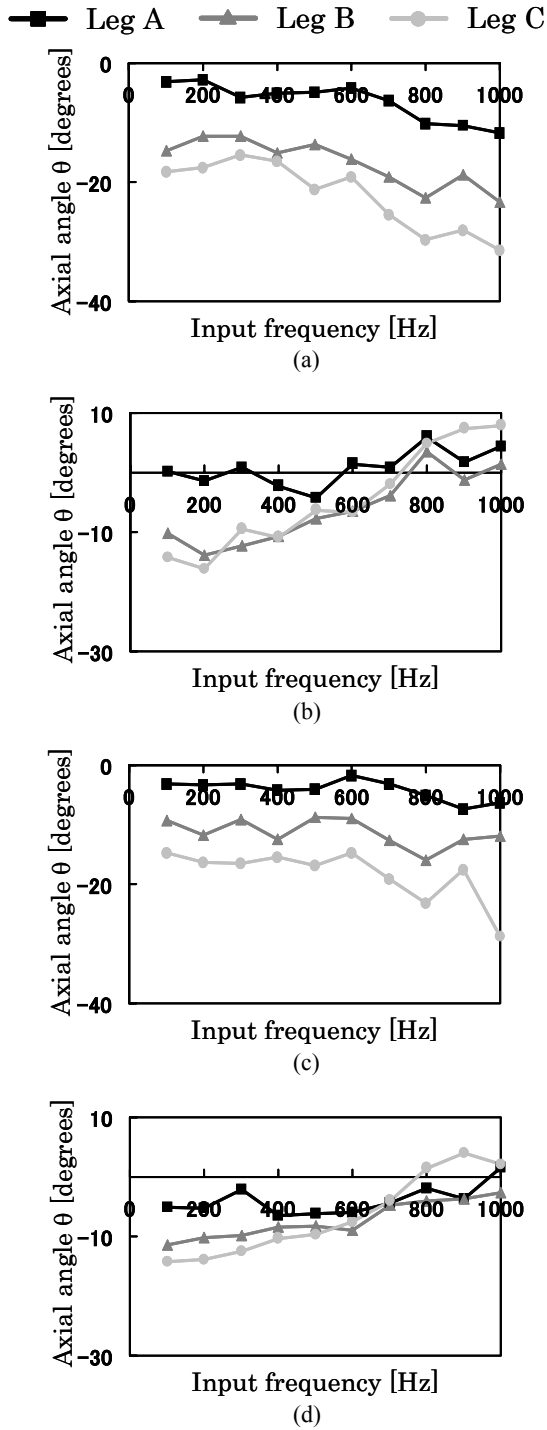


**Fig. 10**  $\theta$  of the legs of each frequency. (a) The control waveform is rectangle, and the direction is the CCW direction. (b) The control waveform is rectangle, and the direction is the CW direction. (c) The control waveform is sinusoidal, and the direction is the CCW direction. (d) The control waveform is sinusoidal, and the direction is the CW direction.

CCW direction. The difference between Fig. 8(a) and (b) is frequency. The difference between Fig. 9(a) and (b) is also frequency. The lines in the trajectories indicate long axis. The numbers in Fig. 8 correspond to those in Fig. 4(a) and numbers in Fig. 9 correspond to those in Fig. 4(b). The trajectories of Fig. 8(a) and Fig. 8(b) are similar. However, the angles of the long axis of Fig. 8(a) are larger than that of Fig. 8(b). The trajectories of Fig. 9(a) and Fig. 9(b) are similar. However, the angles of the long axis of Fig. 9(a) are larger than that of Fig. 9(b). The tendency of the angles in Fig. 9 are similar to Fig. 8. When the frequency changes, the angles differs.

Fig. 10 shows  $\theta$  of the legs of each frequency. The vertical axis denotes the long axis angle and horizontal axis denotes frequency. Fig. 10 is obtained by changing the direction, the waveform, and the frequency. Fig. 10(a) and Fig. 10(b) are obtained when the control waveform is rectangle, and the direction is the CCW direction. Fig. 10(c) and Fig. 10(d) are obtained when the control waveform is sinusoidal, and the direction is the CCW direction. In Fig. 10(a) and Fig. 10(c), as frequency becomes higher, the angles of long axes decrease. In Fig. 10(b) and Fig. 10(d), as frequency becomes higher, the angles of long axes increase. From these results, when the control waveforms is the CCW direction, the angles of long axes decrease as frequency becomes higher, and when the control waveforms is the CW direction, the angles of long axes increase as frequency becomes higher. We suppose that the angle of long axis affect the motion of the miniature robot.

## 6 Conclusions

By changing the input waveforms, we studied the motion of the miniature robot and its legs. In the experiments, the miniature robot, which uses the input frequency of 800 Hz, can rotate properly, and the miniature robot, which uses the input frequency of 300 Hz, can rotate in the wrong direction. The angle of the long axis in each frequency was measured. The angle of the long axis differs according to the frequency and waveform. When the control waveforms is the CCW direction, as frequency becomes higher, the angles of long axes increase. When the control waveforms is the CW direction, as frequency becomes higher, the angles of long axes decrease.

## 7 References

- [1] Akihiro Torii, Yoshiyuki Fukaya, Kae Doki, Akiteru Ueda, (2003) Motion of a Miniature Robot Using Three Piezoelectric Elements Controlled by Rectangular Voltage: Journal of Robotics and Mechatronics Vol. 15 No. 6. 602-608

# Development of IVUS (Intravascular Ultrasound) Driven by Ultrasonic Micromotor -Principle of Drive and Detection Methods-

Tetsuro WADA<sup>1</sup>, Akihei NAKAJIMA<sup>1</sup>, Tadashi MORIYA<sup>2</sup> and Yuji FURUKAWA<sup>3</sup>

<sup>1</sup>Department of Mechanical Systems Engineering, Tokyo University of Agriculture and Technology, <sup>2</sup>Department of Electrical Engineering, Tokyo Metropolitan University, <sup>3</sup>Professional Graduate School, Management of Technology, Tokyo University of Agriculture and Technology

Keywords: IVUS, Ultrasonic Micromotor, Cerebral Thromboses

## Abstract

In this paper, we try to develop a miniaturized ultrasonic angina-pectoris scope, namely, miniaturized IVUS which is rotated by another ultrasonic micro motor for the observation of cerebral thromboses in brain vessels. As a first step of research, a prototype of IVUS with 3 mm outer diameter and 10 mm length has been developed and its torque-rotational speed characteristic was examined. And the principle to detect cerebral thromboses by sending ultrasonic sound to the radius direction of a blood vessel and catching its reflection while it is rotated by a micro motor was proposed and its fundamental characteristics were verified.

## 1 Introduction

As it is desired to operate human bodies without having to cut them open, operations guided by a catheter are widely carried out today for heart and blood vessel diseases. Although ultrasonic angina-pectoris scopes are widely used for the internal observation of blood vessels, it is difficult to apply them for the observation and removal of cerebral thromboses in brain vessels, because their small diameter of less than 2 mm makes it difficult to insert and rotate devices attached at the end of a catheter.

To overcome this problem, in this present study, we tried to develop a miniaturized IVUS which can be rotated by another ultrasonic micromotor. Ultrasonic micromotor is rather easy to miniaturize because of its simple structure, hence, it is expected to be applied in many industries, and outstandingly as a driver of medical devices that operates inside a human body[1][2].

In this report, driving principle and a performance evaluation of a prototype of a ultrasonic micromotor which is applied to a miniaturized IVUS, and the principle and a fundamental experiment of the method of internal observation in a blood vessel by the reception and transmission of the ultrasonic vibration are described.

## 2 Driving principle of ultrasonic micromotor

Fig. 1 a shows the schematic diagram of the ultrasonic micromotor. The prototype micromotor consists of an external vibrator, a waveguide, a stator and a rotor. The thin wire made of SUS receives ultrasonic vibration from the vibrator that is attached to one end of the waveguide (hereinafter, the waveguide is described as the arm part of the coil) and propagates it to a helical coil (stator).

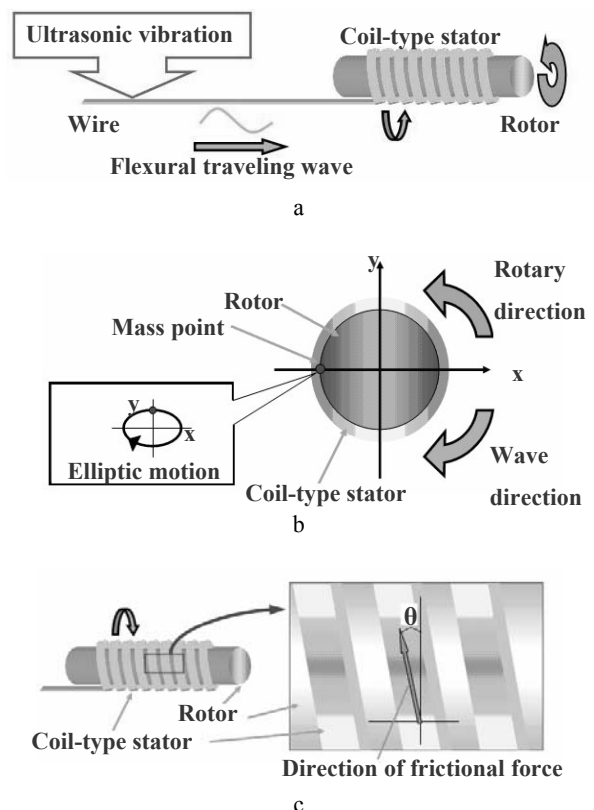


Fig. 1. Driving principle of ultrasonic micromotor

The progressive flexural wave in the helical coil generates micro frictional force at the contact points between the rotor and the coil and the sum of these microfrictions can produce an elliptical motion to rotate the rotor as shown in Fig. 1 b. During this time, the frictional force works oppositely to the forward direction of the progressive wave.

Moreover, the frictional force is not only influenced by the direction of the rotation but also by the axial direction of the rotor because the progressive wave progresses along the spiral structure of the coil (as shown in Fig. 1 c). Therefore, the rotor performs a rotary motion and a translational motion. In the case shown in Fig. 1, the rotor is placed inside the coil, but an opposite location is also possible.

### 3 Prototype of ultrasonic micromotor

A prototype of ultrasonic micromotor with 3 mm outer diameter and 10 mm length has been developed (Fig. 2). It consists of a rotor, a coil, a case, and a stopper. The arm part of the coil has 1.5 m length. The coil is placed around in the rotor and the outer diameter of the coil fits the inner diameter of the rotor. The rotor is covered with the case and the rotor is supported anteroposteriorly and radially by fitting one end of the case with the stopper. The material for the rotor and coil is SUS301 which has a good biocompatibility and that for the case is a TI polymer which has a heat resistance and an abrasion resistance.

When an ultrasonic vibration is applied to the arm part of the coil, it becomes a progressive wave and it spreads from the arm part to the coil part, and the rotor can be rotated according to the principle described in section one.

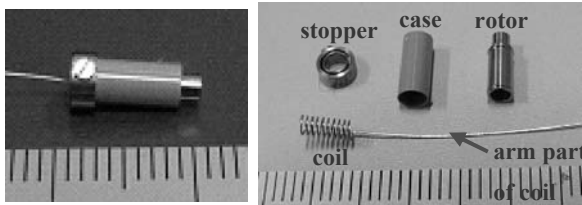


Fig. 2. Prototype of ultrasonic micromotor (left:overall view, right:exploded view)

### 4 Measurement of rotational speed and torque

Fig. 3 shows the apparatus for measuring the rotational speed of the micromotor. The stopper of the micromotor was fixed on the stage and the Langevin vibrator was used as a source of the ultrasonic vibration. A laser beam from the laser displacement meter is irradiated onto a small teeth of the gear (11 mm tip diameter and 7 mm length) which is connected to the tip of the rotor so as to reflect it intermittently, and this reflected light is caught by a laser displacement sensor whose data are stored in the memory of a note PC through the controller. Rotational speed was calculated from a series of pulse outputs. On the other hand, torque was calculated from a rotational angular acceleration

and the moments of inertia of the rotor and gear (the following expression).

$$T = J\dot{\omega} \quad (1.1)$$

$T$ : torque

$J$ : moment of inertia(rotor, gear)

$\dot{\omega}$ : angular acceleration

Fig. 4 shows the results of the measurements of time and angular velocity. From the results, the shape in graph of angular velocity shows a first order lag and the regular rotational speed (approximately 250 rad/s) was seen at about 0.58 seconds in time. Moreover, the time-constant of the micromotor was 0.07 seconds. From the results, the increase and decrease of the value of angular velocity was large, hence, a stable rotation and a control of rotational speed are a problem in the future.

Fig. 5 shows the results of the measurements of rotational speed and torque. From the results, the starting torque is 14.4 $\mu$ Nm and the maximum rotational speed is 2080 rpm. To verify the value of this torque, an experiment to wind up weight was carried out. From the results, it was possible to lift two one yen coin (approximately 20 $\mu$ Nm is necessary to perform the lift). This value is somewhat different from the result of the calculated torque. However, it seems that the method of calculating torque has become a means for presuming torque without measuring the rough torque of the motor.

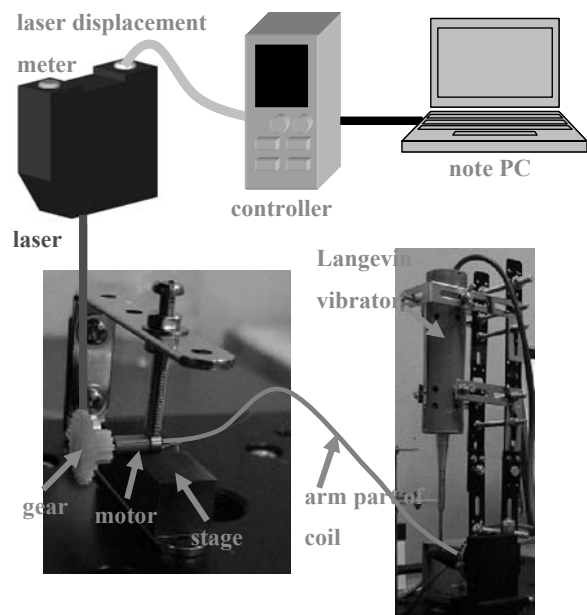


Fig. 3. Apparatus for measuring rotational speed of micromotor

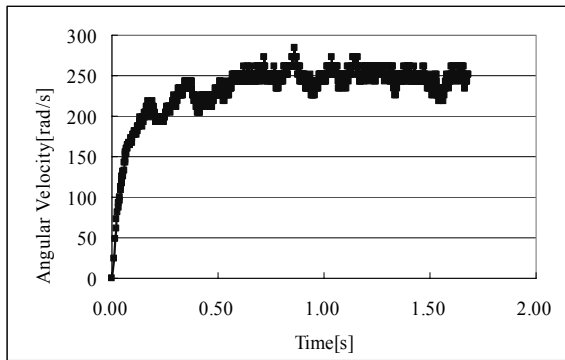


Fig. 4. Results of measurements of time and angular velocity

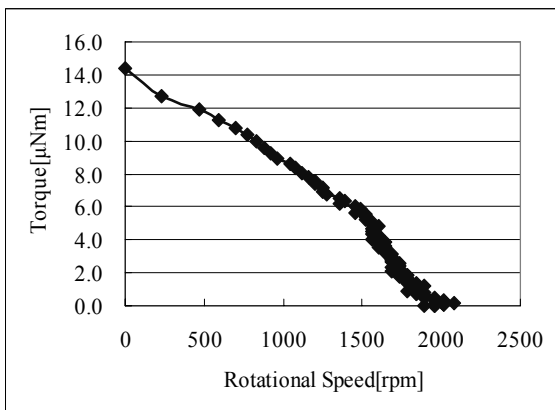


Fig. 5. Results of measurements of rotational speed and torque

### 5 Drive experiment in water

Fig. 6 shows an appearance of the drive experiment of the ultrasonic micromotor that is connected to a 2 mm diameter catheter (TerumoCo., GC-N6JR350NH) in water. The gear (4 mm tip diameter and 5 mm length) is installed on the tip of the rotor, and the rotor is fixed to the stage. The drive of the micromotor was confirmed though the rotational speed decreased. As for the reason why rotational speed decreased, the attenuation of the ultrasonic vibration in the catheter is thought to be the reason.

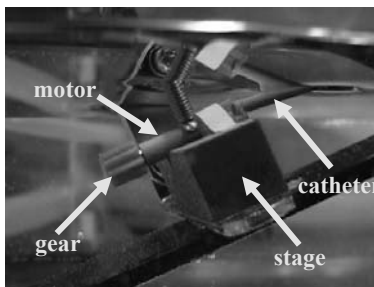


Fig. 6. The drive experiment in water

### 6 Principle of detection method

Fig. 7 shows the reception and transmission mechanisms of the ultrasonic vibration for blood vessel internal shape observation. A 20 MHz oscillator (external size, 1 mm, 1 mm, 0.2 mm) is used for the reception and transmission of ultrasonic vibration. Ultrasonic vibration can be transmitted and received by connecting this oscillator to the ultrasonic wave pulsar/receiver (PANAMETRICS-NDT company, MODEL5800), impressing the voltage of the pulse wave to the oscillator and using the piezoelectric effect of PZT. The direction of the transmitted ultrasonic wave is changed by a reflector and the ultrasonic wave is reflected in the blood vessel inner wall and is received by the oscillator following the same course. The shape of the waves is outputted to a digital oscilloscope (Tektronix Inc., TDS2014) through the ultrasonic wave pulsar/receiver. The distance to the reflection side from the oscillator can be calculated by multiplying sound speed in water (1530 m/s) by the time from sending the ultrasonic vibration to the reception of it. By using this method, the shape of a blood vessel can be determined by measuring the distance to the reflection side and by installing the reflector in the rotor of the ultrasonic micromotor while rotating in the direction of the blood vessel circumference.

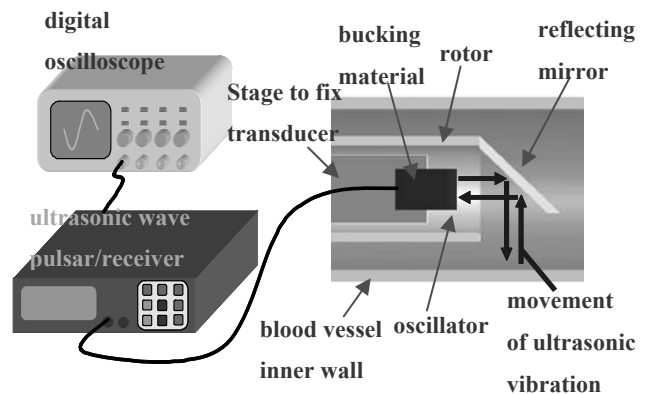


Fig. 7. Schematic diagram of detection method

### 7 Fundamental experiment of detection method

Fig. 8 shows the experimental apparatuses of the fundamental experiment that assumes the ultrasonic wave receiving and sending in a blood vessel. When the DC motor is rotated, the shaft rotates through the gear and the reflecting mirror installed in the shaft point rotates. The silicon tube was arranged by the reflector and the concentric circle and the oscillator was arranged short of the tip of the silicon tube. The ultrasonic vibration transmitted from the oscillator is radially rotated by the reflecting mirror and is reflected in the silicon tube inner wall and received by the oscillator. We examined whether the reception and transmission of ultrasonic vibration in this state to rotate the



reflecting mirror were possible and whether the reception and transmission of ultrasonic vibration by the curved surface were possible in this experiment. The device shown in Fig. 8 was placed in a water tank and the actual experiment was done in water where the diffusion of the ultrasonic vibration was weak. Assumed a blood vessel, the silicon tube (4 mm inside diameter and 6 mm outside diameter) whose dynamic characteristics resemble those of a blood vessel was used (it is often used for the tube as a material for the medical treatment). The reflected wave was received as shown in Fig. 9. From the time from sending the transmission wave to obtaining the reflected wave, we were able to calculate the distance from the oscillator to the inner wall of the silicon tube and confirmed a 2 mm radius of the silicon tube. Moreover, when the rotational speed of the reflecting mirror was changed and the same experiment was carried out, we were able to confirm the shape of the reflected wave even at 2000 rpm, which was the maximum rotational speed of the prototype of the ultrasonic micromotor.

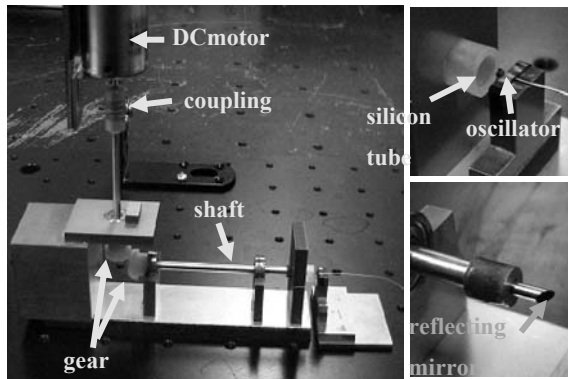


Fig. 8. Apparatus for measuring reflected wave

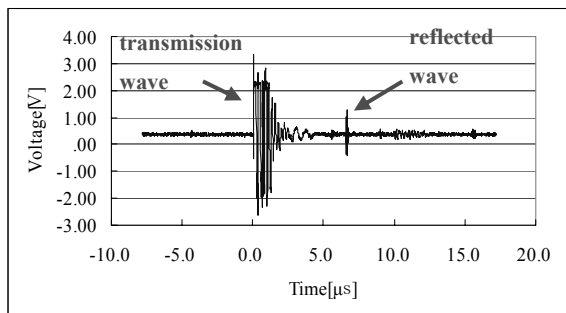


Fig. 9. Results of experiment

## 8 Future perspectives

As future perspectives, miniaturization of prototype of ultrasonic micromotor, improvement of torque, and stabilization of drive of micromotor are going to be performed. Moreover, ultrasonic wave signal reception and transmission experiment that uses parabolic mirror as reflecting mirror are going to be performed. A parabolic mirror can focus the ultrasonic vibration in the focus point, hence, the amplitude of the obtained reflected wave grows, and it is thought it is very effective for image processing. In addition, aiming at practical use, development of prototype of endoscope that combines reflecting mirror, oscillator, and ultrasonic micromotor is going to be performed. Next, using a prototype of endoscope, the internal observation in human blood vessel model is going to be performed.

## 9 Conclusions

The torque-rotational speed characteristics of the prototype of an ultrasonic micromotor were examined, and the performance of the micromotor was examined, and it has been clarified that its starting torque was 14.4 μN, its maximum rotational speed was 2080 rpm and the time-constant of it was 0.07 seconds. Moreover the drive of the micromotor in water was also confirmed. However, its rotational speed and torque were low and its rotational speed was not stable, hence, it is necessary to improve the torque, rotational speed and stable drive of the micromotor for development of prototype of endoscope.

A method for observing internal shape by the transmission and reception of ultrasonic vibration was proposed and a fundamental experiment for measuring reflected wave was performed. The reflected wave could be received in a silicon tube whose mechanical properties are similar to those of a blood vessel and the transmission and reception of ultrasonic vibration were possible in this state of the rotational speed of the micromotor (2080 rpm), thus, it is thought that its application to a prototype of endoscope that installs a reflecting mirror and an oscillator in the motor is possible.

## 10. References

- [1] T. Moriya, Y. Furukawa, Y. Akano, and A. Nakajima, (2005) Experimental Study on a Miniature Ultrasonic Motor Using a Coiled Stator : IECEI Technical Report, No. US2005-29, July, 2005 (in Japanese).
- [2] A. Nakajima, (2006) Development of a New Traveling Wave Ultrasonic Micromotor : MS thesis, Tokyo University of Agriculture and Technology.

---

## Development of Membrane Driven Micropump —Principle of Microbubble Driving Mechanism and Prototype—

Masako Yamada<sup>1</sup>, Yuji Furukawa<sup>2</sup>, Keisuke Morishima<sup>1</sup>

<sup>1</sup>Department of Mechanical Systems Engineering, Tokyo University of Agriculture and Technology, <sup>2</sup>Professional Graduate School, Management of Technology, Tokyo University of Agriculture and Technology

Keywords: Micropump, Microbubble, Membrane, Diffuser

### Abstract

The principle of micropump is proposed, in which, micro bubble by evaporation of liquid as ethanol is utilized for driving force. Microbubble is induced, grown and shrunk by heating/cooling ethanol directly by a micro heater and this bubble pushes and draws a membrane periodically according to sinusoidal input. The main body of pump and the membrane is made by lithographing PDMS. The membrane separates the bubble chamber and micro-channel which has a diffuser to let liquid flow in a same direction. In this paper, fabrication process of a micro-pump we proposed and preliminary experimental results were shown.

### 1. Introduction

Currently there is active research of microsystems such as  $\mu$ -TAS, medical apparatus for in-living-body embedding, and highly efficient micro-chemical analysis equipment. These devices require ultraprecise flux control making the use of micropump indispensable. The development of micropumps has been performed exploiting the excellent features of microbubble. Such pumps have some advantageous characteristics including a low heat capacity of the heater, and a low-voltage drive induced by demagnification. One example of a microsystem using a micropump is an ink-jet printer, which heats liquid (ink) to convey it directly to the target[1],[2]. However this system has some problems. The liquids that it can use are restricted to those suitable for bubble generation, those with a low boiling temperature, and residual air bubbles arise with repeated drives, so that pumping ability needs to be regularly checked. Therefore, we proposed a micropump that uses a membrane. The membrane is between the bubble-generating section and the microchannel. The pump is driven by the power generated from a bubble transmit across the liquid.

In this research, a micropump was developed by the evaporation expansion of a liquid which was the source of a low-voltage drive, and its operation was verified using the principle of a micropump that drives fluid using membrane.

### 2. Principle of micropump

Figure 1 shows the principle of the proposed micropump. A principle of driving a membrane by the evaporation of a liquid at its boiling point was developed to overcome the problems of previous pumps. A liquid with a low boiling point such as ethanol is placed in the bubble generation chamber located on the another surface of the membrane and repeatedly heated and cooled. Ethanol evaporation caused by heating induces microbubble which shrink when the ethanol is cooling. Accordingly, the membrane is periodically driven in a vertical direction. We investigated the dependence of microbubble growth and shrinkage on electric input.

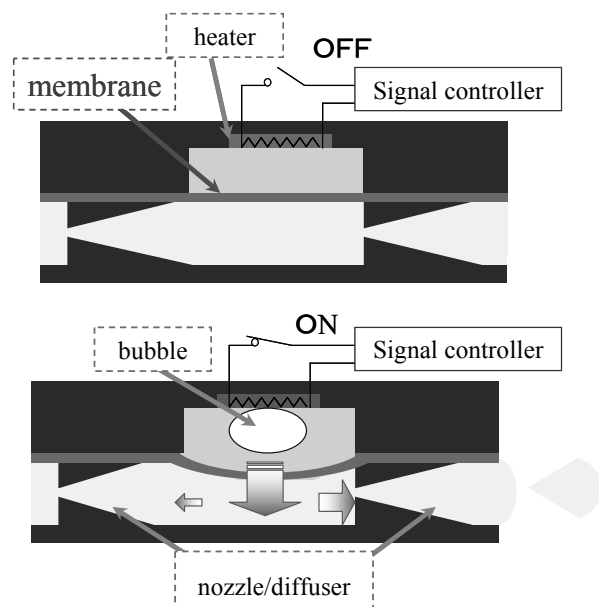


Fig.1 Principle of micropump shown from the side view

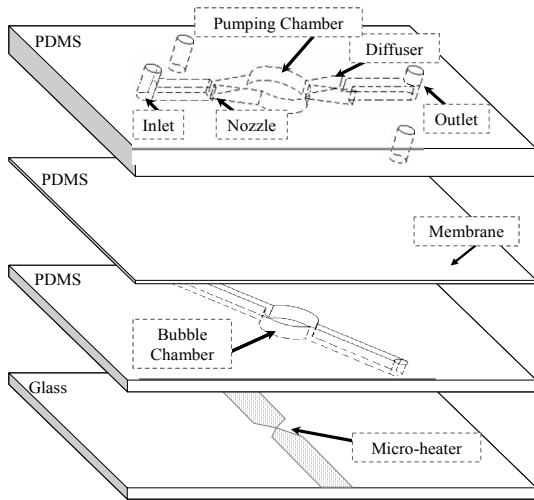


Fig.2 Schematic drawing of prototype micropump

### 3. Micropump design and fabrication

#### 3.1 Design

Figure 2 shows a schematic drawing of the prototype micropump. The pump consists of 4 layers; a microheater, a bubble chamber, a membrane and a microchannel.

PDMS (polydimethylsiloxane), which is a type of silicone rubber, was used as material for all the layers except the heater layer.

The bubble method was not used for microchannel fabrication. Therefore, the microchannel has a simple structure. Figure 3 shows the microchannel of the nozzle/diffuser form. The form has a unidirectional flow. When a microbubble expands on the diffuser side, flow velocity becomes large from the nozzle side. The size of the microchannel was designed to decrease the difference in pressure between nozzle and diffuser side.

#### 3.2 Fabrication

The main bodies of the pump and membrane were fabricated by the lithography of PDMS and by applying MEMS(Micro Electro Mechanical System) technology, respectively, and were combined to produce the prototype. Figure 4 shows the prototype micropump.

##### 3.2.1 Microchannel and bubble chamber

The width of the diffuser side was 40  $\mu\text{m}$  and, nozzle side was 800 $\mu\text{m}$ . The taper angle was 10 degrees.

Figure 5 shows the manufacturing process for the microchannel and bubble chamber. The model was manufactured by photolithography using a purple outdoor daylight resist (SU8). The microchannel has a depth of about 100  $\mu\text{m}$ , and the bubble chamber has a diameter of 2 mm.

PDMS, a transparent material, was poured into these molds, and heat molding was taken off.

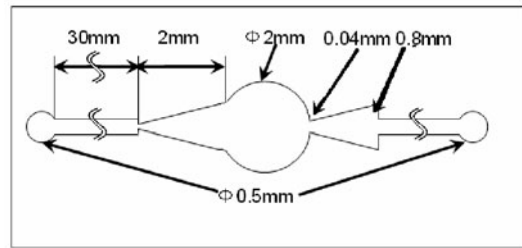


Fig.3 Nozzle/diffuser microchannel

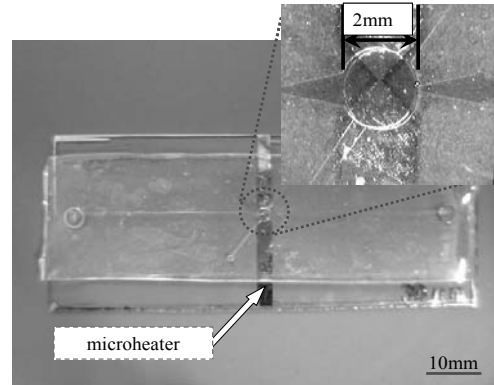


Fig.4 Prototype micropump

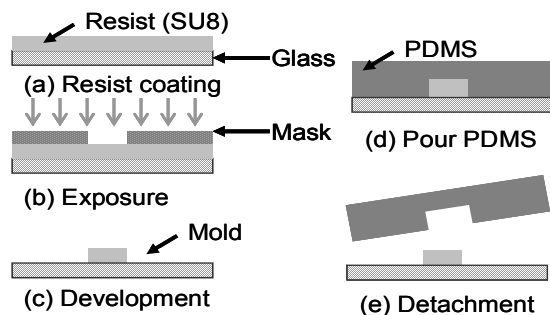


Fig.5 Fabrication process of microchannel and bubble chamber

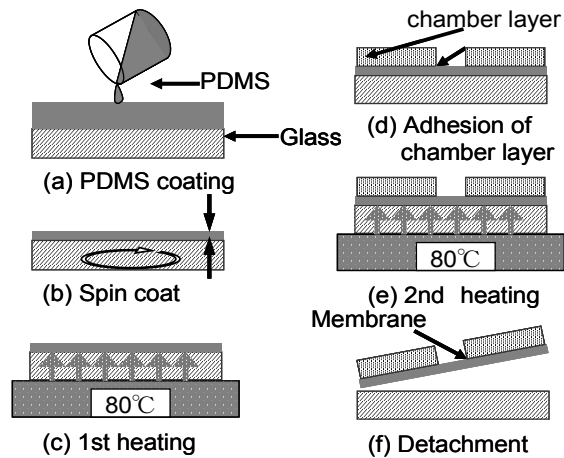


Fig.6 Fabrication process of membrane

## Development of Membrane Driven Micropump

### 3.2.2 Membrane

The membrane was generated on a glass substrate. It was heated for 1 minute, and then placed in the bubble chamber. It was then heated again for 15 minutes at 80 °C. Membrane thickness controlled by changing the number of rotations of a spin coat.

### 3.2.3 Microheater

Metals were sputtered on a glass substrate. Chromium (film thickness 30 nm) was sputtered first, followed by gold (film thickness 80 nm).

Then, to generat a microbubble, a section of the metal thin film was thinned by photolithography. The width of the bubble-generating section can be adjusted by changing mask shape and development time.

## 4. Experimental setup and experiment

### 4.1 Experimental setup

Figure 9 shows an outline of the experimental setup. The bubble chamber was filled with ethanol (99.5%), which has a low boiling point. The microchannel was filled with ultrapure water of 25°C.

An input signal was sent by a function generator (Tektronix AFG 320) to the microheater. The microheater was then heated and cooled to grow and shrink a microbubble, and this cycle of growth and shrinkage was repeated. The generated bubble and bubble chamber were observed by CCD microscopy and images of bubble chamber was recorded on videotape.

### 4.2 Microbubble generation, growth and shrinkage

We determined whether a microbubble would be generated by the micro heater. In addition, the input signal was changed and bubble was observed. The incoming signals were of 4 types; a sinusoidal wave, a triangular wave, a square wave, and a ramp (Table 1). It was driven by input wave of 1 Hz and  $\pm 10.0V$ (pk-pk 20 V). The narrowest part of the microheater used was 32  $\mu m$ . Moreover, the frequency of the input was changed generating a sinusoidal wave of  $\pm 10.0V$ . Bubble growth and shrinkage were observed.

### 4.3 Measurement of membrane displacement

Figure 10 shows the experimental setup. We determined whether a change in membrane displacement results from the growth and shrinkage of a bubble when driven by a sinusoidal wave of 1 Hz and  $\pm 10.0V$ (pk-pk 20 V). Next, membrane displacement was measured and input frequency was changed. We measured the displacement using a laser displacement gaug(KEYENCE LK-G3000V).

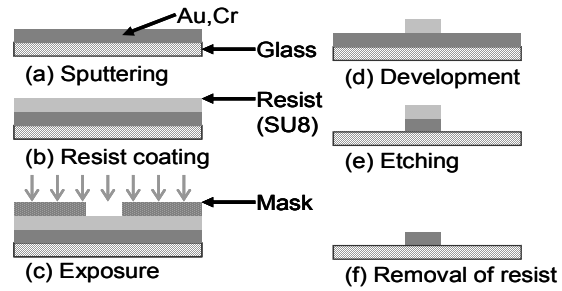


Fig.7 Fabrication process of micro heater

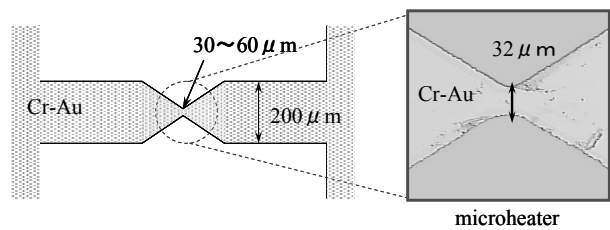


Fig.8 Micro heater and design

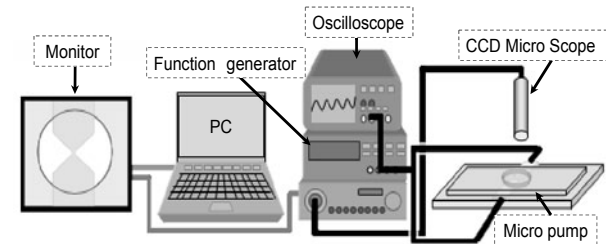


Fig.9 Outline of experimental setup

Table 1 Input wave ( $\pm 10V$ )

Input Wave			
sinusoidal		square	
triangular		ramp	

## 5. Results and Discussion

Figure 11 shows the time change of the bubble generated when inputting a sinusoidal wave. Figure 11 (a) shows the state of maximum expansion, and (c) shows the state of minimum expansion. A microbubble was generated, and after expanding, its shrinkage by natural cooling was observed. The microbubble repeatedly grew and shrank for the sinusoidal wave and triangular wave input signals.

However, the microbubble continued to grow gradually without shirinking for the square and ramp wave input signals. Figure12 shows the change of bubble size.

Figure 13 shows the displacement of the membrane from the bubble generation with an inputting signal of 1 Hz. Two cycles were observed in 1 second.

The microbubble expanded and shrank between each input signal and bubble diameter gradually increased with time. This is because the next heating was started before the microbubble could shrink to its initial size by natural cooling.

Moreover, in several seconds, the microbubble continued to grow until it became in contact with the membrane, thus, distorting the microbubble.

Therefore, to uniformly and repeatedly grow and shrink a bubble regardless of time, it is necessary to optimize the heating and cooling of the heater.

In this experiment, owing to bubble shrinkage not catching up with bubble expansion, the bubble size increased gradually with the low-voltage drive. To use the microbubble as a source of a pump, it must have the capacity to uniformly and repeatedly grow and shrink a bubble. For this reason, an optimal input voltage, an analysis of the heat fluid characteristics of the prototype micropump system and an improvement in the design are necessary.

## 6. Conclusion

We developed a prototype micropump of a membrane drive and observed its bubble generation, growth and shrinkage.

In this experiment, the membrane was driven by controlling the generation growth and shrinkage of a microbubble. Therefore, the possibility that our prototype could be used as a micropump was shown.

For future investigation, we will study how to optimize input vltage control, improve of heater shape, and analyze the heat fluid characteristics and to improve the design of the prototype micropump system.

## 7. Reference

- [1] Jr-Hung Tsai and Liwei Lin, (2002) A Thermal-Bubble-Actuated Micronozzle-Diffuser Pump, Journal of Micromechanical Systems, 665-671
- [2] Kunito Okuyama, Takayuki Tasaki, Shoji Mori, Yoshihiro Iida, (2005) Micro-Pump Using Boiling Propagation Phenomena-Effect of Liquid Composition, The Japanese Society for Multiphase Flow, 225-226

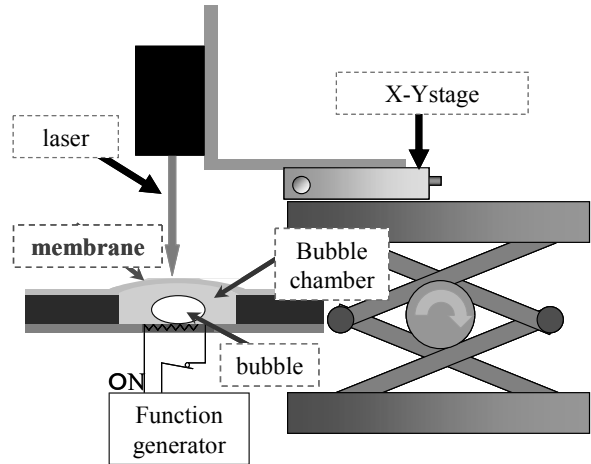


Fig.10 Measurement of membrane displacement of experimental setup

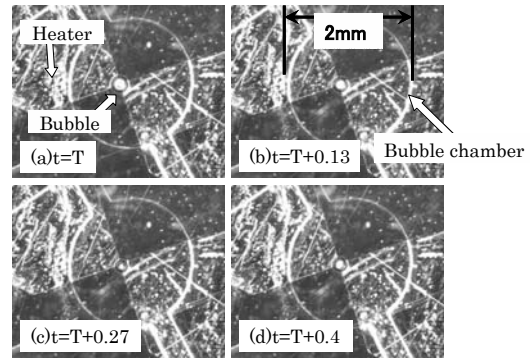


Fig.11 Time change of a microbubble

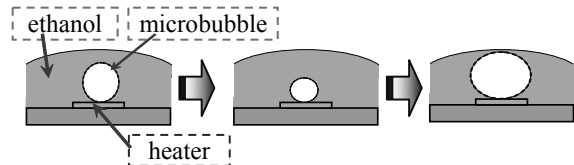


Fig.12 Change of bubble size

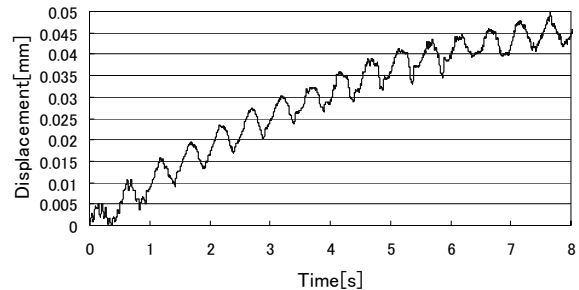


Fig.13 Displacement by 1Hz

---

# A 3-DOF Rotational Precision Positioning Stage using Spring-mounted PZT Actuators

Yung-Tien Liu<sup>1</sup> and Guo-You Lee<sup>2</sup>

<sup>1</sup>Department of Mechanical and Automation Engineering, <sup>2</sup>Institute of System and Control Engineering, National Kaohsiung First University of Science and Technology, Kaohsiung, Taiwan, ROC

## Abstract

A three degree-of-freedom (3-DOF) precision positioning stage with a half-sphere shape is proposed for the applications such as fiber alignment and optical mirror adjustment. An experimental setup consisting of six modularized spring-mounted piezoelectric (PZT) actuators was configured to examine the motion characteristics in  $\pm \theta_x$ ,  $\pm \theta_y$ , and  $\pm \theta_z$  directions. The main experimental results were obtained as follows: the step motions due to 10 times of actuations were recorded as  $0.72 \mu\text{rad}$  and  $37.5 \mu\text{rad}$  along  $\theta_x$ -axis when the applied voltages for the PZT actuator were 80 V and 110 V, respectively. Furthermore, an application example in the fiber alignment was experimentally demonstrated with a loss of light intensity being -0.45 (power efficiency 95%) due to manual operation. According to these experimental results, the proposed stage having precision rotational ability and large operational range was experimentally demonstrated.

Keyword: precision positioning, piezoelectric actuator, impact force, fiber alignment

## 1. Introduction

Nanopositioning technology is increasingly interested in recent precision industry. In nanopositioning devices, the lead zirconate titanate (PZT) actuator is a well utilized key component since it features good performances in controlling precise motion, high-frequency response, and miniaturized size. The most excellent positioning performance can be possibly obtained as high as  $1 \sim 10 \text{ nm}$ , but the total displacement of a PZT actuator is limited to only a few microns. For compensating this main drawback, many special mechanisms such as flexural hinges [1], inchworm actuator [2], impact drive mechanism (IDM) [3], and smooth IDM [4] have been well developed. On the other hand, the structure that the PZT actuator is coupled with a mechanical element such as servomotor [5], voice-coil-motor [6], pneumatic cylinder [7], or spring [8, 9] is also reported as effectiveness in enlarging the operational range. In this paper, a modularized actuating unit that is based on the spring-mounted PZT actuator [8] is proposed for implementing a rotational three degree-of-freedom (DOF) of positioning stage.

Concerning with the positioning stage using the spring-mounted PZT actuator [8, 9], it features two main characteristics: (1) the ultra-small displacement of a PZT actuator is cost-effectively overcome by introducing a passive element of compression spring; (2) the feature of precision motion and heavy load ability is obtained by utilizing the impact force of the PZT actuator. Furthermore, compared to the well-known IDM [3], it features the additional benefit of the simple driving waveform of pulse, thus the controller design is much easier. In the following sections, a modularized actuating unit based on the spring-mounted PZT actuator is described. This is followed by the description of driving process of the positioning stage. The

detail design of the rotational 3-DOF stage and the experimental setup are presented in sections 3 and 4. The fundamental characteristics of the positioning stage are presented in section 5. A perspective application in fiber alignment is shown in section 6. Finally, a conclusion is made in section 7..

## 2. Actuating unit and driving process

### 2.1 The modularized actuating unit

For easy installation and maintenance, a modularized actuating unit consisted of a spring-mounted PZT actuator and a bracket is designed as shown in Fig. 1. The spring-mounted PZT actuator is set inside the bracket and its position relative to the bracket is adjustable. It is consisted of a striking part named as hammer guided by a bush, a PZT actuator, and an inertial body to which a compression spring is fixed. The spring is then fixed to a movable plate for adjusting the positioning of the hammer.

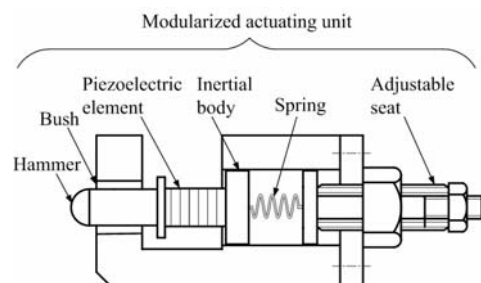


**Fig. 1.** The modularized actuating unit of the spring mounted PZT actuator

## 2.2 Driving process

Figure 2 depicts the driving process of the positioning stage. When assembling the modularized actuating unit to the positioning stage, the bracket is pushed forward and is firmly fixed to the stage. Therefore, the hammer will be forced to contact with the positioning stage and hence the spring will be compressed. Due to the contact of the hammer and the stage, a continuous actuation according to the PZT actuator can be performed. Since the actuating unit will move together with the stage, this can be regarded as a special form of self-moving mechanism having large operational range.

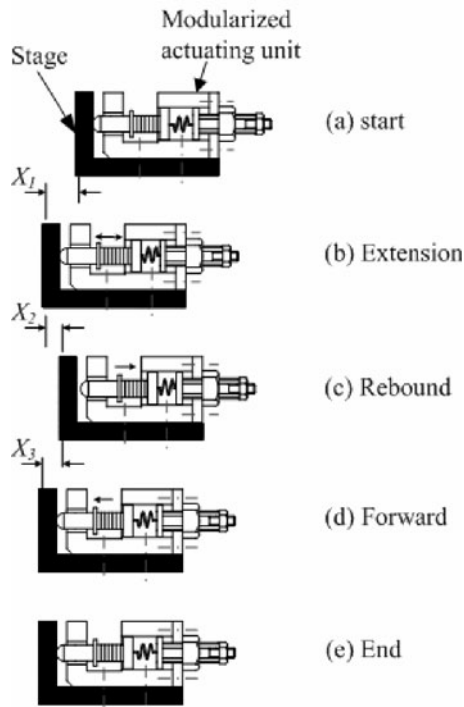


**Fig. 2.** Driving process of the positioning stage

The driving process in one direction of motion is described as follows:

1. In the start stage as shown in Fig. 2 (a), the hammer is in contact with the stage and the PZT actuator is with its natural length.
2. In the extension state as shown in Fig. 2 (b), a pulse voltage waveform is applied to the PZT actuator. Due to the rapid deformation of the PZT actuator, an impulsive force will be generated and then transmitted to the stage through the hammer in the form of contact force. If the contact force is larger than the static frictional force, the positioning stage will start to move by a distance  $X_1$ .
3. In the rebounding state as shown in Fig. 2 (c), due to the contact force acting on both the contact objects in opposite directions, the hammer is forced to rebound right after the actuation for the PZT

actuator. The rebounding motion of the hammer behaves as an inertial force and may result in a backward motion of the stage by a smaller distance  $X_2$  comparing to  $X_1$ .

4. In the forward state as shown in Fig. 2 (d), the returning hammer may cause further movement of the stage with a distance  $X_3$ . Though only one pulse waveform is applied to the PZT actuator, the cyclic process of (3-5) is iterating itself.
5. Finally, the sliding stage will reach to a final position after the hammer damps to standstill. In this state, the PZT actuator is ready for the next actuation from step 2.

## 3. Design of a semi-spherical 3-DOF positioning stage

Due to the special design of the modularized actuating unit, it is much easy to configure a positioning stage having multi-DOF. Figure 3 shows an application example of semi-spherical 3-DOF positioning stage having the positioning ability along  $\theta_x$ -,  $\theta_y$ -, and  $\theta_z$ -axis. Since one actuating unit is capable of acutaing the stage in only one direction of motion, totally, six actuators marked from (a) to (f) are required to performe the 3-DOF of positioning. For examples, the actuators set on the top side of xy plane and marked with (a) and (b) are used for actuating the stage to rotate with respect to  $\theta_z$ -axis; similarly, the actuators units set on the xz plane and marked with (f) and (e) are used for actuating the stage to rotate with respect to  $\theta_y$ -axis as shown in Fig. 4 which is the sectional view A-A in Fig. 3. Figure 5 shows the perspicive schematic drawing of the semi-spherical 3-DOF positionig stage. The friction adjusting mechanism set on the top surface of the stage is used for providing a suitable holding fricritonal force for the rotaional stage.

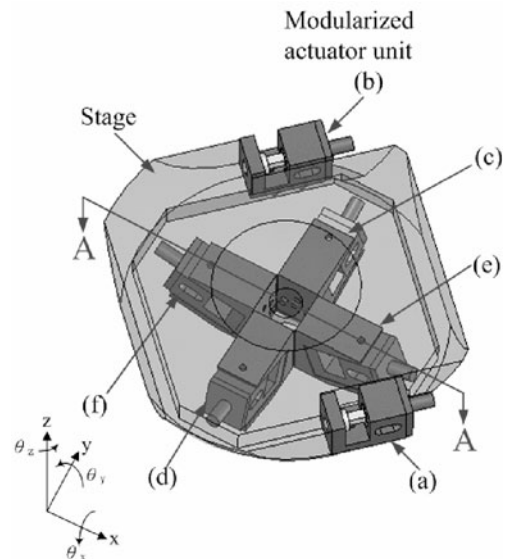


**Fig. 3.** Configuration of the 3-DOF semi-spherical positioning stage

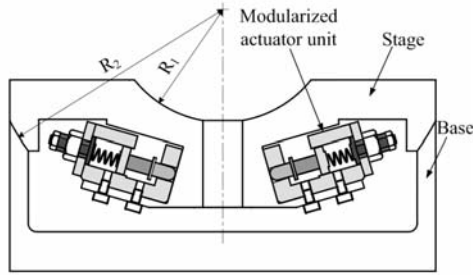


**Fig. 4.** Sectional view of the internally mouted actuating unit.

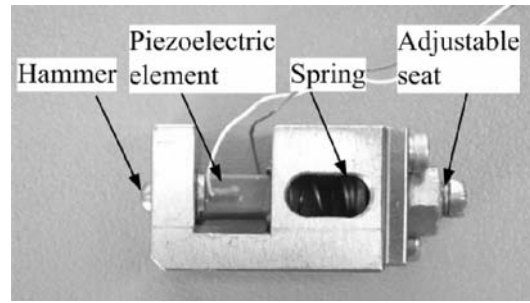


**Fig. 6.** Phtograph of the modularized actuating unit

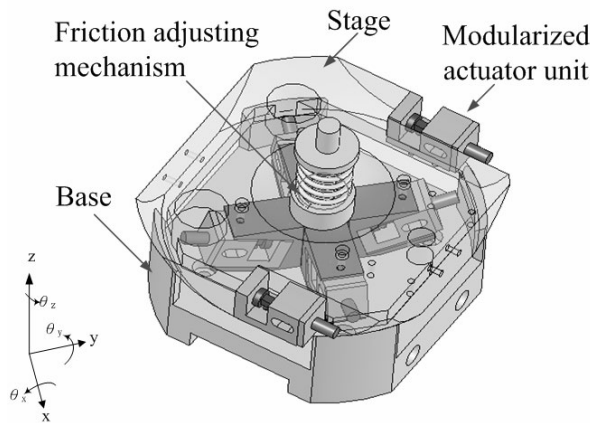


**Fig. 5.** The 3-DOF rotational precision positioning stage

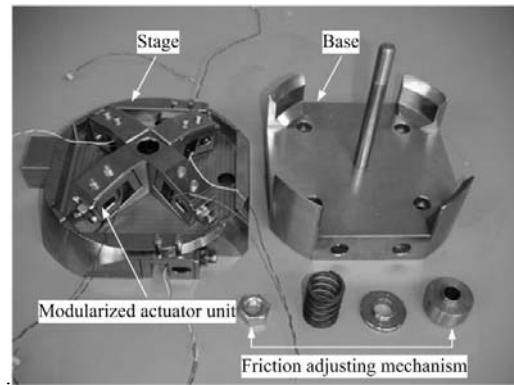


**Fig. 7.** Positioning stage and base.

#### 4. Experimental setup

Figure 6 shows a photograph of the modularized spring-mounted PZT actuator, in which the PZT actuator has the dimension of  $5 \times 5 \times 10$  mm (Tokin). The stiffness of the spring is 0.023 N/mm. Six actuating units are symmetrically mounted to the positioning stage having a radius on the bottom side. The positioning stage made of stainless steel having a mass of 2.6 kg is then set on the base having the same radius on the contact surfaces. Figure 7 shows the positioning stage and the base. Figure 8 shows the 3-DOF positioning stage.

The waveform of applied voltage was generated by LabVIEW, which is a Windows supported graphical programming language. A 16-bit DA/AD converter was used to transform the pulse driving waveform to the power amplifier and then to the PZT actuator. Due to the number limitation of measuring probes, two kinds of gap sensors were used to detect the simultaneous motion behaviors of the positioning stage along three rotation axes. They were the capacitive gap sensor (ADE 5300-5504) and the fiber optic displacement sensors (Fotonic MTI-2100). Their characteristics are, separately, with the bandwidths of 20 kHz and 100 kHz, the measuring ranges of  $\pm 25/250$   $\mu\text{m}$  and  $10/36$   $\mu\text{m}$ , and the corresponding resolutions of 5/50 nm and 1/10 nm.

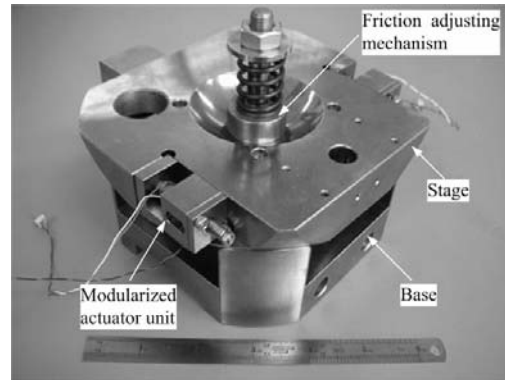


**Fig. 8.** Photograph of the assembly 3-DOF positioning device

Figure 9 shows the overall experimental setup for examining the motion behaviors of the positioning stage. Since the rotation displacement caused by one single actuation of the PZT actuator is expected to be very small, the rotational motion are assumed as the case of linear motion. As shown in the photograph, one capacitive gap sensor was used to measure the rotational motion along  $\theta_z$ -axis, and two fiber optic displacement sensors were used to measure the rotational motions along  $\theta_x$ - and  $\theta_y$ -axis.



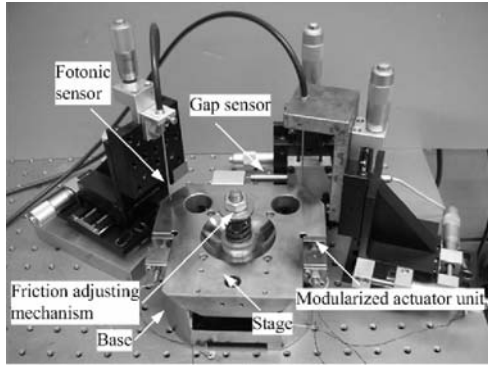


Fig. 9. Photograph of the overall experimental setup

## 5. Experimental results

### 5.1 Step response of 3-DOF rotational stage

The step response of the positioning stage along each rotational axis was separately examined by the same actuating conditions of the amplitude of step waveform being 100 V and the preload of spring force being 0.027 N. Figure 10 shows the measured time history of the motion behaviors of the positioning stage along  $\theta_x$ -,  $\theta_y$ -, and  $\theta_z$ -axis. All the motion behaviors show that the stage would move forward and backward caused by the actuations of step driving waveform. This agrees to the description of the driving process mentioned in section 2.2. Though with vibration motions, the positioning stage would significantly damp to a steady displacement with several micro radians when time was 5 ms. The recorded angular displacements along  $\theta_x$ -,  $\theta_y$ -, and  $\theta_z$ -axis are 2.3  $\mu\text{rad}$ , 2.2  $\mu\text{rad}$ , and 3.8  $\mu\text{rad}$ , respectively.

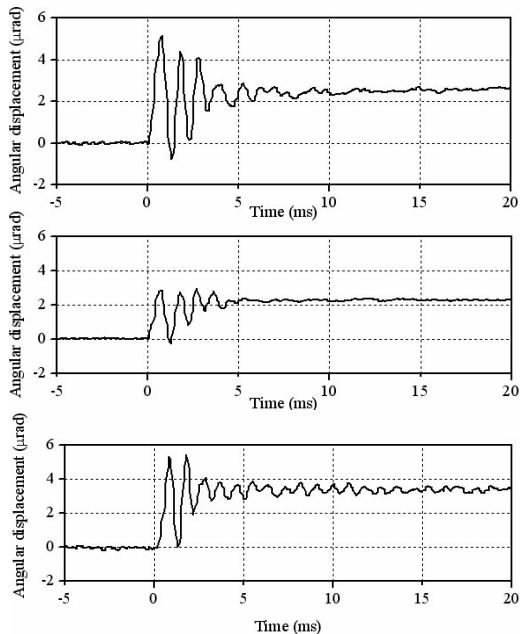


Fig. 10. The step response of rotational positioning stage.

### 5.2 Continuous actuations

The works mentioned above focused on examining the motion behavior of the positioning stage actuated by only one single excitation for the PZT actuator. However, one of the most attractive advantages of the mechanism is that it features large stroke by continuously actuating the PZT actuator.

Figure 11 depicts the experimental results of the continuous actuations with the driving frequency of 2 Hz for four different applied voltages being 80 to 110 V along  $\theta_x$ -axis. It can be seen that the positioning stage could be continuously actuated with clear step motions. However, the vibration motion shown in previous Fig. 10 could not be clearly measured. That is due to a larger time scale. According to the measured angular displacements shown in Fig. 11, the relation that the displacement affected by the applied voltage is arranged to Fig. 12. It can be seen that the displacement is monotonically proportional to the applied voltage. When the applied voltage is 80 V, the average angular displacement along  $\theta_x$ -axis is 0.72  $\mu\text{rad}$ ; when the applied voltage is 110 V, the average angular displacement along  $\theta_x$ -axis is 37.5  $\mu\text{rad}$ .

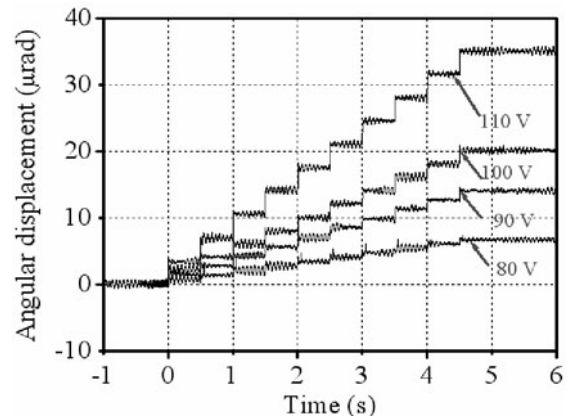


Fig. 11. Continuous motion behaviors of the positioning stage along  $\theta_x$ -axis

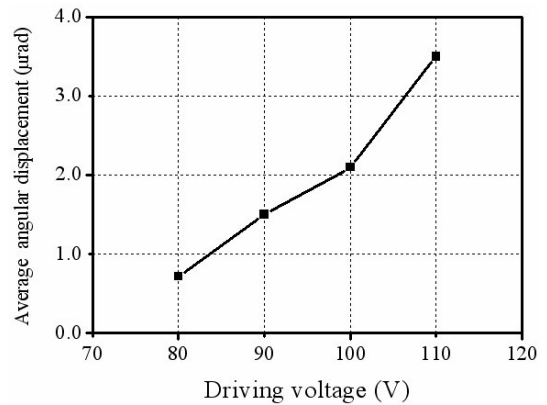


Fig. 12 The angular displacement affected by the applied voltage

5.4 Continuous forward and backward actuations

Since one actuating unit is capable of driving the stage in only one direction, for performing one-DOF of positioning processing, one pair of actuating units is required. Figure 13 shows the recorded angular displacement caused by continuous forward and backward actuations. Though with the same applied voltage being 100 V, it can be seen that the forward actuation is with a larger total displacement of 20  $\mu\text{rad}$  compared to the backward actuation with a smaller total displacement of 17.5  $\mu\text{rad}$ . This problem can be considered as the variations from the dry friction on the sliding surface, and the contact condition of hammer and stage, etc. Because of the variant characteristics, it is necessary to configure a controller for obtaining more precision positioning ability in future applications.

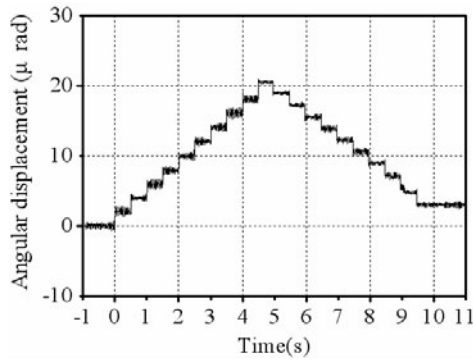


Fig. 13. Continuous forward and backward motion behaviors along  $\theta_x$ -axis

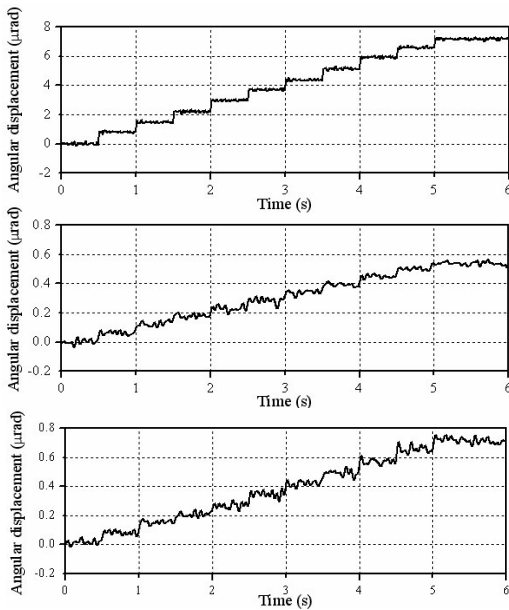
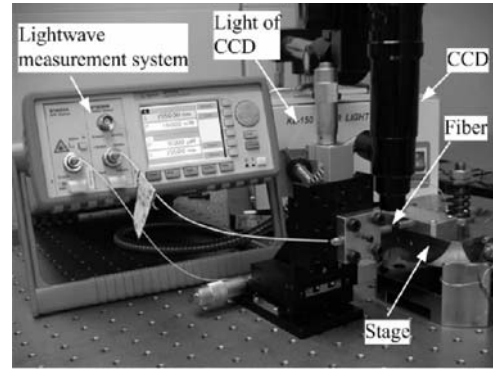


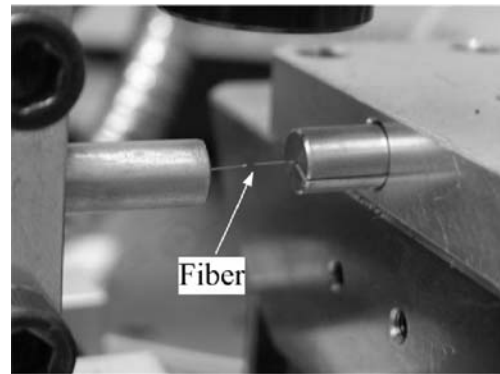
Fig. 14. The simultaneous motion behaviors of the positioning stage due to the actuation in  $+\theta_x$  direction

Table 1 The angular displacements in actuating and non-actuating directions

Actuating direction	Angular displacement ( $\mu\text{rad}$ )		
	$\theta_x$	$\theta_y$	$\theta_z$
$+\theta_x$	0.72	0.055	0.07
$+\theta_y$	0.034	0.81	0.022
$+\theta_z$	0.035	0.015	2.05



(a) Experimental setup for optical fiber alignment



(b) Detail of filaments of optical fibers

Fig. 15. The experimental setup for the alignment work of optical fibers.

5.5 The simultaneous motion behaviors along three rotational axes

In order to examine the simultaneous motion behaviors along three rotational axes, three displacement sensors were used to measure the angular displacements caused by only one directional actuation. Figure 14 shows the measured results for the actuation along  $+\theta_x$  direction with the applied voltage being 80 V and the driving frequency being 2 Hz. It can be seen that the final angular displacement in the actuating  $+\theta_x$  direction is 0.72  $\mu\text{rad}$ , however, the interference angular displacements in the non-actuating directions are much smaller and with 0.055 and 0.07  $\mu\text{rad}$ . Arranging these experimental results for each of the three directional actuations, the differences between the actuating direction and non-actuating directions are shown in Table 1.

## 6. Application in optical fiber alignment

One of the perspective applications of the positioning stage is given as the alignment works for optical fibers. Figure 15 shows the experimental setup for examining the alignment performance of the filaments of optical fibers. One of the filaments of optical fiber is set on the positioning stage for receiving the light intensity from the other filament fixed on a stationary stage. The light source is with the wavelength of 1550 nm and the emitting power of 10 mW from the lengthwave measurement system.

Figure 16 shows the experimental result of alignment work based on manual operation. The positioning process started from the coupling loss being -1.94 dB (power transmission efficiency 80%) and ended with the coupling loss being -0.45 dB (power transmitting efficiency 95%) after 50 times of actuations. The effectiveness of the positioning stage for the application in the alignment work of optical fibers was experimentally demonstrated.

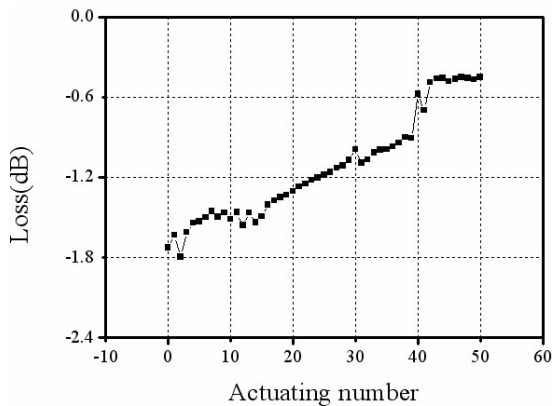


Fig. 16 Coupling loss during manual positioning process

## 7. Conclusion

A 3-DOF rotational positioning stage based on manualized spring-mounted PZT actuators was proposed in this paper. An experimental setup was implemented for examining the fundamental characteristics of the positioning stage. Furthermore, an application example of the alignment work for optical fibers was experimentally demonstrated. Main results are concluded as follows:

1. The positioning stage having a heavy mass of 2.6 kg could be precisely actuated by the impact force of spring-mounted PZT actuator.
2. The rotational positioning stage having self-moving ability featured the angular step motions of 0.72  $\mu\text{rad}$ , 0.81  $\mu\text{rad}$ , and 2.05  $\mu\text{rad}$  along  $\theta_x$ -,  $\theta_y$ -, and  $\theta_z$ -axis with the applied voltages being 80 V.
3. The angular displacement is monotonically proportional to the applied voltage of PZT actuator.
4. The application in the alignment work of optical fibers was experimentally demonstrated with a loss of light intensity being -0.45 dB (power efficiency 95%) due to manual operation.

Future works of this study will be focused on implementing an efficient control algorithm for the alignment automation of optical fibers.

## 8. Acknowledgements

The authors are grateful to the supports from Mitutoyo Association for Science and Technology (MAST, Japan) and National Science Council under Contract No. NSC-93-2212-E-327-002.

## 9. References

- [1] Paros JM, Wesbord L, (1965) How to design flexure hinges. *Machine Design* 37 (27), 151-156.
- [2] Burleigh Instruments, (1975) U.S. Patent: 3,902,084.
- [3] Higuchi T, Watanabe M, Kudou K, (1988) Precise positioner utilizing rapid deformations of a piezoelectric element. *J. JSPE* 54 (11), 75-80.
- [4] Yoshida R, Okamoto Y, Higuchi T, Hamamatsu A, (1999) Development of smooth impact drive mechanism (SIDM). *J. JSPE* 65 (1), 111-115.
- [5] Moriyama S, Harada T, Takanashi A, (1984) Precision X-Y stage with a Piezo-driven Fine-table. *J. JSPE* 50(4), 80-85.
- [6] Liu YT, Higuchi T, (2001) Precision Positioning Device Utilizing Combined Piezo-VCM Actuator. *J. JSPE* 67, (1), pp.70-75.
- [7] Liu YT, Higuchi T, (2001) Precision Positioning Device Utilizing Impact Force of Combined Piezo-Pneumatic Actuator. *IEEE/ASME Trans. Mechatronics* 6(4), 467-473.
- [8] Liu YT, Wang CW, (2002) A Self-moving Precision Positioning Stage Utilizing Impact Force of Spring-mounted Piezoelectric Actuator. *Sens. Actuators A* 102 (1-2), 83-92.
- [9] Liu YT, Higuchi T, Fung RF, (2003) A Novel Precision Positioning Table Utilizing Impact Force of Spring-Mounted Piezoelectric Actuator. *Prec. Eng.* 27(1), 14-21.

---

## Active Damping of a Wafer Loading Robot using Piezoceramic Actuators

Baruch Pletner<sup>1</sup>, Greg Zvonar<sup>1</sup>, Yasunaga Kayama<sup>2</sup>, Takahide Kamiyama<sup>2</sup>, Maki Iwagawa<sup>2</sup>, Shweta Bhola<sup>1</sup>, Grace Rose Kessenich<sup>1</sup>

<sup>1</sup>IPTRADE, Inc., Newton, Massachusetts, USA. <sup>2</sup>Nikon Corporation, Kumagaya, Saitama, Japan

Keywords: Active Vibration Control, Smart Structures, Piezoceramics, Robots

### Abstract

This paper addresses the active treatment of a modal (unforced) vibration problem in a wafer loading robot attached to a microlithography scanner using induced-strain piezoceramic actuators. This type of problem arises often in precision manufacturing equipment such as equipment used in integrated circuit (IC), LCD, and nano/micro device manufacturing. The paper encompasses all stages of the development from diagnostic analysis through feasibility assessment using finite element modeling, followed by the optimal placement of actuators and sensors, determination of optimal control loop configuration, control design and simulation of performance, and finally the design, manufacturing and implementation of a closed-loop active damping system.

### 1 Introduction

While numerous studies have been conducted in the area of active damping with piezoceramics, most involve simple structures such as beams and plates, often with complex control schemes. However in real world applications the actively damped structures tend to be complex, while the control algorithms must be simple to ensure robustness and ease of implementation. Thus the difficulty in deploying active damping systems in manufacturing equipment resides in the proper and extensive use of modeling techniques combined with a flexible and modular design that can accommodate and absorb any departures of the actual structure behavior from the one predicted by the model.

The major innovations reported in the current paper include an integrated modeling approach combining finite element analysis using MSC Nastran with The MathWorks MATLAB and SIMILUNK software, as well as a highly modular piezoceramic active damping system. The control algorithms used are shown to be simple to implement yet highly robust to significant changes in structural dynamics, changes due to various extension positions of the wafer loading arm and the presence or lack thereof of a 300 mm wafer on the arm. High level of active damping performance, well in excess of 20dB, is demonstrated for all operating conditions.

### 2 Feasibility Assessment and Preliminary Design

The loading arm of a wafer handling robot shown in Fig. 2.1 undergoes excessive free vibration during the loading part of the operational cycle. This causes a delay in the loading of the wafer to the chuck and reduces throughput. As is common in these situations, the robot in question is a highly complex instrument and any redesign in order to solve the vibration problem will significantly impact other parts of the design and would cause major delays and expense. A solution is therefore required that can reduce the vibration levels by an order of magnitude while requiring almost no change to the existing design.

The solution chosen for addressing the vibration problem in this robot is active damping using piezoceramic actuators. These actuators belong to the induced-strain actuator class and hence need to be placed over the high strain areas of the target mode or modes. In order to identify these areas a finite element model of the robot was created and a modal analysis performed. Figs. 2.1 and 2.2 show the mode shape of the targeted mode, with high strain area on the linear motor housing due to the free vibration of the robot at the target mode frequency clearly visible in Fig. 2.2.

From Fig. 2.2 it is clear that induced strain actuators will be most effective if placed over the inside bottom corner of the linear motor housing. Naturally in reality there are limitations on actuator size and footprint area, but for the purposes of preliminary design and feasibility estimation we can assume that the entire high-strain area can be covered by a single induced-strain actuator. Modeling induced strain actuation can be rather complicated, but an approximation that has been widely reported in the literature allows the substitution of induced strain actuation by line forces (or moments, depending on the type of element used) applied around the perimeter of the actuator. The underlying assumption for this approximation is the degree to which the host structure is sufficiently stiff to completely constrain the actuator. For infinitely stiff host structure providing complete constraint, the perimeter approximation completely coincides with reality. Since the linear motor housing is

fairly rigid, we utilize the perimeter approximation and apply line moments around the perimeter of the theoretical actuator.

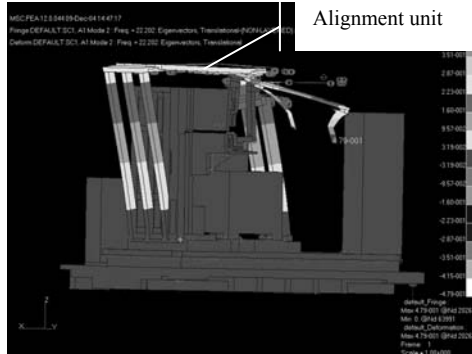


Fig. 2.1 Modal analysis of the wafer handling robot

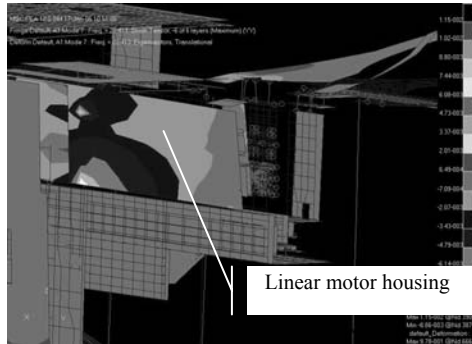


Fig. 2.2 High strain area on linear motor housing

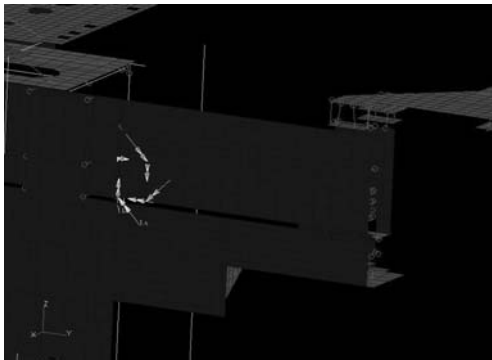


Fig. 2.3 Line moments applied around the perimeter of a theoretical actuator

In order to estimate the feasibility of reducing given levels of vibration using induced strain actuators we need to use some numbers for actuator material and geometric properties. These properties are summarized in Table 2.1.

Table 2.1 Actuator properties

Property	Value	Description
t	2 mm	Thickness of Piezo
b	45 mm	Length/Width of Piezo
$d_{32}, d_{31}$	-180×10 <sup>-12</sup> m/V	Piezo constant
$E_{PZT}$	70×10 <sup>9</sup> N/m <sup>2</sup>	PZT Young's Modulus
C	5 mm	Distance to neutral axis from piezo location

Using the properties in this table we can estimate the actuator authority as bending moment per volt of applied electrical field as follows:

The stress developed in a fully constrained PZT actuator given a certain voltage input is

$$\sigma_{PZT} = \frac{1}{t} E_{PZT} d_{31} V \quad (2.1)$$

The moment applied by the fully constrained PZT patch then becomes

$$M_{PZT} = A_{PZT} \sigma_{PZT} c = cbt \sigma_{PZT} = cbE_{PZT} d_{31} V \quad (2.2)$$

A state space model of the wafer handling robot was derived from the finite element model in order to design a dynamic compensator and perform preliminary performance estimation. The model was derived using *fe2ss*, a MATLAB application produced by IPTRADE, Inc. Fig. 2.4 shows the compensator that was designed for the feasibility phase of this project and Fig. 2.5 shows the preliminary performance in terms of open (no active damping) and closed (with active damping) loop FRF's from vertical floor disturbance to horizontal vibration of the end effector. While these results are far from satisfactory, they do demonstrate the possibility of reducing the targeted mode vibration by 20 dB. A shaped input into the system was designed to mimic the actual disturbance environment during normal robot operations. The effect of applying the shaped input is visible in Fig. 2.6 where only the targeted mode gets excited. When this disturbing input is applied to the closed-loop model, no more than 200 volts peak is required to achieve the desired level of active damping.

We can thus conclude that a reasonable set of piezoceramic actuators in conjunction with a robust broadband compensator can achieve a 20 dB reduction in the end effector vibration while keeping the control voltage to below 200 volts. This concludes the preliminary system design phase and allows us to move to the design optimization phase.

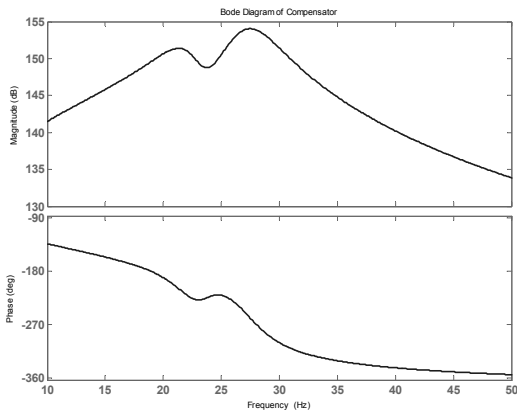


Fig. 2.4. Bode diagram of preliminary compensator

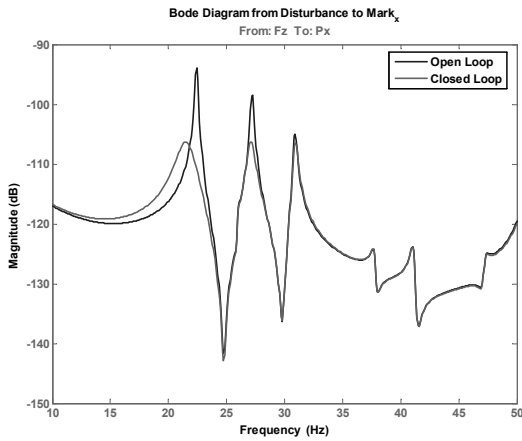


Fig. 2.5. Bode diagram of preliminary compensator

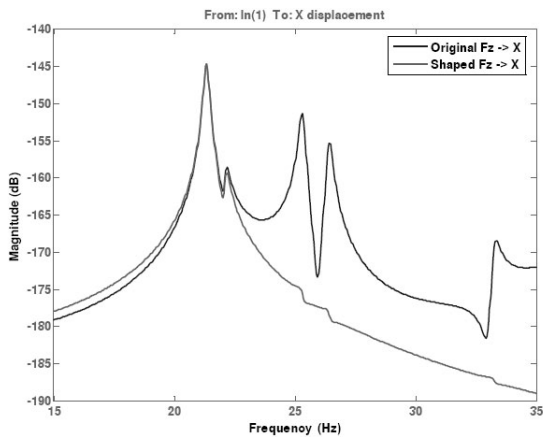


Fig. 2.6. Effect of shaped disturbing input

### 3 Design Optimization

The objective of the design optimization effort is to redesign the piezo control system in a way that makes it possible to

deploy the simplest and most robust compensator with optimal results. Additionally, in this phase of the project we must pay attention to pragmatic considerations such as available sizes of piezoceramic actuators.

In Fig. 2.4 we see that the preliminary compensator that was designed using a single actuator and sensor channel had two peaks to control two resonant modes. In the interest of robustness it is always preferable to optimize hardware design such as actuators and sensors in order to minimize controller complexity. Based on this principle it was decided to split the actuators into two groups thus creating a two-channel control system.

The first actuator group consisted of 6 piezoceramic plates located over the high strain area at the root of the linear motor housing. An additional high strain area was identified at the base of the alignment unit support columns as shown in Fig. 3.1. This area was addressed by Actuator Group II.

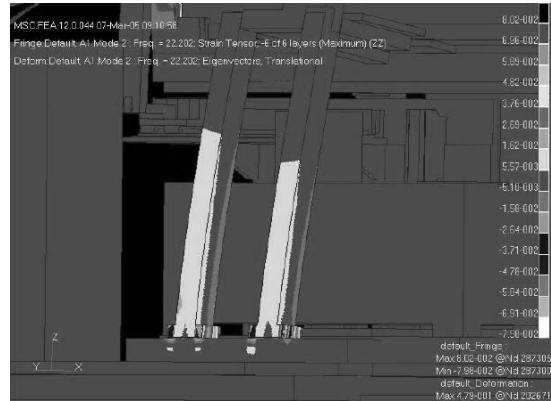


Fig. 3.1. High strain areas at the base of the alignment unit support columns

Fig. 3.2 shows the FRF's from both actuator groups to the feedback sensor at the tip of the end effector. Actuator Group I can address Mode 1 control without difficulty with excellent dynamic range provided by the lightly damped zero immediately following the Mode 1 pole. Actuator Group II FRF however, looks difficult to control due to missing zero between two closely spaced poles.

In order to effectively control Mode 2 with the Group II actuator set, a second feedback sensor was added to the control system. By placing this second accelerometer at the top of the alignment unit, an optimal actuator/sensor set was created for Mode 2 control. Fig. 3.3 shows the Group II FRF after optimization. Mode 1 is rendered completely unobservable and good dynamic range is guaranteed by the lightly damped zero immediately following the Mode 2 pole couple. Also, since new input essentially filters out all of the Mode 1 signal from entering the Mode 2 controller, there is no wasted control authority. In other words, all of the authority of the Actuator Group II will be dedicated to controlling Mode 2 only. Actuator / Sensor optimization thus enables us to use two control channels to address two vibration modes in an almost completely decoupled fashion. This kind of "hardware" decoupling allows the use of pure SISO design for both channels guaranteeing better stability

and performance than anything that can be achieved by a coupled controller, while at the same time optimizing the authority of the individual actuator groups.

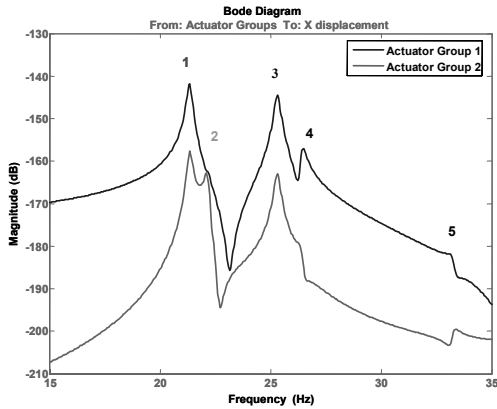


Fig. 3.2. FRF's from both actuators groups to X displacement before optimization

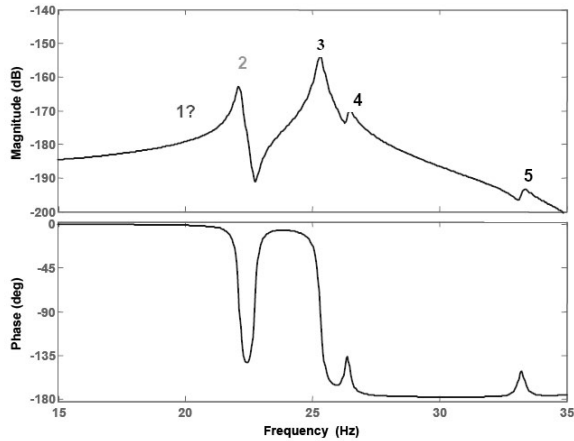


Fig. 3.3. FRF's from Actuator Group II to X displacement after optimization

#### 4 System Implementation and Experimental Results

In December 2005 an active damping system was installed on the Nikon wafer handling robot. A block diagram of the closed loop system is shown in Fig. 4.1. The system was manufactured by IPTRADE, Inc. and consisted of 10 active dampers, two accelerometers and a control computer utilizing the MathWorks xPC Target architecture. The active dampers consisted of a piezoceramic actuator (PZT) and a colocated 200V isolated amplifier shown in Figure 4.2. The size of each amplifier/piezo damper is 105.5mm long by 41.5mm wide by 27mm high. Since the Intellivibe were pre-assembled, installation in the clean room was relatively simple. It only required attaching the Intellivibe units and accelerometers to the robot and then

plugging in cables. 48V DC power to the Intellivibes was delivered over the same CAT5 cable as the signal.

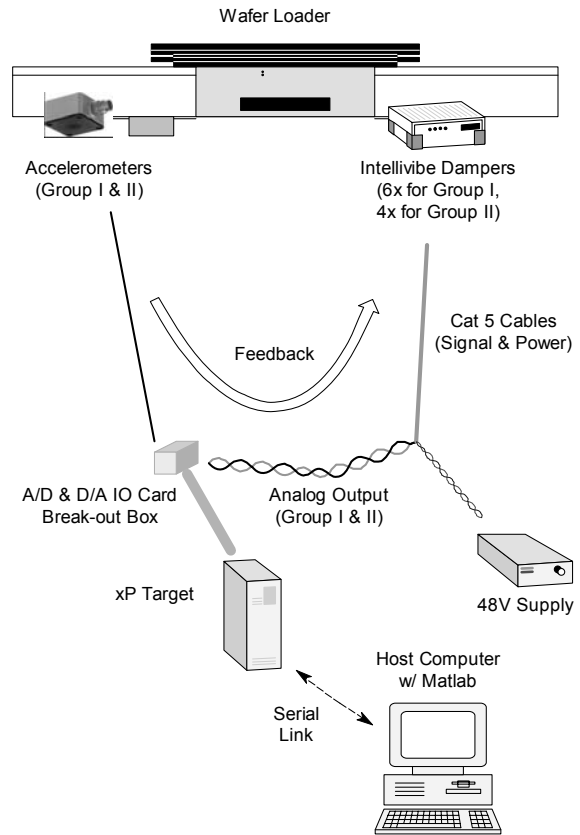


Fig. 4.1. Block Diagram of Closed Loop System



Fig. 4.2. Intellivibe Damper Unit

The six dampers on the linear motor housing and the collocated accelerometer were identified as Control Channel 1, and the four dampers on the alignment unit support column with the accelerometer on the alignment unit table were identified as Control Channel 2. System analysis consisted of collecting frequency response data for both channels. The data was collected with the loading arm in full back position with no wafer (unloading position). A Spectral Dynamics Siglab spectrum analyzer was used to collect high-resolution sine sweep data.

Fig. 4.3 shows the Channel 1 FRF. There are two resonances in the servo control bandwidth for this application: 32.4 Hz and 35.6 Hz. In addition, there is a large resonance at 154 Hz. This resonance is not in the defined control band, but its relative magnitude (30dB higher than

the modes in the control band) makes it highly relevant to the control design process for Channel 1. Fig. 4.4 shows the Channel 2 FRF. In this channel there is only one resonance in the control band. It is a very lightly damped resonance at 23.6 [Hz]. The challenge is then to control the resonance at Channel 2 and the two resonances at Channel 1 in a robust way without destabilizing any frequencies outside of the control band.

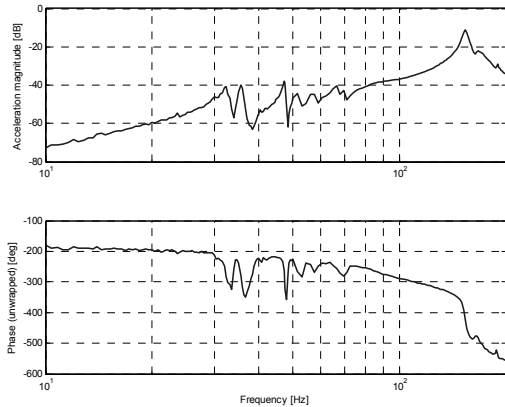


Fig. 4.3. Channel 1 FRF

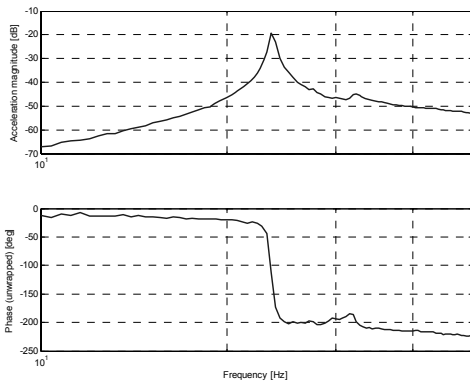


Fig. 4.4. Channel 2 FRF

Fig. 4.5 shows the controller design for Channel 1. The controller features a robust broad band design with a center frequency at 30 Hz and a lightly damped notch at 150 Hz designed to stabilize the lightly damped 150 Hz mode present in the Channel 1 FRF (see Fig. 4.3).

The expected closed-loop performance shown in Fig. 4.6 shows reasonable attenuation of the two targeted modes at about 10 – 12 dB. Fig. 4.7 shows the very robust, broadband Channel 2 controller. The clearly defined resonance at 23.6 Hz with no adjacent dynamics present in this channel allowed us to use a high-gain, high performance controller yielding over 20 dB of attenuation at the targeted frequency (see Fig. 4.8).

Fig. 4.9 and 4.10 are actual open and closed loop measurements of the fully implemented system. Further experiments showed that the controllers retained this high performance and stability over a wide range of robot positions and loads. This result is not unexpected given the

simplicity of the controllers combined with optimal placement of actuators and sensors.

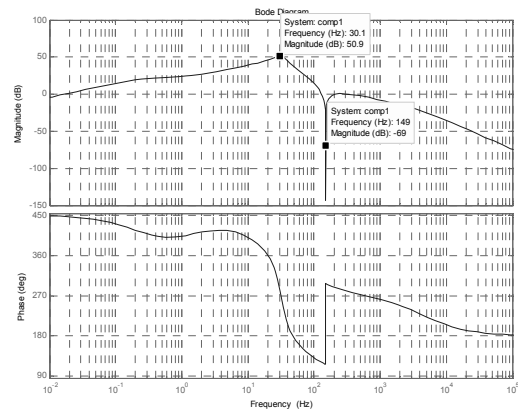


Fig. 4.5. Channel 1 controller showing notch

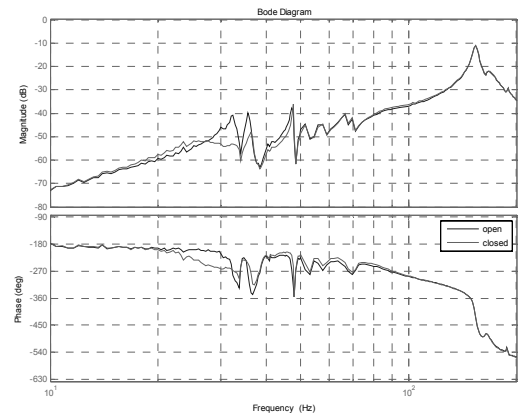


Fig. 4.6. Predicted performance of Channel 1 controller

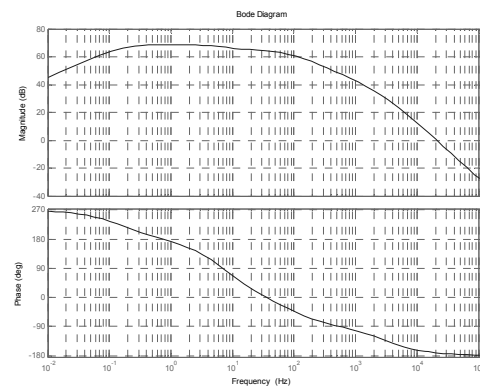


Fig. 4.7. Channel 2 controller



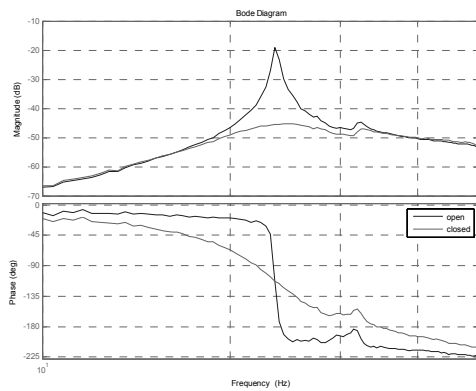


Fig. 4.8. Predicted performance of Channel 2 controller

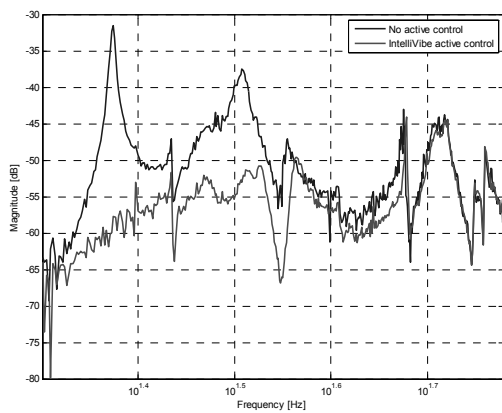


Fig. 4.9. Actual performance of simultaneous Channel 1 + Channel 2 controllers loading arm back, no wafer

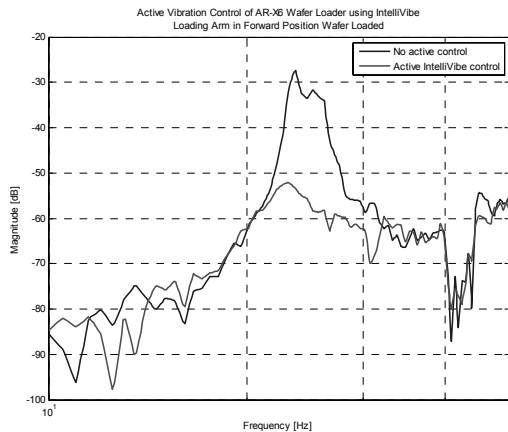


Fig. 4.10. Actual performance of simultaneous Channel 1 + Channel 2 controllers loading arm forward, wafer on

A source of concern was the coupling between the two control channels. Hence an experiment was performed in which the control channels were turned on and off to check for any undesirable cross-coupling effects. Fig. 4.10 shows the effect of Channel 1 control with Channel 2 turned off, Channel 2 control with Channel 1 turned off, and both

channels active simultaneously. It can be clearly observed that Channel 1 addresses only the linear motor housing motor with little or no effect on the alignment unit mode, while Channel 2 affects only the alignment unit mode leaving the linear housing mode unaffected. Both channels active together are an almost perfect superposition of the single channel effects, clearly indicating a very lightly coupled system.

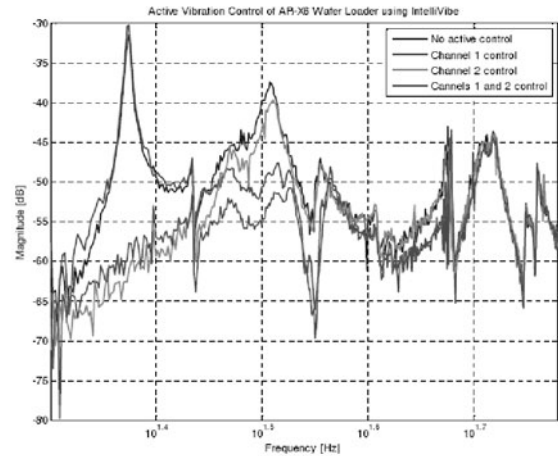


Fig. 4.11. Channel 1, Channel 2 and Channel 1+2 control as compared to open loop system performance

## 5 Summary

This study successfully analyzed a vibration problem in a wafer loading robot, determined that it could be solved by a piezoelectric active damping system, analyzed how such a system would be optimally deployed, simulated performance, and then successfully implemented the system and collected performance evaluation data. The analysis phase allowed us to reduce the actual clean-room installation and tuning time to about 10 hours for a two-channel system. The actual performance closely agreed with the simulation predictions.

## 6 References

- [1] Idan M, Pletner B, Weller T, (1999) Active  $H_{\infty}$  Control of Sound Radiation from Thin Cylindrical Panels. *J. of Guidance, Control, and Dynamics* 22-6:776-783
- [2] Giovanardi M, Pletner B, (2000) Computer aided optimal placement and sizing of induced-strain actuators for broadband structural control. 41<sup>st</sup> AIAA/ASME/ASCE/AHS/ASC Structures, Structural Dynamics, and Materials Conference and Exhibit.
- [3] Pletner B, Abramovich H, (1997) Actuation and sensing in piezo-laminated anisotropic shells. *AIAA Journal* 1798-1808
- [4] Pletner B, Idan M, Weller T, (1997) Active  $H_{\infty}$  control of sound radiation from thin plates. *AIAA Journal* 789-799

---

## Visual Feedback Control of a Micro Lathe

Hiroataka OJIMA<sup>1</sup>, Katsuhiko SAITO<sup>1</sup>, Libo ZHOU<sup>1</sup>, Jun SHIMIZU<sup>1</sup>, Hiroshi EDA<sup>1</sup>  
<sup>1</sup>Ibaraki University

Keywords: Micro lath, Visual feedback, Position control

### Abstract

Micromachining progresses rapidly in recent years. In this research, a micro lathe which is installable and operational inside SEM vacuum chamber has been designed and developed. As a first step, visually guided micro lathe system is developed with image of CCD camera device instead of SEM image. Unlike the conventional feedback control which positions the X-Y table only, this scheme offers a direct control of the position, path and speed of the tool tip. Using proposed method, cutting experiment was achieved, and it is confirmed that developed micro lathe system is effective to do cutting.

### 1 Introduction

Recently, the system capable of producing the micro parts are requested along with the miniaturization<sup>[1]</sup>. Micromachining progresses rapidly in recent years. The exploratory research has approached to a level of accessing a single molecule or atom. As a driving force, MEMS (micro electronic-mechanical system) has been playing a major role in making micro components and devices. However, MEMS is based on the photolithography technology and thereby applicable into limited materials such as silicon monocrystalline. In order to meet the demands of miniaturization in electronic and optical applications, alternative micromachining technology which is able to access a variety of materials in a 3 dimensional way is required<sup>[2]</sup>.

Micro-Meso Mechanical Manufacturing (M<sup>4</sup>) offers accessibility to different kinds of material according to each objective, and attains high repeatability and accuracy with the latest ultraprecision means. There are, however, many scientific and technological barriers encountered in pragmatic implementation of M<sup>4</sup>. One of them is the surface chemistry effects. When machining parts are at micro scale, it is recognized that the surface-area-to-volume ratio will be increased in both chips and the resulting part as compared to conventional (macro) machining process. Another problem is the direct motion and position control. Sensors that are capable of directly measuring the relative displacement between the tool and workpiece are not yet available.

In this research, a micro lathe which is installable and operational inside SEM vacuum chamber has been designed

and developed<sup>[3]</sup>. Fig. 1 shows the concepts of the developed micro lathe. At such oxygen-free condition, cutting tests are conducted to understand surface chemistry effects on micromachining. However, since developed micro lathe is small in size, rigidity of the lathe is low. Thus the position of the tool of the lathe is not able to be controlled accurately with a conventional method which controls X-Y table only. Therefore, the vision guided control method is proposed.

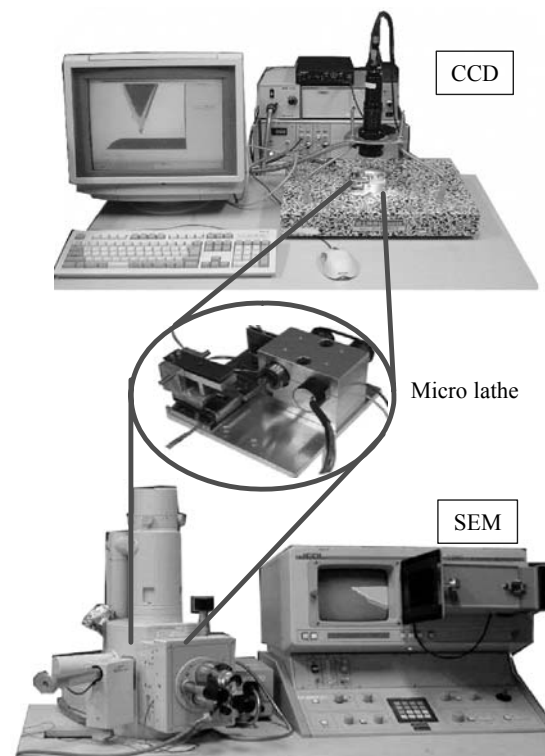


Fig. 1. Concept of the developed micro lathe

The image from the SEM (scanning electron microscope) is digitized by CCD into pixels with 8-bit gray scale. Since each pixel contains 2D positional information, the vision system thus offers an orthogonal coordinate (hereafter referred as the pixel coordinate) for objects in view to refer to. The pixel coordinate is free from the mechanical inaccuracy and offers a direct measurement of

the relative position of tool and workpiece. The resolution increases together with the magnification of the microscope and the number of CCD pixels. In this research, a vision control scheme has been proposed and implemented for feedback control of the tool movements. Unlike the conventional feedback control which positions the X-Y table only, this scheme offers a direct control of the position, path and speed of the tool tip. As a first step, visually guided micro lathe system is developed with image of CCD camera device instead of SEM image.

## 2 Overview of system

Shown in Fig. 2 is the block diagram of developed micro lathe system, which consists of three main modules; the actuating module that drives micro lathe, the sensing module that imports images and the processing module that implements feedback control. Each module is responsible for different function. The actuating module is the core element where the cutting operation is carried out. The sensing module imports images from CCD image device, and obtains the position of the tool and the workpiece. The other tasks including the image processing and feedback control are executed by the processing module. Upper picture of Fig. 1 shows the overall appearance of the system. Table .1 shows the specifications of the system.

The actuating module further incorporates a diamond tool with a XZ linear stage, and the sensing module includes a high resolution CCD image device. Through sensing module, the appearance of the working area is not only displayed on the monitor to the give the operator the visual information, but also converted into digital signal for subsequent processing.

As the control diagram show in Fig. 2, the movements of the diamond tool are governed with the visual feedback control. The sensing module first abstracts the positions of the tool and workpiece by comparing the pre-registered templates with the captured visual information. Corresponding to the relative positions of tool and workpiece, the tool path and speed are calculated and converted into appropriate pulse train.

## 3 Actuating module

The developed micro lathe is shown rightward in Fig. 3. This lathe consists of the main spindle with the collet chuck with the DC motor, the center high adjustment using a piezoelectric actuator and XZ-stage which performs both depth of cut (X-axis) and traverse feed (Z-axis). The XZ-stage is driven by the inertial sliding, and is composed of a piezoelectric actuator and the linear guide.

XZ-stage is shown leftward in Fig. 3. An accurate tool positioning is achieved by driving the XZ-stage precisely. Important points of driving the XZ-stage are the control of the driving direction, distance and velocity. Figure 4 shows the inertial sliding mechanism by the saw-tooth wave. The direction of the movement is decided by the rising/trailing edge of the saw-tooth wave as shown in Fig. 4. For example,

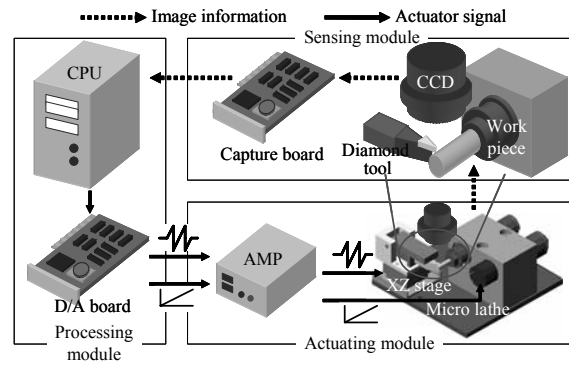


Fig. 2. Block diagram of system

Table 1. Specification of system

Size of micro lathe (W×D×H)	90×90×42 (mm)
Spindle rotational speed	0~8000 (rpm)
Depth of cut × Traverse feed	10×10 (mm)
Center high adjustment	30 (μm)
Tool	Diamond
Nose angle / nose radius	40(°) / 2 (μm)
Scanning rate	20 (frame/s)
Total pixels	0.3 mega pixel

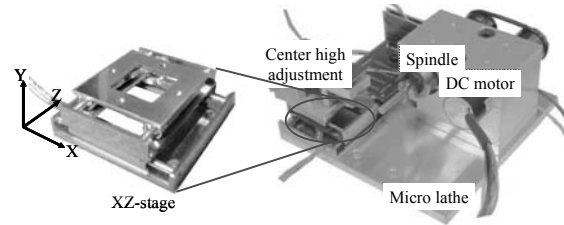


Fig. 3. XZ-stage and micro lathe

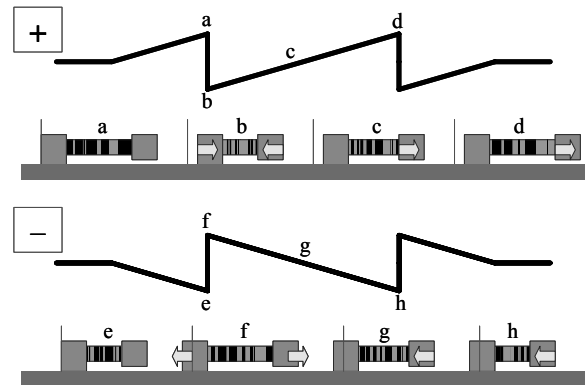


Fig. 4. Driving principle of XZ-stage

the mechanism in the right direction (+) is explained as follows. The voltage gradually rises, and a piezoelectric actuator stretches most in (1). The actuator shrinks based on the centroid in (2) by falling rapidly of the voltage. Only the side where the frictional force is small moves as the actuator stretches gradually with the ascent of the voltage in (3). The actuator is stretches again in (4), and advances toward the right direction. The actuator similarly advances also toward the left direction (-) if a reverse pulse train is given.

Next, the velocity control of this mechanism is described. As shown in Fig. 5, the velocity is proportional to both frequency of the pulse train and driving voltage.

Finally, driving distance can be controlled according to the number of pulses, because the driving distance by one plus is about 500 $\mu\text{m}$  at  $\pm 80\text{V}$  or 250 $\mu\text{m}$  at  $\pm 40\text{V}$ .

#### 4 Sensing module

The diamond tool is mounted on XZ-stage, which uses piezoelectric actuator to drive tool. Those mechanical inaccuracies, mainly caused by thermal expansion, hysteresis/drift in actuators and misalignment of orthogonal axis, may directly deliver a negative effect to the system performance. To solve these problems, a vision control scheme as shown in Fig. 6 is developed. The left picture in Fig. 6 shows the micro lathe and CCD image device located in Y-axis. From the right picture in Fig. 6, the incoming visual information from the CCD is digitized into pixels with 8-bit gray scale by the sensing module. As each pixel bears 2D positional information, the vision system thus offers an orthogonal coordinate (referred as the pixel coordinate) for objects in view to refer to. The pixel coordinate is free from the mechanical inaccuracy and its resolution increases together with the magnification of the CCD.

At a 480 $\times$ 640 pixel frame used in the current research, for example, the resolution of the pixel coordinate is about 6 $\mu\text{m}$  when the view of the CCD is twofold magnified. When the CCD is aligned along Y-axis, the position of the tool tip and workpiece is projected into a 2D pixel coordinate (XZ) which is commonly shared by the XZ-stage and workpiece. Driven and controlled by the pixel coordinate, the tool is able to be positioned and moved at the accuracy of pixel resolution with no effect by the mechanical inaccuracy. In addition, if the rigidity between XZ-stage and tool is low, positioning of tool tip is not achieved by driving XZ-stage accurately. Thus, more importantly, this operation is an effective method of positioning for the micro lathe with a low rigidity.

Figure 7 shows the recognition accuracy that is made by use of shape based pattern matching<sup>[4]</sup> to recognize the actual tool tip repeatedly 500 times. We comprehend from the graph that 88.5% reliability can be achieved within the limes of  $\pm 1\text{pixel}$  (6 $\mu\text{m}$ ).

#### 5 Processing module

For the system which is consisted of the actuating and sensing module in previous section 3 and 4, the visual

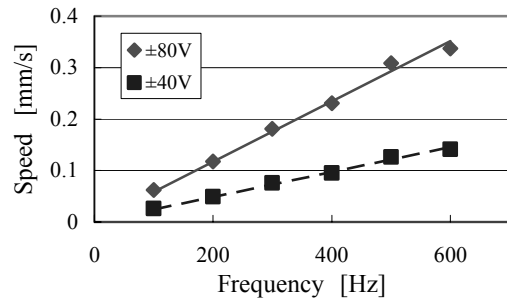


Fig. 5. Velocity change depending on frequency and voltage

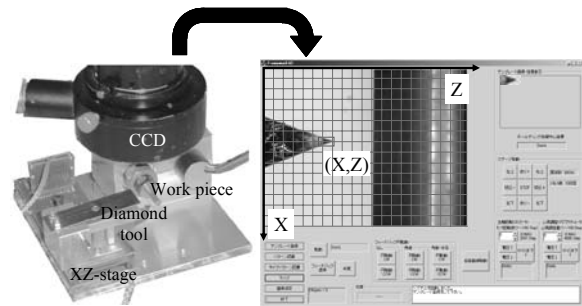


Fig. 6. Visual sensing system

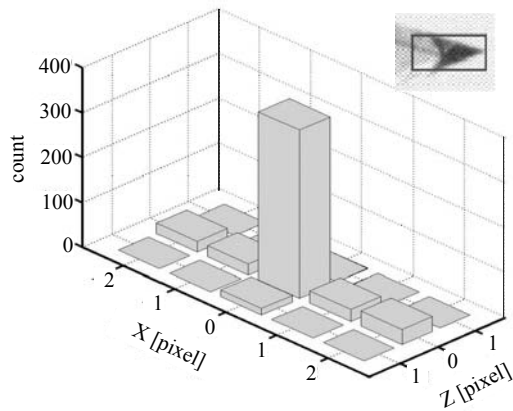


Fig. 7. Recognition accuracy of tool tip

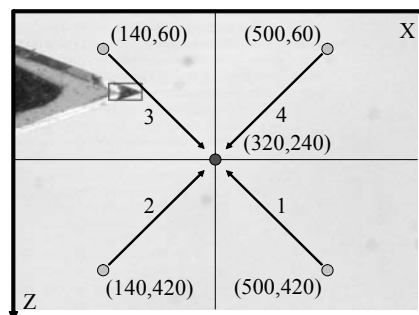


Fig. 8. Experimental condition of linear path control

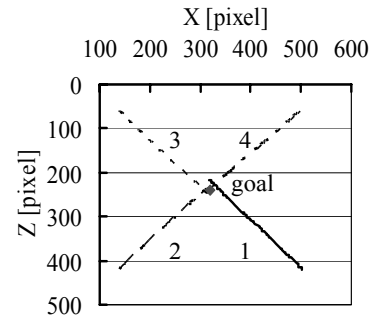
feedback control method is described in this section. The tool tip is driven by visual feedback control method with positions of the tool tip and targets from CCD image device.

As a first step, we examined linear path control and circular path control of the tool tip. In these path controls, driving frequency is 300Hz (162 $\mu$ m/s). At first, linear path control of tool tip is described. As shown in Fig. 8, the target position is defined as (320, 240) which is the center of the image from CCD, and four kinds of path control are examined. In the case of linear path control, the angle formed by the target position and the present position of the tool tip is fed back to achieve the path control.

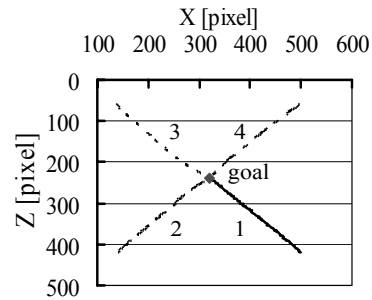
Figure 9 (a) shows the resultant path of the tool tip without feedback control, and (b) shows that with feedback control. In the case of the path without feedback, final errors of four paths are between 5pixels (30 $\mu$ m) and 15pixels (90 $\mu$ m). On the other hand, the path with feedback follows along the target path, and final error is within 2pixels (12 $\mu$ m).

Next, the circular path control which is multi-axial interpolation is described. The condition of the circular path control is shown in Fig. 10. The center of the target circular path is defined as (320, 240) which is the center of the image from CCD, and the radius of the target path is 100pixels (600 $\mu$ m), moreover the tool tip is driven from starting point (220, 240) along counterclockwise direction repeated 3 times. In the case of circular path control, we consider to feed back not only the angle formed the center of the target circular path and the present tool position, but also the deviation of the radius which is the error between the radius of the target circular path and the distance from the center of the target path to the present tool position. In the case of the driving the path without feedback control, the tool is driven by the angles prepared in advance.

Figure 11 (a) shows the resultant path of the tool tip without feedback control, and (b) shows the path with feedback control of the angle only, and (c) shows the path with feedback control of the angle and radius. Figure 11 (a) shows that the resultant path departed from target path, and the center and the radius of the path are deflected from those of the target path. Figure 11 (b) shows the center of the resultant path matches the center of the target path, but extends the radius of the resultant path as the path goes around. Moreover, Fig. 11 (c) shows that the resultant path



(a) without feedback control



(b) with feedback control

Fig. 9. Experimental results of linear path control

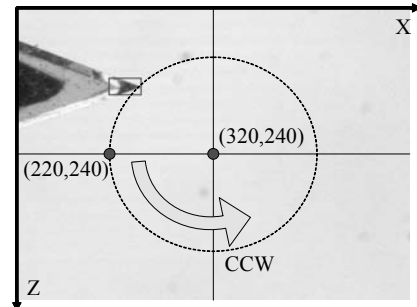
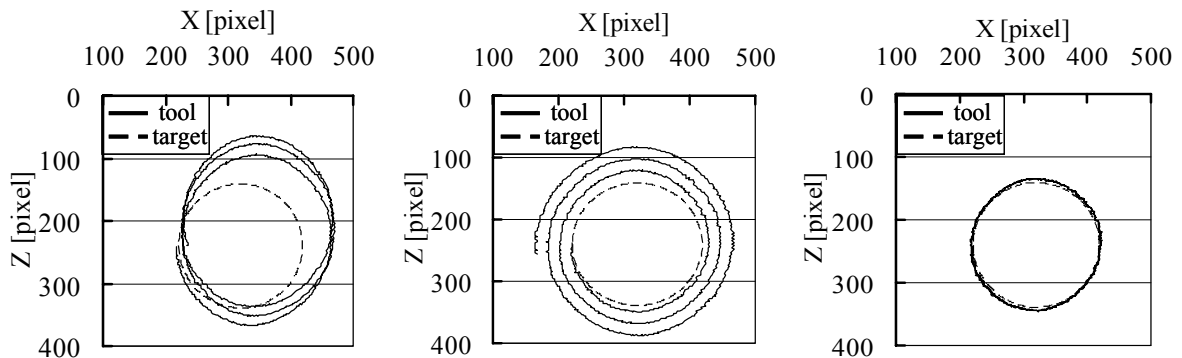


Fig. 10. Experimental condition of circular path control



(a) without feedback control

(b) with feedback control of the angle

(c) with feedback control of the angle and radius

Fig. 11. Experimental results of circular path control

follows the target circular path closely, and errors are  $\pm 5$  pixels ( $30\mu\text{m}$ ). From mentioned above, it is confirmed that proposed feedback control method is effective to position the tool tip of the micro lathe.

Finally, using the proposed control method, cutting of a brass bar is experimented. As shown in Fig. 12, the tool tip is driven with circular and linear paths. The target path moves 1 pixel ( $6\mu\text{m}$ ) rightward every 1 lap, then the tool tip is achieved to cut. In this experiment, total depth of cut is  $150\mu\text{m}$ . Figure 13 shows the appearance of cutting experiment, and cutting of a brass bar advances from (1) to (4). Figure 14 shows the resultant brass bar which is taken a picture by SEM. From this picture, developed micro lathe system can implement cutting well.

### 7 Conclusion

This paper described a vision guided micro lathe which is developed for fundamental research. The system consisted of the actuating module and the sensing module was made up and the visual feedback control method was proposed.

Driving principle of the XZ-stage of the micro lathe was investigated, and control method of the XZ-stage was proposed. Using the CCD image device and image processing, the accurate position of tool and workpiece on the micro lathe was obtained. The visual feedback control method for the system consisted of the actuating module and the sensing module was proposed. Using the proposed control method, linear path control and circular path control was experimented and was able to be controlled that error is within the limes of  $\pm 5$  pixels ( $30\mu\text{m}$ ). Moreover, cutting experiment of a brass bar was achieved, it is confirmed that developed micro lathe system is effective to do cutting.

### 8 References

- [1] Okazaki Y., (2001) NC micro lathe, Journal of Society of Grinding Engineers (in Japanese), Vol.45, No.6: 279-282.
- [2] Libo Z., Kuriyagawa T., (2002) M4 trends in America, Journal of the Japan Society for Abrasive Technology (in Japanese), Vol.46, No.12: 594-597.
- [3] Yokoyama I., Nishida K., Zhou L., Eda H., Kawakami T., (2003) Experiment & Design of Ultra-precision Machine tool, Proceedings of Ibaraki District Conference (in Japanese) : 165-166
- [4] Qiu Z., Zhou L., Nishida K., Shimizu J., Eda H., Ishikawa T., (2004) Development of Cell Manipulation System under Microscope, Proceedings of the 1<sup>st</sup> International Conference on Positioning Technology : 457-461

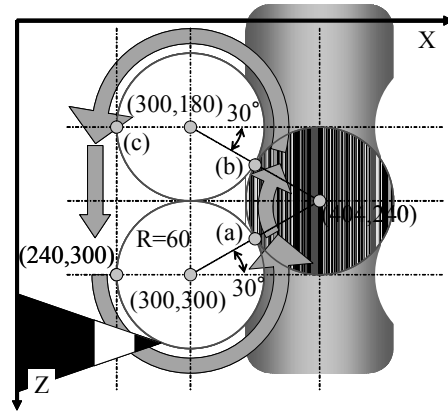


Fig. 12. Tool path strategy

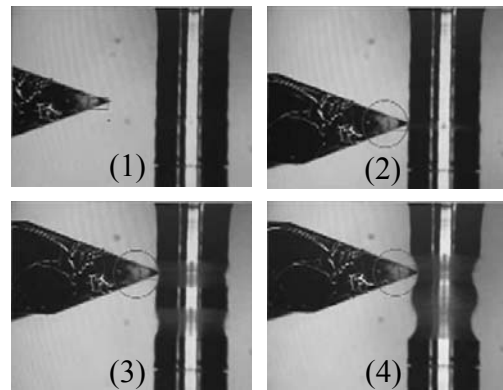


Fig. 13. Experiment of cutting a brass bar

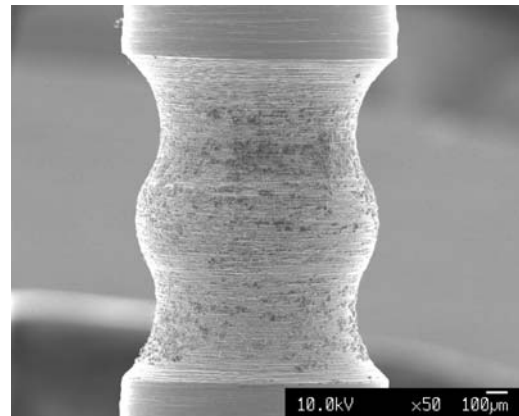


Fig. 14. SEM picture of a resultant brass

---

## An 8-Axis Robot Based Rough Cutting System for Surface Sculpturing

Jiang Zhu<sup>1</sup>, Ryoko Tanaka<sup>1</sup>, Tomohisa Tanaka<sup>1</sup>, and Yoshio Saito<sup>1</sup>  
<sup>1</sup>Tokyo Institute of Technology

Keywords: Robot, Surface Sculpturing, Rough Cutting, Hotwire Cutting,

### Abstract

In this paper, a rough cutting system for surface sculpturing is proposed. The 8-axis machining system is composed of a 6-axis robot and a 2-axis worktable. It carves block of polystyrene foam by hotwire. According to the geometric feature, the system automatically simplifies the input model into a user specified resolution and generates a series of rough cutting models which are composed of large, flat faces. Then according to the cutting tool path generated by the path-planning algorithm, the rough cutting model is sculptured face by face.

### 1 Introduction

Currently there are two conventional methods to fabricate 3D models and freeform surfaces: RP (Rapid Prototyping) and CNC machining[1]. RP process provides a solution with higher speed, easier fabrication and the ability to handle complex structure[2]. While CNC machining provides a solution with higher accuracy, better surface finish and the ability to machine various materials[3]. However, none of them is the ideal solution for producing high quality part within the shortest possible time. Noticed that multi-DOF robot benefits from the faster fashion than traditional RP methods and more flexibility than CNC machines, the idea of utilizing multi-DOF robots to build prototypes has attracted many robotic researchers to the field of 3D fabrication. Tengledor and Vergeest [4, 5] were early to implement robotic arms for this purpose. Also, Chen [6, 7] implemented a robotic system for sculptured surface cutting and later developed a technique that uses layer-based machining to sculpt prototypes made of polymers. Also, Coole evaluated the use of robotic systems in machining full scale prototypes for the sanitary ware industry[8].

In this research, a new rough cutting system based on multi-DOF robot and shaping the 3D work piece by hotwire is proposed, which combines the advantages of high flexibility of RP and high accuracy of CNC. With its flexibility driven from an 8-axis configuration, efficient path planning software for rough cutting, as well as an end effector with hotwire, this rapid prototyping system can carve sculptural surfaces rapidly and efficiently. This system is named "Michelangelo", after an Italian renaissance artist, since it is expected to make sculptures as an artist does.

While most of the traditional RP techniques share the advantage provided by slicing the 3D model into thin 2D layers and consecutively constructing these layers, Michelangelo only simplifies the 3D model into a user specified precision, then generates a series of rough cutting models with continuous volume increase. Then the system cuts the rough cutting model face by face instead of layer by layer.

Michelangelo currently carves blocks of polystyrene foam by heat. Polystyrene foam, for instance, is a polymeric material that is relatively inexpensive, soft to carve, and has a suitable melting temperature. These properties make polystyrene foam a popular material for many fabrication technologies. While this presented work is based on shaping cellular polystyrene foam blocks (with the dimensions of  $100 \times 100 \times 100 \text{mm}^3$ ), Michelangelo is equally capable of carving other soft polymer-based materials with relatively low melting temperatures.

The next section of this paper presents the overall system architecture of Michelangelo. This is followed by a detailed discussion of the Michelangelo subsystems. The main features of hardware and software are also discussed. Finally, summary and potential applications of Michelangelo are addressed.

### 2 System Description

Michelangelo system features a modular design consisting of seven subsystems as depicted schematically in Fig.1. Each subsystem is a module that operates independently as it performs a different function. The subsystems are:

1. Mesh Simplification subsystem simplifies the input 3D models into a user specified precision. Usually the 3D models generated by the CAD software or 3D scanning systems contain tremendous redundant data. Mesh Simplification subsystem reduces the number of polygons needed to represent a model while trying to retain a good approximation to the original shape and appearance.
2. Rough Cutting Model Generation subsystem generates a series of approximations with simple geometrical complexity. The approximations gradually transform the simplified model into a cube

like shape. It will help the system to rapidly remove the redundant material, and approach the final work piece step by step.

3. Tool Path Generation subsystem generates cutting path for the multi-DOF robot. The cutting path is required to guarantee that the system should not interfere with itself, and the cutting tool should not interfere with the work piece.
4. VR (Virtual Reality) Simulator is developed to test the performance of the system, and test the validity of the manipulator motion.
5. 8-Axis Robot is composed of a 6-axis manipulator and a 2-axis worktable, which provides a rich space reach for the cutting tool. The 6-axis manipulator and the 2-axis table are controlled by the interface subsystem according to the motion plan tested by VR simulator.
6. Cutting Tool is composed of a hotwire end effector and a current controller, which provides a suitable temperature for the end effector to perform a smooth cut.
7. Interface provides the on-line control of 8-axis robot and the human-machine interaction with operator. It integrates the software and hardware into a whole system, Michelangelo.

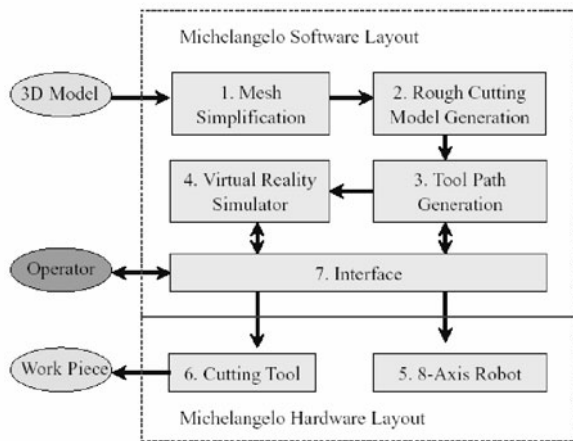


Fig. 1. System modular description

### 3 Hardware Layout of Michelangelo

#### 3.1 8-Axis Robot for Surface Sculpturing

The mechanism of Michelangelo should guarantee an abundant space reach for the end effector, so that the tool can cut any place it could reach on the polystyrene foam block. Because the cutting surface is unfixed, the multi-DOF manipulator alone cannot provide an enough feeding

distance in the cutting direction. Therefore, an 8-axis cooperating robotic system is developed, which is made up of a 6-axis manipulator (Motoman-SV3X, by Yaskawa Electric Co.) and a 2-axis worktable, shown in Fig. 2. It not only conquers the limitation of the manipulator's space reach, but also helps to avoid interference between the manipulator and the work piece.

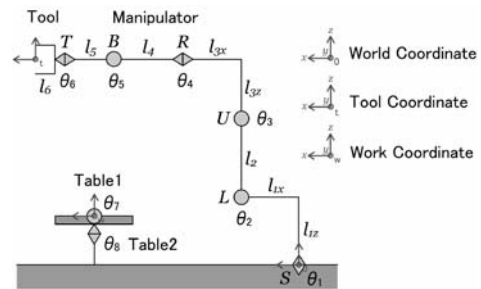
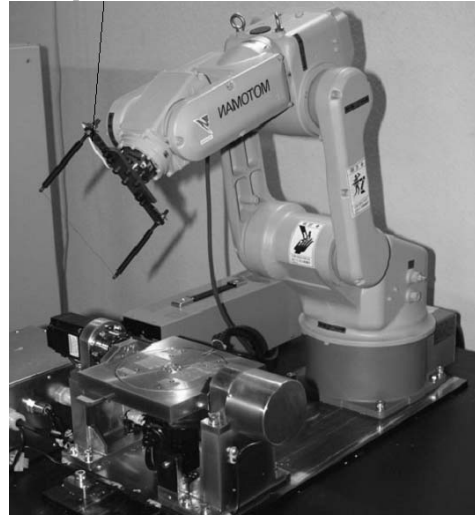


Fig. 2. 8-axis robot for surface sculpturing

#### 3.2 Cutting Tool

Because Michelangelo carves polystyrene foam blocks by heat, hotwire end effector is designed as the cutting tool of this system. To achieve a clean cut of the surface, various variables that affect the performance of cutting tool should be considered. Firstly, proper tuning of the electric current running through the hotwire should be controlled to minimize the unexpected effect. For instance, if the tool is over heated, the polystyrene foam will melt resulting an over cutting of the material and an unacceptable surface finish. Secondly, the temperature rise will cause elongation of hotwire and loss of tension, which will leave wavy traces on the cutting surface. Therefore, proper tension should be adjusted after the hotwire is heated. Finally, the distance between the two poles, which support the hotwire, should be wide enough to prevent the interference between cutting tool and work piece. Considering the above points, a current version of the cutting tool is designed as shown in Fig. 3.



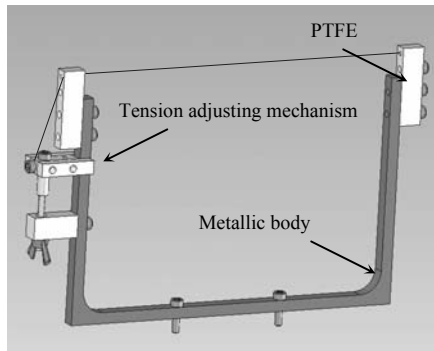


Fig. 3. Hotwire end effector

## 4 Software Layout of Michelangelo

### 4.1 Mesh Simplification

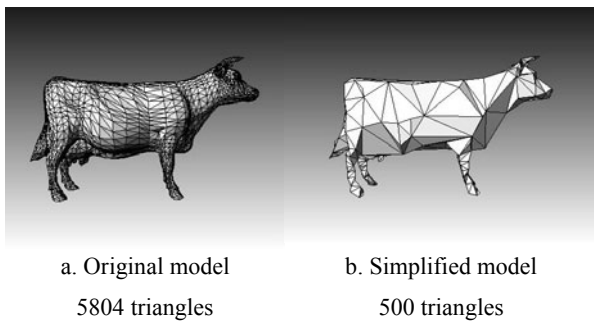


Fig. 4. Cow model

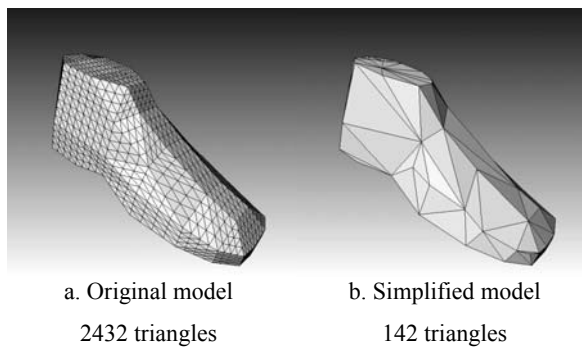


Fig. 5. Shoes model

Michelangelo sculpturing system uses the models generated by CAD software or 3D scanning system as input. Recently, with the rapid development of 3D scanning technology, an accurate representation of a 3D model can easily contain a million triangles. Complex triangle meshes are notoriously difficult to render, store, and transmit. Especially in the field of 3D fabrication, over sampled mesh data will cause much

inconvenience and low efficiency for processing. Mesh simplification subsystem will narrow this discrepancy. It reduces the number of triangles needed to represent the model while trying to retain a good approximation to the original shape and appearance.

A simplification algorithm focusing on the application of surface sculpturing is developed in the previous work [10]. The algorithm uses iterative edge collapse [9] transformation to simplify models, and uses vertex importance value to control the error of the approximation as it is being simplified. It can rapidly produce faithful approximations of the input models. Moreover, the simplified approximation generated by this algorithm is composed of regular shaped and regular sized triangles, which will greatly enhance the model's machinability.

The detailed algorithm description can be found in the previous work [10]. Some simplification results are shown in Fig. 4. and Fig. 5. The simplified approximation will be the model for Michelangelo to cut.

### 4.2 Rough Cutting Model Generation

Before the final work piece is machined, the system needs to cut the block of polystyrene foam into a roughcast, just like the sculptor does. In this step, the system needs to remove the redundant material rapidly and should not miss-cut any part of the final work piece. It requires the rough model generation subsystem to generate a series of approximations with continuous volume increase, and the approximation should be composed of large flat faces [11].

Because generating rough cutting models need not consider shape similarity between the results and the input model, it gives much flexibility to the algorithm. Inspired from the algorithm of simplification envelopes, which was proposed by Cohen J. [12], a rough cutting model generation algorithm is developed. The approximation generated by mesh simplification algorithm is used as the input of this algorithm. It works following below steps:

- First, the algorithm offsets each vertex of the input model along its normal vector by a specific distance. According to the topological feature and connectivity of the input model, an offset surface of the model is generated. It completely includes the input model.
- Then edge collapse transformation is carried out on this offset surface. The input model is used as a boundary limit for the algorithm to guarantee that the simplified results never intersects with the input model. Thus, the simplified outer envelope will be always larger than the input model.

By iteratively carrying out the above two steps with different offset distance, the algorithm generates a series of this kind of rough cutting models. It transforms the model from the work piece into a raw material block. Following the reverse sequence of rough cutting model generation, Michelangelo could approach the final work piece from block of polystyrene foam step by step. Fig. 6. shows the rough cutting models in different rough cutting stages. These rough cutting models are generated based on the simplification result of Fig. 5.

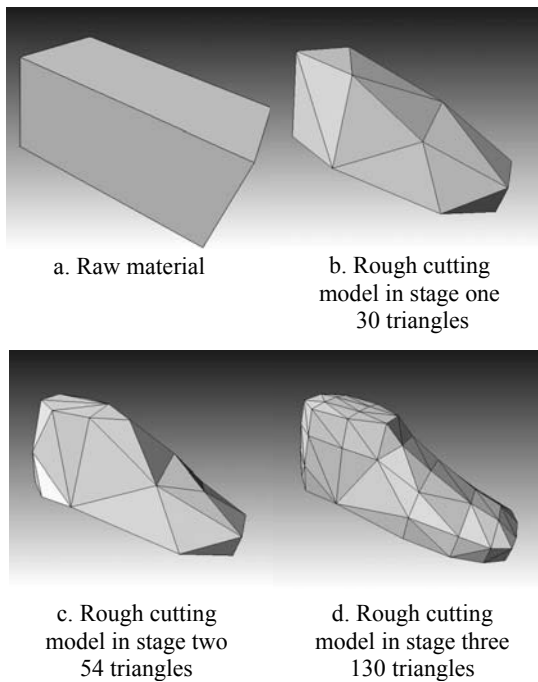


**Fig. 6.** Shoes rough cutting models in different rough cutting stages

### 4.3 Tool Path Generation

Tool path generation subsystem of Michelangelo mainly accomplishes two tasks. The first one is to control the movement of the manipulator cooperating with the worktable. The second one is to avoid the interference between cutting tool and work piece, and to inform the user whenever a face is inaccessible due to the geometric feature of the cutting tool.

#### 4.3.1 Tool Path for Cutting one Face

Considering the process of cutting one face  $T_i$ , which is composed of three vertices  $V_{i1}$ ,  $V_{i2}$ ,  $V_{i3}$ , shown in Fig. 7., firstly, the worktable adjusts the cutting plane to a proper pose, which is easy for the hotwire to cut. Presently, the table adjusts the cutting plane upward or forward to cut.

Then a proper cutting tool direction is calculated, which should avoid all the interferences that will happen. Since the cutting face is composed of three edges, the candidate cutting tool direction is selected among these three directions. The method to select the candidate cutting direction is discussed in the next part of this section. Here the vector of  $\overline{V_{i2}V_{i3}}$  is assumed to be the optimal tool direction for cutting face  $T_i$ .

After that, the path of the hotwire cutting tool is calculated according to the following steps:

1. The manipulator moves the hotwire center  $P$  from the present position to point  $O$ , which is above  $V_{i1}$  along the plane's normal vector, shown as step 1.
2. The hotwire center is moved from point  $O$  to point  $V_{i1}$ , at this moment the hotwire is adjusted to the proper cutting direction, shown as step 2.
3. The surface cutting is executed. The manipulator moves the hotwire center from point  $V_{i1}$  to  $M$ , the perpendicular foot from  $V_{i1}$  to line  $V_{i2}V_{i3}$ , which is shown as step 3.
4. The hotwire moves away from the cutting surface, shown as step 4. And the loop for cutting face  $T_i$  is finished.

By iteratively carrying out the above steps, the sculptural surface can be machined face by face.

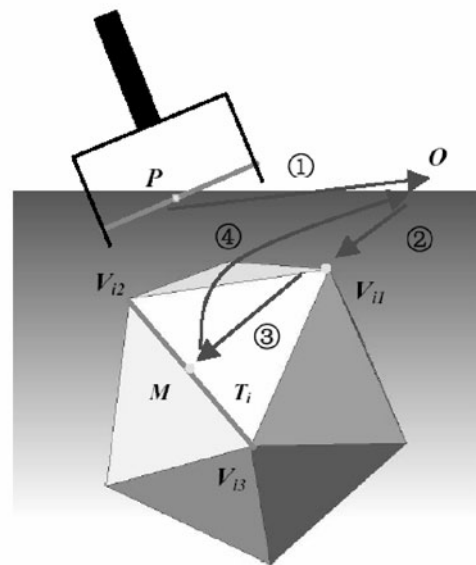


**Fig. 7.** Steps of cutting one face

#### 4.3.2 CD (Collision Detection) for Avoiding Interference

During the machining process, deciding the proper cutting tool direction plays an important role in path planning, since any miss-cut will cause the failure of the whole sculpturing process. A proper cutting path should consider the following requirements:

- The movement of each manipulator joint and worktable joint should not exceed its link limit.
- The manipulator should not interference with itself or with the worktable.
- The hotwire should not miss cut the other part of the work piece during the sculpturing process.

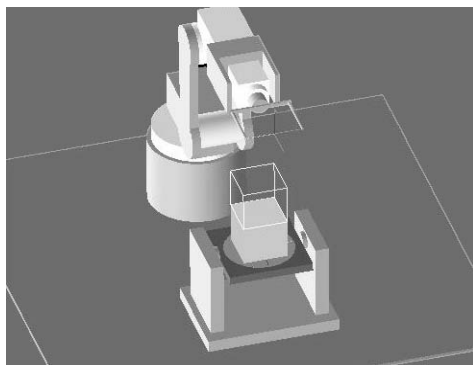
Since the mechanism subsystem introduces an 8-axis distribution of DOF, the position of the cutting face can be adjusted by the movement of worktable. It will prevent the manipulator to exceed its links limits.

In order to prevent the interference phenomenon, CD is introduced into this tool path generation subsystem. Presently, CD methods based on hierarchical bounding

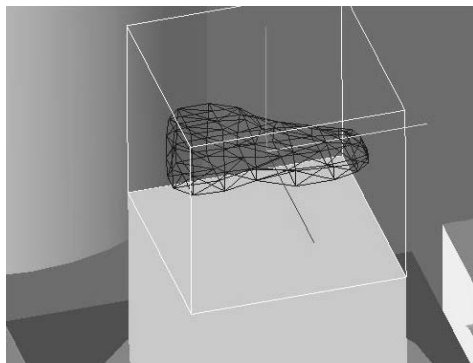
volumes are widely used due to their rapidity and accuracy [13]. Among them AABB (Axis Aligned Bounding Box), Bounding Spheres and OBB (Oriented Bounding Box) are the most popular methods. AABB is the quickest algorithm but with a low precision. Bounding spheres is only proper for objects frequently rotating. OBB [14] is the tightest and most precise one, while requiring huge computation cost. According to the special requirement for this application (no failure is permitted), OBB is introduced into this system.

Before the hotwire attempts to move, the OBB of cutting tool along the cutting surface and the OBB of other faces of the work piece are checked. If there is a proper direction for the hotwire to finish this surface without interference with the other faces of the work piece, the system will output that direction as the cutting tool direction. However, in some cases there will be no valid cutting direction according to the local geometric feature of the model, for instance the bottom of a small concave. In this situation, the system will permit a little error tolerance for this surface. It gives the cutting tool a small offset above the cutting surface and search the proper cutting direction again. If no valid cutting direction can be found under an endurable error tolerance, the system will announce the operator that this surface is inaccessible.

4.4 VR (Virtual Reality) Simulator



a. Whole view of machining system



b. Work piece to be machined

Fig. 8. VR simulator

Virtual Reality is a new emerging technology in computer industry and is one of the hottest research areas in computer graphics fields. The main idea is using computer software and hardware to create a virtual environment that can be visualized, listened and felt [15][16]. In order to test the behavior of the 8-axis robot and visualize the surface sculpturing process, a VR simulator corresponding to the actual Michelangelo mechanism is developed, in which the motion plan can be previewed or simulated before the actual sculpturing. The VR simulator is developed based on CODE99 (Cimetrix Open Development Environment 99) dynamic link library and Visual C++. It is constructed by two kinds of modeling, geometrical modeling and physical modeling. Geometrical modeling builds up the visual foundation of VR simulator. Physical modeling adds physical property to geometric model, and makes the model behave more like that of the actual Michelangelo. Combining the geometrical and physical modeling provides a vivid cutting model visualization and surface sculpturing simulation.

Fig. 8. shows virtual Michelangelo and virtual work piece in VR simulator subsystem.

4.5 Michelangelo Interface

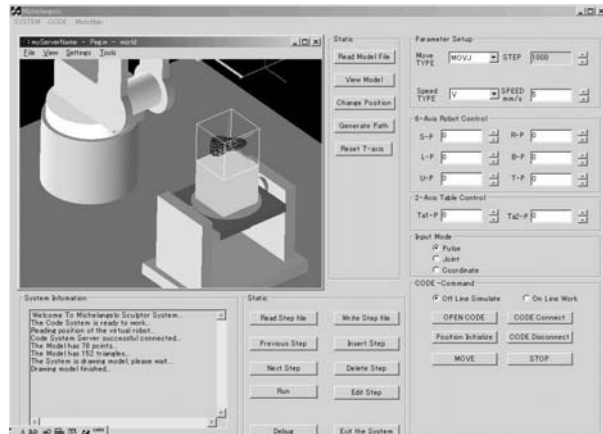


Fig.9. Michelangelo Interface

In order to integrate all the subsystems into a whole system, a well-organized human-machine interface is necessary. The interface of Michelangelo is developed using Visual C++ and MotoCOM open source (provided by Yaskawa Electric Co.). It integrates the functions of on-line control of 8-axis robot, off-line simulation of surface sculpturing process. Fig. 9. shows the appearance of the Michelangelo interface.

The operator can easily manipulate the robot to accomplish various kinds of tasks by operating the control panel on the right side of the interface, and can preview the robot motion trace on the up left VR simulator window. The interface is also capable of visualizing 3D work piece model, previewing sculpturing process, programming robot motion file, and providing proper motion plan.

## 5 Experiment Results

In order to test the capability and performance of Michelangelo, some rough cutting models are sculptured, shown in Fig. 10., including the shoes model shown in Fig. 5. From the experimental result, it can be found that the system currently can make convex structural models with large flat faces very well, such as icosahedron. And the surface finish is very clean. However, in the case of machining models represented by small faces with concave features, such as shoes, it is still a little bit inferior in accuracy. One of the reasons for this shortcoming is that it is difficult to maintain a constant cutting condition regarding to different regions. In some region, which is represented by small faces, the overlap effect with adjacent triangles will cause the hotwire melt the surrounding places, which are quite close to the cutting face, though there is no contact between the cutting tool and such places. It is necessary to examine an appropriate cutting condition for small faces in the future.

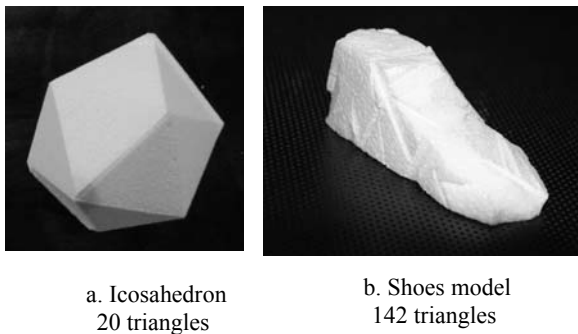


Fig. 10. 3D models sculptured by Michelangelo

## 6 Summary

In this paper, a novel surface sculpturing system based on 8-axis robot and hotwire cutting is presented, which consists of 7 subsystems featuring hardware and software. To sculpture a realistic looking model, what the system needs is only an input 3D model. It can automatically simplify the model into a user specified precision, and generate the rough cutting model. And the final work piece can be sculptured rapidly. In summary Michelangelo is an effective surface sculpturing system, which has great potential applications in the fields of engineering, arts, fabrication, and so on.

## 7 Reference

[1] Copper K.G, (2001) Rapid prototyping technology: selection and application. New York, Marcel Dekker

- [2] Onuh, S.O, Yusuf, Y.Y, (1999) Rapid prototyping technology: Applications and benefits for rapid product development. Journal of intelligent manufacturing, v10, n3: 301-311
- [3] Bob Hassold, (1995) CNC machining as a rapid prototyping technique. Modern machine shop, v 68, n 5: 68-73.
- [4] Tangelder J.W.H, (2004) A survey of content based 3D shape retrieval methods. Proceedings shape modeling international SMI 2004: 145-156
- [5] Tangelder J.W.H, Vergees JSM, (1996) Robot machines rapid prototype. Industrial robot, v 23, n 5, 1996: 17-20
- [6] Chen, Y.H, Hu, Y.N, (1999) Implementation of a robot system for sculptured surface cutting. Part I. rough machining. International journal of advanced manufacturing technology, London, UK, Springer-Verlag, 1999, 15: 624-629
- [7] Hu, Y.N, Chen, Y.H, (1999) Implementation of a robot system for sculptured surface cutting. Part II. finish machining. International journal of advanced manufacturing technology, London, UK, Springer-Verlag, 1999, 15: 630-639
- [8] Coole T.J, (2000) Analysis of robot system capabilities in machining of full scale prototypes for sanitary ware industry. British ceramic transactions, v 99, n 4, 2000: 175-178
- [9] H. Hoppe, (1996) Progressive mesh. SIGGRAPH' 96 Proceedings: 99-108
- [10] J. Zhu, T. Tanaka, Y. Saito, (2005) 3D mesh simplification for freeform surfacing. Tehran international congress on manufacturing engineering: 1180
- [11] J. Zhu, T. Tanaka, Y. Saito, (2005) A new mesh simplification algorithm for the application of surface sculpturing. Proceeding of the first JTU-TIT joint workshop on creative engineering-mechanics, control and advanced robotics
- [12] Cohen J, Varshney A, (1996) Simplification envelopes. SIGGRAPH'96 Proceedings: 119-128
- [13] F.S. Tan, L.N. Sun, W.B. Rong, J. Zhu, (2004) A collision response method in virtual environment of peg-in-hole microassembly. the 5<sup>th</sup> World congress on intelligent control and automation (WCICA2004): 3210-3213
- [14] S. Gottschalk, M. C. Lin, (1996) OBB-tree: a hierarchical structure for rapid interference detection. SIGGRAPH'96 Proceedings: 171-180
- [15] L. N. Sun, F. S. Tan, W. B. Rong, J. Zhu, (2004) Modeling of micromanipulation robot in virtual environment. ACTA Metallurgica Sinca (English Letter), V 17, No.2, Apr, 2004: 194-198
- [16] L. N. Sun, F. S. Tan, W. B. Rong, J. Zhu, (2003) Research on the architecture of virtual reality based on micromanipulation robot. IEEE Conference on RISSP, Changsha, China, Oct, 2003: 960-964

# A New Position Surveying System for the Underground Pipes Using Two Rotary Encoders

Toshiaki HAMANO<sup>1</sup>, Manabu ONO<sup>2</sup> and Shigeo KATO<sup>3</sup>

<sup>1</sup>Technos Corp. , <sup>2</sup>Tokyo Metropolitan College of Technology, <sup>3</sup>Nippon Institute of Technology

Keywords: Position surveying, Optical fiber cable, Underground pipe, In-pipe surveyor, Rotary encoder

## Abstract

We fabricated a position surveying system for underground pipes using two rotary encoders. Two rotary encoders measure distance of right and left walls of the pipe. It was confirmed that the fabricated position surveying system can survey the position of the experimental underground pipe that consists of two 8000 mm straight pipes and 4000 mm curved pipe that has the curvature radius of 36500 mm in the error of 5.6 mm.

## 1. Introduction

Optical fiber cable for the broad bands communication is usually covered by plastic pipe and buried under the ground. Then, we are required to grasp its real buried position before digging at the construction or the maintenance in order to prevent from the cutting of the optical fiber. However, once the optical fiber cable is buried under the ground, it is very difficult to confirm the buried position of the pipe, because the optical fiber cable and plastic cover pipe are not the metal.

A former way to confirm the buried position of the optical fiber cable is the ground penetrating radar method [1]-[5]. The ground penetrating radar method is very useful for the metal. However, the optical fiber cable in plastic cover pipe is not metal. Another method is the elastic wave method [6]. In this method, a vibrator is put on the ground. The wave from the vibrator is detected by many in-lined receivers that are arrayed on the ground. However, the detection is only done at the place where the ground is covered by soil and the accuracy of the surveying is not good at the place where the position of the plastic cover pipe is so deep in the ground or in the different soils.

Fortunately the cover pipe of the optical fiber cable goes through utility holes that are arranged in the hundreds meter interval. If we can insert a surveying mechanism into the cover pipe at the utility holes and detect directly the information of the buried position of the pipe by a new position surveying system that can move itself in the

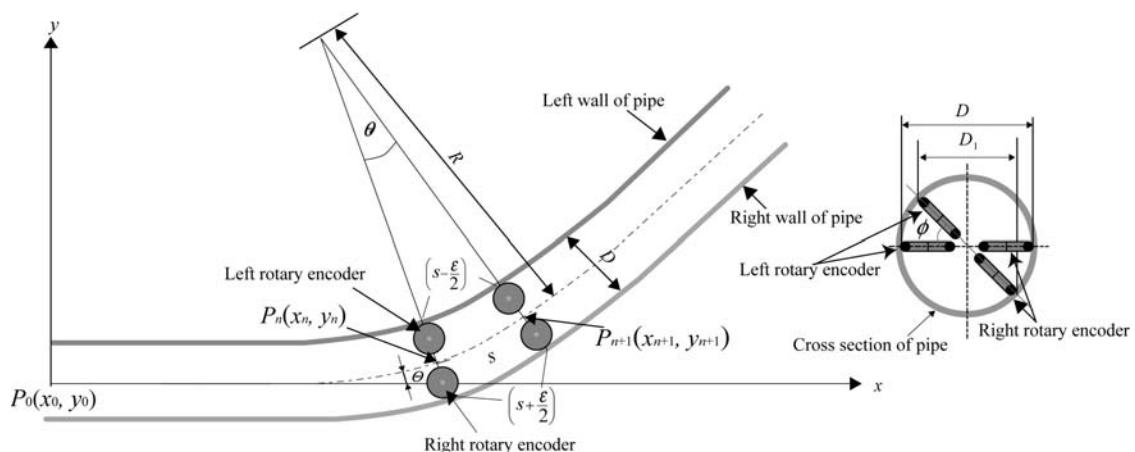


Fig. 1. The principle of the position surveying in the underground pipe by in-pipe surveyor using rotary encoders

pipe, the problem of the former way to confirm the buried position of the optical fiber cable is solved.

This research aims to identify easily the buried position of the pipe, using the information of the buried position from the pipe. We use two rotary encoders that have pulleys contacting right and left walls of the buried pipe in order to detect directly the information of the buried position of the pipe [7]-[9]. Output of the rotary encoder contacting the wall shows the length of the wall. Average of summation of the outputs of the right and the left rotary encoder shows moving distance of a surveying mechanism of the position surveying system. The curvature of the buried pipe is obtained by difference of the outputs of the right and the left rotary encoder. The position of buried pipe is identified by the moving distance and the curvature of the pipe. It is confirmed that the new position surveying system can identify the buried position of a pipe that is 20 m long and has loose curvature in the error of 5.6 mm.

## 2. Principle of position surveying

Length of walls of both side of a pipe is same if the pipe is straight. If the pipe curves toward right, the length of the right wall is shorter than the length of the left wall. We measure the lengths of both side of the pipe by two rotary encoders that have pulleys. The principle of position surveying using two rotary encoders is shown in Fig. 1. Inner diameter of the pipe that has loose curvature is  $D$ . The original point is  $P_0(x_0, y_0)$ . Present position of the surveying mechanism is  $P_n(x_n, y_n)$ . Angle between the tangential line and the  $x$ -axis is  $\Theta$ . It is assumed that a difference  $\mathcal{E}$  is made by the both side rotary encoders when the surveying mechanism moves a small distance of  $s$ . This moved point is  $P_{n+1}(x_{n+1}, y_{n+1})$ . The normal lines that cross points  $P_n(x_n, y_n)$  and  $P_{n+1}(x_{n+1}, y_{n+1})$  make an angle  $\theta$ . The radius of the curvature is assumed as  $R$ . The surveying mechanism may incline by some rolling force. The rolling angle is assumed as  $\phi$ . Projection of the pulley is  $D_1$  and is shown as

$$D_1 = D \cos \phi \quad (1)$$

The difference  $\mathcal{E}$  of the right and left rotary encoders is shown as

$$\mathcal{E} = \left( s + \frac{\mathcal{E}}{2} \right) - \left( s - \frac{\mathcal{E}}{2} \right) = \left( R + \frac{D_1}{2} \right) \theta - \left( R - \frac{D_1}{2} \right) \theta = D_1 \theta \quad (2)$$

Then, the small angle  $\theta$  is obtained as

$$\theta = \frac{\mathcal{E}}{D_1} \quad (3)$$

The  $x$ -coordinates and the  $y$ -coordinates of  $P_{n+1}$  are calculated from the  $x$ -coordinates and the  $y$ -coordinates of  $P_n$  as

$$x_{n+1} = x_n + s \cdot \cos(\Theta + \theta) \quad (4)$$

$$y_{n+1} = y_n + s \cdot \sin(\Theta + \theta) \quad (5)$$

The tangential angle  $\Theta$  is the summation of the small angle  $\theta$  and shown as

$$\Theta = \sum \theta \quad (6)$$

## 3. Pipe for surveying experiment

### 3.1 Coordinates of the pipe for surveying experiment

Pipe for surveying experiment is shown in Fig. 2. The pipe consists of two straight pipes and a curved pipe. The first straight pipe is 8000 mm long. The second curved pipe has a curvature radius of 36500 mm and is 4000 mm long. The third straight pipe that is attached the second pipe and is 8000 mm long. The  $x$ -axis of the pipe for surveying experiment is standardized by a fishing line that is 0.05 mm in diameter and is intensely tightened. Distance from the original point that is the  $x$ -coordinates is measured by a tape measure. The  $y$ -coordinates is measured by steel measure from the standard line of the fishing line. 199  $x$ -coordinates are obtained, because measure is done from the original point to 19800 mm every 100 mm. The  $y$ -coordinates at 19800 mm of the  $x$ -axis is 1121 mm. The distance of 100 mm is divided into 30 in the computer, because 100 mm is coarse. Interval is 3.33 mm and number of the position coordinates is 5941. This is called as the experimental position coordinate. Errors by the division occur at the curved pipe. However, maximum of errors is less than 0.034 mm

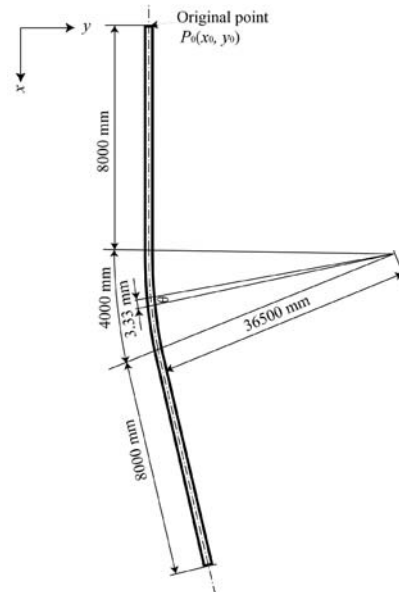


Fig. 2. Pipe for surveying experiment

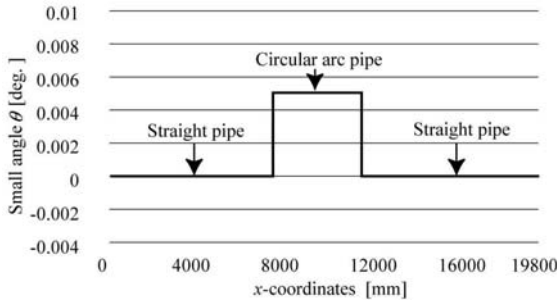


Fig. 3. The small angle  $\theta$  of the ideal pipe

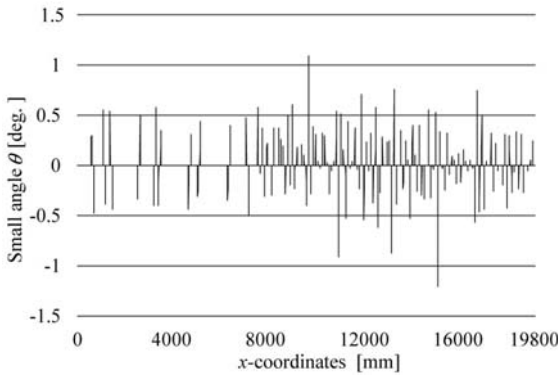


Fig. 4. The small angle  $\theta$  obtained from position coordinates of the pipe for experiment measured by the steel measure

### 3.2 Small angle of the pipe for surveying experiment

Here, the ideal pipe for surveying experiment is assumed to consist from two complete straight pipes and a complete circular arc and the small distance  $s$  is assumed to be 3.33 mm. Then, the small angle is 0 degree at the straight pipes and 0.0053 degrees at the circular arc pipe that exists between 8000 mm and 12000 mm of the  $x$ -coordinates. The small angle  $\theta$  of the ideal pipe is shown in Fig. 3. Using Eqs. (4), (5) and (6), the small angle  $\theta$  and the tangential angle are calculated from position coordinates of 5941 points. Relationship between the small angle  $\theta$  and  $x$ -coordinates is shown in Fig. 4. The small angle of 0.0053 degrees that is shown in Fig. 3 is not seen in Fig. 4, because there exist errors larger than 1 degree.

### 3.3 Averaging process for decreasing of errors

We introduce averaging process in order to decrease large errors. Some small angle  $\theta_n$  is assumed to be an average of three continuous small angles.

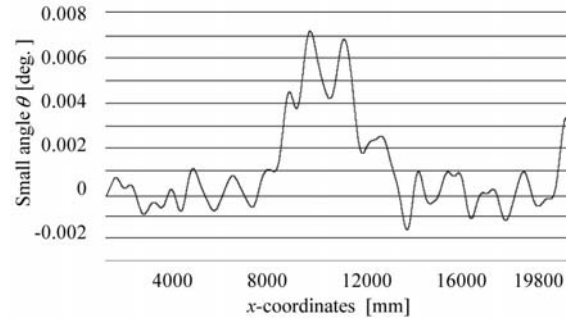


Fig. 5. The small angle  $\theta$  obtained from position coordinates of the pipe for experiment measured by the steel measure and averaged using the averaging process

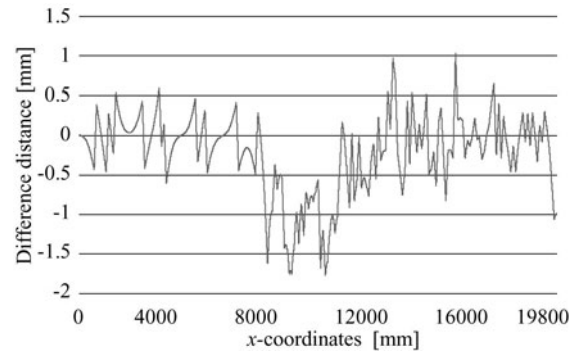


Fig. 6. Difference between the calculated position coordinates and the measured position coordinates

That is,

$$\theta_n = \frac{\theta_{n-1} + \theta_n + \theta_{n+1}}{3} \quad (7)$$

Small angles at both ends do not change. By the averaging process, all small angles except both ends are averaged and changed. The large error is changed to small error. The averaging process of 10000 times is done. The result of the averaging process is shown in Fig. 5. Errors are decreased to the order of 0.001 degrees at the straight pipe. Maximum of small angles at the curved pipe that exist between 8000 mm and 12000 mm of  $x$ -axis are 0.004 degrees or 0.007 degrees. These small angles are approximate as the small angle 0.0053 degrees of the ideal pipe. Substituting small angles shown in Fig. 5 into Eqs. (4), (5) and (6), 5941 position coordinates are obtained. These are called as calculated position coordinates. Difference between the calculated position coordinates and the measured position coordinates is shown in Fig. 6. Maximum difference is about 1.7 mm at the curved pipe. We use the calculated position coordinates as the standard position coordinates, because the error of the measured position coordinates is considered to be decreased by the averaging process of 10000 times.

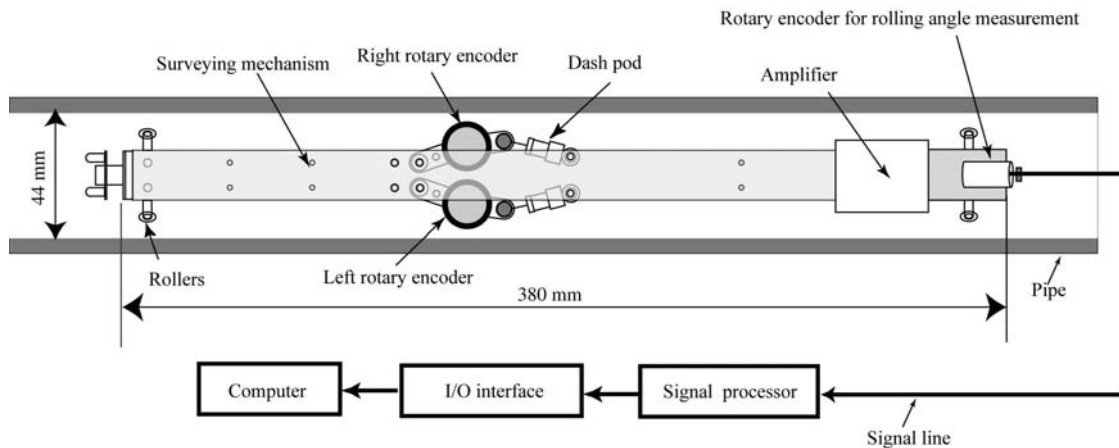


Fig. 7. Structure of the position surveying system

#### 4. Position surveying system

A new position surveying system for underground pipes is shown in Fig. 7. The system consists of a surveying mechanism that carries the right and left rotary encoders, a signal processor, an I/O interface and a computer. The surveying mechanism that is 380 mm long is held to the inside of the pipe by eight small rollers and can move in the inside of the pipe. A weight is attached under chassis in order to prevent rolling of the surveying mechanism. However, rolling of the mechanism can not be prevented perfectly. So, rolling angle  $\phi$  is measured by an another rotary encoder that is attached the chassis. The right and left encoders are held by arms that have pin joints and are attached the chassis of the surveying mechanism. The pulley is pushed to the wall of the pipe by force of 1 N and vibration of the rotary encoder is severely damped, because the arm is suspended by a spring and a dash pod. The signal processor consists of a detecting circuit of clockwise or counter clockwise and a mechanical chattering circuit. The rotary encoder makes 1440 pulses

per one rotation. Resolution of the rotary encoder is 44  $\mu\text{m}$ . The signal from the signal processor is introduced into the computer through the I/O interface. Software in the computer calculates locus of the surveying mechanism. The result of the position surveying is displayed on the screen of the computer.

#### 5. Surveying results by the position surveying system

##### 5.1 Measured small angle

We measure the position coordinates of the pipe for surveying experiment by the surveying mechanism. A sampling frequency from the rotary encoder is 20 Hz. Number of the sample is about 6800. The small distance  $s$  is about 3 mm. Obtained small angles are shown in Fig. 8. The small angle at the ideal straight must be 0 degree.

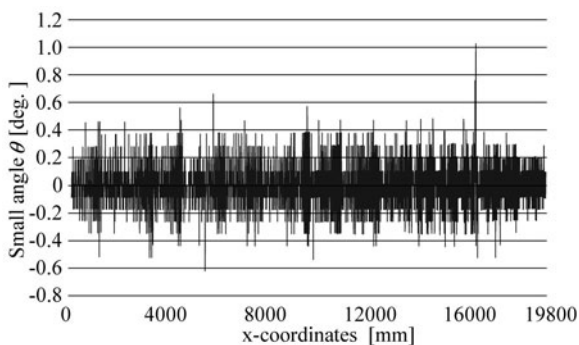


Fig. 8. The small angle measured by rotary encoders of the position surveying system

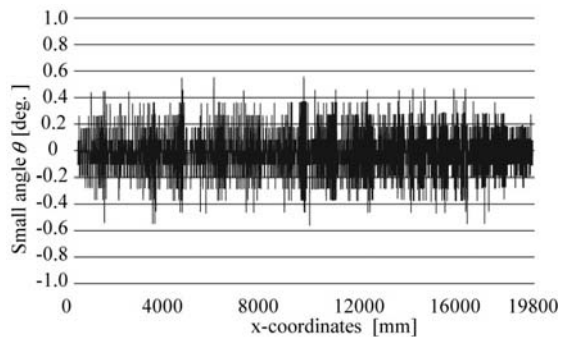


Fig. 9. The small angle eliminated over the optimal threshold



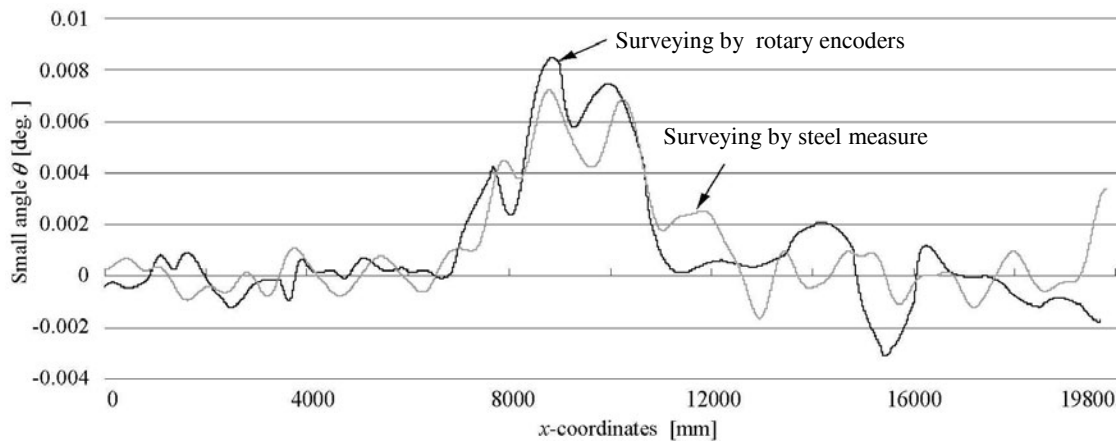


Fig. 10. The small angle after using threshold processing and averaging processing

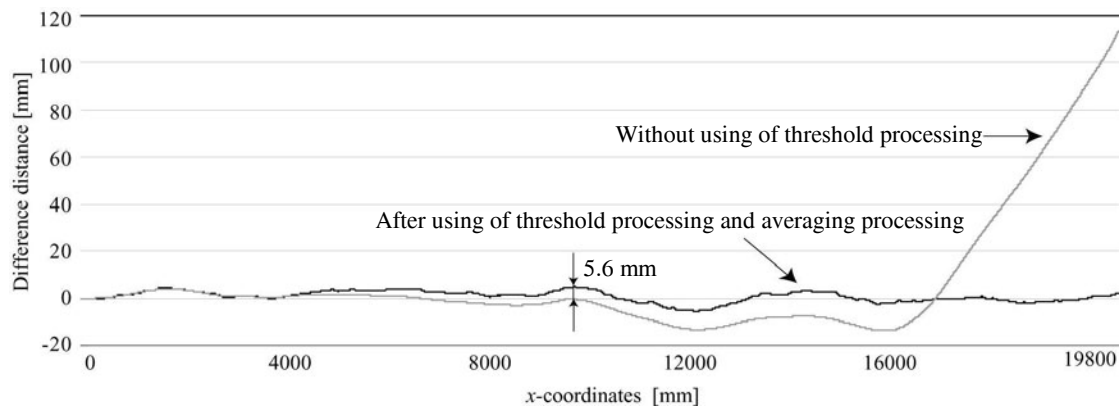


Fig. 11. Difference between the position coordinates measured by rotary encoders and the calculated position coordinates measured by steel measure

However, there exist errors from 0.2 degrees to 0.4 degrees and 1 degree at 16000 mm of  $x$ -axis. The error is considered to occur at the joint bump of pipes that are 4000 mm long.

### 5.2 Decreasing of measured error

Large error must be eliminated, because it severely affects afterwards calculation of the position coordinates. A threshold that is a value of the large error is discussed. Optimal threshold is confirmed to be  $\pm 0.55$  degrees. The difference between the position coordinate by the rotary encoder and the position coordinate by the steel measure is smallest at the optimal threshold. The small angles that are eliminated over the optimal threshold are shown in Fig. 9. The small angles that are measured by rotary encoders are averaged by using Eq. (7). Number of averaging is 10000. The averaged small angles by the rotary encoder are shown in Fig 10 by dark line. The averaged small angles by the steel measure are also shown in Fig 10 by gray line. They are similar.

### 5.3 Result of position surveying

The position coordinate by the rotary encoders and the position coordinate by the steel measure are obtained from the small angles shown in Fig. 10. Difference of both position coordinates is shown in Fig. 11. Maximum of the difference occurs at the curved pipe and is 5.6 mm. Difference of both position coordinates without the threshold processing is also shown in Fig. 11. The threshold processing is confirmed to be very effective.

## 6. Conclusions

1. We fabricated a position surveying system for underground pipes using two rotary encoders. Two rotary encoders measure distance of right and left walls of the pipe.

2. We discussed a threshold of small angles that are obtained by output difference of two rotary encoders. Optimal threshold is  $\pm 0.55$  degrees. Large position surveying error occurs without the threshold processing.
3. Some small angle is assumed to be an average of three continuous small angles. Averaging of 10000 times can decrease the measured error.
4. It was confirmed that the fabricated position surveying system can survey the position of the experimental underground pipe that consists of two 8000 mm straight pipes and 4000 mm curved pipe that has the curvature radius of 36500 mm in the error of 5.6 mm.

## References

- [1] M. Sato, Subsurface Imaging by Ground Penetrating Radar, Society of The Institute of Electronic Information and Communication Engineers Trans. , Vol. J85-C No. 7 (2002), pp. 520-530. (in Japanese)
- [2] M. Tanaka, J. Takayama, S. Ohyama and A. Kobayashi, Imaging Process Based on Bistatic Scanning for Subsurface Radar, Trans. on Society of Instrument and Control Engineering, Vol. 39 No. 4 (2003), pp. 325-331. (in Japanese)
- [3] T. Miwa I. Arai, Estimaion of position of buried pipes using MUSIC algorithm with transmitting and receiving array, Technical Report of IEICE(2001), pp. 65-72 (in Japanese)
- [4] Y. Nagashima H. Yoshida J. Masuda K. Komatu, A Estimation Method of Buried Pipe Location by Using Zero-Crossed Synthetic Aperture, Society of The Institute of Electronic Information and Communication Engineers Trans. ,Vol. J76-B-2 No.7 (1993), pp643-640 (in Japanese)
- [5] T. Nozu M. Suzuki K. Kushima T. Nakauchi H. Nakajima K. Iizuka I. Arai, The Underground Wireless Communication For GPR Data, Technical Report of IEICE (2003), pp. 15-20 (in Japanese)
- [6] Y. Kokubo, Y. Igarashi and K. Ozaki, Development of an Elastic Wave type Position Surveying System for Underground Pipe, EXTEC No. 64 pp. 57-60. (in Japanese)
- [7] T. Hamano, M. Ono, S. Kato, Development of a Position Surveying Robot for the Underground Pipes, Proc. of The 1st International Conference on Positioning Technology (2004), pp. 443-448
- [8] T. Hamano, M. Ono, S. Kato, Fabrication of a Position Surveying Robot in the Underground Pipes, Proc. of 6th International Conference on Mechatronics Technology (2002), pp. 510-515
- [9] T. Hamano, M. Ono, S. Kato, Error Decrease of Leveling Processing in Position Surveying system for the Underground Pipes, Proc. of Japan Society of Mechanical Engineers, 41th Touhoku Meeting. (in Japanese)

---

## Measurement of Cutting Torque by Speed Increasing Spindle

Masashi YAMANAKA<sup>1</sup>, Shinji MIYAMURA<sup>2</sup>, Katsumi INOUE<sup>1</sup>  
<sup>1</sup>Tohoku University, <sup>2</sup> SHOWA CORPORATION

Keywords: Cutting torque, Measurement, Speed increaser, End milling, Planetary gears

### Abstract

A method of measuring cutting torque during milling using a small end mill, using a speed-increasing spindle with planetary gears is proposed. Its viability was confirmed by experiments using three types of end mill and the workpiece of NAK55. By attaching a few parts to a commercially available speed-increasing spindle, torque can be measured at a low cost. Using the torque measurement method proposed, it was experimentally demonstrated that the phenomenon that the higher the cutting speed, the smaller the cutting torque.

### 1. Introduction

The measurement of cutting torque during end milling is effective for the optimization of cutting conditions, the prediction of tool life and the prevention of tool failure [1]-[4]. A cutting force can be detected by attaching a dynamometer to a spindle in the machining center or a workpiece [5]. However, some problems remain; for example, the limitations of the milling range and the shape of the workpiece, and the high cost of equipment. Moreover, the power required for cutting can also be calculated by measuring the power consumption of the spindle motor [6][7]. However, it is difficult to measure a small load applied by a small-diameter tool when using a spindle with a large-capacity motor.

On the other hand, to obtain a good surface by milling using a small end mill, it is effective to increase cutting speed. Accordingly, a speed-increasing spindle may be used. Planetary gears are generally used for increasing speed [8] and planetary rollers with a traction drive are also commercially available [9]. In this study, we propose a method of measuring cutting torque during milling using a small end mill, using a speed-increasing spindle with planetary gears. By attaching a few parts to a commercially available speed-increasing spindle, torque can be measured at a low cost. Here, the principle of measurement and the evaluation of results obtained from the end milling experiments in the torque measurement method proposed are described.

### 2. Principle of Measurement

Planetary gears consist of three elements; namely, a sun gear, a ring gear and a carrier. In most cases, one is fixed and the other two are used as an input and an output. Depending on the transmission torque, a counter torque reacts in the fixed part. Therefore, the transmission torque can be calculated by measuring the magnitude of counter torque. In the case of the speed-increasing spindle with the planetary gears, the carrier and sun gear are used as an input and an output, respectively, and the ring gear is fixed. The end mill is fixed at the sun gear. We devised a mechanism, in which the arm is fixed at the ring gear and a load cell is set between the arm and a stopper, as shown in Fig. 1. The cutting torque applied on the sun gear during end milling can be calculated in the following procedure. The rotary counter force measured at the load cell is multiplied by the distance between the load cell and the center of the rotation, and then, the obtained value is divided by the transmission gear ratio between the ring gear and sun gear.

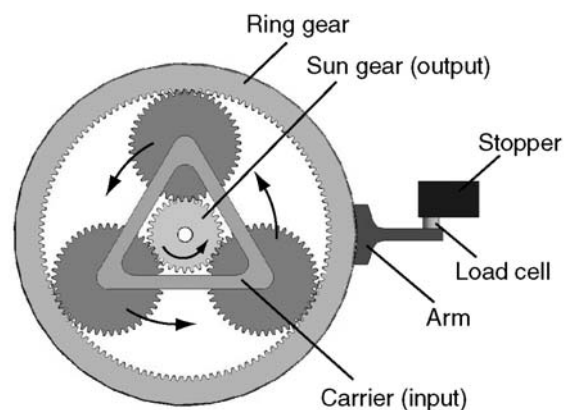


Fig. 1. Principle of torque measurement

### 3. Experimental Setup and Calculation Method of Cutting Torque

To verify that the cutting torque can be measured in the method proposed, a commercially available speed-increasing spindle with planetary gears was modified as shown in Fig. 2. A load cell was set between the arm and stopper, where a preload was applied using a bolt. Therefore, the force to be detected at the load cell is considered to be the sum of preload, force during idling and cutting force. The load cell output was input to a personal computer via an amplifier after A/D translation.

First, a static calibration was carried out in the following procedure. An L-shaped bar was fixed on the chuck, which is for grasping the end mill to be fixed. The bar was pulled with a spring scale in the rotational direction to give a torque. At that time, the load cell output was recorded. As shown in Fig. 3, the output force obtained was proportional to the tensile force, which is in agreement with the theory as mentioned above. Here, the speed increase ratio of the speed-increasing spindle used was 5.

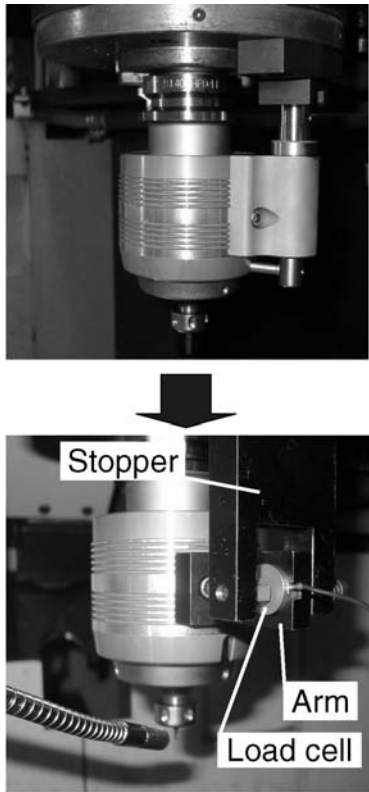


Fig. 2. Photograph of modified speed-increasing spindle with measurement devices

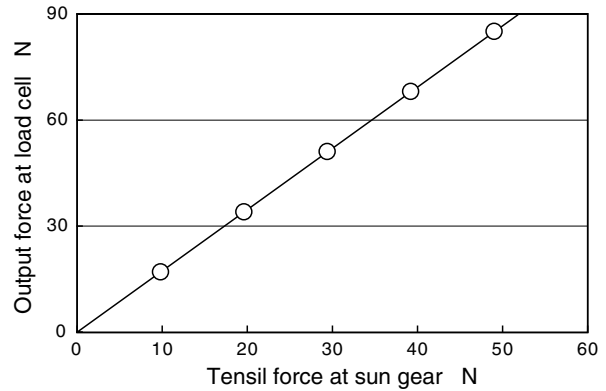
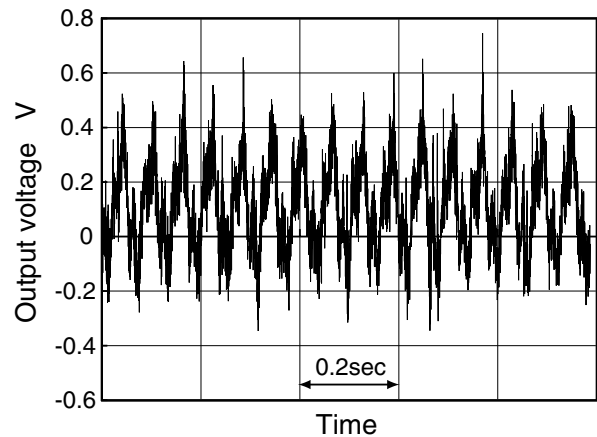


Fig. 3. Result of static calibration

Next, the output time response at the load cell during idling is shown in Fig. 4. The spectrum is also shown to have the characteristics of frequency response. The vertical axis indicates the half amplitude of the time response for the frequency. A strong peak appears at 16.7 Hz in Fig. 4. This is considered to be due to a torque irregularity occurring at the spindle motor because this frequency agrees with that of input rotary speed. Figure 5 shows the output time response at the load cell and its spectrum in the case of the end milling using the  $\phi 2$  2-flute end mill. The amplitude of the time response had few changes compared with that in Fig. 4. In the spectrum, a strong peak was observed at 167 Hz. Because the speed increase ratio of the speed-increasing spindle is 5 and the end mill has two flutes, if the carrier (input) rotates by one turn, the sun gear (output) rotates five times, resulting in a tenfold cutting rate. Accordingly, the peak caused by the milling was considered to appear at 167 Hz, which is the frequency tenfold that of the input waveform. This difference between the frequency component at milling and that at idling is considered to be the increase in frequency due to milling. When this value is converted to power, multiplied by the distance between the load cell and center of the rotation, and then, divided by the transmission gear ratio between the ring gear and the sun gear, which is 4, the cutting torque is obtained. However, real-time measurement has not been realized yet.



(a) Time response

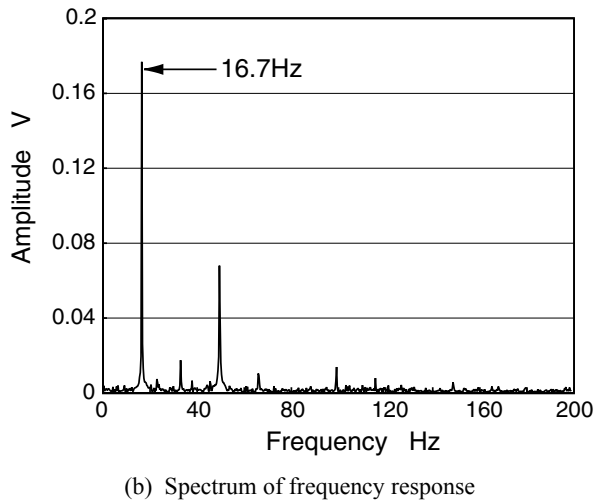


Fig. 4. Output of loadcell at idling

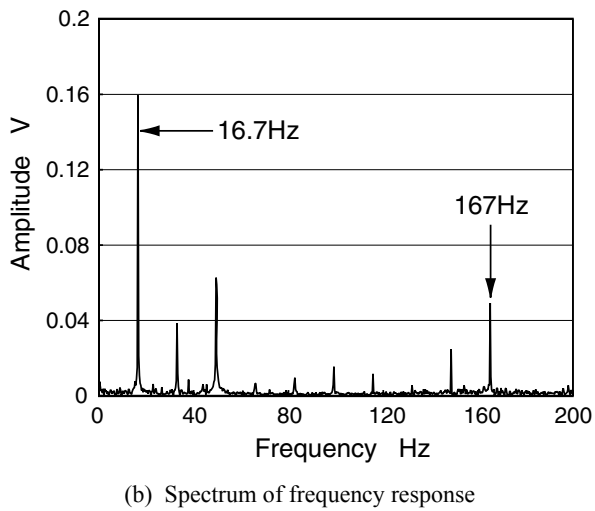
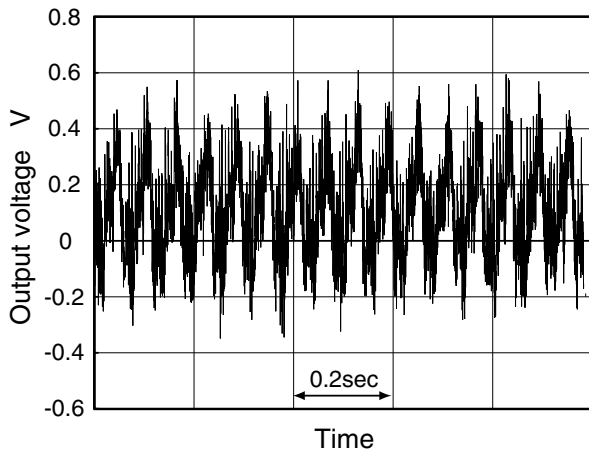


Fig. 5. Output of loadcell during end milling

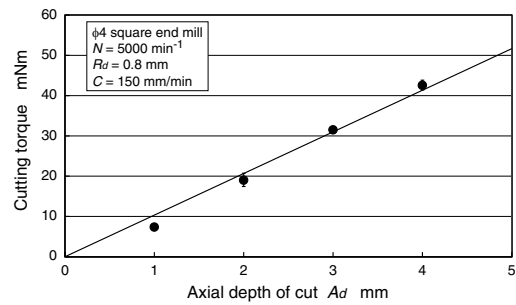
#### 4. Results of Cutting Experiments

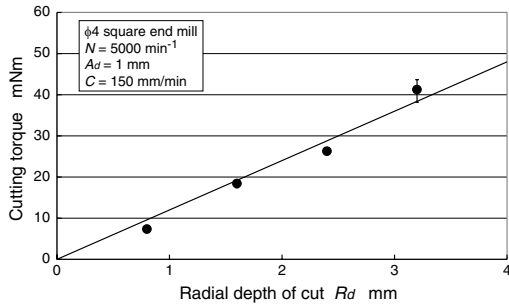
An end milling was carried out under various cutting conditions using three types of carbide end mill shown in Table 1 and cutting torque was measured in the method explained in §3. The material of the workpiece used was NAK55. All cutting conditions are shown in Table 1.

First, the end milling was carried out at a tool rotary speed  $N$  of  $5000 \text{ min}^{-1}$  with a variety of axial depths of cut,  $A_d$ , using a  $\phi 4$  square end mill. The results of torque measurement during the end milling are shown in Fig. 6. The cutting torque was measured five times under each  $A_d$  condition and the mean value and dispersion of five torques measured are shown. The measured cutting torque increased with  $A_d$ . The results of the torque measurement obtained by varying the radial depth of cut,  $R_d$ , and the feed speed,  $C$ , are also shown in Fig. 6. Similarly to  $A_d$ , the values of cutting torque increased with  $R_d$  and  $C$ .

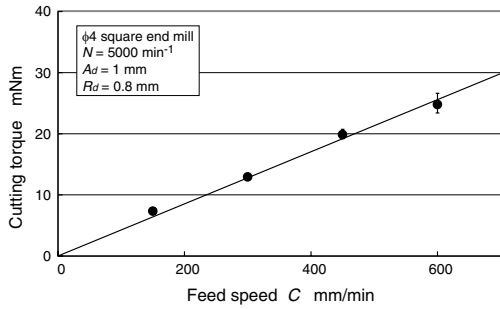
Table 1. Milling conditions

End mill	$\phi 4$ square	$\phi 2$ square	$\phi 2$ ball
Tool rotary speed [min-1]	5000, 20000	5000	
Cutting speed [m/min]	63, 251	31	
Axial depth of cut $A_d$ [mm]	1 - 4	0.5 - 2	0.25
Radial depth of cut $R_d$ [mm]	0.8 - 3.2	0.1 - 0.4	0.3
Feed speed $C$ [mm/min]	150 - 1800	150 - 600	
Workpiece	NAK55		
Coolant	Dry		
Type of milling	Up cut		



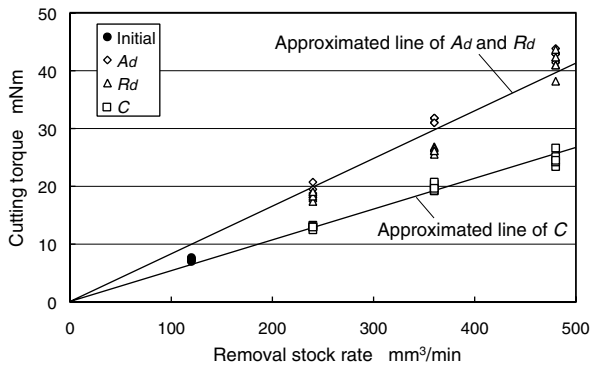


(b) Changing radial depth of cut

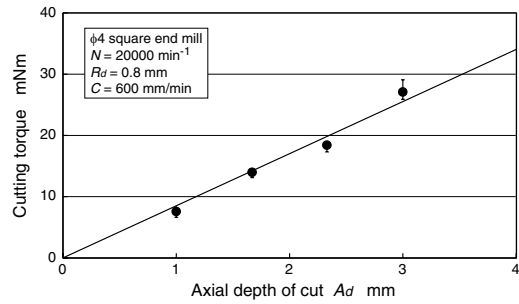


(c) Changing feed speed

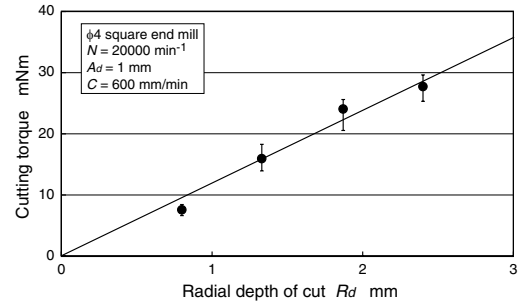
Fig. 6. Relation between cutting torque and milling condition



(a) Changing axial depth of cut



(b) Changing radial depth of cut



(c) Changing feed speed

torque owing to the increase in  $C$  is smaller than those owing to the increases in  $A_d$  and  $R_d$ . From these results, it was confirmed that torque could be measured despite different tool rotary speeds. Figure 10 shows a summary of the results shown in Figs. 7 and 9. When end milling at the same removal stock rate is carried out, the cutting torque in high-speed cutting, in which the tool rotary speed is high, is small. As generally known, this is because the volume of removal stock per revolution decreases when tool rotary speed is increased. Although calibration on the basis of the comparison using the dynamometer was not carried out, such a quantitative comparison is possible, showing the effectiveness of this measurement method.

Fig. 7. Relation between cutting torque and removal stock rate using  $\phi 4$  endmill ( $N=5000$ )

Figure 7 shows the relationship between the removal stock rate and the cutting torque, which was obtained from the results shown in Fig. 6. The result of the measurement at  $A_d = 1$  mm,  $R_d = 8$  mm and  $C = 150$  mm/min is also shown as an “initial” condition. The increased rate of cutting torque owing to the increase in  $A_d$  is almost the same as that owing to the increase in  $R_d$ . Compared with them, however, that owing to the increase in  $C$  is small. This result is in agreement with that in a previous report in which cutting resistance increases with an increase in  $C$  less than that in  $A_d$  or  $R_d$ . Similarly to the experiments shown in Fig. 6, experiments at  $N=2000$  min<sup>-1</sup> were carried out, as shown in Fig. 8. The results had tendencies similar to those in the case of  $N=5000$  min<sup>-1</sup>. Namely, the measured cutting torque increased with  $A_d$ ,  $R_d$  and  $C$ , and the increased rate of cutting

Fig. 8. Relation between cutting torque and milling condition

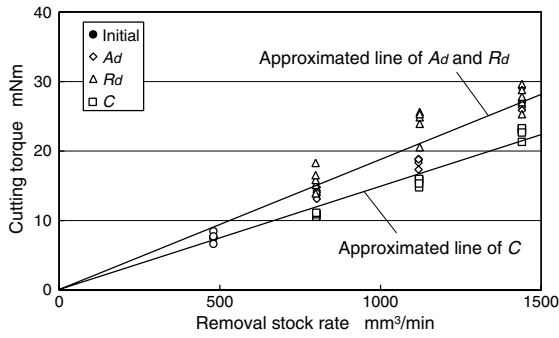


Fig. 9. Relation between cutting torque and removal stock rate using φ4 endmill ( $N=20000$ )

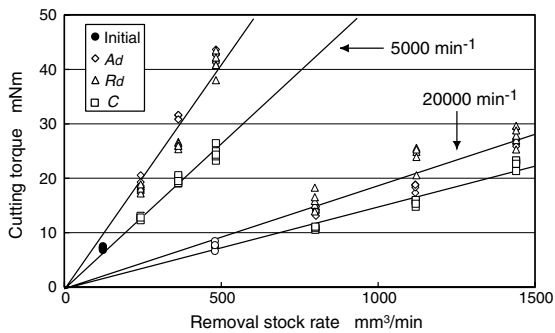


Fig. 10. Effect of high speed cutting

Next, the relationship between removal stock rate and cutting torque in the case of using the φ2 square end mill at  $N=5000 \text{ min}^{-1}$  is shown in Fig. 11. Compared with the case of the φ4 square end mill, even though a little large dispersion was observed, a result similar to that in Fig. 7 was obtained. That is, the measured cutting torque increased with  $A_d$ ,  $R_d$  and  $C$ , and the increased rate of cutting torque owing to the increase in  $C$  was smaller than those owing to the increases in  $A_d$  and  $R_d$ . From this result, it was confirmed that this measurement method is effective for the φ2 square end mill.

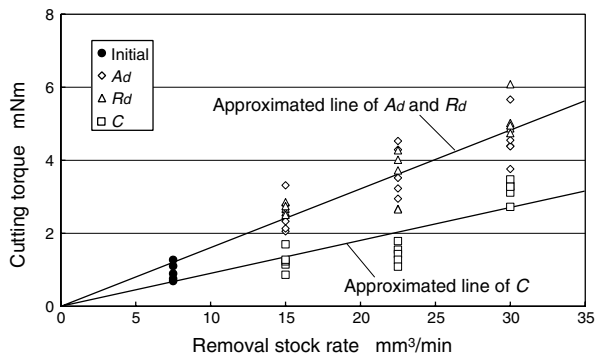


Fig. 11. Relation between cutting torque and removal stock rate using φ2 endmill ( $N=5000$ )

Figure 12 shows an example of the measurement of the cutting torque in the case of using a φ2 ball end mill at  $N=5000 \text{ min}^{-1}$ . Because the magnitudes of  $A_d$  and  $R_d$  are not proportional to the volume of removal stock in the case of end milling using the ball end mill, only  $C$  was varied. When  $C$  was increased, the measured cutting torque increased but the rate of increase in cutting torque decreased gradually. In that way, the characteristics of cutting torque during end milling in the cases of end mills with different shapes can be observed in this method.

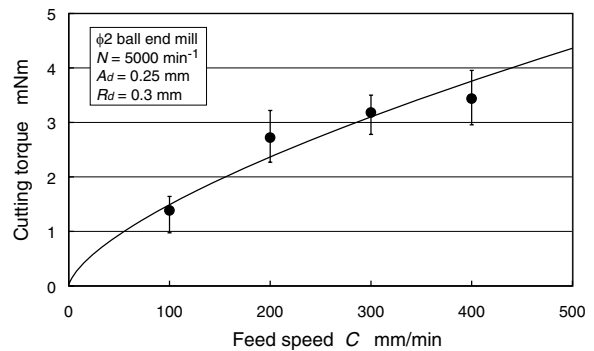


Fig. 12. Relation between cutting torque and feed speed using φ2 ball end mill

## 5. Conclusions

1. A method of measuring the cutting torque using a speed-increasing spindle was proposed and its viability was confirmed by experiments.
2. Using the torque measurement method proposed, it was experimentally demonstrated that the phenomenon that the higher the cutting speed, the smaller the cutting torque.

## 6. References

- [1] Tansel IN, Arkan TT, Bao WY, Mahedrakar N, Shisler B, Smith D, McCool M, (2000) Tool wear estimation in micro-machining. Part I: tool usage-cutting force relationship. *Int. J. Machine Tools & Manufacture* 40: 599-608
- [2] Masuda M, Nogami T, Mizobuchi A, Nagashima T, (2000) The behavior of tool life and cutting temperature on high speed milling of hardened alloy tool steels (in Japanese). *J. Japan Society for Precision Engineering* 66: 1745-1749
- [3] Miyaguchi T, Takeoka E, Masuda M, Iwabe H, (2001) Dynamic cutting force in high-speed milling using small ball end mill (in Japanese). *J. Japan Society for Precision Engineering* 67: 450-455

M. Yamanaka, S. Miyamura, K. Inoue

- [4] Oketani T, Mase Y, Nishigaki Y, Sase N, Fujii H, (1996) Development of a force sensing drill holder for fine drilling. J. Materials Processing Technology 56: 563-570
- [5] Kistler corporation, <http://www.kistler.com/>
- [6] KIM HY, Ahn JH, Kim SH, Takata S, (2002) Real-time drill wear estimation based on spindle motor power. J. Materials Processing Technology 124: 267-273
- [7] Stein JL, Wang CH, (1990) Analysis of power monitoring AC induction drive systems. ASME J. Dyn. Syst. Meas. Contr. 112:239-248
- [8] NT TOOL CORPORATION,  
<http://www.nttool.com/english/index.html>
- [9] SHOWA TOOL CO., LTD,  
<http://www.showatool.com/en/traction/index.html>



---

# Diamond Turning using Water Drive Spindle

Yohichi Nakao, Yuji Sagesaka  
Kanagawa University

Keywords: Water drive spindle, Diamond turning, Spindle runout, Bearing stiffness, Water hydrostatic bearing

## Abstract

A water drive spindle is operated by water flow for driving, supporting and cooling the spindle. The spindle performance, such as bearing stiffness and rotational accuracy, has been measured in this study. The experimental result indicates that the spindle has a comparable performance with the conventional spindle for diamond turning machines. The present paper shows that the diamond turned surface using the water drive spindle has optical quality with the surface roughness of 30 nm. This paper also discusses an influence of pressure pulsation of water flow on the spindle runout.

## 1 Introduction

In ultra-precision machining using diamond turning machine or diamond grinding machine, performance of spindle and machine tool slide are especially important. Since required machining accuracy is very precise, even small error in motion of the spindle and/or the slide often causes unacceptable machining results.

Final objective of the present study is to develop a spindle that is suitable to a diamond turning machine. In this case, important design concerns are rotational accuracy and bearing stiffness of the spindle to be designed. In the present paper, the performance of the water drive spindle is discussed and then the spindle is applied to the diamond turning test that was conducted by the spindle and designed linear slide system. Test results and problems to be considered are also presented.

In general, it is considered that air bearing is suitable to the spindle of diamond turning machine. Accordingly, a number of commercially available diamond turning machines use the air bearings for the spindle. In contrast, a disadvantage of the air bearings is that large stiffness cannot easily be obtained because of high compressibility of air. To cope with the problem of the low stiffness of the air bearing, oil hydrostatic bearings can also be used for the ultra-precision machines. However, it is not necessarily suitable for the bearing that is used for high-speed rotation because of high viscosity of oil.

Water is an alternative to the pressure media for the hydrostatic bearing of the spindle, because water has an intermediate property between air and oil, that is an incompressible fluid with low viscosity. In the previous

study<sup>[1]</sup>, a water drive spindle has been proposed and then developed. A feature of the water drive spindle is that it uses water not only for the pressure media of water hydrostatic bearings but also for working fluid to drive the spindle and for cooling media to cool the spindle. Fundamental performance, such as output power and relationship between supplied flow rate and rotational speed, has been presented<sup>[2]</sup>. In the present paper, bearing stiffness of the water hydrostatic bearing and spindle runout, which will affect on the machining results, are investigated experimentally. In addition, an influence of pressure pulsation on the spindle motion is also discussed. In this study, a linear slide system for in-feed and cross-feed motions was also designed so that diamond cutting tests by the water drive spindle can be conducted. Performance test results of the slide system are presented prior to the results of diamond turning tests.

## 2 Water Drive Spindle

A structure of the water drive spindle is illustrated in Fig. 1. The spindle rotor is supported by the water hydrostatic bearings in the radial and axial directions and it has several flow channels inside the rotor. In order to lead water into the rotor, relatively large channels in the radial directions are made in the middle of the rotor. Water flows inside the rotor, because the main channel passes through the center of the rotor in the axial direction and several flow channels in the radial directions are made for passing the water out from the main channel. The spindle is designed so as to use the water flow effectively to achieve the following three spindle functions.

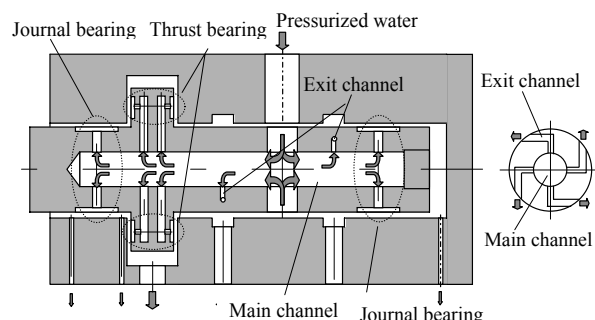


Fig. 1. Water drive spindle

**(i) Water drive motor** The spindle rotor has bend-shaped channels of small diameter, named as the exit channels, connecting between the main channel and the outer surfaces of the rotor. As illustrated in Fig. 1, the exit channels are located at two cross sections of the rotor. These exit channels enable the water flow to pass out from the inside of the rotor. The direction of the water flow changes significantly in the exit channels. Consequently, the torque used to spin the rotor is generated by the large change in the angular momentum of the water flow.

**(ii) Water hydrostatic bearings** Water hydrostatic journal and thrust bearings are designed as follows. Recesses are formed on the outer surfaces of the rotor. In addition, chokes of the bearings are located between the recesses and the main channel. Hence, the lubricant water can pass out from the main channel through the chokes and the recesses in the radial and axial directions. This generates the static pressure distributions around the rotor to support the rotor.

**(iii) Water cooling** In addition to the working and lubricant fluid, water can be used as a coolant, to minimize the thermal deformation of the spindle. The thermal conductivity of water is higher than that of oil and air, which is an advantage for achieving better cooling performance.

### 3 Machine Tool Slide Designed for Diamond Turning Tests

Figure 2 shows a machine tool slide that was designed for diamond turning tests. Performance of the water drive spindle in diamond turning processes was evaluated using this system. In the tests, the spindle was used as a work spindle, and then workpiece was fixed by a holding device at an end surface of the spindle rotor. Diamond face cutting was performed by a single crystal diamond tool. The cutting tool was mounted on the designed machine tool slide that gives the cutting tool cross-feed and in-feed motions. The cross-feed stage has a stroke of 150 mm. The stage was made by alumina ceramics, and is supported by air pressure. A wire driving system moves the air stage. In particular, in order to attain precise linear motion, the driving system was designed so that two pulleys, the drive pulley and idle pulley, are also supported by air bearings in the radial and axial directions. Therefore, there is no friction in the air stage system, except for the friction between motor shaft, drive pulley and driving wire. Two pieces of driving wires, the wire A and wire B, transform the motor torque into the drive force to the air stage. The drive pulley was designed so that it works as a reduction device, reduction ratio 4:1, as well.

Meanwhile, since short stroke is needed for in-feed motion, a piezo actuator was adopted for the in-feed stage, which was mounted on the air stage. The stroke of the piezo actuator is 40  $\mu\text{m}$ . The designed stages are controlled with a PC based controller. As a contrast, rotational speed of the water drive spindle can be adjusted by water flow rate, which was set manually by a flow control valve.

### 4 Performance of Water Drive Spindle

Non-repeatable runout (NRR) of the water drive spindle was measured in the axial and radial directions, respectively. For

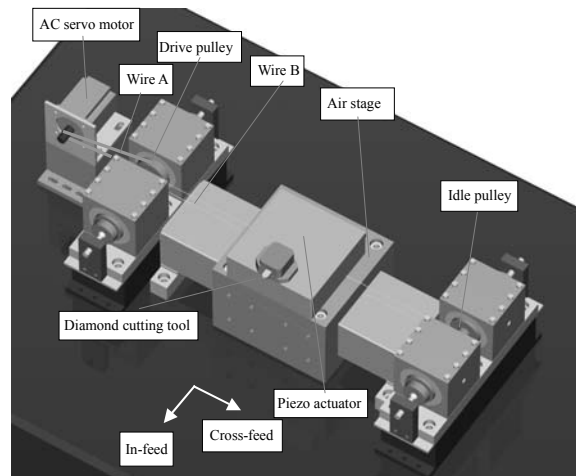
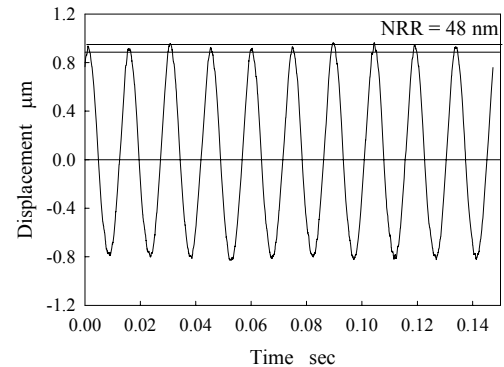
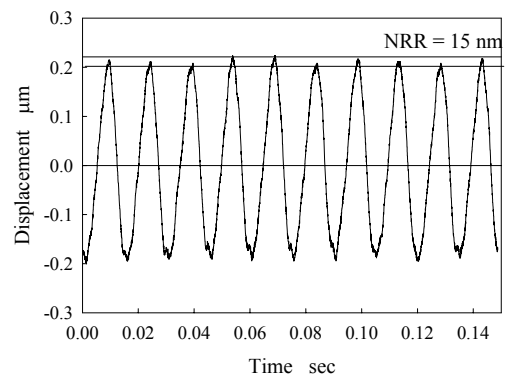


Fig. 2. Designed machine tool slide



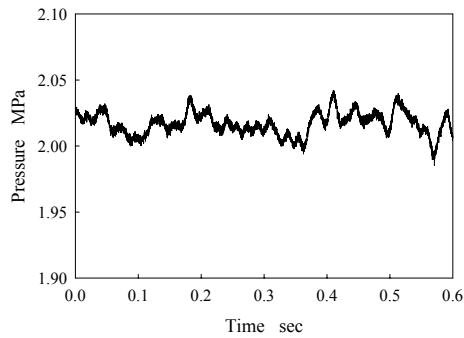
(a) Radial direction



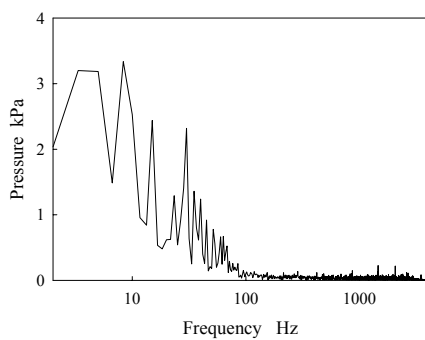
(b) Axial direction

Fig. 3. Non-repeatable runout

the measurements, a steel sphere was fixed on an end surface of the spindle rotor and then centered. The sphericity of the steel sphere is nominally less than 0.7  $\mu\text{m}$ . Spindle runout was then measured by a capacitive displacement sensor, which has a resolution of 2 nm. The displacement sensor was



(a) Time vs. Pressure



(b) Fourier spectrum

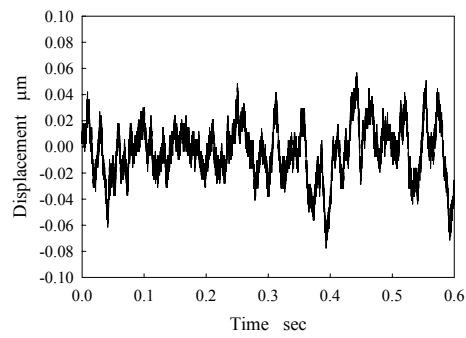
Fig. 4. Pressure pulsation

set so that it can measure runout in the axial and radial directions, respectively.

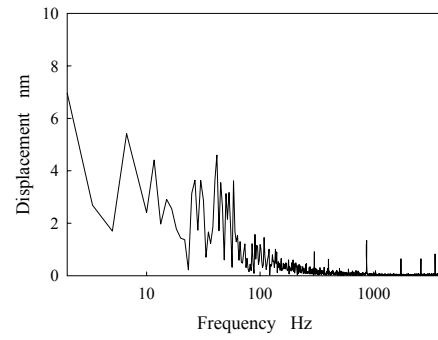
Figures 3 (a) and (b) show the output signal of the displacement sensor. In this case, the spindle speed was 4,000 rpm, the NRR of the water drive spindle were 48 nm and 15 nm in the radial and axial directions, respectively. In addition to the NRR, repeatable runout can be observed, as well. Magnitude of the repeatable runout is comparable to the sphericity of the steel sphere that was mounted with the spindle rotor. It is therefore considered that the repeatable runout was mainly caused by the influence of sphericity of the steel sphere. Further reduction in the spindle runout is expected by reducing off-balance of the rotor body.

In addition to the influence of off-balance of the rotor body on the spindle runout, it is also needed to consider an influence of pressure pulsation of water flow on the spindle runout. Therefore, relationship between the pressure pulsation and spindle runout was examined. In this experiment, radial motion of the spindle rotor was measured because the runout in the radial direction was three times larger than that of the axial direction, as shown in Fig. 3.

The experiment was conducted by supplying no working fluid for the exit channels of the spindle. Accordingly, the rotational speed of the spindle was set to 0 rpm, though the spindle rotor was supported by the water hydrostatic bearings. Therefore, this makes it possible to consider not the influence of the off-balance of the rotor but the influence of the pressure pulsation on the spindle radial vibration. Figures 4 (a) and (b) show the pressure pulsation and its



(a) Time vs. Radial vibration



(b) Fourier spectrum

Fig. 5. Radial vibration

Fourier spectrum. In addition, Figures 5 (a) and (b) show the spindle vibration and its Fourier spectrum.

The result shows that magnitudes of the rotor vibration are approximately 8 nm at 1.7 Hz and also 5.5 nm at 6.7 Hz. It can also be observed that pressure pulsation included considerable magnitude at the same frequencies with the spindle vibration. This indicates that the pressure pulsation affected the spindle vibration. Therefore, we need to consider the influence of the pressure pulsation on the spindle runout as well as the rotational error motion induced by off-balance of the rotor body, in order to reduce the NRR.

Bearing stiffness of the water drive spindle has already

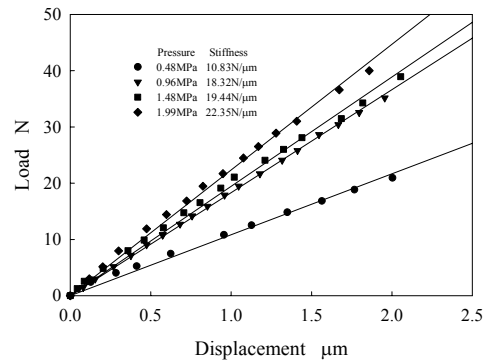


Fig. 6. Relation between load and displacement (Journal bearing)

been presented<sup>[3]</sup>. In order to increase the stiffness, to date, optimum dimensions of the restrictor used for the water hydrostatic bearing have been determined by changing the size of its holes. Then stiffness of the water hydrostatic bearing was re-investigated. Relationship between applied radial forces and the resultant rotor displacement is shown in Fig. 6. Stiffness of the journal bearing was measured as 29.4 N/ $\mu\text{m}$  at 2.3 MPa that is the rated pressure. In this experiment, the radial force was applied to the end of the rotor. By removing the moment effect induced by the radial force, stiffness of journal bearing becomes 374 N/ $\mu\text{m}$  for two journal bearings.

### 5 Performance of Stage

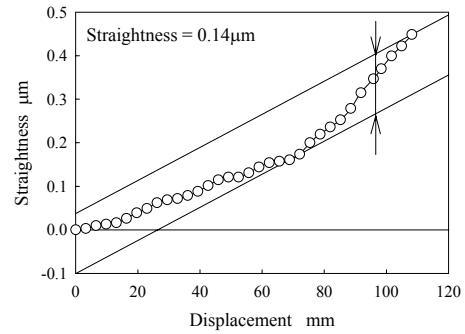
Performance of the machine tool slide, consisting of two stages for in-feed and cross-feed motions, can affect on the machining results, as well as performance of the spindle. Stiffness of the air stage designed for the cross-feed motion was therefore measured in vertical and horizontal directions. Measured stiffness in the vertical and horizontal directions was 234 N/ $\mu\text{m}$  and 110 N/ $\mu\text{m}$ , respectively.

Straightness of motion of the air stage was also measured by a level device. It is found that straightness of the air stage are 0.14  $\mu\text{m}$  in the vertical direction and 0.05  $\mu\text{m}$  in the horizontal direction as shown in Figs. 7 (a) and (b).

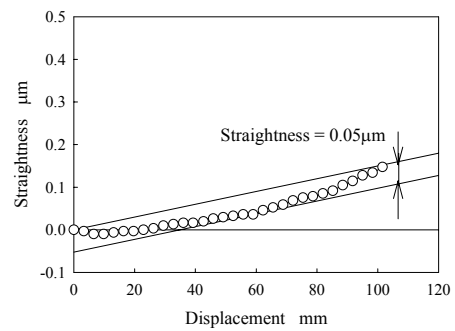
Positioning accuracy of the air stage system including control system was also investigated. Measured positioning accuracy of the stage is presented in Fig. 8. In this test, the motion of the stage was controlled by a minimum step signal from the controller. The result shows the resolution of the air stage is 0.32  $\mu\text{m}$ . A minimum controllable rotational angle of the AC servo motor used in the control system was  $7.2 \times 10^{-3}$  deg. Accordingly, theoretical positioning accuracy of the air stage becomes 0.31  $\mu\text{m}$  because a shaft of the AC servo motor is 7 mm in radius and reduction ratio 1/4. It is then verified that the actual positioning accuracy of the air stage is agreed with the theoretical estimation. It is considered that no-friction characteristics of the air stage including driving system contribute the fine motion. It is also expected that the positioning accuracy will be improved by using a servo motor with high rotational resolution. As well as the air stage, the piezo stage, which is used to generate the in-feed motion, was measured. The result shows the positioning accuracy of the piezo stage is 1.2 nm.

### 6 Diamond Turning Tests

Diamond turning tests were conducted using the water drive spindle and the stages. The designed machine tool system is illustrated in Fig. 9. In the cutting tests, a cutting tool used was a single crystal diamond tool that was set with a tool holder on the piezo stage. The diamond tool nose radius was 2 mm, the rake angle was 0 deg., and the clearance angle was 7 deg. Experiments were performed by supplying mist condition of kerosene. Machined surface was 20 mm in diameter. Workpiece materials used in the diamond turning were aluminum alloy (S3M), oxygen-free high conductivity copper (BsBM) and brass. In the diamond turning, spindle speed was set typically to 4,000 rpm. In addition, depth of



(a) Straightness in vertical direction



(b) Straightness in horizontal direction

Fig. 7. Straightness of air slide system

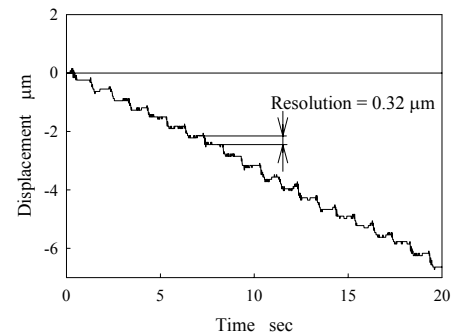
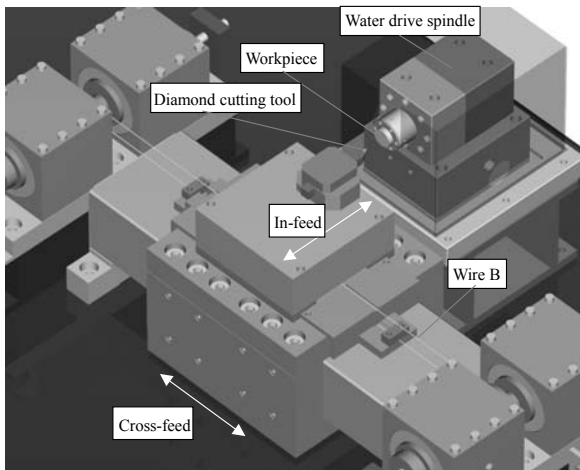


Fig. 8. Positioning accuracy of air slide system

cut and feed rate were set to 3-4  $\mu\text{m}$  and 3  $\mu\text{m}/\text{rev}$ , respectively.

Diamond turned surfaces are shown in Fig. 10. It is verified that optical quality surface can be machined. Surface of the workpiece of brass is given in Fig. 11, showing cutter marks with a constant interval. The interval is 3  $\mu\text{m}$ , which is the same as the feed rate. Surface roughness,  $R_a$ , of the workpiece was 0.03  $\mu\text{m}$ .

This machining result does not reach our goal. In order to improve the machining performance of the spindle, it is



**Fig. 9.** Diamond turning system designed for water drive spindle



**Fig. 10.** Diamond turned workpiece (Aluminum)

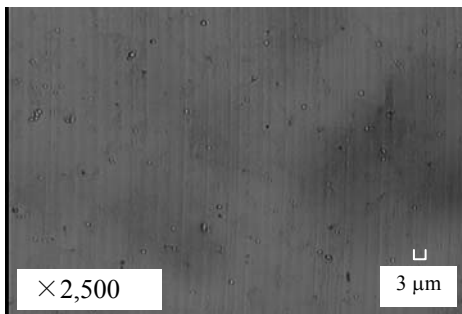


**Fig. 11.** Diamond turned surface (Brass)

needed to improve rotational accuracy of the spindle. This improvement will be attained by reduction of off balance of the rotor body as well as consideration of relationship between the pressure pulsation and the spindle vibration.

In the present paper, an influence of the pressure pulsation on the spindle motion has been examined in Sec. 4.

However, the measurement was made in order to examine an influence of the pressure pulsation on the water hydrostatic bearing. Therefore, in the experiments, the exit channels were plugged by a designed jig, resulting no-rotational motion of the spindle. In this case, since no water was supplied to the exit channels, flow rate was few l/min that is much less than the actual spindle operation. Consequently, in the actual spindle operation, the influence of the pressure pulsation on the spindle vibration would be remarkable. In order to improve the machining accuracy, therefore, further studies focusing on the influence of the pressure pulsation on the spindle rotation will be needed.

## 7 Conclusions

In the present paper, performance of the water drive spindle and machine tool slide were examined. Diamond turning tests were conducted using the developed water drive spindle as well as the machine tool slide designed. The following results are obtained:

- (1) Non-repeatable runout of the water drive spindle was 48 nm and 15 nm in the radial and axial directions, respectively.
- (2) Stiffness of the water hydrostatic journal bearing was 29.4 N/μm. However, by removing the moment effect of the spindle rotor, the stiffness becomes 374 N/μm.
- (3) Pressure pulsation of supplied water flow to the spindle affects the spindle vibration.
- (4) In order to apply the water drive spindle to the diamond turning, a machine tool slide was designed and then fabricated. Performance of the designed slide is examined. The results show that performance of the slide is comparable to that of commercial diamond turning machines.
- (5) Diamond turning tests were conducted for the aluminum, brass and copper alloy. As a result, optical quality surfaces were obtained. In addition, cutter marks with a constant interval were observed.

This research work is financially supported by the Grant-in-Aid for Scientific Research (C) of Japan Society for the Promotion of Science.

## References

- [1] Y. Nakao, M. Mimura and F. Kobayashi, Water Energy Drive Spindle Supported by Water Hydrostatic Bearing for Ultra-Precision Machine Tool, Proc. of ASPE 2003 Annual Meeting, pp. 199-202, (Portland, 2003-10).
- [2] Y. Nakao, F. Kobayashi and Y. Sagesaka, Performances of Water Energy Drive Spindle Supported by Water Hydrostatic Bearing, Proc. of ASPE 2004 Annual Meeting, pp. 241-244, (Orlando, 2004-10).
- [3] Y. Nakao and Y. Sagesaka, Water Drive Spindle for Diamond Turning Machine, Proc. of the third international conference on leading edge manufacturing in 21st century, pp. 449-454, (Nagoya, 2005-10).

---

# Development and Evaluation of a High-Precision Machining Center with Friction-Less Drives

Daisuke Kono<sup>1</sup>, Atsushi Matsubara<sup>1</sup>, Soichi Ibaraki<sup>1</sup>, Hisashi Otsubo<sup>2</sup>, Masaru Tsuboi<sup>2</sup>, Isao Oshita<sup>2</sup>

<sup>1</sup>Machining, Measurement, and Control Laboratory, Kyoto University, Kyoto, Japan

<sup>2</sup>YASDA PRECISION TOOLS K.K., Okayama, Japan

Keywords: Friction-less drive, Motion accuracy, Disturbance force

## Abstract

In order to realize high-speed and high-precision machining, the enhancement of the motion accuracy of NC machine tools is required. It is effective to minimize the friction forces imposed on drive systems to enhance the motion accuracy. From this viewpoint, we developed a high precision machining center using linear motors and hydrostatic guideways for its drive system. The disturbance forces on the developed machining center are measured to evaluate the fundamental motion characteristics. Contouring error trajectories in high-speed circular motions of small radii are also measured for the evaluation of roundness.

## 1 Introduction

For high-speed and high-precision machining with a small diameter endmill, the enhancement of the motion accuracy of NC machine tools and the compensation of machining errors caused by tool deflection are required to realize sub-micron-order geometrical and dimensional accuracy under high-speed machining. Because of the friction imposed on drive systems, it is generally difficult to enhance the motion accuracy to less than 1 $\mu$ m on the conventional machine tools using ball screws and rolling guideways. For sub-micron-order machining, machine tools with friction-less drive systems are promising. For example, a X-Y- $\theta$  table using linear motors and aerostatic guideways has been developed for a compact nano-machine tool [1]. However, aerostatic guideways do not have enough stiffness for the cutting of high hardness material with economical speed.

In order to solve this problem, we developed a high precision machining center using linear motors and hydrostatic guideways for its drive systems. Minimizing the friction force on the drive system enables higher motion accuracy in small and high-speed motions.

This paper presents the fundamental motion characteristics of the developed machining center. The disturbance forces on the developed machining center are measured and compared with friction forces imposed on the conventional ball screw drives. Furthermore, contouring error trajectories in high-speed circular motions of small radii are measured by using the cross grid encoder for the evaluation of roundness.

## 2 Developed machining center

### 2.1 Machine structure

Figure 1 shows the structure of the developed machining center. Table 1 shows the basic specifications. Since the machining center was developed to machine small-size and high-precision dies, the axis travels are set as 250-300mm. As high feedrates are not necessary for such short travels, the maximum feedrate is hold to 20m/s. The acceleration rate is set to 0.8G for shortening positioning times with less vibration.

Linear motors and hydrostatic guideways are selected for the drive systems to minimize the friction force. High-gain control using linear motors also enables higher motion accuracy in high-speed motions. At the same time, it is possible to obtain higher stiffness as well as fine surface roughness by using hydrostatic guideways.

Two motors are employed in each axis so that the motors can cancel the attraction forces. To reduce the table's angular motion (yawing motion), the guideways are located outsides of linear motors of each axis, which compose wide guideway systems. The structure of the machining center is the vertical type with a lower center of gravity, which can realize high stiffness and reduce complex vibration modes.

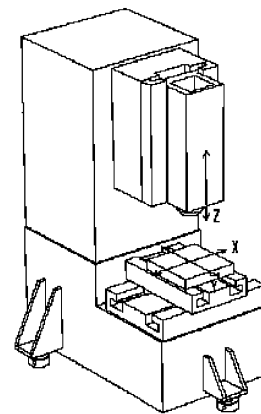


Fig.1 Schematic view of the developed machining center

**Table 1** Specifications of the developed machining center

X-axis travel	300mm
Y-axis travel	250mm
Z-axis travel	250mm
Rapid traverse rate	20000mm/min
Feedrate	10000mm/min
Drive motor	Linear motor
Guideway	Hydrostatic guideway
Scale resolution	7.8nm
Spindle speed	150-30000min <sup>-1</sup>
Spindle nose taper	NT No.30
Spindle bearing	TAC bearing

**2.2 Control system**

Figure 2 shows the block diagram of the drive system. The requirement of the motion accuracy of this machining center is 0.1-0.5μm. In order to meet this accuracy requirement in high-speed motions, nano-order resolution of position command and detection is necessary. Therefore, the position command is interpolated with 1nm step. The scale resolution is 7.8nm.

A digital filter(IIR filter) is installed in the current feedback loop, so that wider bandwidth of the servo loop can be obtained by reducing the resonance by the filter to set the servo gain higher.

On the machine structure mentioned in the previous section and the control system, the position loop gain can be set as high as  $K_p=140s^{-1}$ . The feedforward gain  $FF_p$  is set to 1.

**3 Measurement of the disturbance force on the drive system**

Since the drive systems of the developed machining center are noncontact drive systems, the friction force imposed on the drive systems should be 0N ideally. However, sources of disturbance force such as those from covers to protect the drive system and cableveyors to support cables exist. To evaluate them, the disturbance forces are measured when the table is driven along linear trajectories under a constant feedrate and a vortex trajectory under a variable feedrate. The motor currents are measured to evaluate disturbance forces. The driving forces of the motors are calculated by multiplying measured motor currents by the force constant of each linear motor. These driving forces are regarded as the disturbance forces on the drive systems in linear motions at constant feedrates. In a vortex motion, disturbance forces are calculated by subtracting estimated inertial forces from the driving forces.

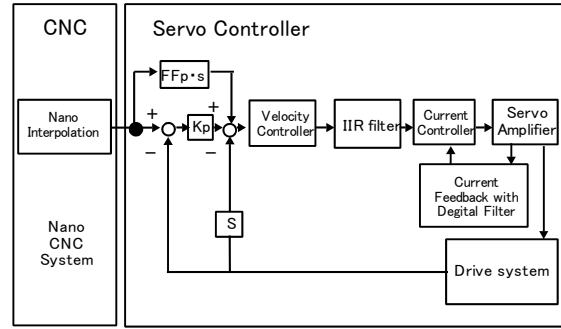


**Fig.2** Block diagram of the drive system

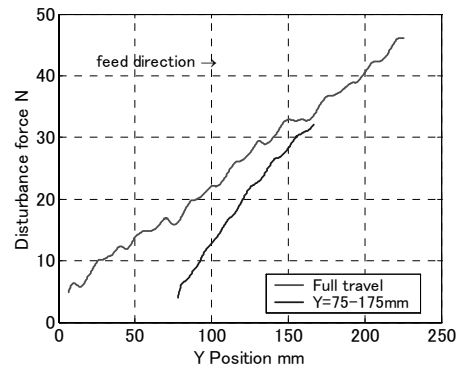


**Fig.3** Relationship between disturbance force and table position

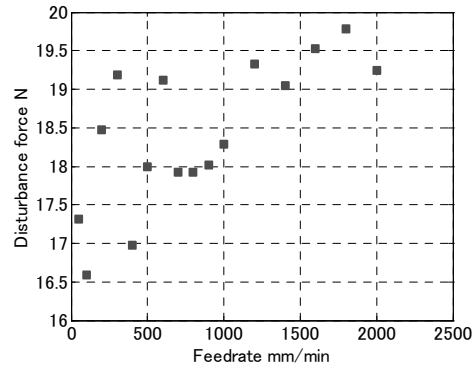


**Fig.4** Relationship between disturbance force and feedrate

**3.1 Disturbance force under linear motions at constant feedrates**

First, the disturbance force when the Y-axis is driven over the full travel ( $Y=10-240mm$ ) at 1500mm/min is measured. The solid line in Figure 3 shows the result of the measurement. It can be seen that the disturbance force increases gradually from 5N to 45N.

Second, we investigate whether the fluctuation of the disturbance force depends on the table position or not. The disturbance force when the Y-axis is driven between  $Y=75-175mm$  at the same feedrate (1500mm/min) is measured.

The dashed line in Figure 3 shows the result. In the result at  $Y=75-175\text{mm}$ , it can be seen that the disturbance force increases gradually from  $5\text{N}$  to  $32\text{N}$ . As shown in Figure 3, the fluctuation of the disturbance force depends on the table position, but it is not only factor to determine the disturbance force.

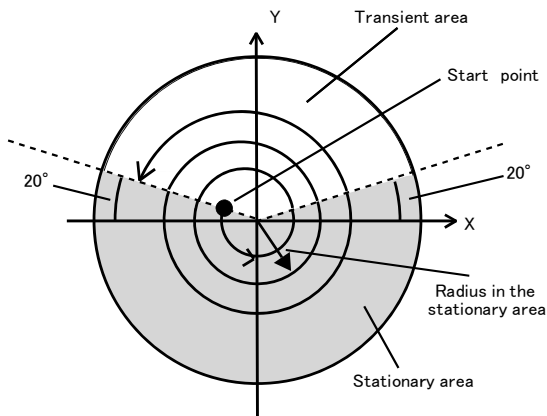
Finally, we investigate whether the disturbance force changes at different feedrates. Figure 4 shows the mean values of the disturbance force measured at each feedrate when the table is driven between  $Y=75-175\text{mm}$  at various feedrates from  $50\text{mm/min}$  to  $2000\text{mm/min}$ . As shown in Figure 4, the mean value of the disturbance force varies within  $3\text{N}$ , but the influence of the feedrate to the disturbance force is small.

**3.2 Disturbance force under a vortex motion with variable feedrate**

Figure 5 shows the tool center trajectory used in the measurement. In this figure, the start point is inside the vortex, and the vortex motion has 22 cycles. The stationary area and the transient area are defined as shown in the figure. While the tool center is in the stationary area, the feedrate is constant. While it is in the transient area, the radius and the feedrate gradually change to the values in the following stationary area. The feedrate changes from  $3800\text{mm/min}$  to  $1000\text{mm/min}$ , and the radius changes from  $2.2\text{mm}$  to  $8.7\text{mm}$ . These conditions are decided from the typical cutting conditions for dies and molds.

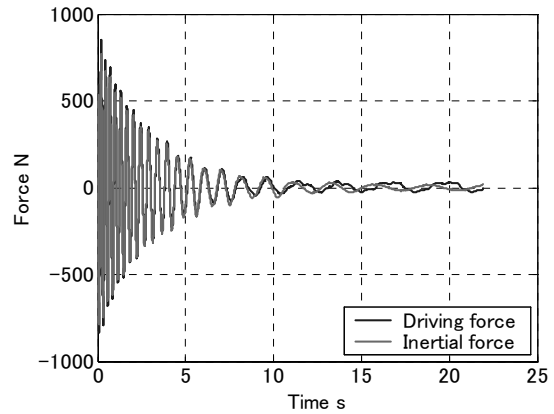
The estimated inertial force is calculated by multiplying the acceleration rate and the mass of the driven object for each axis. The acceleration rate is obtained by taking the second derivative of the position feedback signal. The mass is calculated from the design information of the machine.

Figure 6 shows the driving force of the motor and the inertial force in the X-axis drive. Figure 7 shows the disturbance force in the X-axis drive. Compared with the inertial force, the disturbance force is quite small. However, the disturbance force varies from  $0\text{N}$  to  $70\text{N}$ . As shown in Figure 7, the disturbance force decreases in the first 13 cycles and increases in the next 6 cycles and reaches stationary cycles after that.



**Fig.5** Vortex trajectory used in the measurement

For comparison, Figure 8 shows the disturbance force measured on a conventional machining center (medium-size machine) using ballscrews and rolling guideways. The pattern of the disturbance fluctuation shown in Figure 7 is different from that shown in Figure 8. This implies that the



**Fig.6** Driving force and estimated inertial force in the vortex motion

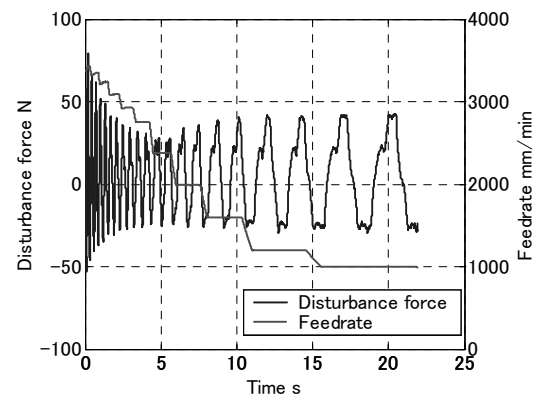


**Fig.7** Disturbance force and feedrate in the vortex motion

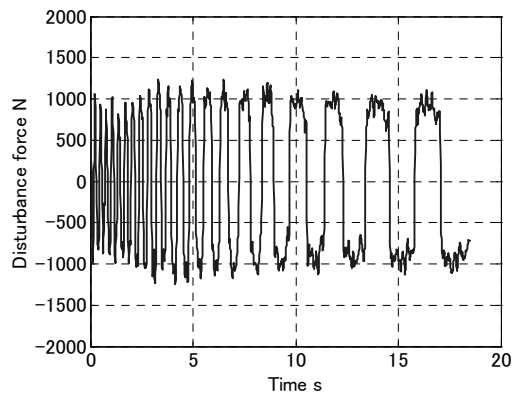


**Fig.8** Disturbance force in the conventional ballscrew drives



disturbance force observed on the developed machine is not completely caused by the Coulomb friction.

Two possible reasons are considered to explain this difference. The first reason is that the identification error of the mass of the driven object may generate the estimation error of disturbance forces. The second reason is that the cableveyors and/or the covers may disturb table motion.

#### 4 Measurement of the motion accuracy

As the disturbance forces in circular motion in the developed drive systems are estimated less than 50N and position loop gain is  $140 \text{ s}^{-1}$ , we can expect higher contouring accuracy in high speed motions. In order to evaluate the motion accuracy, high-speed circular motion tests in the X-Y plane with small radii are conducted. The measurement instruments is the cross grid encoder (KGM181 made by HEIDENHAIN). The nominal measurement accuracy of KGM181 is  $\pm 2\mu\text{m}/140\text{mm}$ , which is enough for circular motion tests with small radii. The measurement conditions are shown in Table 3. In each measurement condition, the drive table rotates three times clockwise. The measured trajectory data at the second cycle for each condition is selected as its feedrate is stationary. The measured X-Y data is transferred to r- $\theta$  coordinate, and average radius is calculated for radius compensation. By radius compensation, the roundness change due to the feed change is investigated.

**Table 3** Measurement conditions

Radius mm	Feedrate mm/min
0.6	465, 657, 805, 930, 1039
2.5	949, 1342, 1643, 1897, 2121
6.4	1518, 2147, 2629, 3036, 3394

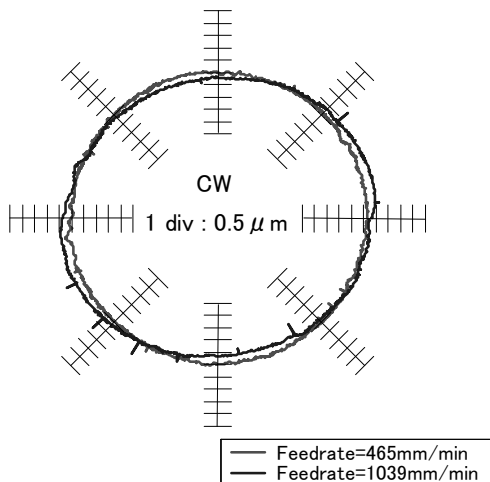


**Fig.9** Motion error traces (radius is 0.6mm)

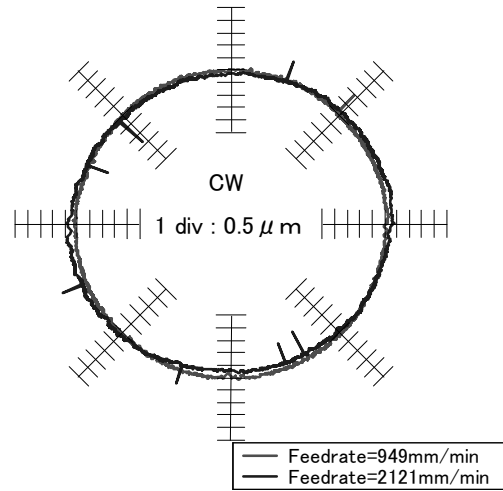


**Fig.10** Motion error traces (radius is 2.5mm)

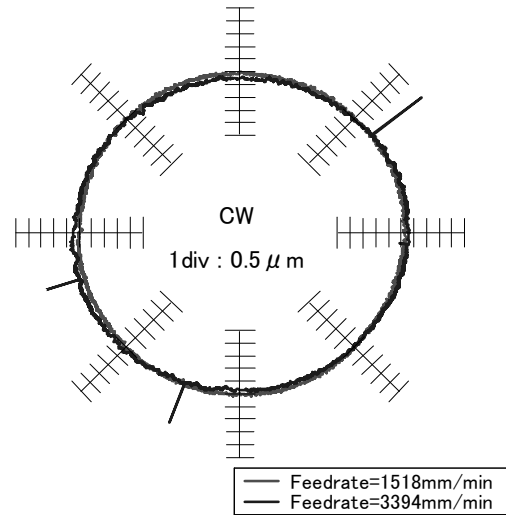


**Fig.11** Motion error traces (radius is 6.4mm)

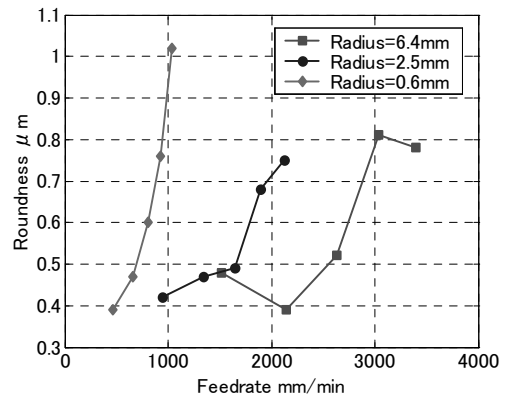


**Fig.12** Relationship between : feedrate and roundness

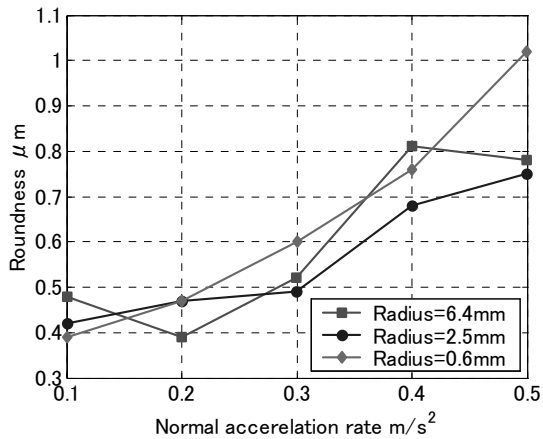


**Fig.13** Relationship between normal acceleration rate and roundness

Figures 9, 10, and 11 show measured roundness in different radii. Stick motion errors at the quadrant changes are not observed in each result. The spike type errors are seen in several results, but these are due to the noise in the measurement system. This noise is not considered in the following consideration. As the feedrate is getting faster, the roundness is getting larger due to the ellipse-type distortion in each radius condition. Directions of the major lines of the ellipses seem to be same.

Figure 12 shows the roundness change due to the variation of the feedrate. The roundness is less than about 1 $\mu$ m in all conditions and increases in parabolic curve in each radius condition. Figure 13 shows the relationship between the normal acceleration rate and roundness. As

shown in this figure, roundness depends on the normal acceleration rate, which suggests dynamic difference between X and Y drives [2].

## 5 Conclusions

A high-precision machining center using linear motors and hydrostatic guideways for its drive systems was developed. From the measurement results of the disturbance force and the roundness in high-speed circular motions on X-Y plane, the following conclusions are obtained.

1. Disturbance forces less than 70N exists in the machine drive.
2. Roundness in the circular motion is less than about 1.0 $\mu$ m.
3. Roundness of the motion trajectories depends on the normal acceleration rate, which suggests dynamic difference between X and Y drives.

## References

- [1] H.Shinno, H.Hashizume, H.Yoshioka, K.Komatsu, T.Shinshi, K.Sato, 2004, X-Y- $\theta$  Nano-Positioning Table System for a Mother Machine, Annals of the CIRP Vol.53/1,337-340
- [2] M.Hamamura, J.Fujita, Y.Kakino, A.Matsubara, 2003, The Influence of Inertia and Viscous Friction on Contouring Errors in Circular Interpolation, Journal of the JSPE, Vol.69, No.9, 1306-1311

# Machining Feature-Driven 5-Axis CNC Machine Tools

Satoshi Mitsui<sup>1</sup>, Fumiki Tanaka and Takeshi Kishinami<sup>2</sup>  
<sup>1</sup>Asahikawa National College of Technology and <sup>2</sup>Hokkaido University

Keywords: Machining feature, 5-axis machine tool, STEP, ISO14649

## Abstract

With a 5-axis CNC machine tool that is built according to the new CNC data model, a user considers information about only the motion of tools, such as the machining shape, the machining operation, and the cutting condition. The user can work without being influenced by the structure of the machine. Our studies aimed at two goals: making a CNC machine tool that directly inputs CNC model data and realizes 5-axis machining, and verifying the CNC model. Our CNC machine tool had a CNC-model data interpreter, built-in tool-path generation, and driving-axes control capability.

## 1 Introduction

For a manufacturing company to increase its competitive position, it must increase the efficiency of its production activity. To do so, the company must integrate and share

product information among its manufacturing systems. However, since the databases that the systems use differ in their schema structures, neither the sharing nor the exchanging of data is easy.

In the field of machining, ISO 14649 standardizes [1-3] a high-level NC language based on the CNC data model of the next-generation machining system, as shown in Figure 1.1. This CNC data model is based on the STEP product model (ISO 10303) and incorporates process plan information. The basis for the necessary information technologies is a set of data models and exchange formats. ISO 10303 meets all the requirements for product data. Now, research and development is progressing on the use of a 3-axis CNC machine tool that is constructed according to the CNC data model.

To maintain a good cutting state in machining a free-form surface, it is useful to have a 5-axis machine tool to which the orientation of a tool can be changed. Since the motion of a 5-axis machine tool is complicated, its dependence on CAM or a post processor is high. And, the machining data changes with the structure of the machine tool, so there is no compatibility of data among machine

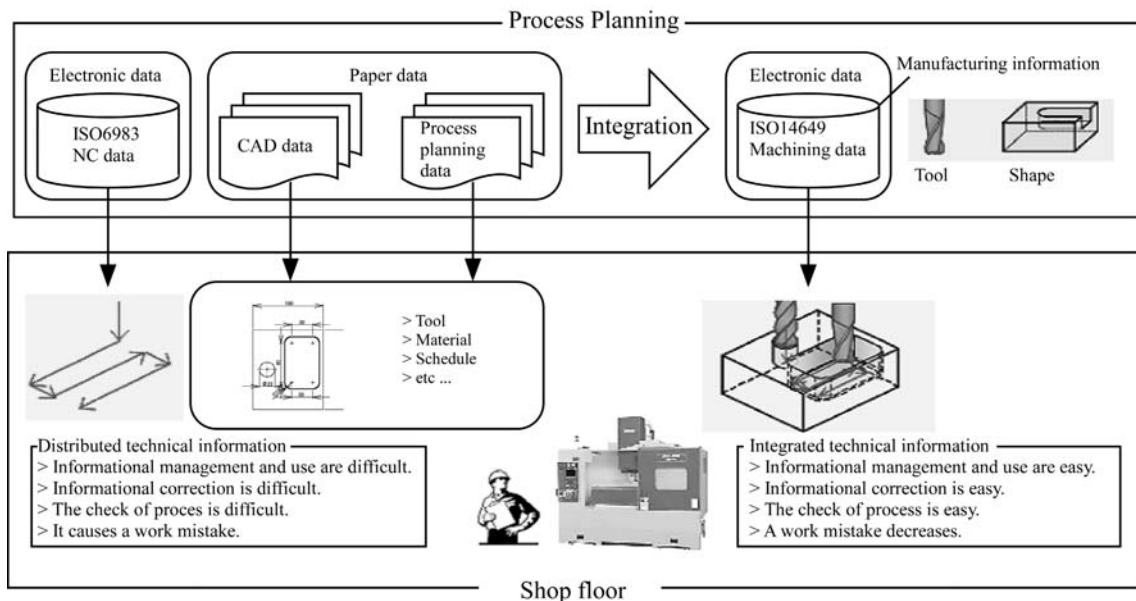


Fig. 1.1. Current state of product development and manufacturing

tools. Since the machining information that is based on ISO 14649 is related to the motion of a tool, compatibility of information can be gained among machines. Although 5-axis machining CNC data can be described by adding the orientation data of a tool to 2.5-axis machining data in ISO14649, there is only limited research and development about 5-axis machining. The 5-axis machine tool didn't have the benefit of CNC model based on ISO14649.

The purpose of our research is to verify the application and validity of the data model to the 5-axis machining system. Therefore, we develop the machining feature-driven model for a 5-axis CNC machine tool and conducted a verification experiment on the data model. The information is described by using Web/XML because the system is run in a networked environment and the users can be visible the information.

## 2 Background and purpose

To share and manage product information among production systems, a data model and an exchange format are required. In the field of machining, the current CNC language, or so-called M&G codes (ISO 6983), have been used since the 1950s. This language is a low-level one that mainly specifies the position and feed rate of a cutting tool. Because this CNC data changes according to the structure of the machine tool, there is no compatibility of data among the different types of tools.

ISO 14649 is a new standard for transferring data between CAD/CAM systems and CNC machines. The standard specifies information content and semantics for various CNC manufacturing processes. The CNC data model that is based on ISO 14649 can both describe the machining and working information and take this information into account in the management and operation method of a particular system. To close one of the gaps that would prevent a complete and continuous information flow, ISO 14649 provides a standard that includes an interface for a machining system with its working flow. Recently, a new and comprehensive language for CNC, called STEP-NC [4-9], has been developed by ISO TC184 SC1 and SC4. Since the new language accommodates various types of information that relate to work plans, geometry, technologies, tools, and materials, STEP-NC can perform various intelligent functions that cannot be performed by the conventional CNC based on ISO 6983.

With a 5-axis CNC machine tool that is built according to the new CNC data model, a user considers information about only the motion of tools, such as the machining shape, the machining operation, and the cutting condition. The user can work without being influenced by the structure of the machine. In 2005, the OMAC STEP-NC Working Group tested on 5-axis parts using AP-238 CC1 machine-independent tool paths. To verify the CNC data model and show its compatibility with an existing 5-axis machine tool, the test changed the data from the CNC data model to the G/M code in a postprocessor.

Our studies aimed at two goals: making a CNC machine tool that directly inputs CNC model data and realizes 5-axis

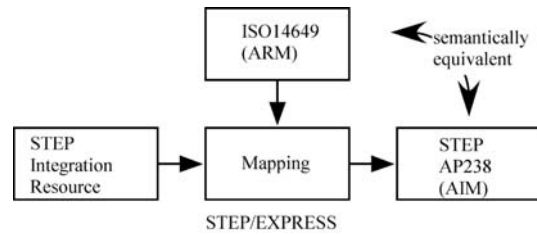


Fig. 2.1. STEP AP238 and ISO14649

machining, and verifying the CNC model. Our CNC machine tool had a CNC-model data interpreter, built-in feature driven tool-path generator, and driving-axes controller. ISO 14649 is ARM version on STEP (ISO10303) and STEP AP238 is AIM version of ISO14649 as shown in Figure 2.1. Therefore, STEP AP238 and ISO14649 is equivalent semantically. Since implementation of the CNC model based on ISO14649 is easy, we indicate the practicality to 5-axis machining of machining feature using its CNC model. We will use STEP AP238, if practicality is checked in future work. Improving 5-axis machining accuracy by determining the optimal tool-path control method, deviation compensation, and so on was not the object of our research.

## 3 Information content of ISO 14649

ISO 14649 is described as a structured, feature-based representation of the process plans for such manufacturing processes as milling operations and turning operations. The CNC data model to be formalized as ISO 14649 is based on

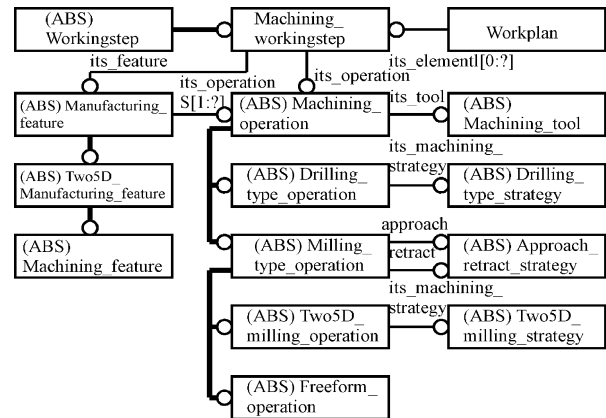


Fig.3.1. Structure of Workingstep

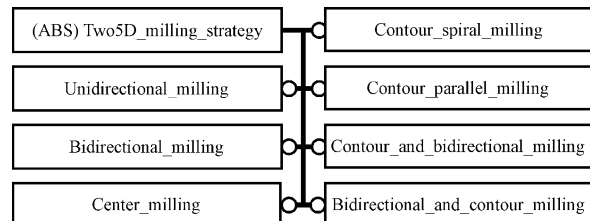


Fig. 3.2. Structure of Two5D\_milling\_strategy

the STEP product model (ISO 10303), which incorporates process-plan information. The CNC data model of ISO 14649 is composed of descriptions that relate to tasks, technologies, tools, and geometry.

Figure 3.1-3.4 contains a simplified abstract of the machining information as defined in Part 10 of ISO 14649. The figure shows geometry, manufacturing features, and operations defined separately and then combined into a Workingstep. As shown in figure 3.1, a Workplan has a list of the simple Workingsteps and can be processed. The Workingstep includes manufacturing features for 2.5D (two5D\_manufacturing\_feature) and 3D milling operations (region). Furthermore, each Workingstep defines which Operation must be executed, based on a geometrical item such as a machining feature (for example, planar face, step, boss, hole, pocket, or slot, as shown in figure 3.2) or a free-form surface. The Operation itself is one more piece of object-oriented machining information that contains technological information, tool information, and the process strategy as shown in figure 3.3. It is important that the tool-path specification in ISO 14649 is optional, unlike in the G&M codes where the tool path, in terms of driving axes, is the main information content. The orientation of a tool can be described by adding optionally a Tool\_direction the Operation. The Toolpath describes a feature's geometry and explicitly makes use of a predefined cutter contact, cutter location, and tool-orientation curve so that 5-axis machining can be performed using the CNC data model of ISO 14649. As shown in figure 3.4, in approaching or retracting the orientation of a tool can be described by the Approach\_retract\_strategy. In this way, 5-axis machining CNC data can be described by adding the orientation data of a tool to 2.5-axis machining data

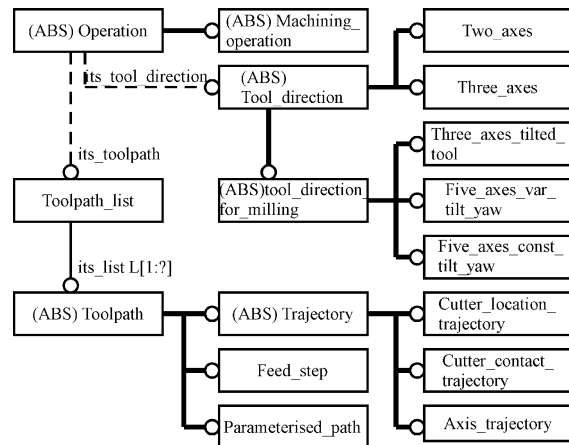


Fig. 3.3. Structure of Operation

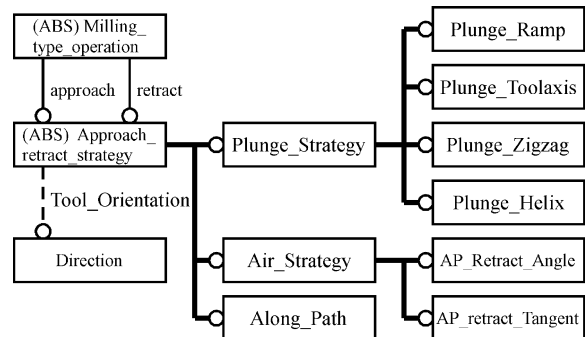


Fig. 3.4. Structure of Approach\_retract\_strategy

## 4 The 5-Axis CNC machine tool

### 4.1 Structure of the 5-Axis CNC machine tool

We developed a 5-axis CNC machine tool that uses the machining feature model based on ISO 14649. The structure of this machine tool combines a tool (A-axis) and table (C-axis) tilt. The machine tool contains a CNC-model data interpreter; the CNC kernel, with built-in tool-path and tool-orientation generation capabilities, executes the programmed Working\_step. Furthermore, the CNC machine tool computes the position and angle of the driving axes by coordinate transformation processing, and it controls the driving axes. These functions are built into a personal computer.

Since the CNC machine tool performs the coordinate transformation processing with the structure of itself, the CNC-model data does not need to take the structure of the machine into consideration. Therefore, the CNC model describes information related to the cutter contact position, and the data is compatible according to the standard.

Each driving axis of X, Y, and Z of this machine tool uses an AC linear motor in which high speed and high positioning are possible. An AC rotary motor is used for driving each A and C axis. The specification of the machine

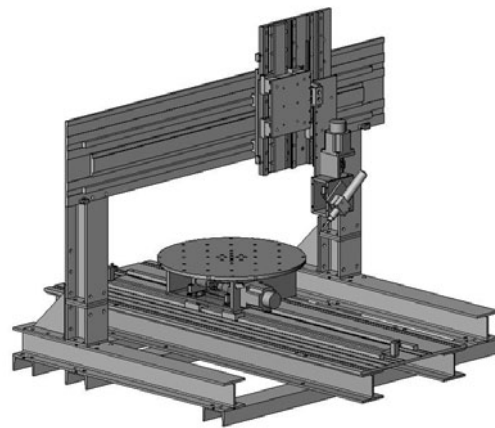


Fig. 4.1. Configuration of 5-axis machine tool

Table 4.1. The specification of the machine tool

Axis	Movable range	maximum speed
X	1000 mm	1000 mm/sec
Y	1000 mm	1000 mm/sec
Z	250 mm	1000 mm/sec
A	± 90 degree	150 rpm
B	360 degree	50 rpm

is shown in Table 1. This machine, which was made for the purpose of machining material such as wax and urethane foam, equips a brushless motor with a maximum speed of 25,000 rpm. The speed is manually set. Although the cutting position changes depending on the orientation of the tool, and the cutting speed changes along with it, the spindle speed control cannot be adjusted.

If the amount of movement and the speed of the driving axes are set on the motor control board that is built into the computer, the board will send a pulse to the motor driver and control the driving axes.

This machine is characterized by nonlinear kinematics due to the two additional degrees of freedom that control tool orientation. The function of the 5-axis control loops is to track the reference position commands that are generated by the interpolator. For each loop, the controller objective is to minimize the position error along the driving axes.

#### 4.2 Machine tool structure model

This machine has one rotary axis on the table and one on the tool. Figure 4.2 illustrate the coordinate frames of the 5-axis machine tool. The machine can be modeled as an open kinematic chain with several links connected in series by prismatic and rotational joints. The index 1 and 2 represent respectively initial and rotated state. Theremore the index a and c represent respectively the coordinate frames of A- and C- axis.

The cutter contact position vector of the workpiece coordinate frame is  $\mathbf{P} = [x, y, z]$ . The axis position vector is  $\mathbf{P}' = [X, Y, Z]$ . The tool orientation vector, represented by the unit directional vector  $\mathbf{N} = [i, j, k]$ , is determined by two rotary axes.  $\mathbf{S} = [X_s, Y_s, Z_s]$  is the work offset vector relating between the workpiece coordinate frame and the table coordinate frame. The tool vector is  $\mathbf{L} = [0, 0, L]$ , and the parameter L is tool length.

The A- and C-axis angle can be expressed as follows using the unit directional vector.

$$A = \cos^{-1} k, \quad C = \tan^{-1} i/j \quad (4.1)$$

The relationship between the axis position vector and the cutter contact position vector of the workpiece coordinate frame can be expressed as follows. Where  $R(\text{angle})$  and  $T(\text{vector})$  indicates respectively transformations of rotate and translate.

$$Q' = R(A) \cdot L \quad (4.2)$$

$$W = T(-L) \cdot T(Q') \cdot P' \quad (4.3)$$

$$W = T(-S) \cdot R(C) \cdot T(S) \cdot P \quad (4.4)$$

$$P' = T(L) \cdot T(-Q') \cdot T(-S) \cdot R(C) \cdot T(S) \cdot P \quad (4.5)$$

The function model of the target 5-axis machine tool can be derived easily by using equation (4.4) and (4.5), and can be explicitly expressed as follows. If the driving axis translate to  $\mathbf{P}'$ , the tool tip becomes the cutter point.

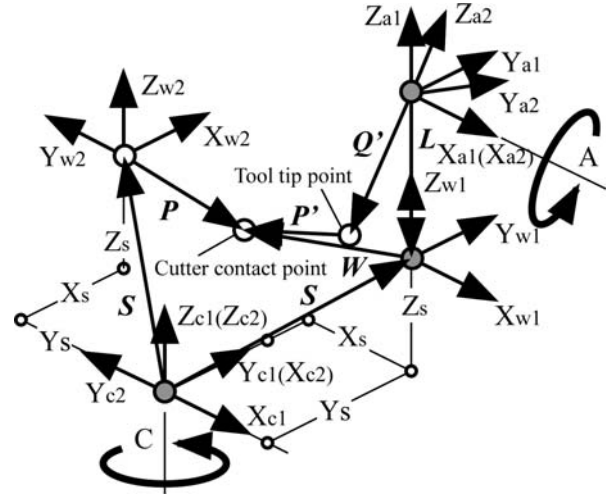


Fig. 4.2. Coordinate frames of 5-axis machine tool

$$\begin{bmatrix} X \\ Y \\ Z \\ 1 \end{bmatrix} = \begin{bmatrix} \cos C & -\sin C & 0 & X_s \cos C - Y_s \sin C - X_s \\ \sin C & \cos C & 0 & X_s \sin C + Y_s \cos C - Y_s - L \sin A \\ 0 & 0 & 1 & L \cos A - L \\ 0 & 0 & 0 & 1 \end{bmatrix} \begin{bmatrix} x \\ y \\ z \\ 1 \end{bmatrix} \quad (4.6)$$

The velocity of each five driving axes can be derived by using the jacobian matrix expressed as follows.

$$\begin{bmatrix} \dot{X} \\ \dot{Y} \\ \dot{Z} \\ \dot{A} \\ \dot{C} \end{bmatrix} = \begin{bmatrix} \cos C & -\sin C & 0 & 0 & -(x + X_s) \sin C - (y + Y_s) \cos C \\ \sin C & \cos C & 0 & -L \cos A & (x + X_s) \cos C - (y + Y_s) \sin C \\ 0 & 0 & 1 & -L \sin A & 0 \\ 0 & 0 & 0 & 1 & 0 \\ 0 & 0 & 0 & 0 & 1 \end{bmatrix} \begin{bmatrix} \dot{x} \\ \dot{y} \\ \dot{z} \\ \dot{A} \\ \dot{C} \end{bmatrix} \quad (4.7)$$

#### 4.3 Data processing procedure

The data processing procedure in the 5-axis CNC machine tool is shown figure 4.3. The ISO 14649-compliant CNC-model data is created by EDM (EXPRESS Data Manager). The data is described in either the STEP Part21 file format or the XML (eXtensible Markup Language) format. The CNC machine tool reads the data, interprets the contents by using MSXML according to DOM (Document Object Model), and carries out internal generation of the tool path and tool orientation for each Workingstep.

Linearization is performed, and the tool path and tool orientation are corrected so that collision of the tool is avoided and any deviation from the desired tool path is compensated for. The coordinate transformation processing is performed from the generated position or orientation of the tool, and the position, angle, speed, and angular velocity of the individual axis are computed. Coordinate transformation is for a tool- and table-tilt type. The five driving axes are controlled by the pulse series, which are generated based on this driving data. Thus, CNC machine tools that carry out the internal feature driven generation of tool paths and orientations and that control the driving axes

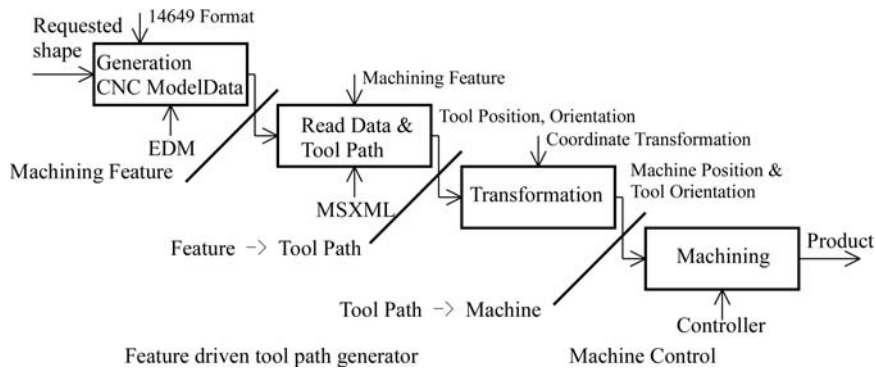


Fig. 4.3. Procedure of Data processing

may become the system that realizes highly precise machining at a high speed.

#### 4.4 Tool-path generation and interpolation

The 5-axis machining is characterized by nonlinear kinematics due to the two additional degrees of freedom that control tool orientation. As the result of the required machining accuracy is not satisfied.

Furthermore, to carry out linear movement on the work coordinate system while the tool changes orientation, the tool path on the machine coordinate system becomes a cycloid curve. An easy example of a machining error occurs when a tool (A-axis) and table (C-axis) tilt type compound machine tool has a tool path with a collision.

Generally, CAM or a post processor performs linearization processing, which gives a small rate of interpolation until the 5-axis machining accuracy is satisfied, and generates NC data based on this interpolation. For this reason, 5-axis machining has used an extraordinary amount of labor and time, so it is necessary to solve these problems.

In this CNC machine tool, the tool trajectory is represented by a linear interpolation. The interpolation function of this 5-axis machine tool generates the position and orientation of the tool for every sampling time of a control system. Furthermore, the position and velocity of each driving axis is computed by coordinate transformation processing, and the position and orientation of the tool are controlled. The 5-axis CNC machine tool constructs the functions of the tool-path generation and interpolation, so that the 5-axis machining can be independent of CAM system.

### 5 Practical results

To verify the CNC data model, the machining data of a hemisphere was created by EDM, and the hemisphere was machined with a 5-axis machine tool using the data. A hemisphere was created by machining a free-form surface, and Cutter\_Location\_trajectory described the instance of a tool path. The center position and ordinate of the tool were

```
ISO-10303-21;
.....
DATA;
#1= PROJECT('Hello world',#2,$,$,$);
#2= WORKPLAN($,#3,$,$);
#3= MACHINING_WORKINGSTEP($,$,$,#5,$);
#5= FREEFORM_OPERATION(#6,$,$,$,$,$,$,$,$);
#6= TOOLPATH_LIST((#7));
#7= CUTTER_LOCATION_TRAJECTORY($,$,$,$,$,#11,#3770,$);
#11= POLYLINE($,#13,#15,#17,#19,#21,#23,#25,#27,.....
#13= CARTESIAN_POINT($,(0,0,.5));
#15= CARTESIAN_POINT($,(0,.45,.5));
.....
#39= CARTESIAN_POINT($,(0,.44.8903823312964,-41.8609596769032));
#41= CARTESIAN_POINT($,(0,.44.5620632257812,-38.7372113989472));
.....
#3770= POLYLINE($,#3772,#3774,#3776,#3778,.....
#3772= CARTESIAN_POINT($,(0,0,1));
#3774= CARTESIAN_POINT($,(0,0,1));
#3776= CARTESIAN_POINT($,(0,-0.156434467332172,0.98768834023213));
.....
#7528= CARTESIAN_POINT($,(0,0,1));
ENDSEC;
END-ISO-10303-21;
```

Fig. 5.1. Description of CNC model data using STEP part 21

```
<machining_workingstep id="i944">
  <its_operation>
    <freeform_operation xsi:nil="true" ref="i946" />
  </its_operation>
</machining_workingstep>
<freeform_operation id="i946">
  <its_toolpath>
    <Toolpath_list xsi:nil="true" ref="i947" />
  </its_toolpath>
</freeform_operation>
<toolpath_list id="i947">
  <its_list ex:cType="list">
    <cutter_location_trajectory xsi:nil="true" ref="i948" />
  </its_list>
</toolpath_list>
<cutter_location_trajectory id="i948">
  <its_technology>
    <milling_technology xsi:nil="true" ref="i950" />
  </its_technology>
  <basiccurve>
    <polyline xsi:nil="true" ref="i953" />
  </basiccurve>
  <its_toolaxis>
    <polyline xsi:nil="true" ref="i4712" />
  </its_toolaxis>
</cutter_location_trajectory>
<milling_technology id="i950">
  <cutspeed>0.833</cutspeed>
</milling_technology>
<polyline id="i953">
  <points ex:cType="list">
    <cartesian_point xsi:nil="true" ref="i955" />
    <cartesian_point xsi:nil="true" ref="i957" />
    <cartesian_point xsi:nil="true" ref="i959" />
  </points>
</polyline>
```

Fig. 5.2. Description of CNC model data using XML

specified by Polyline, and Cartesian\_point described each point. The orientation of the tool was a unit normal vector. Figures 5.1 and 5.2 both show the processing of the CNC-model data of a hemisphere that has a diameter of 80 mm; the data is described by the STEP Part21 format and the XML format, respectively.

The 5-axis CNC machine tool input this data and machined urethane foam using a ball end mill with radius of 3 mm as shown in figure 5.3. The cutting conditions were a feed rate of 500 mm/min and a spindle speed of 25,000 rpm. The practicality of the CNC data model was thus able to be shown.

## 6 Summary

Our research, which used a machining feature-driven 5-axis CNC machine tool that is based on ISO 14649, verified the usefulness of the CNC data model for 5-axis processing and can be summarized as follows:

- A 5-axis CNC machine tool that directly inputs 5-axis machining data based on ISO 14649 and that can machine parts was manufactured. Then, it was verified that the CNC data model could fully equal that of existing 5-axis machining.
- Since the CNC-model data was information about a tool tip course, it could be used regardless of the structure of a machine. The advantage of the CNC data model in providing compatibility of data has thus been verified.
- By describing the CNC-model data using XML, data exchange was possible and Web representation was made easier.
- The 5-axis CNC machine tool constructed the functions of the tool-path generation and interpolation, so that the 5-axis machining could be independent of CAM system.

## Reference

- [1] ISO 14649 , (2004)Data model for Computerized Numerical Controllers Part 10: General Process Data
- [2] ISO 14649 , (2004)Data model for Computerized Numerical Controllers Part 11:Process Data Milling
- [3] ISO 14649 , (2004)Data model for Computerized Numerical Controllers Part 111:Tools for Milling Machines

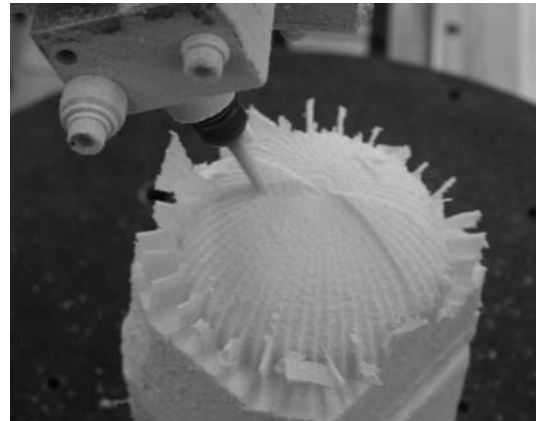


Fig. 5.3. Machining using CNC model data

- [4] M Weck, Jochen Wolf, Dimitris Kinitsts, (2001) STEP-NC - The STEP compliant NC Programming Interface: IMS Forum
- [5] S T Newman, R D Allen and R S U Rosso Jr, (2002) CAD/CAM solutions for STEP Compliant CNC Manufacture: Proceedings of the 1st CIRP(UK) Seminar on Digital Enterprise Technology: 123-128
- [6] S.H. Suh, B.E. Lee, D.H. Chung, S.U. Cheon, (2003) Architecture and implementation of a shop-floor programming system for STEP-compliant CNC: Computer-Aided Design 35: 1069-1083
- [7] X.W. Xu, Q. He, (2004) Striving for a total integration of CAD, CAPP, CAM and CNC: Robotics and Computer-Integrated Manufacturing 20: 101-109
- [8] A. Nassehi, S.T. Newman, R.D. Allen, (2006) The application of multi-agent systems for STEP-NC computer aided process planning of prismatic components: International Journal of Machine Tools & Manufacture 46: 559-574
- [9] O. Remus Tutunea-Fatan, Hsi-Yung Feng, (2004) Configuration analysis of five-axis machine tools using a generic kinematic model: International Journal of Machine Tools & Manufacture 44: 1235-1243
- [10] Chih-Ching Lo, (2002) A tool-path control scheme for five-axis machine tools: International Journal of Machine Tools & Manufacture 42: 79-88
- [11] W.T. Lei, Y.Y. Hsu, (2003) Accuracy enhancement of five-axis CNC machines through real-time error compensation: International Journal of Machine Tools & Manufacture 43: 871-877



---

# Selective Anodising Technologies for Obtaining Translucent Micro Structures

H.N. Hansen<sup>1</sup>, P. Møller<sup>1</sup>, C. Jarnov<sup>1</sup>, J. Staun<sup>1</sup>, J.P. Prichystal<sup>2</sup>

<sup>1</sup>Department of Manufacturing Engineering and Management, Technical University of Denmark,

<sup>2</sup>Bang & Olufsen Operations a/s

Keywords: Translucent metallic micro structures, selective anodising, processing

## Abstract

Anodising of aluminium is a well-known technology usually applied to surface treatment. With this technology a transparent layer of oxide is established on the surface of a workpiece. For the establishment of components in aluminium with certain light transmitting areas anodising was investigated. A process sequence involving application of photoresist, lithography using UV light, development of photoresist and subsequent anodising was established and investigated. The effect of various process parameters, material composition as well as pattern layout on the final component quality was investigated. It was found that with this technology it is possible to create light transmitting areas on aluminium workpieces consisting of either dot-like structures or continuous patterns.

## 1 Background

Information displays became invisible in inactive state when placed behind transparent or semi-transparent materials such as plastic or glass. Different technologies for obtaining such displays are commercially available including metallisation of plastic or glass in order to render the impression of a metal surface. However, if the bulk material were to be all metal very few known solutions exist. This has to do with the fact that extremely thin metal layers are required for light to penetrate. Theoretical models will result in transmission curves as illustrated in figure 1. It is obvious that obtaining metal layer thicknesses of the order of 10-40 nm is far from trivial using any technologies available today. Furthermore, regions with a wall thickness of this magnitude most probably will not be able to withstand any forces. The present paper addresses methods for obtaining such nano sized structures in bulk aluminium, in particular selective anodising.

Methods for obtaining translucent areas in bulk metal have so far all been based on material removal processes (ref. 1). Successful application of femto second laser machining combined with an advanced detection and process control loop has rendered good results as presented in ref. 2.

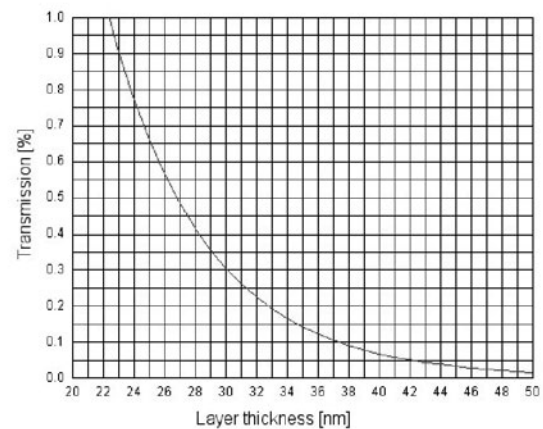


Fig. 1. Light transmission in metals (ref. 2).

Material removal processes applied to bulk aluminium displays result in a matrix of holes as illustrated in figure 2. In each hole the bottom aluminium layer has to be controlled precisely not to jeopardise light transmittance. Therefore a new process is suggested and tested that involves material transformation instead of material removal. This new process, selective anodising, is based on the fact that aluminium can be transformed into translucent aluminiumoxide by means of an anodising process. By applying the anodising process selectively a matrix of light transmitting pixels is created. Figure 3 illustrates the principle.

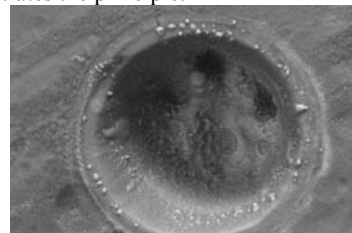
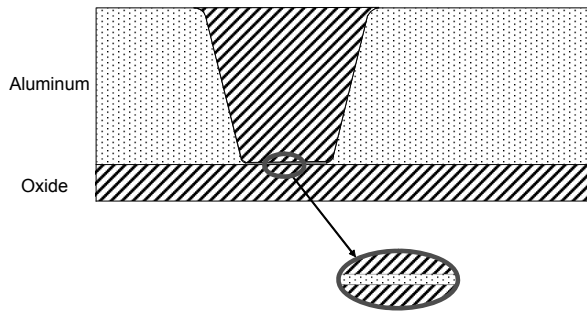


Fig. 2. SEM micrograph of hole obtained using femtosecond laser. Diameter approximately 40  $\mu\text{m}$  (ref. 2).



**Fig.3.** Principle of creating translucent areas in aluminium by selective anodising.

## 2. Selective anodising

Anodising of aluminium is a well-known technology usually applied to surface treatment. With this technology a transparent layer of oxide is established on the surface of a workpiece. The oxide layer (or coating) can be obtained on aluminium by using a wide variety of electrolytes with AC, DC or a combination of both voltage types (ref. 3). In order to generate an anodic layer the aluminium workpiece acts as the anode and another suitable metal or alloy acts as the cathode (ref. 4).

A new variant of the anodising process is proposed. A pre-machined workpiece in bulk aluminium is exposed to photolithography in this way covering defined regions of the surface with a polymer. Upon development of the photoresist, anodising is performed. Only those areas not protected by the polymer are subject to the anodising process, and in this way aluminium is transformed into translucent aluminiumoxide in selected areas only. The principle is illustrated in figure 4.

The process is heavily inspired by traditional microelectronics processes, where photolithography is used intensively in combination with both etching and electrodeposition (ref. 5). The new aspect is found in the fact that aluminium is a polycrystalline material (in contrast to silicon) and that the process control of the anodising process is less predictable than etching of semiconductors. Due to the nature of the anodising process, there is a limit as to how thick the bulk material can be. Operational experience shows that the thickness preferably has to be less than 0.5 mm if all aluminium is to be transformed into transparent aluminiumoxide. Therefore some kind of pre-machining is necessary. The four criteria initially set up to evaluate the selective anodising process are:

1. Translucency in aluminium. Can the desired translucent effect be obtained with the same result as proven with material removal processes?
2. Selectivity. Can the selectivity of the process be controlled in a sufficiently precise manner?

3. Mechanical stability. Can the microstructures obtained using selective anodising be included into assemblies?
4. Invisibility. Can the symbols be identified when the display is turned off?

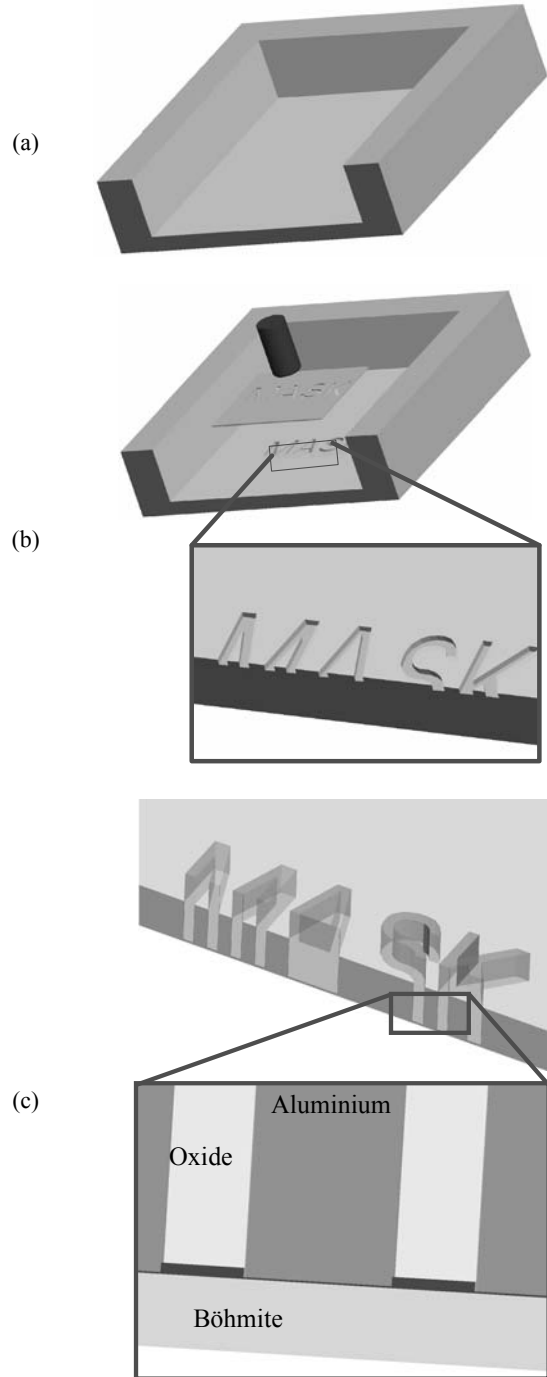


**Fig. 4.** Main steps of selective anodising: (a) Pre-machining, (b) lithography including development of resist, (c) anodising.

### 2.1 Translucency in aluminium

Three different aluminium foils were investigated with respect to the possibility of obtaining translucency through anodising (A: 90  $\mu\text{m}$  foil, 1000 alloy. B: 300  $\mu\text{m}$  plate, 5000 alloy. C: 11  $\mu\text{m}$  foil, 8111 alloy). Initial experiments confirmed the hypothesis that translucency in aluminium can be obtained by anodising using the above mentioned types of materials. For foil C conventional DC anodising could be used whereas pulsed anodising was necessary for the thicker foils and plate.

### 2.2 Selectivity

The first approach to selectivity was based on simple shadow masking using chemically resistant tape. This method of course was not able to render satisfactory resolutions so subsequently selectiveness was performed with UV-photolithography using a positive resist and a mask. By exposing the resist with a UV lamp through a mask it was possible to produce consistent structures with a diameter of 66  $\mu\text{m}$  and a center-to-center distance of 200  $\mu\text{m}$ . If dedicated lithography equipment were used, resolutions down to or even below 1  $\mu\text{m}$  is expected. The resist needs to be able to withstand sulphuric acid for a relatively long time (>10 minutes). Practical experiments showed that this particular requirement was hard to fulfill with the resist and lithography method used in the present investigation (figure 5).

Masks with varying pixel diameters from 50  $\mu\text{m}$  to 1000  $\mu\text{m}$  were produced and tested. Besides the pixel size also the total area exposed to the electrolyte had to be considered because the current density is one of the key process parameters. Figure 6 shows a 3D scan of the resist after development obtained using an optical profilometer. As expected, the resist is very uniform and the exposed areas of the aluminium is very close to the nominal dimensions of the mask.

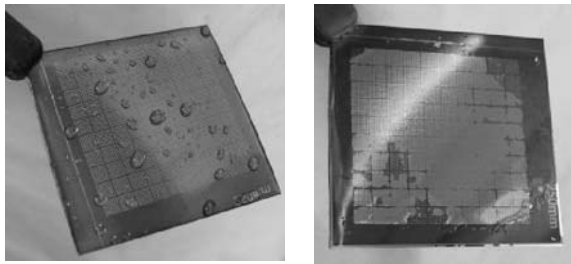


**Fig. 5.** Examples of resist adhesion in sulphuric acid. Left: good adhesion. Right: poor adhesion.

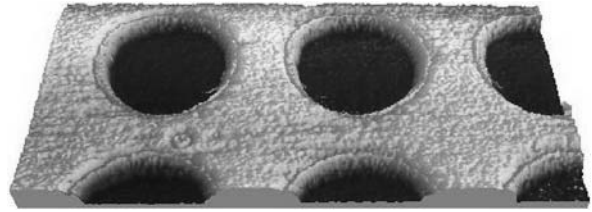


**Fig. 6.** 3D visualisation of photoresist on aluminium. Pixel size  $\varnothing$  500  $\mu\text{m}$  with a center distance of 1000  $\mu\text{m}$ . Thickness of the resist approximately 2.5  $\mu\text{m}$ .

The subsequent anodising process is another key step in obtaining translucency. Investigation of conventional DC anodising revealed that it was not possible to obtain translucency for the 90  $\mu\text{m}$  foil even with very long process times. However, for pulsed anodising translucency was obtained after approximately 60 minutes. After this period of time the oxide was observed to break down at the same rate at which it was formed. The anodising process requires electrical contact to the aluminium areas to be transformed. If the process is not entirely uniform, oxide may be formed at different speeds in different areas resulting in isolated “islands” of aluminium without electrical contact to the remaining aluminium. If this situation occurs the anodising process will stop locally and “islands” of non-translucent material may be observed in otherwise translucent oxide. This effect was primarily observed for pixel diameters larger than 500  $\mu\text{m}$ . Figure 7 shows translucency of anodised aluminium foil (type A) as observed in a light optical microscope using back light. No translucency has been achieved for the 125  $\mu\text{m}$  pixels. Furthermore islands of aluminium are observed in the 2000  $\mu\text{m}$  pixels. Figure 8 shows cross sections of 90  $\mu\text{m}$  anodised foils. Translucency is clearly observed because of the transparent oxide regions.

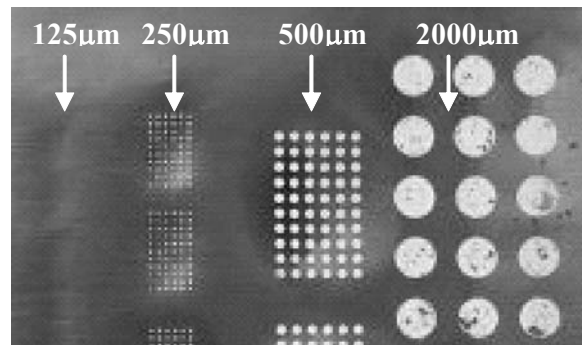


**Fig. 7.** Translucency obtained in 90  $\mu\text{m}$  aluminium foil. Numbers indicate nominal pixel diameters.

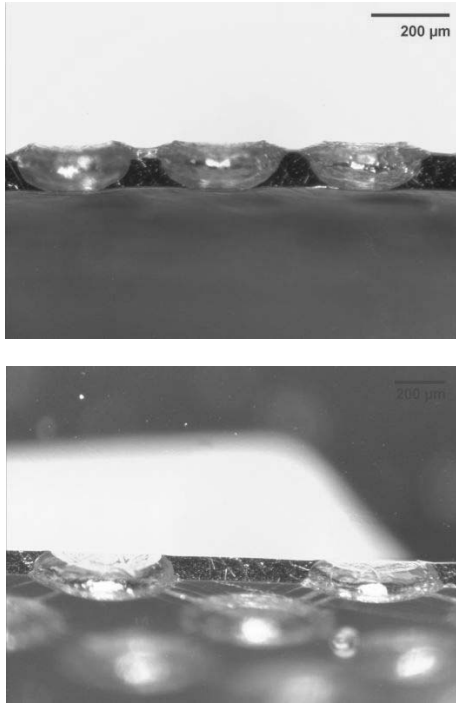


**Fig. 8.** Light optical microscope pictures of  $\varnothing$  250  $\mu\text{m}$  (top) and  $\varnothing$  500  $\mu\text{m}$  (bottom) pixels.

Figure 8 also illustrates that the oxide has a different crystal structure, and therefore it expands relatively to the aluminium. This results in local compressive stresses in the aluminium. Due to this fact different anodising strategies were investigated. First a process where the front side of the workpiece was anodised and sealed as in conventional anodising. This treatment was then followed by a selective anodising process from the back side. The result is illustrated in figure 9. The larger volume of the oxide is clearly seen. If the workpiece was anodised simultaneously from both sides, the result is seen in figure 10. Here the process has reached the phase where oxide is created and broken down at the same speed.

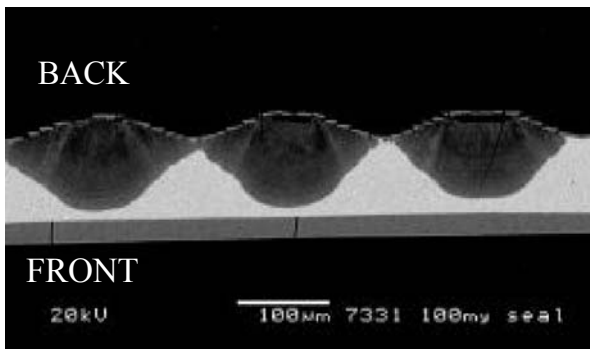


**Fig. 9.** SEM micrograph of cross section of selectively anodised aluminium. Initial thickness 90  $\mu\text{m}$ . Anodised from backside only. Frontside sealed. Dark material indicates oxide.

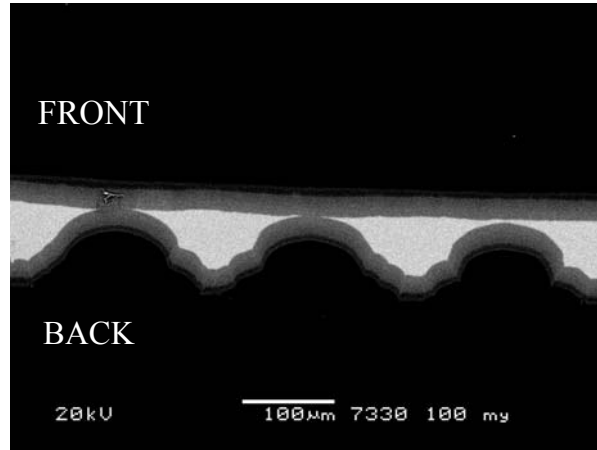


**Fig. 10.** SEM micrograph of cross section of selectively anodised aluminium. Initial thickness 90  $\mu\text{m}$ . Anodised from both sides simultaneously. Dark material indicates oxide.

### 2.3 Mechanical stability

Anodizing the whole way through from the rear side to the front can result in bulging areas on the front. Anodizing from the front in areas covering the bounded areas can reduce bulging. This is closely related to the discussion about oxide and aluminium volume. Figure 11 shows the effect of bulging on a 50 mm \* 50 mm plate of 90  $\mu\text{m}$  thickness. The amount of supporting aluminium not active in the anodising process is critical to the mechanical stability of the final product. Finite element simulations showed that the deformation could be significantly minimized by increasing the centre-to-center distance of the pixels. Furthermore, the thickness of the supporting oxide layer on the front side (e.g. figure 9) has a direct correlation to the mechanical stability of the workpiece.

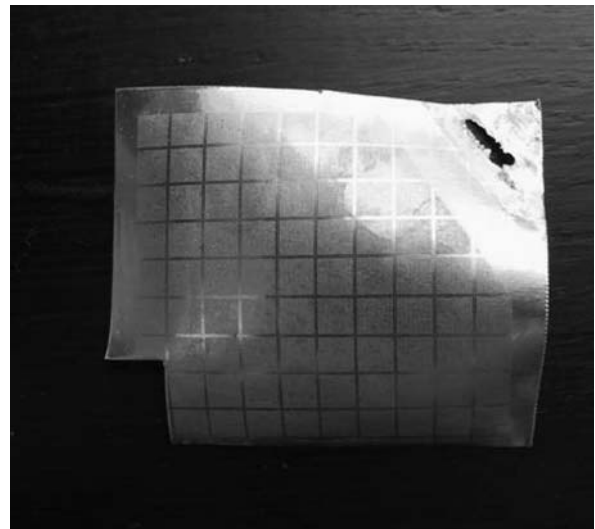


**Fig. 11.** Bulging as a result of selective anodising.

## 2.4 Invisibility

In order for the pixels to be invisible at the front side there needs to be a nanometer thin aluminium layer left or the transparent oxide “channels” need to be smaller than the resolution of the human eye (i.e.  $< 20 \mu\text{m}$ ). Invisibility was not fully achieved since some of the oxide channels and local deformations were visible to the viewer. Furthermore the macroscopic bulging of the thin foils clearly is a problem even though the single pixels might be invisible. Figure 12 illustrates the front side of the aluminium workpiece without and with backlight.

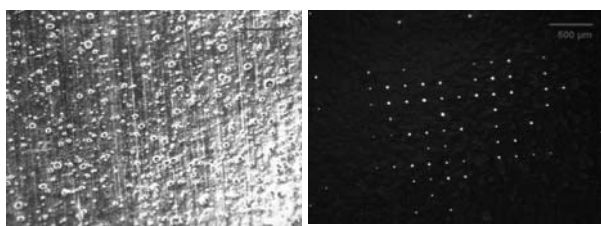


**Fig. 12.** Front side of selectively anodised workpiece. Anodised from back side only. Scale indicates  $500 \mu\text{m}$ . Left: front side as seen in microscope. Right: front side with backlight illumination.

## 3. Conclusion

For the establishment of components in aluminium with certain light transmitting areas selective anodising was investigated. A process sequence involving application of photoresist, lithography using UV light, development of photoresist and subsequent anodising was established and investigated. In particular the structures created in this way varied in size from  $\varnothing 60 \mu\text{m}$  to  $\varnothing 400 \mu\text{m}$  with varying centre distances. The effect of various process parameters, material composition as well as pattern layout on the final component quality was investigated. It was found that with this technology it is possible to create light transmitting areas on aluminium workpieces consisting of either dot-like structures or continuous patterns. The structure of the anodised layer before sealing is nano-scale and can be controlled by controlling parameters in the anodising process. With this technology it is possible to establish microstructures directly in an aluminium matrix consisting of a different material with different material properties. In this case the light transmittance was the desired property, but other effects may be achieved. The up-scaling of the technology to industrial production schemes is relatively easy.

## 4 References

- [1] Prichystal, J.P., Hansen H.N., Bladt H.H.; (2005) Invisible Display in Aluminum, Photon Processing in Microelectronic and Photonics, IV (Proc. of SPIE, Bellingham, WA, 2005), Vol.5713:215 – 222.
- [2] Bladt H., (2003) Read-out Device and Procedure for its Manufacture, International patent publication WO 03/019505 A1, World Intellectual Property Organization.
- [3] Juhl A.D., Eis M., Rasmussen J., Møller P., (1994) Review of Pulse Anodising. State of the Art of Square Pulse Anodising, ISFE 94, Birmingham, 28-30/3 1994.
- [4] Sheasby P.G., Pinner R., (2001) The surface treatment and finishing of aluminium and its alloys, Finishing Publications Ltd., Stevenage.
- [5] Senturia S.D, (2001) Microsystem design, Kluwer Academic Publishers, Boston, USA.

---

## Development of Rectangular Microblasting Nozzle

Masaki SUGIMOTO<sup>1</sup>, Toshihiko SHAKOUCHI<sup>1</sup>

<sup>1</sup>Graduate School of Engineering, Mie University

Keywords: Microblasting, Rectangular nozzle, Gas-solid two phase flow, Machining characteristics

### Abstract

In this study, in order to improve the machining productivity of microblasting, the new rectangular microblasting nozzle with a large aspect ratio is proposed and the flow characteristics and cutting performance are examined precisely by experimental and numerical analyses. The main results show that (1) setting the circular vane in the nozzle can diffuse particle flow uniformly at the nozzle exit, making the high cutting accuracy, (2) larger cutting efficiency is obtained comparing with the conventional circular blasting nozzle.

### 1 Introduction

The machining technology supporting the rapid growth industries, such as semiconductor, electrical and electronic industries, fine processing of drilling, grooving, etc, with high accuracy and high efficiency have been desired.

There are many methods for fine processes, such as wet and dry etching, laser, electronic discharge, ultra sonic and so on. However, microblasting process by particle laden impinging air jet flow with the order of 10 $\mu$ m particles has been increasing in order to process the brittle materials, such as glass or ceramic as the fine process for high accuracy and productivity<sup>[1]</sup> (where, the microblasting is the machining process that masks a micro fracture by impinging high speed gas-solid two phase jet flow with fine particle to workpiece surface. Pattern accuracy is controlled by a high accuracy photolithography resist masking.).

In microblasting, a circular nozzle is used commonly, yet it takes a large number of scanning times to process a wide area, and then a long machining time. Recently, use of a two-dimensional rectangular nozzle, slot nozzle, has been considered to process a large area with high efficiency<sup>[2],[3]</sup>. However, it is difficult to obtain uniform and high accuracy for cutting depth over nozzle width.

In this study, in order to improve the cutting performance of a microblasting nozzle, a new rectangular nozzle with a large aspect ratio is proposed and the flow characteristics and cutting performance are examined precisely by experimental and numerical analyses. As a result, the new rectangular nozzle showed a high accuracy over the nozzle width and high cutting performance.

### 2 Experimental apparatus and procedure

#### 2.1 Nozzle

Figure 1 shows the newly proposed nozzle and coordinate system. Figure 1 (a) represents the basic nozzle designed in reference to the conventional diffuser<sup>[4]</sup>. It has a two-dimensional rectangular nozzle with a large aspect ratio. Particle laden flow with a constant mass loading ratio is introduced into the nozzle inlet (square cross section : 32 $\times$ 32mm) from the circular pipe ( $\phi$ = 32mm) and then it diverges to 100mm width in  $y$  direction (expansion angle :  $\alpha = 38^\circ$  ). The width of nozzle outlet is constant at 100mm. The depth of nozzle ( $z$  direction) converges linearly to 1mm (nozzle height,  $h$ ) from nozzle inlet to the 10mm upstream of nozzle outlet, and the 10mm length from there to nozzle outlet is parallel to the 1mm depth (hereafter, it is called the 1st nozzle).

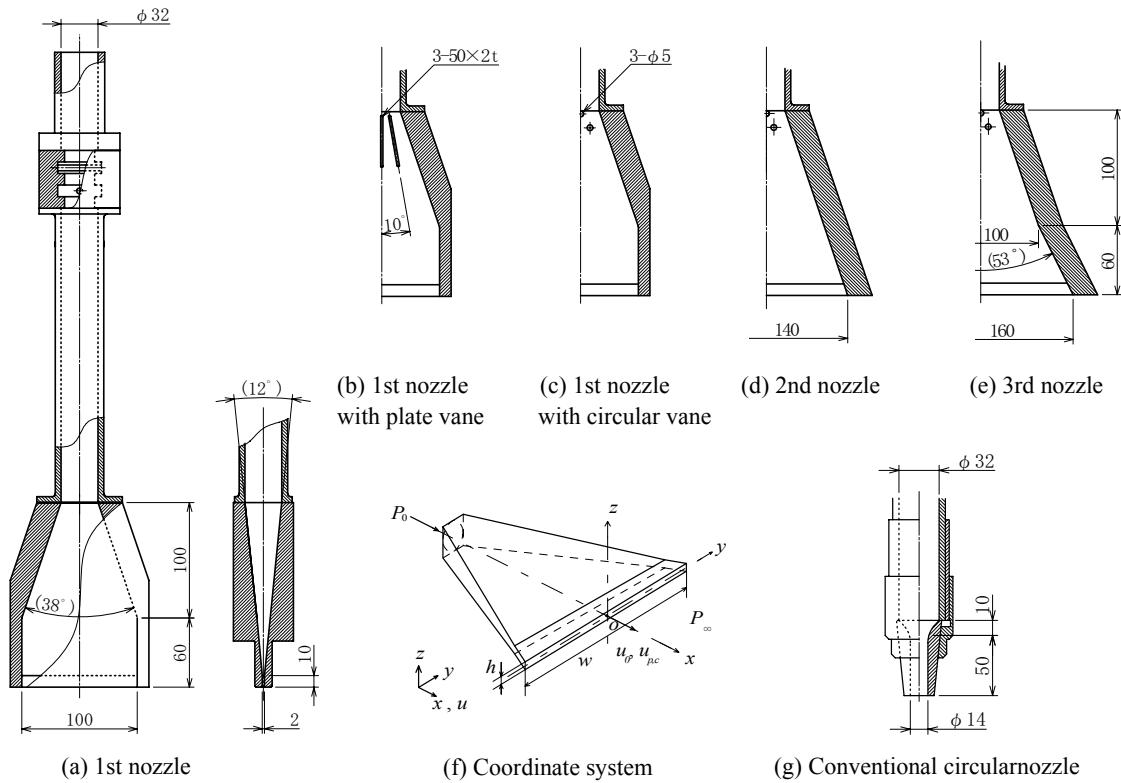
The other nozzles in Figs.1 (b) and (c) with the vane, plate or circular shaped vane are also used in order to make uniform air flow and to diffuse particle uniformly at the nozzle outlet. Figures 1 (d) and (e) show the new nozzles for uniforming more the air flow at the nozzle exit. Figure 1 (d), the 2nd nozzle, shows the nozzle with 140mm width at the outlet where diverges with a constant angle from nozzle inlet to outlet, and Fig.1 (e), the 3rd nozzle, shows the nozzle with 160mm width at the outlet which more expands linearly from the middle section of nozzle.

Figure 1 (f) shows some symbols and the coordinate system used. The coordinate origin  $o$  is located on the nozzle center at the outlet,  $x$ ,  $y$  and  $z$  coordinates are taken as in the downstream, width and height directions, respectively. The velocity of the  $x$  direction is  $u$ , maximum velocity at the nozzle outlet is  $u_0$  and centerline air and particle velocities are  $u_c$ ,  $u_{p,c}$ , respectively.  $p_0$ ,  $p_\infty$  are a supplied air pressure and ambient pressure, respectively.

For the purpose of comparison of the process efficiency, conventional microblasting nozzle with a circular outlet which is shown in Fig. 1(g) is also used.

#### 2.2 Experimental apparatus

Figure 2 shows the experimental apparatus. The air from air compressor is introduced into the nozzle after adjusting the flow rate by inverter for motor control and air valves and



**Fig. 1.** Details of new rectangular nozzle and conventional nozzle

then issued into the atmosphere from nozzle exit.

The jet temperature was measured by thermocouples set at inner pipe wall surface located in upstream of nozzle. The jet velocity  $u$  was measured by Pitot tube with 0.8mm inner diameter and the effect of compressibility of air was considered because the nozzle exit velocity was a little large, almost 200m/sec in most cases.

In incompressible region of  $0 < M < 0.3$ , the jet velocity can be calculated by  $u = (2gh \rho_{Hg} / \rho_a)^{1/2}$ .

In compressive region,  $M > 0.3$ , the relation of supplied pressure and total pressure can be expressed by

$$\frac{P_0}{P_s} = \left(1 + \frac{\kappa - 1}{2} M^2\right)^{\frac{\kappa}{\kappa - 1}} \quad (1.1)$$

Mach number can be obtained by measuring static pressure, and then the jet velocity is

$$u = M \sqrt{\kappa R T_a} \quad (1.2)$$

Microblasting experiment was carried out as follows. First, the glass plate as a work-piece is set normal to the mainstream of nozzle-plate distance  $H/h = 15 = \text{const}$ . Second, the screw type particle feeder feeds the particle constantly within  $\pm 5\%$  of feeding accuracy into the upstream of nozzle and then the particle laden jet with a uniform concentration is issued from the nozzle and impinges on a work-piece. Particle was collected in dust collector after impinges on the workpiece. The nozzle was fixed and work-piece was transferred in  $z$  direction with the 3mm/sec speed.

The cutting depth was obtained by measuring the cutting cross section by surface roughness measurements (Tokyo-Seimitsu, Surfcom-1400D). In this study, the accuracy of cutting depth was defined by the rate of difference of maximum and minimum cutting depths,  $d_{max}$  and  $d_{min}$ , in the area of 80% length  $l_i$  of cutting width.

$$\zeta = \pm \left( \frac{d_{max} - d_{min}}{2d} \right) \times 100 \quad (1.3)$$

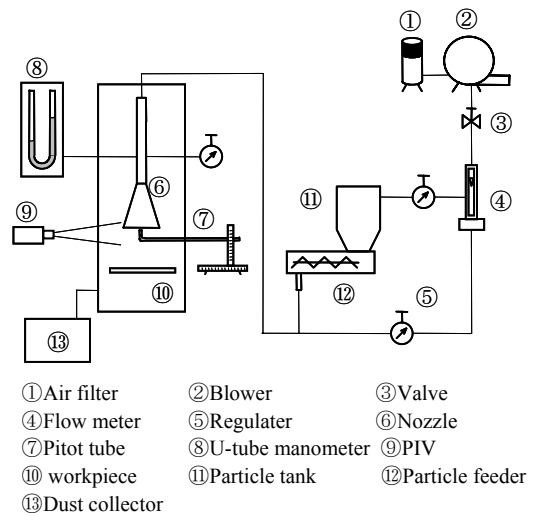


**Fig. 2.** Model of experimental apparatus

Removal weight of work-piece was measured by electrical precision balance (A&D, GR-200).

The behavior and velocity of particle was measured by particle image velocimetry, PIV (TSI, 2D-PIV System) to analyze image data by CCD camera. The Nd-Pb YAG laser (New Wave Research, Solo- I-15Hz, 15mJ/cm<sup>2</sup>) was used as a light source for flow visualization. The laser-light which expands like a sheet by cylindrical lens illuminates the flow field at time interval of 3.0μsec, and the CCD camera could take the flow region of 200×260mm. The velocity vector was analyzed in a small fragments divided into 1.0×1.0mm area. The average value of velocity vector of 50 times measurements (100 frames) was used as the experimental value. The errors of particle velocity measured by PIV were within 15%. In order to visualize the particle concentration, the reflection light from the particle was also taken by CCD camera.

### 2.3 Experimental condition

Table 1 shows the particle properties and experimental conditions. For the experiment of flow characteristics, measurements of velocity and pressure distributions, of air single-phase flow, the supplied air pressure at upstream of nozzle is  $(p_0 - p_\infty) = 0.025\text{MPa}$  ( $u_0 \doteq 200\text{m/sec}$ ). For microblasting experiment,  $(p_0 - p_\infty) = 0.1\text{MPa}$  ( $u_0 \doteq 360\text{m/sec}$ ), and for the experiment of machining efficiency  $(p_0 - p_\infty)$  was changed from 0.050 to 0.200MPa. The test particle was silicon-carbide abrasive (mean particle diameter : 25μm), and for the measurement of particle velocity vector the mass loading ratio was  $LR = 0.06 =$

**Table 1.** Experimental condition

Item	Data
Particle (abrasive)	JIS-GC#600 (Ave. dia. 25μm) Specific gravity : 3170kg/m <sup>3</sup>
Loading ratio, $LR$	0.06 ~ 0.38
Impinging distance, $H$	15mm ( $H/h=15$ )
Supplied pressure, $(p_0-p_\infty)$	0.025 ~ 0.200MPa
Workpiece transfer speed	3mm/sec
Workpiece material	Soda lime glass ( $\text{Na}_2\text{CaO5SiO}_2$ )

### Nomenclature

$C_D$ : Drag coefficient	$C_p$ : Pressure coefficient	$d_p$ : Particle diameter
$F_{b,i}$ : Body force	$H$ : Distance from nozzle to workpiece	$h$ : Depth of nozzle outlet
$k$ : Turbulence kinetic energy	$LR$ : Mass loading Ratio	$M$ : Mach number
$o$ : Coordinate origin	$P_s$ : Static pressure	$P_\infty$ : Atmospheric pressure
$P$ : Supplied power	$Q$ : Mass flow rate of air	$R$ : Universal gas constant
$p$ : Pressure	$T$ : Temperature	$t$ : Time
$S$ : Shape factor	$v$ : $y$ direction velocity component	$W$ : Removal weight of workpiece
$u$ : $x$ direction velocity component	$x, y, z$ : Coordinate system (see Fig.1.1)	$\varepsilon$ : Turbulence dissipation rate
$w$ : Width of nozzle outlet	$\delta$ : Jet width	$\kappa$ : Specific heat ratio
$d$ : Cutting depth of workpiece	$\eta$ : Cutting efficiency	$\tau$ : Relaxation time
$\zeta$ : Cutting accuracy	$\rho$ : Density	
$\mu$ : Viscosity	$\bar{\cdot}$ : Fluctuating value	
<i>Superscript</i>		
$\bar{\cdot}$ : Time average		
<i>Subscript</i>		
$a$ : Air	$c$ : Centerline	$0$ : Initial
$\max$ : Maximum	$\min$ : Minimum	$0.5$ : Half width
		$p$ : Particle
		$\text{Hg}$ : Mercury

$$\frac{\partial \rho}{\partial t} + \frac{\partial (\rho u_j)}{\partial x_j} = 0 \quad (1.4)$$

$$\frac{\partial}{\partial t} (\rho u_i) + \frac{\partial}{\partial x_i} (\rho u_i u_i) = -\frac{\partial p}{\partial x_i} + \frac{\partial}{\partial x_j} \left\{ \mu \left( \frac{\partial u_i}{\partial x_j} + \frac{\partial u_j}{\partial x_i} \right) \right\} \quad (1.5)$$

$$\begin{aligned} \frac{\pi}{6} d_p^3 \rho_p \frac{du_{p,i}}{dt} &= \frac{\pi}{8} d_p^2 \rho_a C_D |u_{p,i} - u_i| (u_{p,i} - u_i) \\ &\quad - \frac{\pi}{6} d_p^3 \frac{\partial p}{\partial x_i} + \frac{\pi}{12} d_p^3 \rho_a \left( \frac{du_i}{dt} - \frac{du_{p,i}}{dt} \right) \\ &\quad + \frac{3}{2} d_p^2 \sqrt{\pi \rho_a \mu} \int_{t_0}^t d\tau \frac{d\tau}{\sqrt{t-\tau}} + \frac{\pi}{6} d_p^3 \rho_p F_{b,i} \end{aligned} \quad (1.6)$$

const. and for microblasting experiment  $LR = 0.10 = \text{const.}$ , and for the machining efficiency the mass flow rate was  $m = 1000\text{g/min} = \text{const.}$  ( $LR = 0.15$  to  $0.38$ ).

In this study, in order to estimate the effect of various parameters on the flow characteristics in nozzle and jet flow, two-dimensional numerical analysis by the software (Fluid technology, CFD-2000) was introduced, which consists of mass and energy conservation laws expressed Eq.(1.4) and (1.5), respectively, and the standard  $k-\varepsilon$  turbulence model was used for turbulent flow analysis. Also, particle behavior was calculated by momentum Eq.(1.6).

The numerical analysis was carried out under  $(p_0 - p_\infty) = 0.025\text{MPa} = \text{const.}$

## 3 Results and discussions

### 3.1 Cutting performance of the 1st nozzle

Figure 3 shows the cutting cross section of the work-piece by the 1st nozzle. The cutting depth  $d$  takes a maximum value at the center of nozzle ( $y/h = 0$ ), and the cross section is a concave shape of almost symmetric with the center. In the left and right half of Fig. 4 show the particle concentration and particle velocity vector of the 1st nozzle, respectively, because the profiles were symmetric with the center. The particle concentration becomes maximum at the center and decreases to the nozzle edge, with almost no particle in the area of  $y/h < -35$ . The particle can't spread in  $y$  direction because of a large inertia force of



particle<sup>[5]</sup>.

The particle velocity distribution shows a convex shape with a minimum at the center and a maximum at the nozzle edge. The particle velocity decreases at around the center of nozzle by particle-particle and particle-wall interactions.

As a result, the cutting accuracy depends on the particle concentration and velocity. Therefore, in order to improve the cutting accuracy, a uniform particle concentration and velocity distribution in  $y$  direction are needed.

### 3.2 Uniformity of particle concentration

In order to diffuse the particle in  $\pm y$  direction uniformly, the plate and circular shaped vanes shown in Figs. 1 (b) and (c)

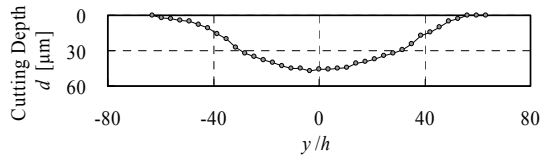


Fig. 3. Cutting cross section by microblasting (1st nozzle)

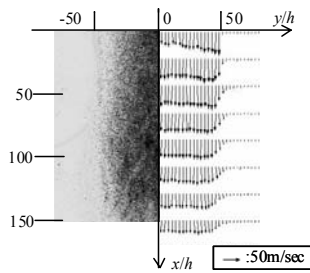
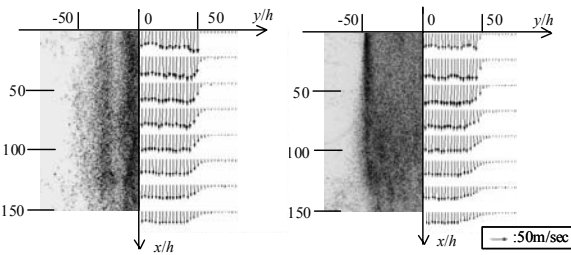


Fig. 4. Particle concentration and velocity vector of gas-solid free jet (1st nozzle)



(a) 1st nozzle with plate vane (b) 1st nozzle with circular vane

Fig. 5. Particle concentration and velocity vector of gas solid free jet (1st nozzle with plate or circular vane)

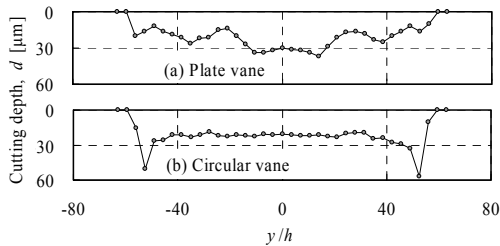


Fig. 6. Cutting cross section for each vane (1st nozzle)

were used.

Figures 5 (a) and (b) show the particle velocity vector and particle concentration for the 1st nozzle with plate and circular vanes, respectively. For the plate vane, the particle concentration decreases at the downstream of vane but it spreads in  $y$  direction a little more than the basic nozzle without vane. The velocity distribution also shows a non-uniform profile.

For the circular vane, the particle concentration shows a uniform profile except the nozzle edge area. The particle velocity distribution also shows a uniform profile.

Figures 6 (a) and (b) show the profile of cutting cross section ( $z=0$ ) for the nozzles with plate and circular vanes, respectively. Each cutting cross section shows a non-uniformity, and the shapes following the particle concentration. For the circular vane, the cutting accuracy shows  $\zeta = \pm 7.5\%$  at  $-40 < y/h < 40$ , however for the plate vane, it shows  $\zeta = \pm 60\%$  at the same region. It is clear that the circular vane has an advantage for diffusing the particle in  $y$  direction and cutting accuracy.

Then particle diffusion in  $y$  direction and uniformity result in improvement of cutting accuracy.

### 3.3 Uniformity of air velocity distribution and cutting performance

In this section, the relationships between uniformity of air velocity distribution and microblasting characteristics by the 2nd and 3rd new nozzles appeared in Figs. 1 (d) and (e) were considered.

#### 3.3.1 Pressure distribution (centerline)

Figure 7 shows pressure distributions on the centerline for each nozzle. Pressure distribution was shown by pressure coefficient  $C_p$ ,

$$C_p = \frac{P_s - P_\infty}{P_0 - P_\infty} \quad (1.7)$$

Pressure distribution shows almost same distribution for each nozzle and calculation value agree it well. The pressure has a constant value at  $x/h < -40$ , and it decrease rapidly to atmospheric pressure toward nozzle exit.

#### 3.3.2 Velocity distribution ( $x$ - $y$ plane, $z = 0$ )

Figure 8 shows the experimental results of velocity distribution ( $x$ - $y$  plane,  $z=0$ ) of air free jet for each nozzle. The velocity distribution for each nozzle shows a uniform one over the nozzle width at nozzle outlet, but it does not keep at the outsides of downstream.

The 1st nozzle shows a saddle-shaped velocity distribution that is known as general characteristics of a rectangular jet. For the 2nd nozzle, the velocity distribution does not show a saddle-shaped one and it has a wide uniform profile since it is extended at constant angle from nozzle inlet to outlet. The velocity near the edge of jet decreases gradually comparing with the 1st nozzle since it has the  $y$  direction component. For the 3rd nozzle, the maximum velocity appears again near the edge of jet. It depends on the separation of flow from the extended nozzle wall but the most wide uniform-profile is obtained. The 2nd and 3rd nozzles can give the uniform velocity distribution at  $0 < x/h < 15$  and  $30 < x/h$ , respectively.

3.3.3 Velocity distribution ( $x$ - $z$  plane,  $y = 0$ )

Figure 9 shows the experimental results and calculation of velocity distribution of air free jet. Jet issued from the nozzle exit indicates rectangular air velocity distribution at the nozzle exit, and it expands to  $z$  direction at downstream. All of air velocity distributions for each nozzle show same distribution on each cross section of  $x$ . Calculation value fits well.

3.3.4 Particle behavior

Figure 10 shows the particle concentration and particle velocity vector for the 2nd and 3rd nozzles. The uniform particle concentration can be seen over the nozzle width for the two nozzles since the circular vane was set in the nozzle. It is thought that the high concentration area near the nozzle edge shown in Fig. 5 (b) is diffused in  $y$  direction since nozzle outlet was extended.

For the 2nd and 3rd nozzles, the magnitude of particle velocity vector shows a uniform distribution results from uniform particle concentration same as the case of 1st nozzle and the direction indicate outer direction slightly, however 1st nozzle have inner direction.

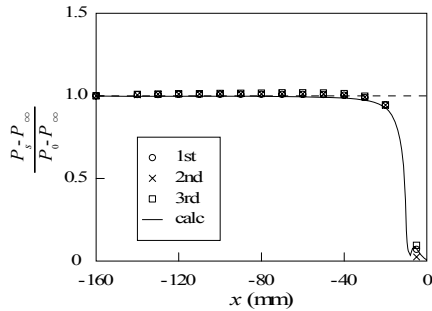


Fig. 7. Static pressure distribution

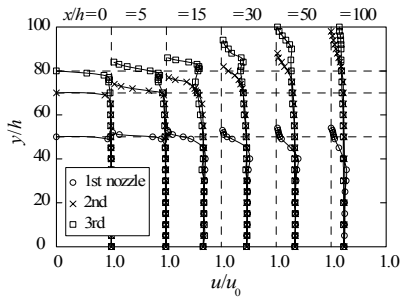


Fig. 8. Velocity distribution,  $u/u_0$  ( $x$ - $y$  plane,  $z = 0$ )

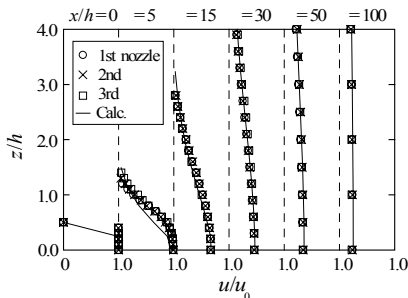


Fig. 9. Velocity distribution in  $z$  direction ( $x$ - $z$  plane)

3.3.5 Flow characteristics of particle laden free jet

Figure 11 shows the velocity distributions in  $x$ - $y$  plane ( $z = 0$ ) of particle and air for the 3rd nozzle. The velocity distribution of air is the results for a single-phase air jet flow at the same mass flow rate like as the particle laden free jet. The spread of particle corresponds to the air and it has wide and uniform velocity profile in  $y$  direction.

Figure 12 shows the centerline velocity distribution of air  $u_c$  and particle  $u_{p,c}$  obtained by the experimental and numerical analyses. The calculation condition is as follows. The particle shape is sphere and the particle-particle interaction and particle-nozzle wall interaction are not considered. The interaction between air flow and particle is not also considered. The maximum velocity  $u_c$  decreases to the downstream after the potential core region ( $0 < x/h < 5$ ). The transition region is in ( $5 < x/h < 9$ ) and the developed region is in ( $9 < x/h$ ). In the developed region,  $u_c$  can be expressed by

$$u_c/u_0 \propto (x/h)^{-0.5} \tag{1.8}$$

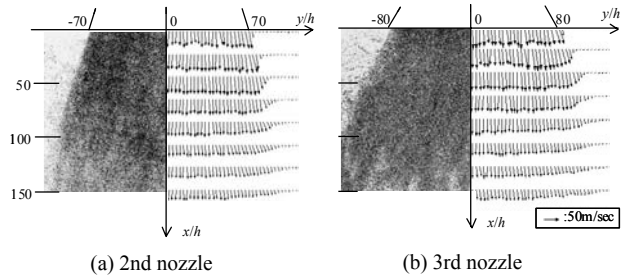


Fig. 10. Particle concentration and velocity vector of particle laden free jet

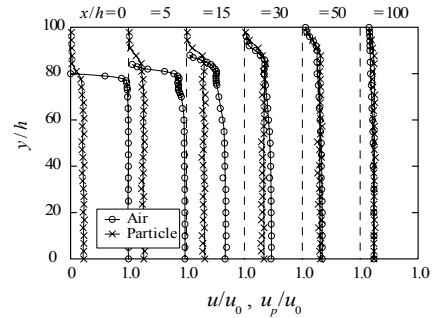


Fig. 11. Particle velocity distribution of 3rd nozzle

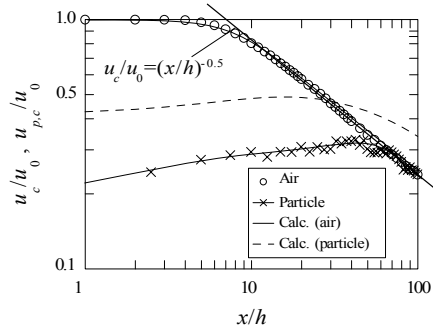


Fig. 12. Centerline air and particle velocity distributions of 3rd nozzle

It corresponds to the just two-dimensional free jet<sup>[6]</sup>. The numerical analysis of air flow, velocity and pressure distributions, agreed well with the experimental results. The numerical results were used to check the effect of various parameters on the behavior of flow.

The particle velocities obtained by the numerical and experimental analyses were considerably different. It results from particle-nozzle wall and particle-particle interactions in the actual flow. The both profiles were similar, and the change of particle velocity  $u_{p,c}$  can be divided into the gradual accelerating region with nearly constant gradient ( $0 < x/h < 30$ ), the transition region ( $30 < x/h < 70$ ), and the decreasing region ( $70 < x/h$ ). The decreasing rate at the decreasing region corresponds to the air. On the other hand,  $u_{p,c}$  is only 20% of the air at the nozzle outlet since the particle has a large specific gravity comparing with the air and then the particle does not accelerate enough by air flow. It takes the maximum value at  $x/h = 40$  and decreases gradually with decreasing of air velocity.

3.3.6 Cutting performance

Figure 13 shows cutting cross section by microblasting using the 2nd, 3rd nozzle. As nozzle outlet becomes wider, excess cutting region of nozzle edge shown in Fig 6 (b) decreases, and then high flatness, cutting accuracy can be obtained. The cutting accuracy shows a high quality of  $\zeta = \pm 8.9\%$  at  $-70 < y/h < 70$  for the 3rd nozzle. The high cutting accuracy in a wide range results from the uniform particle diffusion and uniform air velocity.

3.3.7 Cutting efficiency

Figure 14 shows the relation between supplied power and removal weight for conventional nozzle (Fig. 1 (g)) and the 3rd nozzle which was proposed newly. The 3rd nozzle takes the large removal weight comparing with the conventional nozzle, for example, cutting efficiency of the 3rd nozzle improves by 20% of the conventional circular nozzle at the

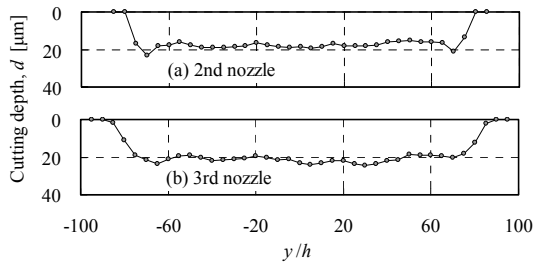


Fig. 13. Cutting cross section of 2nd and 3rd nozzles

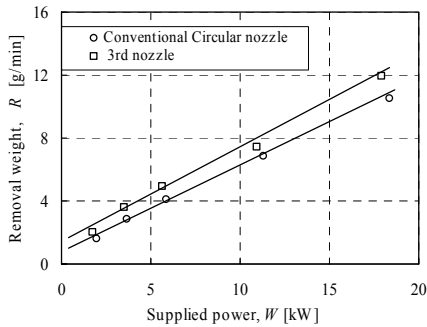


Fig. 14. Cutting efficiency

supplied power of  $W = 10\text{kW}$ . Removal of the particle and cutting material after the particle-laden jet impinges on the work-piece is a significant factor in order to improve the cutting efficiency of microblasting. If the particle and cutting material remain on and around the work-piece after particle impinges on the work-piece, a newly coming particle impinges on the remaining particle, then the energy of particle is spent to only interaction between the particle and particle remaining on the work-piece. Removal of the particle and cutting material for conventional nozzle is not enough because the particle converges on one area but the 3rd nozzle has a narrow impingement width and it makes easy to removal of the particle and cutting material. As a result, cutting efficiency of the 3rd nozzle is improved considerably comparing with the conventional nozzle.

4 Conclusion

In this study, in order to develop a new advanced microblasting nozzle flow characteristics of particle laden high speed air jet flow, behavior of fine particle and cutting performance of for a two-dimensional rectangular new nozzle are examined by experimental and numerical analyses. Major results are as follows.

1. Uniform particle concentration and velocity distributions can be obtained by the new nozzle with circular vane.
2. The particle velocity shows a maximum at  $y/h = 40$  since it has a large inertia force comparing with the air. The particle is accelerated only by 20% of air velocity at the nozzle outlet.
3. The cutting accuracy shows a high quality of  $\zeta = \pm 8.9\%$  at  $-70 < y/h < 70$  for the 3rd nozzle. The high cutting accuracy in a wide range results from the uniform particle diffusion and uniform air velocity distribution.
4. The 3rd nozzle takes the largest removal weight comparing with the conventional nozzles, for example, cutting efficiency of the 3rd nozzle improves by 20% of the pressure type nozzle at the supplied power of  $W = 10\text{kW}$ .

5 Reference

- [1] M.Hirayama, et al., Micro-blasting Technology, Trans. of the JSAT, 46-3, (2002) 5.
- [2] N.Ogawa, et al., Study of Large Scale Micro Processing, Proc. of Two-phase flow modeling and experimentation, 3 (1999) 1727-1732.
- [3] T. Kuriyagawa, et al., Machining Characteristics of Abrasive Jet Machining, Trans. of the JSPE, 64, 6 (1998) 881.
- [4] Robert D. Blevins, Applied Fluid Dynamics Handbook, (1984) 153-155.
- [5] H. Matsufuji, E. Hasegawa, Wall Collision of Small Particle at Stagnation Point, Trans. of the JSME, 46, 409, (1980) 1647
- [6] A. Krothapalli, D. Baganoff and K. Karamcheti, On The Mixing of a Rectangular Jet, J.Fluid Mech. 107 (1981), 201-220.

---

# Thick SU-8 Mask for Micro Channeling of Glass by using Micro Abrasive Jet Machining

Agung Shamsuddin Saragih, Ji Hyeung Lee, Tae Jo Ko, Hee Sool Kim

School of Mechanical Engineering, Yeungnam University

Keywords: abrasive jet machining, SU-8 mask, micro channel

## Abstract

In this paper, we present the implementation of thick SU-8 layer as a mask for micro abrasive jet machining (micro-AJM) process. We obtained micro channel with aspect ratio 0.33. The micro channel was semicircular shape with 190  $\mu\text{m}$  width and 70  $\mu\text{m}$  depths. We also showed some phenomena happened along the processes which are important to have attention for achieving qualified micro channel for micro fluidic application. We think that repeated sequence of the proposed steps give possibility to fabricate 3D micro channel on a single glass slide.

## 1. Introduction

Glass is became important material nowadays. Because of its high resistance to chemicals and transparency, glass is widely use in many fluidic application. In micro-fabrication area, many researcher use glass substrate to develop micro fluidic devices [1, 2]. Commonly, glass chip fabrication use wet etching process technique such as HF etching steps, such as by Berthold et al. [3]. The HF acid etching technique is complex, expensive and can be very dangerous if mishandled. It needs an enclosed area, equipment and materials for its exclusive use. Although it has good result in resolution, accuracy and surface quality, but the etching rate is slow, very time consumptive. On the other hand, for faster techniques by using conventional machining technologies has been difficult since thermal and/or chemical machining methods (such as chemical etching, laser and electron beam machining, EDM, and electrolytic machining) cause an excessive heat affected zone, while using mechanical machining methods like micro-milling [4], which is a simple process and uses standard drilling equipment, is not suitable for batch production and has limitation in accuracy.

Micro abrasive jet machining (micro-AJM) is a process of using impact energy from high pressurized air with micro-abrasive particles. In its basic machining principle, micro-abrasives (tens of  $\mu\text{m}$ ), accelerated by highly compressed air or gases, are forced through a micro-nozzle, and collide with hard and brittle workpieces at a very high velocity and density. This method is characterized by a very high etching rate (1 mm/min), typically two orders of magnitude higher than obtained by dry and wet etching techniques, and does not require a cleanroom environment, which makes it extremely attractive for low cost industrial applications.

Since the material removing process of micro-AJM is performed by an integration of brittle mode machining based on micro-crack propagation similar to a Vickers indentation experiment [5], there is very little heat, chipping, and crack generation in the workpiece. Because the productivity is high and heat affected layers caused by material removal are very thin, it has been considered one of the most appropriate micro-machining methods for hard and brittle materials such as glass, ceramics, etc, which generally difficult-to-machine due to the properties of extreme hardness, brittleness, corrosion resistance and melting temperature.

As fast and flexible technique for micro patterning of glass, micro-AJM usually combines with patterned mask from high-erosion resistance materials to excellent photolithographic property materials. From all the masking material, photosensitive materials are most widely used due to economic reason and required resolution offered.

Since its introduction by researchers at IBM (1989), the epoxy-based SU-8 chemically amplified (CA) photosensitive resist has been used in a wide range of applications to fabricate high aspect ratio structures by optical lithography specifically designed for ultra-thick, high type applications. Several important properties of SU-8 make it suitable for such applications. First of all, the material has a low molecular weight enabling it to be dissolved in a variety of organic solvents to form highly concentrated solutions (72%–85% solids by weight). Ultra-thick coatings can be easily formed by a multi-spinning process. Secondly, the absorption for SU-8 in the UV spectrum is very low, thus allowing the patterning of thick coatings. It is well known that if the optical absorption of a photoresist is too high, even high doses of UV light will fail to penetrate a thick resist layer to generate clean, sharp images [6]. Thirdly, since the resist has high functionality, a high degree of cross-linking can be obtained, permitting a high aspect ratio and straight sidewall to be achieved in lithographic applications.

To our knowledge, with above advance properties of SU-8, it will be suit the requirement as a mask for micro-AJM process. The excellent photolithography properties will let us to apply complex design of micro pattern. And for any applications that may need multi process of micro-AJM where in some place they need an aligning process (for example to fabricate 3D micro-mixer in a piece of glass slide), is possible due to transparency of SU-8 mask. Mean while, a high degree of cross-linking can be obtained which permitting a high aspect ratio and straight sidewall to be achieved, can be used as thick mask to against erosion effect of micro-AJM. By this way, we want to get the micro-

channel profile on glass using micro-AJM process by applying thick SU-8 mask with micro pattern.

## 2. Experimental Details

### 2.1 Material

For all the experiments we used the commercially available NANO™ SU-8 2100 formulation from MicroChem Corp. (Newton, MA).

Glass substrates which were used throughout this work were soda lime glass with Knoop Hardness: 585 kg/mm<sup>2</sup> + 20 and cut into 25mm x 25 mm square and thickness 1mm. They were cleaned in a solution of hot Piranha (75% H<sub>2</sub>SO<sub>4</sub> : 25% H<sub>2</sub>O<sub>2</sub>) and dehydrated on a 200 °C convection oven for 10 min to get hydrophilic surface which can increase adhesion with the mask.

The abrasive particle used for micro-AJM process was Aluminum Oxide (AL<sub>2</sub>O<sub>3</sub>) with average grain size 17.5 μm.

### 2.2 Process Flow

The total process flow of micro-channeling process using micro-AJM is illustrated in Fig. 4. As shown in the figure, the total process is composed of the following three steps:

1. *Masking process:* The masking process is used to prepare the specimens having required patterns for micro-AJM. Photolithography process was applied to produce SU-8 mask. It started by spin coating. To spend minimum amount of SU-8, we control the volume of SU-8 being dispense about 6 ml for each specimen. The resist was dispensed statically by using syringe. Than spin coat with a spread cycle at 500 rpm for 20s , and 1000 rpm/s for 40s. We found that by this procedure can give us a fixed value of approximately 250 μm thickness (after soft baking) measured using surface profiler. And than softbake on hotplate from room temperature to 95°C, keep there for 60 minutes and another 30 minutes for cooling down back to room temperature. Exposure was taken with 600 mJ/cm<sup>2</sup> under UV-light with 360-365 nm wavelengths. Post Exposure Baking (PEB) was applied on convection oven to avoid surface wrinkle. It kept at 95°C for 15 minutes and took longer time for cooling down compared to hotplate, around 60 minutes. But this longer time is useful to avoid crack on the mask. The samples were developed using MicroChem SU-8 Developer for 5 minutes and followed by direct spraying using syringe to reach the edge of micro pattern. This procedure closed by rinse with isopropyl alcohol, deionized water and dry using N<sub>2</sub> gun.
2. *Abrasive jet machining process:* micro-AJM is performed on SwamBlast micro abrasive sandblaster by Crystal Inc. Here, the regions, where masks are removed in the developing process, are selectively

machined. The process parameters, such as distance between nozzle and work piece, diameter of the nozzle, blasting air pressure, and flow rate of micro-abrasives, are maintained at constant through the process. Applied process parameters for the experiments are listed in Table 1.

**Table 1.** Process parameters for micro-AJM process

Parameters	Value
Nozzle size (rectangle size)	0.18X3.75mm
Stand-off distance	30 mm
Air pressure	300 kPa
Flow rate	0.8 gr/min
Scanning speed	0.3 mm/s
Number of scanning	10 times

3. *Mask removing and cleaning process:* After the machining process is finished, any remaining mask adhered to the workpiece surface is removed. We sued Piranha solution Piranha (75% H<sub>2</sub>SO<sub>4</sub> : 25% H<sub>2</sub>O<sub>2</sub>) for this process. It is cheap, compare with SU-8 removal provide from its manufacturer, and fast, although it need fumehood in the process to remove the gas and smell produced. No need external heat, because it's exothermic. And after rinsed by acetone, methanol and DI-water, the specimen ready for repeating the process with different applied micro pattern if needed.

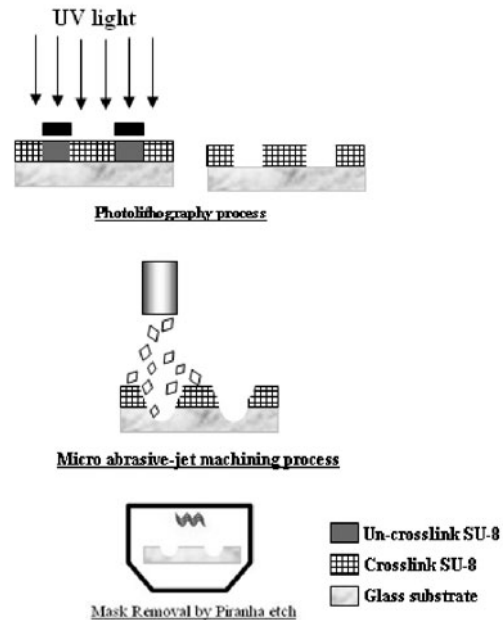


**Fig. 1** Process flow of micro patterning process of glass by micro-AJM

### 3. Result and Discussion

#### 3.1 Mask pattern and thickness

We determined quality of mask by sharp pattern and even surface. The problem usually appeared on mask making was distortion of the mask after PEB which was indicated by wavy mask surface in result. This problem appeared mostly every time we tried to get mask thickness around 300  $\mu\text{m}$  and above. This distortion affected pattern resolution greatly. The dimension of micro patterns were change compare to master film.

We suspect the distortion was happened mainly caused by the cross-link reaction. The material changed from a linear oligomer to a cross-linked network structure during thermal curing. The photo-acid generator in the resist system absorbed photons and produced a strong acid when being exposed to UV light. The strong acid acted as the catalyst for the cross-linking reaction during PEB. The reaction rate of the cross-link reaction related with the concentration of the catalyst, which was decided by the UV dosage. At higher mask thickness only part of the photo-acid generator can change to acid and the concentration of the catalyst was low, so the cross-link reaction was not uniform, this can cause the distortion. Unfortunately, increasing UV dosage gave burning sensation on SU-8 mask, which was indicated by brown color of the mask layer. In this condition, the mask become self-crosslink before PEB process which gave very hard on developing, or we can say that we almost have no micro pattern after developing. Based on our equipment, the best mask quality obtained on 250  $\mu\text{m}$  thickness with process parameter as mention above. Finding out way to obtain good result on ultra thick patterned SU-8 mask (>300  $\mu\text{m}$  thickness) can be main interest of next experiment due to expected micro channel result through that thickness.

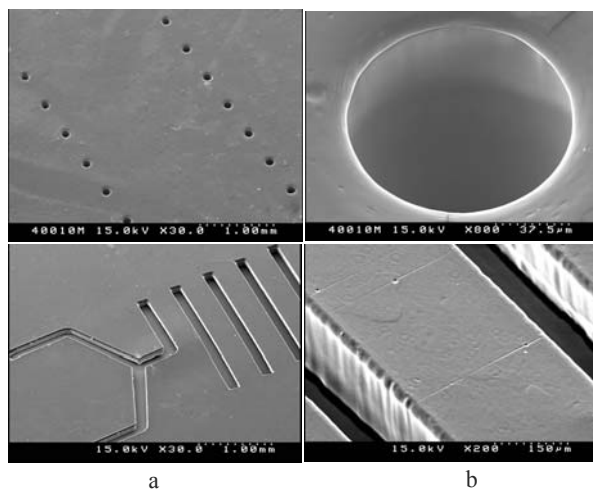


**Fig. 2** Patterned SU-8 mask on glass substrate, with good quality (sharp pattern resolution and even surface) and highly repeatable at 250  $\mu\text{m}$  has shown in a) and b)

#### 3.2 Micro channel result

The purpose of using thick mask for this experiment was to achieve desired channel depth by sacrificing mask material. Thickness of mask layer which eroded by blasting process will be compensated to become channel depth on glass. We used master film with 200  $\mu\text{m}$  width of micro pattern to fabricate the mask. And after micro-AJM process, we got semicircular shape channel with average width 190  $\mu\text{m}$  and depth 70  $\mu\text{m}$ . This 0.3 aspect ratio micro channel was obtain with parameter mention in process flow section. Combination of contact surface profiler HOMMELWERKE Turbo Roughness V3.44 and non-contact surface profiler from NanoSystem co. ltd. were used to determine thickness, depth and width of mask and machining result. By micro Vickers hardness test we got the hardness value of SU-8 mask was 25 hardness values. If we compare with glass hardness value, we can assume that the mask was much more ductile. This lead us to expected to get deeper channel depth by increasing scanning time of micro-AJM process.

Fig. 3b shows observation of machining result under scanning electron microscopy (SEM). We found that the mask suffer for under cut after micro-AJM process when the scanning time was increased twice, which gave different result as expected. This under cut indicated a phenomenon happened on micro-AJM process called "blast lag effect", mentioned by Henk et al in his paper [7].

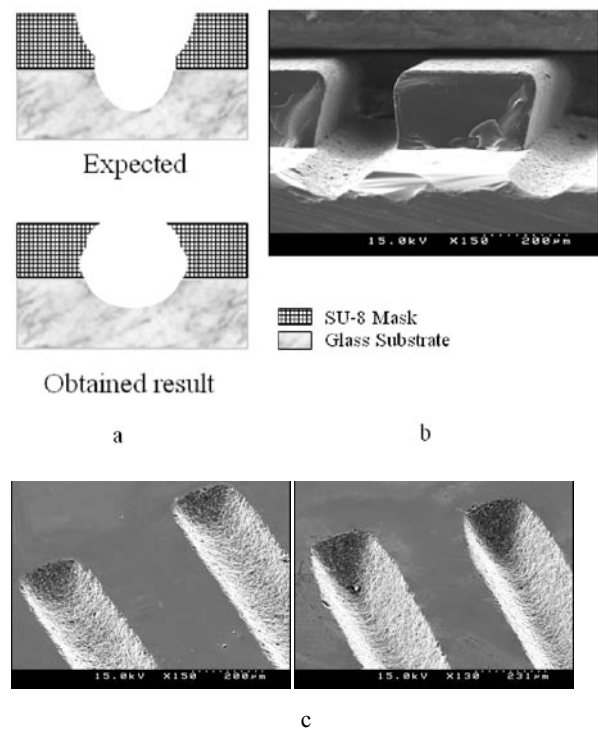


**Fig. 3** Illustration of expected result of the purpose of using thick mask for micro AJM process a) SEM image that contrary the expected result b) longer blasting process to reach deeper channel will result in widen channle width c)

He said that, this phenomenon was caused by the decrease of particle impact angle to sidewall. Blast lag defined as small channels etch slower compared to wider channels. It happened due to the impact angle dependent etch rate. The lower impact angle on the sidewalls result in a lower etch rate, with respect to the perpendicular impacts, as seen in Fig. 4. During blasting, the two sidewalls of a channel grow. At this point the channel only consists of sidewalls and consequently the etch rate drops. The smaller the channel, the sooner this effect occurs [7]. So, it seem that in our case the blast lag effect occur when the channel reach 70  $\mu\text{m}$  in depth. And if the blasting process still continued when the blast lag effect had occurred, the etching direction will redirect to horizontal direction (increase erosion rate in horizontal direction and decrease in vertical direction), which gave the mask under-cut profile and wider the channel width in result.

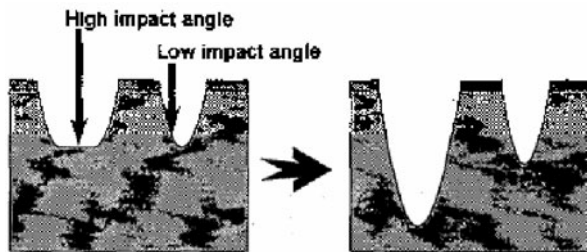


Fig. 4 The formation of a blast lag [7]

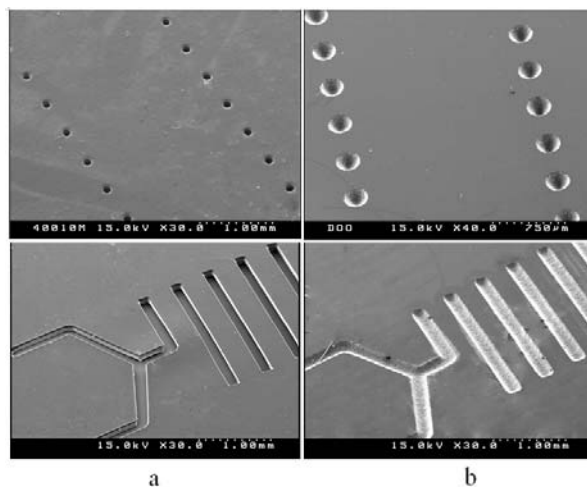


Fig. 5 250  $\mu\text{m}$  thickness SU-8 mask with micro pattern and its micro-AJM result. The channel depth is around 70  $\mu\text{m}$ . This sequence of process, if repeated, can be use to develop 3D micro chnnel on single glass slide (a): masked pattern, (b) machined channel

#### 4. Conclusion

The results of this study, on using thick SU-8 mask to fabricate micro channel on glass by micro-AJM, can be summarized as follows:

- With thickness around 250  $\mu\text{m}$ , we can get SU-8 2100 mask on glass substrate with good micro pattern and highly repeatable in result.
- Erosion profiles of the channel show U-type shapes. Thus, it is very difficult to machine accurate square type channel due to the basic characteristics of micro-AJM. Except if we can figure out the way to get ultra thick SU-8 mask wih homogenous cross-link structure and good pattern resolution than we can explore erosion profile through that thickness.
- Due to the wear of the mask film and "blast lag effect" at the boundaries, measured dimensions of the machined specimens are slightly larger than the masking patterns.
- SU-8 mask in this experiment was easy to remove from the glass substrate by Piranha Etch. It gave advantage for application which need multi process of micro-AJM, such as channeling on both side of substrate to build 3D micro channel on a single glass slide.

#### 5. Reference

- [1] Grosse A., Grewe M. and Fouckhardt H., 2001 Deep wet etching of fused silica glass for hollow capillary optical leaky waveguides in microfluidic device *J. Micromech. Microeng.* 11 252–62
- [2] Stjernstrom M. and Roeraade J., 1998 Method for fabrication of microfluidic system in glass *J. Micromech. Microeng.* 8 33–8
- [3] A. Berthold, F. Laugere, H. Schellevis, C.R. De Boer, M. Laros, R.M. Guijt, P.M. Sarro and M.J. Vellekoop, Fabrication of a glass-implemented microcapillary electrophoresis device with integrated contactless conductivity detection, *Electrophoresis* 23 (2002), pp. 3511–3519.
- [4] G. Minas, J.S. Martins, J.C. Ribeiro, R.F. Wolfenbittel and J.H. Correia, Biological microsystem for measuring uric acid in biological fluids, *Sens. Actuators A* 110 (2004), pp. 33–38.
- [5] Slikkerveer P. J., Bouten P. C. P., in't Veld F. H. and Scholten H., 1998 Erosion and damage by sharp particles *Wear* 217 237–50
- [6] Zang J., Tan K. L. and Gong H. Q., 2001 Characterization of the polymerization of SU-8 photoresist and its application in MEMS polymer teseting 20 (201) 693-701
- [7] H. Wensink, U. Berenshot, H.V. Jan seu, M.C. Elwenspoek, High resolution powder blast micromachining, in: Proceedings of the IEEE Micro Electro Mechanical Systems (MEMS), 2000, pp. 769–774.

# Fabrication of Self-assembled Microstructure using Controlled Liquid Spreading on Textured Surface

Arata KANEKO, Nobuyuki MORONUKI, Michihiro MOGI, and Yuta YAMAMURA  
Tokyo Metropolitan University

Keywords: Self-assembly, Microstructure, Spreading, Textured surface

## Abstract

This paper proposes a novel process for micro-sphere assembly. Grooved substrate was prepared to give a controlled wettability of the surface and then it was drawn up from suspension in which  $\phi 1\mu\text{m}$ -polystyrene spheres were dispersed. This process can produce position-controlled structure of micro-spheres because the suspension selectively spread in the groove due to the controlled wettability and constitute hexagonally-packed structure. Some factors that affect the coverage, such as groove depth and width, were examined by experiments and it was found that deeper grooves and slightly raised local humidity enhanced the selective spreading and thus the coverage.

## 1 Introduction

Development of manufacturing technology in micro/nano-level spherical particles (micro-sphere) allows fabrication of innovative optical devices such as photonic crystal and channel waveguide [1], [2]. Namely, two- or three-dimensionally assembled micro-spheres on required position generate interesting property because of various interactions between them and light [3], [4]. However, the assembly technique has not been established to fulfill some requirements such as throughput (productivity), accuracy, and compatibility to another technology. It is well known that dip coating technique can successfully fabricate uniform monolayer structure of micro-sphere structure [4 – 6]. In this process, a hydrophilic substrate is drawn up from suspension in which micro-spheres disperse in liquid. They are hexagonally self-assembled by capillary force between them with the advance of the liquid evaporation.

It has been found that the dip coating to specially patterned substrate can fabricate microstructure with desired profile such as line-and-space [7], [8]. However, appropriate control of spreading and drying of suspension is necessary to obtain good results. Geometrically structured surface, or “textured” surface, can control liquid spreading [9 – 12]. For example, surface wettability can be set to hydrophilic or hydrophobic by texturing. The authors are proposing a new assembly technique of micro-spheres by a dip coating to a textured substrate as shown in Fig. 1. Namely, supposing that capillary force also affects the liquid spreading in

narrow grooves as well as in tube, the local spreading of liquid helps the micro-spheres self-assembled. In this paper, it is demonstrated that micro-spheres can be assembled selectively on grooves. Then, the effect of groove specifications on the self-assembly process is discussed based on the local liquid spreading.

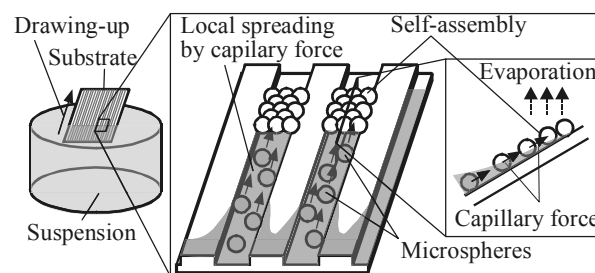


Fig. 1. Schematic illustration of dip coating to grooved surface for self-assembly of micro-spheres.

## 2 Experimental procedure

Textured surfaces, micro-grooves, were fabricated on Si substrate by electron beam lithography and dry etching. Although the substrate size was  $10 \times 10 \times 0.45$  mm, the grooves were fabricated on  $500 \times 500 \mu\text{m}$  region. The specification of textured surface is characterized by groove depth  $h$ , width  $w$ , and pitch  $p$  ( $= 2w$ ). Figure 2 shows the AFM image of typical textured surface. Straight micro-groove and mesa with same width were alternately placed on the surface. The groove depth  $h$  and width  $w$  were 90 nm and  $4 - 50 \mu\text{m}$  respectively. The groove depth was shallow compared to the diameter of micro-spheres. The groove surface is slightly rougher than the mesa surface. In the case of groove depth above  $1 \mu\text{m}$ , the groove width was slightly wider than the design and their edges were rounded because of side etching. However, these geometries seem not to be serious problem for dip coating. The surface of textured substrate was chemically treated in HF-solution (10 wt%) for 120 s before the experiment for cleaning and conditioning. The contact angles of un-etched region (mesa) and etched



region (groove) were approximately 60 and 40 degrees. The reason for difference in contact angle is considered as the effect of surface roughness [11], [12].

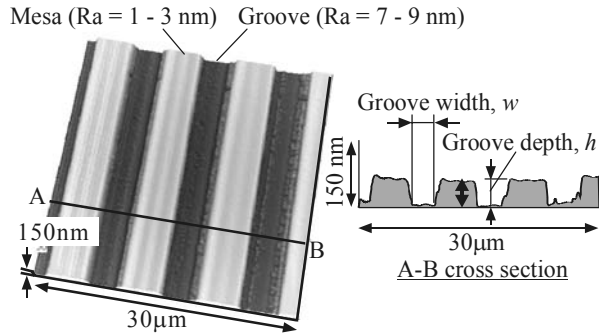


Fig. 2. AFM image of typical grooved surface.

Figure 3 shows a schematic illustration of the dip coating system. This system consists of an inchworm actuator, a rotational stage, a reservoir, and a CCD microscope. The inchworm actuator can draw up a substrate at required drawing speed  $V$  in the range from 0.7 to 15  $\mu\text{m/s}$ . Although the rotational stage can adjust a drawing angle  $\phi$  in the range from 0 to 90 degrees, the drawing angle  $\phi$  was fixed at 90 degrees in the following experiments. A reservoir is filled up with a suspension in which polystyrene spheres (1  $\mu\text{m}$  diameter) disperses in pure water at 1 % concentration. The reservoir size was  $\phi 20 \times 5 \text{ mm}$ . This system is set in clean room where temperature and humidity are kept at 20 centigrade and 50 % respectively.

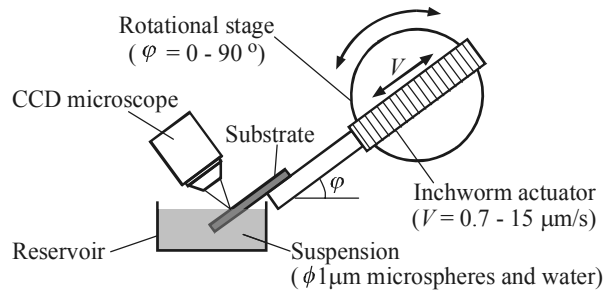


Fig. 3. Experimental setup.

### 3 Results and discussion

#### 3.1 Demonstration of local spreading

The textured surfaces were drawn up from pure water at 2.1  $\mu\text{m/s}$  to investigate the effect of micro-grooves on spreading of liquid. Figure 4 shows CCD microscope images of contact line profiles on micro-grooves. Pure water locally spread in micro-grooves. Namely, it was demonstrated that micro-grooves make water locally spread. The height of local spreading in 2  $\mu\text{m}$  width groove was much longer than that

of 8  $\mu\text{m}$  width groove. Figure 5 shows the relationship between groove width  $w$  and height of local spreading  $l$ , where groove depth  $h$  was 120nm. The height is approximately inversely proportional to the groove width. Generally, the height of raised liquid by capillary force in tube is also inversely proportional to tube diameter. Therefore, it is considered that the local spreading shown in Fig. 5 was also caused by the capillary force. This result clearly suggests that geometry of local spreading can be controlled by the groove width. Therefore, it is considered that the geometry affects the assembly process of microspheres in the application of dip coating to grooved surface.

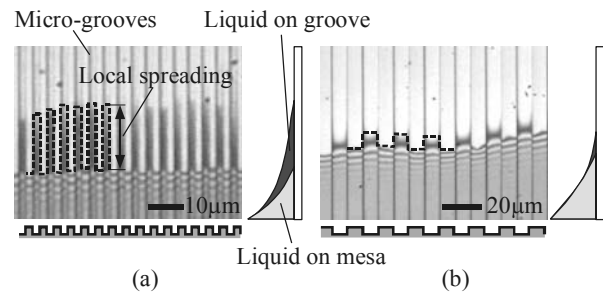


Fig. 4. Local spreading pure water in microgrooves by capillary force; groove width is 2  $\mu\text{m}$  (a) and 8  $\mu\text{m}$  (b), and depth is 120nm.

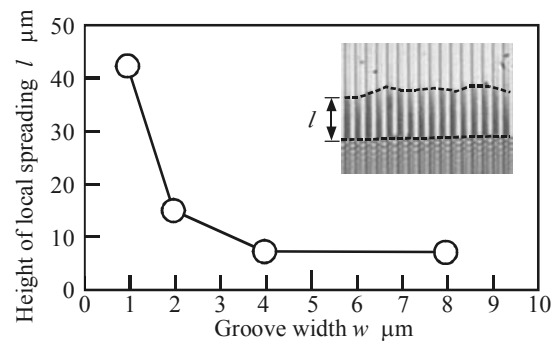
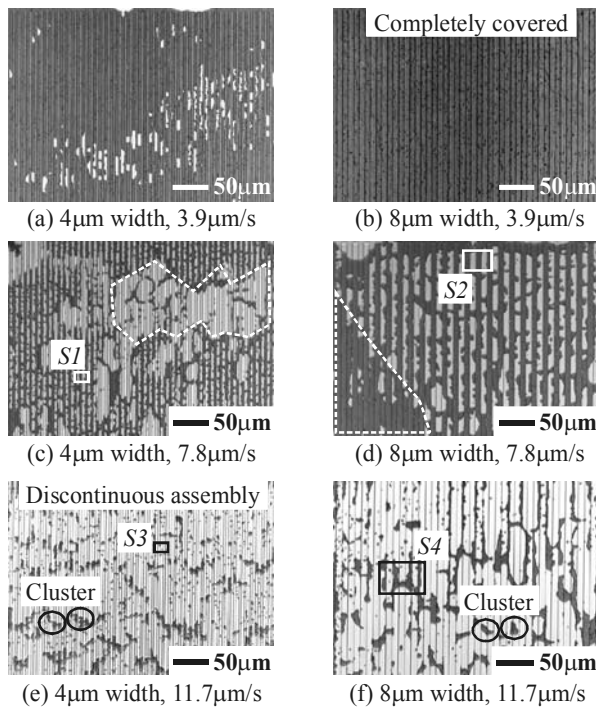


Fig. 5. Relationship between groove width and height of local spreading in micro-grooves; groove depth 120nm.

#### 3.2 Effect of groove width and drawing speed on dip coating

Straight grooved substrates, the depth and width of which were 90 nm and 4 – 50  $\mu\text{m}$  respectively, were drawn up from suspension at 3.9 – 11.7  $\mu\text{m/s}$ , in which polystyrene spheres 1  $\mu\text{m}$  in diameter were dispersed in pure water. The substrates were also treated in HF-solution as describe in the previous section. *In-situ* CCD microscope observation was not operated in this experiment. Figure 6 shows the laser microscope images of typical dip-coated surface of textured substrate (4 and 8 width micro-grooves). The colour of these images can be classified into two; dark and bright. The dark and bright colour indicates micro-spheres and substrate surface, respectively. In the case of drawing speed 3.9  $\mu\text{m/s}$ ,

the substrate surface was almost or completely covered with micro-spheres without regard to groove or mesa, Fig. 6(a) and (b). These results indicate local spreading could not selectively supply micro-spheres into the micro-grooves. On the other hand, in the case of  $7.8 \mu\text{m/s}$ , most of the mesa-regions were not covered with micro-spheres as shown in Fig. 6(c) and (d), so that micro-spheres could be selectively supplied into the micro-grooves. However, uncovered or over-covered regions, enclosed by broken line in the images, were observed on the substrate. In the case of  $11.7 \mu\text{m/s}$ , practically no micro-spheres were found on the substrate surface as shown in Fig. 6(e) and (f). Considerably small cluster of micro-spheres scattered everywhere. These results can be concluded as follows. It is possible to assemble micro-spheres by using locally controlled spreading selectively on micro-grooves that were enough shallow as compared with micro-sphere diameter as shown in Fig. 6 (c), (d). However, the other conditions like drawing speed should be properly adjusted to improve the selectivity of assembly.



**Fig. 6.** Effects of groove width  $w$  and drawing speed  $V$  on dip coating to grooved surface.

Then, the structure of micro-spheres on the substrate was observed by scanning electron microscope (SEM). Figure 7 shows typical SEM images of assembled micro-spheres. These observed regions correspond to the  $S1 - S4$  in Fig. 6 (c) - (f). Regardless of groove or mesa, most of micro-spheres were hexagonally packed. The hexagonal package was orientated to specific direction because one or both sides of micro-grooves was restricted and fixed along the side of micro-grooves. This result elucidates the self-assembly process shown in Fig.1. Narrowly assembled micro-sphere and completely isolated clusters of micro-spheres were placed on the side edge of micro-groove (c), (d). There were

some vacancies as indicated by arrowheads. These observation results suggest that local spread suspension.

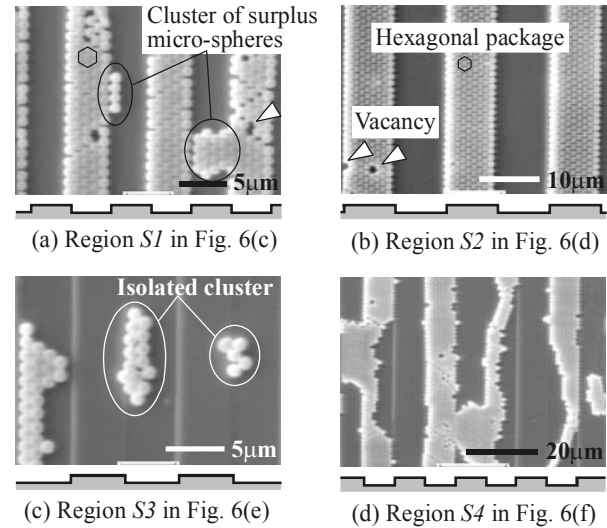


**Fig. 7.** Scanning electron microscope images of textured surface after dip coating;  $S1 - S4$  means observation area shown in laser microscope images (See Fig. 6).

The authors define the following two parameters, “groove coverage”  $\theta$  and “selectivity”  $\sigma$  to characterize the geometry of assembled micro-spheres quantitatively as shown in Fig. 8,

$$\theta_g = A_g / A \quad (1)$$

$$\theta_m = A_m / A \quad (2)$$

$$\sigma = \theta_g / (\theta_g + \theta_m) \quad (3)$$

where  $A$  denotes the areas of referred groove or mesa, and  $A_g$  and  $A_m$  are the area of assembled micro-spheres on groove and mesa respectively. It is noted that vacant space between microspheres and/or side edge of groove was neglected in the calculation. High groove coverage means that the groove is densely filled with micro-spheres. High selectivity means that the number of assembled spheres on grooves is larger than that on mesa. Ideally both of  $\theta_g$  and  $\sigma$  should be 100 %. Figure 9 shows the relationship between groove coverage or selectivity and groove width. These data were obtained by analyzing the images in Fig. 6 and 7 and other experiments. In the case of drawing speed 3.9 and  $7.8 \mu\text{m/s}$ , the groove coverage and selectivity were constant regardless of groove width. However, in the case of  $11.7 \mu\text{m/s}$ , the wider groove made them decreased. This result corresponded to the relationship between groove width  $w$  and length of local spread suspension  $l$  as shown in Fig. 5. To sum up major characteristics of these results, there found a conflict between the effect of drawing speed on groove coverage and high selectivity. In other words, the groove coverage decreases while selectivity is raised up. Furthermore, the higher drawing speed made the dependence of groove

coverage and selectivity on groove width clearer. It is noted that high coverage and selectivity could not be realized for wide groove above 20  $\mu\text{m}$  in these experimental conditions.

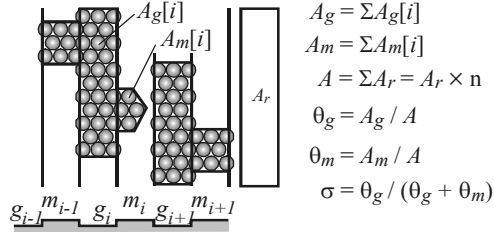


Fig. 8. Definition of groove coverage  $\theta_g$  and selectivity  $\sigma$ .

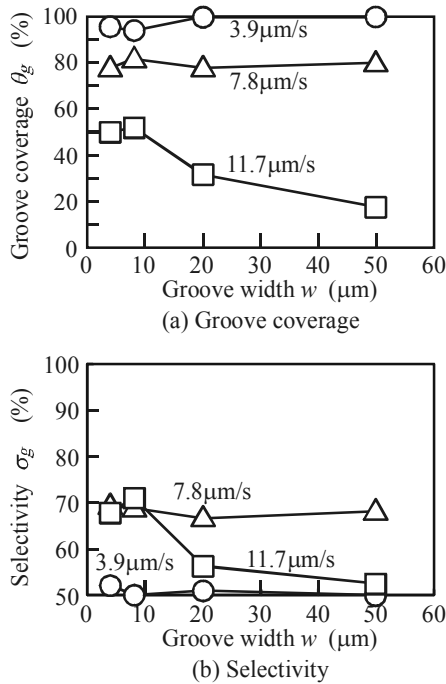


Fig. 9. Relationship between groove width and groove coverage (a), and selectivity (b) at 90nm depth.

### 3.3 In-situ observation of self-assembly

Figure 10 shows the results of *in-situ* CCD microscope observation of dip coating at 10.2  $\mu\text{m/s}$ , where the groove width and depth are 4  $\mu\text{m}$  and 90 nm respectively. This observation reveals important characteristics of the self-assembly process. Image (b) shows the same position of image (a) after 0.5 seconds. Although micro-spheres moved in drawing direction, there is clear difference in the characteristic of motion between on groove and on mesa. Micro-sphere moved independently or separately and continuously on groove, and finally was assembled into a cluster of micro-spheres. Namely, the cluster was composed of hexagonally packed micro-spheres and grew gradually. On the other hand, small cluster of micro-spheres moved intermittently on mesa. The velocity of micro-sphere on

groove was different from that on mesa. It could be estimated from micro-sphere(s)  $M_A$  and  $M_B$  of the images. The former one was isolated single micro-sphere on the groove, and the latter one was cluster of 5 micro-spheres on the mesa. The velocity of  $M_A$  and  $M_B$  were 25 and 13  $\mu\text{m/s}$ , respectively. The average velocity of micro-sphere on mesa was practically slower still because of intermittent moving. The velocity means flux of micro-spheres defined as supplied number per unit time. It can be considered that the difference in moving velocity caused a selectivity of self-assembly between groove and mesa. It should be noted that the substrate temperature seemed to be slightly raised up because of light for CCD microscope in this experiment. Therefore, the result could not be simply compared with the other results without CCD microscope observation shown in Fig. 6 and 7.

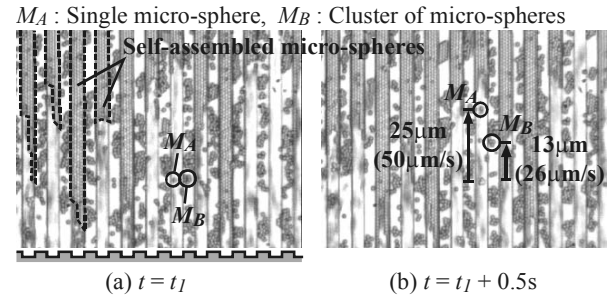


Fig. 10. *In-situ* CCD microscope observation of dip coating process; groove width  $w$  and depth  $h$  were 4  $\mu\text{m}$  and 90 nm respectively, drawing speed was 10.2  $\mu\text{m/s}$ .

### 3.4 Discussion about mechanism of dip coating to textured surface

This section discusses the mechanism of selective self-assembly by dip coating to textured surface based on the results in the previous sections.

The mechanism of selective self-assembly can be considered as follows: Local spreading of suspension on the micro-grooves is necessary condition for the following process because it causes the concentration gradient of micro-spheres [5], [6], while the liquid was evaporated from the edge of spread suspension. This concentration gradient and liquid evaporation made the micro-spheres flow in the drawing direction. The selectivity of assembly can be considered from viewpoint of evaporation rate that is defined as volume of evaporated liquid per unit time. The thickness of locally spread suspension on groove was thinner than that on mesa as shown in Fig. 4. Thinner liquid generally increases the evaporation rate. Furthermore, it was demonstrated that coverage of micro-spheres is inversely proportional to evaporation rate, in specific dip coating like continuous convective method [6]. Therefore, the flux of micro-spheres also resulted from the evaporation rate which is controlled by the textured surface, so that it determined both of the groove coverage and selectivity.

The evaporation should proceed constantly and continuously at the top edge of suspension to obtain

continuum self-assembly because intermittent evaporation generates discontinuous cluster of assembly as shown in Fig. 6(c), (d). Furthermore, the evaporation rate should be appropriately controlled to avoid surplus assembly shown in Fig. 6(a), (b) regardless of controlled liquid spreading. The evaporation rate depends on temperature, humidity, drawing speed, and geometry of spread suspension. It was found that, in the experiments shown in Fig. 6, drawing speed around  $7.8 \mu\text{m/s}$  gave appropriate evaporation rate for selective assembly on  $8 \mu\text{m}$  width grooves.

#### 4 Dip coating under modified condition

As describe in the previous section, it can be considered that both of the appropriate selective spreading and evaporation rate are important to realize accurately self-assembly of micro-spheres on micro-grooves. The authors tried to apply modified conditions to dip coating to improve the groove coverage and selectivity. This section shows some results and describes a discussion for effective self-assembly.

Spread height by capillary force is inversely proportional to the tube diameter in “closed” tube. Since the textured surface dose not have “closed” tube but “open” groove, it is considered that capillary force can not effectively work the spreading of suspension in grooves as compared with tube. Therefore, deeper micro-grooves were prepared to increase the surface area of groove, and thus to enhance the local (selective) spreading of suspension.

Figure 11 shows the results of dip coating on the textured surface with 1 and  $5 \mu\text{m}$  depth. The common characteristics of two results are that both of groove coverage and selectivity were accurately kept 100 % near the top edge of grooves. The regions were indicated as dotted lines with specific length  $l_s$  in the images. Namely, it was found that the coverage and selectivity can be improved by groove depth. The specific length covered with micro-spheres became longer as groove was separated from the center of textured area as clearly shown in image (b).

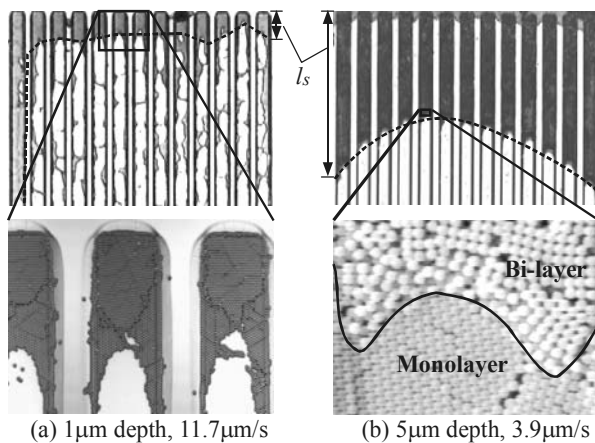


**Fig. 11.** Effect of groove depth  $h$  on dip coating; both groove widths  $w$  were  $25 \mu\text{m}$ . Comparing these geometries with that of groove depth  $90 \text{ nm}$  shown in Fig. 7 clearly shows the difference in groove coverage and selectivity.

These results suggest that supply of micro-spheres was suddenly stopped at the position. As described in the section 2, textured surface was fabricated within  $500 \times 500 \mu\text{m}$ . As average level of suspension sank below the bottom of textured area, locally spread suspension was also drained from micro-grooves. Therefore, these textured areas were drawn up from suspension before sufficient micro-spheres were supplied into micro-grooves. It is considered that the elongation of textured area can improve this problem. It should be noted that most of micro-spheres were packed in bi-layer structure in the case of  $5 \mu\text{m}$  (b). Arrangement of upper microspheres was not hexagonal but disorder in the bi-layer structure. The results seemed to result from thicker spread suspension in deeper micro-grooves. These results can be summarized as follow. The deeper groove is preferable to obtain higher groove coverage and selectivity, however, the groove depth needs to be approximately comparable to diameter of micro-sphere to avoid fabrication of multi-layer structure.

Then, the effect of local humidity is focused, which determines the evaporation rate on textured surface. The dip coating system was placed in a clean room in which temperature and humidity were kept at 20 centigrade and 50 % respectively. However, the local humidity near the substrate or inside the reservoir during dip coating must be different from the nominal humidity in the room. Although it is difficult to measure or control the local humidity, it is possible that the evaporation rate is kept lower using tall reservoir where the dissipation of the vapor is restrained and humidity becomes high. Therefore, another reservoir  $\phi 20 \times 35 \text{ mm}$  was prepared, and then it was filled with the same volume of suspension as that of previous reservoir  $\phi 20 \times 5 \text{ mm}$  as shown in Fig. 12.

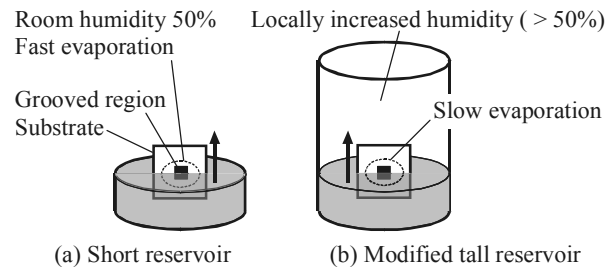
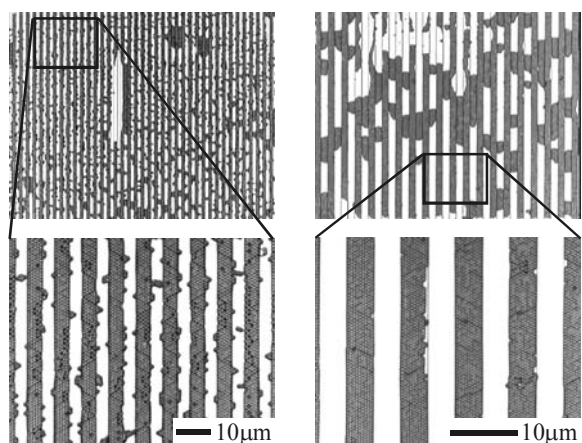


**Fig. 12.** Schematic illustration of controlled evaporation rate using reservoir height; (a) short reservoir used in previously shown results (Fig. 6 – 9) and (b) modified tall reservoir.

Figure 13 shows the results of dip coating from the tall reservoir. It was found that the selectivity was considerably improved. The mesa was not covered with micro-spheres as like Fig. 6(a), (b), though both drawing speeds were slower ( $0.7$  and  $2.1 \mu\text{m/s}$ ). These results suggest that modified local humidity relatively restricted evaporation of suspension on mesa to that on groove while suspension was kept selectively spread. It was also demonstrated that the local humidity strongly affects the self-assembly process. However, there were also some clusters of assembled micro-spheres on mesa and uncovered groove, and these structures were not periodically observed. It is considered that a series of

assembly process was discontinuous by some undesirable factors like contamination on the substrate and/or the roughness of sidewall of the groove, because it was demonstrated that the contamination and roughness affect spreading or dewetting (evaporation) of liquid [13], [14]. These results concluded that slightly high humidity can improve the groove coverage and selectivity at drawing speed less than  $3.9 \mu\text{m/s}$  although it is difficult to control the local humidity successfully and dynamically. Therefore, control of both drawing speed and local humidity may improve the coverage and selectivity on wider groove.



(a)  $4 \mu\text{m}$  width,  $120\text{nm}$  depth, and drawing speed  $0.7 \mu\text{m/s}$  (b)  $8 \mu\text{m}$  width,  $120\text{nm}$  depth, and drawing speed  $2.1 \mu\text{m/s}$

**Fig. 13.** Effect of evaporation rate on dip coating. Modified reservoir was used to control evaporation rate. These geometries of assembled micro-spheres can be compared with that of Fig. 6 and 7.

Finally, special arrangement of micro-spheres is introduced. In the previous sections, groove widths were enough to assemble micro-spheres hexagonally. The authors also prepared another grooves with  $1 \mu\text{m}$  width and  $120\text{nm}$  depth. The groove width was narrower than that of hexagonally assembled micro-spheres in two lines, and wider than that of straightly aligned them in 1 line. Figure 14 shows the result. The micro-spheres were alternately attached each side of groove, so that they aligned zigzag. It was demonstrated that narrower groove can change arrangement of micro-spheres.

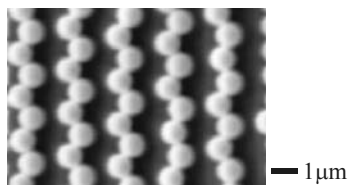


**Fig. 14.** Zigzag-assembled micro-spheres on  $1 \mu\text{m}$  width micro-grooves.

## 5 Conclusions and future works

The paper can be concluded as follows.

- (1) It was demonstrated that dip coating was applied to textured (grooved) surface for fabrication of microstructure.
- (2) The micro-spheres were mainly hexagonally packed on the grooves.
- (3) The coverage and selectivity of assembled micro-spheres depend on local humidity as well as drawing speed, groove width and depth.

The authors will try to improve the groove coverage and selectivity using modified drawing conditions, and apply dip coating to various textured surface as future works.

## 6 References

- [1] V. N. Astratov et al., Photonic band gaps in 3D ordered fcc silica matrices, *Phys. Lett. A*, **222** (1996) 349.
- [2] V. N. Astratov et al., Photonic band structure of 3D ordered silica matrices, *Superlattices and Microstructures*, **22**, 3 (1997) 393.
- [3] G. Pan, R. Kesavamoorthy, and S. A. Asher, Optically Nonlinear Bragg Diffracting Nanosecond Optical Switches, *Phys. Rev. Lett.*, **78** (1997) 3860.
- [4] Y. Xia, B. Gates, and Z. -Y. Li, Self-Assembly approaches to three-dimensional photonic crystals, *Adv. Mater.*, **13** (2001) 409.
- [5] S. I. Matsushita, T. Miwa, D. A. Tryk, and A. Fujishima, New mesostructured porous  $\text{TiO}_2$  surface prepared using a two-dimensional array-based template of silica particles, *Langmuir*, **14** (1998) 6441.
- [6] K. Nagayama, *J. Soc. Powder Technol.*, **32** (1995) 476.
- [7] Y. Masuda, M. Itoh, T. Yonezawa, and K. Koumoto, Low-dimensional arrangement of  $\text{SiO}_2$  particles, *Langmuir*, **18** (2002) 4155.
- [8] Y. -H Ye, S. Badilescu, and V. -V. Truong, Self-assembly of colloidal spheres on patterned substrates, *Appl. Phys. Lett.*, **79**, 6 (2001) 872.
- [9] A. Kaneko and N. Moronuki, Control of droplet profile with directional wettability on the textured surface, *Proc. of 5th International conference of euspen, Montpellier, France*, **2** (2005) 739.
- [10] N. Moronuki, K. Ryu, and A. Kaneko, Control of wettability with surface texturing and its application, *Proc. ASPE Annual Meeting, CD-ROM*, (2004).
- [11] J. Bico, C. Tordeux, and D. Quere, Rough wetting, *Europhys. Lett.*, **55**, 2 (2001) 214.
- [12] J. Bico, C. Marzolin, and D. Quere, Pearl drops, *Europhys. Lett.*, **47**, 2 (1999) 220.
- [13] G. Nadkarni and S. Garoff, An investigation of microscopic aspects of contact angle hysteresis, *Europhys. Lett.*, **20** (1992) 523.
- [14] C. Andrieu, C. Sykes, and F. Brochard-Wyart, Average spreading parameter on heterogeneous surfaces, *Langmuir*, **10** (1994) 2077.

---

# Improving Performance of Direct Photosynthetic/Metabolic Micro Bio Fuel Cell (DPBFC) by Gene Manipulation of Bacteria

Akihiro Furuya<sup>1</sup>, Takeyuki Moriuchi<sup>1</sup>, Makoto Yoshida<sup>2</sup>, Masahiro Ota<sup>2</sup>, Keisuke Morishima<sup>1</sup> and Yuji Furukawa<sup>3</sup>

<sup>1</sup>Tokyo University of Agriculture and Technology, Koganei, Japan, <sup>2</sup>Tokyo Metropolitan University, Japan, <sup>3</sup>Management of Technology, Tokyo University of Agriculture and Technology, Japan

Keywords: Photosynthetic, Metabolic, Micro Bio Fuel Cell, Genetic manipulation, Bacteria

## Abstract

In our laboratory, we have developed mediator-less direct photosynthetic/metabolic bio fuel cell (DPMFC) in which microparticles of polyaniline were adopted as electrodes to draw electrons from bacteria. We selected purple photosynthetic bacteria (PPBs) which is activated by organic compounds as well as emitting hydrogen in photosynthetic and metabolic processes for improving the electron generation efficiency of PPB by applying gene manipulation to inhibit hydrogen emission. Our hypothesis is that more electrons will be stored inside PPB if hydrogen emission is inhibited. As a result, the power density of Gene manipulated bacteria became  $10\mu\text{W}/\text{cm}^2$ , that is higher than the normal one.

## 1 Introduction

The fuel cell is expected to be a new energy technology that can offer an effective solution to energy and environmental problems. Furthermore, portable equipment is becoming increasingly sophisticated and will require the miniaturization of high-output power sources in the future. To realize such power sources has received the greatest attention, fuel cells have been developed of which the direct methanol fuel cell (DMFC) is the most watched. However, it requires rare metals and uses methanol, a toxic material. To solve these problems, bio fuel cells that use electrons released from biocatalytic reactions have been developed.

Lin et al. have developed a micro-photosynthetic/metabolic bio fuel cell that is composed of cyanobacteria and that could make electricity by photosynthesizing and metabolizing[1][2]. This bio fuel cell requires mediators such as methylene blue to extract electrons from cyanobacteria. However, in this cell, bacteria are killed once mediators attack them; furthermore, such mediators lose their function rapidly when exposed to light. To overcome these problems, we have developed a novel mediatorless direct photosynthetic/metabolic bio fuel cell (DPBFC) in which microparticles of polyaniline were adopted as electrodes to draw electrons directly from bacteria. Our bio fuel cell resulted in an increase output by more than ten-fold that of Lin et al. Nevertheless, the output

is still low and must still be increased at least ten-fold. To realize this, the electron generation efficiency of the bacteria must be improved. We selected PPBs because they have special characteristic such as being activated by organic compounds as well as emitting hydrogen in photosynthetic and metabolic processes. We improved the electron generation efficiency of PPB by applying gene manipulation technology to hydrogen emission. Our hypothesis is that more electrons will be stored inside PPB if hydrogen emission is inhibited. The objective of this research is to evaluate the usefulness of gene manipulation in increasing what output.

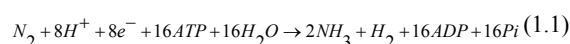
## 2 Biology of Purple Photosynthetic Bacteria

### 2.1 Biological Characteristics of PPB

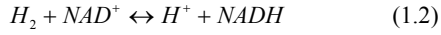
In this research, we used three types of PPB; accumulation-type PPB, emission-type PPB, the biological character of which was changed by gene manipulation, and normal-type PPB. All these types of PPB are anaerobic and heterotrophic. They absorb organic compounds in photosynthetic and metabolic processes. The PPBs were cultivated by anaerobic culture in PYS medium which contains organic compounds under light.

#### 2.1.1 Biological Characteristics of Normal-Type PPB

Fig.1 shows the photosynthetic and metabolic mechanisms of the normal-type PPB. Normal-type PPB absorbed organic compounds for the production of the energy-storing molecule ATP (adenosine triphosphate), which is synthesized from ADP (adenosine diphosphate). Normal-type PPB has a nitrogen-fixing enzyme (nif) that uses ATP energy, inevitably releasing H<sub>2</sub> from this reaction.



Some H<sub>2</sub> released is taken up into normal-type PPB cell using the hydrogen-uptake enzyme (hup), which provides reducing power in the form of electrons.



Therefore, the removal of these enzymes enables us to control electron generation capacity. However, these enzymes have susceptibility to oxygen.

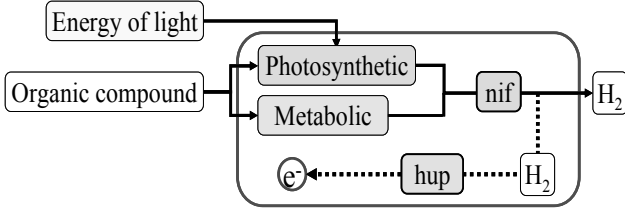


**Fig.1.** Photosynthetic and Metabolic Mechanisms of Normal-Type PPB

**2.1.2 Biological Characteristics of Accumulation-Type PPB**  
 Fig.2 shows the photosynthetic and metabolic mechanisms of the accumulation-type PPB. This PPB was developed by removing the gene *nif* from normal-type PPB. Hydrogen emission is inhibited as a result of *nif* removal; therefore, more electrons will be stored these bacteria than normal-type PPB.

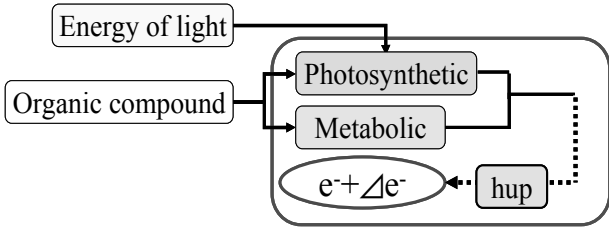


**Fig.2.** Photosynthetic and Metabolic Mechanisms of Accumulation-Type PPB

**2.1.3 Biological Characteristics of Emission-Type PPB**  
 Fig.3 shows the photosynthetic and metabolic mechanisms of the emission-type PPB. This PPB was developed by removing the gene *hup* from normal-type PPB. The accumulation of electrons is inhibited as a result of *hup* removal, and hydrogen emission is enhanced by *nif*.

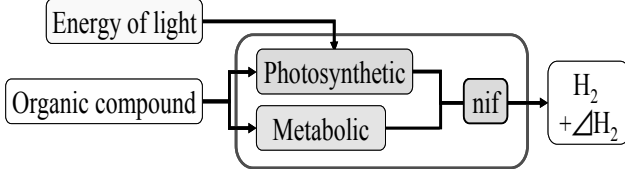


**Fig.3.** Photosynthetic and Metabolic Mechanisms of Emission-Type PPB

**2.2 Biological Characteristic change by Gene Manipulation of PPB**

Table 1 shows the biological characteristic change of PPB. The accumulation-type PPB stores more extractable electrons in the cell, therefore, the DPBFC performance which used the accumulation-type PPB will be expected to improve. Furthermore, the direct supplementation of organic compounds to PPB can improve the performance, because all types of PPB become activated.

**Table 1.** Biological Characteristics of PPB

Type of PPB	Hydrogen Emission	Electron Accumulate	Effect of organic compound
Normal-Type	○	○	○
Accumulation-Type	×	⊙	○
Emission-Type	⊙	×	○

**3 Working Principle of DPBFC**

**3.1 Principle of Electric Generation**

Fig.4 shows a schematic of the working principle of DPBFC. DPBFC has an anode chamber (left side) and a cathode chamber (right side) separated by a proton exchange membrane (PEM). Electrons are extracted from the electron transport chain of PPB, which is in contact with an electrode consisting of polyaniline, thus generating electricity.

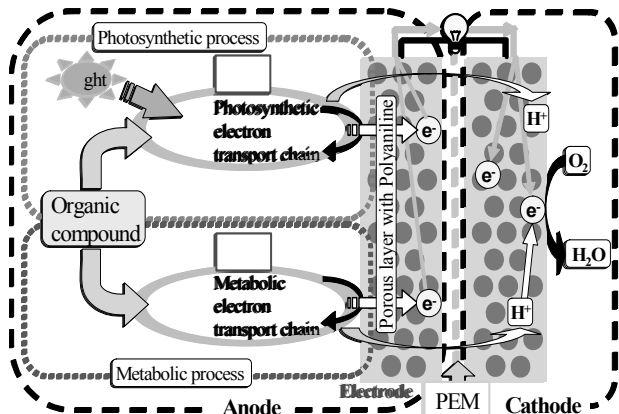


**Fig.4.** Working Principle of DPBFC

### 3.2 Electron Extraction Mechanism from PPB Cell

Fig.5 shows the electron extraction mechanism from PPB cell. The cell of PPB is composed of cytoplasm, periplast, periplasm space and cell wall from the inside. The thickness of periplast and cell wall becomes several nanometer (5~10nm) when the diameter of the cell is assumed to be 1 $\mu$ m. Electron which was raised in photosynthetic and metabolic processes was transported on electron transport chain in periplast.

The electron transfer mechanism between polyaniline and PPB cell are two processes. One is that electrons in the periplast were extracted by polyaniline's redox potential through cell wall, and the other is that, polyaniline nano sized particle sticks into the cell walls and contact to periplast directly. These reactions enable to draw electrons more directly, therefore, the DPBFC performance was improved more than ten-fold compared to the performance of using mediators[3].

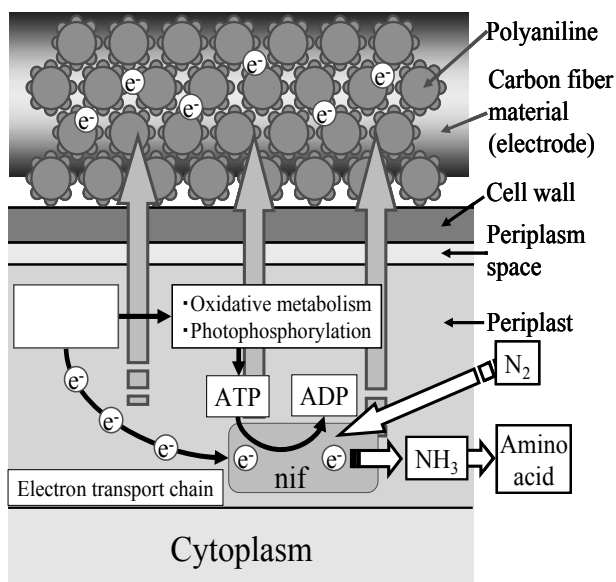


Fig.5. Electron Extraction Mechanism from PPB Cell

### 4 Structure of DPBFC

Fig.6 shows the structure of the prototype DPBFC. An MEA (membrane electrode assembly) was fabricated using Nafion117 (DuPont Co. Ltd.) and carbon paper (0.19 mm or 0.11 mm thick) or carbon cloth (0.33 mm thick). To collect current, MEA was sandwiched between two copper electrodes (0.3 mm thick) manufactured by electric discharge machining. To make space for anolyte and catholyte injections, an O-ring of internal diameter 18 mm and 1.5 mm thick was used. Finally, the fuel cell was sandwiched between layers of acrylic, which is an optically transparent material. The DPBFC was 40 mm $\times$ 40 mm with a reactive area of 2.54 cm<sup>2</sup>.

### 5 Processing of Prototype MEA

MEA was fabricated using PEM and a carbon fiber electrode. Nafion117, used as PEM, was treated with H<sub>2</sub>O<sub>2</sub> (3-5 wt. %) at 80 $^{\circ}$ C for 1 hour, and then boiled in deionized water for 1 hour. Carbon fiber, which has an excellent electric characteristic and a steric structure, was used as the catalyst carrier. Polyaniline solution was placed on carbon paper or carbon cloth, and dried. Then, two electrodes were hot-pressed in to one piece with a pretreated Nafion117 membrane to at 150 $^{\circ}$ C, 50 kg/cm<sup>2</sup> for 3 minutes complete the MEA.

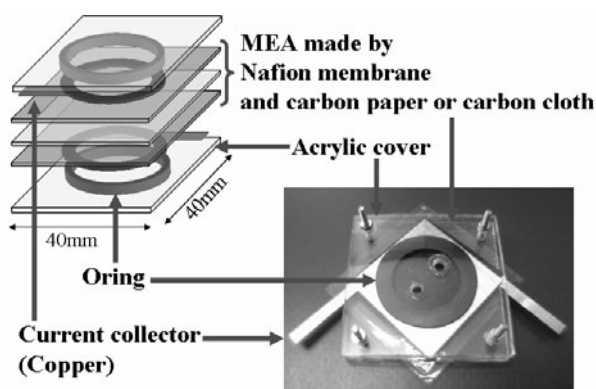


Fig.6. Structure of Prototype DPBFC

### 6 Factors Determining DPBFC Performance

Fig.7 shows a schematic of the two factors determining DPBFC performance; PPB status and DPBFC structure. To confirm the effects of PPB status, we used two evaluations, and to confirm those of DPBFC structure, we used the evaluation shown in Fig.7.

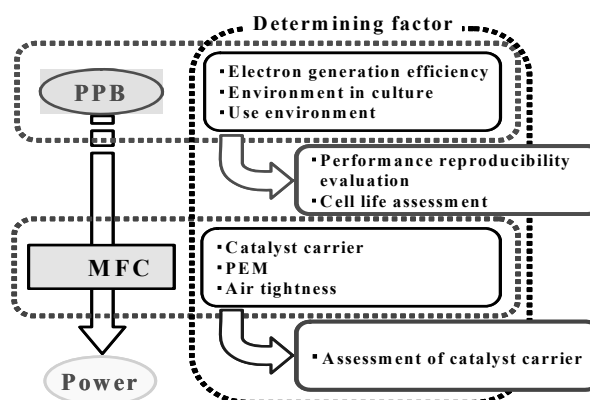


Fig.7. Schematic of Factors Determining DPBFC Performance



## 7 Experimental Methods

DPBFC performance was evaluated on the basis of electric power, which was measured by connecting resistors, from 10 Ω to 1 kΩ, to DPBFC. The voltage of the resistor was measured with a data logger (Kyowa Co. Ltd. PCD320A) and current was measured with a digital multimeter (Advantest Co. Ltd. AD7461A). PPB cultured for 3 days was used in all the experiments.

### 7.1 Performance Reproducibility Evaluation

Gene manipulation in PPBs influences the stability of their DPBFC performance. Therefore, to confirm the stability of DPBFC performance after gene manipulation, electric power was measured five times under the same conditions. Carbon cloth was placed on as the catalyst carrier, and the amount of polyaniline used was 0.3 ml.

### 7.2 Cell Lifespan Assessment

If the lifespan of PPBs is extended, allowing for the storage of more electrons PPBs, the cell life of DPBFC will be extended. To determine the cell life extension after gene manipulation, open circuit voltages, electric power as determined by connecting 100 Ω resistors and the pH of PPB culture before and after the experiment were measured. Carbon paper (0.11 mm thick) was placed on as the catalyst carrier, and the amount of polyaniline used was 0.4 ml.

### 7.3 Assessment of Catalyst Carrier

Table 2 shows the experimental conditions. A changing in the structure of the catalyst carrier can increase the area of contact between PPB and polyaniline; thus, this contact area was varied. To determine the optimal structure of the catalyst carrier in DPBFC, the electric power was measured while changing the structure of the catalyst carrier. The amount of polyaniline used was 0.4 ml.

## 8 EXPERIMENTAL RESULTS & DISCUSSION

### 8.1 Result of Performance Reproducibility Evaluation

Table 3. shows the experimental result of the performance reproducibility evaluation. Gene manipulation did not clearly increase electric power, and the electric power observed was unstable. This may result from nif and hup's susceptibility to oxygen. The PPBs were exposed to air; therefore, the performance of nif and hup were suppressed because of their susceptibility to oxygen. Furthermore, MEA performance was determined by evaluating the states of the polyaniline coating, joint of Nafion117 and catalyst carrier. It was difficult to measure these states quantitatively. Therefore, a strict management of PPB cultures, an airtight DPBFC structure and quantitative

processing of MEA are necessary to improve and achieve performance reproducibility.

**Table 2.** Experimental Conditions of Assessment of Catalyst Carrier

Experimental number	Anolyte (Type of bacteria)	Catalyst carrier
No.1	Normal	Carbon paper 0.19mm thick
No.2	Accumulation	Carbon paper 0.19mm thick
No.3	Emission	Carbon paper 0.19mm thick
No.4	Normal	Carbon cloth
No.5	Accumulation	Carbon cloth
No.6	Emission	Carbon cloth
No.7	Normal	Carbon paper 0.11mm thick
No.8	Accumulation	Carbon paper 0.11mm thick
No.9	Emission	Carbon paper 0.11mm thick

**Table 3.** Result of Performance Reproducibility Evaluation

Experimental number	Power density[ $\mu$ W/cm <sup>2</sup> ]					Average
	1	2	3	4	5	
Normal	7.8	5.3	3.5	5.4	2.2	4.9
Accumulation	7.6	8.1	4.0	4.5	2.8	5.4
Emission	6.6	4.5	4.6	3.1	4.6	4.7

### 8.2 Results of Cell Lifespan Assessment

Fig.8 shows the open-circuit voltage performance of DPBFC, and Fig.9 shows the electric power performance of DPBFC. From time course of electric power, the cell lifespan was about 2 hours. Although it was forecast that the cell lifespan of the accumulation-type PPB would be longest, the cell lifespan of the normal and emission-types were actually longest. This was a result of nif and hup's susceptibility to oxygen. With a decrease in pH, a proton permeability decrease due to Nafion117 drying, and an ion electron imbalance between the anode and cathode chambers occurred. Therefore, it is important to determine a method of injecting H<sub>2</sub>O, which was generated in the cathode chamber, into Nafion117 of the MEA, and developing a more airtight structure of DPBFC to protect nif and hup from oxygen.

## Improving Performance of Direct Photosynthetic/Metabolic Micro Bio Fuel Cell by Gene Manipulation of Bacteria

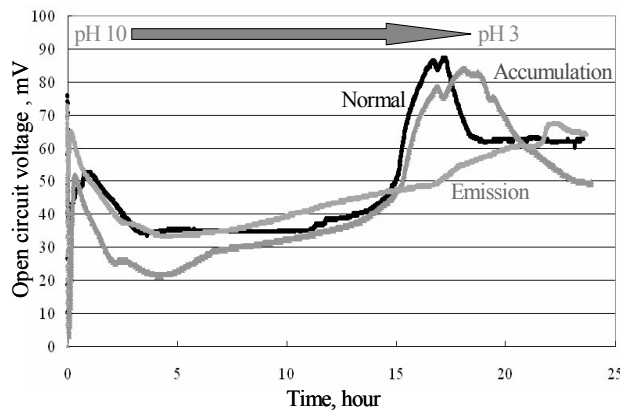


Fig.8. Open-Circuit Voltage Performance of DPBFC

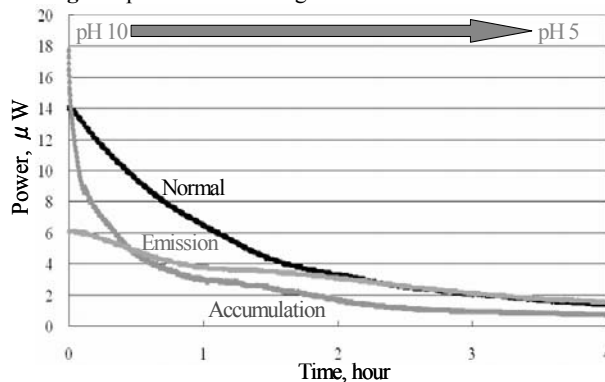


Fig.9. Electric Power Performance of DPBFC

### 8.3 Result of Assessment of Catalyst Carrier

Fig.10 and Table 4 show the experimental results of the assessment of the catalyst carrier. DPBFC performance was improved using a thin and highly porous material, namely, carbon paper (0.11 mm thick), to increase the area of contact between the PPBs, polyaniline and Nafion117, and the reaction between electrons and protons was promoted. Moreover, the accumulation-type PPB generated the highest electric power of all the catalyst carriers. Therefore, to generate high electric power, the accumulation-type PPB should be used.

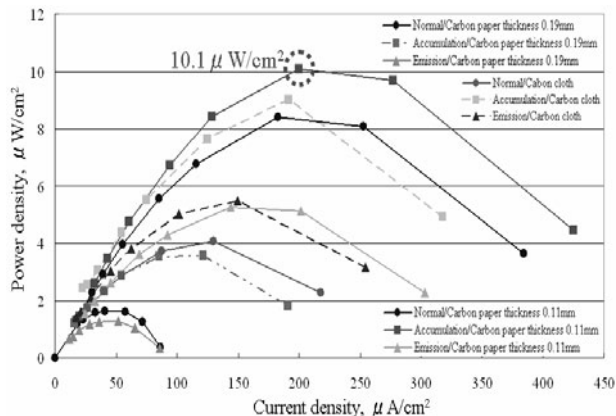


Fig.10. Results of Assessment of Catalyst Carrier

Table 4. Results of Assessment of Catalyst Carrier

	Power density [ $\mu\text{W}/\text{cm}^2$ ]		
	Carbon paper 0.19mm thick	Carbon cloth	Carbon paper 0.11mm thick
Normal	1.6	4.1	8.4
Accumulation	3.6	9.0	10
Emission	1.3	5.5	5.3

## 9 Conclusions

No clear improvement in DPBFC performance by applying gene manipulation in PPB was accomplished in this research. Nevertheless, it is highly possible that gene manipulation can improve the electric power output of accumulation-type PPB. The DPBFC performance was low because PPB can not stably produce electric power; therefore, it is necessary to improve PPB stability to develop a useful fuel.

Prospects for future studies include the direct supplementation organic compounds to PPB, and the development of an airtight and miniature structure of DPBFC to increase electric power output and improve PPB stability. Such improvements will allow DPBFC to output a high electric power. Furthermore, the development of a flexible structure DPBFC or medium reflux DPBFC will allow widespread application.

## 10 References

- [1] M.Chiao , K.B.Lam and L.Lin, (2000) Micromachined Microbial Fuel Cells, in Proc. IEEE Conf. on Micro Electro Mechanical Syst. (MEMS 2000), Kyoto, Japan, Jan.19-23.
- [2] K. B. Lam, M. Chiao, and L. Lin, (2003) A Micro Photosynthetic Electrochemical Cell, in Proc. IEEE Conf. on Micro Electro Mechanical Syst. (MEMS 2003), Kyoto, Japan, Jan. 19-23, pp. 391-394.
- [3] Y. Furukawa, T. Moriuchi, and K. Morishima , (2005) Design Principle and Prototyping of Direct Photosynthetic/Metabolic Bio Fuel Cell (DPBFC), PowerMEMS 2005, Tokyo, Japan, pp.182-185.
- [4] U.Schroder , J.Niessen and F.Scholz, (2003) A Generation of Microbial Fuel Cells with Current Outputs Boosted by More Than One Order of Magnitude, Angew.Chem., 115, pp.2986-2989.
- [5] K.V.P.Nagashima , A.Hiraishi , K.Shimada and K.Matsuura, (1997) Horizontal Transfer of Genes Coding for the Photosynthetic Reaction Centers of Purple Bacteria, Journal of Molecular Evolution , pp.132-136.

---

# Nanometer Deflection Control of AFM Probe by Irradiating Polarized Laser and its Application to Nano-Structuring Process

Daisuke MEZAKI<sup>1</sup>, Ken-ichiro CHUMA<sup>1</sup>, Akira KAKUTA<sup>2</sup>, Yuji FURUKAWA<sup>1</sup>  
<sup>1</sup>Tokyo University of Agriculture and Technology, <sup>2</sup>Tokyo Metropolitan University

Keywords: AFM, Polarization Laser, Nano-Processing, Cantilever, Single Crystal Si, Single Crystal SiC

## Abstract

Scanning probe microscopy (SPM) is expected most as a tool for a processing size of a single nanometer order. We present a new technique of processing that combined atomic force microscopy (AFM) with a polarization laser. It is a method of irradiating the laser on the lever of a cantilever for AFM. As a result of this method, we succeeded in generating the groove with less than 5 nm width and less than 2 nm depth on a gold thin film. We experimentally verified factors for this processing, evaluated experimental results, and aimed to improve processing accuracy and speed.

## 1 Introduction

For device production, a decrease in processing size is increasingly desired because the demand for the miniaturization of electronic devices increases every year. Photolithography plays the most important role in the processing of semiconductor device. However, it is impossible to obtain a processing size of a single nanometer order because processing size is limited to the wavelength of light in this method. Thereafter, some attentions are given to scanning probe microscopy (SPM) as one of the new techniques for a processing size of a single nanometer order. This method can move each atom theoretically and the D.M.Eigler's group moved each atom and wrote the character named IBM by scanning tunneling microscopy (STM) in 1990<sup>[1]</sup>. Similarly, the minimum processing size of fabrication by SPM is certainly attractive, but many problems exist in its industrial application. An atom or a molecule cannot be handled if the condition is not under ultrahigh vacuum and low temperature. Moreover, the worst problem is processing speed. Therefore, it is necessary to develop a new fabrication technique that uses SPM to improve processing speed under room temperature.

Next, some methods of combining a laser with SPM were studied<sup>[2-4]</sup>. These are a method of irradiating laser under the probe tip. The mechanism of this method remains unclarified although it is reported to be the thermal expansion of the probe tip or the enhancement in the electric field by the laser. However, this method has not yet been industrially applied.

Thus, we proposed a new technique of processing that combined atomic force microscopy (AFM) with a polarization laser. This is a method of irradiating the laser on the lever of a cantilever for AFM. The factors for this processing may be the changes in the particle size of the cantilever by the irradiating laser and atomic force between the probe tip and the sample. In this study, we experimentally verified these factors for this processing, evaluated experimental results, and aimed to improve processing accuracy and speed.

## 2 Processing Principle

### 2.1 Particle Size Change in Metal by Irradiating Polarized Laser

In a previous experiment for irradiating two lasers (wavelength, 267 nm; pulse length, 150 fs; repetition rate, 10 Hz and wavelength, 800 nm; pulse length, 40 fs; repetition rate, 10Hz) on TiN, Yasumaru's group formed periodic nanostructures on the surface at the low laser fluence, that is, within ablation threshold. In addition, they proved that the size of this nanostructure can be changed by the laser wavelength and laser fluence<sup>[5]</sup>. Fig. 1 shows the changes in particle size at various laser fluences and Fig. 2 shows the changes in particle size at various laser wavelengths.

Moreover, in a previous experiment for irradiating polarization laser (wavelength, 355 nm; pulse length, 15 ps; repetition rate, 80 MHz) on SiC wafer, Chuma discovered that the shapes of the nanostructures were orthogonal in the direction of the polarization<sup>[6]</sup>. Fig. 3 shows the changes in particle shape at various directions of polarization.

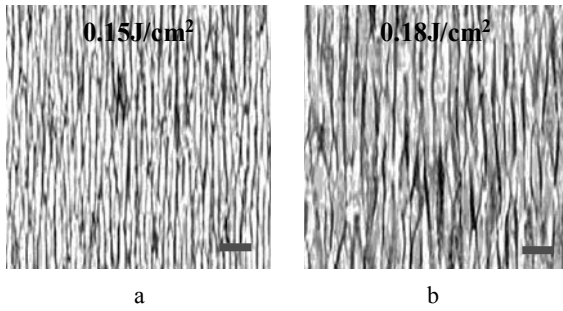


**Fig. 1.** Changes in particle size at laser fluences  
a. 0.15 J/cm<sup>2</sup>; b. 0.18J/cm<sup>2</sup> (J. Kiuchi, N. Yasumaru, [5])

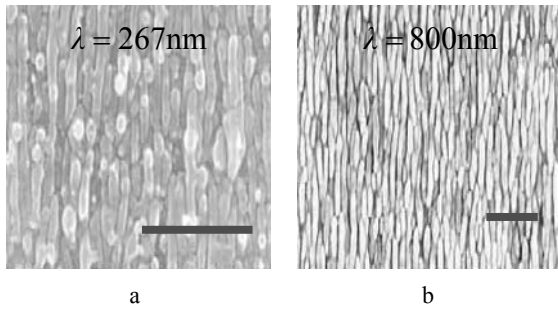


**Fig. 2.** Changes in particle size at wavelengths  
a. 267nm; b. 800nm (J. Kiuchi, N. Yasumaru, [5])

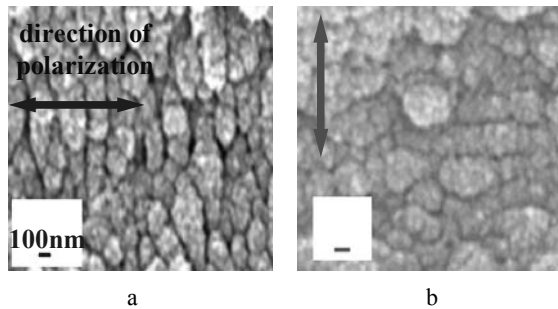


**Fig. 3.** Changes in particle shape at polarization directions  
a. *p* polarization; b. *s* polarization (K. Chuma, [6])

## 2.2 Processing Principle

From the above-mentioned results, if a polarization laser is irradiated on the lever of a cantilever for AFM which is a continuous molecular solid material, its particle size may change statically and/or dynamically on a nanometer order. Consequently, the force produced by a change in particle size is added to atomic force between the sample material and the probe tip, so as to exceed the intermolecular attractive force of the material and the material atoms can be taken out according to the movement of the probe tip. Fig. 4 shows the image of the processing principle.

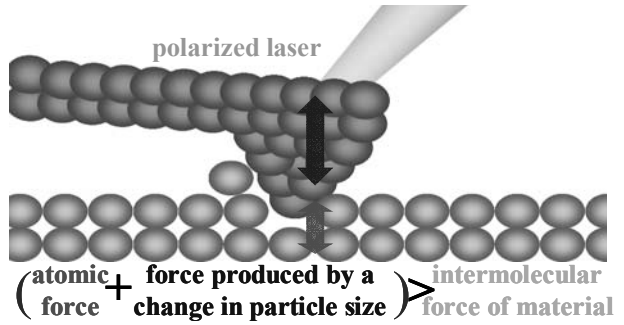


**Fig. 4.** Processing principle

## 3 Experimental Details

Fig. 5 shows the experimental setup. A UV laser (PALADIN™, COHERENT) with a pulse length of 15 ps was used. Its wavelength is 355 nm and its repetition frequency is 80 MHz. The laser beam was focused by lens whose focal length was 200 mm (UDL, SIGMA KOKI CO., LTD.). The laser spot diameter was approximately 90 μm. The laser beam was irradiated to the lever of cantilever with the mirror. During imaging and processing, AFM system (SPM-9500J3, Shimadzu) was used for scanning in the contact mode. A cantilever (OMCL-TR-800PSA-1, OLYMPUS) made of Si<sub>3</sub>N<sub>4</sub> was used. The sample was a gold thin film of approximately 100 nm thickness on Si wafer. The gold thin film was made by sputtering.

First of all, it was confirmed whether it was actually feasible for the proposed technique to process at the nanometer order. Next, it was verified how the processing factors, such as atomic force, effected on the nanostructuring. Atomic force can be changed at operating point, that is at the level of push-in force, and the particle size can be changed with laser fluence and the direction of polarization. Therefore, the actual processing factors were the operating point, laser fluence, and polarization. In addition, the irradiating time and scanning speed were changed because other processing factors were considered. Moreover, the difference in the two cantilevers was compared using a cantilever (OMCL-AC240TS-C2, OLYMPUS) made of single crystal Si. In addition, considering to the industrial applications, the Si wafer that was used as the material of the semiconductor device, the SiC thin film on Si wafer, and the SiC wafer that would be used for the future device were used as the sample materials.

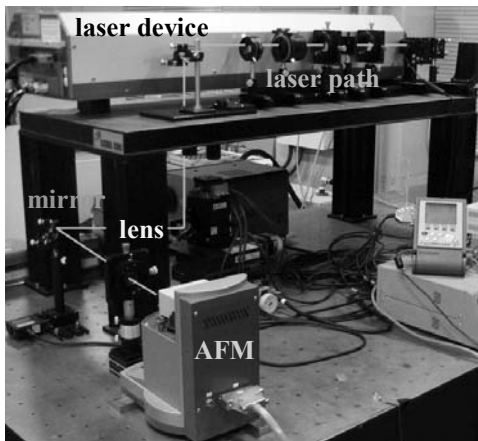


Fig. 5. Experimental setup

### 4 Results and Discussion

Fig. 6 shows the AFM images of the generated groove with less than 10 nm width and less than 5 nm depth. It was made under laser fluence of  $9.6 \mu\text{J}/\text{cm}^2$ , which is the minimum value of the UV laser, irradiating time of 1 s, scanning speed of 200 nm/s, *p* polarization, scanning area of  $500 \text{ nm} \times 500 \text{ nm}$ , and operating point of 2 V using  $\text{Si}_3\text{N}_4$  cantilever and gold thin film. When five experiments were repeated under the same condition, the width and depth of grooves were in the range of 9-16 nm and 3-12 nm, respectively. It is thought that these were caused by the laser irradiation position not constant. This might be solved by using the lens with smaller spot diameter.

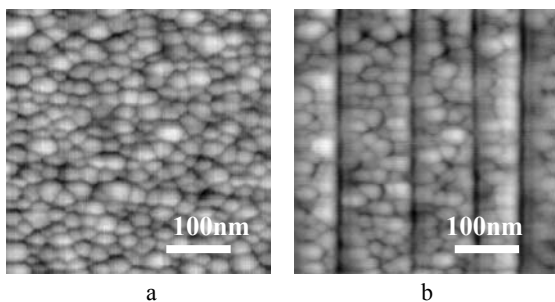


Fig. 6. AFM images  
a. before processing; b. after processing

#### 4.1 Operating Point

Fig. 7 shows the effect of the operating point. It is shown that the processing size increased by increasing push-in force, that is operating point. Consequently, it means that the atomic force between the sample material and the probe tip is one of the processing factors in the new processing technique.

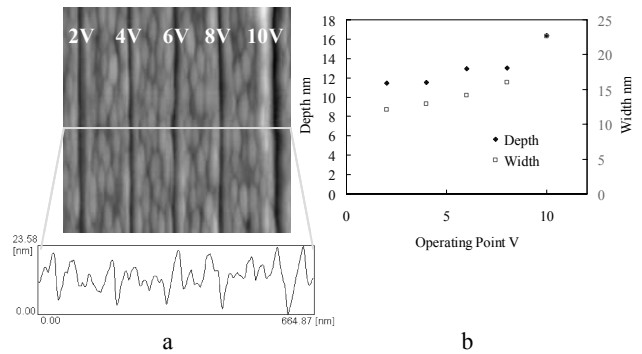


Fig. 7. Results for operating point change  
a. AFM image and cross section; b. graph

#### 4.2 Laser Fluence

Fig. 8 shows the effect of the laser fluence. It is shown that the processing size increased markedly by increasing laser fluence. Consequently, it means that the force produced by the change in particle size is one of the processing factors affecting this new technique. Moreover, a laser that is not irradiated on the lever might be diffracted and thus influence processing.

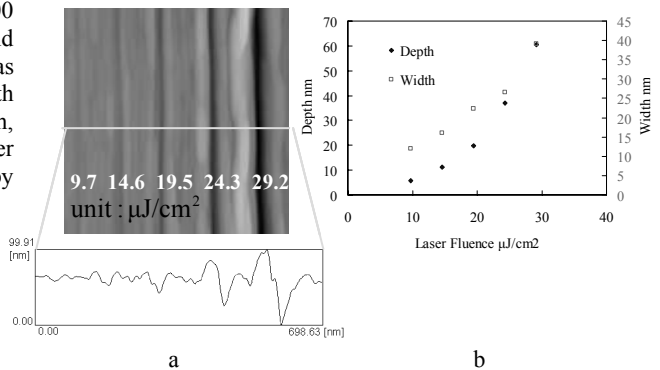
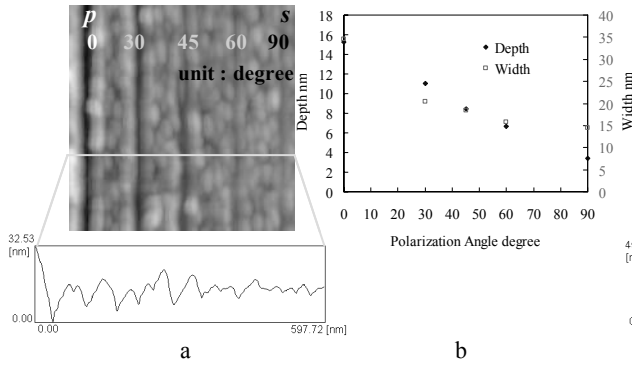


Fig. 8. Results for laser fluence change  
a. AFM image and cross section; b. graph

#### 4.3 Polarization

Fig. 9 shows the effect of the polarization direction. It is shown that *p* polarization was larger than *s* polarization for a processing size. Moreover, the angles near *p* polarization were larger than these near *s* polarization. As a result, the particle shape might change into the axial direction of the probe tip in case of *p* polarization. In case of *s* polarization, particle shape might change at right angles with the probe tip.



**Fig. 9.** Results for polarization change  
a. AFM image and cross section; b. graph

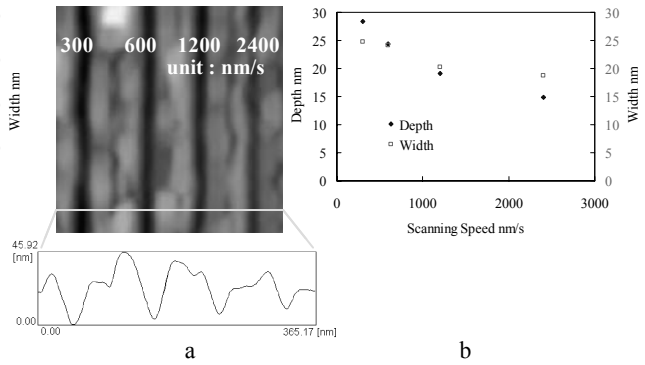


**Fig. 11.** Results for scanning speed change  
a. AFM image and cross section; b. graph

#### 4.4 Irradiating Time

Fig. 10 shows the effect of the irradiating. It is shown that the processing size is proportional to the irradiating time. The processing size has increased by the number of processing lines increasing with the irradiating time. Moreover, the temperature of the cantilever increased with irradiating time. This phenomenon might have caused the heating of the probe tip or the increase in particle size.

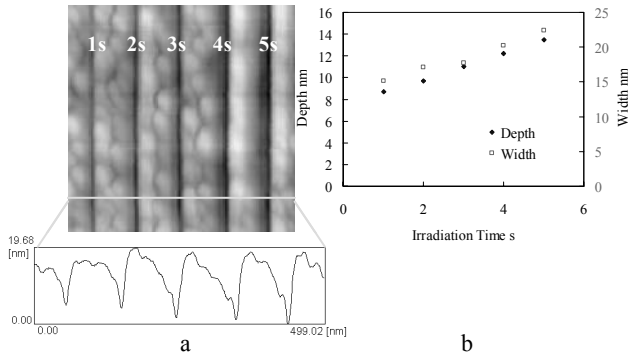


**Fig. 10.** Results for irradiating time change  
a. AFM image and cross section; b. graph

#### 4.5 Scanning Speed

Fig. 11 shows the effects of the scanning speed. It is shown that the processing size increased as the scanning speed decreases. This phenomenon might have occurred by increase of the irradiating time with scanning time.

#### 4.6 Cantilever

Fig. 12 shows the effect of the Si and Si<sub>3</sub>N<sub>4</sub> cantilevers. Because the area of the lever of the Si cantilever was small, the laser fluence of the processing threshold of the Si cantilever was 14.6 μJ/cm<sup>2</sup>. Using the same laser fluence, the processing size of the Si cantilever was smaller than that of the Si<sub>3</sub>N<sub>4</sub> cantilever. Because the probe tip of the Si cantilever was longer than that of the Si<sub>3</sub>N<sub>4</sub> cantilever, the attenuation of energy for the Si cantilever might be larger, and the change in particle size in the point of the probe tip might be smaller. Moreover, because the Si<sub>3</sub>N<sub>4</sub> cantilever was harder than the Si cantilever, the Si<sub>3</sub>N<sub>4</sub> cantilever removed many gold atoms.

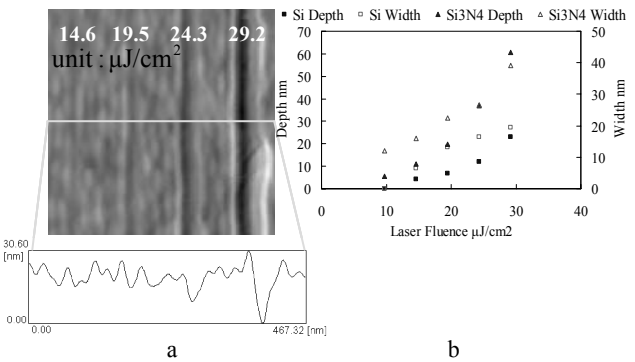


**Fig. 12.** Results for Si and Si<sub>3</sub>N<sub>4</sub> cantilevers  
a. AFM image and cross section using Si cantilever;  
b. graph for Si and Si<sub>3</sub>N<sub>4</sub> cantilevers

#### 4.7 Si Wafer

The Si wafer was processed under irradiating time of 4 s, scanning speed of 200 nm/s, *p* polarization, scanning area of 500 nm×500 nm, operating point of 2 V and using Si<sub>3</sub>N<sub>4</sub> cantilever. Fig. 13 shows the AFM images at the processing thresholds of 14.6 μJ/cm<sup>2</sup> and 39.0 μJ/cm<sup>2</sup>. The processing threshold of the laser fluence for the Si wafer was 14.6 μJ/cm<sup>2</sup> against 9.6μJ/cm<sup>2</sup> in the gold thin film because it was harder than the gold. The maximum laser fluence in these

experiments was  $39.0 \mu\text{J}/\text{cm}^2$ , because the AFM might be damaged at a higher laser fluence. At  $14.6 \mu\text{J}/\text{cm}^2$ , the width and depth of groove was 43.4 nm and 0.40 nm, respectively. At  $39.0 \mu\text{J}/\text{cm}^2$ , the width and depth was 49.4 nm and 0.93 nm, respectively. For depth, 2-3 pieces of Si atoms were removed because the diameter of the Si atom was 0.234 nm. However, the accuracy of the measurement worsens so that many noises may enter under the present environment. Therefore, a better environment is necessary to measure this range.

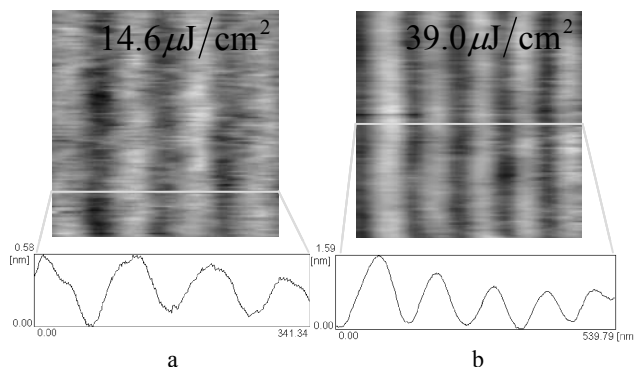


**Fig. 13.** AFM images and cross sections of processed Si wafer at laser fluences a.  $14.6 \mu\text{J}/\text{cm}^2$ ; b.  $39.0 \mu\text{J}/\text{cm}^2$

#### 4.8 SiC Thin Film and SiC Wafer

The SiC thin film and wafer were processed under irradiating time of 4 s, scanning speed of 200 nm/s, *p* polarization, scanning area of 500 nm×500 nm, operating point of 2 V and using  $\text{Si}_3\text{N}_4$  cantilever. Fig. 14 shows the AFM images of the processed SiC thin film. It is shown that the processing of the SiC thin film might have succeed because the grooves were observed faintly. However, the probe tip broke because we were not able to take the image after processing at a high laser fluence.

For the SiC wafer, we were not able to process it even at a high laser fluence. Therefore, using a harder cantilever may enable a SiC thin film and a wafer to process.

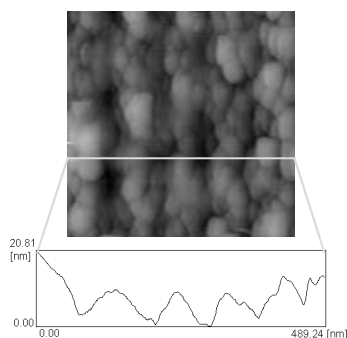


**Fig. 14.** AFM image and cross section of processed SiC thin film

## 5 Conclusion

A groove with less than 5 nm width and less than 2 nm depth was made on a gold thin film by irradiating a polarization laser on the lever of a cantilever for AFM. We succeeded in generating a groove with less than 1 nm depth on the Si wafer. We confirmed that the processing factors were atomic force and changes in particle size by an irradiating laser. Moreover, laser diffraction and the heat of the probe tip contribute to fabrication of nanostructures. However, the force produced by changing the size of a particle may be the main factor for the processing because the influence of the laser was the largest in these experimental conditions.

The processing size was controlled at a single nanometer level by the these parameters. The processing time was very short because of the use of irradiating laser only. Moreover, if a harder cantilever and AFM for this new technique are developed, its industrial application may be realized

## 6 References

- [1] D. M. Eigler, E. K. Schweizer, (1990) Positioning single atoms with a scanning tunnelling microscope: *Nature* 344:524-526
- [2] V. A. Ukraintsev, J. T. Yates, Jr., (1996) Nanosecond laser induced single atom deposition with nanometer spatial resolution using a STM: *Journal of Applied Physics* 80:2561-2571
- [3] M. H. Hong, S. M. Huang, B. S. Luk'yanchuk, T. C. Chong, (2003) Laser assisted surface nanopatterning: *Sensors and Actuators A* 108:69-74
- [4] A. Kisanov, A. Kiselev, A. Stepanov, N. Polushkin, (2003) Femtosecond laser-induced nanofabrication in the near-field of atomic force microscope tip: *Journal of Applied Physics* 94:6822-6826
- [5] J. Kiuchi, N. Yasumaru, (2003) Femtosecond -laser-induced nanostructures formed on hard thin films of TiN and DLC: *Applied Physics A* 76:983
- [6] K. Chuma, (2005) A study on surface integrity of SiC/Si layer and its nano-structured surface: MS thesis, Tokyo University Agriculture and Technology

---

# Investigation on Fabricating 3D Structures Using Inkjet Printing Technology

Mustaffa IBRAHIM<sup>1</sup>, Takayuki OTSUBO<sup>2</sup>, Hiroyuki NARAHARA<sup>3</sup>, Hiroshi KORESAWA<sup>4</sup> and Hiroshi SUZUKI<sup>5</sup>  
Department of Mechanical Information Science and Technology, Kyushu Institute of Technology

Keywords: Rapid prototyping, Inkjet printing, Piezoelectric, Inkjet device

## Abstract

Recently a rapid prototyping method for building parts layer-by-layer has led to interest in fabrication of electrical circuits and optical devices by inkjet printing. In this study a Java program was developed to control a commercial piezoelectric inkjet printer whose nozzles are about 30  $\mu\text{m}$  with experiments focusing on the drop positioning and arrangement required to fabricate three-dimensional structure layer by layer. A single nozzle inkjet device whose nozzles are about 100  $\mu\text{m}$  was also fabricated to study the basic operating parameters affecting the fluid drop formation such as cavity length, viscosity and amplitude voltage.

## 1. Introduction

An inkjet printer patterns material by ejecting tiny droplets of liquid ink from its printhead nozzles or orifices as it moves in two dimensions approximately 1 mm above a substrate. The prospect of adopting inkjet printing technology in various advanced manufacturing processes is very promising due to its apparent simplicity, the fact that it is data-driven, its high material deposition speed, reduced waste of costly materials and elimination of cross-contamination on surfaces because it is a non-contact process.

With this broader view of the technologies encompassed by the term “inkjet printing”, applications in electronics, optics, displays, virtual reality, medical diagnostics, and medical procedures have been developed using inkjet fluid microdispensing as an enabling technology [1]. The characteristic feature of the inkjet process is to print dots, but for printing 3D functional parts, lines and areas with good dot-to-dot conductivity are a necessity, as for example in electrical and thermal conduction applications.

This study intends to utilize Java program to manipulate CAD design data and interface them with a modified commercial 357-nozzle piezoelectric printer with experiments focusing on the drop positioning and arrangement required to fabricate 3D patterns. In order to study the parameters affecting drop formation of a piezoelectric inkjet printer, a single nozzle inkjet device whose nozzle diameter is about 100  $\mu\text{m}$  was also fabricated to study basic parameters affecting fluids drop formation such as voltage amplitude, firing frequency and fluid viscosity.

The printing quality and resolution of an inkjet printhead are closely related to the characteristics of the ejected droplet and therefore it is important to gain insights into how the liquid droplet is formed and ejected in a piezoelectric inkjet printing device. Without a clear knowledge of the operating parameters for the printhead, optimal droplet ejection and printing quality cannot be realized.

## 2. Experimental Details

In this study, two experimental works were done: deposition experiment using the modified inkjet printer and drop deposition experiment that uses a single nozzle inkjet device.

### 2.1 Drop deposition using inkjet printer

The focus of the experiments was to study the area covered by ink deposited horizontally and vertically in order to print 3D patterns using the modified inkjet printer. Although in our previous study, silver nanoparticle ink was successfully printed and can function as a conductive circuit [2], a more thorough understanding of printer capabilities in arranging dots in both the X and Y axis and in patterning 3D patterns needed to be reached.

A Java program was developed to manage CAD data manipulation, control the printer without its software and independently customize the fluid cartridges selection to avoid simultaneous deposition when data was sent and creating problems in fabricating multi-material 3D structure[s]. The Java program also synchronizes installed motorized stages with the printing movement so that it was possible to deposit materials selectively layer by layer.

This study used the printer’s original ink, with a surface tension of approximately 28.7 mN/m and viscosity at room temperature of approximately 3.59 mPa [3]. The positioning of deposited ink is important because failure to deposit ink in some areas would have a significant effect if functional inks such as conductive or magnetic ink were used. The modified printer horizontal movement is not modified, but the mechanical paper feed mechanism was replaced by motorized stages as depicted in Figure 2.1. In these experiments, micro slide glass was used as the substrate material.



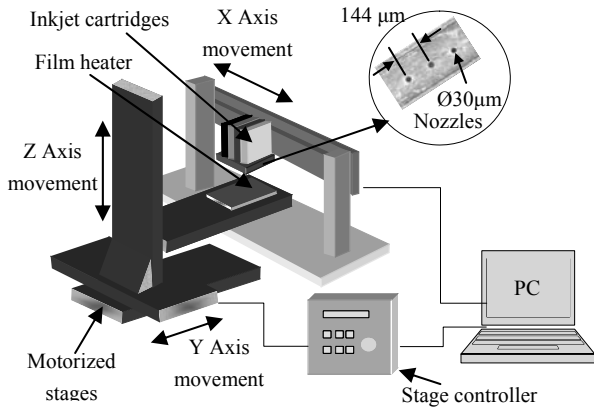


Fig. 2.1. Inkjet printing system

2.1.1 Single drop deposition

An inkjet printer’s horizontal resolution is defined by the firing frequency of the printhead and the linear speed of its horizontal movement, while vertical resolution depends on the positioning accuracy of the mechanical paper feed. In this study, however, since the mechanical paper feed was removed and replaced by motorized stages, ink positioning accuracy on the vertical axis was determined by overlaying the ink between the two adjacent nozzles, which were 144  $\mu\text{m}$  apart. In this experiment however, only one nozzle of the printer head was used to deposit inks so that a coverage area and thickness from a single drop could be determined.

The deposited single ink drop shape changed from a circular to an ellipse shape after drying due to solvent evaporation and measures about 90  $\mu\text{m}$  horizontally and about 54  $\mu\text{m}$  vertically as depicted in Figure 2.1.1 (a). The drops were then overlaid in the X and Y direction as seen in Figure 2.1.1 (b) according to a specific distance as denoted in Table 2.1.1.  $R_a$ , a parameter for measuring the average roughness of a surface and  $R_y$ , the maximum peak to lowest valley vertical distance within a single sample length was measured to study the effect of overlaying distance on the flatness of the deposited drops.

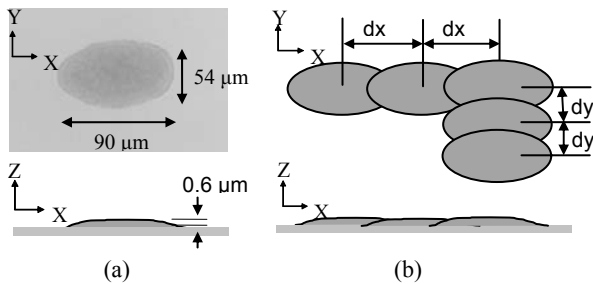


Fig 2.1.1. Description of a. a single drop coverage area; b. the overlaying of drops in the X axis and the Y axis.

Table 2.1.1. Overlaying distance

Distance dx( $\mu\text{m}$ )	92	80	68	56	44
Distance dy( $\mu\text{m}$ )	52	40	28	16	

2.1.2 Printing 3D patterns

The ability of inkjet printing technology to arrange dots precisely to create layers of material makes it interesting in layering multiple materials integrated into one part. This experiment however is trying to arrange dots of ink to fabricate 3D patterns based on the distance in the X and Y axis gathered from the previous experiment. Two patterns were fabricated, a rectangular pattern and a pyramid pattern as shown in Figure 2.1.2 (a) and Figure 2.1.2 (b). The patterns was chosen to study the ability of deposited ink drops to be arranged in a flat and inclined shaped so that deposition sequence can be better understood.



Fig 2.1.2. Description of a. rectangular pattern; b. pyramid pattern..

2.2 Drop deposition using inkjet device

The objective of this experiment is to investigate drop formation from a drop-on-demand piezoelectric ink jet device and by studying the dependence of several operating characteristics the physical phenomena underlying the operation of such a device can be better understood when fluids with different characteristics compared to normal inkjet inks were used.

The apparatus used in the investigations consists of a squeeze mode piezoelectric disc with external diameter measuring 25.4 mm, inner diameter 6.35 mm and thickness 2.54 mm (APC International, Ltd) which surrounds a glass Pasteur pipette bonded together by epoxy. The bottom end of the Pasteur pipette is closed off by a 0.2 mm thick aluminum plate, which contains a nozzle hole with an aperture dimension typically of 100  $\mu\text{m}$  in diameter, drilled using a microdrill. The piezoelectric assembly forms the cavity length of the apparatus where the upper and lower surfaces of the piezoelectric ring are plated to provide electrodes which rectangular pulses are applied as depicted in Figure 2.2.

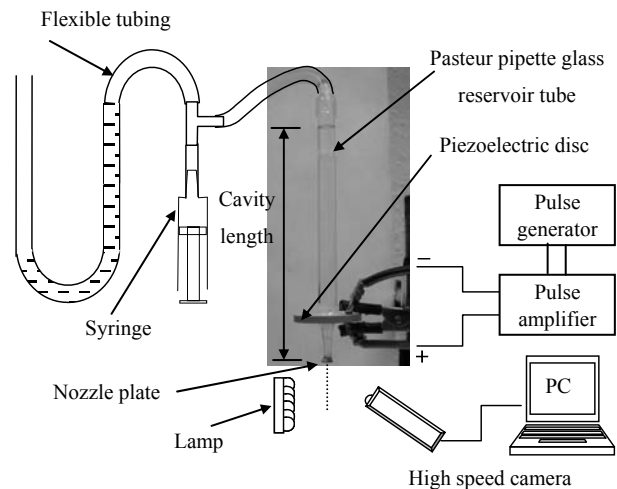


Fig 2.2. The piezoelectric assembly device apparatus

The piezoelectric disc produces fluid ejection by operating in compression, which contracts the volume of the glass fluid reservoir in the region of the hole in the driver disc. This produces a pressure pulse that forces out a fluid jet from the nozzle [4]. The device must be carefully prepared to remove all air from the pipette, since air bubbles absorb the pressure waves produced by the piezoelectric disc preventing a drop from forming. To avoid fluid buildup or leaking at the end of the nozzle when the drop ejector is in static mode, a manometer tube pressure control device was utilized to create a negative pressure to control the volume of air at the rear of the inkjet device reservoir. Too much negative pressure will draw air bubbles inside the device and insufficient negative pressure can cause fluid buildup at the end of the nozzle.

2.2.1 Cavity Length Effect

Experiments were done firstly on the relation of some operation parameters on the different length of fluid cavity. This was done by changing the cavity length while varying the voltage amplitude needed to produce a stable straight jet deposition. The amount of negative pressure required to avoid fluids from dripping was also recorded. De-ionized water was used for the purpose of this experiment. A high speed camera was also used to capture the image of de-ionized water deposited at variable frequency to investigate the frequency effect on drop velocity.

2.2.2 Variable Viscosity Deposition

In order to deposit fluid through the nozzle which diameter is about 100 μm, viscosity and surface tension which are crucial parameters were measured to confirm their capability to be deposited using the inkjet device. Generally, the fluid property requirements for demand-mode inkjet dispensing are as follows, the viscosity should be Newtonian and less than 40 cp, and the surface tensions should be greater than 20 dynes/cm (mN/m) [5]. Among fluids tested were de-ionized water (D.W) and ethylene glycol (E.G) because of their material properties and because they are commonly used as the base fluids for inks in inkjet printing. Their surface tensions are rather similar, but their viscosities are quite different. Inkjet ink was also tested as a comparison. Apart from that, water based low viscosity conductive silver ink was also tested. In this experiment frequency between 3 kHz and 5 kHz was used while maintaining the cavity length.

3. Experiment Results

3.1 Drop deposition using inkjet printer

In these experiments, a film heater was installed under the slide glass at temperature 80°C to evaporate the solvents in the ink and the ink dries in about 10 seconds.

3.1.1 Single drop deposition

Experiments were carried out to establish X and Y axis overlay distance that would give better surface flatness result. Figure 3.1.1 (a) shows the result of Ra and Ry when the dots

were overlayed on the X axis and Figure 3.1.1 (b) shows the result of Ra and Ry when the dots were overlayed on the Y axis. The results shows that the best surface flatness can be achieved when overlaying the dots at a distance of 68 μm on the X axis and 40 μm on the Y axis.

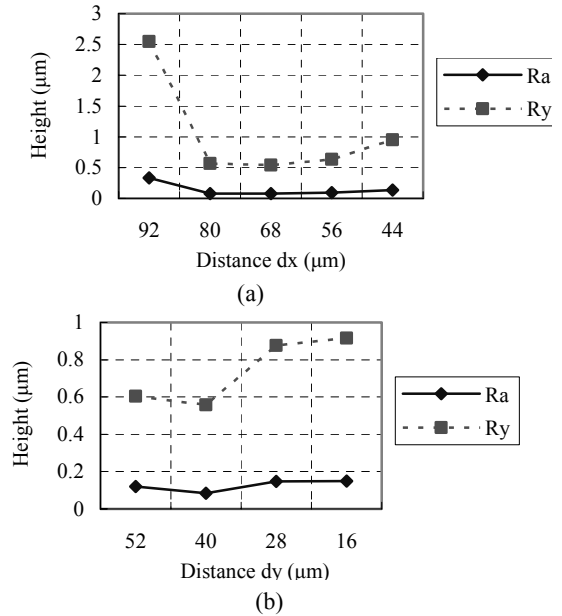


Fig. 3.1.1. Surface flatness on a. X axis; b. Y axis

3.1.2 Printing 3D patterns

Experiment result on printing a rectangular pattern shows that the ink seems to sink at the intersection area of dots as described in profile 1 and profile 2 shown in Figure 3.1.2 (a). Experiment done in arranging the dots to fabricate a pyramid pattern also show that there is a sinking setback with the deposited pattern as can be seen in profile 1 and profile 2 shown in Figure 3.1.2 (b).

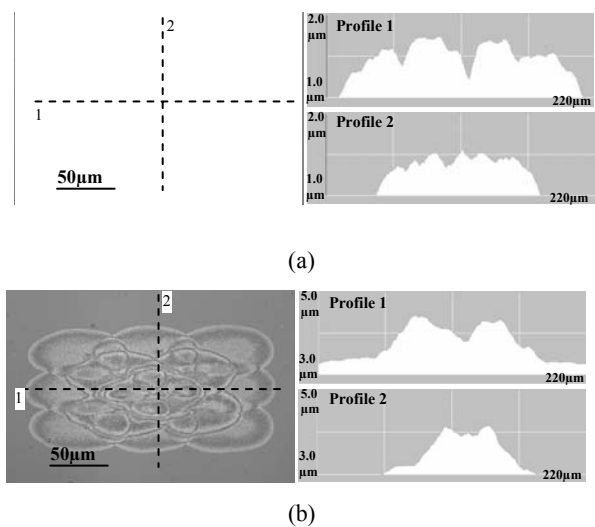


Fig. 3.1.2. Surface profile of the a. rectangular pattern; pyramid pattern

### 3.2 Drop deposition using inkjet device

As it is difficult to verify the droplets coming out of the nozzle with naked eyes, droplets formation were monitored using the Phantom v5.0 high speed digital imaging system.

#### 3.2.1 Cavity Length Effect

From experiments done to study the relation of some operation parameters on the different length of fluid cavity, observation showed that the voltage pulse amplitude needed to eject drops increased when cavity length of the inkjet device is reduced almost at a constant rate while the negative pressure hold the fluid from dripping reduced as shown in Figure 3.2.1. This means that if a fixed voltage amplitude wished to be used, a fluid filling mechanism have to be installed to maintain the fluid level for a stable drop formation. Experiments to investigate the frequency effect on drop velocity shows that as frequency increased the distance between drops and drop velocity reduced as shown in Table 3.21 and Figure 3.2.1.1. The relationship between the frequency, distance between drops and drop velocity is very important if the inkjet device system was to be used to direct write functional materials using.

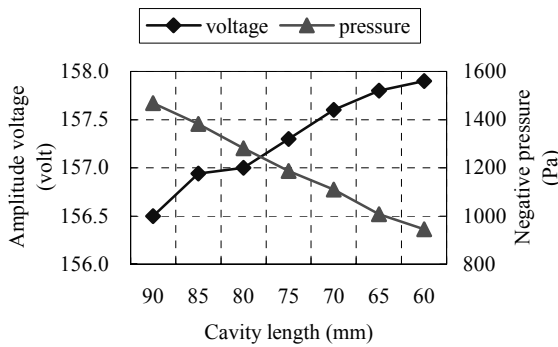


Fig. 3.2.1. Inkjet printing system

Table 3.2.1. Frequency effect on drop velocity

Frequency (kHz)	2.5	2.6	2.7	3.0
Distance between drops (mm)	1.74	0.84	0.58	0.19
Drop velocity (m/s)	2.24	1.08	0.75	0.43

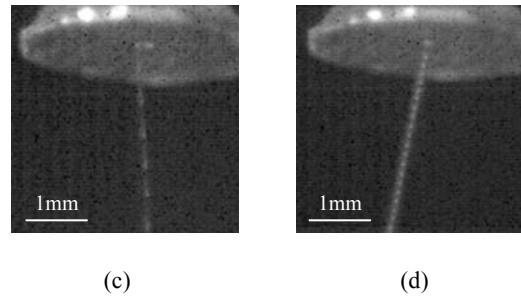
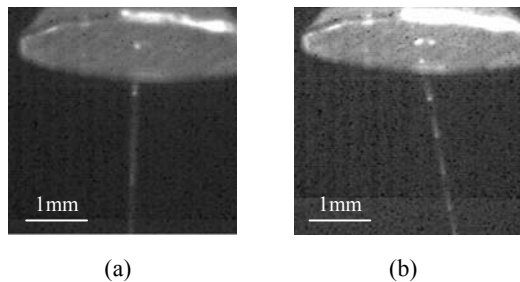


Fig 3.2.1.1. Drop deposition at frequency a. 2.5 kHz; b.2.6 kHz; c. 2.7 kHz; d.3.0 kHz..

#### 3.2.2 Variable Viscosity Deposition

The results of viscosity and surface tension measurement of the fluid materials were shown in Table 3.2.2. From the experiments done on depositing the materials, it seems that more voltage pulse amplitude is needed to eject fluid material with higher viscosity as shown in Figure 3.2.2. Fluids with different material characteristic require different parameter setting. In this experiment, the same cavity length was used to test all the fluid materials due to its effect on the voltage amplitude. Fluids filtering will also help reduce the possibility of the nozzle being clogged due to foreign particles.

Table 3.2.2. Fluid material properties

Fluid Material	Viscosity (mPa.s)	SurfaceTension (mN/m)
D.W	1.14	55.2
E.G 25% D.W 75%	1.79	62.6
E.G 50% D.W 50%	3.44	56.7
Printer Ink	3.59	32.2
Silver Ink	1.81	53.9

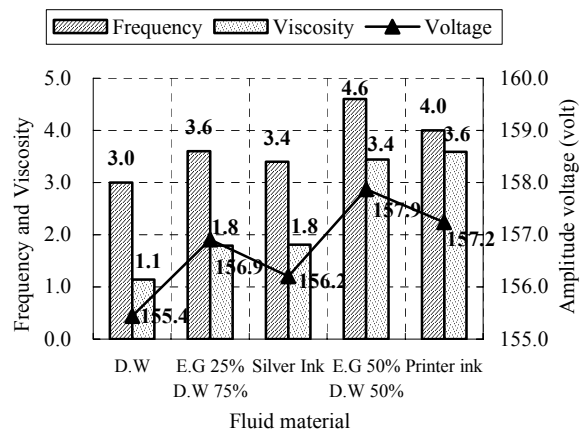


Fig 3.2.2. Variable viscosity deposition

#### 4. Discussion

The ability to convert CAD design data and control an inkjet printing machine within a Java program provides the flexibility to harmonize different equipment in the same environment. Although there are still many improvements to be made in terms of hardware and software, the capability of the inkjet printing technology in depositing material layer by layer to build 3D structures is promising. Fabricating multi-material 3D structures using inkjet printing technology require arrangement and overlaying the deposited dots in a manner that will create a dense and flat layer pattern. In order to direct write patterns with the deposited fluid, the movement of the additional axes must be synchronized with the ink deposition rate. A study of inkjet printing resolution using normal printing ink was necessary prior to printing with functional inks because fluids such as metal-filled conductive inks or polymer inks are not cheap and extra care must be taken in handling these materials.

From the experiments done using print head nozzle 30  $\mu\text{m}$  in diameter, 144  $\mu\text{m}$  apart and printed at a horizontal resolution of 360 dpi, the smallest dot can be printed is about 90  $\mu\text{m}$  horizontally and about 54  $\mu\text{m}$  vertically. Overlaying the ink in a controlled environment provides the flexibility in programming the drops deposition both on the X and Y axis. The drops positioning however must be improved to get smooth surface 3D patterns. The ability of the program to control fluid deposition with different sizes will inevitably improve the print resolution because circular dots tend to leave void areas at their corners, making it difficult to fabricate sharp edges.

The drop deposition experiment using the inkjet device shows that depositing fluids with precise control trajectory requires control of its operating parameters such as amplitude voltage, pulse frequency and cavity length. These parameters have big influence on the capability of fluids to be deposited, their velocity, distance between drops and some of these parameters are related to each other. The information is very useful in fabricating multi-material 3D structure using the inkjet printing system. The imaging system however must be improve so that deposited drop size could be measured. The inkjet device fabricated is also capable to deposit fluids without having in contact with the piezoelectric material and this makes it possible to test fluids that require special consideration.

#### 5. Conclusion

The ability to build multiple-material prototypes or models from a rapid prototyping machine will inevitably bring manufacturing technology to another dimension. The inkjet printing machine that was built shows flexibility in depositing fluid of multiple materials generating one ink cartridge (tool) path file for every different material. From the experiments done to explore ink deposition resolution using a commercial piezoelectric printer, a few conclusions can be made:

- ◆ The minimum dot size achievable which is from a single drop is about 90  $\mu\text{m}$  in the X axis and about 54  $\mu\text{m}$  in the Y axis.

- ◆ The overlaying distance to arrange the drops that gives a more flat pattern is about 68  $\mu\text{m}$  in the X axis and 40  $\mu\text{m}$  in the Y axis.

The inkjet device also gives valuable information on deposition of drops using a piezoelectric device. Among the conclusions that can be made are:

- ◆ The cavity length or the fluid volume in the reservoir will give a significant effect on the drop deposition. Fluid cavity of 90 cm required frequency of 3.7 kHz and amplitude voltage of 156.5 volt while fluid cavity of 60 cm required frequency of 4.7 kHz and amplitude voltage of 157.9 volt to be deposited.
- ◆ The cavity length or the fluid volume in the reservoir will also give a significant effect on the negative pressure needed to hold the fluid from dripping. Fluid cavity of 90 cm will require a negative pressure of 1468 Pa while fluid cavity of 60 cm will require a negative pressure of 945 Pa.
- ◆ Frequency will give significant effect on the drops characteristic. A frequency of 2.5 kHz will deposit drops with velocity of 2.24 m/s and distance between drops of about 1.74 mm while a frequency of 3 kHz will deposit drops with velocity of 0.43 m/s and distance between drops of about 0.19 mm.
- ◆ Fluids with different material characteristic require different parameter setting. To deposit inkjet ink with viscosity of 3.59 mPa.s require frequency of 4.0 kHz and amplitude voltage of 157.24 volt while conductive silver ink with viscosity of 1.81 mPa.s require frequency of 3.4 kHz and amplitude voltage of 156.2 volt.

#### 6. References

- [1] Wallace D.B. and Hayes D.J. (2002), "Solder Jet™ - Optics Jet™ - AromaJet™ - Reagent Jet - Tooth Jet and other Applications of Ink-Jet Printing Technology", in Proceedings, NIP18: International Conference on Digital Printing Technologies, San Diego, CA.
- [2] Mustaffa B.I., Narahara H. and Suzuki H. (2004), "Electronic Circuit Fabrication Using Inkjet Printed Silver Nanoparticles For SFF", in Proc. of Japan Society for Precision Engineering National Conference, pp. 83-84, Tokyo
- [3] Mustaffa B.I., Narahara H., Koresawa H. and Suzuki H. (2004), "Integration of Silver Nanoparticle Inkjet Printing and Layered Manufacturing Technology", Proc The 7<sup>th</sup>. Intl. Conf. Quality in Research (QIR) 2004 (Mech. Engineering), ME-DM-04-1-4, Jakarta, Indonesia, August.
- [4] Eric R. Lee (2003), Microdrop Generation, CRC Press, pp. 166.
- [5] Wallace D.B., Cox W.R., and Hayes D.J. (2002), "Direct Write for Ink-Jet Techniques", in A. Pique and D.B. Chrisey, eds, Direct Write Technologies for Rapid Prototyping Applications- Sensors, Electronics, and Integrated Power Sources, Academic Press, New York.

---

# Miniaturization of Dot Pattern by Metal Forming for Direct Marking of 2D Barcode Symbols

Hiroshi IKE<sup>1</sup>  
<sup>1</sup> (RIKEN, Japan)

Keywords: microforming, dot impact, 2D bar code, direct marking, Data Matrix.

## Abstract

To create information delivering ability on metal surfaces by microforming, a direct marking system of 2D bar code symbols (Data Matrix) on a metal plate as surface microcavities using a dot impact forming machine is developed via symbol images. Miniaturization of dot pattern was further enabled by introducing an x-y microstage to reduce the pitch of dots from 119 $\mu$ m to 30  $\mu$ m, resulting in 2D symbols at 840 DPI with successful rapid decoding by a PC-based optical system compatible with direct marking.

## 1. Introduction

Micro-metalforming has been developed during the last ten to fifteen years intensively to find its superiority on other processing mainly for efficiency in mass-production [1]-[3]. However, intelligent and less speedy way of application can be another acceptable direction of development. One of those applications can be found among abilities of surface microgeometry formed on metal surfaces. It is expected that such properly defined arrays of surface asperities can deliver information inherent to the parts on which the surface asperities are formed. This enables metallic parts to play the role of durable, high temperature resistant, chemically stable media for information transmission. This idea can be realized through direct marking of two dimensional bar codes, among which Data Matrix [4] and QR Code [5] are popular. Specifically their symbol patterns are composed of orthogonal arrays of white and black square cells, which can be replaced by circular dots if appropriate decoding software is used. This feature is suitable for direct marking of 2D bar codes on metal surfaces. Data Matrix is used in the present study, however, similar availability is confirmed for QR Code as well [6].

Currently available methods of direct marking include micro-drilling, dot impacting (=micro-metalforming) and laser marking. Micro-drilling and dot impacting are usually used in a semi-micro range (order of 0.X mm)[7]. Though laser marking is microscopic (order of 10  $\mu$ m), the apparatus is expensive and the geometry of the marking has some problems. The methods of information acquisition, common among those marking are acquiring grey scale images of dotted patterns using appropriate lighting, a macro-lens and

an image sensor, and then these images are processed and decoded into text.

The author studied forming of surface micro-geometry by coining [8] [9] and special rolling [10] and confirmed that microcavities with diameter of some tens of micron can be formed without serious problems because of secure contact between tool and workpiece during indentation. In the present paper microforming ability of metal sheets are fully utilized by sequential micro-dot impacting and the ability of information delivery of the formed surface cavities.

In the previous paper [6], the author constructed a laboratory system of encoding arbitrary text into 2D barcode symbols of Data Matrix and QR Code, marking of 2D barcodes by a dot impact pin in terms of progressive micro-metalforming and successful and speedy image acquisition and decoding by a CCD sensor with PC-based direct marking decoding software. In the previous experiments dotting was made in both x and y directions at a fixed pitch of 119  $\mu$ m (210 DPI) because of the performance of the dotting machine. In the present paper, for realizing higher density marking and decoding system, a computer controlled micro x-y stage is introduced. Finally direct marking of 16 times higher density at a pitch of 30  $\mu$ m, that is 840 DPI marking, was achieved and successfully decoded by the current system. The limitation of further miniaturization is discussed.

## 2. Basic experimental method [6]

### 2.1 Microforming process and equipment

The experimental procedure is shown in Fig. 1. Information expressed by characters or numerals are encoded to Data Matrix by a commercial software to obtain symbol images in a BMP file format. The images are imported to a so-called "metal printer" (Metaza MPX60) in a manner that one dot corresponds to one cell of the 2D barcode image. The metal printer makes arrays of dots at a pitch of 119  $\mu$ m at an average speed of 65 cell/s including black cells (no dots) and feeding time. The tested specimen material is an austenitic stainless steel SUS304 of 1.47 mm thickness (MVH: 217.1) and the surface is mirror-finished to have a clear image of symbols. The head of dot impact pin made from tungsten

carbide has a cone shape with a cone angle of 90 degrees and a rounded head of about 10 μm diameter. The impact force is adjustable to obtain cavity diameter of 29 to 65 μm for the current tested specimen.

**2.2 Measurement and decoding**

Fig. 2 shows a measuring system of direct marked 2D bar code. The image of the dotted pattern is acquired by a CCD camera with a macro-zoom lens and close-up lenses. This system totally zooms up actual 1mm to 16.7 to 96.6 pixels in the VGA monitor at a working distance of 138mm. Lighting direction is slanted by 50 degrees from sample plane normal. Under this lighting, as schematically shown in the expanded figure of Fig. 2, the original plane surface looks dark and the surface cavities formed by a dot impact pin look bright, because of optical geometry to cause normal reflection at the rounded bottom. However, of course, a reverse image is also obtainable in terms of image processing software. The speed of shutter was fixed at 1/60 s. The samples were placed normally to the optical axis. Image acquisition and decoding was repeated automatically as soon as one cycle is completed to check the repeatability and average time of decoding.

**3. Experimental results**

**3.1 Simple example**

Fig. 3 shows a barcode symbol of “International Conference on Precision Engineering” in Data Matrix (ECC200) (a) and the corresponding dot pattern image (b) obtained from a dotted stainless steel sample by the optical system shown in Fig. 2. It has 28x28 cells including quiet zone of 1 cell width around its square. A Data Matrix symbol has a characteristic L shape at the left and bottom sides and alternating black and white cells on the top and right sides to detect the size, location and rotation of the symbol.

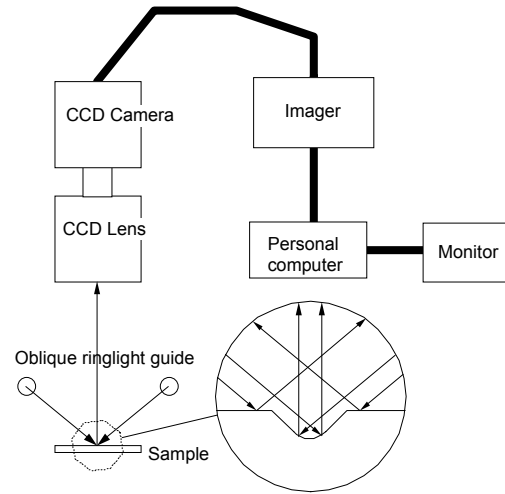


Fig. 2. System of measuring direct marked 2D bar-code symbols [6].

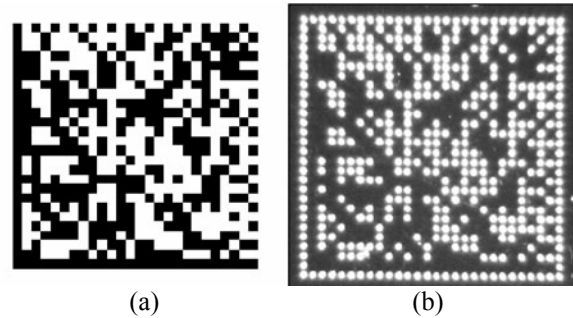


Fig. 3. Data Matrix Symbol of “International Conference on Precision Engineering” (a) and the corresponding decodable dot pattern image (b) obtained by the optical system shown in Fig. 2. Dot pitch: 119μm. 28x28 cells including quiet zone. Global size: 3.30 mm. Marking time: 24s.

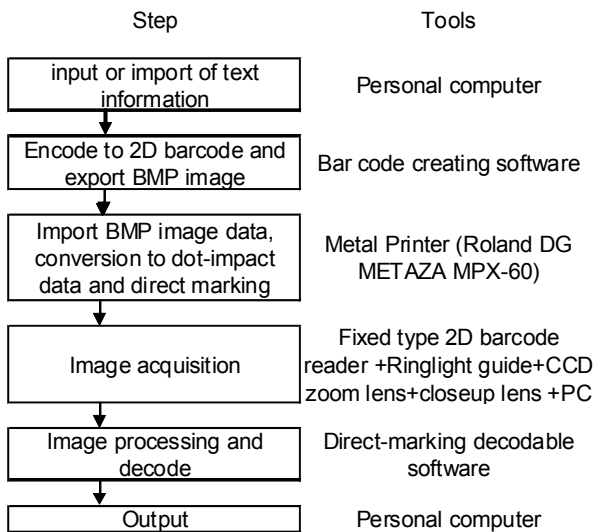
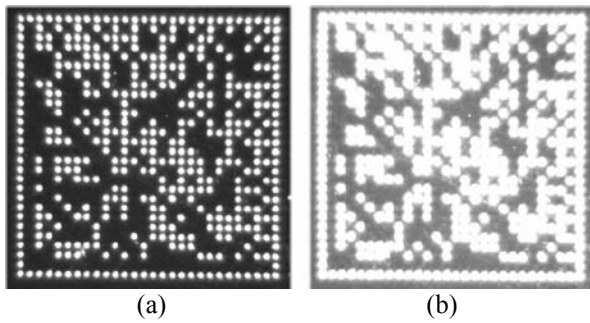


Fig. 1. Experimental procedure and the related tools [6].

The image Fig. 3 (b) varies with variation of diameter of the dotted cavities and/or illumination. An increase in diameter of the dotted cavities results in a slight increase in the enlarged white marks in the acquired image. However, an increase in illumination overrides the effect of cavity diameter. Fig. 3(b) is the darkest limit of the image that can be decoded with 100% success. Fig. 4(a) shows an even darker example that can not be decoded at all and Fig. 4 (b) shows bright limit that can be decoded with 100% success. Figs. 3 and 4 show that the decodable range of illumination is wide.

Apart from the optical system shown in Fig.2, for laboratory purposes, one can decode Data Matrix ECC200 symbols in the following manner: acquire an original image (for example as in Fig. 5(a)) using a normal flat-bed scanner with high resolution of 3200 DPI or higher and then apply “dilate” filter a few times by an image processing software to transform the image into Fig. 5 (b). Finally, the image Fig. 5 (b) can be decoded by a conventional (=direct-marking incompatible) decoding software. However, in this method decoding is sensitive to the degree of dilation of the images.



**Fig. 4.** Variation of the images by illumination. (a) An undecodable dark image. (b) Bright limit image decodable with 100% success. Dot pitch: 119 $\mu$ m. Size: 3.30 mm.

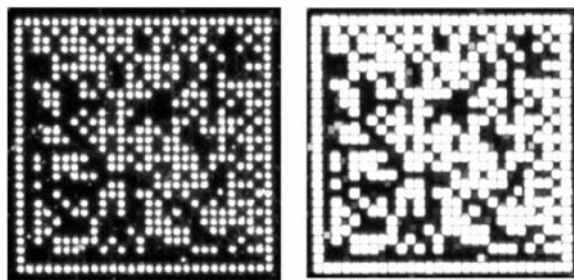


**Fig. 5.** An image taken by a flat-bed scanner (a) and the dilated image (b) that is decodable by normal software. The same marking as in Figs. 3 and 4.

### 3.2 Further miniaturization - 4 times high density dots

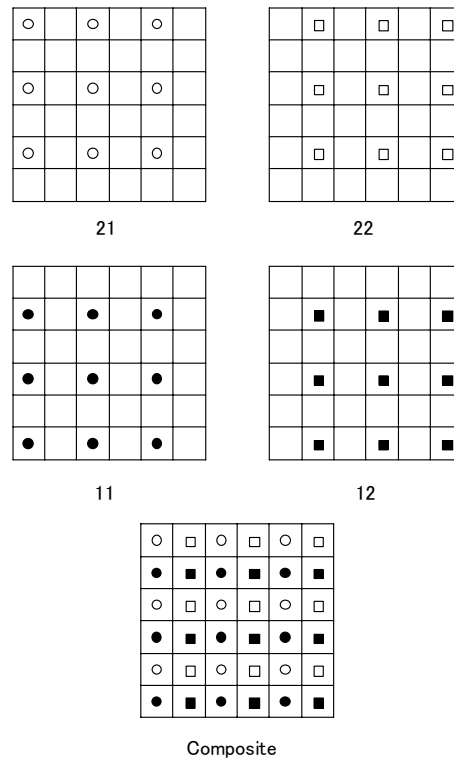
The used machine produces dots at a fixed pitch of 119 $\mu$ m presumably for simplicity of the machine mechanism and for the high rate of marking. To realize further miniaturization, a computer-controlled x-y stage was introduced. For example, to produce dots at a pitch of 60  $\mu$ m, the original orthogonal dots are decomposed into 4 overlapping groups of dots as shown in Fig. 6 as 11, 12, 21 and 22. Each group is marked at a normal pitch of 119 $\mu$ m but with or without a shift of the sample at 60  $\mu$ m in x-y axes made by the motion of the x-y stage among the groups. The final overlapping pattern of dots is shown at the bottom figure as “composite”, where the distance of the neighbouring dots is 60  $\mu$ m.

Fig. 7 shows an example of dots at a 60  $\mu$ m pitch that is of 4 times-high density compared to Fig. 3(b).

### 3.3 Extreme miniaturization - 16 times high density dots

The above technique is naturally extended to 16 times high density dots, where the pitch of dots is 30  $\mu$ m and the dotting pattern is decomposed into 16 partial patterns. Fig. 8 shows an example of 16 times high-density dots that were decodable by the current measuring system.

The 16 times high density dots is useful if the text capacity is large. Fig. 9 (a) shows such an example of Data Matrix Symbol of 436 characters including spaces taken from the topics of the 11th ICPE as follows: “Topics of the conference include, but are not limited to, the following:   
Advanced Manufacturing Systems   
Ultra-Precision Machining and Micro Machining   
Nanotechnology for Fabrication and Measurement   
Rapid Prototyping and Production Technology   
New Materials and Advanced Processes   
Computer Aided Production Engineering   
Manufacturing Process Control   
Planning and Scheduling for Production   
CAD/CAE/CAM”. The cell size is 76x76 including quiet zone of 2 cell width. Fig. 9(b) shows the corresponding decodable dots of the 16 times high-density. The global size of the dots is 2.28 mm while the size of original dots at a pitch of 119  $\mu$ m is 9.04 mm. The marking was achieved in 94 s for the original dots and the decoding of this pattern takes for 0.30 to 0.35 s irrespective of marking density.



**Fig. 6.** Method of decomposition of orthogonal symbols into 4 groups and integration of the dots.



**Fig. 7.** Dots of 4 times high density compared with Fig.3 (b). Dot pitch: 60  $\mu$ m. Size: 1.66 mm.



**Fig. 8.** Dots of 16 times high density compared with Fig.3 (b). Dot pitch: 30  $\mu\text{m}$ . Size: 0.83 mm.

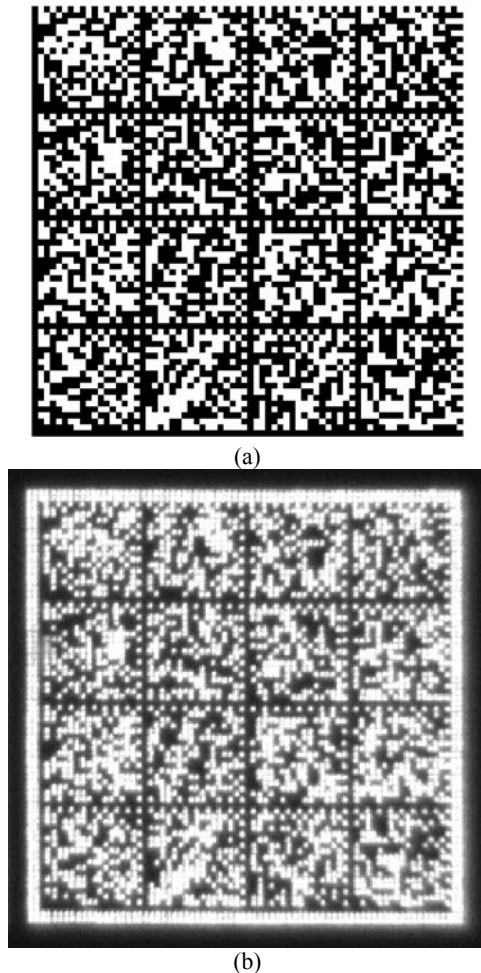


**Fig. 9.** An example of large symbol. (a) Data Matrix symbol of 436 characters taken from Topics of the 11th ICPE. 72 x72 cells. (b) Dots of 16 times high-density compared with Fig. 3 (b). Dot pitch: 30  $\mu\text{m}$ . Size: 2.28 mm.

## 4. Discussion

### 4.1 Optical requirements to decode symbols

As the dot pitch decreases, requirements to the optical system become severe. Under the current optical system, where both the height of ring light and the intensity of the light are adjustable, the limiting optical condition seems to be magnification of the total optical system. For example, with 16times high-density dots at a pitch of 30  $\mu\text{m}$ , magnification of 71.2 pixel/mm or higher was required. This corresponds to 2.14 pixel/cell. At this limiting condition, the

alignment of CCD camera, illumination, and so on were severe and at 96.6 pixel/mm (=2.9 pixel/cell) they became moderate.

### 4.2 Dot size requirements

If the dot pitch is fixed, for example, at 30  $\mu\text{m}$ , an important limiting condition of dot size (=diameter) is imposed. In the present system, dot size can be fairly small comparing with the cell size: dot size of 28.5  $\mu\text{m}$  at a dot pitch of 119  $\mu\text{m}$ , *i.e.*, 24% in diameter and 4.5% in area, was quite decodable if the illumination is slightly increased. However, in the case of small cell size, dot size must be smaller than a certain value. Fig. 10 shows scanning laser micrograph of decodable dots (a), (b) and undecodable dots (c), (d). Dotted cavities are rather independent and undeformed in Fig. 10 (a) and (b), while dots are severely interfered by the neighbouring dots in Fig. 10 (c) and (d). The limiting condition of decoding depends whether the central bright area of each dot (rounded bottom) is maintained or destroyed by the neighbouring (subsequent) dots. For example, in Figs. 10 (a) to (d), the second row from the top is formed at the initial stage of marking and is the most vulnerable to the subsequent dots (upper and lower). So in Fig. 10 (c) and (d) central bright area of the second row vanished. Judging from Fig. 10, the decodable limiting size of free dots is about 36  $\mu\text{m}$  when the dot pitch (=cell size) is 30 $\mu\text{m}$ . It means that the dot diameter slightly larger than the dot pitch is allowed. With the impact force lower than that in Fig. 10 (a), the dots diameter get unstable presumably because of reduced normal stress and of a scatter in deforming resistance of crystallographic grains based on preferred orientation. In order to decrease the diameter of dots further, the rounded bottom should be reduced in size though it is fixed at about ten  $\mu\text{m}$  in the current machine.

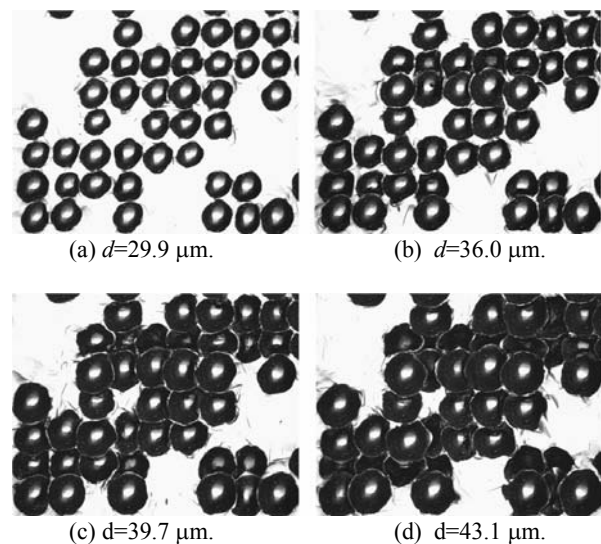


**Fig. 10.** Effect of dot size on decoding. Dot pitch: 30  $\mu\text{m}$ .  $d$ : average diameter of free dots. (a) and (b): decodable. (c) and (d): undecodable. Scanning Laser Micrograph.



## 5. Conclusion

To create information delivering ability on metal surfaces in a micro scale, patterns of 2D bar codes are micro-formed using a dot-impact metal printer, and the pattern was successfully decoded by a direct-marking compatible measuring system. Though the dot pitch is originally fixed at 119  $\mu\text{m}$  depending on the machine performance, an additional x-y stage under the sample enabled to make a 16 times high-density dots at a pitch of 30  $\mu\text{m}$  (840 DPI), resulting in successful decoding. The limitation of miniaturization is found with interference of dots to destroy neighbouring dots to vanish central rounded bottom. For this reason, the dot size should be below 120% of dot pitch. Optical magnification should be also as high as about 2.5 pixels / cell for stable decoding.

The author expresses his sincere appreciation for the financial aid by The Ministry of Education, Science, Sports and Culture of Japan (Grant-in Aid for Scientific Research (C) 16560643).

## 6 References

- Geiger M, Kleiner M, Eckstein R, Tiesler N, Engel U, (2001) Microforming. Ann. CIRP 50: 1-18.
- Engel U, Eckstein R, (2002) Microforming - from basic research to its realization. J. Mater. Process. Technol. 125-126: 35-44.
- Engel U, Geißdorfer, S, (2006) Microforming technology - history and future. Proc. ESAFORM 2006 ed. Juster N, Rosochowski A: 11-12, Akapit.
- Information technology - International symbology specification – Data Matrix, ISO/IEC 16022.
- ibid*, QR Code, ISO/IEC 18004.
- Ike H, (2006), Microforming of Cavities for Direct Marking of Two-Dimensional Barcode Symbols, Proceedings ESAFORM 2006, ed. Juster N, Rosochowski A: 551-554, Akapit.
- Mortimer J, (2005) BMW first to adopt data matrix for engine “track and trace”. Assembly Automation: 25/1: 15-18.
- Ike H, Plancak M, (1998) Coining Process as a Means of Controlling Surface Microgeometry. J. Mater. Process. Technol. 80-81:101-107.
- Ike H, Plancak M, (1999) Controlling Metal Flow of Surface Microgeometry in Coining Process, Advanced Technology of Plasticity 1999, ed. Geiger M: 907-912, Springer.
- Ike H, (1996) Properties of Metal Sheets with 3-D Designed Surface Microgeometry Prepared by Special Rolls, J. Mater. Process. Technol. 60: 363-368.

---

## Plasma Etching Based Processes for the Fabrication of Micro Structured Linear Guide

A. Phataralaoha, S. Büttgenbach  
Institute for Microtechnology, Technical University Braunschweig  
Alte Salzdahlumer Str. 203, 38124 Braunschweig, Germany  
Tel: +49 531 391 9759; Fax: +49 531 391 9751  
E-mail: a.phataralaoha@tu-bs.de

Keywords: inductively coupled plasma etching, barrel plasma etching, micro structure, linear guide

### Abstract

This abstract is focused on the fabrication of low friction silicon micro guides. The novelty of this work is related to the fabrication process using an inductively coupled plasma etching and a barrel etching process for silicon micromachining. This simple technology allows the fabrication of silicon micro guides with only two photolithographic steps. Micro patterns on support structures of the stationary parts were fabricated to minimize the contacting area of the micro linear guide and as a result to reduce a sliding friction as well as a coefficient of friction.

### 1 Introduction

Friction is an unavoidable characteristic of mechanisms comprising movable components which are in contact with each other. The effects of friction increase significantly as the system dimensions decrease. Therefore, friction becomes critical on the microscale and is one of the fundamental limitations in the design and implementation of reliable, efficient MEMS devices.

In the last decade various types of actuating principles used in micromachines have been reported [1, 2]. Great efforts have been made to improve the reliability of the devices but the understanding of friction, wear and other related phenomena is still insufficient. Several guide and support structures based on two categories were demonstrated for use in micromachines: contact and non-contact type bearings. In contact type bearings, support structures are in direct contact with the moving parts. Due to the tribological contact, the reliability of such devices suffers drastically from friction and wear. The non-contact type structures use more complicated mechanisms like electrostatic [3], electromagnetic [4] or aerostatic bearings [5]. These systems show much less friction and wear compared to contact type systems, however, as major drawbacks, their fabrication is rather complex and the stability of the moving plate falls off. In spite of less friction, contact type rolling motion ball bearings also have a serious disadvantage [6]. The unpredictable, mixed movement between rolling and sliding motion of the balls causes

instability of the moving plate. Therefore, tribological guides seem to be well suited for MEMS applications, due to the fact that the guide mechanism is relatively simple, whereas the structures can be fabricated with a couple of photolithographic and etching steps. In addition, the guide structures provide a stable and robust support for the moving plates.

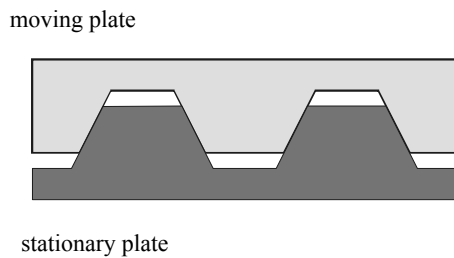
Micro linear guides are inevitable parts of active micro systems driven by micro linear motors. A micro linear guide was designed in order to reduce the static and also the kinetic friction between the moving micro plates. Concerning the previously developed silicon linear micro guides [7], both the moving and the stationary plate were fabricated by wet chemical etching. The typical V-grooves of (111)-planes provide a self-alignment between both plates. An average coefficient of friction (COF) of the linear guide of 0.2 was determined. Because of the small size of micro actuators, the resulting driving force of micromachines is very limited, so that the friction of the guides has to be reduced as far as possible. To achieve a COF of less than 0.1 optimized linear guides are needed.

Several approaches have been introduced to improve the tribological behavior of sliding motion, such as mono- or multilayer coating of lubricating films [8]. Another approach is the optimization of contact areas, due to the fact that the COF verifiably depends on the topography of contact areas. A COF of sliding friction of 0.04 can be observed when the contact area is reduced to 1% [9]. Thus, the further development of the micro linear guide is focused on the reduction of the contact area. Using plasma based etching processes the contact area of micro structures can easier be controlled as in wet chemical etching.

This paper focuses on the fabrication of silicon micro guides using a dry etching based process. The novelty of this work is related to the fabrication process. It uses an inductively coupled plasma etching process (ICP) and a barrel etching process for silicon micromachining and allows the production of monolithic micro structures. ICP etching is used to fabricate the main support structures and barrel etching is used to pattern the contact area on top of these structures.

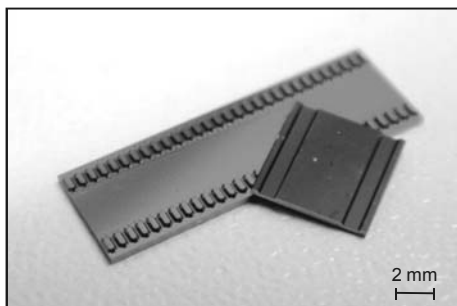
## 2 Micro linear guides

A basic concept of linear guides consists of two matching long parallel tracks on a stator (stationary plate) and grooves on a slider (moving plate), which can be fabricated using micromachining techniques, such as wet chemical etching of silicon. A schematic view of the previous design of the micro linear guide is shown in Fig. 1. Parallel V-grooves are etched into the moving plate (5 mm x 5 mm x 0.45 mm) made of a (100)-silicon wafer. On the stationary plate, V-shape tracks are also etched wet chemically. The gap between both plates is determined by the opening size of the masking layer.



**Fig. 1.** Schematic view of the wet chemically etched linear guide

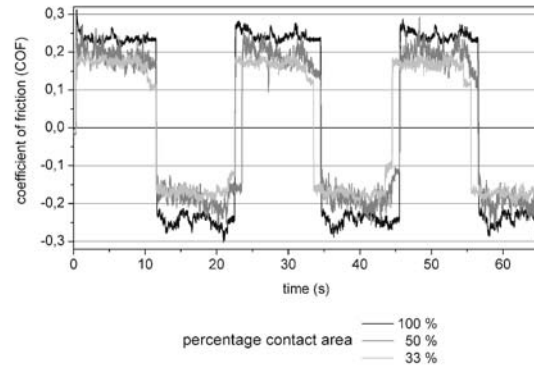
For this design the contact area is on the (111)-plane of the etched surface which assures the lateral accuracy between stator and slider. Therefore, undercut of the (111)-plane has no effect on the fitting accuracy of the guide. Preliminary investigations of sliding friction of flat and patterned specimens have shown that the patterned specimens have lower static as well as kinetic friction as the flat specimens. For this reason, the long V-shape tracks of the stator are micro structured to exhibit small bosses. Fig. 2 shows a micro guide with micro structured rails on the stationary plate and V-grooves on the moving plate.



**Fig. 2.** Stator with micro structured rails and slider of a silicon micro linear guide

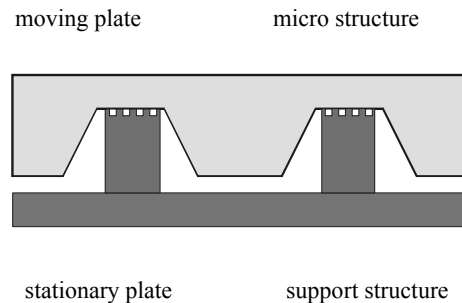
Through the micro structures of the rails the contact area was reduced from 2.6 mm<sup>2</sup> to 1.3 mm<sup>2</sup> (50 %) and to 0.91 mm<sup>2</sup> (33 %) by boss distances of 250 μm and 500 μm, respectively. Fig. 3 shows the kinetic COF of the micro linear guides, where the sign of COF denotes the moving direction of the samples. In this experiments the slider was

driven in oscillating motion using a friction tester described in [10] with a sliding speed of 100 μm/s and constant normal load of 30 mN.



**Fig. 3.** Kinetic COF of the micro linear guide

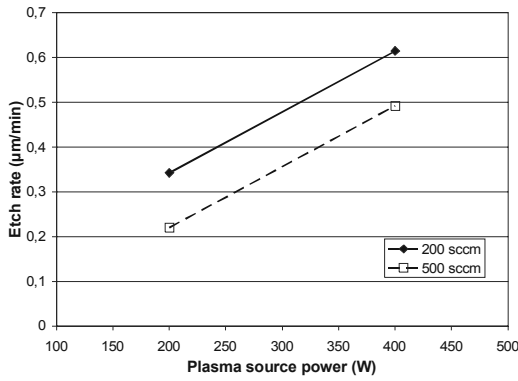
The micro guide with a contact area of 33 % has the minimum average COF of 0.17. For a contact area less than 33 %, an even lower COF can be expected. For our requirements, the COF of micro linear guides has to be less than 0.1. Due to anisotropy and undercut, the variation of the shape of micro guides using a wet chemical etching process is very limited. Hence, plasma dry etching processes are the key technologies for fabricating optimized micro linear guides.



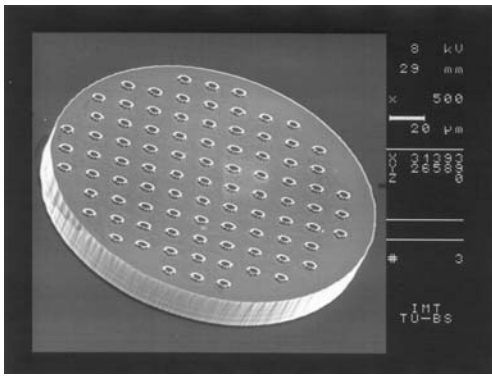
**Fig. 4.** Schematic view of the plasma assisted etched linear guide

Fig. 4 shows a schematic view of the micro linear guide, the stator of which is fabricated by plasma dry etching. The V-grooves of the slider are still produced using wet chemical etching, but instead of the (111)-plane the contact surfaces of this linear guide are on the bottom of the grooves. A groove depth of 10 μm has been defined, so that the bottom width closely fits into the support structures. The cylindrical support structures of the stator are fabricated by ICP dry etching. The top surfaces of the structures are used as the contact area, which are patterned into an array of bosses with a diameter of 10 μm using isotropic barrel etching. The accuracy of the V-grooves depth determines the laterally fitting tolerance of the guides.





**Fig. 7.** Silicon etch rate versus source power and CF<sub>4</sub> flow rate



**Fig. 8.** SEM picture of a patterned cylindrical support structure with a diameter of 200 µm

Fig. 8 shows a patterned support structure with a diameter of 200 µm. The ICP dry etching process with a low etch rate assures a high uniformity and a high aspect ratio. For 20 µm etch depth the overall deviation of the depth is less than 2 µm over the whole 4" wafer. The thick resist can be used as a reliable masking layer, especially for this application, due to the short etching time of 17 min. For very deep etching or long process times (more than 30 min.) the resist will be damaged because of the high process temperature which causes the decrease of lateral accuracy and surface quality of the etched structures.

## 5 Experiment results

Two different designs of the micro linear guides are tribologically investigated using the friction tester. Both designs have the support structures with a diameter of 200 µm and a distance to each other of 2.5 mm, so that the moving plate with a length of 5 mm is placed on only four support structures. The first design has a flat surface on the top of the support structures of the stationary plate. For the second design the micro pattern is fabricated on the top surface of the support structures. The moving plates which have a mass of 19.5 mg, with wet chemically etched

V-grooves are used for both designs. Furthermore, both the stationary plates and moving plates were coated with a thin amorphous carbon (a-C) layer with a thickness of 0.5 µm used as a dry lubricating layer. The moving plate is placed on the stationary plate, which moves for 1 mm with a velocity of 100 µm/s. The dynamic friction force is simultaneously measured using a micro force probe [11]. All measurements are performed in steady room environment at a temperature of 25°C and a relative humidity of 35%RH.

Different weights are applied onto the moving plate to study the effects of the normal load on the friction force. The four measurements are made at each weight on diverse positions of the linear guides. Fig. 9 shows the friction force versus the normal load. Each point in the diagram represents the average friction force of each experiment.

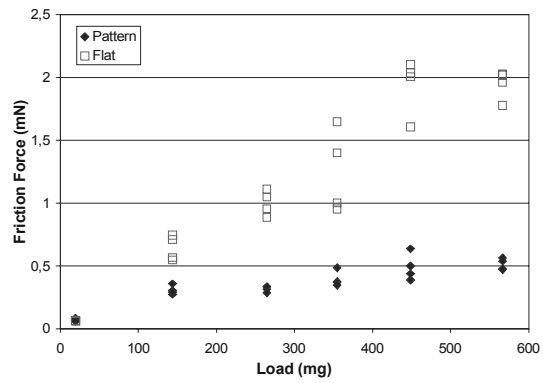


**Fig. 9.** Friction force of the micro linear guides with and without micro pattern on the support structures with varied normal load

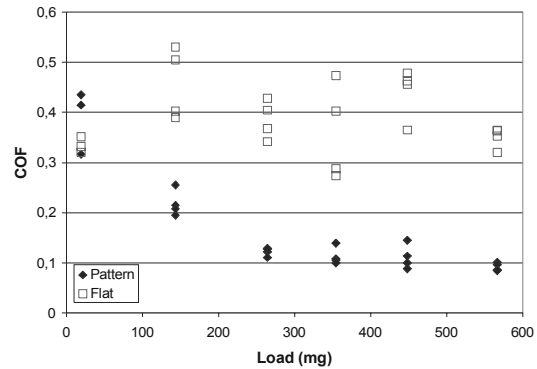


**Fig. 10.** Dynamic COF of the micro linear guides with and without micro pattern on the support structures with varied normal load

A dynamic friction force of 0.06 to 0.08 mN is measured at the lowest load for both guide designs. In case of increasing normal loads, the friction force of the first design significantly increase compared to the friction force of the second design. Furthermore, a strong scattering of the friction force of the first design can be observed. For the maximum load of 566 mg the friction force of the first

design is approx. 2 mN, in contrast to the friction force of approx. 0.5 mN of the second design.

Fig. 10 shows the COF of both designs at the same range of the normal loads. The first design of the linear guides has an average COF in a range of 0.3 to 0.5. The COF of the second guide design has the same amount as the COF of the first design at the minimum load of 19.5 mg. On increasing the normal load the COF of the second design drastically declines at the beginning and approaches approx. 0.1 at the maximum load.

## 6 Conclusion

This paper presents the development of micro linear guides and the necessity for improvement of their tribological properties. Compared to wet chemical etching, the plasma dry etching process provides more flexibility and more possibilities to design various shapes of micro structures independent of the silicon crystal orientation. With this major advantage plasma etching is used to fabricate tribologically optimized micro linear guides.

We have demonstrated the fabrication process of the micro guide, which can be finished in only two photolithography steps with two different etching processes: barrel plasma and ICP etching. The ICP etching process allows the production of support structures with high aspect ratios and high lateral accuracy. In order to improve the tribological properties of the micro guides, the contact area on top of the support structure has to be reduced by patterning using isotropic barrel plasma etching. Due to the isotropy, the contact area can be varied by etch depth. We have described the effect of two major parameters on the silicon etch rate, the plasma source power and the etching gas flow rate.

Micro guides with various contact areas have been fabricated using the processes described above. The tribological properties of two designs of the linear guides have been investigated. In order to improve the tribological properties of the guides, a dry lubricating coating of a thin a-C layer has been deposited on the contact surfaces. The linear guides with flat support structures exhibit considerably the higher friction force and the COF compared to the guides with patterned support structures. Furthermore, the COF of the guides with flat support structures scatter in a wide range for all applied normal loads. In contrast, the COF of the guides with patterned support structures decrease by increasing normal loads.

The results show, the increase of contact surface pressure by arising normal load and the micro pattern can obviously reduce the dynamic friction force of the micro linear guides. Nevertheless, the further investigations of tribological properties of the micro pattern are necessary. Furthermore, the different forms of the micro patterns can also affect on the tribological properties. The optimization of the form and size of the micro patterns concerning the frictional behavior is hence required, in order to assure the functionality of the linear guides for the application on the active micro systems.

## 7 Acknowledgements

This work is supported by the Deutsche Forschungsgemeinschaft (DFG) in the framework of the Collaborative Research Center 516 "Design and Fabrication of Active Micro Systems".

## 8 References

- [1] Feldmann, M., Ruffert, C., Gatzert, H.H., Büttgenbach, S.: Fertigung von Funktionskomponenten für elektromagnetische Mikroaktoren; Kolloquium Mikroproduktion - Fortschritte, Verfahren, Anwendungen, Mainz Verlag, 2005:295-303
- [2] Mehregany, M., Nagarkar, P., Senturia, S. D., Lang, J. H.: Operation of microfabricated harmonic and ordinary side-drive motors; Proceeding 3<sup>rd</sup> Annual IEEE Microelectromechanical Systems Workshop, 1990:1-8
- [3] Kumar, S., Cho, D.: A proposal for electrically levitating micromotors; Sensors Actuators A, Vol.24, 1990:141-149
- [4] Denkena, B., Li, J.: Untersuchung einer magnetischen Mikroführung - Modellierung und Simulation, wt Werkstattstechnik online, 2005, H. 5:357-361
- [5] Denkena, B., Li, J., Kopp, D.: An Aerostatic Linear Guidance for Microsystems, Production Engineering, Annals of the German Academic Society for Production Engineering (WGP), Vol. XI/2, 2004:203-208
- [6] Lin T., Modafe A., Shapiro B., Ghodssi R.: Characterization of dynamic friction in MEMS-Based microball bearings; IEEE Transaction on Instrumentation and Measurement, Vol.53, No. 3, 2004:839-845
- [7] Phataralaoha, A., Büttgenbach, S., Schiffmann, K., Sick, J.-H., Bandorf R., Küster, R.: Tribologische lineare Mikroführungen; Mikrosystemtechnik Kongress, 2005:789-792
- [8] Bandorf, R., Lüthje, H., Henke, C., Wiebe, J., Sick, J.-H., Küster, R.: Different carbon based thin films and their microtribological behaviour in MEMS applications; Surface & Coatings Technology, Vol. 200, 2005:1777-1782
- [9] Bandorf, R., Küster, R., Henke, C., Sick, J.-H., Neumeister, C., Phataralaoha, A., Büttgenbach, S., Gatzert, H. H., Bräuer, G.: Tribologie von MEMS-Komponenten; Kolloquium Mikroproduktion - Fortschritte, Verfahren, Anwendungen, Mainz Verlag, 2005:225-232
- [10] Phataralaoha, A., Büttgenbach, S.: Microscopic Friction Force Measuring System for the Investigation of Micro Components; 4th Euspen Conference, 2004:310 – 311
- [11] Phataralaoha, A., Büttgenbach, S.: Proceeding of Eurosensor, 2005:WPb31

---

# Ultraprecision Finishing of Photomask Substrate by Utilizing Atmospheric Pressure Plasma

Kazuya Yamamura<sup>1</sup>, Akihiro Fujiwara<sup>1</sup>, Koji Ueno<sup>1</sup>, Yasuhisa Sano<sup>1</sup>, Masafumi Shibahara<sup>2</sup>, Katsuyoshi Endo<sup>1</sup>, Yuzo Mori<sup>1</sup>  
<sup>1</sup>Osaka University, <sup>2</sup>Hyogo Prefectural Institute of Technology

Keywords: atmospheric pressure plasma, PCVM, photomask, quartz glass, flatness

## Abstract

In the case of the atmospheric pressure plasma, localized high density plasma is generated around the electrode. Therefore, free figuring without mask pattern is realized by scanning the localized reactive etching area. And we developed new ultra precision machining method which is named plasma chemical vaporization machining (PCVM) utilizing atmospheric pressure plasma. In this paper, we report the performance of the PCVM in the finishing process of photomask substrate made of quartz glass. And as a result of the correcting process of the flatness of the 6 inches square substrate, the flatness of 100 nm or less without degradation of the surface roughness was achieved.

## 1 Introduction

The figure accuracy of the photomask substrate utilizing in the semiconductor lithography process is very high, because the focal depth of an optical projection system is very small. In the case of a photomask substrate for the next-generation extreme ultraviolet lithography (EUVL) system, flatness of 50 nm or less and roughness of 0.15 nm rms or less are required for an area 152 mm square. It is difficult to obtain such flatness with a high efficiency by the conventional mechanical polishing, and the flatness of commercial photomask substrate is about 300 nm order. Recently, required specification for the EUVL photomask substrate about the flatness has been achieved by applying the magneto-rheological finishing (MRF) [1], but roughness specification is not satisfied yet.

On the contrary, atmospheric pressure plasma is utilizing in various processes, such as etching, deposition, and surface modification. In the case of the atmospheric pressure plasma, high density plasma region is localized around the electrode because of small mean free path. Therefore, free figuring without mask pattern is realized by scanning the localized reactive area. And plasma etching process is insensitive to the external disturbances such as vibration or thermal deformation of the process machine compared with the conventional mechanical machining process, because the plasma process is a noncontact process. Furthermore, electronic and optical properties of the material are never degrade, because kinetic energy of the collision ion is very low. So, the atmospheric pressure plasma process is an ideal

method for figuring or surface treatment of the ultra precision optical or electronic device. And we have developed a new ultraprecision machining method named plasma chemical vaporization machining (PCVM) utilizing the atmospheric pressure plasma. By utilizing a numerically controlled PCVM (NC-PCVM), large size (400 mm) silicon plane mirror<sup>[2]</sup>, elliptical mirror for hard x-ray focusing which has 3 nm order figure accuracy<sup>[3]</sup>, and silicon on insulator (SOI) wafer which has 13 nm±5% thickness distribution of silicon layer<sup>[4]</sup> have already achieved. Furthermore, as a result of the correcting process of the thickness distribution of the AT cut quartz crystal wafer, thickness uniformity was improved to 10 nm level<sup>[5]</sup>.

## 2 Machining apparatus and NC procedure

Figure 1 shows the NC-PCVM machine developed for ultraprecision figuring. This machine has a rotary electrode for generating the plasma, and the diameter of the electrode is 300 mm. The surface of the rotary electrode is covered with alumina ceramics that formed by plasma spraying for preventing an arc discharge. Owing to this coating, stable dielectric barrier discharge (DBD) is realized even in the atmospheric pressure atmosphere. In the case of the chemical machining process such as the plasma etching, contaminations of the workpiece surface induce etching irregularity, and as a result, surface roughness is degraded. Therefore, the hydrostatic bearings that worked by high-pressure process gas are applied to the supporting mechanism of the rotary electrode and the xy-table for avoiding the generation of abrasion particle and vaporization of lubrication oil those pollute the surface of the workpiece. The servo motors for driving the rotary electrode and the xy-table are installed in the air-tight sealed box, and driving forces are transmitted through the magnetic fluid sealing, and hydrostatically floated xy-table is pulled by stainless steel belt. Furthermore, NC-PCVM machine is installed in the clean room of class 1. The inside air of the chamber is evacuated to 10<sup>-4</sup> Pa, and it filled up to 0.1 MPa with process gases. And strokes of the xy-table are 500 mm in x-direction and 200 mm in y-direction.

The flatness correction procedures of the photomask substrate are as follows. Firstly, the flatness of the photomask substrate is measured by Fizeau-type laser interferometer that installed in the temperature controlled

room. Secondary, a scanning speed distribution of the worktable in each point of the photomask substrate is determined by deconvolution calculation. Thirdly, numerically controlled plasma correcting is performed, and finally, the flatness of the photomask substrate is verified by laser interferometer again. The flatness correction process is performed only one time for each photomask substrate because the productivity is taken into consideration.

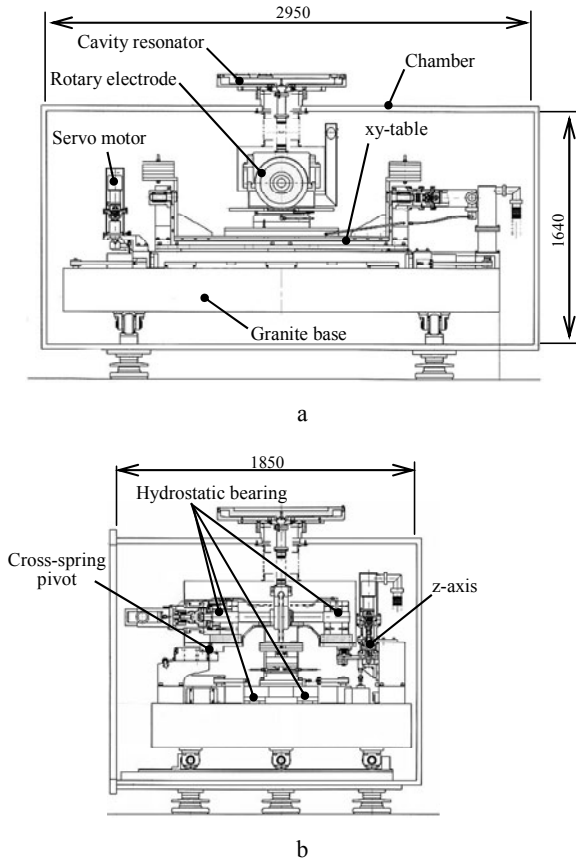


Fig. 1. Schematic view of NC-PCVM machine; a. front view; b. side view

### 3 Machining characteristics of quartz glass

In the case of the EUVL system, coefficient of thermal expansion (CTE) of the photomask substrate should be 30 or less ppb. To satisfy that specification, low thermal expansion glasses such as the Zerodur<sup>®</sup> (Schott) or the ULE<sup>®</sup> (Corning) are utilizing. However, the Zerodur<sup>®</sup> glass contains various elements which are difficult to remove by plasma reaction. On the contrary, ULE<sup>®</sup> glass is composed by only SiO<sub>2</sub> and TiO<sub>2</sub>, and these components are easily removed as the fluorine compound in the plasma reaction. Therefore, we selected the ULE<sup>®</sup> glass as a target material which is finished by NC-PCVM. In this paper, synthetic quartz glass substrate (152 mm × 152 mm × 6.35 mm<sup>t</sup>) is used instead of the ULE<sup>®</sup> glass for acquiring the machining characteristics of the plasma CVM, because the ULE<sup>®</sup> glass substrate is very expensive.

Figure 2 shows example of the shape of the removal spot that formed by PCVM on the surface of the quartz glass, and process parameters are shown in Table 1. The shape of the removal spot in the direction of electrode rotation is asymmetry to the center of the rotation, since the maximum depth point of the removal spot is shifted to the downstream of the gas flow that generated by rotation of the electrode. On the contrary, shape of the removal spot is symmetry in the transverse direction of the gas flow. In the case of the machining of the silicon, maximum depth point of the removal spot is closer to the center of the rotary electrode than in the case of the quartz glass. Therefore, it seems that electronic property of the material affects the shape and the position of the removal spot.

Table 1. Machining parameters in Fig. 2

<b>Gas Composition</b>	CF <sub>4</sub> :0.3%, O <sub>2</sub> :0.075% (He balance)
<b>VHF Power (f=150MHz)</b>	550 W
<b>Machining Gap</b>	750 μm
<b>Electrode Rotation Speed</b>	10 m/s
<b>Machining Time</b>	1 min

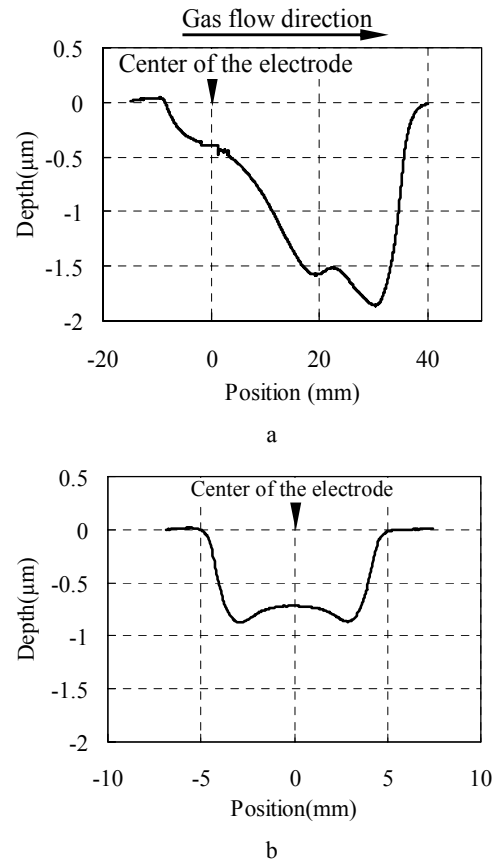


Fig. 2. The shape of the removal spot that formed on the surface of the quartz glass; a. gas flow direction; b. transverse direction of gas flow



Figure 3 shows the relationship between the volumetric removal rate and various process parameters. In the case of utilizing  $CF_4$  as the etching gas, the removal rate increases by the addition of  $O_2$ . However, excessive addition of  $O_2$  causes decreasing of the removal rate, so that optimal mixture ratio of  $CF_4$  and  $O_2$  exists around  $O_2/CF_4=0.25$ . This tendency is also seen in the conventional plasma etching of the silicon which used  $CF_4$  and  $O_2$  as the process gases<sup>[6]</sup>. Moreover, the removal rate increases in monotonically to the increasing of the RF power, and is insensitive to the gap distance (machining gap) between the electrode and the workpiece surface. Figure 4 shows the relationship between the volumetric removal rate and the surface roughness, and the exposure time of the plasma. This figure shows that the increase of plasma exposure time causes increase of removal rate and degradation of the surface roughness. Figure 5 shows the relationship between the removal cross section per pass and the inverse scanning speed of the worktable in the machining of silicon and quartz glass, the machining parameters of which are shown in Table 2. In the case of machining of the quartz glass by PCVM, the relationship between the removal volume and the inverse scanning speed of the worktable is nonlinear, although is linear in the case of the machining of silicon. Figure 4 and 5 show that the machining characteristics of the quartz glass substrate is strongly affected by rising of the surface temperature caused by heat transfer from the plasma. On the contrary, in the case of the machining the silicon wafer, removal volume in scanning is perfectly proportional to the inverse scanning speed of the worktable. It seems that the difference in the machining characteristic in removing of quartz glass and silicon results from the difference in both thermal conductivities. Therefore, in order to achieve the ultraprecision finishing property of the quartz glass substrate by applying the PCVM, avoiding the rising of the surface temperature is indispensable.

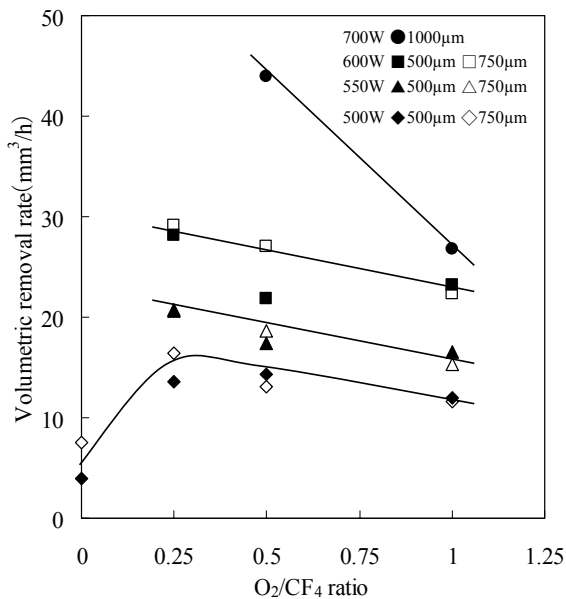


Fig. 3. The relationship between the volumetric removal rate and various process parameters

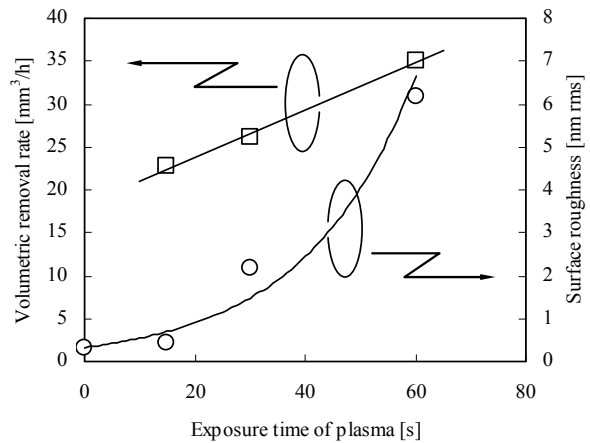


Fig. 4. The relationship between the volumetric removal rate and the exposure time of the plasma. (He:CF<sub>4</sub>:O<sub>2</sub>=99.55:0.3:0.15, machining gap : 1000 µm, rotation speed of the electrode : 10 m/s, RF power : 700 W)

Table 2. Machining parameters in Fig. 5

Parameters	Silicon	Quartz Glass
Gas Composition	CF <sub>4</sub> : 0.3%, O <sub>2</sub> : 0.075% (He balance)	CF <sub>4</sub> : 0.3%, O <sub>2</sub> : 0.075% (He balance)
VHF Power (f=150 MHz)	140 W	550 W
Machining Gap	1000 µm	750 µm
Electrode Rotation Speed	10 m/s	10 m/s

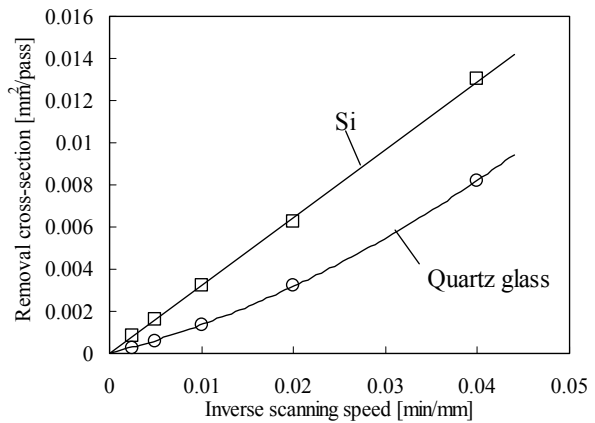


Fig. 5. The relationship between the removal cross section per pass and the inverse scanning speed of the worktable

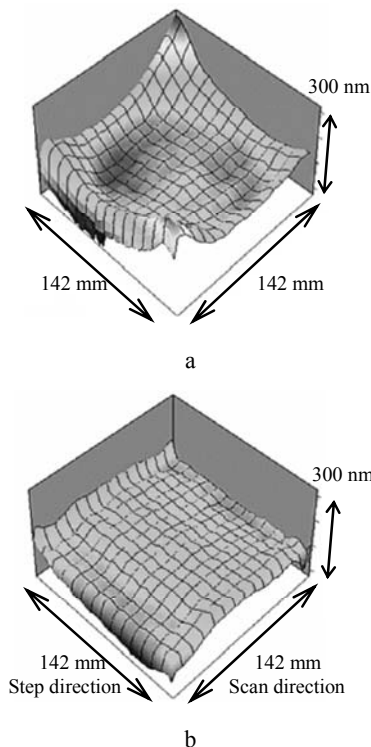
#### 4 Flatness correction of photomask substrate

Figure 6 shows the result of finishing the photomask substrate made of synthesized 6 inches quartz glass by the NC-PCVM. In this case, to reduce the influence of the

temperature rising of the surface, the plasma was generated by pulse modulated power supply and machining parameters are shown in Table 3. Before correcting, the shape of the photomask substrate was concave, and the flatness is 442 nm. On the contrary, the flatness was improved to 94 nm by only one time NC-PCVM correcting process. And Fig. 7 shows the AFM image of the surface of the photomask substrate processed by PCVM. In this case, there is no degradation of the surface in the high-spatial frequency roughness (HSFR) domain. However, the figure accuracy of both ends of the substrate in the scanning direction is not so good. The temperature of the edge part of the substrate tends to rise, because cooling period is short by changing of scanning direction of the plasma. Therefore, excessive removal tends to occur in both ends of the substrate. So, some changes of the process parameter such as increasing the scanning speed are required for improving the figuring accuracy of the NC-PCVM.

**Table 3.** Machining parameters in NC-PCVM

<b>Gas Composition</b>	CF <sub>4</sub> :0.3%, O <sub>2</sub> :0.075% (He balance)
<b>VHF Power</b> ( $f=150$ MHz, Pulse modulation)	400 W (Average) (on:10 $\mu$ s, off:20 $\mu$ s)
<b>Machining Gap</b>	750 $\mu$ m
<b>Electrode Rotation Speed</b>	10 m/s



**Fig. 6.** Improvement of flatness of photomask substrate by NC-PCVM; a. before correction 442 nm p-v; b. after correction 94 nm p-v

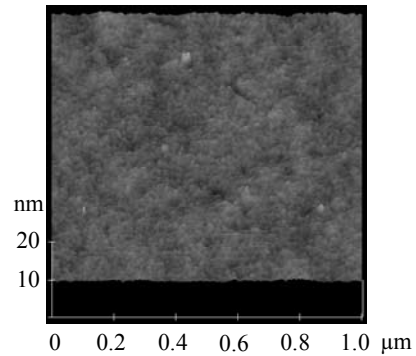


**Fig. 7.** AFM image of the surface of the photomask substrate processed by NC-PCVM

## 5 Conclusions

We have developed a new ultraprecision machining method named plasma CVM, which utilizes atmospheric pressure plasma. This method was applied to the finishing process of photomask substrate made of synthetic quartz glass for lithography. And as a result of numerically controlled plasma CVM, flatness of the photomask substrate was improved from 442 nm p-v to 94 nm p-v.

## 6 References

- [1] Paul E. Murphy, James T. Mooney, Thomas P. Courtney, (2003) Fabrication of EUV components with MRF, Proc. of SPIE 5193:29-38
- [2] Yuzo Mori, Kazuya Yamamura and Yasuhisa Sano, (2000) The study of fabrication of the X-ray mirror by numerically controlled plasma chemical vaporization machining: Development of the machine for the X-ray mirror fabrication, Rev. Sci. Instrum. 71:4620-4626
- [3] K. Yamamura, K. Yamauchi, H. Mimura, Y. Sano, A. Saito, K. Endo, A. Souvorov, M. Yabashi, K. Tamasaku, T. Ishikawa, and Y. Mori, (2003) Fabrication of elliptical mirror at nanometer-level accuracy for hard x-ray focusing by numerically controlled plasma chemical vaporization machining, Rev. Sci. Instrum. 74:4549-4553
- [4] Yuzo Mori, Kazuya Yamamura and Yasuhisa Sano, (2004) Thinning of silicon-on-insulator wafers by numerically controlled plasma chemical vaporization machining, Rev. Sci. Instrum. 75:942-946
- [5] M. Shibahara, K. Yamamura, Y. Sano, T. Sugiyama, K. Endo and Y. Mori, (2005) Improvement of thickness uniformity of quartz crystal wafer by numerically controlled plasma CVM, Proc. SPIE 5869:58690I
- [6] J. W. Coburn and Harold F. Winters, (1979) Plasma Etching – A Discussion of Mechanisms, J. Vac. Sci. Technol., 16:391-403

## **Acknowledgements**

This work was partially supported by Grant - in - Aid for 21st Century COE Research (H12) from the Ministry of Education, Culture, Sports, Science and Technology, Japan.

---

# Development of Ultra Precision Finishing Method for Quartz Crystal Wafer Utilizing Atmospheric Pressure Plasma

Masafumi Shibahara<sup>1</sup>, Yusuke Yamamoto<sup>2</sup>, Kazuya Yamamura<sup>2</sup>, Yasuhisa Sano<sup>2</sup>, Katsuyoshi Endo<sup>2</sup> and Yuzo Mori<sup>2</sup>  
<sup>1</sup>Hyogo Prefectural Institute of Technology, <sup>2</sup>Osaka University

Keywords: quartz crystal, quartz resonator, atmospheric pressure plasma, plasma CVM, thickness distribution

## Abstract

To improve the thickness distribution of quartz crystal wafer, we developed new machining process which utilizing an atmospheric pressure plasma. The thickness distribution was corrected by numerically controlled machining which scanning of the quartz crystal wafer to the localized high-density plasma. In the result of performing the numerical control machining of an AT cut quartz crystal wafer, the thickness distribution in the area of 13.5 mm × 16.8 mm was substantially improved from 272 nm [peak to valley (p-v)] to 55 nm (p-v) within 330 s. Moreover, unwanted spurious mode of the resonance curve in the machined quartz crystal wafer was reduced.

## 1 Introduction

The crystal resonator is often used as a high-performance clock source of various watches, the communication equipments and electric devices. It is made from a quartz crystal substrate divided from a quartz crystal wafer processed thin. As an AT cut crystal resonator made from an AT cut quartz crystal substrate has the very high stability of resonator frequency to temperature fluctuation, it is most often used among the several kind of crystal resonators.

Conventionally, thinning of a quartz crystal wafer is performed by double-sided polishing machine by sun-and-planet motion. To improve the productivity, many crystal resonators are formed on one quartz crystal wafer. However, in the mechanical polishing process, distribution of polishing pressure results in the thickness distribution of one quartz crystal wafer<sup>1</sup>. The oscillation frequency ( $f$ ) of an AT cut crystal resonator is in inverse proportion to the thickness ( $t$ ) of a crystal substrate, using following relationship,  $f$  (MHz) = 1670 /  $t$  ( $\mu$ m). Thus, manufacturing many crystal resonators on one crystal wafer, such thickness distribution causes the variation in the oscillation frequency of each resonator, so that additional correcting process for adjusting the resonance frequency is indispensable. Therefore, in order to reduce the number of processes, development of new fabrication process which reduces a thickness distribution of the quartz crystal wafer is necessary<sup>1</sup>.

Furthermore, to produce a high-frequency resonator, the wafer must be thin. In case of the polishing by sun-and-

planet motion, the steel carrier for holding a quartz crystal wafer is required. Although it is necessary to make thickness of the carrier thin if the quartz crystal wafer becomes thin, it becomes easy to break for the mechanical strength to decline. Therefore, the limit thickness of quartz crystal wafer produced by double-sided mechanical polishing is about 30  $\mu$ m. Computer controlled polishing (CCP) which utilizing a small tool or ion beam figuring (IBF) can be considered as a method of improving a thickness uniformity of a quartz crystal wafer. However, as for the CCP, fracture and introducing of deformed layer are caused by mechanical force, and also as for the IBF, machining speed is low and surface damages are introduced by ion collision<sup>2</sup>. Since the deformed layer causes degradation of the resonance characteristic of a quartz resonator, it is necessary to avoid generation of surface damage as much as possible. On the other hand, wet etching using HF or NH<sub>4</sub>F- HF has a high etching rate to the quartz crystal wafer, and a deformed layer is not generated at all. But there is no spatial controllability of removal depth, so that, it is very difficult to correct the thickness distribution of the quartz crystal wafer.

On the contrary, plasma chemical vaporization machining (PCVM) which utilizing atmospheric pressure plasma has an enough machining speed and also has good spatial resolution for figure error correction, because density of reactive species is very high and plasma region is localized around the electrode<sup>3</sup>. Furthermore, since PCVM is a non-contact chemical machining method without mechanical force to the workpiece, deformed layer is not generated in the removal process. By utilizing a numerically controlled PCVM (NC-PCVM), large size (400 mm) silicon plane mirror<sup>4</sup>, elliptical mirror for hard x-ray focusing which has 3 nm order figure error<sup>5</sup>, and silicon on insulator (SOI) wafer which has 13 nm  $\pm$  5 % thickness of silicon layer<sup>6</sup>, have already achieved.

So, NC-PCVM is an optimum machining method for a brittle material like a quartz crystal wafer. We proposed new machining process of AT cut quartz crystal wafer for improving a thickness distribution and for thinning by utilizing NC-PCVM which applied combination of cylindrical rotary electrode and pipe electrode, called "the two-step correction process"<sup>1</sup>. In the first correction process, the long-spatial-wavelength component of the thickness error is corrected by 1-dimensional NC-scanning, which utilizes a cylindrical rotary electrode. In the second correction process, fine correction for removing the residual thickness error is

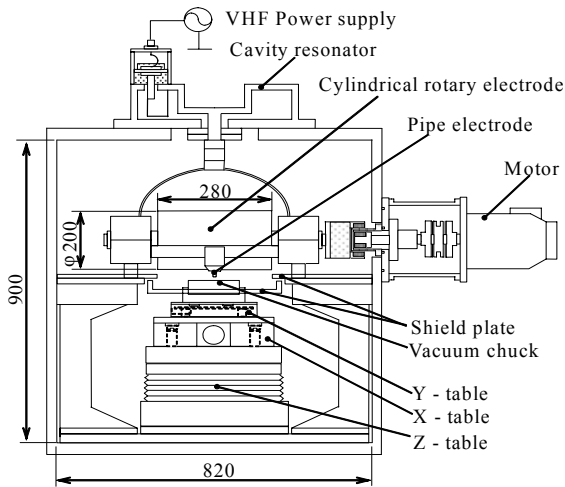


Fig. 1. Schematic diagram of the process chamber

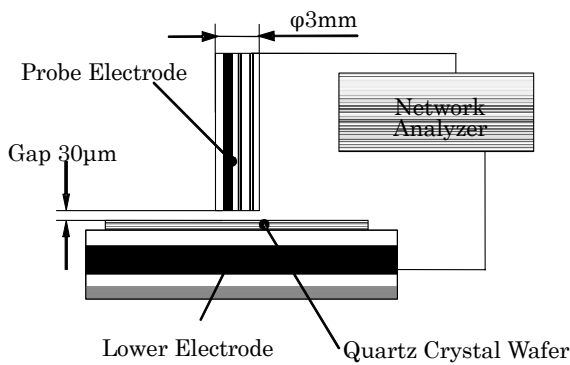


Fig. 2. Schematic diagram of resonance frequency measuring instrument

carried out by 2-dimensional NC-scanning, which utilizes a small pipe electrode. As concern with the removal rate, rotary electrode is faster than pipe electrode about 10 times since removal area is large. Therefore, the combination of these two processes realizes a high efficiency and highly precise correction of the wafer thickness distribution.

## 2 Experiment procedes

NC-PCVM machine is composed of a process chamber, a power supply and a process gas controller<sup>1</sup>. The schematic diagram of the process chamber is shown in Fig. 1. The inside of the chamber is divided by metal plate for shielding a high frequency electric field, and the cylindrical rotary electrode (200 mm diameter, 280 mm width) is installed in the upper part of the chamber. The pipe electrode (outer diameter  $\phi 3$  mm, inner diameter  $\phi 0.5$  mm) is attached to the housing of the rotary electrode, so that type of the electrode can be selected according to the purpose of machining. The XYZ tables for performing a NC processing are installed in the lower part of the chamber. The workpiece is AT cut quartz crystal wafer (25 mm  $\times$  20 mm  $\times$  62  $\mu$ m), and is held by a vacuum chuck made of aluminum alloy. The chamber

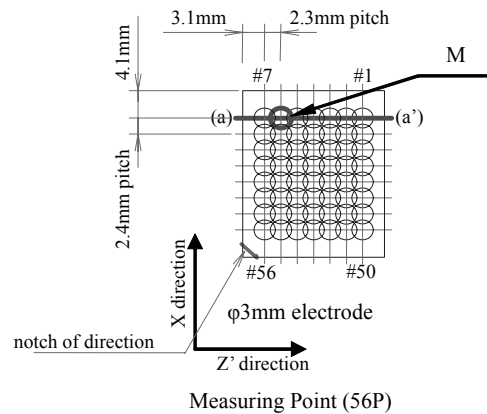


Fig. 3. Schematic diagram of resonance frequency measuring point on a quartz crystal wafer

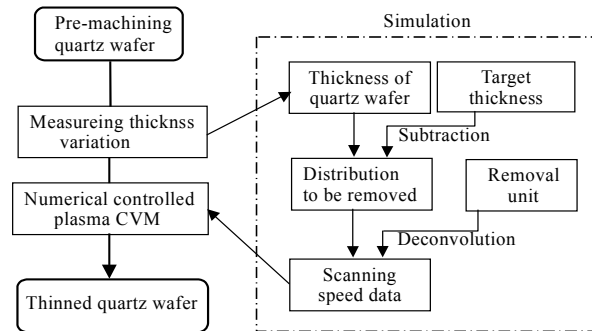


Fig. 4. Procedures of the figuring process utilizing NC-PCVM

Table 1. Target value of correction

	Pre-machined	After-corrected
<b>Resonance frequency</b>	26.892~27.01 MHz ( $\Delta f=119$ kHz)	27.014MHz $\pm$ 23kHz ( $\Delta f=46$ kHz)
<b>Thickness</b>	61.827~62.09MHz ( $\Delta t=272$ nm)	61.820 $\mu$ m $\pm$ 52.5nm ( $\Delta t=105$ nm)

Table 2. Machining parameters

Reactive gas	RF power	Suction rate	Machining gap
He:CF <sub>4</sub> :O <sub>2</sub> = 98:1:1	200 W	0.13 liter/min	600 $\mu$ m

is evacuated to 1 Pa, and filled to 0.1 MPa with process gas. The composition of the process gas to remove quartz crystal is several percent CF<sub>4</sub> and O<sub>2</sub>, which was diluted with helium. The region of the plasma is localized around the electrode under the atmospheric pressure condition, so figuring without a mask pattern can be performed by scanning the

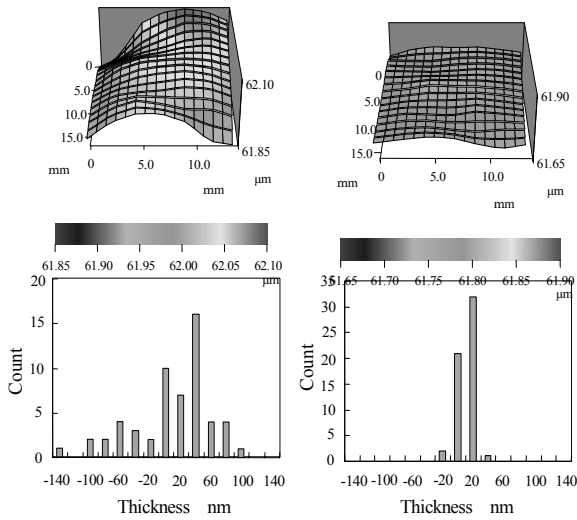


Fig. 5. Thickness distribution of AT cut quartz crystal wafer

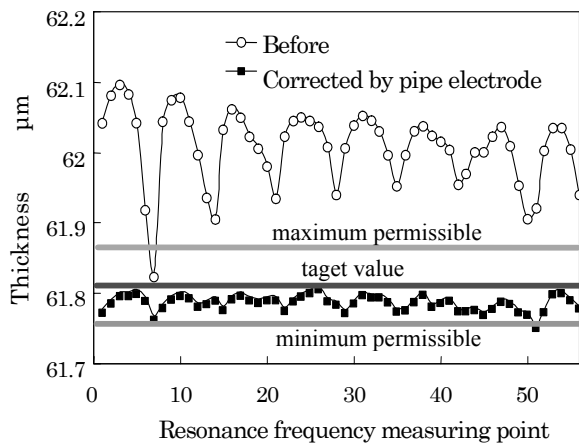


Fig. 6. Relationship between pre-machined thickness and actual thickness after corrected by pipe electrode

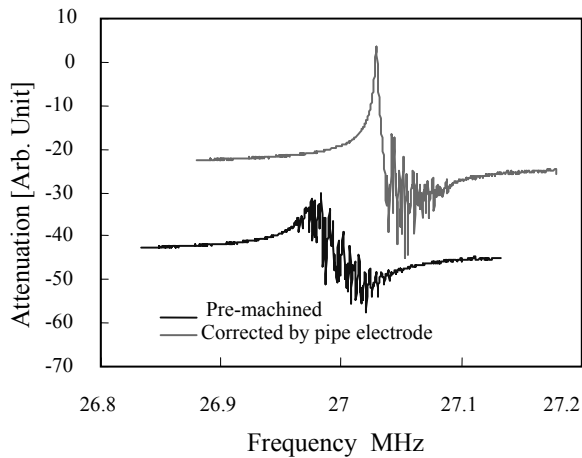


Fig. 7. Resonance curve of AT cut quartz crystal wafer in stage of the correction process (measuring position is M point in Fig. 3)

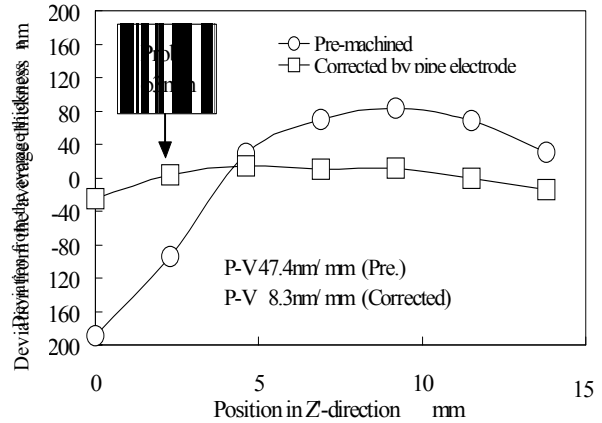


Fig. 8. Relationship between deviation from the average thickness in z'-direction and position of probe electrode (probe position is M point in Fig. 3)

plasma region relatively to the workpiece surface. The frequency of the power supply is 13.56 MHz or 150 MHz.

Thickness of the quartz crystal wafer is acquired by measuring the resonance frequency using a small capacitively probe electrode (diameter  $\phi 3$  mm). In case of the AT cut quartz wafer, a thickness ( $t$ ) is calculated from the resonance frequency ( $f$ ) using following relationship,  $t$  ( $\mu\text{m}$ ) =  $1670 / f$  (MHz). The schematic diagram of non-contact resonance frequency measuring instrument is shown in Fig. 2. It makes the quartz crystal wafer resonate, hanging an electric field in the condition which installed between the upper probe electrode and the lower ground electrode with small air gap about  $30 \mu\text{m}$ . And resonance frequency characteristic is analyzed in the resonance-curve using network analyzer which connected with this instrument. The measuring specifications of the network analyzer are assumed that resonance-curve measurement section is 0.3 MHz, number of the measuring point is 1201. Since the size of probe electrode is 3 mm diameter, the measuring of resonance frequency is divided 56 points on a quartz crystal wafer as shown in Fig. 3, acquiring the thickness distribution of the wafer.

The figuring process utilizing NC-PCVM is performed according to the following procedures as shown in Fig. 4<sup>1</sup>.

- (1)The figure of the pre-machined AT cut quartz crystal wafer is acquired by the measuring the resonance frequency, calculating the thickness from the resonance frequency.
- (2)The figure error distributions are determined by subtracting the target thickness from the acquired shape.
- (3)The distribution of the scanning speed of the table is determined by deconvolution calculation of the figure error distribution and the removal spot shape that is obtained in unit time.
- (4)The numerically controlled correcting process is carried out by the distribution of the scanning speed of the table.

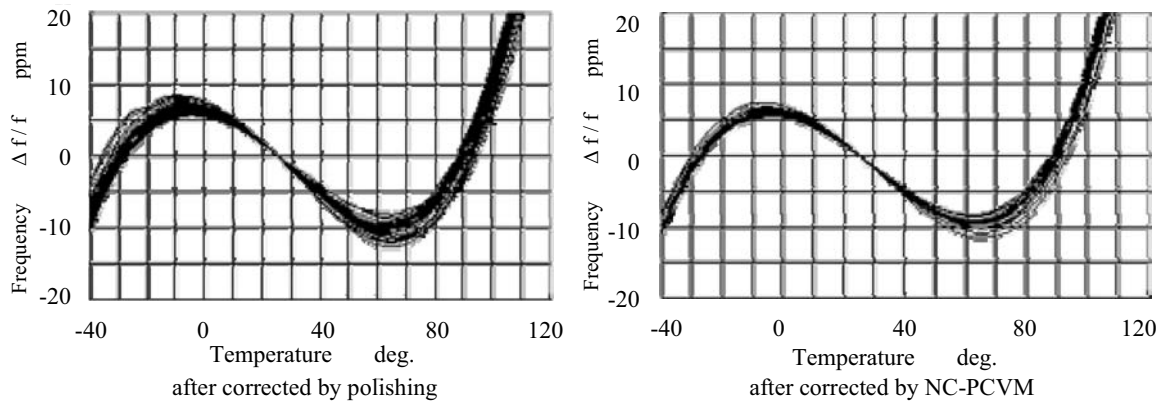


Fig. 9. Frequency-temperature characteristics

### 3 Results and discussion

In this paper, the thickness distribution of the AT cut quartz crystal wafer is corrected utilizing NC-PCVM, at the same time adjusting the thickness to target value. Table 1 shows target value of correction. Incidentally, since the figure error of using pre-machined quartz crystal wafer is small comparatively, NC-PCVM is carried out utilizing only a pipe electrode. Table 2 shows machining parameters.

Fig. 5 shows the thickness distribution of the AT cut quartz crystal wafer. After correction process, the thickness distribution of the wafer was improved from 272 nm p-v ( $\Delta f = 119$  kHz) to 54 nm p-v ( $\Delta f = 27$  kHz) within 330 sec in the area of 13.8 mm  $\times$  16.8 mm. These values are a half with target value as shown in Table 1. Moreover, the thickness of quartz crystal wafer is attained adjusting approximately to target value, as shown in Fig. 6.

Fig. 7 shows the resonance curve of the AT cut quartz crystal wafer in stage of the correction process of the thickness distribution (measuring position is M point in Fig. 3). Before the correction, there are many spurious peaks in the resonance curve. But, after the correction processes progress, the number of spurious peaks decreases, and the main resonance peak remains.

Fig. 8 shows relationship between deviation from the average thickness in z'-direction and position of probe electrode (probe position is M point in Fig. 3). The diameter of the capacitively probe electrode for measuring a resonance curve is 3 mm. The parallelism of the area facing the measuring probe electrode is improved from 47.4 nm/mm to 8.3 nm/mm. Thus, if the improvement in the parallelism of the area facing the measuring probe electrode is achieved, the resonance property of the AT cut quartz crystal wafer is also improved as result.

Fig. 9 shows characteristic of the crystal resonator manufactured on actually such quartz crystal wafer. It works as well as the crystal resonator manufactured on a quartz crystal wafer corrected by polishing.

Therefore, this correction process is useful for improving the productivity of a crystal resonator.

### 4 Conclusion

As a result of performing the numerical control machining

of an AT cut quartz crystal wafer, the thickness distribution in the area of 13.5 mm  $\times$  16.8 mm was substantially improved from 272 nm p-v to 54 nm p-v within 330 sec. The parallelism of the quartz crystal wafer was improved at the same time, so that unwanted spurious mode of the resonance curve in the machined quartz crystal wafer was reduced. Moreover, the thickness of quartz crystal wafer is attained adjusting approximately to target value. Actually, the crystal resonator manufactured on such quartz crystal wafer work very well. Therefore, it was proved that the thickness distribution of quartz crystal wafer was corrected by utilizing our newly developed finishing process without any problem.

### 5 Acknowledgements

This work was partially supported by Grant - in - Aid for Young Scientists (A) (No. 15686007) and 21st Century COE Research (H12) from the Ministry of Education, Culture, Sports, Science and Technology, Japan.

We also acknowledge EPSON TOYOCOM CO.,LTD for the donation of AT cut quartz crystal wafer.

### 6 References

- [1] M. Shibahara, K. Yamamura, Y. Sano, T. Sugiyama, K. Endo and Y. Mori, (2005) Improvement of the thickness distribution of a quartz crystal wafer by numerically controlled plasma chemical vaporization machining. *Rev. Sci. Instrum* 96: 1031– 1034
- [2] Y. Nagaura and S. Yokomizo, (1999) Manufacturing method of high frequency quartz oscillators over 1GHz. *Proc. IEEE Int. Freq. Control Symp.* :425-428
- [3] Y. Mori, K. Yamauchi, K. Yamamura and Y. Sano, (2000) Development of the machine for the x-ray mirror fabrication. *Rev. Sci. Instrum.* 71:4627-4632
- [4] Y. Mori, K. Yamamura and Y. Sano, (2000) The study of fabrication of the X-ray mirror by numerically controlled plasma chemical vaporization machining: Development of the machine for the X-ray mirror fabrication, *Rev. Sci. Instrum.* 71:4620-4626
- [5] K. Yamamura, K. Yamauchi, H. Mimura, Y. Sano, A. Saito, K. Endo, A. Souvorov, M. Yabashi, K. Tamasaku, T. Ishikawa, and Y. Mori, (2003) Fabrication of elliptical mirror at nanometer-level

Development of Ultra Precision Finishing Method for Quartz Crystal Wafer Utilizing Atmospheric Pressure Plasma

- accuracy for hard x-ray focusing by numerically controlled plasma chemical vaporization machining, Rev. Sci. Instrum. 74:4549-4553
- [6] Yuzo Mori, Kazuya Yamamura and Yasuhisa Sano, (2004) Thinning of silicon-on-insulator wafers by numerically controlled plasma chemical vaporization machining, Rev. Sci. Instrum. 75:942-946



## Sub-nanometer Smoothing of Diamond-turned Metal Surfaces using Ion Beams

Frank Frost<sup>1</sup>, Hideo Takino<sup>2</sup>, Renate Fechner<sup>1</sup>, Axel Schindler<sup>1</sup>, Namiko Ohi<sup>2</sup>, and Kazushi Nomura<sup>2</sup>  
<sup>1</sup>Leibniz-Institute for Surface Modification Leipzig, <sup>2</sup>Nikon Corporation

Keywords: Smoothing, Ion beam, Diamond turning, Metal, Roughness, Copper, Nickel-phosphor

### Abstract

We investigated the smoothing effect of ion beam etching with the aid of a sacrificial layer on smoothly cut metal surfaces. Electroplating copper and electrolessplating nickel-phosphor were used as specimens to compare their smoothness characteristics. The surfaces were turned by a single-crystal diamond tool, applied with photoresist as a sacrificial layer, and then processed using ion beams. As a result, the heights of the tool marks were successfully reduced on both surfaces, improving the surface roughness. In particular, for the nickel-phosphor, this technique was proven efficient for improving the surface roughness, allowing an rms surface roughness of sub-nanometer order.

### 1 Introduction

Ion beam technology has been attracting considerable interest due to its many advantages in industrial applications [1]. A surface planarization technique using ion beams with the aid of a sacrificial layer has been proposed by Johnson et al [2, 3]. We have investigated the smoothing characteristics of this technique for various materials, such as fused silica, silicon, nickel, and copper, that are favorable for obtaining optical surfaces [4]. However, to our knowledge, this technique has not yet been applied to the planarization of metal surfaces with a smoothness level of nm.

In this study, we investigate its smoothing effects on metal surfaces smoothly cut using a single-crystal diamond tool. We examine two metals, copper (Cu) and nickel-phosphor (NiP), as specimens to compare their smoothing characteristics. Since both metals can be easily cut with a single-crystal diamond tool to produce high-quality surfaces, the cut surfaces can be used as optical surfaces. However, in general, the diamond-turned surfaces exhibit tool marks with an amplitude of nm even if they are cut to have a high smoothness level. To smoothen such cut surfaces, it is essential to remove the tool marks from the surfaces. Thus, in this study, we particularly investigate the removal of the tool marks and the smoothness of the resultant surfaces by the planarization technique.

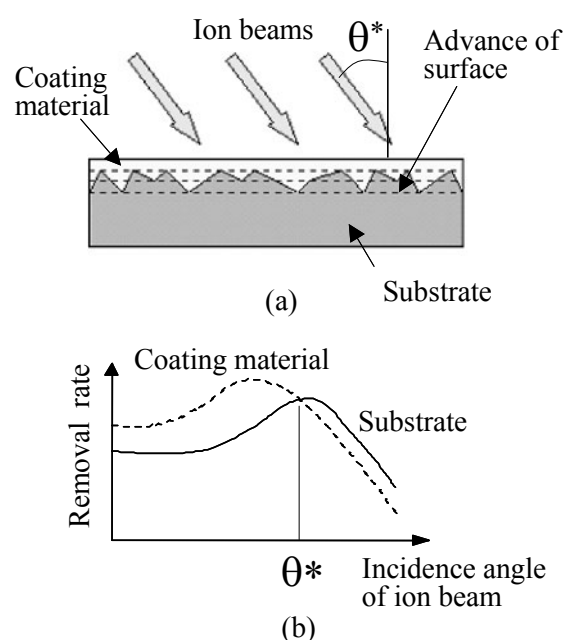


**Fig. 1.** Principle of smoothing technique. (a) Schematic drawing of ion beam bombardment on coated substrate, and (b) relationship between incidence angle and removal rate.

### 2 Principle of Smoothing Technique

The principle of the smoothing technique is as follows. The targeted substrate is coated with a material that enables a reduction in substrate roughness, as shown in Fig. 1(a). The coated layer corresponds to a sacrificial layer for the subsequent ion beam process. The substrate is processed using ion beams with an appropriate incidence angle. The

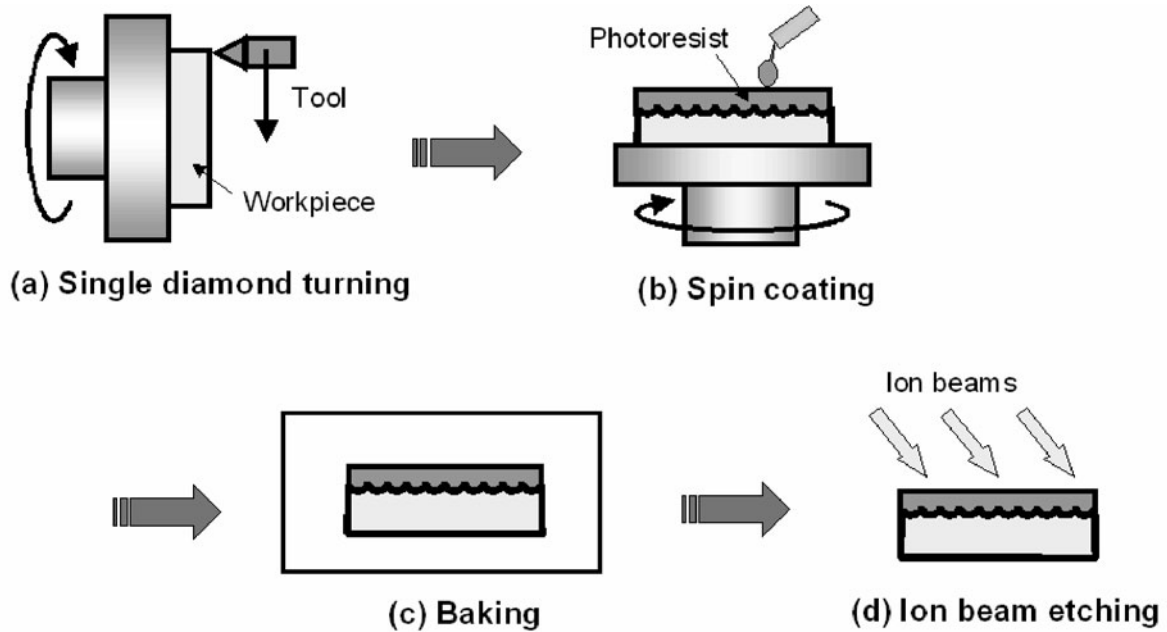


Fig. 2. Experimental procedure.

removal of the coated substrate surface progresses during the ion beam process, as shown by dotted lines in Fig. 1(a).

The incidence angle for smoothing is optimized on the basis of the removal rates of both the substrate and coating material as follows. Here, we assume that the relationships between the incidence angle and the removal rate are known for the coating material and the substrate, as schematically shown in Fig. 1(b). In this case, the incidence angle is optimized as  $\theta^*$ , which is referred to as the planarization angle, at which the removal rate of the coated material is identical to that of the substrate. Thus, ion beam etching at planarization angle  $\theta^*$  results in the uniform removal of the coated substrate surface.

### 3 Experimental

The experimental procedure used is schematically shown in Fig. 2. Steel blocks applied with electroplating Cu or with electrolessplating NiP were prepared as specimens. The surfaces of the specimens to be processed were approximately 10 mm X 20 mm in size. As shown in Fig. 2, in the first step, the surfaces of the specimens were turned

using an ultraprecision machine with a single-crystal diamond tool.

Next, the turned surfaces were further improved by the ion beam planarization technique. In this planarization step, the surface with the tool marks was coated with a suitable sacrificial layer using a spin coater to reduce the surface roughness. A photoresist was used as the sacrificial layer material. After the baking of the photoresist, the surface was etched using Ar ion beams at an ion energy of 700 eV, an ion current density of  $200 \mu\text{Acm}^{-2}$ , and a planarization angle of 30 deg. This planarization angle of 30 deg was chosen for both Cu and NiP according to the results of preliminary experiments. We repeated the process from photoresist coating to ion beam etching in Fig. 2.

For Cu surfaces, after performing this planarization process twice, we performed additional ion beam etching without the photoresist. The conditions for this additional etching were as follows: an ion energy of 500 eV, an ion current density of  $100 \mu\text{Acm}^{-2}$ , and an incidence angle of 85 deg.

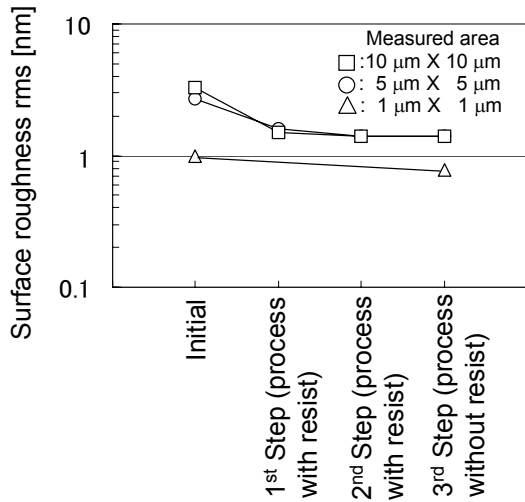


Fig. 3. Change in surface roughness for Cu surfaces.

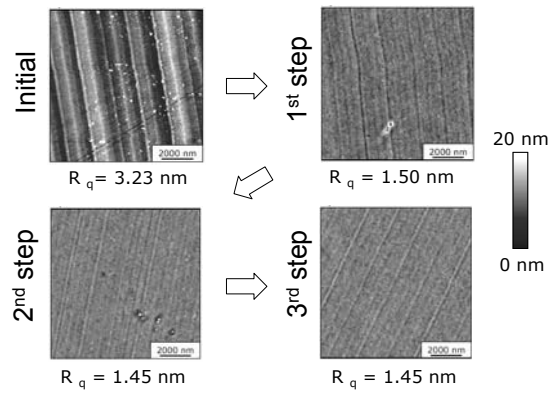


Fig. 4. Surface topographies in area of 10 μm X 10 μm for Cu.

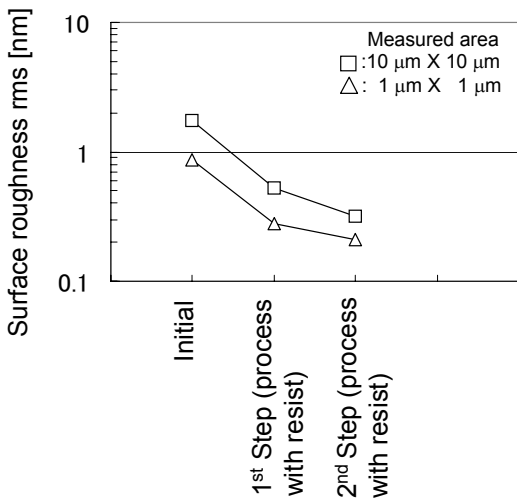


Fig. 5. Change in surface roughness for NiP surfaces.

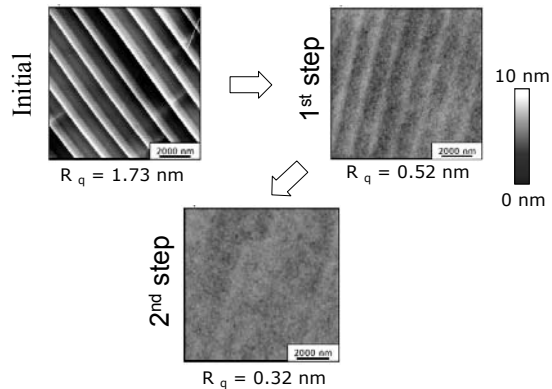


Fig. 6. Surface topographies in area of 10 μm X 10 μm for NiP.

## 4 Results and Discussion

### 4.1 Cu Surfaces

Figure 3 shows the change in the roughness of Cu surfaces obtained by each process. Figure 4 shows examples of surface topographies within an area of 10 μm X 10 μm. The surfaces were measured with an atomic force microscope

(AFM). The initial surface, a diamond-turned surface, has a roughness of 3.23 nm rms with a tool mark spatial wavelength of approximately 1.8 μm. This spatial wavelength corresponds to the feed rate of the tool for the turning. Figures 3 and 4 reveal that this technique enables a reduction in the height of tool marks. The surface roughness is reduced from 3.23 nm rms to 1.45 nm rms by the present technique. On the other hand, the additional ion beam etching process had little effect on the surface roughness. As shown in Figs. 3 and 4, the surface roughness seems to be not improved to less than approximately 1.45 nm rms.

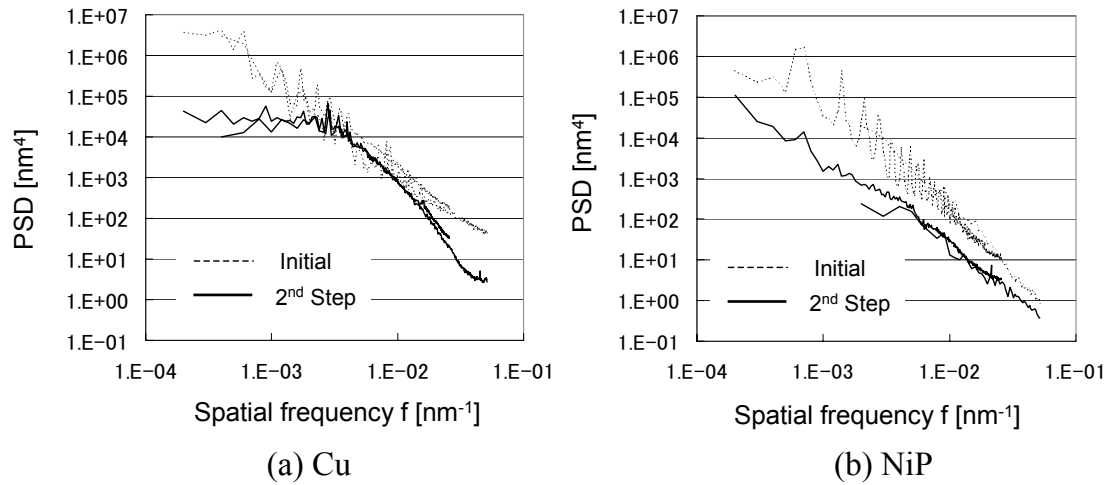


Fig. 7. Power spectrum density distributions.

#### 4.2 NiP Surfaces

Figures 5 and 6 show the results of the processes for NiP surfaces. The initial surface has a roughness of 1.73 nm rms with a tool mark spatial wavelength of approximately 1.5  $\mu\text{m}$ . Figures 5 and 6 reveal that the height of tool marks is reduced, and that the degree of reduction seems to be higher than that of the Cu surfaces. The roughness of the NiP surfaces is improved by the present technique to less than 1.45 nm rms in contrast to that of the Cu surfaces, and reaches 0.32 nm rms.

#### 4.3 Spatial Frequency Analysis of Processed Surfaces

To investigate the smoothing effect of this technique in detail, we calculated the power spectrum density (PSD) distributions for the spatial frequencies of the roughnesses of the initial and processed surfaces, as shown in Fig. 7. On the PDS curves for the initial surfaces of both Cu and NiP, the peaks at spatial frequencies from about  $1 \times 10^{-4}$  to about  $1 \times 10^{-3} \text{ nm}^{-1}$  are considered to correspond to the tool marks. These curves reveal that the heights of the tool marks were reduced on both surfaces, improving the surface roughness.

As shown in Fig. 7, for Cu surfaces, it was difficult to improve the roughness in the spatial frequency range from about  $1 \times 10^{-3}$  to about  $1 \times 10^{-2} \text{ nm}^{-1}$ . This is considered to be a reason why the roughness of Cu surfaces was not improved to less than 1.45 nm rms. On the other hand, for the NiP surface, the roughness was improved in the entire spatial frequency range shown for these curves. Thus, this technique was found to be efficient for improving the roughness of NiP surfaces.

Generally, the polycrystalline surfaces are known to be roughened by ion beam etching. Electroplating Cu is polycrystalline, although electrolessplating NiP is amorphous. Therefore, during the ion beam process on the Cu surfaces it is considered that the reduction in the height of the tool marks and the roughening of the surface occurred

simultaneously. On the other hand, the roughening did not occur for the NiP surfaces, which resulted in the NiP surfaces becoming smoother than the Cu surfaces.

## 5 Conclusions

Two surfaces, Cu and NiP, cut to a smoothness level in the order of nm were processed by the ion beam planarization technique. The heights of the tool marks were successfully reduced on both surfaces, improving the surface roughness. Particularly for NiP surfaces, this planarization technique was proven very efficient for improving the surface roughness, allowing an rms surface roughness of 0.3 nm. In many cases, Cu surfaces are difficult to polish with abrasives owing to the easy generation of scratches. Thus, this technique is expected to be effectively used for this purpose.

## References

- [1] Schindler A, Haensel T, Nickel A, Fechner R, Neumann H, Bigl F, (1993) Broad ion beam processing of large surfaces areas with nanometer precision, Proc. of the 7th International Precision Engineering Seminar (IPES), 88-99
- [2] Johnson LF, Ingersoll KA, Kahng D, (1982) Planarization of patterned surfaces by ion beam erosion, Appl. Phys. Lett. 40, 7:636-638.
- [3] Johnson LF, Ingersoll KA, (1983) Ion polishing with the aid of planarizing film, Appl. Opt., 22, 8:1165-1167
- [4] Fechner R, Schindler A, Haensel T, Bigl F, (1999) Sub-nanometer polishing of optical surfaces by ion beam planarization technique, Proc. of the 9th International Conference on Precision Engineering (ICPE), 249-254

---

# Laser Machining of Cobalt Cemented Tungsten Carbides

Prof. Dr.-Ing. habil. Bernhard KARPUSCHEWSKI; Dipl.-Ing. Eckart WOLF; Dipl.-Ing.(FH) Mathias KRAUSE

## Abstract

In comparison to the far greater acceptance of laser beam machining, little is still known on how the two-phase material responds to the impact of the laser beam (surface damage). Currently, few scientifically grounded, technological data are available on the removal of hard metals by using laser beams.

This study investigates the impact of laser radiation (wavelength of 1,064 nm) in ns pulse range on various hard metal configurations. In addition to the removal behaviour, the resulting surface damage as well as surface roughness were studied as target parameters that can be influenced. As radiation source, a Q-switch-Nd:YAG laser is employed, as is common in the majority of 3D laser micro machining concepts. In experiments, the impact of influencing parameters relevant to the process is determined, such as the light's current intensity, repetition rate, and scanner feed velocity, on the qualitative and quantitative target values of surface roughness, layer removal rate, and surface integrity impact.

Comparative investigations of hard metals with different grain sizes were performed to determine the impact of this material characteristic on the machining process. In this research the mean grain diameters of tungsten carbide were varied by using grain sizes ranging from ultra fine to standard grains.

The results on laser machining of cobalt cemented tungsten carbide demonstrate the suitability for micromachining small three-dimensional geometries. A possible application field for micro tools is shown in the paper.

## 1. Introduction

In recent years, industry has witnessed an increasing demand of tools capable of quickly giving parts most diverse geometries. Part of this development are keywords such as rapid prototyping or the machining of new materials which are difficult or impossible to machine with traditional processes such as milling, grinding or EDM. For these fields of application, the innovative laser beam removal process seems to be a suitable answer [1]. Advantages of removing material using laser radiation include:

- high process flexibility and a high degree of automation based on NC-controls and linkage to CAD-CAM process chains
- production of nearly any structure without the need to change tools or high production costs for suitable tool electrodes, and
- touch-free and consequently force-free machining of extremely hard and non-conducting materials.

Laser beam machining may be used, for instance, for machining fully sintered hard metals, e.g. for chip breaker geometry into a fully sintered disposable cemented-carbide insert, as is common in everyday industrial practice [2]. In this case, laser beam machining competes with the traditional machining processes of EDM and grinding. These technologies possess however individual process borders, which favour the employment of laser beam machining.

So far there has been a lack of reliable information on the removal behaviour of hard metals using a pulsed Nd:YAG laser so that problems may occur with regard to attaining a reproducible surface and machining quality. By applying suitable process parameters the hard metal should, if possible, evaporate completely, and be removed from the machining zone by the generated steam pressure. Otherwise, surface quality may deteriorate due to droplet formation.

Information is also sparse on removal rates and surface qualities attainable when submitting hard metals to a pulsed laser beam machining process. Recent research performed at the Institute of Manufacturing Technology and Quality Management at Magdeburg University has focused on determining optimal laser and process parameters.

One current study aims at thoroughly investigating the geometrically determined two-dimensional machining of hard metals. As a radiation source, a cw-Q-switch-Nd:YAG laser is employed, as is common in the majority of 3D laser micro machining concepts. In experiments, the impact of influencing parameters relevant to the process is determined, such as the light's current intensity, repetition rate, and scanner feed velocity, on the qualitative and quantitative target values of surface roughness, layer removal rate, and surface integrity impact. One aspect of the study, which has already been completed, focused on determining technological performance characteristics for removal and roughness behaviour occurring in two-dimensional laser beam machining processes.

Comparative investigations of hard metals with different grain diameters were performed to determine the impact of this material characteristic on the machining process. In this research the mean grain diameters of tungsten carbide were varied by using an ultra fine grain hard metal, a fine grain hard metal, and a standard grain hard metal. In addition, only pure WC-CO hard metals containing 6% of binder metal was used to counteract the impact of other structural constituents and different concentrations of the cobalt binder.

The study also focused on changing the raw laser beam diameter from 1.3 mm to 1.8 mm, which causes a change in the effective focus diameter. So it was possible to estimate the relationship between the effective beam surface parameter and the removal rate or quality because it is highly relevant to the process, similar to the tool diameter analogous to face milling.

## 2. Process overview

Laser beam machining is a well-known process, which has been studied scientifically since a laser was first put into practice more than 40 years ago. First, drilling with the help of laser radiation was given priority. One of the first industrial applications of the laser technology included the drilling of gemstones for watches in 1968, followed by the drilling of cooling bores in turbine blades. Nowadays, laser drilling has found a variety of industrial applications with a tendency to improve the shape of the bore or to increase the aspect ratio [4]. Since the beginning of the 1990s, laser machining has been used in a number of fields to produce dies and to structure surfaces. Figure 1 shows a qualitative grouping of major micro-machining technologies in terms of minimum lateral structural dimension and surface roughness. Geometrical accuracy is closely linked to the roughness, which may be obtained [9].

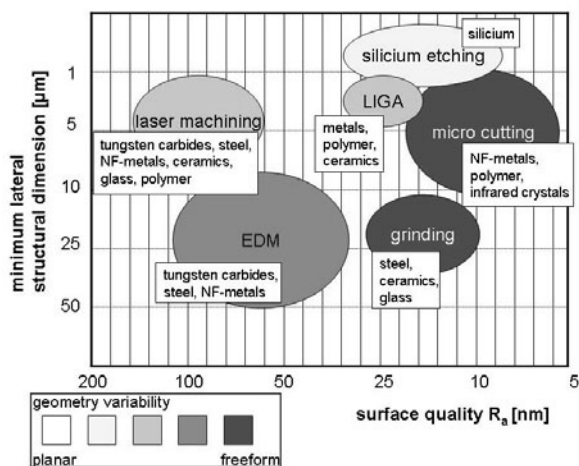


Fig. 1. Qualitative grouping of micromachining technologies, under aspects of possible machined materials and geometry variability [9]

Furthermore the comparison shows the still clearly existing advantages of the cutting technologies, like the high flexibility with the producing of complex three-dimensional

geometries and the high attainable surface qualities. To expand the laser removal process, developments aim at decreasing structural size and tolerances, extending the range of materials to be machined, and with priority improving surface quality [12].

To remove material with laser beams, excimer lasers ( $\lambda = 193\text{-}351\text{ nm}$ ) and to some extent copper vapour lasers ( $\lambda = 511\text{ nm}$ ) have been used so far as radiation sources in addition to  $\text{CO}_2$  ( $\lambda = 10.6\text{ }\mu\text{m}$ ) and Nd:YAG-laser systems ( $\lambda = 1064\text{ nm}$ ) [10]. The Nd:YAG concept has a number of decisive advantages compared to the previously most used  $\text{CO}_2$  lasers, including the mechanically simple and compact setup of its radiation source as well as its easy beam positioning and formation through optics made of quartz glass. These can be used because of their wavelength of 1064 nm, which is 10 times shorter than that of  $\text{CO}_2$  radiation and guarantee a high degree of absorption on metallic surfaces [3]. In comparison to  $\text{CO}_2$  lasers, drawbacks of these radiation sources include the fact that the pump light source is prone to wear-and-tear and their poor quality at lower attainable powers. Such Nd:YAG lasers with a power of up to some 100 W are often used for fine welding, fine cutting, drilling, and removing material [13].

Depending on the type of excitation principle employed, Nd:YAG lasers can be grouped into flash-pumped or laser diode pumped pm (pulse mode) Nd:YAG lasers and cw (continuous wave) Nd:YAG lasers with arc lamps. The latter may be operated in pulse mode during Q-switch operation. Such cw-Q-switch-Nd:YAG sources are able to generate pulses exceeding 100 kW with pulse length between 30 and 300 ns at repetition rates within 10 and 50 kHz. However, the electric or acoustic-optical Q-switch limits maximum medium power to approximately 100 W [5].

In combination with a scanner positioning system, this type of beam source may be used for special applications. It is already widely used for engraving jobs, combining the advantages of highly dynamic beam deflection with galvanometer-driven tilted mirrors with a type of radiation that can be modulated within the kHz range. Typically, computer aided design is also involved in obtaining a particular geometry [8].

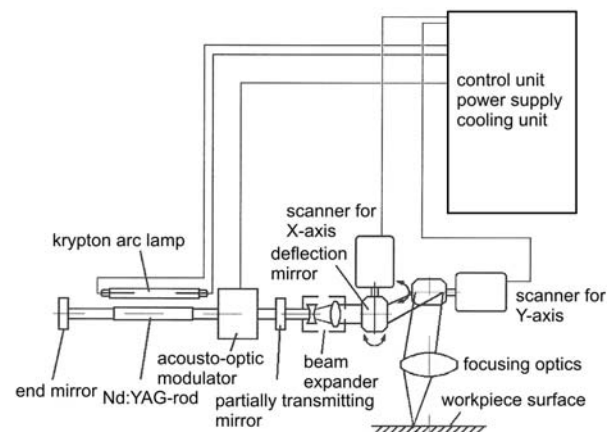


Fig. 2. Schematic set-up of the laser system [15]

In the presented research such system was used (Figure 2). The DMU 60L three-axis Nd:YAG laser machining system stands out in the field of laser beam machining as its basic unit consists of a CNC controlled three-axis milling machine with a built-in cw-Q-switch-Nd:YAG laser source providing milling and laser beam machining successively. The laser beam machining process is a thermal process where the optical energy absorbed is converted into heat. Depending on the material to be machined and the particular process control, it is possible to heat up, melt, and evaporate the material [11].

Usually, the laser beam is perpendicular to the laser feed direction. It scans the workpiece within the surface area that is to be removed in overlapping tracks like a cutter. If the depth of removal required cannot be reached with one laser scan, the laser scans the surface repeatedly, cutting deeper layer by layer. Figure 3 shows the definition parameters for laser machining during the removal process.

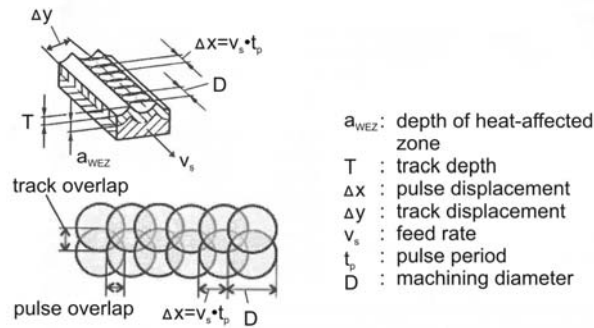


Fig. 3. Laser machining parameters at material removal according to DIN EN ISO 11145 [14]

The removal process dominating the laser beam machining process of hard metals may be defined as sublimation where most material is removed through evaporation. As a result of the high vapour pressure prevailing in the interaction zone, the melt created on a limited scale will be ejected. Since the thermal energy applied will be largely removed from the machining zone together with the metal vapour generated, the heat impact zone is relatively small [6] [7]. Due to the high thermal conductivity of metals, sublimation removal is only possible at pulse durations starting in the microsecond range. Longer pulses will cause heat to increasingly spread into adjacent areas of the workpiece, forming more melted material. Overall, the amount of energy applied to the workpiece is relatively large since the specific evaporation energy must be generated, too [9]. The high resulting intensities may also cause plasma to form in the metal vapour flowing off, binding more energy. If incorrect setting parameters are selected, the plasma may also shield the surface of the workpiece from the laser beam. In summary, sublimation facilitates high geometrical accuracy and relatively low removal rates [10].

### 3. Experiment

For a basic technological study of two-dimensional machining of hard metals using Nd:YAG radiation, target values such as removal behaviour, roughness behaviour, and

peripheral zone impact had to be determined. In particular, the impact of various WC grain sizes on the removal process would be of interest.

To this end and because of the wide range of hard alloys, the research was limited to the hard metal group with the largest market share. This group of WC-Co-hard metals without additional elements providing hardness includes alloys with grain sizes ranging from ultra fine to standard grains with Co contents of 6-16 % by weight. From this group of hard metals, WC-Co-alloys containing 6 % cobalt in their structure were selected, used primarily for cutting tools. For research purposes, three grades of hard metal were used, with the designations E410, MG12, and H15Y (Table 1).

Table 1. Material properties of the investigated hard metals

hard metal type	E410	MG12	H15Y
composition [mass %]	WC: 93,0 % MC: 0,8 % Co: 6,0 %	WC: 93,2 % MC: 0,8 % Co: 6,0 %	WC: 93,7 % MC: 0,3 % Co: 6,0 %
WC grain size	ultra finest grain 0,2 $\mu\text{m}$ - 0,5 $\mu\text{m}$	finest grain 0,5 $\mu\text{m}$ - 0,8 $\mu\text{m}$	standard grain > 1,3 $\mu\text{m}$
hardness (HV <sub>10</sub> ) DIN 3878	1950 $\pm$ 60	1820 $\pm$ 60	1730 $\pm$ 60

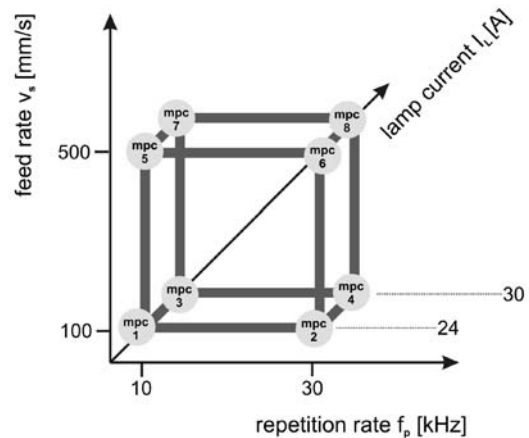


Fig. 4. Three-dimensional model of the input machining parameter matrix with the limit values of the parameter range (mpc = machining parameter combination)

In order to determine the characteristics of machining and roughness behaviour, it was necessary to study allvariations of the technological parameters in a set matrix (Figure 4). The technological parameters used, largely cover the parameter range provided by the machine. Moreover, they are within the limits determined in preliminary experiments, where it seemed possible to remove an efficient amount of hard metals using laser beams.

The experiment also focused on changing the raw laser beam diameter as an indication of the effective spot diameter. Introducing the mode-aperture contained in the laser resonator into the beam path and limiting the raw beam to diameters of 1.3 mm and 1.8 mm respectively achieved this. In order to demonstrate the dependency between the parameters spot diameter and removal behaviour, roughness behaviour, and surface integrity impact, the entire experiment plan had to be run with a 1.3 mm aperture (test series 1) and a 1.8 mm aperture (test series 2). This allows comparing directly removal behaviour and roughness behaviour at these different beam constellations.

In order to investigate the impact of the differing grain diameters of the hard metal on the machining process, the hard metal test materials E410, H15Y, and MG12, described above, were each treated in the test series 1 and 2, adding up to a total of 600 cubes machined, which could be analysed.

#### 4. Results

Experimental research showed that best machining results in terms of surface roughness and layer removal can only be obtained within a particular intensity and pulse overlap. Furthermore, the surface structures generated could be subdivided into three individual phases depending on energy intensity. However, these phases start at different energy intensity depending on the laser aperture diameter (Figure 5). Both the intensity at work and the pulse overlap decisively influence the surface roughness that may be obtained. The pulse overlap is calculated by using the effective machining diameter, repetition rate, and feed velocity. As a result, surface roughness is minimal in Phase III, the intensity phase relevant for machining, at increasing pulse overlap.

The amount of material removed increases with intensity and the pulse overlap. As the amount of material removed increased, at first it is an increase in roughness observed, too. After exceeding this intensity-depending partial removal phase (Phase II), surface roughness decreased due to the full removal of the hard metal. Consequently, there is a certain phase with a suitable parameter combination in Phase III, where best surface quality is obtained at maximum amounts of layer removal.

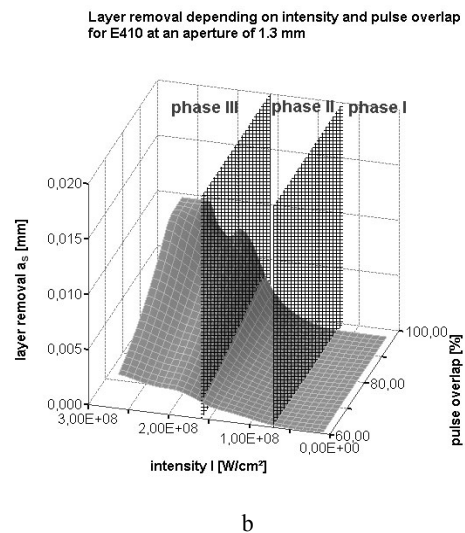
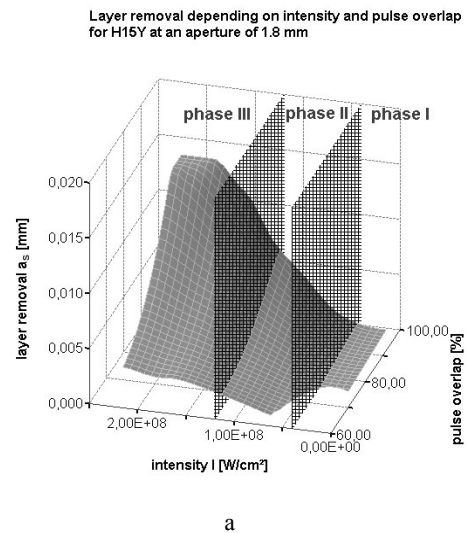
Changes in the hard metal structure relate only to a limited extent to the laser beam machining process. When WC grain sizes become smaller (finest grain, ultra finest grain), only a slight increase was noted in the amount removed at a minimally decreasing roughness. However, this dependence only occurs at the smaller aperture diameter.

The influence of the increased aperture diameter results in increased material removal due to the larger beam impact area. Surface quality is not influenced decisively by this change. Consequently, a suitable method for the laser machining of hard metals producing high-quality results can be derived to select the optimum parameter combination in Phase III to minimize surface roughness.

After such laser machining, the surface is covered with a layer of melted material, which can be characterized by phase changes and residual stresses. This layer forms in its size independently of the machining parameters, as soon as the necessary melting energy is applied. Therefore in Phase I only individual melted particles at the surface were proven.

The thickness of the amorphous layer of melted material in the Phases II and III is equally 1 to 2  $\mu\text{m}$  (Figure 6). On the surface of the layer cracks are to be observed, which are caused through residual stresses induced by temperature- and phase changes.

As already described, the main mechanism for laser material removal involves energy absorption, which leads to heat transfer and phase transition. With pulses in ns-range, heat transfer to the bulk of the material by thermal conductivity results in heat-affected zones where changes in the material structure can be observed. These heat-affected zones have a negative effect on material properties and introduce residual stresses. In order to reduce the development of the heat-affected zone, the optimum parameter combination (Phase III) has to be chosen. As mentioned before, a recast layer on hard metal surface was observed. This layer of melted material, not acceptable for the later use of the workpiece, should be removed. As finishing process and simple reworking method, micro-blasting with ceramic particles was used.





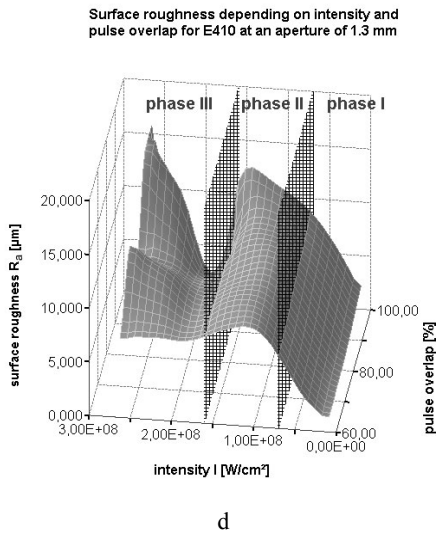
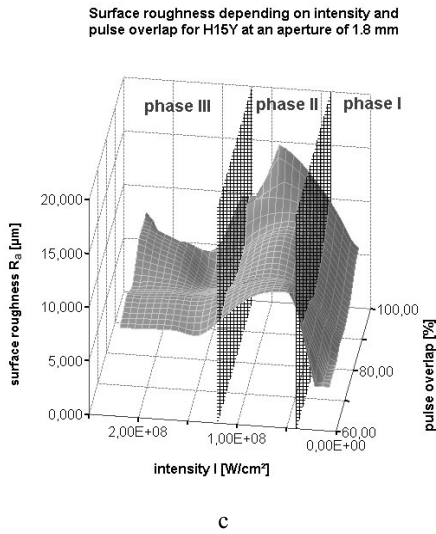



**Fig. 5.** Layer removal (a,b) and surface roughness (c,d), depending on intensity and pulse overlap, divided into three removal phases for H15Y at an aperture of 1.8 mm and for E410 at an aperture of 1.3 mm

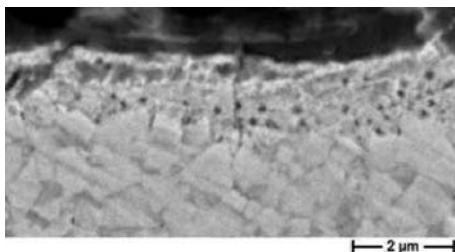


**Fig. 6.** Material structure of a phase III machined H15Y hard metal with an amorphous layer of melted material above the basic structure

The resulting characteristic diagrams for the material removal and roughness behaviour with laser machining of the used tungsten carbide configurations can serve the potential users of the procedure as basis for the process optimization. The surface roughness was proved as primary factor for the choice of the technological characteristic values. Therefore in the first step the selection with consideration of demanded, maximally permissible surface roughness should take place. Afterwards the user should consider the minimum acceptable layer removal and commit under attention of further limiting parameters (operating time etc.) a useable working strategy. By the integration of the innovative technology laser machining into the process chain for the manufacturing of smallest tungsten carbide tools the possibility to save time and costs is given (Figure 7). Since the conventional way over eroding and the electrode production as a time intensive procedure can be void. Besides the laser machining allows manufacturing filigree structures directly into the workpiece surface because of the small laser diameter (60µm).

Development + Design	Production + Preparation	Manufacturing			
CAD	CAM	Prepare blank	Milling electrode	EDM	Finishing
CAD	CAM	Prepare blank	Laser machining	Finishing	

 Saving time + costs

**Fig. 7.** Innovative process chain by using laser machining to save time and costs in production

A necessity for laser machining is the presence of STL data (polygonized surface data), which can be generated from the 3D-CAD data of the micro tool. Similarly as with the milling process thereby the difference volume between blank and desired final contour is used as basis. In order to study the capabilities for laser machining of cobalt cemented tungsten carbides through the described process chain, some tungsten carbide tools were designed and machined (Figure 8).

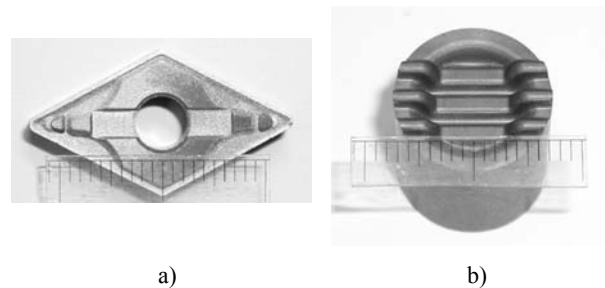


**Fig. 8.** Laser machining examples: insert with new chip breaker geometry - machining time 48min (a), tungsten carbide micro transforming stamp - machining time 7h 23min (b)

The tool material was ultra finest grain tungsten carbide, chosen to facilitate the achievement of a good surface quality. Accordingly laser machining offers a cost-effective and time-efficient solution for manufacturing small three-dimensional geometries in tungsten carbides. Of course it is not the suitable technology for mass production, but the ideal technology for prototype testing and tool development. By iterative use of this fast and precise technology the final geometry for mass production moulds can be determined.

## 5. Summary

In this paper the capabilities of laser machining on cobalt cemented tungsten carbides as a manufacturing process were introduced. With the resulting process parameter combinations a suitable method for the laser machining of hard metals producing high-quality results can be derived. It was demonstrated here that cobalt cemented tungsten carbides can be machined without requiring expensive special tools.

Nevertheless, the laser machining process, being in its infancy as a manufacturing technology, requires further study to define effective process windows for different types of material and also research into new application areas. The accuracy, surface finish, surface integrity and productivity achieved with the process and its operational costs should be investigated in greater detail. The laser machining is a promising new technology that, when used appropriately, can make a significant impact on current manufacturing practice and open new areas of application for advanced materials like cobalt cemented tungsten carbides. Work is being carried out to integrate laser machining with other manufacturing processes, so as to exploit their strengths and overcome their limitations. This should help to make laser machining an attractive proposition for a wider range of manufacturing problems.

## 6. Acknowledgement

This study on "Laserstrahlabtragen von Hartmetall" ("Laser Machining of Hard Metal") is funded by the Ministry of Education and Culture of the federal state of Saxony-Anhalt as well as by the European Union's EFRE Structural Funds. The authors would like to thank all sponsors for supporting the project.

## 7. References

- [1] Lierath F., Pieper H.-J., Wolf E., Krause M., "Laser machining – a modern procedure for mould making", proceedings "Int. Conference on laser technologies in welding and materials processing" LTWMP 2003, Katseveli Town, 19./23.05.2003, pp. 202-205, ISBN 966-95847-3-6
- [2] Dübner L., Pieper H.-J., Wolf E., Krause M., "Laserstrahlabtragen ein zukunftsweisendes Rapid Tooling Verfahren", 4 Int. Konferenz "Moderne Technik und Technologie" 2003, Sewastopol, ISSN 0372-6053
- [3] Weissmantel S., Reisse G., Rost D., "Preparation of superhard amorphous carbon films with low internal stress", *Surface & Coatings Technology*, 188–189, 2004, pp. 268–273
- [4] Malshe A., Deshpande D., "Nano and microscale surface and sub-surface modifications induced in optical materials by femtosecond laser machining", *Journal of Materials Processing Technology*, 149, 2004, pp. 585–590
- [5] Heyl P., "Mikrostrukturierung von Hartmetallen mit UV-Laserpulsen im Nanosekundenbereich", Dissertation, Heidelberg, 2004
- [6] Rizvi N. H., Apte P., "Developments in laser micro-machining techniques", *Journal of Materials Processing Technology*, 127, 2002, pp. 206–210
- [7] Andrä G., Bergmann J., Bochmann A., Falk F., "Herstellung und Bearbeitung von Mikrowerkzeugen aus Hartmetall mit einem Femtosekundenlaser", *J. Univ. Appl. Sci. Mittweida*, 16th Int. Scientific Conf. Mittweida, Nr. 1, *Lasertechnologien*, 2003, pp. 12-15
- [8] Förster D., Müller W., "Laser in der Metallbearbeitung", Fachbuchverlag Leipzig im Carl Hanser Verlag, 2001
- [9] Fischer S.W., *Fertigungssysteme zur spanenden Herstellung von Mikrostrukturen*, Shaker Verlag, 2000, ISBN 3-8265-7856-2
- [10] Li T., Lou Q., Wei Y., Huang F., Dong J., Liu J., "In situ diagnosis of pulsed UV laser surface ablation of tungsten carbide hardmetal by using laser-induced optical emission spectroscopy", *Applied Surface Science*, 185, 2001, pp. 114-122
- [11] Lässig B., "Kontrollierter Formabtrag durch Sublimation mittels Laserstrahlung", Shaker Verlag, Dissertation, Aachen, 1995
- [12] Haferkamp H., Alvensleben F. v., Becker H., Lindemann K., Czerner St., "Lasereinsatz zur Vergütung und Reparatur im Werkzeugbau" (Laser Zentrum Hannover), Fachbericht, wt - Werkstatttechnik, 1989
- [13] Beck M., "Verbundprojekt: Abtragen mit Laserphotonen- Laserpräzisionsbearbeitung keramischer Hochleistungswerkstoffe: Bauteile und Werkzeuge aus Verbundwerkstoffen und Siliziumnitrid", Daimler Benz AG, Forschung und Technologie, Hannover, 2000
- [14] Optics and optical instruments – Lasers and laser-related equipment, DIN EN ISO 11145
- [15] Pham D.T., Dimov S.S., Petkov P.V., Petkov S.P., "Laser milling", *Proceedings of the Institution of Mechanical Engineers*, Bd. 216, 2002, 5, pp 657-668

---

## Study of Thermal Deformation of a Base Sheet Caused by Laser Cutting

Masayuki NUNOBIKI<sup>1</sup>, Koichi OKUDA<sup>1</sup>, Toshiyuki YOSHIDA<sup>2</sup>, Shohei KITA<sup>3</sup>

<sup>1</sup>University of Hyogo, <sup>2</sup>Yamato Trackwork System Co., Ltd., <sup>3</sup>Sanyo Special Steel Co., Ltd.

Keywords: Laser cutting, Thermal deformation, Deformation of a base sheet, Control of deformation, Cutting sequence

In case that a lot of products were cut out from a wide base sheet by laser cutting, the sheet had been much deformed so that the error occurred in a height regulator. This paper deals with thermal deformation of a base sheet caused by laser cutting. We clarified that the thermal deformation was influenced by the cutting sequence in the case of SUS304 sheets of 1mm thickness. The workpieces bent upward in inward sequence, and the workpieces bent downward in outward sequence. It is expected that the deformation was able to be controlled by cutting sequence.

### 1 Introduction

Laser material processing has been widely used in industry. Highly localized heat input to the workpiece minimizes its deformation compared with conventional heat cutting. In case that a lot of products were cut out from a wide base sheet in some laser cutting conditions, the sheet had been much deformed so that the error occurred in a height regulator. If the error occurs in the unmanned process, the waste of the time and money follow it. Many studies investigated the influence of the cutting parameters on the quality of products and some researches investigated relationship between heat input and HAZ along the cutting edge. There are few studies which treated the deformation of the base sheet of which the products were cut out.

The relationship between laser cutting parameters and quality of cut edges were already discussed at following studies. B. Yilbas et al. investigated the penetration time during CO<sub>2</sub> laser cutting of mild steel at various pressures of the cutting gas<sup>(1)</sup>. K. Chen and V. Modi investigated the interaction of a supersonic jet with workpiece by simulations and experiments<sup>(2)</sup>. C. Bagger and F. Olsen described how the laser cutting process could be optimized to obtain high quality cut edges<sup>(3)</sup>. S. Lee and D. Dornfeld investigated the material property changes and cutting kerf shape to develop an effective way of automated deburring of precision component<sup>(4)</sup>. B. Yilbas identified the influence of cutting parameters on the resulting cut quality based on factorial analysis<sup>(5, 6)</sup>. P. Sheng and V. Joshi developed a numerical analysis for the HAZ<sup>(7)</sup>.

Some research has been devoted to understand thermal deformation mechanisms as for laser forming<sup>(8,9)</sup>. The mechanism of thermal deformation caused by laser cutting differed from that by laser forming in some respect. In laser cutting of metal sheet, laser beam is absorbed at the cutting

front and the generated heat is conducted into the surrounded material. Molten material forms the melt film and the thickness of the melt film increased with depth. The molten material at the cutting front becomes heat source until it is ejected at the bottom of kerf. In addition, the dross attached at the bottom of workpiece became heat source too. The temperature of the bottom of workpiece became higher than the top of workpiece. Therefore, it was expected that the deformation mechanism of laser cutting was different from the mechanism of laser forming.

This paper deals with thermal deformation of a base sheet caused by laser cutting. We selected a simple kerf for the shape of product to examine an influence of the cutting sequence upon the thermal deformation. We made several kerfs on a stainless sheet 29×58×1mm by using CO<sub>2</sub> laser and measured the deformation of the sheet. The workpieces were cut by various cutting sequences. We investigated the deformation of the base sheets. This study aimed the clarification of the relationship between the deformations of the base sheet and the cutting sequence.

### 2 Experimental procedure

We used a 1600W CO<sub>2</sub> laser system provided by Mitsubishi electric Co. Ltd.. The laser beam exhibited a near TEM<sub>00</sub> mode pattern. A 127mm ZnSe focusing lens was used to focus the laser beam to a spot size of 0.1mm. The focal point was set on the surface of the workpiece. A pulse wave CO<sub>2</sub> laser was used to cut workpieces. Oxygen was introduced coaxially with the laser beam through a nozzle with 1.5mm diameter. The stand-off distance between nozzle and workpiece was 1.0mm. The workpiece were cut by pulse laser at average power of 156W, frequency of 200Hz, duty factor of 13%, cutting velocity of 0.3m/min and pressure of oxygen gas of 274kPa.

All workpieces were SUS304 and 29×58×1mm in size. We made the direction of all workpieces the same. The right edge of each workpiece was fixed by a jig. We cut several kerfs in each workpiece. The kerf configuration and coordinate system were set as shown in Fig. 1. The side with a free end was named outer side and the side with a fixed end was named inner side. We arrayed the kerfs in two rows. The distance between two rows was 3mm. The kerfs were located at intervals of 4mm. We numbered each of the kerfs.

We called a set of two kerfs located in the same x coordinates a column of kerfs. We numbered each of the columns sequentially from outer column to inner column. For example, a set of kerf 1 and 2 was called 1<sup>st</sup> column of kerf and a set of kerf 9 and 10 was called 5<sup>th</sup> column of kerf. The rhombic marks represented the piercing points, and we cut each kerf from the piercing point toward the center of the workpiece. The length of each kerf was 10mm.

In our experiments, we cut the kerfs in several cutting sequences. We classified the cutting sequences into inward sequence, outward sequence and others. In inward sequence, processing is advanced from the kerf on the outer side to the kerf on the inner side. In outward sequence, processing is advanced from the inner kerf to the outer kerf. The displacement of the surface of workpiece was defined by the difference between waviness profiles which measured after and before laser cutting as shown in Fig.2. We measured the waviness profiles along the x-axis by using a profilometer SURFCOM 570A provided by Tokyo Seimistu Co. Ltd.

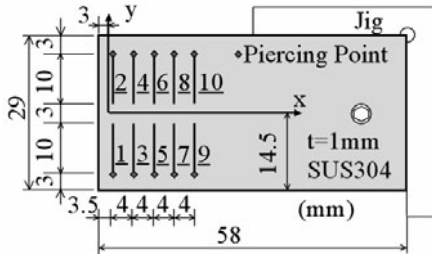


Fig. 1. Geometry of workpiece and kerf configuration

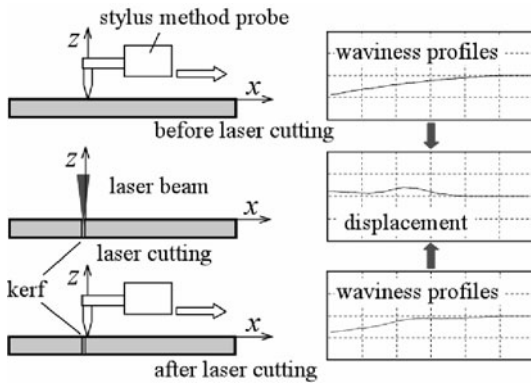


Fig. 2. Definition of displacement of workpiece

### 3 Displacement in inward and outward sequences

We cut six kerfs in each workpiece in inward sequence and outward sequence. Figure 3 shows the displacements of the top and bottom surfaces when six kerfs were cut on a workpiece in inward sequence. The free edge displaced upward. The displacement took positive when the free edge of the workpiece displaced upward. The broken line is a mean line of them and indicates the deformation of workpiece. Figure 4 shows the displacements of the top and

the bottom surfaces in the case of outward sequence. The free edge displaced downward. In both sequence, the plastic deformation was occurred at the bottleneck places between two kerf ends. The workpieces bent at these bottleneck places. Figure 5 shows the results of five experiments obtained by the inward sequence. All workpieces bent upward similarly. Figure 6 shows the results of five experiments obtained by the outward sequence. All workpieces bent downward although the amounts of displacements were a little different.

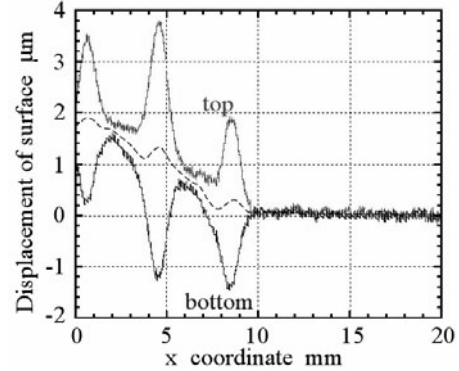


Fig. 3. Deformation of workpiece in thickness of 1mm when six kerfs were cut in inward sequence

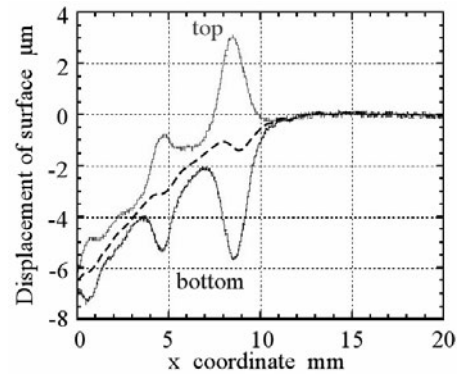


Fig. 4. Deformation of workpiece in thickness of 1mm when six kerfs were cut in outward sequence

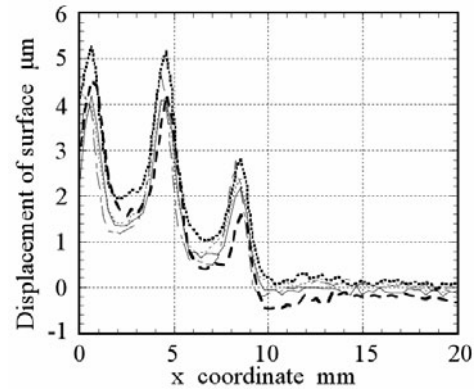
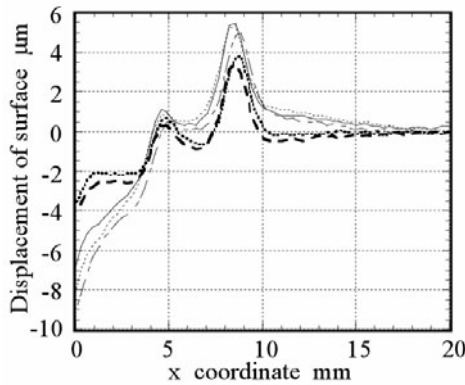


Fig. 5. Results of five laser-cut experiments in inward sequence

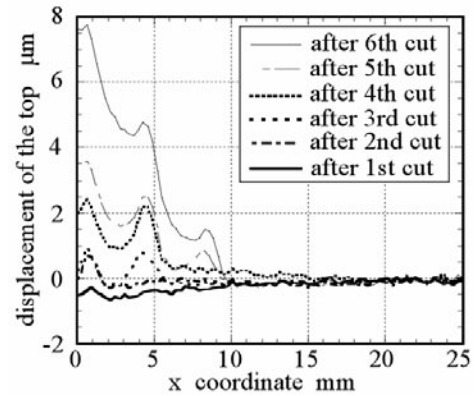


**Fig. 6.** Results of five laser-cut experiments in outward sequence

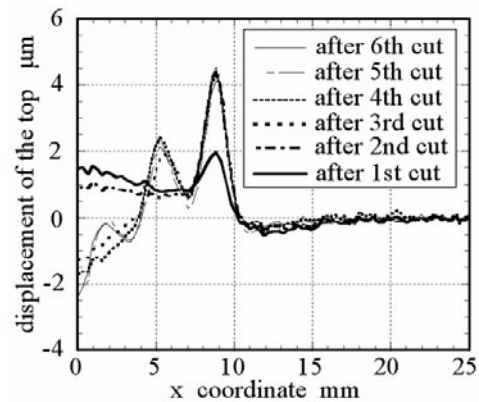
When the shapes of each deformation were compared, the following similarities and differences were observed. The convexes appeared at the bottleneck places between two kerf ends in both sequences. We considered that the plastic deformation was occurred at the bottleneck places and the expansion in the z direction was caused by compression in the x direction. In laser cutting of metal sheet, laser beam is absorbed at the cutting front and the generated heat is conducted into the surrounded material. Because the cutting front becomes heat source, the top and bottom surfaces around the cutting front were heated. The heated area expanded and compressed by the surrounding of low temperature. The workpiece bends in a direction of the surface strongly compressed i.e. a direction of the surface with bigger convex than another. The convex has become small more than the convex previously made excluding first convex in inward sequence.

Figure 7 shows the process of deformation caused by laser cutting in inward sequence. Six curves represented the displacements from initial surface which were measured after having cut corresponding kerf. Whenever we cut one kerf, we measured the waviness profile of top surface. After the workpiece had been cooled to the room temperature, we cut following kerf. The displacement increased gradually as the process advanced. Figure 8 shows the process of deformation caused by laser cutting in outward sequence. Until second cutting, the workpiece bend slightly upward. After third cutting, the workpiece bent downward as the process advanced.

In both sequence, the workpieces hardly bent at laser-cut of 1st column of kerfs, and it bent largely after laser-cut of 2nd column of kerfs. Even if we cut kerfs at long intervals, the same displacement at the continuous cutting was observed. Therefore, we considered that the temperature distribution before laser cutting does not influence the direction of deformation so much. And we consider that the position of the existing kerfs influences the direction of deformation. When the adjacent kerf exists at the outer side of the kerf which will be cut, the workpiece bends upward. And when the adjacent kerf exists at the inner side of the kerf, the workpiece bent downward. These results indicated that the processing sequence influenced the direction of bend of the workpiece and the deformation of workpiece can able to be controlled by the cutting sequence.



**Fig. 7.** Process of deformation when six kerfs were cut in a workpiece of 1mm thickness in inward sequence



**Fig. 8.** Process of deformation when six kerfs were cut in a workpiece of 1mm thickness in outward sequence

#### 4 Displacement in four cutting sequences

We cut eight kerfs in a workpiece in three cutting sequences shown in Fig. 9 First is an inward sequence. Second is an outward sequence. Last is a mixed sequence which consists of the inward sequence and the outward sequence. In cutting of the kerfs encircled by continuous line, the adjacent kerf exists at the outer side and it is predicted that the workpiece bend upward. In cutting of the kerfs encircled by broken line, the adjacent kerf exists at the inner side and it is predicted that the workpiece bend downward. Figure 10 shows the deformation of the workpiece caused by laser cutting in three sequences. In inward sequence, the workpiece bent upward. In outward sequence, the workpiece bent downward. In the mixed sequence, the displacement of workpiece was smaller than two of the previous sequences.

We cut ten kerfs in a workpiece in four cutting sequences shown in Fig. 11. The first is an inward sequence. The second is an outward sequence. The third is a mixed sequence which consists of the inward sequence and the outward sequence. The last is a dividing sequence in which new kerf is cut in the middle of existed kerfs. Figure 12 shows the deformation of the workpiece caused by laser cutting in the sequences. In inward sequence, the workpiece

bent upward. In outward sequence, the workpiece bent downward. In the mixed sequence, the workpiece bent downward at the inner columns of kerfs, and bent upward at the outer columns of kerfs. The displacement was smaller than two of the previous sequence. In the dividing sequence, the displacement was smallest than other sequences. These results indicate that the deformation of workpiece can be controlled by the cutting sequence in the case of SUS304 sheet of 1mm thickness.

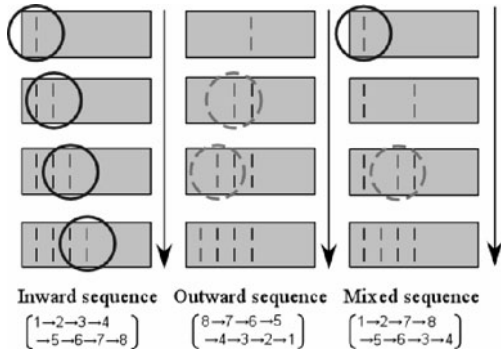


Fig. 9. Cutting sequences for eight kerfs

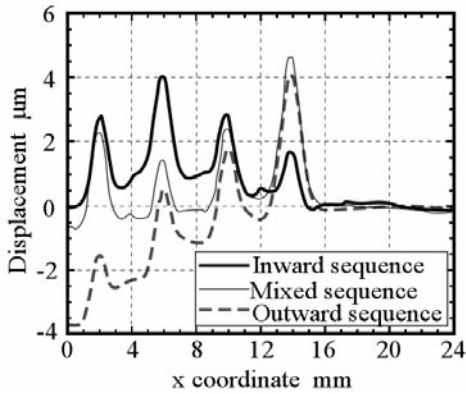


Fig. 10. Deformation of workpiece in thickness of 1mm when eight kerfs were cut in each sequence

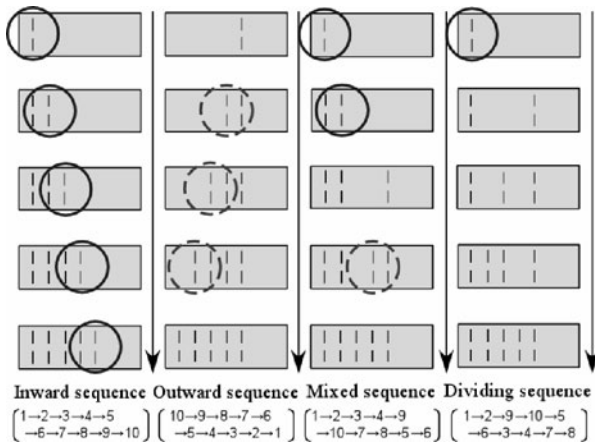


Fig. 11. Cutting sequences for ten kerfs

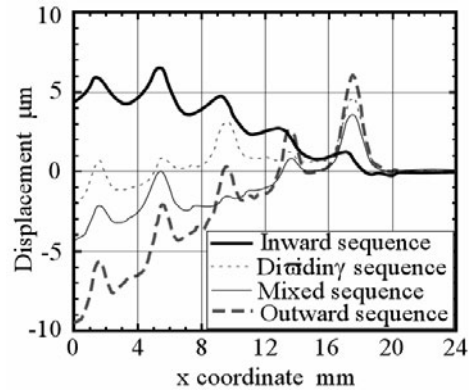


Fig. 12. Deformation of workpiece in thickness of 1mm when ten kerfs were cut in each sequence

### 5 Influence of thickness of base sheet

We investigated whether same effect of cutting sequence was observed in laser cutting of SUS304 sheet of 2mm thickness. We cut ten kerfs in a workpiece in four cutting sequences shown in Fig.11. Figure 13 shows the deformation of the workpiece caused by laser cutting in these sequences. Unlike the laser cutting of SUS304 sheet of 1mm thickness, all workpieces bent upward in all sequence. The workpiece which was cut in the inward cutting bent larger than the workpiece in case of the outward sequence.

Figure 14 shows the process of deformation in the case of inward sequence. Six curves represented the displacements measured after having cut corresponding kerf. Whenever we cut one kerf, the workpiece had been cooled to the room temperature. The displacement increased gradually as the process advanced. Figure 15 shows the process of deformation in case of the outward sequence. While there were some differences in process of deformation between the outward sequence and the inward sequence when we cut kerfs at long intervals, the terminal deformation in each sequence was similar to others when we cut kerfs continuously.

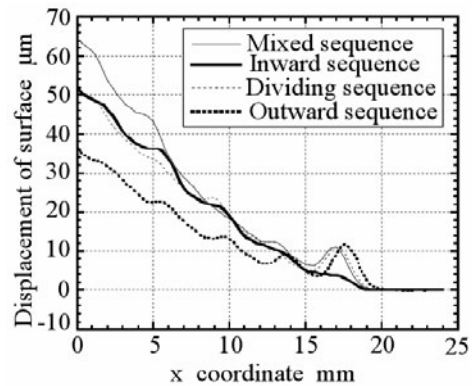


Fig. 13. Deformation of workpiece in thickness of 2mm when eight kerfs were cut in each sequence

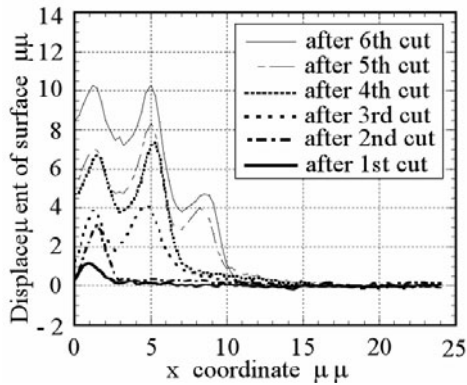


Fig. 14. Process of deformation when six kerfs were cut in a workpiece of 2mm thickness in inward sequence

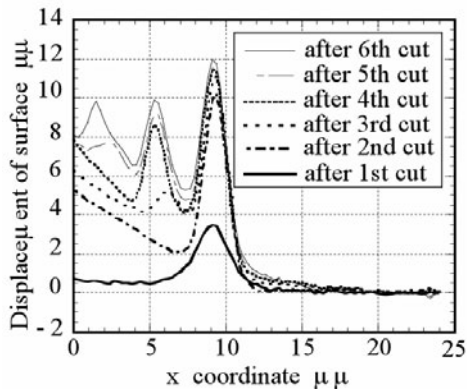


Fig. 15. Process of deformation when six kerfs were cut in a workpiece of 2mm thickness in outward sequence

### 6 Temperature of base sheet during laser cutting

We investigated the influence of thickness upon the deformation around the kerf under laser cutting. We measured the temperatures of top and bottom surfaces around a kerf during laser cutting. Experimental setup is shown in Fig. 16. We cut one kerf in a workpiece and measured temperature at several points on x-axis by using a Type K (Chromel-Alumel) thermocouple.

Figure 17 shows the maximum temperature in the vicinity of the kerf during cutting of workpiece of 1mm thickness. A continuous line and a broken line were the regression lines. Figure 18 shows the maximum temperature in the case of 2mm thickness. In both case, the maximum temperature at a point of the bottom was higher than the temperature at corresponding point of the top where the same distance parted from the kerf. At the points close to the kerf in the of 1mm thickness, there was little temperature difference between the top and the bottom. In the case of 2mm thickness, the temperature difference between top and bottom was larger than the difference in the case of 1mm thickness.

We considered the cause of temperature deference as follows. In laser cutting, laser beam is absorbed at the cutting front and the generated heat is conducted into the surrounded material. Molten material forms the melt film and the thickness of the melt film increased with depth. In addition, the dross attached at the bottom become heat source too. The temperature of the bottom became higher than the top.

In the case of laser cutting of thick sheet, the temperature difference between top and bottom became dominant factor for the deformation of workpieces. When thickness of sheet increased, it become difficult to control of deformation by cutting sequence.

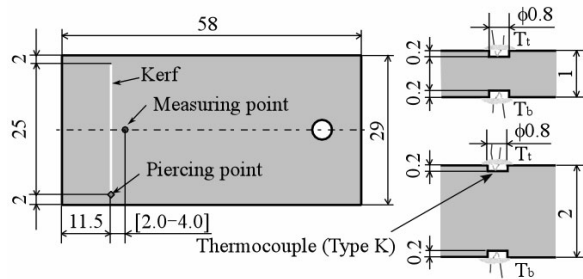


Fig. 16. Experimental setup

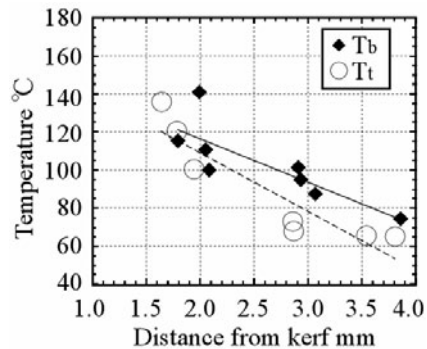


Fig. 17. Temperature of top and bottom surface in the vicinity of a kerf when a kerf was cut in a workpiece

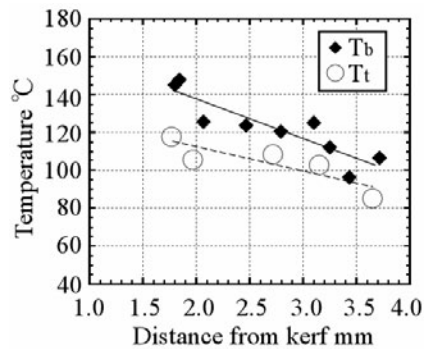


Fig. 18. Temperature of top and bottom surface in the vicinity of a kerf when a kerf was cut in a workpiece

## 7 Conclusions

This study investigated the thermal deformation of a base sheet when a lot of products were cut out from the base sheet.

It was clarified that the thermal deformation was influenced by the cutting sequence in the case of laser cutting of SUS304 sheets of 1mm thickness. The workpieces bent upward in inward sequence, and the workpieces bent downward in outward sequence. This tendency was observed even if we cut kerfs at long intervals or continuously. It is expected that the deformation of the base sheet was able to be controlled by cutting sequence.

In the case of SUS304 sheet of 2mm thickness, the workpieces bent upward even if we cut kerfs in inward sequence or outward sequence. In the case of laser cutting of thick sheet, the control of deformation was difficult as long as kerfs were cut continuously.

## 8 References

- [1] B. S. Yilbas, R. Davis and Z. Yilbas, (1990) Study into the measurement and prediction of penetration time during CO<sub>2</sub> laser cutting process, Proc. Instn. Mech. Engrs Vol.204, pp105-113
- [2] K. Chen and V. Modi, (2000) Gas jet – workpiece interactions in laser machining, ASME, J. Manuf. Sci. Eng. Vol.122 August, pp.429-438.
- [3] C. Bagger and F. O. Olsen , (2001) “Pulsed mode laser cutting of sheets for tailored blanks”, Journal of Materials Processing Technology, Vol. 115, 1, pp.131-135.
- [4] S. Lee and D. Dronfeld, (2001) Precision laser deburring, ASME, J. Manuf. Sci. Eng. Vol.123 November, pp.601-608.
- [5] B. S. Yilbas, (1996) Experimental investigation into CO<sub>2</sub> laser cutting parameters, Journal of Materials Processing Technology, Vols. 58, pp.323-330
- [6] B. S. Yilbas, (2004) Laser cutting quality assessment and thermal efficiency analysis”, Journal of Materials Processing Technology, Vols. 155-156, pp.2106-2115.
- [7] Joshi, V. and P. Sheng, (1995) Analysis of Heat-Affected Zone Formation for Laser Cutting of Stainless Steel, Journal of Materials Processing Technology, Vol. 53, No. 3-4, pp. 879-892.
- [8] W. Li and Y. Yao, (2000) Numerical and experimental study of strain rate effect in laser forming, ASME, J. Manuf. Sci. Eng. Vol.122 August, pp.445-451.
- [9] J.Cheng and Y. yao, (2002) Microstructure integrated modeling of multiscan laser forming, ASME, J. Manuf. Sci. Eng. Vol.124 May, pp.379-388.



---

## Laser Welding of Transparent Resin Plates

Shinya Hayakawa<sup>1</sup>, Tadashi Miura<sup>1</sup>, Takashi Nakamura<sup>1</sup>, Fumihiro Itoigawa<sup>1</sup> and Tatsuya Hasegawa<sup>2</sup>  
<sup>1</sup>Nagoya Institute of Technology, <sup>2</sup>Nagoya University

Keywords: Laser welding, Transparent resin, Absorptivity

### Abstract

A new method of the laser welding of thermoplastic resin plates is developed to apply the laser welding process to the welding of transparent resin plates. The welding surface of the transparent resin plate is pretreated by sandblasting in order to increase the absorptivity of the laser beam. It is found that the laser welding of two transparent PMMA plates can be realized and the optical property of the welded region returns to transparent. It is also found that the transparency of the welded region can be improved when the hot pressing is used for the pretreatment.

### 1 Introduction

The laser welding of thermoplastic resin parts [1] is now practically used for many products such as automobile components. In the usual laser welding process, two thermoplastic resin parts are lapped and a laser beam is irradiated from the transparent resin side. In this process, one of the parts must be transparent in order to transmit the laser beam and the other must be opaque in order to absorb the laser beam. If laser welding can be realized for two parts that are both transparent, the application of laser welding will be much broader. It is also expected that the environmental burden can be reduced because the usage of adhesive will decrease; in other words, the amount of emission of organic solvent will decrease. In this paper, a new method of laser welding thermoplastic resin plates is developed in order to apply the laser welding process to the welding of transparent resin plates.

## 2. Laser welding of different materials

### 2.1 Principle of laser welding

First, the principle of laser welding two different materials [2, 3], which is the basis of laser welding transparent resin plates, is explained. Figure 1 shows the principle of the usual laser welding of thermoplastic resin plates [1]. A

transparent resin plate is placed on an opaque resin plate and a laser beam is irradiated from the transparent resin side. The irradiated laser beam is transmitted through the transparent resin plate and is absorbed on the bonding plane of the opaque resin plate. Therefore, the opaque resin plate generates heat at the laser-irradiated spot and the temperature at that point is locally raised. The generated heat is transferred to the transparent resin plate by conduction and its temperature is also raised. If the temperatures of the two plates around the laser-irradiated spot exceed the melting point of the material, the two plates are welded at that area. In this welding process, the two parts must be made of the same thermoplastic resin; one of them must be transparent in order to transmit the laser beam and the other must be opaque in order to absorb the laser beam.

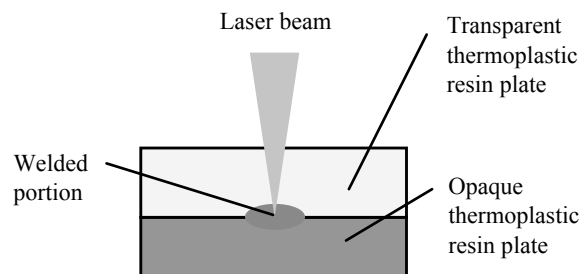
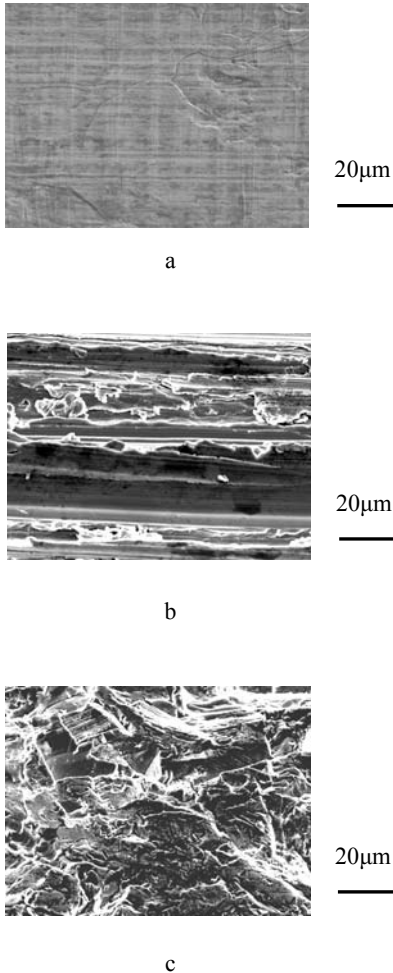


Fig. 1. Principle of laser welding

### 2.2 Laser welding of thermoplastic resin and metal

The authors applied the laser welding process described above to the welding of thermoplastic resin and metal [2,3]. The feature of our method is that the welding surface of metal is pretreated by sandblasting, sandpaper processing or any other machining process. Figure 2 shows a comparison of tin surfaces with and without the treatment. Innumerable microgrooves or microasperities are formed on the metal surface by the treatment. These microgrooves and microasperities increase the laser absorptivity of metal. Therefore, when the transparent thermoplastic resin plate is placed on the pretreated metal plate and a laser beam is irradiated from the transparent resin plate side, the

temperatures of the metal and resin are raised around the laser-irradiated spot as in the case described above. In the case of the welding of resin and metal, however, the temperature at the laser-irradiated point may not exceed the melting point of metal but do so the melting point of resin because the melting point of metal is higher than that of resin. Therefore, melted resin material may flow in the microasperities formed on the metal surface, which means that the microgrooves and microasperities formed by the pretreatment also develop the anchor effect. In this way, the welding of metal and transparent thermoplastic resin can be realized. Figure 3 shows an example where a tin plate and a transparent PMMA plate are welded. The authors also successfully applied this method for welding different kinds of thermoplastic resins. From these results, it can be expected that if the laser absorptivity of transparent resin is increased by forming microasperities, the welding of transparent resins will be realized.



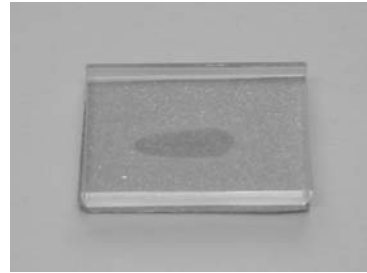
**Fig. 2.** SEM photos of tin surface a. without treatment; b. with sandpaper treatment; c. with sandblast treatment

### 3. Laser welding of transparent resin plates

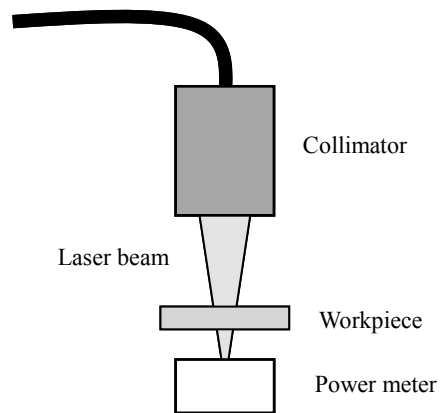
#### 3.1 Measurement of laser absorptivity

When transparent resin is treated by sandblasting, microasperities are formed on the treated surface and the transparency at that area is reduced. In other words, the transparent resin is clouded. This means that the absorptivity and/or reflectivity of the transparent resin are/is increased. Therefore, the absorptivity of the transparent resin is estimated by the following method. First, the laser beam is directly irradiated to a power meter and the actual output power from the laser device is measured. Then, the treated transparent resin plate is placed between the laser device and the power meter as shown in Fig. 4, and the transmittance of the plate is measured. When the nontreated transparent resin plate is used for the measurement of transmittance and the absorptivity of the workpiece is assumed to be zero, the reflectivity on the nontreated workpiece surface can be measured. Then, the absorptivity on the treated workpiece surface can be obtained as follows.

$$absorptivity = 1 - transmittance - reflectivity \quad (1.1)$$



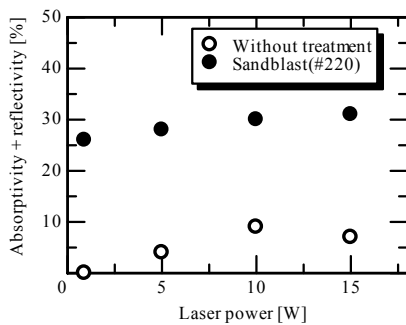
**Fig. 3.** Welding of tin and transparent PMMA



**Fig. 4.** Method of measuring laser absorptivity

**Table 1** Machining conditions of sandblasting

Abrasive grain	SiC
Grain size	#220
Injection pressure	0.6MPa
Working distance	300mm
Processing time	1s

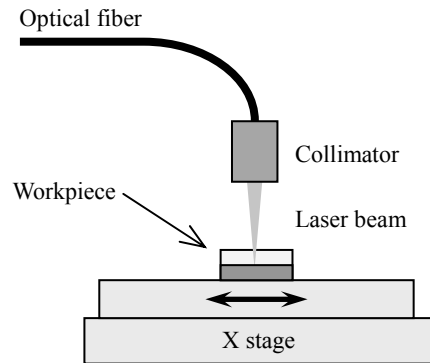
**Fig. 5.** Measured absorptivity

Transparent PMMA 3mm thick is used as the workpiece and one side of its surface is treated by sandblasting. The machining conditions of sandblast treatment are listed in Table 1. A diode laser with a 920nm wavelength is used for laser irradiation. In this experiment, absorptivity may change when resin material melts. Therefore, the diameter of the laser-irradiation spot is set to be sufficiently large in order to avoid workpiece melting.

Figure 5 shows the measured values of the sum of absorptivity and reflectivity. The measured results for the nontreated workpiece may indicate the reflectivity of the workpiece surface. If the reflectivity of the treated workpiece surface is assumed to be equal to that of the nontreated workpiece surface, the absorptivity of the sandblasted transparent PMMA can be obtained as 20 to 25%.

### 3.2 Experimental setup for laser welding

Figure 6 shows the experimental setup for laser welding. A diode laser is used for the experiments. Laser light is transmitted from the laser oscillator to the collimator through an optical fiber and irradiated to the workpiece. The emitted laser beam is focused on the interface of lapped workpieces where the welding surface is located. Welding workpieces are pressed under closely attached conditions using workpiece holding equipment. The equipment is mounted on an X stage in order to scan the laser beam.

**Fig. 6.** Experimental setup**Table 2** Experimental conditions of laser welding

Wavelength	820nm
Maximum output power	15W
Beam mode	TEM00
Spot diameter	1mm
Scanning rate	0.5mm/s
Scanning length	10mm
Number of scanning	1 (One way)
Workpiece holding pressure	1MPa

The experimental conditions are listed in Table 2. A laser diode with a 820nm wavelength and a 15W maximum output power is used for this experiment. Transparent PMMA 3mm thick is used for the workpiece. The welding surface of one of the workpieces is pretreated by sandblasting (#220).

### 3.3 Experimental results

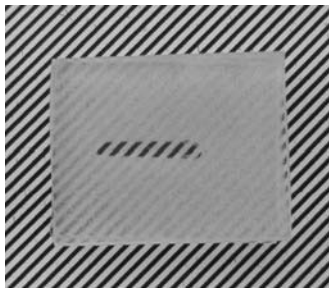
Laser welding of transparent PMMA plates, one of which is pretreated by sandblasting and the other is non-treated is carried out. Experimental results show that the welding can be realized. Figure 7 shows examples of welded workpieces. In the case of Fig. 7(a), a transparent straight line is drawn on a clouded background. In this case, the overall welding surface of one workpiece is sandblasted and then a thin laser beam is scanned linearly. Any graphics and characters can be drawn by beam scanning. It is found that the transparency of the welded region is recovered because microasperities formed by the pretreatment are melted away. Figure 7(b) shows a welded workpiece that is transparent throughout. In this case, the workpiece surface except for

the welding area is masked during sandblast pretreatment. Therefore, microasperities are formed in a portion of the workpiece surface. Since the asperities are melted away during the laser welding process, an entirely transparent welded workpiece can be obtained.

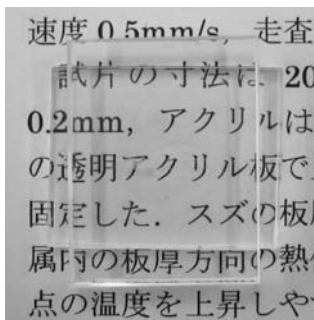
Concerning the laser welding of transparent resin parts, some techniques have been developed [4, 5]. In those methods, a special kind of absorbent, which is transparent for visible wavelengths but not transparent for the wavelength of a diode laser, is used. Fine Device has developed a welding method in which the special absorbent is daubed on a welding surface by solving in organic solvent [4]. BASF has developed a transparent resin in which the special absorbent is kneaded [5]. In contrast, the method proposed in this paper enables us to weld the usual transparent resin without using the special absorbent and organic solvent, which may have advantages in cost, material recycling efficiency and environmental-friendliness.

#### 4. Improvement of transparency of welded workpiece

In the case of Fig. 7(b) where sandblast pretreatment is carried out for a portion of the workpiece surface and the welded workpiece is entirely transparent, there are some cases in which clouded spots are left at the edge of the welded region. If the laser beam is irradiated again to such an area, those clouded spots cannot be melted away. The cause of the defective transparency is thought to be residual interspace on the welded interface. Since the removal process such as sandblasting is used for the pretreatment of the welding surface, material volume must be lacking and therefore interspace should be left at the end point of the welding pass. Figure 8 shows the measured profile of the cross section of the pretreated PMMA plate. In this case, sandblast pretreatment is carried out for a portion of the workpiece surface for 5s. The measured result shows that the depth of the material removal extends to  $10\mu\text{m}$ . The lack of the material volume would lead to residual interspace at the welded interface, which may cause the defective transparency. To improve the transparency of the welded area, following methods of pretreatment are attempted.



a



b

Fig. 7. Examples of laser welding of transparent resin plates a. example 1; b. example 2

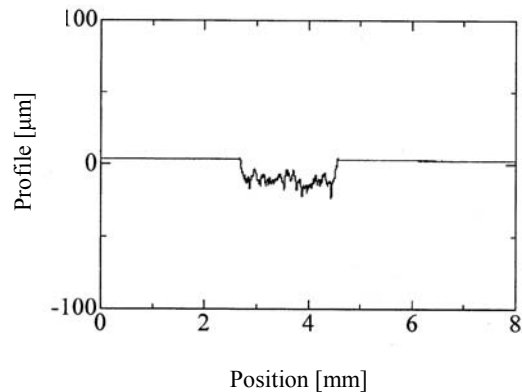


Fig. 8. Profile curve of cross section of PMMA plate pretreated by sandblasting

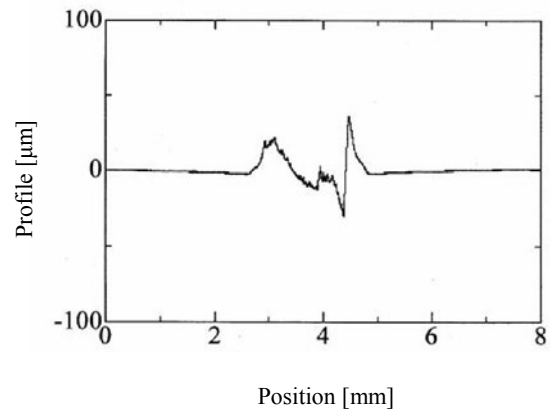


Fig. 9. Profile curve of cross section of PMMA plate pretreated by hot pressing

*(a) Shortening of processing time of sandblast pretreatment*

Considering the fact that the depth of material removal is proportional to processing time, the processing time of the sandblast pretreatment in the case of Fig. 8 seems to be too long. Therefore, processing time is shortened to 1s. Even if this modification decreases the laser absorptivity of the treated surface, it can be recovered by increasing laser power. Although the fact that material is removed by the pretreatment is not essentially changed, experimental results show that clouded spots are not found in the welded workpiece and therefore defective transparency is improved. It is found that this simple solution is useful.

*(b) Hot pressing*

To form microasperities on the surface of transparent PMMA without material removal, pretreatment by hot pressing is attempted. A die, which is textured by sandblasting, is heated and pressed against the transparent PMMA to replicate the surface profile of the die. The temperature of the die is set at nearly the melting point of PMMA and loading pressure is set as very light, such as touching lightly with the hands. An example of the profile of the cross section of the workpiece partially pretreated by hot pressing is shown in Fig. 9. Experimental results show that clouded spots are not found in the welded workpiece and therefore defective transparency is improved. It is also found that hot pressing is useful for the pretreatment of transparent resin parts.

## 5. Conclusions

A new method of laser welding transparent thermoplastic resin plates is developed. The laser absorptivity and transparency of the welded workpiece are experimentally investigated and the following conclusions are obtained.

1. By forming microasperities on the welding surface of transparent resin parts, the absorptivity of a laser

beam is increased and laser welding can be realized.

2. The welded workpiece is transparent because microasperities formed by the pretreatment are melted away by the welding process.
3. The pretreatment method without material removal can be used to avoid defective transparency of the welded workpiece.

## Acknowledgment

The authors would like to express their thanks to Mr. Tomio Motoyama and Mr. Tetsushi Yamada for their contribution to the experiments. This work is funded by the Ministry of Education, Culture, Sports, Science and Technology of Japan (Grant-in-Aid for Scientific Research, Project No. 1576079).

## References

- [1] Tatsuya Hasegawa, Tomohiro Maeda, Shuichi Nakahara, Yuichiro Takai and Takashi Nakamura: Trans. Japan Society of Mechanical Engineers, Vol.67, No.C-661 (2001) pp.3997-3001. (in Japanese)
- [2] Shinya Hayakawa, Ikumi Takashima, Tadashi Miura, Takashi Nakamura, Fumihiro Itoigawa and Tatsuya Hasegawa: Proc. Annual Meeting of Japan Society of Electrical-Machining Engineers, (2003) pp.41-44. (in Japanese)
- [3] Shinya Hayakawa, Tadashi Miura, Takashi Nakamura, Fumihiro Itoigawa and Tatsuya Hasegawa: Proc. Annual Meeting of Japan Society Electrical-Machining Engineers, (2004) pp.53-56. (in Japanese)
- [4] Kenichi Aoki: Handout of Lecture Meeting of The Society of the Plastics Technology, No.1082 (2003) pp.4.1-4.20. (in Japanese)
- [5] Yoshio Otsuka: Handout of Seminar of Technical Information Institute, No.511411 (2005). (in Japanese)

---

# Fabrication of Carbon Nanotube Reinforced Hydroxyapatite Coating on Stainless Steel 316L by Laser Surface Treatment

Chi Tat Kwok, Department of Electromechanical Engineering, University of Macau

Keywords: Biomaterials, Laser surface treatment, Carbon nanotube, Hydroxyapatite, Stainless Steel, Corrosion

## Abstract

Carbon nanotube reinforced hydroxyapatite composite coating (HA/CNT) was fabricated on stainless steel 316L by laser surface alloying (LSA) with a 2.5-kW CW Nd:YAG laser. Metallographical, compositional and phase analysis of the laser-fabricated composite coating were studied by means of scanning electron microscopy (SEM), energy dispersive spectrometry (EDS) and X-ray diffractometry (XRD). In addition, the corrosion behavior of the composite coating was investigated by means of potentiodynamic polarization technique and electrochemical impedance spectroscopy. A strong metallurgical bond was formed between the substrate and the coating which was presence of microcracks. The existence of CNT in laser fabricated layer was confirmed by XRD analysis. In addition, the data of electrochemical corrosion studies illustrated the HA/CNT composite coating possessed outstanding corrosion properties compared with the 316L substrate.

## 1 Introduction

Austenitic stainless steel 316L is often used in orthopedic surgery and dentistry due to its good corrosion resistance, high mechanical strength and relative cheap price. However, it is not suitable for bone binding because of its inertness. Hydroxyapatite (HA) is a biocompatible calcium phosphate ceramic which resembles the mineral constituents of human bones and teeth. However, sintered HA is not suitable for biomedical applications especially under load-bearing conditions because it is too brittle and weak. Because of its simplicity and versatility, plasma spraying is currently the only commercial process for fabricating HA coating on metallic implants. Nevertheless, long-term stability of the plasma sprayed coatings is an exigent problem because of their high degree of porosities, poor bond strength, non-stoichiometric composition and amorphous structure [1-4]. Recently, the bioceramic or composite coatings of hydroxyapatite have been successfully fabricated on stainless steel 316L [5], pure titanium [6] and Ti-6Al-4V [7] by mean of laser surface treatment. In addition, coating of HA reinforced with carbon nanotubes (CNT) on Ti-6Al-4V by LSA was reported to be a viable route for forming a tailor-made surface composite due to the excellent mechanical

properties and chemical stability of CNT [8]. However, the major drawbacks of using titanium and its alloys as the substrate are too expensive and large difference in thermal expansivity compared with HA. Moreover, the corrosion properties of the laser-fabricated HA coating on the substrate alloy are merely reported. The aims of present study are to study the feasibility of fabricating HA/CNT coating on the 316L substrate with a 2.5-kW CW Nd:YAG laser for enhancing its corrosion resistance.

## 2 Experimental details

The as-received austenitic stainless steel AISI 316L (designed as AR-316) was in form of rectangular bar. Its nominal composition in wt% is: Fe-17.6Cr-11.2Ni-2.5Mo-1.4Mn-0.4Si-0.03C. The bar was cut into the specimens with dimensions of 20 mm x 20 mm x 12 mm and the surface was mechanically ground with 80 grits silicon carbide paper. Reagent grade hydroxyapatite [HA,  $\text{Ca}_{10}(\text{PO})_4(\text{OH})_2$ ] powder with average particle size ranging from 30 to 50  $\mu\text{m}$  and commercially available multiwalled carbon nanotubes (CNT) with diameter from 20 to 40 nm and length from 5 to 15  $\mu\text{m}$  in the ratio of 80 wt% and 20 wt% respectively were mixed with the polyvinyl alcohol (PVA) for forming a paste. The paste was preplaced on the surface the 316L specimens and followed by drying. The thickness of pre-deposited HA/CNT layer was about 0.1 mm. Subsequent laser melting of the pre-deposited layer was carried out using a 2.5-kW CW Nd:YAG laser (Lumonics MW2000). A defocused spot of 4-mm diameter scanning at a speed of 15 mm/s with laser power of 1 kW at the specimen was used for achieving surface melting. Argon flowing at 15 l/min was used as shielding gas. The melt surface was achieved by overlapping of successive melt tracks at 50% track width interval.

After laser surface treatment, the specimens were etched with acidic ferric chloride solution (25 g  $\text{FeCl}_3$ , 25 ml HCl and 100 ml  $\text{H}_2\text{O}$ ) for investigating the microstructure by optical microscopy and scanning electron microscopy (SEM, JEOL JSM-6335F). The average chemical compositions of the specimen were taken from various locations by energy dispersive spectrometry (EDS, JEOL EX-64125JMU). The phases existed in specimen were analyzed by X-ray diffractometry (XRD, Philips PW3710). The radiation source used in XRD was Cu  $K\alpha$  with nickel filter and generated at

40 kV and 35 mA. The longer Cu  $K_{\alpha}$  wavelength (0.15406 nm) was used so that only a thin layer of about 10  $\mu\text{m}$  was diffracting (i.e. shallow penetration). The scanning range was  $20^{\circ} \leq 2\theta \leq 80^{\circ}$  and the scan rate was 1.5  $^{\circ}/\text{min}$ .

Prior to the corrosion tests, the surface of the specimen was cleaned, degreased and dried. To investigate their electrochemical corrosion behavior, the laser-fabricated specimens were embedded in cold-curing epoxy resin, exposing a surface area of 1  $\text{cm}^2$ . Open-circuit potential (OCP) measurement and potentiodynamic polarization scans for the specimens were conducted in 0.9 wt% NaCl solution at  $37 \pm 1$   $^{\circ}\text{C}$  (open to air) using a potentiostat (PAR VersaStatII) according to ASTM Standard G61-94 [9]. All potentials were measured with respect to a saturated calomel electrode (SCE, 0.244V versus SHE at 25  $^{\circ}\text{C}$ ) as the reference electrode. Two parallel graphite rods served as the counter electrode for current measurement. Potential scans started after the 4-hour OCP measurement for allowing the specimen to reach a steady state. Then the potential was increased at a rate of 0.1667  $\text{mV s}^{-1}$ , starting from 200 mV below the OCP.

The measurement of electrochemical impedance spectroscopy (EIS) was performed at the OCP. A sine wave of 10 mV (rms) was applied at the OCP of the system. The spectra were obtained in a  $10^{-2}$  to  $10^5$  Hz frequency range by an EIS system (VoltaLab 10, PGZ100). Impedance spectra were represented in both Nyquist plot and Bode plot. In the Nyquist plot, the imaginary component of the impedance ( $Z_i$ ) is plotted as a function of the real component ( $Z_r$ ), whereas the Bode plot represent the logarithm of the total impedance  $|Z|$  as a function of the logarithm of applied frequency  $f$ .

### 3 Results and Discussion

#### 3.1 Microstructural and metallographic analysis

The cross-sectional appearance of laser-alloyed specimen (designated as HA/CNT-316) is shown in Fig. 1. The thickness of laser-alloyed layer is about 100  $\mu\text{m}$ . The alloyed layer (AL) and the heat affected zone (HAZ) are observed at higher magnification as shown in Fig. 2. The surface of the specimen is free of porosities but microcracks are observed [Fig 2(c)]. The HA/CNT composite coating was strongly bonded to the 316L substrate by metallurgical bond after laser surface treatment. In the AL, the minute needle-like and granular structures with diameters range from 1 to 5  $\mu\text{m}$  are observed. By EDS analysis, the atomic ratio of Ca and P in the AL were found to be 64.6% and 16.2% respectively. The Ca/P ratio is 3.99 and greatly deviates from the normal Ca/P ratio of HA (1.68). The HAZ with thickness of approximately 80  $\mu\text{m}$  is observed beneath the AL. A few of tiny HA/CNT particles are entrapped in the dendritic austenite ( $\gamma\text{-Fe}$ ).

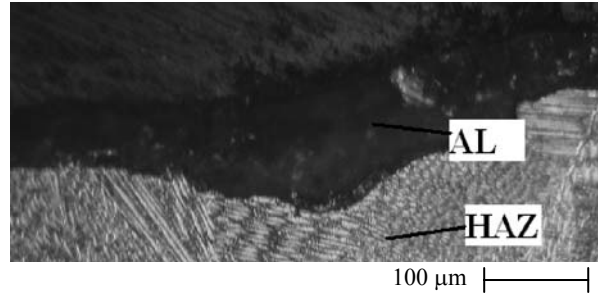


Fig. 1. Cross-sectional view of HA/CNT-316

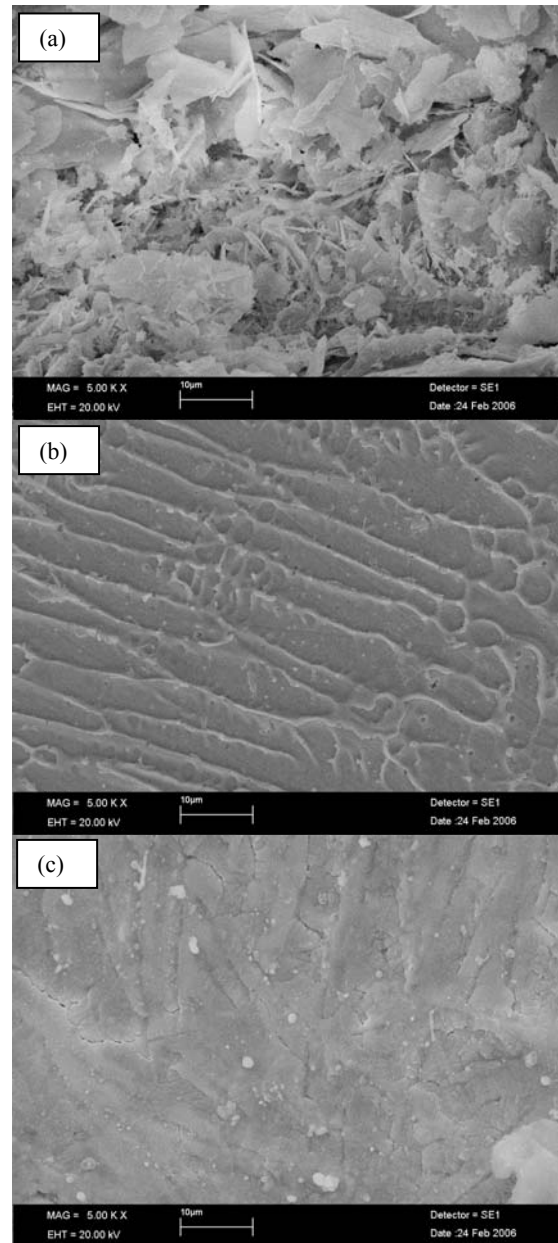


Fig. 2. SEM micrographs showing the microstructure of HA/CNT-316: (a) AL, (b) HAZ and (c) surface of AL at higher magnification

The XRD spectra of the HA and CNT powder, and the laser-alloyed specimen HA/CNT-316 are shown in Fig. 3. Fig. 3(c) shows that HA/CNT-316 possesses higher crystallinity than the plasma sprayed HA coating [10]. In the AL, the peaks of HA and CNT were detected in the XRD spectrum of HA/CNT-316. This shows that the HA coating is reinforced with CNT by laser surface treatment. Chen et al reported that no CNT peaks were found by XRD in the laser-alloyed coating of HA/CNT on Ti-6Al-4V but the existence of residual CNT was confirmed by TEM examination [8]. It is well known that CNT possesses excellent mechanical properties and chemical stability. HA reinforced with CNT is the excellent coating as the high-loading-bearing implants [6]. The diffraction peaks of austenite were also detected in the AL indicating that the 316L substrate has been diluted into the AL. The high temperature involved in laser surface treatment could result in decomposition of HA so calcium phosphate was also detected.

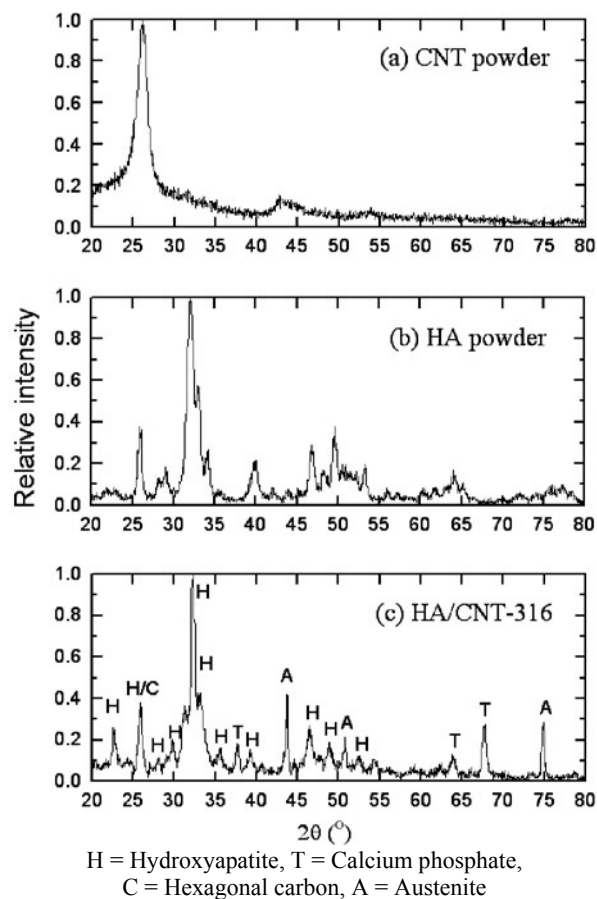


Fig. 3. XRD spectra for (a) CNT powder, (b) HA powder and (c) HA/CNT-316

The EDS spectrum of the surface of HA/CNT-316 is shown in Fig. 4, which indicates its elemental composition. Intense peaks for Ca and P were obtained. Small peaks corresponding to Fe, Cr, Ni present in the specimen were also detected. The presence of intense peaks for Ca and P suggests HA is the major constitute in HA/CNT-316.

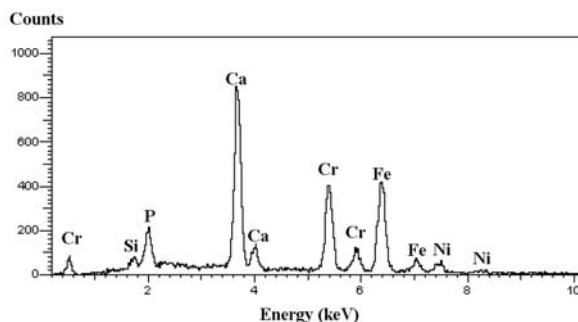


Fig. 4. EDS spectrum of HA/CNT-316

### 3.2 Open circuit potential-time measurement

The plot of OCP against time of the specimens AR-316 and HA/CNT-316 in 0.9% NaCl solution (open to air) at 37 °C is shown in Fig. 4. After four hours, their OCP become steady and are summarized in Table 1. Compared to AR-316, the OCP of HA/CNT-316 shifted towards noble direction and reached a potential of -150 mV (increased by 110 mV). Similar behavior where the OCP of 316L increases after coated with HA has been reported by Eliaz et al [11]. The present results show that thermodynamic stability of the HA/CNT-316 in 0.9% NaCl solution at 37 °C. According to the result of EDS analysis, although some metallic elements have been introduced in the AL, the noble corrosion behavior of HA/CNT-316 is attributed to the laser-alloyed coating with good insulating property.

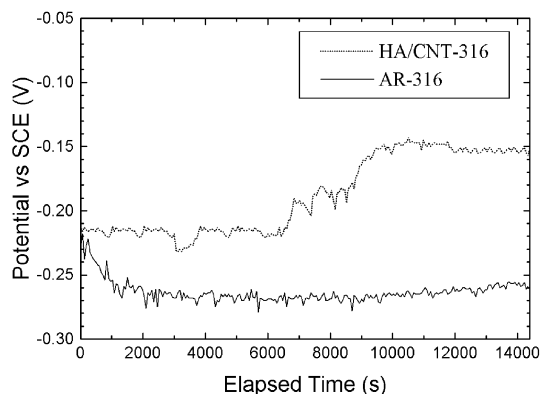


Fig. 4. Plot of OCP vs time of AR-316 and HA/CNT-316 in 0.9% NaCl at 37 °C

### 3.3 Polarization study

Potentiodynamic polarization curves of AR-316 and HA/CNT-316 are shown in Fig. 5 and the corrosion parameters are summarized in Table 1. The laser-alloyed specimen HA/CNT-316 exhibited better values for all the corrosion parameters. The corrosion current densities ( $I_{corr}$ ) of the specimens were determined from the curves using Tafel extrapolation method. The  $I_{corr}$  of AR-316 and



HA/CNT-316 were 78 and 25 nA/cm<sup>2</sup> respectively. Similar results (in the order of magnitude of nA/cm<sup>2</sup>) have been reported for the uncoated and coated 316L with HA by plasma spraying [12]. The specimen AR-316 showed pitting corrosion after polarization test (Fig. 5). On the contrary, HA/CNT-316 possessed very high pitting resistance as reflected by a wide passive range and lower  $I_{corr}$  compared with those of AR-316. No pitting corrosion occurred in HA/CNT-316 up to 3.8 V. By metallographic examination, no evident pit was observed on the surface of HA/CNT-316 after polarization test. In addition, the overall current density of HA/CNT-316 is lower than that of AR-316. This indicates that the AL can act as a good barrier in arresting pit growth. The improved corrosion resistance can be attributed to the fact that the HA/CNT composite coating has high passivity although some metallic elements has been diffused into it during high temperature melting by laser irradiation.

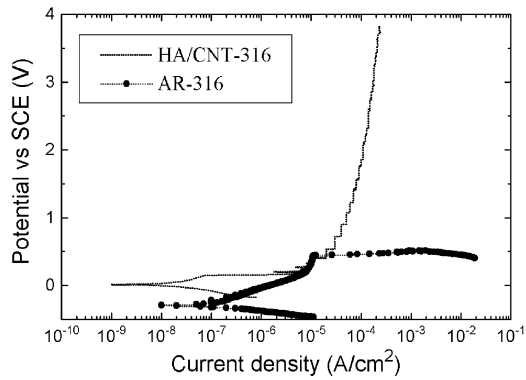


Fig. 5. Potentiodynamic polarization curves of AR-316 and HA/CNT-316 in 0.9% NaCl solution at 37 °C

Table 1. Corrosion parameters of various specimens

Specimen no.	OCP (mV)	E <sub>pit</sub> (mV)	I <sub>corr</sub> (nA/cm <sup>2</sup> )
AR-316	-260	430	78
HA/CNT-316	-150	No pitting	25

### 3.4 Electrochemical impedance spectra

The impedance spectra of AR-316 and HA/CNT-316 obtained at OCP after immersed in 0.9% NaCl solution for 2 hours are presented in the Nyquist and Bode plots (Fig. 6). Although the Nyquist plot of AR-316 and HA/CNT-316 demonstrate insignificant feature, the Bode plot shows that the total impedance  $|Z|$  has increased for HA/CNT-316. The thin passive oxide film on the surface of AR-316 became less protective in the presence of chloride ions at 37 °C. For HA/CNT-316, the increase in  $|Z|$  at high frequency indicated the enhanced passivity as good protective coating. These results were complimentary to those obtained by OCP-time measurement and polarization study.

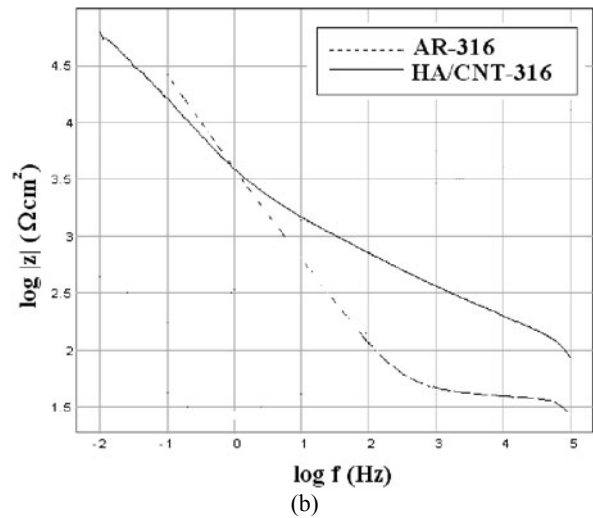
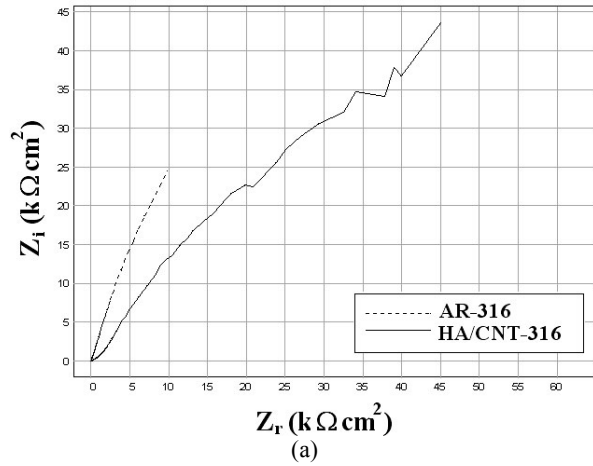


Fig. 6. (a) Nyquist plot and (b) Bode plot measured at various intervals for AR-316 and HA/CNT-316 in 0.9% NaCl solution at 37 °C

## 4 Conclusions

The carbon nanotube reinforced hydroxyapatite composite coating (HA/CNT) was successfully fabricated on the stainless steel 316L by laser surface treatment. A strong metallurgical bond was formed between the substrate and the coating with microcracks. The existence of CNT in laser-alloyed layer was detected by XRD. Compared to the as-received 316L, the pitting corrosion resistance of the HA/CNT composite coating on 316L was significantly improved, as evidenced by noble shift of open circuit potential, a wide passive range, low corrosion current density and high total impedance.

## 5 Acknowledgements

The authors wish to acknowledge the support from the infrastructure of the University of Macau.

## 6 References

- [1] Lacefield WR (1993), An Introduction to Bioceramics. 2<sup>nd</sup> ed., Plenum Press, NY, Ch5:79-115.
- [2] Chen J, Wolke JGC, de Groot H, (1994) Microstructure and crystallinity in hydroxyapatite coatings. *Biomaterials* 15:396-399.
- [3] Kay JF, (1992) Calcium phosphate coatings for dental implants. *Dent Clin North Am* 36:1-18.
- [4] Zeng HT, Lacefield WR, (2000) XPS, EDX and FTIR analysis of pulsed laser deposited calcium phosphate bioceramic coatings: effect of various process parameters. *Biomaterials* 21:23-30.
- [5] Wang YC, Li YM, Yu HL, Ding JJ, Tang XH, Li JG, Z YH, (2005) In situ fabrication of bioceramic composite coatings by laser cladding. *Surface & Coatings Technology* 200:2080-2084.
- [6] Cheng GJ, Pirzada D, Cai M, Mohanty P, Bandyopadhyay A (2005), Bioceramic coating of hydroxyapatite in titanium substrate with Nd-YAG laser. *Materials Science and Engineering C* 25:541-547.
- [7] Lusquinos F, Pou J, Arias JL, Boutinguiza, Leon B, Perez-amor M (2002), *Journal of Materials Science: Materials in Medicine* 13:601-605.
- [8] Chen Y, Zhang YQ, Zhang TH, Gan CH, Zheng CY, Yu G (2006), Carbon nanotube reinforced hydroxyapatite composite coatings produced through laser surface alloying. *Carbon* 44:37-45.
- [9] ASTM Standard G61-86 (2003) Standard Method for Conducting Cyclic Potentiodynamic Polarisation Measurements for Localised Corrosion Susceptibility of Iron-, Nickel-, or Cobalt-Based Alloys, in Annual Book of ASTM Standards, Vol. 03.02, ASTM, Philadelphia.
- [10] Ding SJ, Huang TH, Kao CT (2003), *Surface & Coatings Technology*, 165: 248-257.
- [11] Eliaz N, Sridhar TM, Mudali UK, Raj B (2005), Electrochemical and electrophoretic deposition of hydroxyapatite for orthopaedic applications. *Surface Engineering*, 21:238-242.
- [12] Fathi MH, Salehi M, Saatchi A, Mortazavi V, Moosavi SB (2003) In vitro corrosion behavior of bioceramic, metallic, and bioceramic-metallic coated stainless steel dental implants. *Dental Materials* 19:188-198.

---

## Novel Abrasive-free Planarization of Si and SiC using Catalyst

Hideyuki Hara<sup>1</sup>, Yasuhisa Sano<sup>1</sup>, Hidekazu Mimura<sup>1</sup>, Kenta Arima<sup>1</sup>, Akihisa Kubota<sup>2</sup>, Keita Yagi<sup>1</sup>, Junji Murata<sup>1</sup> and Kazuto Yamauchi<sup>1</sup>

<sup>1</sup>Osaka University, <sup>2</sup>Kumamoto University,

Keywords: Silicon Carbide, Polishing, Etching, Catalyst, Hydrofluoric Acid and Platinum

### Abstract

We propose a new chemical planarization method using a catalyst as a polishing plate. A sample is placed on the polishing plate in a solution that is a source of reactive species. Since the catalyst generates reactive species that activate only next to the catalyst surface, this method can efficiently planarize. This processed surface is not damaged by chemical removal. We named this method CAtalyst-Referred Etching (CARE). CARE was applied to SiC planarization. The processed surfaces were observed by atomic force microscopy and optical interferometry. These observations presented a marked reduction in surface roughness.

### 1 Introduction

The planarization of metals and semiconductors is important for the fabrication of electronic devices. Single-crystal silicon (Si) wafers must satisfy stringent requirements for flatness, surface integrity and contamination control. The sequence of producing wafers from a Si ingot consists of slicing, lapping, wet-chemical etching, rough polishing, final polishing such as chemical mechanical polishing (CMP), and cleaning. Such steps for Si wafers are well established. Other materials, for example, silicon carbide (SiC), gallium nitride (GaN) and diamond have some difficulties in planarization. The preparation of well-ordered SiC to realize high-performance electronic power devices is difficult because of SiC's mechanical hardness and chemical inertness.

Current SiC preparation methods are mechanical polishing using a diamond abrasive with a hard lapping plate,<sup>1,2</sup> CMP<sup>3-5</sup>, and hydrogen etching at high temperature.<sup>6,7</sup> Although the mechanical polishing can flatten wafer surfaces, it causes crystallographic damage. CMP reduces surface damage but cannot remove it completely. In addition, waviness increases during the processing because elastically soft pads are employed in CMP. Hydrogen etching is an indispensable pretreatment method for epitaxial layer growth for removing crystallographic damage and contamination on

substrates. However, its removal rate is low and a large electrical energy is required to produce a high temperature.

In this study, we show that Si and SiC are planarized using a new abrasive-free planarization method that we have proposed. We named this method CAtalyst-Referred Etching (CARE).<sup>8</sup> As mentioned above, Si and SiC planarization processes require many sequences for electrical devices. Although the surfaces are required to have good flatness, low microroughness and low crystallographic damage, no methods can simultaneously fulfill these requirements. Wafer flattening methods such as lapping involve a strong abrasion between a wavy wafer and a flat polishing plate for the preferential removal of the topmost wafer surface in contact with the flat polishing surface. This abrasive method deforms the surface crystalline structure owing to the mechanical removal that deteriorates microroughness. In contrast, chemical etching removes wafer surfaces without causing surface damage but cannot efficiently improve flatness because the wafer surface is randomly etched without reference to a flat surface. CMP has both the features of chemical removal and mechanical removal. Microroughness is reduced by the wafer surface removal depending on the shape of the powder particles used because the removal mechanism is a reaction between the powder particles and the wafer surface. However, wafer waviness increases owing to the use of elastically soft pads in CMP.

We consider that the most efficient planarization would chemically remove and simultaneously realize a flat surface, and this can be achieved using a catalyst as a polishing plate. If the catalyst generates reactive species that are activated on the catalyst surface, the wafer is chemically removed in the areas in contact with the reactive flat catalyst. In this regard, it is important that the reactive species are activated only next to the catalyst surface and deactivated when they move away from the catalyst surface. If the reactive species are activated away from the catalyst surface, the removal is without reference to the flat catalyst surface, and will be the same as conventional chemical etchings.

## 2 Concept of CARE

### 2.1 Selection of catalysts and reactive species

For the fulfillment of CARE, a catalyst and reactive species appropriate to a processed material are selected. We considered F and OH radicals as reactive species for the removal of Si and SiC because these species chemically remove Si and SiC in aqueous solutions<sup>9, 10</sup> and plasma<sup>11</sup>.

We performed an initial experiment in which a Pt wire was used as the catalyst and moved relative to and in contact with SiC in hydrogen fluoride (HF) solution. The results show that hard SiC can be removed. The reason for using Pt and HF is as follows: Pt has catalytic properties, such as the ability to dissociate various molecules<sup>12</sup>, and the interaction between Pt surfaces and hydrogen fluoride molecules in an aqueous solution can generate F and OH by self-dissociation.

To investigate the role of Pt and HF in the process, we carried out some etching experiments on a SiC surface using different combinations of a pad and an etchant with the same contact pressure as that of the Pt pad. The results show that SiC can be removed with a the combination of Pt and HF (Table.1). There was no removal of SiC using a polycarbonate pad instead of a Pt pad which clearly indicates that the removal mechanism is not based only on mechanochemical phenomena but that the catalytic nature of Pt also plays a critical role.

**Table 1.** Assessment of removal rate with various combinations

Material	Catalyst	Etchant	Removal rate ( $\mu\text{m}/\text{h}$ )
SiC	Pt	Hydrofluoric acid	0.1-0.2
SiC	Pt	Water	< 0.001
SiC	Polycarbonate	Hydrofluoric acid	< 0.001
Si	Pt	Hydrofluoric acid	1.0-1.5

### 2.2 Setup

CARE setup has a catalytic polishing pad made of Pt placed on a rotational table. Wafers are fixed on the sample stage using wax and are placed on the pad with a controlled pressure of 0.02 MPa, which is noticeably lower than that in conventional CMP. The polishing pad and sample are immersed in 2 mol/l hydrofluoric acid. The rotation speeds of the sample stage and pad were fixed at 20 rpm and 19 rpm, respectively. The removal rates of Si and SiC are 1.0-1.5  $\mu\text{m}/\text{h}$  and 0.1-0.2  $\mu\text{m}/\text{h}$ , respectively, under such conditions. The SiC wafers (4H n-type) are lapped to expose the (0001) Si plane on-axis and have resistivities and micropipe densities of 0.02-0.03  $\Omega\text{cm}$  and 50-100  $\text{cm}^{-2}$ , respectively.

Firstly the processed surfaces were observed by Nomarski differential interference contrast (NDIC) microscopy. Then, the surface qualities were evaluated by optical interferometry (ZYGO Corp., NewView 200 CHR), atomic force microscopy (AFM, SII Nanotechnology, Inc., SPA400+SPI3800N) and low-energy electron diffraction (LEED) analysis.

## 3 SiC-processed surfaces

### 3.1 Surface damage removal

The NDIC images in Fig. 1. show that microcracks on the SiC surfaces were reduced progressively by CARE. Many of the micro cracks observed on the surfaces shown in Fig.1. (a) were introduced during lapping, which generates and accumulates scratches and cracks on the surface. After CARE with a removal depth of 1  $\mu\text{m}$ , some micro-cracks were not removed, for example the micro crack marked by the arrow in Fig.1. (b) corresponds to the deep micro crack marked by the arrow in Fig.1. (a). As removal increased, such micro cracks were completely removed (Fig.1. (c)). The results show that CARE preferentially removes the topmost wafer surface in contact with the pad surface, and that the frictional force between the pad and SiC surfaces was sufficiently small to not introduce mechanical scratches or cracks.

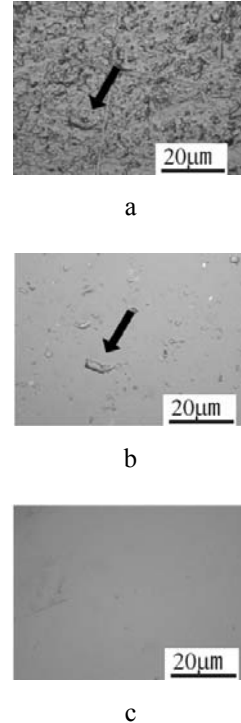


**Fig.1.** NDIC  $60 \mu\text{m} \times 80 \mu\text{m}$  images of a 4H-SiC wafer: (a) as-lapped surface, (b) CARE-processed surface with removal depth of 1  $\mu\text{m}$ , and (c) with

removal depth of 2  $\mu\text{m}$ . Many cracks were markedly reduced by CARE.

### 3.2 Comparisons between CMP and CARE

#### 3.2.1 Optical interferometry

A CARE-processed surface with a removal depth of 3  $\mu\text{m}$  from the lapped surface and a surface of commercially obtainable SiC wafer prepared by conventional CMP were observed by optical interferometry (Fig.2.). The maximum height of the surface irregularity (P-V) and root-mean-square roughness (RMS) of the CARE-processed surface were evaluated to be 1.236 nm and 0.142 nm, respectively. The roughness of the CARE-processed surface is markedly lower than that of the CMP surface, which suggests that CARE has a higher potential as a planarization method than conventional CMP.

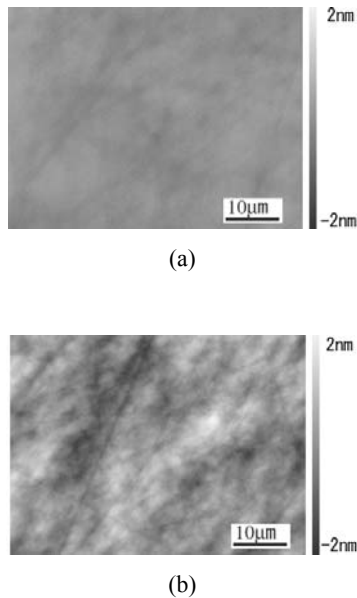


**Fig. 2.** Optical interferometry images of a 4H-SiC wafer: (a) CARE-processed surface with removal depth of 3  $\mu\text{m}$ ; RMS: 0.142 nm [P-V: 1.236 nm, Ra: 0.114 nm] and (b) as-received (after CMP) surface; RMS: 0.548 nm [P-V: 3.856 nm, Ra: 0.436 nm].

#### 3.2.2 AFM

The surface morphology of the processed surface was measured by AFM (Fig.3.) in a  $500\text{nm} \times 500\text{nm}$  area. A step terrace with a step height of approximately 3  $\text{\AA}$ , corresponding to the thickness of a single bilayer of Si and C structures was observed on the CARE-processed surface. Such a surface structure strongly indicates that the removal

mechanism is based on chemical phenomena, and that a type of step-flow removal occurs on the (0001) Si surface of SiC.

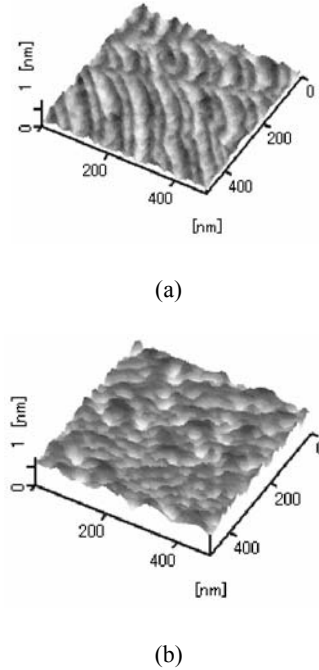
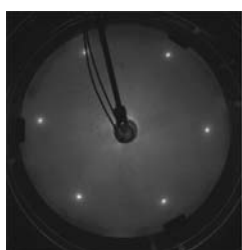


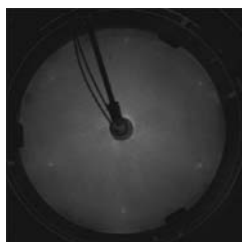
**Fig. 3.** AFM images of a 4H-SiC wafer: (a) CARE-processed surface with removal depth of 3  $\mu\text{m}$ ; RMS: 0.093 nm [P-V: 0.724 nm, Ra: 0.076 nm] and (b) as-received surface; RMS: 0.174 nm [P-V: 1.761 nm, Ra: 0.131 nm]. A step-terrace structure was observed on CARE-processed surface.

#### 3.2.3 Damage estimation

To estimate the crystallographic properties of the CARE-processed surface, CARE-processed and CMP-processed surfaces were observed by LEED analysis with a probe beam energy of 65eV corresponding to an estimated thickness of 0.4nm (Fig.4.). LEED analysis is used for the estimation of crystal structures in a surface. When an electron beam penetrates a well-ordered crystalline structure in a surface, a sharp diffraction spot is observed on a detection screen. The estimated thickness is determined by electron penetration depth. Sharp LEED spots were observed from the CARE-processed surface (Fig.4.(a)) compared with the CMP surface, in which only diaphanous and blurry spots were observed under such low-energy probe beam conditions (Fig.4.(b)). The results show that the removal mechanism of CARE is not mechanical but chemical because the crystalline structure of the CARE-processed surface is well-ordered.



(a)



(b)

**Fig. 4.** Photographs of LEED spot with probe beam energy of 65 eV corresponding to estimation thickness of 0.4nm: (a) CARE-processed surface with removal depth of 3  $\mu\text{m}$  and (b) as-received (after CMP) surface. Sharp LEED spots, which show a crystallographically well-ordered surface, are observed in the CARE-processed surface.

## 4 Summary

We proposed a new abrasive-free planarization method for Si and SiC wafers that is called CAtalyst-Referred Etching (CARE). CARE planarization uses a Pt polishing pad as a catalyst that activates hydrofluoric acid to generate reactive species and removes SiC chemically. Optical interferometry and atomic force microscopy images showed a marked reduction in surface roughness compared with that possible with CMP. Furthermore, LEED analysis showed that a crystallographically well-ordered surface was realized. The results show that CARE is a more efficient planarization process than CMP.

## 5 Acknowledgements

This research was partially supported by a grant for the 21st Century COE Program, "Center for Atomistic Fabrication Technology", from the Ministry of Education, Culture, Sports, Science and Technology of Japan and Industrial Technology Research Grant Program in 2005 from New Energy and Industrial Technology Development Organization (NEDO) of Japan.

## 6 References

- [1] W. Qian, M. Skowronski, G. Augustine, R. C. Glass, H. McD. Hobgood, and R. H. Hopkins, (1995) Characterization of polishing-related surface damage in (0001) silicon carbide substrates. *Journal of the Electrochemical Society* 142:4290-4294.
- [2] J. A. Powell and D. J. Larkin, (1997) Process-induced morphological defects in epitaxial CVD silicon carbide. *Physica Status Solidi B-basic Reserch* 202:529-548.
- [3] L. Zhou, V. Audurier, P. Pirouz, and J. A. Powell, (1997) Chemomechanical Polishing of Silicon Carbide. *Journal of the Electrochemical Society* 144:L161-L163.
- [4] M. Kikuchi, Y. Takahashi, T. Suga, S. Suzuki, and Y. Bando, (1992) Mechanochemical Polishing of Silicon-Carbide Single-crystal with chromium(III) Oxide Abrasive. *Journal of American Ceramic Society* 75:189-194.
- [5] C. Li, I. B. Bhat, R. Wang, and J. Seiler, (2004) Electro-chemical mechanical polishing of silicon carbide. *Journal of Electronic Materials* 33:481-486.
- [6] F. Owman, C. Hallin, P. Martensson, and E. Janzen, (1996) Removal of polishing-induced damage from 6H-SiC(0001) substrates by hydrogen etching. *Journal of Crystal Growth* 167:391-395.
- [7] C. Hallen, F. Owman, P. Martensson, A. Ellison, A. Konstantinov, O. Kordina, and E. Janzen, (1997) In situ substrate preparation for high-quality SiC chemical vapour deposition. *Journal of Crystal Growth* 181:241-253.
- [8] H. Hara, Y. Sano, H. Mimura, K. Arima, A. Kubota, K. Yagi, J. Murata and K. Yamauchi, (2006) Novel abrasive-free planarization of 4H-SiC(0001) using catalyst. *Journal of Electronic Materials* accepted.
- [9] A. Kubota, H. Mimura, K. Inagaki, K. Arima, Y. Mori, and K. Yamauchi, (2005) Preparation of Ultrasmooth and Defect-Free 4H-SiC(0001) Surfaces by Elastic Emission Machining. *Journal of Electronic Materials* 34:439-443.
- [10] Y. Ichii, Y. Mori, K. Hirose, K. Endo, K. Yamauchi and H. Goto, (2005) Electrochemical etching using surface carboxylated graphite electrodes in ultrapure water. *Electrochimica Acta*, 50:5379-5383.
- [11] Y. Mori, K. Yamauchi, K. Yamamura, and Y. Sano, (2000) Development of plasma chemical vaporization machining. *Review of Scientific Instruments*, 71:4627-4632.
- [12] F.T. Wagner and P.N. Ross, Jr. (1988) Long-range structural effects in the anomalous voltammetry on ultra-high vacuum prepared Pt (111). *Journal of Electroanalytical Chemistry* 250:301-320.

---

## Polishing of Single Crystal SiC with the LHA Pad

Makoto Sato<sup>1</sup>, Kazuhiro Okuda<sup>1</sup>  
<sup>1</sup>Noritake co., limited

Keywords: Single-crystal SiC, Polishing, Polishing pad, LHA pad, Abrasive grain, pH, ORP.

### Abstract

Conventionally, the final polishing of single-crystal silicon carbide has been performed by loose abrasive grain polishing. However, its removal rate was low and it required a very long time. In this study, an advanced-type Loosely Held Abrasive (LHA) pad for polishing was examined; this pad comprised abrasive grains, and water or a polishing lubricant containing an additive agent was supplied in order to improve the polishing process. Consequently, it was clarified that by adjusting the amount of supply of water or the polishing lubricant containing the additive agent, a high removal rate could be attained during free abrasive grain polishing.

### 1 Introduction

Single-crystal silicon carbide (single-crystal SiC) is in considerable demand as a support substrate of GaN-LED. Since it has an excellent electrical property, its application to high frequency devices, power devices, etc. is expected in the future. However, it is very difficult to process single-crystal SiC. In particular, the processing efficiency for polishing is low.

The fixed abrasive polishing pad has attracted attention as a scouring pad for realizing global planarization and low waste. However, since it is difficult to reconcile a high removal rate and scratch-free polishing by using conventional fixed abrasive pads, fixed abrasive polishing methods have been attempted.[1][2] We are shown that it is effective in the loosely held abrasive (LHA) structure raising a polishing performance in polishing of a silicon wafer and an oxidation film wafer.[3][4][5] An LHA structure is carrying out intension of the grain into a polishing pad.

In this study, a polishing pad with an LHA structure (LHA pad) that is used for polishing of single-crystal SiC is reported; this pad improves the polishing performance; further, the influence of pH and oxidation reduction potential (ORP) of the polishing lubricant supplied to the LHA pad on the polishing performance is investigated.

## 2 Experimental

### 2.1 Polishing pad preparation

The LHA pad was prepared by mixing silica beads with an average particle diameter of 250 nm and poly-ether sulphone (PES) resin in N,N-dimethylformamide (DMF) solvent. The mixture was poured into a mold in order to evaporate the DMF solvent. A 500 × 500 × 2 mm sheet was created and cut to the required size. **Fig. 1** shows a section of the polishing pad. **Table 1** shows the compositions of the polishing pad.

**Table 1.** Component of polishing pad

Polishing pad	Silica abrasive grain	Matrix resin
LHA pad	26 vol %	28 vol %

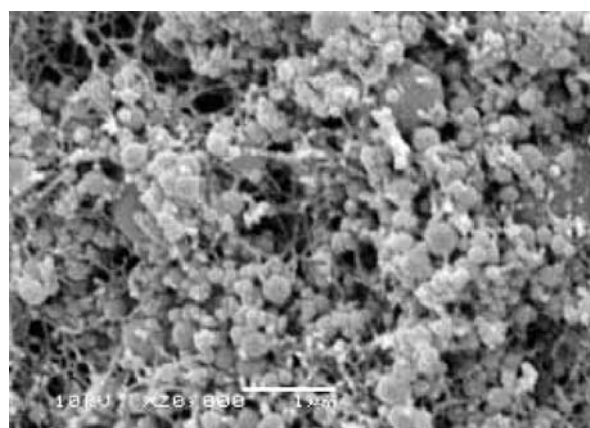


**Fig. 1.** SEM micrographs of the LHA pad cross section

## 2.2 Polishing experiments

The polishing performance was examined and evaluated by using an equipment shown in Fig. 2. The polishing experiment was conducted to investigate the polishing performance (removal rate and surface roughness) of the single-crystal SiC. The details of the polishing pad used in conjunction with a polishing fluid (slurry or lubricant) are shown in Table 2. The polishing conditions are outlined in

**Table 2.** Polishing pad and fluid

Experimental number	Polishing pad	Polishing fluid
1	IC1000	Water + silica (250nm) 12.5w%
2	IC1000	HCl (0.1mol/l) + silica (250nm) 12.5w%
3	IC1000	KOH (0.1mol/l) + silica (250nm) 12.5w%
4	IC1000	KMnO <sub>4</sub> (0.1mol/l) + silica (250nm) 12.5w%
5	IC1000	KMnO <sub>4</sub> (0.1mol/l) + HCl (0.1mol/l) + silica (250nm) 12.5w%
6	IC1000	KMnO <sub>4</sub> (0.1mol/l) + KOH (0.1mol/l) + silica (250nm) 12.5w%
7	IC1000	K <sub>2</sub> S <sub>2</sub> O <sub>3</sub> (0.1mol/l) + silica (250nm) 12.5w%
8	IC1000	K <sub>2</sub> S <sub>2</sub> O <sub>3</sub> (0.1mol/l) + HCl (0.1mol/l) + silica (250nm) 12.5w%
9	IC1000	K <sub>2</sub> S <sub>2</sub> O <sub>3</sub> (0.1mol/l) + KOH (0.1mol/l) + silica (250nm) 12.5w%
10	LHA pad	Water
11	LHA pad	HCl (0.1mol/l)
12	LHA pad	KOH (0.1mol/l)
13	LHA pad	KMnO <sub>4</sub> (0.1mol/l)
14	LHA pad	KMnO <sub>4</sub> (0.1mol/l) + HCl (0.1mol/l)
15	LHA pad	KMnO <sub>4</sub> (0.1mol/l) + KOH (0.1mol/l)
16	LHA pad	K <sub>2</sub> S <sub>2</sub> O <sub>3</sub> (0.1mol/l)
17	LHA pad	K <sub>2</sub> S <sub>2</sub> O <sub>3</sub> (0.1mol/l) + HCl (0.1mol/l)
18	LHA pad	K <sub>2</sub> S <sub>2</sub> O <sub>3</sub> (0.1mol/l) + KOH (0.1mol/l)

**Table 3.** The temperature of the platen was controlled by a cooler and maintained at 298 K. A foam polyurethane pad (Nitta Haas IC1000) was used as a general purpose polishing pad in loose abrasive polishing. The polishing performance using silica slurry (particle diameter of 250 nm) was comparatively evaluated. The removal rate ( $R_r$ ) is derived by dividing the stock removal (thickness) by polishing time.

$$R_r = \frac{V}{t} \quad (1)$$

Where,  $R_r$  = Removal rate,  $V$  = Polishing thickness,  $t$  = Polishing time.

The surface roughness ( $R_a$ ) was used to evaluate the surface quality.  $R_a$  was measured by using an optical interference microscope (Zygo New View 200). The SiC used as the work piece was a single-crystal (6H), and it was used to convert the crystal face (0001) into a polishing face.

## 2.3 Measurement of oxidation reduction potential and pH

The oxidation reduction potential (ORP) and pH were measured by using a pH-ORP meter (Eutech instruments, Cyber Scan 200).

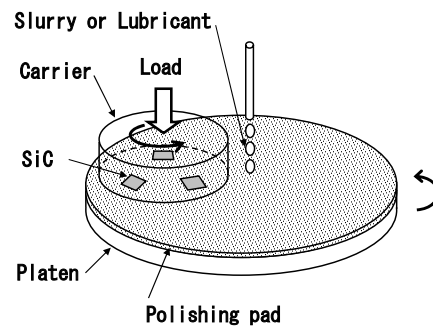


**Fig. 2.** Aschematic of the polishing experimental setup

## 3 Results and discussion

The relation between ORP and pH is shown in Fig.3. The value of the ORP and pH of the polishing fluid is shown in Table 4. K<sub>2</sub>S<sub>2</sub>O<sub>3</sub> (reducing agent) and KMnO<sub>4</sub> (oxidizing agent) were used for the adjustment of ORP of the polishing fluid. HCl and KOH were used for adjustment of pH. The ORP and pH of SiC was measured as follows. The SiC particles of size 2 μm were distributed in water to make a slurry. The slurry was adjusted by the addition of HCl and KOH, and the ORP and pH of nine points were measured. The line approximated by the least-square method by using the values of the 9 points is the broken line shown in Fig.3. In this figure, when the value of ORP in an area is above (below) this line, it is considered that the polishing fluid acts as an oxidizing (reducing) agent for SiC in that area.[6] This shows that Exps.1–3 and Exps.10–12 differ only in terms of the pH; the polishing fluid does not act as either an oxidizing agent or a reducing agent. Moreover, this shows that Exps.1,



4, and 7 and Exps.10, 13, and 16 differ in terms of ORP; however, they have almost the same pH (weak acidity).

**Table 3.** Polishing conditions

Item	Contents
Polishing machine	Lapmaster LP-15 (Taisei lapping system)
Polishing pad size	300mm
Platen revolutions	1s <sup>-1</sup> (60 rpm)
Work piece	Single crystal SiC 6H (0001)
Work piece size	10 x 10 x 0.26 mm (3 piece)
Carrier revolutions	1s <sup>-1</sup> (60 rpm)
Polishing pressure	24.6 kPa (251 gf/cm <sup>2</sup> )
Fluid flow	IC1000 : 0.167 cm <sup>3</sup> /s (10 ml/min) LHA pad : 0.0067cm <sup>3</sup> /s (0.4 ml/min)
Polishing time	7200 s (120 min)
Conditioner	SD#325

**Table 4.** Oxidation reduction potential and pH of polishing fluid

Experimental number	ORP mV	pH
1	560	4.5
2	755	1.4
3	241	11.5
4	1016	5.4
5	1359	1.3
6	683	11.5
7	266	5.2
8	148	2.0
9	137	12.4
10	565	5.0
11	648	1.3
12	166	12.8
13	1012	5.7
14	1382	1.2
15	735	13.3
16	361	6.2
17	137	1.5
18	40	13.0

**Fig. 4** shows removal rate in loose abrasive polishing, and **Fig.5** shows surface roughness in loose abrasive polishing. **Fig. 6** shows removal rate in the LHA pad, and **Fig.7** shows surface roughness in the LHA pad. The polishing examination result of Exps.1-18 and the virtual curved surface which connects them with the correlating method are drawn on these figures.

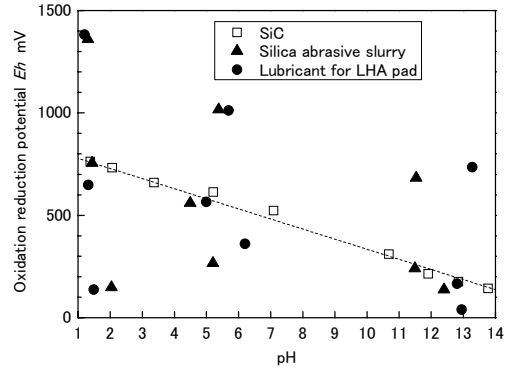


**Fig. 3.** Correlation with oxidation reduction potential and pH

**Table 5.** Removalrate and surface roughness

Experimental number	Removal rate nm/h	Surface roughness Ra nm
1	117	1.43
2	232	0.54
3	167	1.57
4	250	0.53
5	308	0.24
6	162	0.24
7	183	0.62
8	28	0.71
9	35	0.53
10	217	0.63
11	150	1.06
12	200	1.35
13	450	0.35
14	400	0.59
15	100	0.83
16	67	0.48
17	34	0.44
18	50	1.07

The value of the polishing examination result of Exps.1-18 is shown in **Table5**.

With regard to the removal rate, loose abrasive polishing is represented by Exp.4; the LHA pad—represented by Exp.13—exhibits the highest value. The oxidizing agent is contained in both Exp.4 and Exp.13. The removal rate for Exp.13 is 1.8 times that for Exp.4. Exp.3 has almost the same ORP and pH as commercial slurry for silicon wafer polishing. The removal rate for Exp.13 is 2.7 times that for Exp.3. Thus, the removal rate improves by the addition of an oxidizing agent to the polishing fluid. In addition, the removal rate improves further by the use of the LHA pad. From the virtual curved surface in **Fig.4** and **Fig.6**, it is found that the removal rate is high in the domain with acidity and high ORP (oxidation), and the removal rate is low in the domain of strong acidity and low ORP (reduction). Thus, in the polishing of single-crystal SiC by silica, since ORP has a greater influence than pH, it is considered that the

oxidization (reduction) reaction has occurred.

With regard to the comparison of surface roughness Ra, loose abrasive polishing yields the finest surface at Exp.4; the LHA pad yields the finest surface at Exp.13. These are the points at which the removal rate is the highest. On the other hand, loose abrasive polishing yields the coarsest surface at Exp.3, and the LHA pad yields the coarsest surface at Exp.12. Each of these points have strong alkalinity and do not have an oxidizing or a reducing action. From the virtual curved surface of **Fig5** and **Fig7**, it is expected in an acid domain that surface roughness is fine. Moreover, it is expected in an un-oxidizing, non-returning and strong alkalinity domain that surface roughness is coarse.

As these data suggest, it is considered that the C atom is oxidized to CO<sub>2</sub>, thus making its escape from single-crystal SiC easy; the removal rate improves if the polishing of single-crystal SiC by silica promotes oxidation reaction.

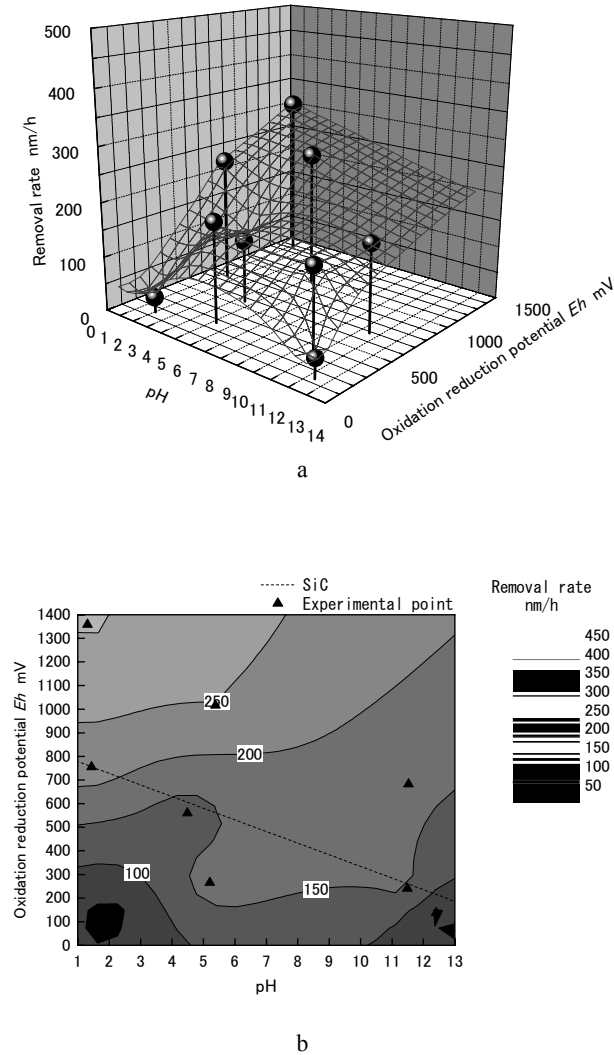


**Fig. 4.** Correlation with removal rate and oxidation reduction potential-pH on loose abrasive. a.3D-graph; b. contour drawing

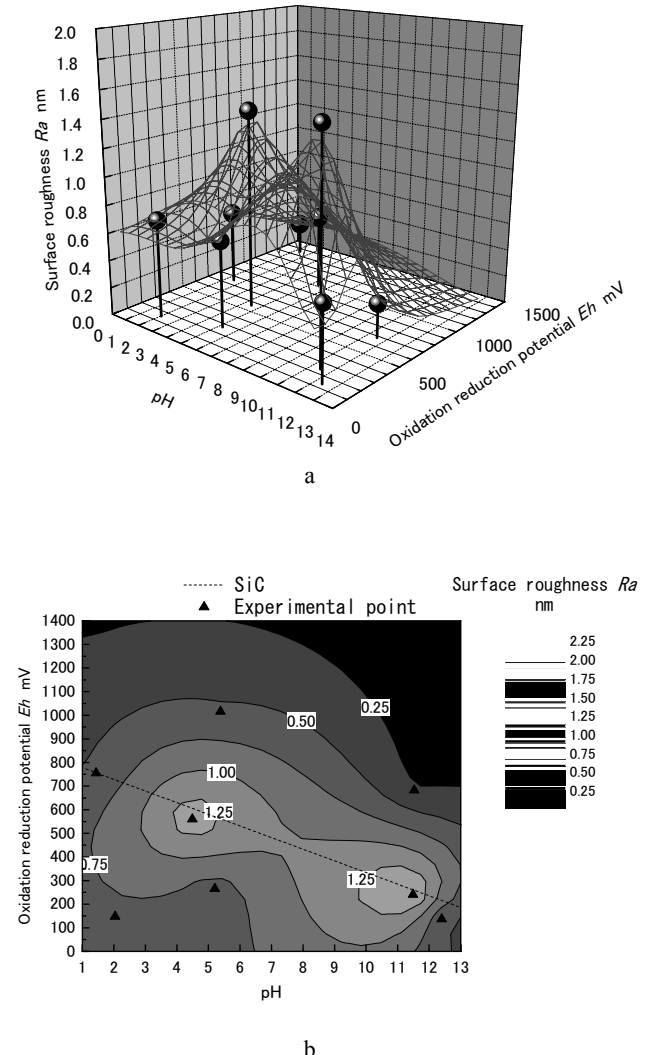


**Fig. 5.** Correlation with surface roughness and oxidation reduction potential-pH on loose abrasive. a.3D-graph; b. contour drawing

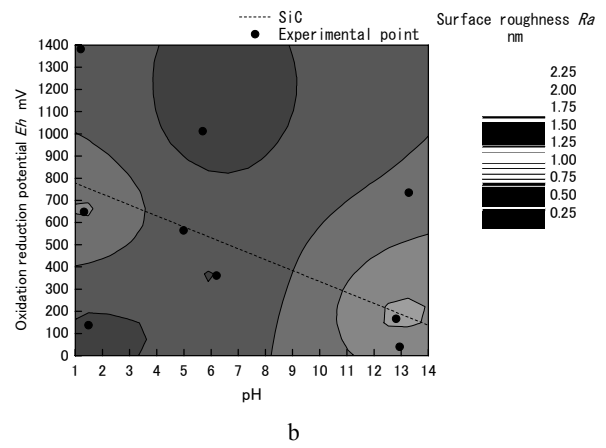
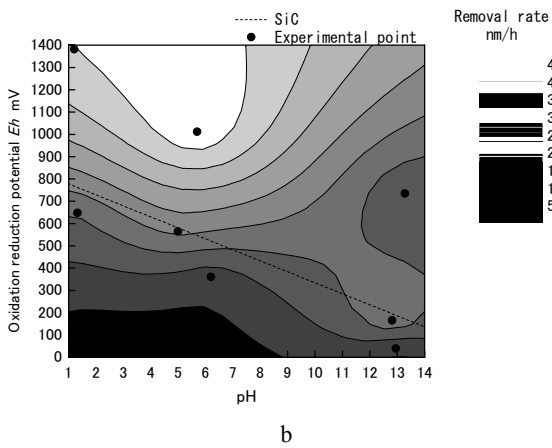
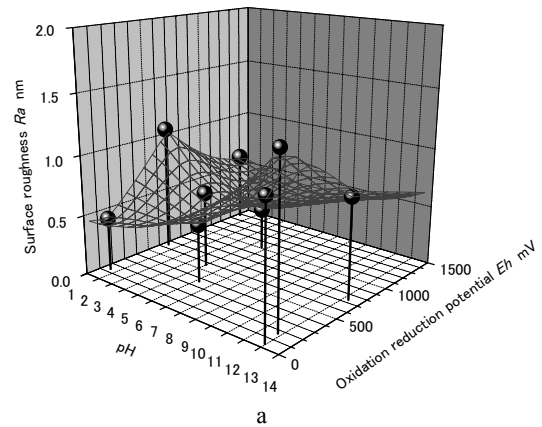
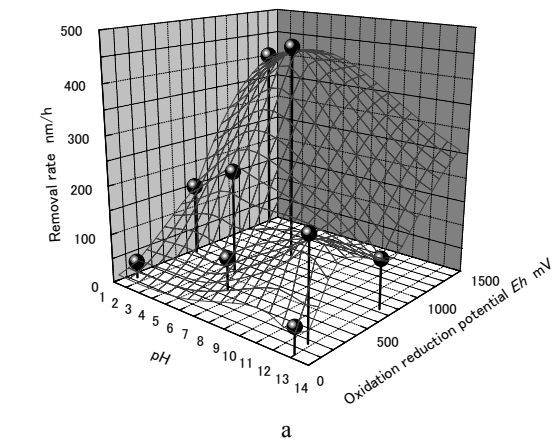


**Fig. 6.** Correlation with removal rate and oxidation reduction potential-pH on LHA. a.3D-graph; b. contour drawing

**Fig. 7.** Correlation with surface roughness and oxidation reduction potential-pH on loose abrasive. a.3D-graph; b. contour drawing

The research by Watanabe and Doi et al.[7] has also suggested that oxidation influences the polishing of single-crystal SiC. Moreover, it is considered that the mechanical power of the LHA pad is strong since it restrains the motion of abrasive grains in contrast to loose abrasive polishing; moreover, the removal rate of the LHA pad is further improved under the influence of the oxidizing action.

#### 4 Conclusion

The LHA pad leads to an improvement in the polishing of single-crystal SiC. Moreover, if the oxidation reaction is promoted, the polishing performance can be improved further. By using this knowledge, it expects that the cost cut of polishing of single-crystal SiC will be attained, and it is expected that fertilization will be promoted. In the future, we want to prepare an LHA pad that exhibits oxidizing action.

#### 5 References

- [1] K. Ishiguro, *Electronic Parts and Materials*, **39**, 5 (2000) 83
- [2] K. Koh, Y. Tani and Y. Uemura, *Proceedings of JSPE Autumn Meeting*, (2001) 406
- [3] M. Sato, T. Nonami, J. Ishizaki, *Journal of the Ceramic Society of Japan, Supplement*, **112**, 5(2004) s1341
- [4] M. Sato et al., *Proceedings of JSPE Spring Meeting*, (2003) 259
- [5] M. Sato, T. Kameyama, T. Nonami, *JSPE*, **72**, 1(2006) 79
- [6] M. Pourbaix, "Atlas of electrochemical equilibria in aqueous solutions", National association of corrosion engineers (1974)
- [7] S. Watanabe, T. Doi, J. Ikeno, *Proceeding of JSPE Autumn Meeting*, (2005) 339

# A Computational Study on Slurry Flow between a Wafer and CMP Pad with Grooves

Katsuya NAGAYAMA, Hirofumi MORISHITA, Keiichi KIMURA, Kazuhiro TANAKA,  
Panart Khajornrungruang and Yousuke INATSU  
Dept. of Mechanical Information Science & Technology, Kyushu Institute of Technology

Keywords: CMP, wafer, pad, slurry, numerical simulation, flow visualization

## Abstract

Slurry flow in CMP (Chemical Mechanical Polishing) process between the wafer and the polishing pad was studied using CFD (Computational Fluid Dynamics). Simulations were carried out for several pads, such as without groove, with circular grooves, and with radial grooves. One role of grooves is to replace old slurry to new slurry quickly by transporting the slurry. Another is to carry particles away, which are removed from the wafer surface, through grooves to prevent deep scratches. These roles are analyzed from the flow field and concentration of new slurry.

## 1 Introduction

In recent years, CMP (Chemical Mechanical Polishing) greatly has taken its role as technology of planarizations to produce multi-level interconnections. While slurry is flowing on a polishing pad in CMP, the polishing pad is in contact with the wafer to polish the wafer surface. The various types of groove layout pattern are set on the polishing pad in, such as concentric circular, radial, lattice, and spiral form. Grooves are expected to supply slurry evenly, improving the wafer surface flatness and efficiency in removal rate, and to remove wasted particles, preventing deep scratches and processing defects. However, the relationships among groove design, slurry flow and polish performance are not still clarified. CFD (Computational Fluid Dynamics) is a strong tool to investigate the slurry flow by various grooved pads [1, 2], and to find any relationships with polish performances.

Our study aims at developing the design of the best layout patterns of grooves and their cross-section shape. By predicting slurry flows between wafers and polishing pads in CMP using CFD, the influence of the slurry flow by the grooved pad can be analyzed. In this paper, simulations were carried out for three cases: without groove, with circular grooves, and with radial grooves. With analysis of the flow field, how grooves affect the velocity distributions are studied. We also simulated the replacement of old slurry to new slurry, and the roles of the grooves are discussed.

## 2 Simulation Model

### 2.1 Mathematical Model

For this analysis, we used FLUENT6.2 which is the heat fluid analysis code. The governing equations consist of continuity equation, Navier-Stokes equations (2), and diffusion equations (3). Eqn. (1) and (2) are for flow simulation and the following symbols are used.  $v$ : velocity components of each axis-of-coordinates direction,  $p$ : pressure,  $\rho$ : the density of fluid,  $\mu$ : viscous coefficient, and  $F$ : external force vector. Eqn. (3) is used for slurry transportation,  $C$  is concentration of new slurry, and  $D$  is diffusion coefficient. These equations are discretized by the limited volume method.

$$\frac{\partial \rho}{\partial t} + \nabla \cdot (\rho \vec{v}) = 0 \quad (1)$$

$$\frac{\partial}{\partial t} (\rho \vec{v}) + \nabla \cdot (\rho \vec{v} \vec{v}) = -\nabla p + [\mu (\nabla \vec{v} + \vec{v}^T)] + \vec{F} \quad (2)$$

$$\frac{\partial}{\partial t} (\rho C) + \nabla \cdot (\rho \vec{v} C) = \rho D \nabla^2 C \quad (3)$$

### 2.2 Model Description

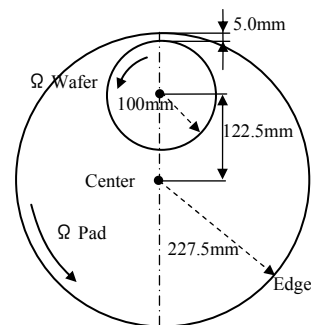


Fig. 1 Configuration of CMP model

Figure 1 shows the configuration of wafer and polishing pad of the CMP equipment. In order to clarify the influence of slurry flow by pad grooves, three cases of pad, which are groove-less, concentric-circular grooves, and radial grooves, are studied for comparison.

### 3 Simulation Conditions

The flow was treated as steady flow in case of groove-less and concentric-circular grooves, while unsteady flow in case of radial grooves in the simulations. Time step is  $10^{-3}$  s, and the physical property of water is used instead of slurry. The rotational speed of wafer and pad are both  $60 \text{ min}^{-1}$ . The pressure at the wafer edge is set to 0 Pa as boundary conditions. Simulations were carried out within gaps between wafer and polishing pad, and the influence of the pad groove was evaluated.

#### 3.1 Simulation Conditions for Non-grooved Pad and Circularly Grooved Pad

Figure 2 shows calculation domain for circularly grooved pad. The groove designs are pitch 2.0 mm, groove width 1.0 mm, land width 1.0 mm, groove depth 1.0 mm, and gap at land  $10 \mu\text{m}$  in Fig.2. Hexagonal lattice is used, and the numbers of lattice are 400,000 for non-groove case while 1,000,000 for concentric-circular grooves case.

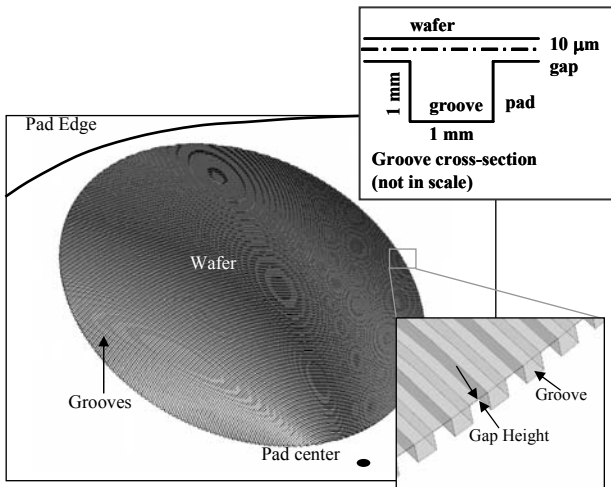


Fig. 2 Computational model between wafer and grooved pad

#### 3.2 Simulation Conditions for Radially Grooved Pad

For radial grooves, grooves in radial direction are located from the center of the pad. They rotate with axis at the pad's center, passing through under the wafer. These motions are modelled using sliding mesh function in Fluent. The groove design are the angle between the groove  $11.25$  degree, pitch 2.0 mm, groove width 1.0 mm, and groove depth 1.0 mm. The gap at land is set to be  $10 \mu\text{m}$ . Hexagonal lattice is used, and the numbers of lattice are 600,000.

## 4 Results and Discussions

### 4.1 Slurry Flow in Non Groove and Circular Groove

Fig. 3 shows the velocity distributions in tangential direction at  $5 \mu\text{m}$  from a wafer surface (center in the  $10 \mu\text{m}$  gap). Result (a) is for the non-groove pad, and (b) is for radially grooved pad. Basically, tangential velocity at the land position increases from the pad center toward its edge, due to the pad rotation for both cases. Due to low Reynolds number flow, velocity at the land largely depends on just pad and wafer velocity, and velocity at the gap center at land is almost the mean of their value. Maximum tangential speed is  $1.0 \text{ m/s}$  at the pad edge, and minimum speed is at the wafer edge close to the pad center.

In case of circular grooves as shown in Figure 4, striped pattern can be found, which indicates the difference in velocity between the land and the groove. In the grooved region, wafer drag is dominant at the upper region ( $5 \mu\text{m}$  from the wafer surface). On the other hand, both drag of wafer and land wall affect the flow in the land region.

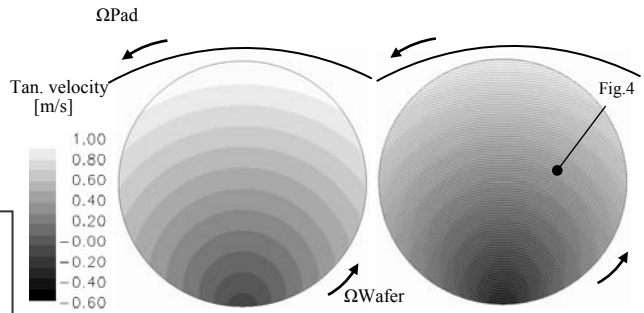


Fig.3 Tan. Velocity magnitude at center of wafer-pad gap

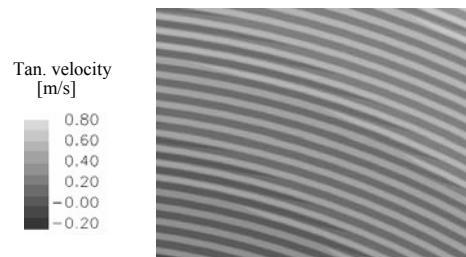


Fig.4 Groove/land velocity difference

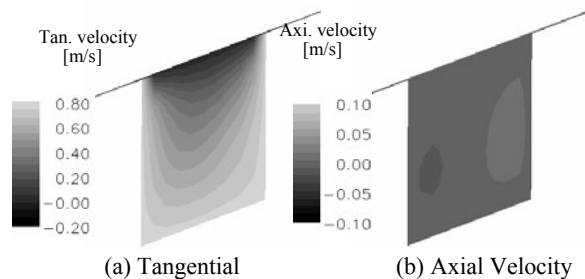
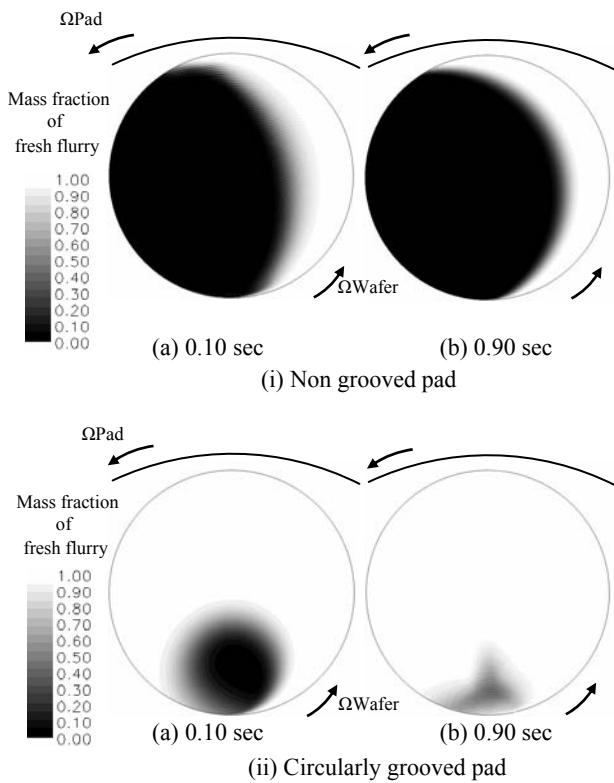


Fig.5 Velocity magnitude in a groove cross-section

Figure 5 shows the velocity distribution at the cross-section of the groove at the position shown in Figure 4. In tangential velocity in (a), slurry flows almost the same as grooved wall. As getting close to the wafer surface, tangential velocity becomes close to that of wafer. Axial velocity in the groove is very small as shown in (b), which indicates axial flow is negligible in case of circular grooves.

**4.2 The Effect of Circular Groove in Slurry Replacement**

Fig. 6 shows the mass fraction of fresh slurry at 5  $\mu\text{m}$  from the wafer surface, comparing with non-groove pad and radially grooved pad. At time 0, old slurry is assumed to be filled under the wafer, and afterwards, new slurry flows in from the wafer edge. Using the solution of steady flow as initial conditions, a diffusion coefficient is set to 2000  $\mu\text{m}^2/\text{sec}$ , and the time step to  $10^{-3}$  sec. After 0.1 sec, in both the cases of non-grooved pad and radially grooved pad, new slurry is flowing in from the wafer's right-side edge, due to the rotation of the pad. At 0.9 sec, old slurry still remains partially in non-grooved pad. The reason is tangential velocity of pad, and wafer in opposite direction diminishes the tangential velocity of slurry. On the other hand, very little of old slurry remains in case of circularly grooved pad. It can be assumed that the circular groove transports slurry in the groove, thus the slurry diffuses to the wafer surface. These results clearly indicate that circular grooves help slurry's transportation and replacement.



**Fig.6** Slurry mixing dynamics in pad-wafer gap

**4.3 Comparison with Experimental Results**

To verify simulation result, an experiment of slurry flow visualization was conducted for circularly grooved pad. The same size of wafer and pad are used here. In the experiment, synthetic silica glass was used as a substitute of a wafer. Fluorescence agent is mixed with water instead of slurry. The fluorescence agent was dropped on the polishing pad, being irradiated by the ultraviolet ray from UV lamp and emit visible light.

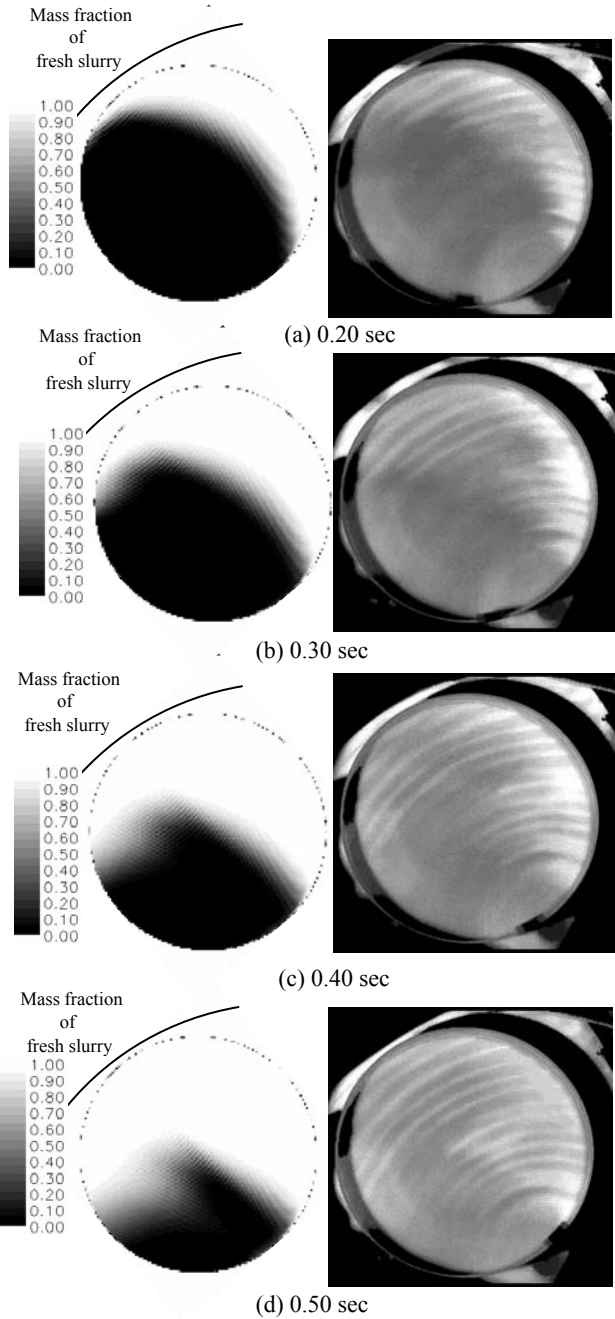


**Fig.7** Comparison of simulation and experiment

The visualized flow was monitored with a video camera. Circularly grooved pad is used, and as conditions for an experiment and simulation, pad rotates at  $30 \text{ min}^{-1}$  and wafer rotates at  $30 \text{ min}^{-1}$  here.

Simulation results and experimental results are shown in Fig.7. At time 0, new slurry is filled around the wafer in simulation, and fluorescence agent starts to enter wafer-pad gap from the right edge of wafer in experiment. Both experimental result and an analysis result after 0.2 and 0.3 [sec], show that slurry is flowing in from the right side and top edge of the wafer. Near the pad edge, velocity tangential to pad rotation is large, and slurry is expected to flow quickly. That is similar at 0.4 and 0.5 sec. Old slurry tends to remain at the area close to the pad center, while replacement is almost finished close to the pad edge. Thus, simulation result is validated by the experimental results.

#### 4.4 Results for Radially Grooved Pad

Fig. 8 shows tangential velocity distributions at  $5 \mu\text{m}$  from wafer (gap center at land). Fig. 8 (a) is after 0.10 sec from an initial state, and (b) is after 0.9 sec. We can see the groove position, where the tangential velocity is slightly different, but overall velocity distribution is similar. Even in a few time steps, the flow field in land becomes steady state. This is because the gap between the wafer and pad is very small (very low Re number flow), viscous diffusion is dominant, and flows become steady states very quickly.

Fig. 9 shows the mass fraction of fresh slurry at  $5 \mu\text{m}$  from the wafer surface for a radially grooved pad. For the case of the circularly grooved pad, the grooves replace old slurry to new slurry quickly, compared to the non-grooved pad case. As for radially grooved pad, this tendency is more obvious. After 0.9 sec, new slurry spreads all over under the wafer. This happens because, while circular groove does not pass through all the surface of wafer, radial grooves pass through all the surface of a wafer, and diffusion arises from the groove. As shown, radial groove seems most effective from the standpoint of slurry replacements.

## 5 Concluding Remarks

Numerical simulations of the slurry flow in CMP for non-grooved, circularly grooved, and radially grooved pad were carried out. In all the cases, velocity at the center of the gap in the land region is close to the mean of wafer and pad velocity. Maximum tangential speed is  $1.0 \text{ m/s}$  at the pad edge, and minimum speed is at the wafer edge, close to the pad center. At the bottom of circular groove, slurry at the lower part flows almost at the pad rotational speed, and slurry flows slowly as it goes to the groove upper part. It turns out that slurry inside a groove hardly flows in axial direction.

In the aspects of slurry replacements for non-grooved pad, old slurry remains close to the pad center for a long time, which is not preferable for CMP. Circular grooves promote the slurry replacement by carrying the new slurry in the groove. Experimental visualization was also conducted. The interface of the fluorescence agent and slurry in the

experiment matched qualitatively between new and old slurry in the simulation.

Slurry replacement takes place evenly and effectively performed in case of radially grooved pad, because groove, including new slurry, passes through the entire bottom of the surface of a wafer, and thus, diffusion arises.

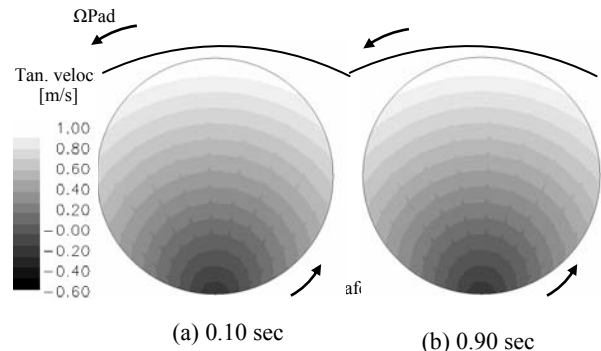


Fig.8 Tangential velocity magnitude in pad-wafer gap

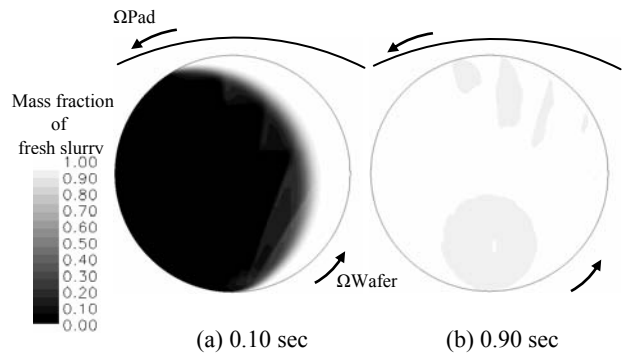


Fig.9 Slurry mixing dynamics in pad-wafer gap

## References

- [1] G.P.Muldowney, "Characterization of CMP Pad Surface using a Porous-Media Flow Approach", Proceedings of AIChE Annual Meeting (2003)
- [2] G.P.Muldowney and D.P.Tselepidakis, "A Computational Study of Slurry Flow in Grooved CMP Polishing Pads", Proceedings of CMP-MIC (2004)

---

# Multilevel Computer Generated Hologram on a Curved Surface for High Power CO<sub>2</sub> Laser Beam Shaping

Hideki Hagino<sup>1</sup>, Choong Sik Park<sup>1</sup>, Hisao Kikuta<sup>2</sup> and Koichi Iwata<sup>1</sup>

<sup>1</sup> Technology Research Institute of Osaka Prefecture, <sup>2</sup> Osaka Prefecture University

Keywords: computer generated hologram, beam shaping, high power CO<sub>2</sub> laser, curved surface, laser processing

## Abstract

A multilevel computer generated hologram (CGH) on a curved surface was developed for the laser beam shaping of a high-power CO<sub>2</sub> laser. The CGH with eight height-levels was fabricated by direct-writing laser-beam lithography and the copper electroplating. The fabricated CGH changes a laser beam profile from a Gaussian distribution to a Rectangle-Gaussian distribution. The measured diffraction efficiency was 68%. When a steel surface was exposed to the shaped laser beam, a uniform melted zone was obtained. We investigated the melted zone with respect to the irradiated conditions experimentally.

## 1 Introduction

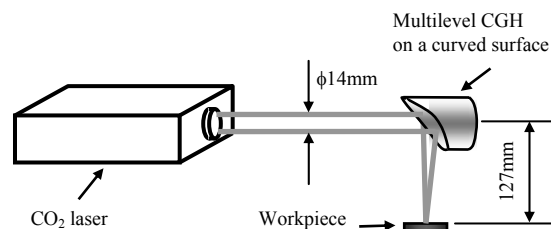
High power lasers are used for a wide variety of material processing such as cutting, marking, welding, laser transformation hardening and surface modification. The laser beams with Gaussian distribution profile are employed in many cases. But the Gaussian distribution is not always suitable for the laser processing. Shaping the laser beam profile improves the quality and efficiency of the laser processing. There are various techniques for shaping a laser beam. An aspheric beam shaper<sup>1)</sup>, a segmented mirror and a light-pipe waveguide<sup>2)</sup> are used commonly.

Computer generated hologram (CGH) is also utilized for the laser beam shaping. Especially CGH is suitable for realizing a complex beam profile with a small energy loss<sup>3)</sup>. For a high-power infrared laser beam shaping, silicon<sup>3-4)</sup>, zinc selenide (ZnSe)<sup>5)</sup> and copper<sup>6-8)</sup> substrates were used as material of CGH substrate. Silicon and ZnSe substrates are less heat-resistant because of low thermal conductivities. Copper not only has a high thermal conductivity but also is easy to be formed by machining process. We fabricated CGH on a parabolic reflection mirror of copper for a few kW high-power CO<sub>2</sub> laser<sup>7)</sup>. The CGH was cooled efficiently so as not to be damaged in laser processing. The fabricated CGH surface consisted of two phase levels. The laser beam was shaped into a desired intensity distribution on the focal plane of the parabolic mirror.

In this study, a multilevel CGH has been fabricated on a parabolic copper mirror to improve the diffraction pattern for the high-power CO<sub>2</sub> laser beam shaping. The CGH with 8 phase levels was realized by the direct-writing laser-beam lithography and the copper electroplating. This paper describes a fabrication of the multilevel CGH and its optical performance. Furthermore a steel surface was exposed to the shaped laser beam for the surface modification. We compared the modified surfaces with experimental results of a conventional defocused laser beam.

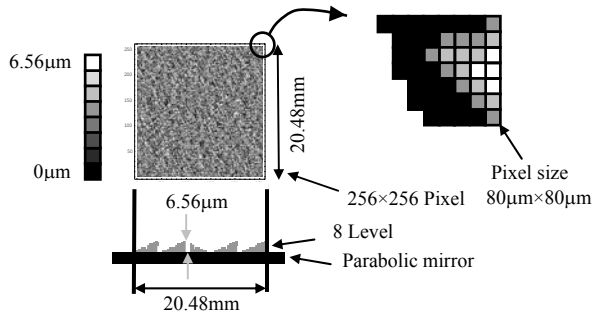
## 2 Design of CGH

Figure 1 shows the system configuration of laser beam shaping with the multilevel CGH on the parabolic mirror. The CO<sub>2</sub> laser outputs a 10.6μm-wavelength light beam with a Gaussian intensity distribution. The beam diameter is 14mm, which is defined as the waist at which the intensity is down by a factor 1/e<sup>2</sup> compared to the maximum value on the axis. The incident laser beam is reflected down by the CGH. A focal plane of the parabolic mirror lies 127mm away. The desired intensity distribution is formed on the focal plane.



**Fig.1** Basic configuration of beam shaping system using multilevel CGH on a curved surface





**Fig.2** Schematic diagram of the CGH

Figure 2 shows the schematic diagram of the 8-level copper CGH. The area of CGH is a square 20.48mm on a side. The CGH consists of 256×256 pixels and each pixel is a 80µm×80µm square. The surface height is reduced to 8-levels shown by the gray scale in Fig.2. The maximum and minimum step heights of the CGH are 6.56µm and 0.94µm, respectively.

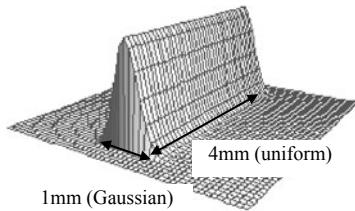


**Fig.3** Desired intensity distribution

The desired intensity distribution is shown in Fig.3. The shaped beam profile is Rectangle-Gaussian for laser transformation hardening. The intensity is uniform and 4mm-wide in a longitudinal direction and 1mm-wide Gaussian distribution in the other direction. The surface profile of CGH has been designed with GS algorithm<sup>9)</sup> which is an iterative design method based on Fourier transform algorithm. Since the curvature of the parabolic mirror surface is not large, the CGH is designed for a flat surface. And the resultant surface relief is superimposed on the parabolic mirror surface.

**3 Fabrication of CGH and the optical performance**

The parabolic mirror was made of oxygen-free copper. The copper substrate was 4mm thick. The mirror surface was fabricated with the CNC high precision machining and a mirror bowl was 0.77mm in depth.

The direct-writing laser-beam lithography and the mask-electroplating method<sup>8)</sup> were used for fabricating the multilevel copper CGH. The laser-beam writer has a

mechanism of z-axis control for writing on a curved surface. After making the photoresist pattern on the parabolic copper mirror, a copper thin film is plated on the bare surface. The remaining photoresist was removed by organic solvent. By repeating this process three times with different photoresist patterns, the eight-level surface profile was obtained.

The photo-resist was 4µm thick which was larger than the maximum plating thickness. The plating thickness could be controlled by plating time, current density and bath temperature. The deposition rate was about 0.2µm/min. The fabricated CGH was coated by a gold thin film to improve reflectance for the infrared light.

Figure 4 shows the fabricated CGH. The surface profiles were measured at 4×4 points with a scanning white light interferometer (Zygo New View 5020). Measurement results are shown in Table 1. Deviations of the mean plating thickness from the designed thickness are smaller than 0.1µm. And the standard deviation of plating thickness is 0.03~0.06µm. The fabrication error of step height increases the 0th-order diffraction light which appears as a conspicuous spot in the shaped beam. According to optical simulation results of CGH, when the plating thickness has a fabrication error of 0.1µm in standard deviation, the intensity of the 0th-order diffraction light increases by 10% and the diffraction efficiency decreases by 1.5%. Then the above step-height errors are not significant for the beam shaping.

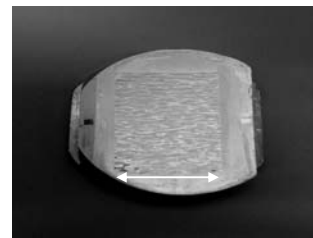


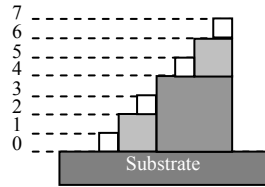
**Fig.4** Fabricated multilevel CGH on a curved mirror

**Table 1** Plating thickness of the CGH [µm]

	Plating times		
	1st.	2nd.	3rd.
Mean	3.81	1.80	0.91
Maximum	3.88	1.90	0.99
Minimum	3.71	1.70	0.88
Standard deviation	0.045	0.057	0.030
Designed thickness	3.75	1.88	0.94

**Table 2** Surface roughness of the CGH

Level (Plating times)	Roughness Ra [nm]
0 (0)	38
1 (1)	151
2 (1)	124
3 (2)	146
4 (1)	91
5 (2)	148
6 (2)	149
7 (3)	157



The surface roughness of CGH became worse as repeating the copper electroplating. The surface roughness decreases diffraction efficiency and messes the beam profile. The measured surface roughness for each level is shown in Table 2. The lowest level surface which was just finished machinely has the roughness of 38nm in Ra. For the plated surfaces the roughness was 100~160nm in Ra, which was much smaller than 10.6μm wavelength of the CO<sub>2</sub> laser.

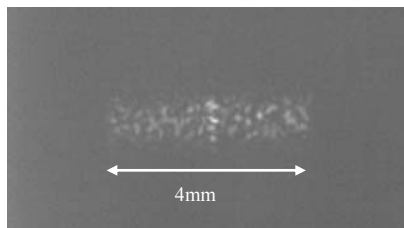


**Fig.5** Shaping beam image for a low power laser

To investigate an optical performance of the fabricated CGH, we observed the shaped beam profile using an infrared camera system (Mitsubishi Electric IR-U300M) and a low power CO<sub>2</sub> laser (SYNRAD 48-1W). The collimated light beam to the CGH has a Gaussian profile 14mm in diameter. The shaped beam profile was observed by the infrared camera which was placed on the focal plane of the parabolic mirror as CGH substrate. An observed image of the shaped beam is shown in Fig.5. An outline of the beam profile is 1mm×4mm. A speckle noise appeared in the shaped beam. But this noise is not significant for the laser transformation hardening. The diffraction efficiency was 67.8%, which was defined as a ratio of the total power within the shaped beam area (1mm×4mm) except the 0th-order diffraction light to the power of incident beam.

The CGH was tested for a high power CO<sub>2</sub> laser beam. The laser beam was 2kW power and 14mm in diameter. The beam profile was not the Gaussian distribution but was distorted slightly. The CGH was irradiated with the high power CO<sub>2</sub> laser without damage. The CGH was held in an aluminum holder which had a water cooling channel in it.

Figure 6 (a) shows the shaped beam profile measured with a laser beam profiler (Prometec Laser Scope UFF100). Fig.6 (b) and (c) are the intensity distribution on dashed lines shown in Fig.6 (a). The beam profile is a nearly rectangle shape. But the outline is larger than 1mm×4mm and the profile is not uniform in a longitudinal direction. The loss of shape in the high power laser beam was caused by a mode distortion of the laser beam.

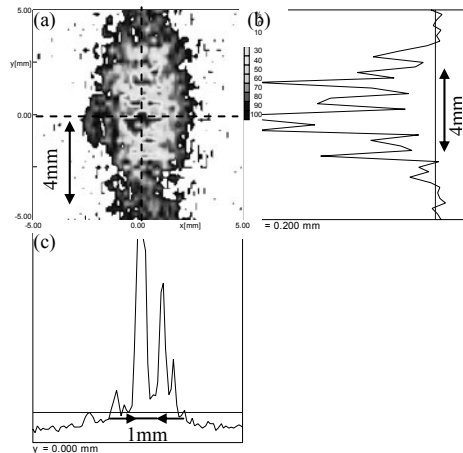


**Fig.6** A beam profile shaped by the CGH for a high power laser; (a) 2D intensity distribution, (b) cross sectional intensity for flat top direction, (c) Gaussian direction

#### 4 Laser Processing for Using Shaped beam

The shaped beam was applied to the laser surface processing. The 1.5-kW CO<sub>2</sub> laser described above was used for the processing. A plate workpiece was exposed to the shaped laser beam. The workpiece was tool steel (SKD11). A surface of the workpiece was treated by grass beads blast. The workpiece moved in a direction orthogonal to a longitudinal direction of the shaped beam. The laser power was 1.0~1.5kW and the traverse speed was 2.5~10.0mm/s. The same experiments were made for a defocused laser beam. We used a lens for defocusing the laser beam. Its focal length was 127mm which was equal to that of the parabolic mirror of CGH substrate. The defocus beam diameter was 4mm which was equal to the longitudinal beam width of the shaped beam.

Figure 7 (a) and (b) show macrographs of the cross sections of steel plates exposed to the shaped beam and the defocused beam respectively. The laser power was 1.5kW and the traverse speed of the workpiece was 5mm/s. White areas in the figures had been melted once by exposing to the laser beams. The width of melted area, i.e. bead width, is equal to that of each other. However the depth of melted area is shallow and uniform compared with results of the defocused beam.

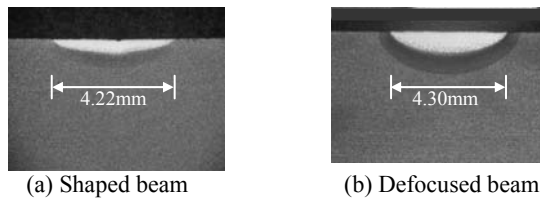


**Fig.7** Cross sectional macrographs of laser irradiated steel (SKD11). Laser power : 1.5kW, Traverse speed : 5mm/s

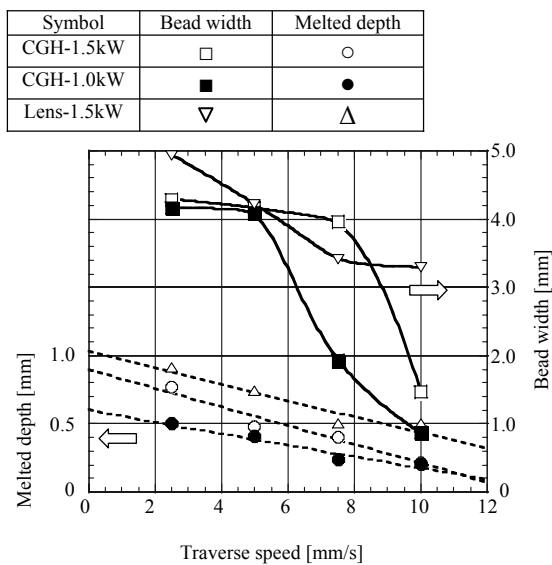


**Fig.8** Relationship between laser irradiate parameter and melted zone size

We investigated the bead widths and melted depths for different irradiated conditions. Figure 8 shows the bead width and melted depth with respect to the traverse speed of the workpiece. The results of the shaped beam are denoted by *CGH*, and the results of the defocused beam are denoted by *Lens*. The bead widths for the shaped beam are constant at 4mm at traverse speed slower than 7.5mm/s at a power of 1kW and 5mm/s at 1.5kW. For higher traverse speeds the bead widths decrease suddenly. The threshold speed of the sudden decrease in a bead width depends on the laser power. But the ratio of laser power to the traverse speed at the threshold is equal to each other. This ratio represents the

exposed energy. For the defocused laser beam there is no threshold of the sudden decrease and the bead width depends on the traverse speed.

On the other hand, the melted depths decrease monotonically with respect to the traverse speed for both beam profiles. Therefore the melted depth for the shaped laser beam can be controlled by the traverse speed. In the case of the defocused laser beam it is not easy to control the bead width and melted depth simultaneously.

## Conclusions

The multilevel CGH was fabricated on a parabolic mirror of copper by means of the direct writing laser beam lithography and the mask electroplating method. The CGH shaped a high power CO<sub>2</sub> laser beam into the rectangle beam profile without a lens. The diffraction efficiency was 68% for the low power CO<sub>2</sub> laser beam. When the fabricated CGH was used for the laser surface processing with a 1.5kW high power laser, the steel plate surface was melted uniformly in the beam width. The bead width did not depend on the traverse speed slower than a certain threshold speed, and the melted depth depended on the traverse speed. The melted depth will be controlled by the traverse speed without reducing the bead width.

## References

- [1] Ebata K, Shiozaki M, Okada T, Fuse K, Nanba H, Proc. SPIE 4443 (2001):125-134
- [2] Miyamoto I, Maruo H, Proc. SPIE 1031 (1988):512-519
- [3] Haupt Ch, Pahlke M, Krupka R, Tiziani HJ, Appl. Opt. 36 (1997):4411-4418
- [4] Cole CE, Noden SC, Tyrer JR, Hilton PA, Proc. ICALEO (1998):84-93
- [5] Kurisu K, Hirai T, Ushiro T, Fuse K, Okada T, Ebata K, Proc. SPIE 4830 (2003):313-318
- [6] Tyrer JR, Noden SC, Hilton PA, Proc. SPIE 2789 (1996):174-185
- [7] Hagino H, Park CS, Kato N, Mitsumata M, Kikuta H, Iwata K, J. Jpn. Soc. Prec. Eng. 69 (2003):417-421 (in Japanese)
- [8] Hagino H, Park CS, Yokoi M, Kato N, Mitsumata M, Kikuta H, Iwata K, J. Jpn. Soc. Prec. Eng. 70 (2004):1180-1185 (in Japanese)
- [9] Gerchberg RW, Saxton WO, Optik 35 (1972):237-246

---

# Milling-Combined Laser Metal Sintering System and Production of Injection Molds with Sophisticated Functions

Satoshi Abe<sup>1</sup>, Yoshikazu Higashi<sup>2</sup>, Isao Fuwa, Norio Yoshida<sup>3</sup>, Takeshi Yoneyama<sup>4</sup>  
<sup>1</sup>Matsushita Electric Works, Ltd., <sup>2</sup>Matsushita Electric Works, Ltd., <sup>3</sup>Matsushita Electric Works, Ltd., <sup>4</sup>Kanazawa University

Keywords: Rapid Tooling, laser sintering, milling, injection molding, cooling, accuracy, molding cycle time

## Abstract

The first system of milling-combined laser metal sintering is developed, combining a laser-assisted metal sintering and a milling process. In this process, the periphery of the sintered layers is machined by endmill in each several sintering steps. Smooth surface is obtained after the one process.

Applying to the mold manufacturing process, many characteristics is achieved. Firstly, it halved the lead time required in the conventional machining processes. Secondly, the mold with deep ribs can be manufactured in one process. Thirdly, adequate cooling channel can be composed freely. These sophisticated functions improve the injection mold accuracy and mold cycles.

## 1 Introduction

Manufacturing in Japan is exposed to the crisis of the hollowing out of industry owing to the gap of the labor cost with the foreign countries. Especially, the mold industry which is one of the basis industries in Japan receives a big blow. Under such a condition, the innovation of a mold manufacturing system is demanded for mold industry.

Also, the information machinery products such as the mobile phone become popular rapidly. To support eclectic needs in the market, new products incorporated with the latest technology are developed one after another. The characteristic of these products is that the lifetime is very short. As the speed of developing a product becomes the key point in the competition, it is required to minimize the development period and to reduce the production cost.

As the tool to shorten development time, the stereo lithography system was developed<sup>[1]</sup>. It has been expected to shorten the period of manufacturing prototypes, because the model shape designed by the 3D CAD is evaluated in a few days using this system. However, because the materials of the prototypes made by this system are different from those of the end product, they cannot be used for the evaluation of the features and the performances such as the lifetime, the strength of the products etc. We must manufacture the real injection molds to evaluate these items.

After that, the material resin has been developed to manufacture the molds directly by stereo lithography system.

Injection molding is also available using the mold<sup>[2]</sup>. But, only the hundreds shots can be molded because the strength is weak as the injection molds.

Next, laser-assisted metal sintering system<sup>[3]</sup> (the stereo lithography system which sinters metal powders with a laser and piles layers to manufacture metal parts or molds directly) has been developed. However, this system cannot be used for the mass production of the molds because both the dimensional accuracy and the surface roughness are poor in quality.

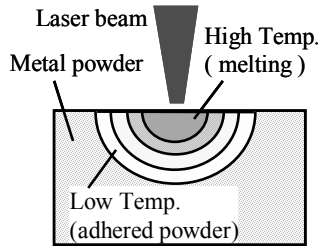
To solve these problems, we have developed a system of Milling-Combined Laser Metal Sintering, combining the laser-assisted metal sintering process and the high-precision and high-speed milling process to manufacture high-precision molds for the mass production in very short lead time. This process is an "additional" process, unlike conventional milling and electro discharge machining (EDM) processes, which are "removal" processes. Applying to injection mold processing, even the molds with deep ribs can be manufactured in one process. Moreover, adequate cooling channel such as spiral holes that have not been possible in the conventional machining process along the mold profile can be composed. These sophisticated functions improve the dimensional accuracy and the molding cycle time in the injection molding

In this paper, the overview of the milling-combined laser metal sintering system and the injection molds which have sophisticated functions by applying this system are described.

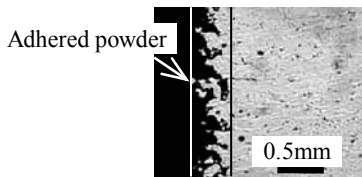
## 2 Problems of the conventional laser assisted metal sintering process

The laser-assisted metal sintering process is the method of manufacturing three dimensional shapes by sintering the metal powders that are irradiated by the infrared laser and piling it layer by layer. The characteristic of this process is that it is possible to manufacture the mold shapes which are designed by the 3D CAD just as it is, and the complex shapes can be easily manufactured. However, the limit of the dimensional accuracy of the product is  $\pm 100 \mu\text{m}$ . This is far from the required accuracy of the injection mold. Dimensional accuracy is approximately caused by the laser scanning accuracy. In the stereo lithography system, the

differential transducer type galvanometer mirrors are generally applied. But, they are easy to be influenced by the temperature and the humidity. Specially, because the infrared laser is used in this system, when a laser beam is reflected by the mirror, the mirror absorbs energy and becomes hot. It is one of the factors that dimensional accuracy is aggravated. Moreover, in the conventional laser-assisted metal sintering system, the upper limit of the surface roughness is 100  $\mu\text{m Rz}$ . The cause is that "The powder adhesion area" (the unnecessary metal powders which adhere to around the surface) has been formed. As shown in Fig. 2.1, the powders around the melting part is also heated by the spreading heat to adhere to the melting part. They cover the melting surface. Such accuracy and the surface roughness cannot be accepted to the molds in mass production. Therefore, a lot of processes are necessary as the milling and the EDM processes, and the mold manufacturing period is not shortened.



(a) Temperature distribution in laser irradiation



(b) Cross section of sintered work

Fig. 2.1. Mechanism of metal powder sintering

### 3 Milling-Combined Laser Metal Sintering Process

#### 3.1 Process of the Milling-Combined Laser Metal Sintering

Milling-Combined Laser Metal Sintering is the process that combines the laser assisted metal sintering and the milling by the end mill, within one equipment to solve both problems of dimension accuracy and surface roughness. The concept of the process is shown in Fig. 3.1 Components of the system and the photograph of processing chamber are shown in Fig. 3.2 and Fig. 3.3 respectively. The procedure of the process is shown as follows.

- (1) Metal powder material is applied onto the base plate at fixed thickness, then, material is selectively sintered by the irradiated infrared laser and joined with the base plate.
- (2) Composing layers by repeating supplying metal powder material and sintering powders by the laser irradiating.
- (3) The powder adhesion area is removed by the end mill when the height of the sintered layers reached the effective cutting edge length of the end mill.
- (4) Repeating (2) and (3) steps.

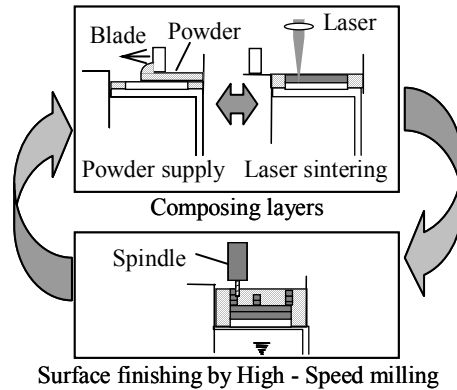


Fig. 3.1. Concept of Milling-Combined Laser Metal Sintering process

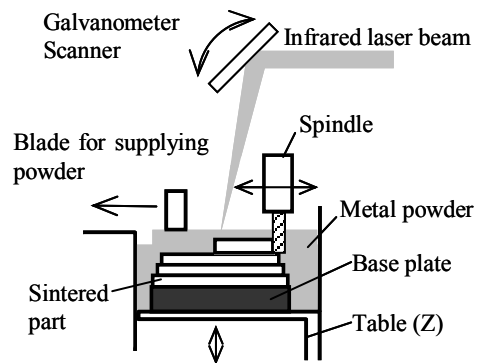


Fig. 3.2. Components of the Milling-Combined Laser Metal Sintering System

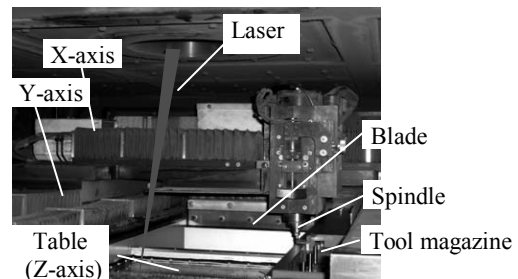
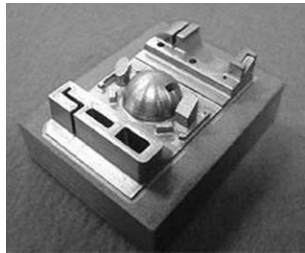


Fig. 3.3. Processing chamber of Milling-Combined Laser Metal Sintering System

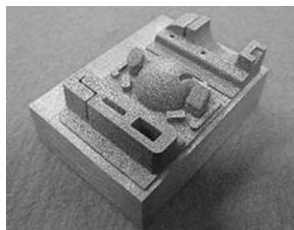
The characteristic of this process is to repeat sintering and milling, not milling an entire surface after all layers are sintered. In this process, the end mill with the short effective cutting edge length can machine the deep ribs which was impossible in the past. Therefore, the molds which needed the EDM can be manufactured in one process and the dimension accuracy and the surface roughness are equal to the one made by a machining center.

Fig.3.4 shows the sample which is manufactured in this system. The surface is the same as milled surface. The dimension accuracy is  $\pm 0.03$  mm and the surface roughness is  $20 \mu\text{m Rz}$ . They are improved together remarkably than the conventional laser assisted metal sintering system. The powder material is the iron based powder<sup>[4]</sup>. Ball end mill of the diameter 0.6 mm and the effective cutting edge length 1.2 mm is used. Table 3.1 shows the milling conditions. Milling process is inserted when the height of the sintered layers have reached 0.5 mm. Milling path type is contour line path. In this sample shape, the width of the thinnest rib is 1.5 mm and the depth is 10 mm. The rib depth is about 8.3 times as large as the effective cutting edge length of the used ball end mill. Because corner R in the rib is 0.5 mm, the tool of diameter 0.6 mm (R0.3) is used. In this way, in this process, it is the one of the characteristics that the short end mill can be used. Therefore, the influence of the bend and breakage of the tool which is caused by the stiffness of the tool is small and it is possible to mill stably.



Dimensional accuracy :  $\pm 0.03$  mm  
Surface roughness :  $20 \mu\text{m Rz}$

(a) By Milling-Combined Laser Metal Sintering system



Dimensional accuracy :  $\pm 0.10$  mm  
Surface roughness :  $150 \mu\text{m Rz}$

(b) By conventional Laser-assisted Metal Sintering

**Fig. 3.4.** Comparison of dimensional accuracy and surface roughness

**Table 3.1.** Milling conditions

Spindle speed	50,000 min <sup>-1</sup>
Feed rate	800 mm/min
Axial depth of cut	70 $\mu\text{m}$
Radial depth of cut	70 $\mu\text{m}$

### 3.2 Reduction of the mold manufacturing period

In the conventional machining process, molds are designed on the assumption that they are machined, assembled with many divided blocks and applied by EDM process. Because the molds of complex shape (for example deep ribs) can not be milled by the reason that there is a limit in the length of the end mill used for milling. In Milling-Combined Laser Metal Sintering process, molds don't have to be divided into the blocks but manufactured as one part and EDM process is substantially reduced. In the following, the cases which this developed process have been applied to the molds are described.

Fig.3.5 shows the mold manufactured by the developed process. The comparison on the period of the manufacturing between the developed process and the conventional machining process on this mold is shown in Fig. 3.6 This mold with a lot of deep ribs can also be manufactured as one part. A period of the manufacturing of the mold is reduced 62 % at the whole processes flow. In detail, design time is about 67 %, CAM process time is about 90 % and machining time is reduced about 47 %.



Process Time  
72 Hours

(a) Mold manufactured by the developed process



Injection resin  
ABS

(b) Molded part

**Fig. 3.5.** Example of mold and molded part

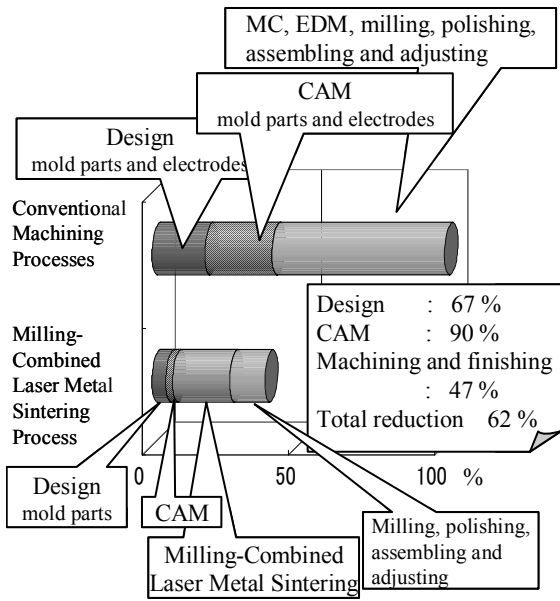


Fig. 3.6. Reduction ratio of the mold manufacturing period

#### 4 Application to sophisticated function mold

In the conventional machining process, only straight cooling channels can be formed by drilling and the EDM process. Cooling channels sometimes cannot be passed through the area to be cooled owing to the shape of the molded parts and the mold construction. It causes a lot of problems that the dimension accuracy of the molded parts becomes low by warp and that the cycle time becomes long.

On the other hand, applying Milling-Combined Laser Metal Sintering process, three dimensional complex cooling channels can be formed in the mold, because the inside structure can be freely composed in this process. It is possible to insert cooling channels intensively for cooling the area where heat is stored up with the molding process. The channels can be formed to avoid the ejector pins and the leader pins in the mold.

In the following, the effect of the mold with three-dimensional cooling channels on the injection molding process is described.

##### 4.1 Precise molding using three-dimensional cooling channels

Molding accuracy improvement is attempted on the work piece of the flat plate which has ribs on one side with changing length in turn as shown in Fig. 4.1 This work piece is easy to warp remarkably because the heat flow from the ribs rises the temperature of the core mold around the ribs. Therefore, the thermal balance has collapsed, and after the mold release, the thermal shrinkage is different between the cavity and the core side.

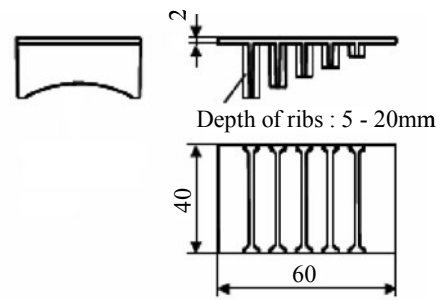


Fig. 4.1. Dimension of Work piece

Cancel of the warp is attempted by arranging a cooling channel among the ribs on the core side to cool around the ribs efficiently. The arranged cooling channel is shown in Fig. 4.2. One spiral channel is led between the ribs in the core. The channel of the cavity is meandered through parallel with the surface of the work piece. The cross-section shape of the channel in the core is an ellipse, the major axis diameter is 5 mm and the minor one is 3 mm to get enough flow rate even among the narrow ribs. Steel mold (S50C) is manufactured to compare with the conventional machining process. Because it is impossible to arrange the same cooling channel in that, a straight one by drilling is arranged under the ribs. Core and cavity of the molds which is manufactured by Milling-Combined Laser Metal Sintering process and the molded part are shown in Fig. 4.3.

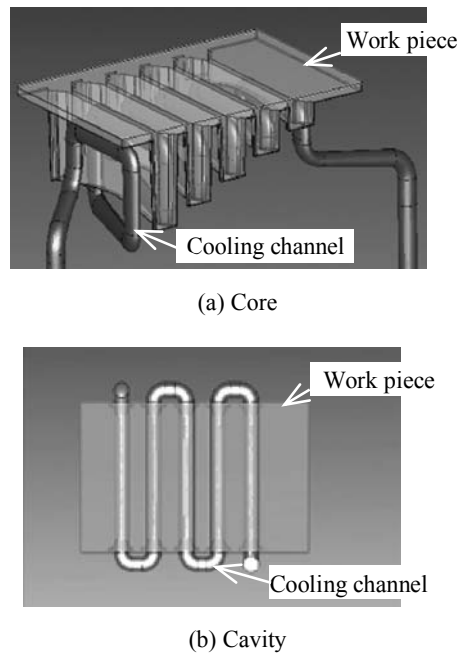


Fig. 4.2. Construction of cooling channels

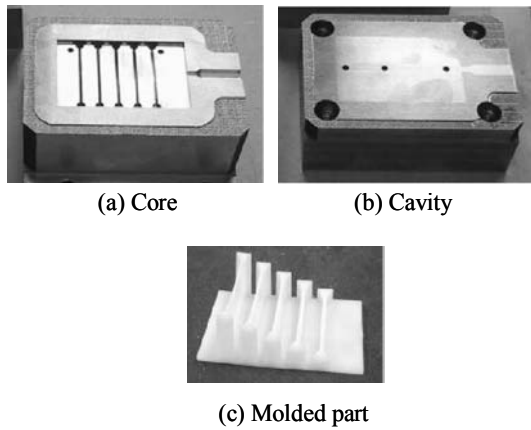


Fig. 4.3. Developed molds and molded work piece

By making the temperature of cavity higher than the temperature of the core, the amount of the warp of the work piece molded by developed molds are compared with those by conventional steel molds. Polyacetal (POM) is chosen for injection resin. The amount of the warp is evaluated in the straightness in the longer direction profile on the top flat board of the molded workpiece. The profile is measured by the three dimensional coordinate measuring machine. Fig. 4.4 shows the measuring points.

Fig. 4.5 shows the profiles of the molded work pieces in each temperature condition. Fig. 4.6 shows the relation between the warp and the temperature difference of core and cavity. In case of the set temperature of core and cavity are 50°C together, the warp is 0.8 mm by the developed molds, but is about 1.0 mm by the steel molds. The molding accuracy improved by 20 % by using the developed mold. When the temperature difference is 20 °C, the warp is about 0.27 mm. Temperature difference of 40 °C is necessary to make the same warp in the steel mold. On the contrary, the temperature difference 40 °C in the developed mold makes the warp of the work piece to the opposite side.

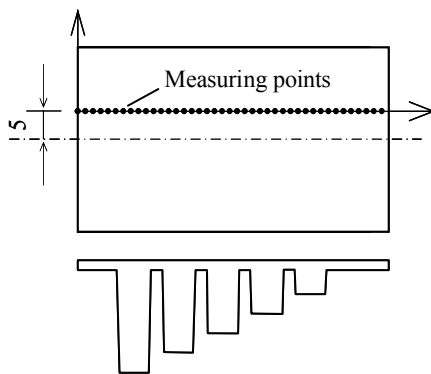
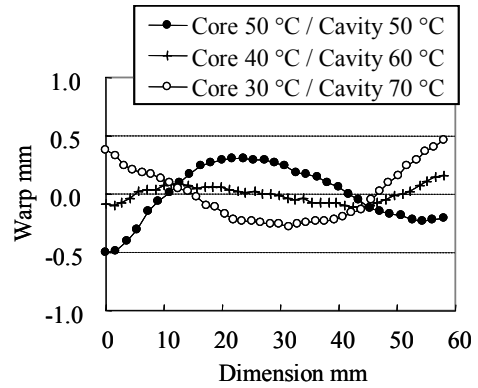
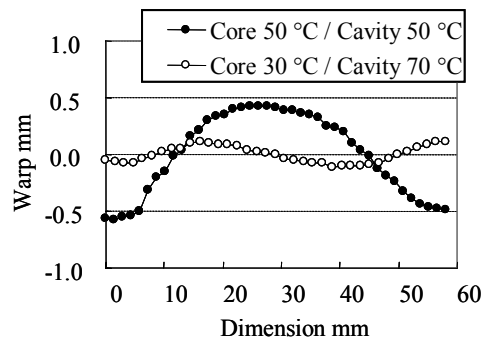


Fig. 4.4. Measuring points



(a) Profiles of molded work pieces - Developed mold



(b) Profiles of molded work pieces - Steel mold

Fig. 4.5. Profiles of the molded work pieces in each temperature condition.

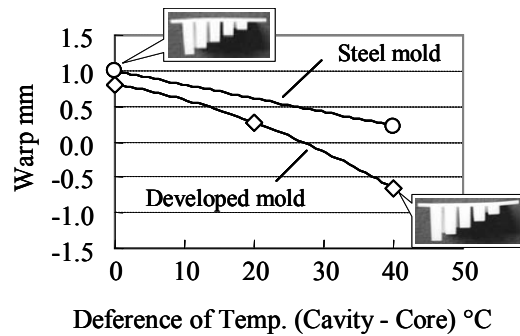


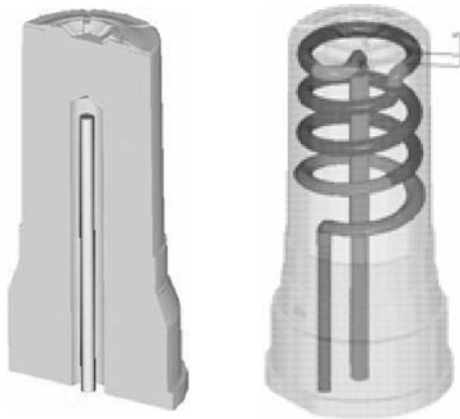
Fig. 4.6. Relation between the warp and the temperature difference of core and cavity

It becomes clear that the accuracy (the warp) of the molded part can be sensitively changed by arranging the cooling channels in the area where the heat accumulates and by controlling the temperature of the molds using Milling-Combined Laser Metal Sintering.



**4.1.2 Reduction of molding cycle time by the three dimensional cooling channels**

It is difficult to set uniform heat distribution in the case of deep cup shape. High cycle molding is realized by applying the three dimensional cooling channels to the mold core of this part. In the conventional molds, baffle type channel was used as shown in Fig. 4.7 (a). The cooling efficiency was not so good because the distance from the channel to the mold surface is far. Milling-Combined Laser Metal Sintering mold which arranged a three-dimensional spiral channel near the mold surface is manufactured as shown in Fig. 4.7 (b) The developed mold is cooled rapidly and equally because the distances of the arranged channels from the mold surface are very short and equal. Fig. 4.8 shows the comparison of the molding cycle time between the developed mold and the steel mold. The whole cycle time is reduced 37 %, specifically the cooling time is reduced 50 %. To reduce molding cycle contributes the production cost reduction directly.



(a) Conventional cooling channel (baffle type) (b) Developed cooling channel (spiral pipe)

**Fig. 4.7.** Construction of cooling channel

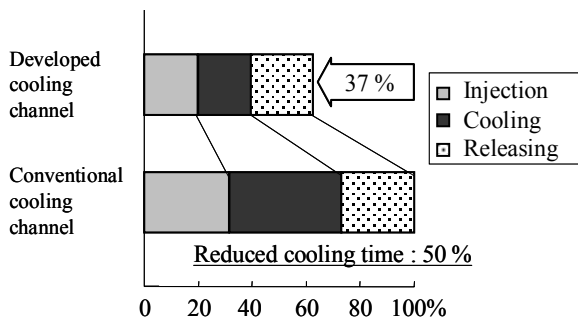


**Fig. 4.8.** Comparison of the molding cycle time

**5 Conclusion**

We have developed the first system of Milling-Combined Laser Metal Sintering in the world and applied to the injection mold for the mass production. The characteristic of this system is to repeat laser assisted metal sintering and high speed milling. In the process more than one layer are sintered by the laser and then, before the height of the sintered layers reaches the effective cutting edge length of the end mill, milling process is inserted. Therefore, the short end mill can mill even the shapes such as deep ribs that were impossible in the past. Because the mold is fabricated in one process, mold manufacturing time is substantially reduced.

Moreover the dimensional accuracy improved remarkably compared with conventional laser assisted metal sintering process because it achieves the same level finishing as the machining center. We have attempted to improve the molding accuracy and high cycle molding applying three dimensional complex cooling channels on the mold using the characteristic of developed process which can freely compose the inside structure.

We have achieved the following.

- $\pm 0.03$  mm dimensional accuracy and  $20 \mu\text{m}$  Rz surface roughness of the mold by applying developed Milling-Combined Laser Metal Sintering System .
- Reduction by half in the mold manufacturing period.
- Improvement and controll of the molding dimensional accuracy is easy by arranging three dimensional cooling channels in the area where the molding heat accumulates.
- High cycle molding is possible by applying the three dimensional cooling channels.

**6.1 References**

[1] Jacobs P. F., et al. (1992) Rapid Prototyping & Manufacturing, Fundamentals of StereoLithography, Society of Manufacturing Engineers, Dearborn

[2] Takeo Nakagawa, Masato Imamura, Yi XU, (1997), Overview of Rapid Prototyping Research and Development in Japan, Proceedings of the 8th ICPE, 3-16

[3] Andre Danzig, M. Shellabear, V. Junior, (2001), Laser Sintering – from Rapid Prototyping to Rapid Manufacturing, ICS Workshop on Computer Aided Materials Engineering and Prototyping

[4] Isao Fuwa, (2000), Laser Sintering of Steel-Based-Powder, Proceedings of the 8th International Conference on Rapid Prototyping, 413-418

---

# Development of Optical Elements with ELID-grinding and MRF Synergistic Finishing Process

W. Lin, H. Ohmori, Y. Uehara, Y. Watanabe, T. Suzuki, and S. Yin  
Discovery Research Institute, RIKEN (The Institute of Physical and Chemical Research)

## 1. Introduction

In the Laser optical system, many high quality aspheric mirrors are used. Appropriate optical components used in that system must have the ability to withstand damage caused by radiation and high heat load, which limits material selection. Fused silica, single crystal silicon, silicon carbide, etc. are the most commonly used materials. However, both very low surface roughness and very high form accuracy are required simultaneously for optical surfaces. Fabrication of them is very difficult, especially when short wave light source is applied in the optical system. Usually lapping is implemented to obtain the required form accuracy, and then polishing is carried out to attain the desired surface roughness. But the form accuracy is very difficult to maintain during the polishing process in which soft elastic polishing pad and loose abrasive were employed. One of the authors has proposed a new grinding technique that produces high surface quality: “ELID (electrolytic in-process dressing)-grinding”. This new technique is expected to contribute greatly to precision grinding particularly in the field of mirror finishing hard and brittle materials. The ELID-grinding can produce ultra precision grinding performances for aspheric optical elements especially under the specific machine specifications such as hydrostatic bearing and submicron feeding control.

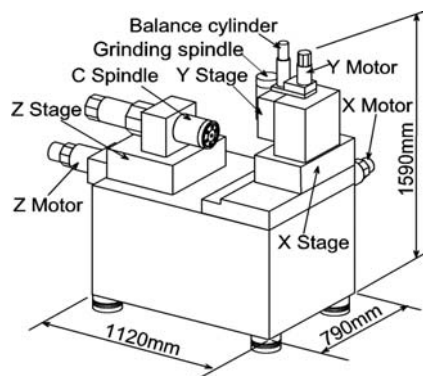


Figure 1 Schematic of ELID-grinding machine.

In this paper, we proposed a complex finishing process of ELID grinding and the MRF, and applied this method to nano-precision finishing of silicon mirrors. ELID grinding, as the pre-finishing, was employed to obtain high efficiency and form accuracy, and then, MRF, as the final finishing, was used to improve furthermore surface quality and figure accuracy. Several sets of finishing experiments for silicon mirrors have been performed to verify obtainable surface figure precision and surface roughness by use of this new synergistic process. Surface accuracy of  $0.333\mu\text{m}$  peak-to-valley and surface micro-roughness less than 10 Angstrom for silicon mirror were produced in high efficiency.

## 2. ELID-grinding and MRF equipments

The truing and ELID grinding processes were conducted on an ultra-precision 4-axes grinding machine (Figure 1) with a maximum resolution of 1nm for 3-axis linear feeding. The specifications of the grinding machine are summarized in Table 1. This machine employs ultraprecision guideways using needle rollers for 3-axes linear feeding. The linearity evaluations of three axes are shown in Table 2. Excellent linearity of 150nm at the full stroke of 300mm for the X-axis was stably achieved on the machine. A characteristic small waviness in the linear movement of approximately 20 to 40nm due to the rolling of the needles was observed.

Figure 2 shows the MRF machine. A workpiece is installed at a fixed distance from a moving spherical wheel. An electromagnet located below the wheel surface generates a gradient magnetic field in the gap between the wheel and workpiece. When the MR fluid is delivered to the wheel, it is pulled against the wheel surface by the magnetic field gradient. The fluid acquires the wheel velocity, develops high stresses, and becomes a subaperture polishing tool. Specifications of the MRF machine are shown in Table 3. The system is based on a five-axis CNC platform ( X, Y, Z, A, B) with a positioning accuracy of a micron. Axis-asymmetric and symmetric lens or mirror can be finished. Two main toolpath, the spiral toolpath is for axisymmetric, and the parallel toolpath for non-axisymmetric.

Table 1 Major specifications of grinding machine.

Linear axes (Ultraprecision roller guide)	Range: X300mm, Y75mm, Z150mm Scale resolution: 1nm Maximum feeding speed: 1,000mm/min
C axis (Air hydrostatic bearing)	Maximum rotating speed: 3,000min <sup>-1</sup> Rotating accuracy: 0.03μm Rotary encoder resolution: 1/10,000deg.
Tool spindle (Air hydrostatic bearing)	Maximum rotating speed: 20,000min <sup>-1</sup> Rotating accuracy: 0.02μm Stiffness: 50N/μm(axial), 16N/μm(radial)

Table 2 Linearity evaluation of grinding machine.

Axis	Direction	Straightness/Full stroke	Waviness
X	Horizontal	150nm/300mm	Approx. 20nm
	Vertical	80nm/ 300mm	Approx. 20nm
Y	Horizontal	60nm/ 75mm	Approx. 40nm
	Vertical	50nm/ 75mm	Approx. 20nm
Z	Horizontal	90nm/ 150mm	Approx. 20nm
	Vertical	120nm/150mm	Approx. 20nm

Table 3 Specifications of MRF machine

Workpiece diameter range	φ10~200mm
Workpiece radius range	φ150mm Tooling: cvx hemisphere- 90 mm cc φ50mm Tooling: cvx hemisphere- 35 mm cc
Maximum workpiece weight	7.25kg (including lens holder)
Spindle speed range	10~500min <sup>-1</sup>
Moving range(mm)	X:350; Y:225; Z:220; A:∞°; B: ±100°
Positioning accuracy (mm)	X:±0.01; Y:±0.001; Z:±0.001; A:±4arcsec; B:±4arcsec
CNC machine control	Siemens Simo Drive 611Dw/Sinumerik 840D
Abrasive in MR polishing fluid	Cerium oxide abrasive and diamond abrasive

Table 4 ELID grinding conditions

Grinding machine	Ultraprecision mirror surface 4-axes grinding system with 1nm resolution
Grinding wheel	CIB diamond wheel, φ60×W5 mm, #325, #1200, #4000 Straight type, Concentration: 75
Grinding conditions	Wheel rotational speed: 3000min <sup>-1</sup> , Workpiece rotational speed: 500min <sup>-1</sup> , Feed-rate: 5mm/min, Depth of cut: 1-5μm/pass
ELID conditions	Open circuit voltage ( <i>E<sub>o</sub></i> ) : 80V, peak current ( <i>I<sub>p</sub></i> ): 10A, On/off-time ( <i>τ<sub>on</sub>/τ<sub>off</sub></i> ) : 2/2μs, Pulse wave: Square
Workpiece	Material: Silicon; Size: φ40mm
Grinding fluid	Chemical-solution-fluid (2% dilution of water)

### 3. Grinding and experimental results

#### 3.1 Grinding experimental conditions

Several concave silicon specimens (Full aperture 40mm, Clear aperture 35mm in diameter, 1800mm radius of curvature) were generated by ELID-grinding in an ultra-precision machining system. Several cast iron bonded (CIB) diamond wheel SD#325, SD1200, SD4000 were computer-controlled to scan the workpiece to generate required sphere (Figure 3). Grinding and ELID conditions are shown in Table 4. Grinding wheel was trued by #140 truing wheel in assistance with ELID.



Figure 2 MRF polishing machine



Figure 3 ELID-grinding of silicon mirror

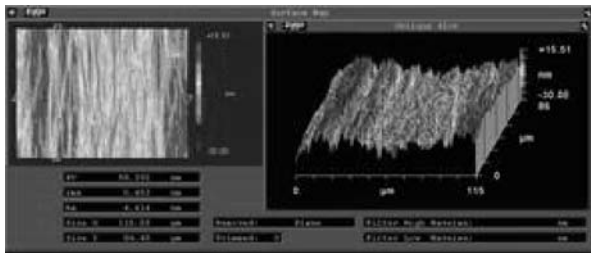


Figure 4 Surface roughness of #4000 ELID grinding

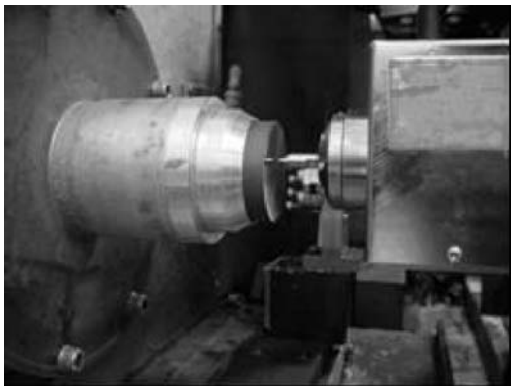


Figure 5 On-machine measuring of form error

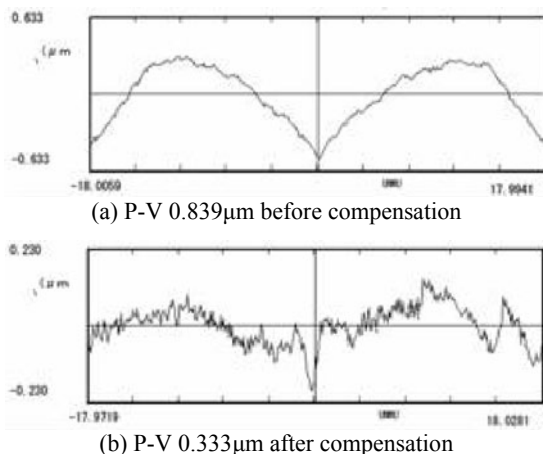


Figure 6 Form deviation profile measured by on-machine measure system

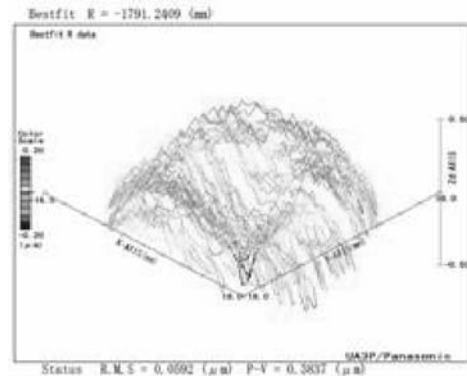


Figure 7 Form deviation profile measured by AFP

### 3.2 Grinding results

Figure 4 shows ground surface optical map. As shown in Figure 4, ground surface by #4000, generated in ductile mode, surface micro-roughness less than rms 5.45nm was obtained.

The ground surface figure by #4000 wheel was measured with on-machine measure system as shown in Figure 5. Form deviation profile from the designed curved surface after fitting is shown in Figure 6(a). Form accuracy in X-direction was about 0.839 $\mu\text{m}$  p-v. Tool path compensation, initial tool diameter compensation were conducted. Initial ground surface was measured for calculating the distribution of the form deviation profiles. With these deviation profiles, the NC data was compensated. As shown in Figure 6(b), form accuracy was improved remarkably to 0.333 $\mu\text{m}$  P-V. Form deviation profile measured by AFP(Atomic Force Plofilometer) are shown in Figure 7, measured result was 0.384 $\mu\text{m}$  P-V. This data was very near to the result measured by on-machine measure system.

### 3.3 MRF experiments and results

Table 5 shows the MRF conditions, and Figure 8 shows the external view of MRF for silicon mirror. Figure 9 shows the removal "spot" for silicon mirror, immersed in the MR suspension for 3 second (conditions described in Table 5). The peak removal rate may be calculated to be about 3.09 $\mu\text{m}/\text{min}$  and the volume removal rate is 0.021 $\text{mm}^3/\text{min}$ .

The finished surface form was measured by AFP. The form accuracy was improved down to 0.22 $\mu\text{m}$  in P-V (Figure 10) from 0.39 $\mu\text{m}$  p-v before MRF (after ELID grinding, Figure 5). From this result we know that the figure corrective ability is high. It is seen that extremely high form accuracy and surface micro-roughness could be realized simultaneously in a high efficiency. As a result, surface micro-roughness rms 0.96nm down to from rms 5.45nm was improved. In a short time (17min), a silicon mirror surface could be finished to sub-nanometer surface micro-roughness. Figure 11 shows the polished sample.

Table 5 MRF conditions

MRF machine	Q22Y MRF system
Finishing mode	Uniform removal & figure correction
Workpiece	Materials: silicon, $\phi$ 40mm, concave surface, curvature radius R1200 mm
Delivery system setting	Magnet: 12A; Wheel revolution :450rpm;Suction pump revolution :120rpm; Centrifugal pump revolution: 2800rpm
Delivery system reading	Pressure:6.84PSI; Flow rate:0.2l/m; Viscosity: 37.0cP;
Ribbon parameters	Wheel: 50mm; Ribbon height:0.97mm; Gap: 0.66mm; Depth 0.33 mm
MR Fluid	diamond abrasive
Finishing time	15 min



Figure 8 External view of MRF for silicon mirror

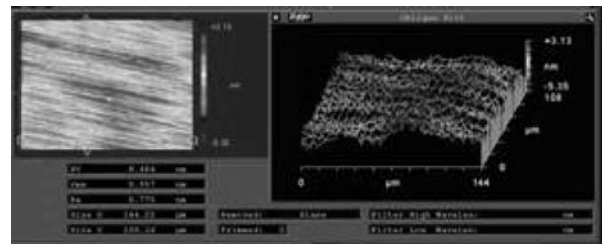


Figure 11 Optical roughness map of surface after MRF

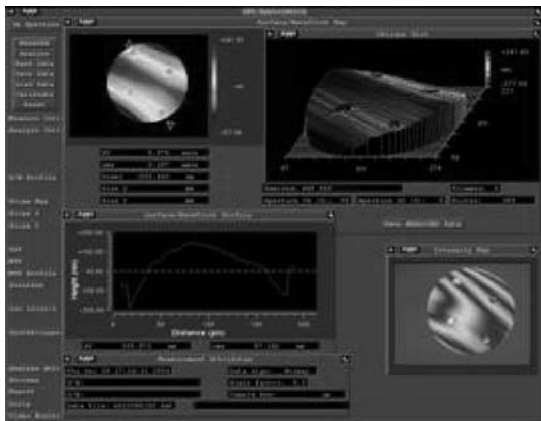


Figure 9 Surface roughness after taking spots

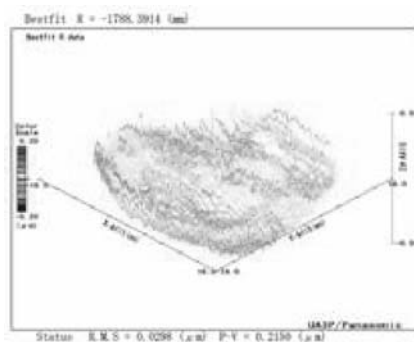


Figure 10 3D surface profile map measured by AFP

#### 4. Conclusions

By applying the ultraprecision synergistic finishing process of ELID-grinding and MRF, surface accuracy of the 0.333  $\mu$ m peak-to-valley and surface micro-roughness less than 10 Angstrom for silicon mirror were successfully produced in a high efficiency.

#### 5. References

- [1] H.Ohmori, et al: Mirror Surface Grinding of Silicon Wafer with Electrolytic In-Process Dressing, Annals of the CIRP, 39, 1 (1990), 329-332.
- [2] H.Ohmori, et al: Analysis of Mirror Surface Generation of Hard and Brittle Materials by ELID (Electrolytic In-Process Dressing) Grinding with Superfine Grain Metallic Bond Wheels, Annals of the CIRP, 44, 1 (1995), 287-290.
- [3] H.Ohmori, et al: Improvement of Mechanical Strength of Micro Tools by Controlling Surface Characteristics, Annals of the CIRP, 52, 1 (2003), 467-470.
- [4] H.Ohmori, et al: Advanced Desktop Manufacturing System for Micro-Mechanical Fabrication, Laser Metrology and Machine Performance VII, Lamdamap 2005, euspen (2005), 16-29.
- [5] H.Ohmori, et al: Investigation of Substrate Finishing Conditions to Improve Adhesive Strength of DLC Films, Annals of the CIRP, 54, 1 (2005), 511-514.
- [6] A.Nakao, M.Kaibara, et al: XPS and SERS studies of cell adhesion controlled polymer modified by Ne-ion bombardment, Surf.Inter.Anal.24 (1996), 252-257.
- [7] F. Yatagai: Mutation Induced by Heavy Charged Particles. Biol. Sci. Space, 18 (2005), 224-234.

---

## Fabrication of Ultraprecisely Figured Mirror for Nano Focusing Hard-x-ray

Hirokatsu Yumoto<sup>1</sup>, Hidekazu Mimura<sup>1</sup>, Satoshi Matsuyama<sup>1</sup>, Souichiro Handa<sup>1</sup>, Kazuya Yamamura<sup>2</sup>, Yasuhisa Sano<sup>1</sup>, Katsuyoshi Endo<sup>2</sup>, Yuzo Mori<sup>2</sup>, Makina Yabashi<sup>3</sup>, Yoshinori Nishino<sup>4</sup>, Kenji Tamasaku<sup>4</sup>, Tetsuya Ishikawa<sup>4</sup>, and Kazuto Yamauchi<sup>1</sup>

<sup>1</sup>Department of Precision Science and Technology, Graduate School of Engineering, Osaka University, <sup>2</sup>Research Center for Ultra-Precision Science and Technology, Graduate School of Engineering, Osaka University, <sup>3</sup>Spring-8/Japan Synchrotron Radiation Research Institute (JASRI), <sup>4</sup>Spring-8/RIKEN

Keywords: hard X-ray mirror, X-ray nanofocusing, At-wavelength wave-front metrology, surface metrology

### Abstract

We developed a novel at-wavelength metrology for the surface figure of hard x-ray focusing mirrors. The metrology, which evaluates the wave-front error of the focusing beam, is based on the numerical calculation of intensity distribution profiles around the focal point. We demonstrated the at-wavelength metrology of a total reflection mirror. The recovered phase error profile of the test mirror using the at-wavelength metrology was in good agreement with the profile measured using an optical interferometer. This result indicates the effectiveness of the developed metrology. This technique is expected to be applied to manufacturing processes for realizing diffraction-limited nano focusing optics.

### 1 Introduction

Precision engineering encourages the development of industries and progress in the fields of scientific technologies. In recent years, a combination of third-generation synchrotron radiations and optical elements, which are based on ultraprecision machining technology, has enabled the realization of hard x-ray nanobeams with lateral beam sizes less than 100 nm. Hard x-ray nanobeams are applied to scanning hard x-ray microscopy, microdiffraction analysis, and spectromicroscopy in analyses in medicine, chemistry, materials science, and other science fields. The spatial and contrast resolutions of these microscopes are determined not only by the focusing size of the hard x-ray beam, but also by the intensity distribution properties of the focused beam. An ideally focused beam, the so-called diffraction-limited focused beam, allows one to obtain an excellent resolution of the microscope used. There are many types of hard x-ray focusing optics, which utilize refraction, reflection, and diffraction effects, such as Fresnel Zone plates, Kirkpatrick-Baez (K-B) mirrors, compound refractive lenses, Bragg-Fresnel lenses, and capillaries. The focusing probes generated using K-B mirrors, which utilize two glancing-angle concave mirrors to collect and focus x-rays in both vertical and horizontal axes, have a high efficiency

compared with other optics. A two-dimensional hard x-ray focused beam of  $36 \times 48 \text{ nm}^2$  full width at half maximum (FWHM) that was nearly a diffraction-limited beam at an x-ray energy of 15 keV was obtained using K-B mirrors in our previous research [1].

The quality of the focusing probes obtained by K-B mirrors is influenced by optical design, surface figure accuracy, degree of coherence of illumination light, and alignment accuracy. We have developed the manufacturing process of directly figured elliptical mirrors for diffraction-limited focusing in hard x-rays and applied them to a scanning x-ray microscope [2]-[4]. Computer-controlled plasma chemical vaporization machining (PCVM) [5] and elastic emission machining (EEM) [6] can figure mirror surfaces to a peak-to-valley (PV) accuracy better than 1 nm and lateral resolutions close to 0.1  $\mu\text{m}$  [1],[7],[8]. In addition, surface figure metrology combining microstitching interferometry (MSI) [9] with relative angle determinable stitching interferometry (RADSI) [10] can measure the surface profiles of an x-ray mirror to a PV accuracy higher than 3 nm and a spatial resolution close to 10  $\mu\text{m}$ .

One of the most important matters regarding hard x-ray focusing is the improvement of the focusing beam size. To realize a smaller focusing size, mirrors with steeply curve having a larger numerical aperture (NA) are necessary. In this study, we designed a multilayer mirror for focusing hard x-rays to a sub-10-nm size. As we will describe, we examined the acceptable tolerance of wave-front error to realize diffraction-limited sub-10-nm focusing. The wave-front aberration tolerance places extremely high demands on the fabrication of mirror substrates and multilayer coatings, and even higher demands on the metrology tools required evaluating mirror surface qualities. Conventional surface metrologies are not sufficient for evaluation of the sub-10-nm focusing mirrors. Wave-front metrology is an essential tool for the development of the optical systems for the extreme ultraviolet (EUV) lithography [11]. In addition, the system performance, composed of the geometric figure of the substrate surface and the properties of the multilayer coatings, is measurable only at the operational wavelength.

In this study, we suggest a new method of at-wavelength metrology for evaluating diffraction-limited focusing mirrors

**Table 1.** Optical parameters of designed mirror

Mirror length	100 mm
Length of ellipse	500.075 m
Breadth of ellipse	135.9 mm
Focal length	150 mm
Glancing angle on optical axis	11.1 mrad
Acceptance width	1.1 mm
Surface coating	Multilayer

in the hard x-ray region. At-wavelength metrology for estimating the wave-front aberration on reflected x-rays is based on the numerical calculation method using the intensity distribution around the focal point.

We demonstrated the at-wavelength metrology for total-reflection mirror at 15 keV. An experiment for measuring the focusing intensity profile was performed at the 1-km-long beamline (BL29XUL) of SPring-8. The calculated profile was in good agreement with that measured by an optical interferometer, which indicates effectiveness of the developed method.

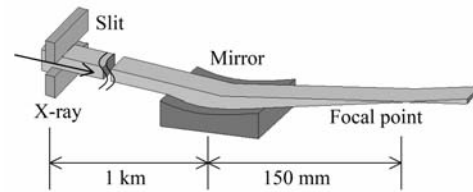
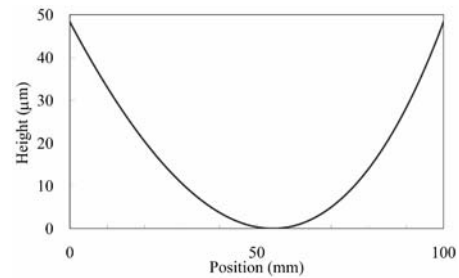
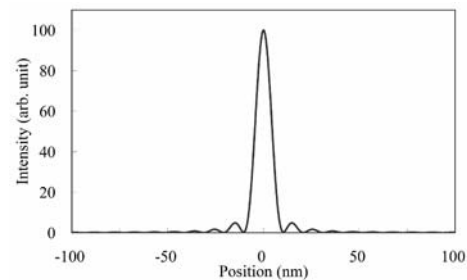
## 2 Optical design for sub-10-nm focusing

### 2.1 Design of optical parameter

We designed the line-focusing mirror with a large NA having a 1.1 mm aperture size and a 100 mm long working distance assuming application of this mirror in a microscope system. Figure 1 shows the schematic drawing of the layout of optical system for line focusing. Table 1 lists the optical parameters of the sub-10-nm focusing system. Figure 2 shows the figure profile of the designed 100-mm-long mirror substrate. The substrate surface shape is part of an elliptical function in which one focal point is the light source and the other is the focal point. The mirror was designed for the 1-km-long beamline [12] of SPring-8 where the mirror aperture can be coherently illuminated. The incidence angle on the optical axis is 11.1 mrad. By coating graded multilayers [13], which fulfill the Bragg diffraction condition, a high reflectivity can be maintained at an incidence angle larger than the critical angle of the substrate material. Figure 3 shows the predicted intensity profile at a focal plane at an x-ray energy of 15 keV, which is obtained using a wave-optical simulator [14] coded on the basis of the Fresnel-Kirchhoff diffraction integral theory. The ideal focusing size is 9.2 nm (FWHM).

### 2.2 Acceptable tolerance of wave-front error

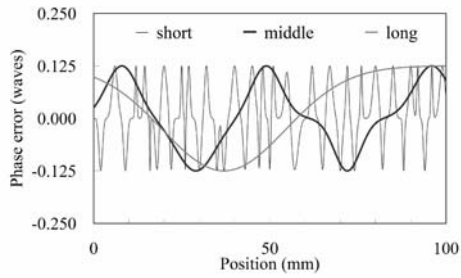
We examined the acceptable tolerance of wave-front error to realize the diffraction-limited sub-10-nm focusing in this optical system. A wave-front accuracy of  $1/4 \lambda$  ( $\lambda$  is wavelength) is required in accordance with Rayleigh's


**Fig.1.** Schematic drawing of layout of optical system for line focusing with single reflective mirror.

**Fig.2.** Surface figure profile of designed mirror substrate for nanofocusing of hard x-rays.

**Fig.3.** Intensity profile of ideally focused x-ray beam at 15 keV, which is calculated using wave-optical simulator.

quarter wavelength rule [15]. The wave-front error  $\varphi$ , attributed to the figure error height  $d$ , is expressed by the following equation in grazing-incidence total reflection mirror optics.

$$\varphi = 2 d k \sin \theta. \quad (1.1)$$

Here,  $\theta$  is the glancing angle of an incident beam at the reflecting point, and  $k$  is the wave number. Wave-front error corresponds to the figure error in this optical system. The mutual relationships between the figure error characteristics and the focusing performances were investigated using the wave-optical simulator. Figure 4 shows the phase error profiles characterized in short, middle, and long spatial wavelength ranges in the longitudinal direction of the mirror. The PV phase error height is  $1/4 \lambda$ , which is equal to a figure error height of 0.93 nm at the optical axis of this mirror. Figure 5 shows the calculated intensity profiles of focused x-ray beams using the elliptical mirror having the phase errors shown in Fig. 4. This simulation results indicate that the phase errors in the middle spatial wavelength range deform the shape of the focal beam profiles and that the phase errors



**Fig. 4.** Phase error profiles assumed on mirror surface characterized in short, middle, and long spatial wavelength ranges used in simulation for estimating wave-front aberration tolerance. PV phase error height corresponds to  $1/4 \lambda$ .

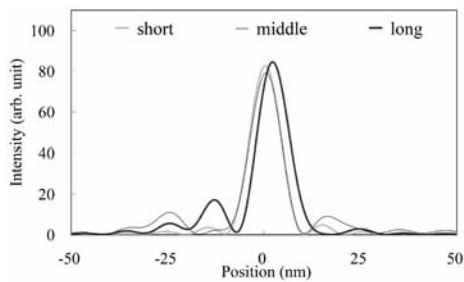


**Fig. 5.** Calculated intensity distribution profiles of focused x-ray beams using designed mirror having phase error shown in Fig. 4 at an x-ray energy of 15 keV.

in the short spatial wavelength range decrease the intensity of the focused beam. From these results, a PV figure error height of lower than 0.93 nm equal to a phase error of  $1/4 \lambda$  accuracy is necessary for metrology to realize the diffraction-limited focusing beam. By using the optical interferometer, the short spatial wavelength range is measurable with a 0.1 nm height accuracy. Metrology in the middle spatial wavelength range is desired.

### 3 At-wavelength metrology

We developed an evaluating method of phase error on the focusing wave-front x-ray due to the imperfection of the mirror. The observable physical value is the reflected intensity distribution without its phase information from the test mirror. Reconstructing the phase only from the intensity information is referred to as a phase problem. A Fourier-based iterative algorithm [16]-[18] and other algorithms [19],[20] have been used to perform such a reconstruction. We developed two types of phase-retrieval program in this study. One is based on an iterative transform algorithm and the other one is based on linear optimization algorithms. In the two retrieval programs, we applied the designed optical arrangement and propagation model in the developed wave-optical simulator for investigating the intensity distribution reflected by the test mirror. Furthermore, we assumed a point light source or a transverse coherence length of infinity at the

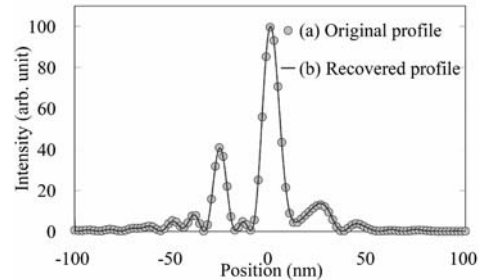


**Fig. 6.** Results of numerical simulation of phase retrieval algorithm. Intensity distribution profiles at focal point. (a) Original intensity profile. (b) Reconstructed intensity profile.

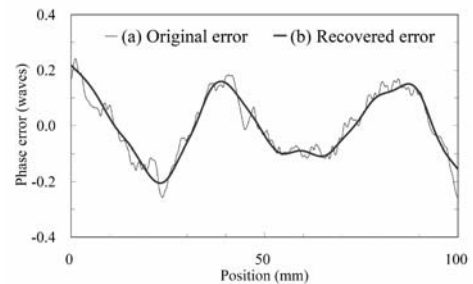


**Fig. 7.** Results of numerical simulation of phase retrieval algorithm. Phase error distribution on ideally shaped mirror surface. (a) Original phase error. (b) Phase error distribution reconstructed from intensity at focal point.

light source in the model, because this enables significant simplification of the algorithm. In the designed optical system, x-rays illuminating the mirror are produced at an undulator and propagate for long distance of 1 km. The system provides reasonable estimation of the light source.

#### 3.1 Iterative transform method

The wave-front error of the focusing beam is calculated on the basis of an error-reduction algorithm [21]. The mirror is assumed to shift the phase of the reflected wave and change the known intensity, because of its imperfections. Mirror acts as a pure phase object in the developed phase retrieval program. Wave-front error calculation was performed from a single intensity distribution. The intensity on the mirror and at the focal point are sampled to satisfy the conditions of Nyquist's sampling theorem. In this program, the intensity of the focal point and on the mirror surface is replaced with the measured amount and the phase is recovered gradually in each iterative procedure.

Simulation was performed to explore the characteristics of the phase retrieval algorithm. The phase on a perfectly elliptical shape surface is taken as the initial point of the iteration algorithm. The surface figure of the mirror can be measured approximately using the optical interferometer. The simulated optical system is the designed one to achieve sub-10-nm focusing and the assumed phase error on the mirror surface is shown in Figure 7 (a). Figure 6 shows the focusing intensity profiles recovered (b) and set as the original value (a). Figure 7 (b) shows the recovered phase



error on the ideal surface curve. Approximately 1000 iterations were performed to obtain the result. From the intensity profile including no measurement noise, accuracy on the order of 0.030 waves root-mean-square (RMS) was simulated under these conditions.

The Fourier transform of the complex amplitude distribution on the focusing light wave becomes a complex amplitude distribution at the focal point. From this viewpoint, the intensity distribution at the focal point is more sensitive to the middle and long spatial wavelength ranges than the short one. This wave-front metrology has a higher potential for evaluating focusing optics than optical interferometer.

### 3.2 Linear optimization method

The other approach to determining wave-front error is the iteration method, which minimizes the differential intensity between experimental and simulated data only by solving a direct problem. A wave-front error is expressed as a weighting function of unit phase error. The error parameters are composed of PV height and spatial wavelength in the longitudinal direction of the mirror. This method is sure to find the solution even if the measured intensities have noise. One of the main problems of this phase retrieval method is the long computation time. To overcome this difficulty, the coded program was substantially simplified. An iterative procedure is continued until no further improvement is observed.

To avoid the local minimum problem, the two developed algorithms are combined to calculate wave-front error using the measured intensity distribution. Additional intensity measurements around the focal point can be of assistance in performing high-precision computation.

## 4 Experiment

At-wavelength wave-front metrology was demonstrated using a total reflection mirror at an x-ray energy of 15 keV. An experiment was performed at the 1-km-long beamline (BL29XUL) of SPring-8. The test mirror has a much smaller NA compared to the designed sub-10-nm focusing mirror. So the test mirror surface shape can be measured with a high accuracy by MSI. In addition, focusing intensity profiles of 200 nm (FWHM) can be detected accurately using a wire scanning method. The optical parameters of this mirror are shown in Table 2. Figure 8 shows (a), (b) the measured intensity profile and (c) the recovered intensity profile using the retrieval algorithm at the focusing point. The intensity profiles were detected at 25 nm and 50 nm intervals independently. Figure 9 shows the phase error profiles on the test mirror surface (a) measured by MSI and (b) recovered using the retrieval algorithm. In this optical system, the phase error of  $1/4 \lambda$  corresponds to a figure error height of 7.4 nm at the mirror center. Although the retrieval accuracy depends on the intensity measurement precision of the focusing beam, the difference in wave-front error between the two phase errors is 0.052 waves RMS. The good agreement between the two figure error profiles in the middle spatial wavelength range proves the high capability

**Table 2.** Optical parameters of test mirror.

Substrate material	CZ-Si (111) single crystal
Surface coating	None
Effective mirror length in longitudinal direction	90 mm
Length of ellipse	500.15 m
Breadth of ellipse	24.25 mm
Focal length	300 mm
Glancing angle on optical axis	1.40 mrad
Acceptance width	130 $\mu\text{m}$

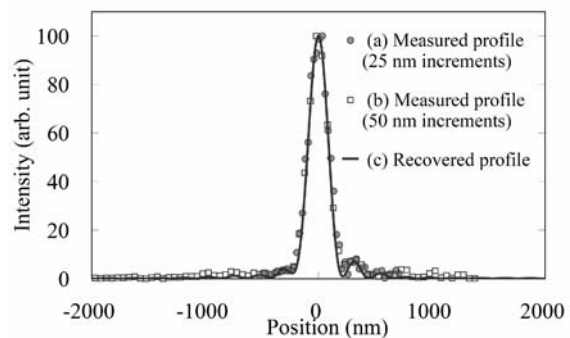


**Fig. 8.** Experimental results of at-wavelength metrology. Intensity distribution profiles at focal point at an x-ray energy of 15 keV. (a), (b) Measured intensity profile using wire-scanning method. (a) Circles denote 25 nm increments and (b) open squares denote 50 nm increments. (c) Reconstructed intensity profile using phase retrieval algorithm.

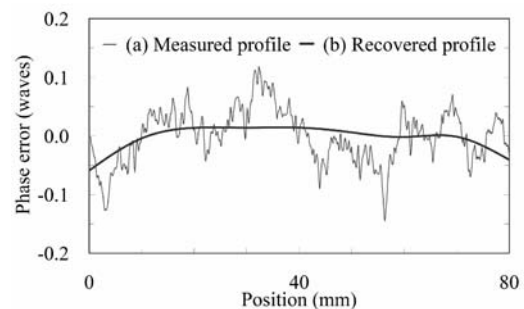


**Fig. 9.** Experimental results of at-wavelength metrology. Phase error distribution on ideal shape plane of focusing mirror. (a) Measured profile using optical interferometer. (b) Reconstructed profile from measured intensity profile at focal point.

of the developed metrology not shared by conventional surface metrologies to realize diffraction-limited focusing.

## 5 Results

We have developed and demonstrated efficient at-wavelength wave-front metrology. Realization of the sub-10-nm diffraction-limited focusing require a manufacturing process consisting of the at-wavelength assessment of the fabricated mirror and the phase correction of wave-front aberration on the basis of the estimated phase error. Therefore, the at-wavelength wave-front metrology presented here is an indispensable tool. The phase correction of the multilayer mirror in the hard x-ray region has been shown possible by an additional deposition method [22]. One of the technical considerations of the process is the accuracy of the characterizing method for the sub-10-nm focusing intensity distribution. Several techniques have been used to evaluate the nanobeams [23]-[27], however, these have not been demonstrated in the sub-10-nm region.

At-wavelength wave-front metrology is also applicable to microdiffraction, in which the illuminated x-ray wave-front over the object must be known. Sub-10-nm hard x-ray probes with extremely intense light will revolutionize the field of microscopy. This technique offers the ability to realize nondestructive analyses of the internal structure of materials with the same spatial resolution as electron microscopy and AFM (atomic force microscopy), and moreover, to realize monomolecular resolution analyses.

## 6 Acknowledgement

This research was supported by Grant-in-Aid for Scientific Research (S), 15106003, 2004 and the 21st Century COE Research, Center for Atomistic Fabrication Technology, 2004 from the Ministry of Education, Sports, Culture, Science and Technology.

## 7 References

- [1] H. Mimura et al., (2005) Hard X-ray Diffraction-Limited Nanofocusing with Kirkpatrick-Baez Mirrors. *Jpn. J. Appl. Phys.* 44, 539
- [2] S. Matsuyama et al., (2005) Diffraction-limited two-dimensional hard-x-ray focusing at the 100 nm level using a Kirkpatrick-Baez mirror arrangement. *Rev. Sci. Instrum.* 76, 083114
- [3] H. Yumoto et al., (2005) Fabrication of elliptically figured mirror for focusing hard x rays to size less than 50 nm. *Rev. Sci. Instrum.* 76, 063708
- [4] S. Matsuyama et al., Scanning hard-X-ray microscope with spatial resolution. *Jpn. J. Appl. Phys.* in press.
- [5] K. Yamamura et al., (2003) Fabrication of elliptical mirror at nanometer-level accuracy for hard x-ray focusing by numerically controlled plasma chemical vaporization machining. *Rev. Sci. Instrum.* 74, 4549
- [6] K. Yamauchi, H. Mimura, K. Inagaki, and Y. Mori, (2002) Figuring with subnanometer-level accuracy by numerically controlled elastic emission machining. *Rev. Sci. Instrum.* 73, 4028
- [7] H. Mimura et al., (2004) Image quality improvement in a hard X-ray projection microscope using total reflection mirror optics. *J. Synchrotron Rad.* 11, 343
- [8] K. Yamauchi et al., (2003) Two-dimensional Submicron Focusing of Hard X-rays by Two Elliptical Mirrors Fabricated by Plasma Chemical Vaporization Machining and Elastic Emission Machining. *Jpn. J. Appl. Phys., Part 1* 42, 7129
- [9] K. Yamauchi et al., (2003) Microstitching interferometry for x-ray reflective optics. *Rev. Sci. Instrum.* 74, 2894
- [10] H. Mimura et al., (2005) Relative angle determinable stitching interferometry for hard x-ray reflective optics. *Rev. Sci. Instrum.* 76, 045102
- [11] H. Meddecki, E. Tejnil, K. A. Goldberg, and J. Bokor, (1996) Phase-shifting point diffraction interferometer. *Opt. Lett.* 21, 1526
- [12] K. Tamasaku, Y. Tanaka, M. Yabashi, H. Yamazaki, N. Kawamura, M. Suzuki, and T. Ishikawa, (2001) SPring-8 RIKEN beamline III for coherent X-ray optics. *Nucl. Instrum. Methods Phys. Res. A* 467–468, 686
- [13] Ch. Morawe, P. Pecci, J. Ch. Peffen, and E. Ziegler, (1999) Design and performance of graded multilayers as focusing elements for x-ray optics. *Rev. Sci. Instrum.* 70, 3227
- [14] K. Yamauchi et al., (2005) Wave-optical evaluation of interference fringes and wavefront phase in a hard-x-ray beam totally reflected by mirror optics. *Appl. Opt.* 44, 6927
- [15] M. Born and E. Wolf, *Principles of Optics*, 6th ed. (Cambridge University Press, 1997), p. 468.
- [16] J. Miao, P. Charalambous, J. Kirz, and D. Sayre, (1999) Extending the methodology of X-ray crystallography to allow imaging of micrometre-sized non-crystalline specimens. *Nature (London)* 400, 342
- [17] Y. Nishino, J. Miao, and T. Ishikawa, (2003) Image reconstruction of nanostructured nonperiodic objects only from oversampled hard x-ray diffraction intensities. *Phys. Rev. B* 68, 220101
- [18] H. M. Quiney, A. G. Peele, Z. Cai, D. Paterson, and K. A. Nugent, (2006) Diffractive imaging of highly focused X-ray fields. *Nature Physics* 2, 101
- [19] A. Souvorov, M. Yabashi, K. Tamasaku, T. Ishikawa, Y. Mori, K. Yamauchi, K. Yamamura, and A. Saito, (2002) Deterministic retrieval of surface waviness by means of topography with coherent X-rays. *J. Synchrotron Rad.* 9, 223
- [20] J. R. Fienup, (1993) Phase-retrieval algorithms for a complicated optical system. *Appl. Opt.* 32, 1737
- [21] J. R. Fienup, (1982) Phase retrieval algorithms: a comparison. *Appl. Opt.* 21, 2758
- [22] S. Handa et al., Wavefront phase correction of X-ray multilayer mirror by additional layer deposition: Simulation study. *Nucl. Instrum. Methods Phys. Res. A*, submitted.
- [23] Y. Suzuki, A. Takeuchi, H. Takano, and H. Takenaka, (2005) Performance Test of Fresnel Zone Plate with 50nm Outermost Zone Width in Hard X-ray Region. *Jpn. J. Appl. Phys.* 44, 1994
- [24] W. Liu, G. E. Ice, J. Z. Tischler, A. Khounsary, C. Liu, L. Assoufid, and A. T. Macrander, (2005) Short focal

H. Yumoto, H. Mimura, S. Matsuyama, S. Handa, K. Yamamura, Y. Sano, K. Endo, Y. Mori, et al

- length Kirkpatrick-Baez mirrors for a hard x-ray nanoprobe. *Rev. Sci. Instrum.* 76, 113701
- [25] O. Hignette, P. Cloetens, G. Rostaing, P. Bernard, and C. Morawe, (2005) Efficient sub 100 nm focusing of hard x rays. *Rev. Sci. Instrum.* 76, 063709
- [26] C. G. Schroer et al., (2005) Hard x-ray nanoprobe based on refractive x-ray lenses. *Appl. Phys. Lett.* 87, 124103
- [27] H. C. Kang, J. Maser, G. B. Stephenson, C. Liu, R. Conley, A. T. Macrander, and S. Vogt, (2006) Nanometer Linear Focusing of Hard X Rays by a Multilayer Laue Lens. *Phys. Rev. Lett.* 96, 127401

## Surfaces Formation of Precision ELID Grinding Rock Minerals

Jianyun Shen<sup>1</sup>, Weimin Lin<sup>2</sup>, Hitoshi Ohmori<sup>2</sup> and Xipeng Xu<sup>1</sup>

<sup>1</sup> Provincial Key Research Lab for Stone Machining, Huaqiao University, China

<sup>2</sup> Materials Fabrication Laboratory, The Institute of Physical and Chemical Research, Japan

Keywords: ELID Grinding, Rock, Surface Roughness, Surface Texture

### Abstract

In this study, several kinds of rock minerals with different chemical compositions were finely ground to study the characteristics of smooth stone surface formation. These rock minerals used in the grinding tests were the typical components for decorative stone materials. In order to get precision surfaces, the Electrolytic In-Process Dressing (ELID) grinding technology with different mesh size diamond wheels was applied in experiments. The changes of surface roughness of different rock minerals were measured during the grinding process. The finally ground rock specimens surfaces were analyzed with 3D surface texture analyzer. Based on the micro-observation of rock specimen surfaces, it was found that the rock minerals used in the tests could be finished to smooth surfaces with ELID grinding technology. The results also showed that rock minerals surfaces with different chemical compositions revealed different surface patterns during the grinding process.

### 1 Introduction

Natural stone materials, including granite and marble, are popularly used as surface decorative materials of buildings in architecture industry for their beautiful color and splendid glossiness. The stone surface glossiness is one of the most important quality criterions for the natural stone products. It is closely associated with the material properties and finished surface quality. However, for the complexity of the mineral compositions and texture of stone, it is difficult to describe the formation mechanisms of stone surfaces ground with diamond tools well. In the past research, surface behaviours of ground natural stone were studied to show that the formation of gloss on the surface was mainly related to the grinding technology and its natural defects [1-3].

The ELID grinding technology with metal bond superabrasive diamond wheels have been proven to successfully finish mirror surface for various brittle materials [4,5]. In order to get the basic knowledge for the mechanism of surface formation on stone surface, in the present study, several kinds of rock minerals with different chemical compositions were finely ground with ELID system on a precision surface grinder. With the measurement of surface roughness on ELID-ground surfaces at each grinding stage

and micro-observation of surface texture on the smooth surfaces, the characteristics of rock mineral surface formation were discussed.

### 2 Experimental Methods

In this study, grinding tests of rock minerals were conducted on a MITSUI High-tech precision surface grinding machine with ELID system as illustrated in Figure 1. Three cast iron bond diamond wheels in 205mm diameter with mesh sizes #140, #1200, and #4000 were applied in these experiments, and the depths of cut were 15 $\mu$ m, 2 $\mu$ m, and 1 $\mu$ m separately. The spindle rotational speed was 2000rpm for the whole grinding process, and the condition of ELID grinding system in the tests was also illustrated in Figure 2.



Fig. 1. ELID grinding setup

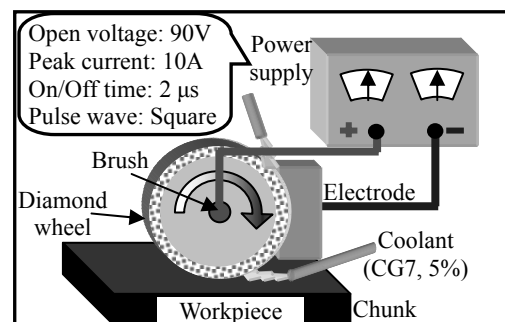


Fig. 2. Illustration of ELID grinding system in the test

The selected rock specimens in the grinding tests were with different chemical compositions, and they were the main components for natural stone, including of granite and marble. There were twelve rock material workpieces used in the experiments, and these workpieces could be classified into four kinds of rock minerals according to the chemical composition: quartz, calcite, fluorite and feldspar. The rock specimens were shown in Figure 3, and the chemical composition for these minerals were  $\text{SiO}_2$ ,  $\text{CaCO}_3$ ,  $\text{CaF}_2$  and  $\text{K(AlSi}_3\text{O}_8)$  respectively. There were five quartz minerals, which were mined from USA, Brazil and South Africa. Four calcite minerals were mined from Mexico. Two fluorite minerals were respectively exploited from Mexico and USA, and the feldspar was from USA. Quartz and feldspar are main mineral compositions of granite, and calcite is main mineral compositions of marble.



Fig. 3. Rock mineral specimens used in the tests

The surface roughness of ground rock surfaces during the grinding process was measured with a non-contact roughness analyzer (Mitaka NH-3) in the measurement length of 4mm. In order to evaluate the micro structure of the finally finished surfaces of rock minerals, the micro characteristics of ground minerals surfaces were analyzed with 3D surface texture analyzer (ZYGO Newview 5032).

### 3 Results and Discussions

#### 3.1 The Surface Roughness of Rock Minerals During the ELID Grinding Process

In the experimental study, all the rock specimens were ELID ground with three mesh size cast iron bond diamond wheels step by step. The topographies of ground surfaces gradually changed from rough to smooth with the decreasing of grit size applied in the grinding tests as shown in Figure 4, which were the typical surface roughness curves of calcite mineral at the different grinding stages. In the past studies, it has been stated that the surface glossiness of stone materials has a non-linear relationship with surface roughness[1,2]. The measurement of surface roughness on the ground stone

surface could be influenced by the natural defects of stone materials. The rock specimens used in the grinding tests were mostly monocrystals with less defects. Therefore, the ground surface topographies of other rock minerals were similar to the roughness curves of calcite mineral.

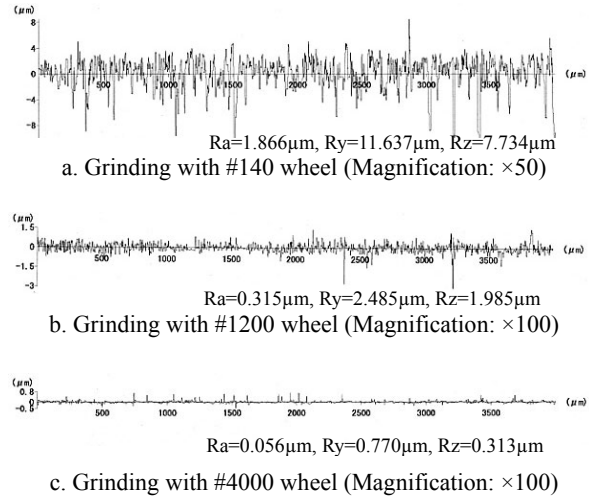


Fig. 4. Surface roughness of the calcite mineral during the grinding process

The surface roughness values of four types of rock mineral workpieces during the ELID grinding process were measured carefully and the average data were calculated to plot the statistic chart in the Figure 5. It can be found that all the rock minerals could be ground to smooth surfaces with the ELID grinding technology in the tests. Because of the rock specimens used in the grinding experiments were monocrystals, and the measurement of surface roughness were picked up on the ground crystal surfaces, the surface roughness in the measurement length of 4mm exhibited similarity under the same grinding condition. The values of surface roughness for these rock minerals were also nearly equal to each other as the statistic data listed in the chart.

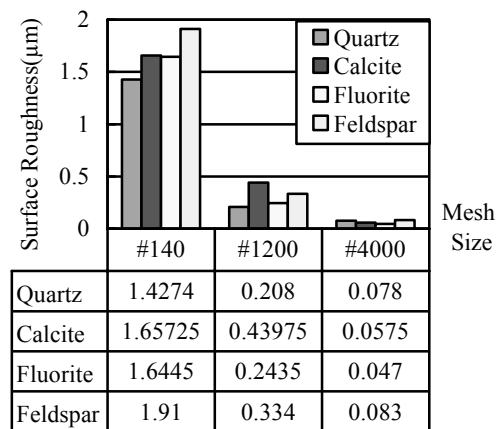
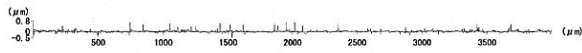


Fig. 5. Surface roughness of rock minerals during the ELID grinding process

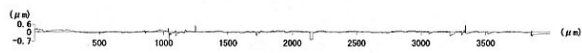
### 3.2 Surface Topographies of Rock Minerals after the Precision ELID Grinding

In order to get smooth ground surface for discussing the surface characteristics of rock minerals, precision ELID grinding with mesh size #4000 cast iron bond diamond wheel was applied as the final stage for the grinding process. After the finely grinding, the surface roughness of four types of rock minerals was measured with non-contact analyzer and the curves were plotted in Figure 6.



Ra=0.053 $\mu$ m, Ry=0.945 $\mu$ m, Rz=0.668 $\mu$ m

a. Quartz (Magnification:  $\times 100$ )



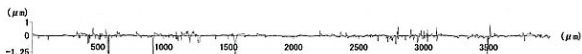
Ra=0.057 $\mu$ m, Ry=0.770 $\mu$ m, Rz=0.313 $\mu$ m

b. Calcite (Magnification:  $\times 100$ )



Ra=0.068 $\mu$ m, Ry=0.992 $\mu$ m, Rz=0.573 $\mu$ m

c. Fluorite (Magnification:  $\times 100$ )



Ra=0.083 $\mu$ m, Ry=1.802 $\mu$ m, Rz=0.972 $\mu$ m

d. Feldspar (Magnification:  $\times 100$ )

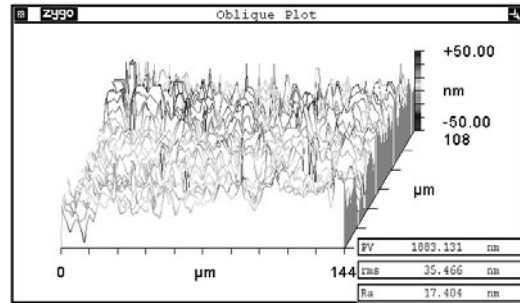
**Fig. 6.** Surface topographies of rock minerals after finely ELID grinding

From the surface topographies, it can be found that all the precision ground rock minerals revealed smooth topographies. The arithmetic average values of roughness Ra listed in the Figure 6 were near to nanometer scale and in the same order of magnitude. However, the peak value of roughness Ry for the ground rock mineral surface showed to be very large. It was really different from precision grinding of artificially synthesized single crystal. From the roughness curves plotted in the Figure 6, it could be seen that there were intermittent irregularity along the roughness curves. Especially, the topography of feldspar mineral was more rough than that of the other rock minerals. It must be due to the micro structure of the rock mineral.

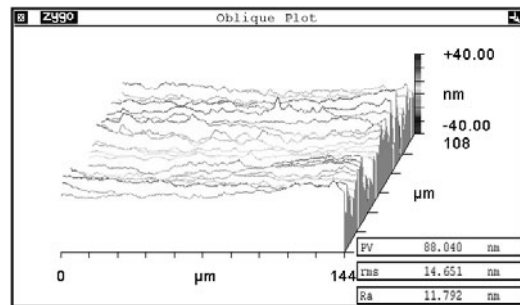
### 3.3 Micro Surface Texture of the Finely Ground Rock Mineral Specimens

For the difference between the surface topographies of different rock minerals, it was necessary to conduct micro observation of precision ground surfaces to analyze the surface characteristics. In the present study, micro observation of the finely finished rock surfaces were carried

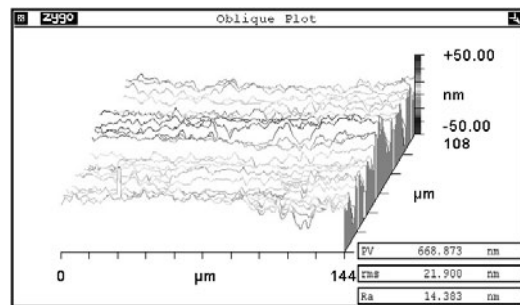
on the 3D surface texture analyzer in detail. The surface texture of these rock specimens was examined and showed in the Figure 7.



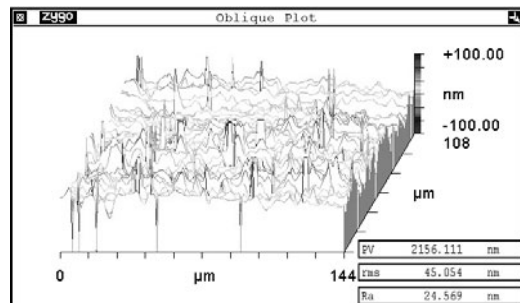
a. Quartz



b. Calcite



c. Fluorite



d. Feldspar

**Fig. 7.** Micro surface texture of finely ELID ground rock minerals

For grinding of brittle material, it has been widely reported that the surface quality is nearly determined by material removal mode during machining process. Usually, high surface quality is generated from extensively ductile regime grinding [6]. From the micro observation of these ground rock material surfaces with surface texture analyzer as shown in Figure 7, ductile removal took place on the surfaces of calcite and fluorite minerals during the precision ELID grinding process. However, the surface texture of quartz and feldspar were much coarser than that of calcite and fluorite minerals, and the coarse surface inevitably led to large values of Ra and PV as the data listed in the Figure 7. The characteristics of micro surface texture should be related to the mechanism of material removal during the grinding process and the natural properties of these rock specimens. The Mohs Hardness of these rock minerals were listed in the Table 1. The quartz and feldspar minerals is harder than calcite and fluorite minerals. Therefore, the machinability of calcite and fluorite should be much better than that of quartz and feldspar minerals, and it led to the perfect ground surfaces in the experiments. Moreover, the feldspar mineral used in the test was with complex chemical composition and rock structure. The results in the Figure 7 also indicated that the natural defects of the mineral caused to comparatively coarse surface after precision ELID grinding.

**Table 1.** Mohs Hardness of rock specimens

Rock Minerals	Quartz	Calcite	Fluorite	Feldspar
Mohs Hardness	7	3	4	6

On the other hand, from the pictures shown in the Figure 3, the texture of the same rock material was also different from one to another for the complexity during the diagenesis process. Therefore, the rock minerals with the same chemical composition but different structure revealed different surface topographies after finely grinding, although these minerals were monocrystals. The micro surface texture of another quartz material was shown in the Figure 8. Compared with the ground quartz surface shown in Figure 7a, it showed that the surface quality of the quartz mineral was much better. The phenomenon was also existed in the precision grinding of other rock minerals.

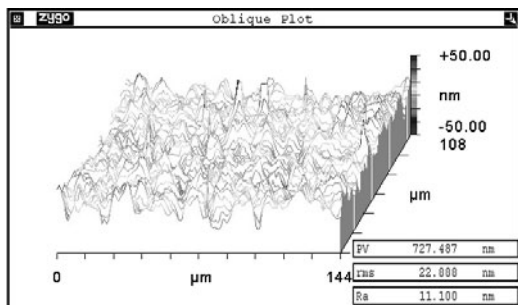


**Fig. 8.** Micro surface texture of finely ELID ground quartz mineral

#### 4 Conclusions

The surface characteristic of ground rock material is determined by not only the grinding process but also the inherence of the natural material. The ELID grinding with superabrasive diamond wheel applied in the tests could finish different natural rock minerals with super smooth surfaces perfectly. However, the original defects of these materials brought great effects to the surface quality and surface roughness characteristics, although these rock minerals were monocrystalline materials. The macroscopic measurement of surface roughness for these rock minerals showed nearly the same surface topographies. But the different chemical composition and structure of natural rock specimens led to different surface behaviours during the grinding process. The micro surface texture showed that the surface quality of rock with higher hardness were with coarser topographies and the natural defects of the mineral caused to comparatively coarse surface after precision ELID grinding.

#### 5 Acknowledgements

The authors would like to give gratefully thanks to Dr. J.C. Guo, Mr. T. Suzuki, and Dr. Y. Watanabe in the Materials Fabrication Lab of RIKEN, for their sincere cooperation in ELID grinding system preparing and micro-observation of ground surfaces. The work was supported by Grant No. 50275055 from the National Natural Science Foundation of China (NSFC) and by Science and Technology Foundation (2003H030, 2002J003) of Fujian Province in China.

#### 6 References

- [1] Wright DN, Rouse C, (1993) Stone polishing measurement of surface finish. *Industrial Diamond Review* 53:10–13
- [2] Xu XP, Huang H, Gao Y, Xu HJ, (2003) Processes for the generation of glossiness on ground granite and ceramics. *Key Engineering Materials* 238–239:99–104
- [3] Shen JY, Lin W, Ohmori H, Xu XP, (2005) Characterization of ELID-ground granite surfaces. *Key Engineering Materials* 291–292:127–132
- [4] Ohmori H, Nakagawa T, (1990) Mirror surface grinding of silicon wafers with Electrolytic In-Process Dressing. *Annals of the CIRP* 39:329–332
- [5] Ohmori H, Nakagawa T, (1995) Analysis of mirror surface of hard and brittle materials by ELID (Electronic In-Process Dressing) grinding with superfine grain metallic bond wheels. *Annals of the CIRP* 44:287–290
- [6] Bifano TG, Dow TA, Scattergood RO, (1991) Ductile regime grinding: a new technology for machining brittle materials. *Transactions of the ASME, Journal of Engineering for Industry* 113:184–189

---

# Dressing of Coarse-Grained Diamond Wheels for Ductile Machining of Brittle Materials

D. Grimme<sup>1</sup>, K. Rickens<sup>1</sup>, Q. Zhao<sup>2</sup>, C. Heinzl<sup>1</sup>

<sup>1</sup>University of Bremen, Laboratory for Precision Machining, <sup>2</sup>Harbin Institute of Technology, Center for Precision Engineering

Keywords: Dressing, Ductile Machining, Diamond Grinding Wheels

## Abstract

Grinding of large optical components in ductile mode with high form accuracy and low subsurface damage is difficult to achieve with fine grained diamond grinding wheels due to wheel wear and the necessity of recurrent dressing. An advanced high precision conditioning method for electroplated coarse-grained diamond grinding wheels for grinding large optical components in optical quality without recurrent dressing is proposed in this paper. This method is used to truncate the tips of each diamond grain on the periphery of the grinding wheel generating a uniform envelope. Therefore a bronze bond diamond cup wheel was applied. Since rapid glazing of the cup wheel occurs during the conditioning process, either the electrolytic in-process dressing technique (ELID) [1] is used or an alumina oxide stick is applied intermittently for dressing the conditioning wheel.

## 1 Introduction

Ductile grinding of brittle materials to achieve mirror-like surfaces with low subsurface damage is typically realized by using fine-grained resin bonded diamond grinding wheels. However, these wheels exhibit certain disadvantages e.g. high wear rate, which limits the achievable figure accuracy and low material removal volume, especially in case of ductile grinding of large optical surfaces. To solve these problems, a new diamond wheel type is applied with a coarse grit size. These monolayer nickel electroplated coarse-grained diamond grinding wheels with grain sizes of approximately 100  $\mu\text{m}$  are conditioned with an advanced technique to meet the high demands of form accuracy, surface quality and low subsurface damage in grinding of large optical components.

Kanai et al. [2] proposed a new design of diamond wheels with mono-crystalline, columnar diamonds co-linearly aligned.

Brinksmeier et al. [3, 4] have proposed a conditioning technique for coarse-grained electroplated diamond wheels using a diamond cup wheel as a dressing tool. Finally a radial run-out error of less than 2  $\mu\text{m}$  was achieved and ductile mode taper grinding was realized on optical glasses.

One problem in manufacturing electroplated nickel diamond wheels is the grain homogeneity of grain concentration and grain protrusion height.

Wakuda et al. [5] have proposed a truncating method to dress a coarse-grained CBN wheel in grinding hardened steel and a mirror-like surface with Ra 0.05  $\mu\text{m}$  was obtained.

T. W. Hwang et al. [6, 7, 8] have used unconditioned electroplated diamond wheels for high speed grinding of silicon nitride and the occurring wheel wear, wheel life, wheel topography and grinding mechanism were investigated. However, there have been no reports so far of the successful application of coarse-grained diamond wheels on ductile contour grinding of optical glasses.

In this research, a conditioning technique integrated with an in-situ wheel run-out monitoring system was successfully developed to condition precisely and efficiently a monolayer nickel electroplated coarse-grained diamond wheel. To determine the applicability of these conditioned grinding wheels grinding experiments on BK7 glass and a PVD-TiNiN coating were carried out.

## 3. Experimental Setup

The general experimental setup is shown in figure 1. The ultra-precision machine tool, used in this investigation, shows 3 hydrostatic linear axes with nanometric resolution and two aerostatic rotary axes. In order to achieve an efficient conditioning process the conditioning diamond bronze bonded cup wheel and the electroplated diamond grinding wheel rotate in counter direction.

For the conditioning process a speed ratio of  $q_d = -0.2$  was applied. The applied general depth of cut  $a_{ed}$  (infed of the conditioning wheel in Z direction) was 1  $\mu\text{m} \div 2 \mu\text{m}$  and the feed rate  $v_{fd}$  (feed speed of conditioned grinding wheel in X direction) was 5 mm/min.

During the conditioning process, the conditioned grinding wheel surface status was monitored in-situ by a coaxial optical distance measurement system with a sampling rate of about 100 Hz. During the runout measurement the grinding wheel rotated with approx. 4 rpm, while dressing the wheel rotated with 3800 rpm ( $v_{cd} = 15 \text{ m/s}$ ). For every 40  $\mu\text{m}$  interval of dressing infed  $a_{ed}$  in Z direction three run-out error measurements at different locations on the wheel peripheral envelope were conducted.



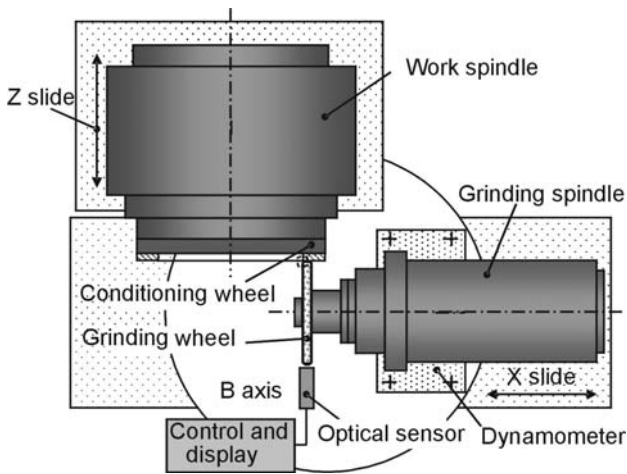


Fig. 1. Experimental setup of the conditioning process

The corresponding wheel surface topography was replicated to investigate the dressing improvement during the conditioning process. A 3-channel dynamometer was used to monitor, both, conditioning and grinding forces. A white light interferometer (WLI) and a precision profilometer were applied to measure the ground surface quality. A large chamber scanning electron microscope (SEM) was used to monitor the diamond grain status of the conditioned grinding wheel; the replica (resin replica duplicated by vinyl polysiloxane impression material) of the conditioned grinding wheel surface morphology were documented by SEM.

#### 4. Experimental Results and Discussion

Figure 2 shows the improvement of the grinding wheel runout error and the corresponding wheel surface topography before and after conditioning with a  $91 \mu\text{m}$  conditioning cup wheel and an overall dressing infeed  $a_{ed} = 200 \mu\text{m}$ . As the conditioning process went on the wheel run-out error decreased from about  $18 \mu\text{m}$  to  $1 \mu\text{m}$ - $2 \mu\text{m}$ . There are different initial run-out-errors distributed alongside the wheel peripheral envelope not only due to the wheel core manufacturing error, but also due to the uneven electroplated nickel layer thickness in wheel axial direction, resulting in different material removal rate and, hence, different convergent velocities of wheel run-out errors.

With regard to the improvement of the coarse diamond grain topography during the conditioning process (figure 2), it can be seen that there are no flattened grains before the conditioning process. As the conditioning process proceeds, more and more diamond grains were contacted and truncated resulting in flattened grains tops, and hence, the average grain protrusion height was decreased and the numbers of active grains were increased. After the conditioning process the diamond grinding wheel is dressed with an ELID-process for enhancement of the diamond grain protrusion height.

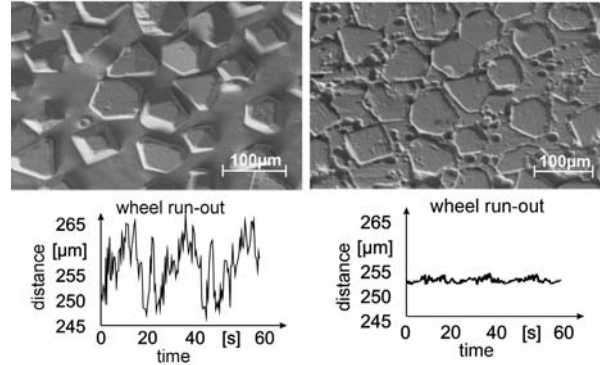


Fig. 2. Wheel run-out error improvement and wheel surface topography before and after a conditioning and electrolytic dressing

During conditioning of the grinding wheels the grain tips are truncated and the bearing ratio of the grinding wheel topography increases (figure 3). The improvement of the bearing ratio (defined as the ratio of the area of flattened grain surface relating to the whole wheel surface) of the coarse diamond grains was analysed on identical diamond grains. As the conditioning process proceeds, the bearing ratio increases from 0% to about 40%.

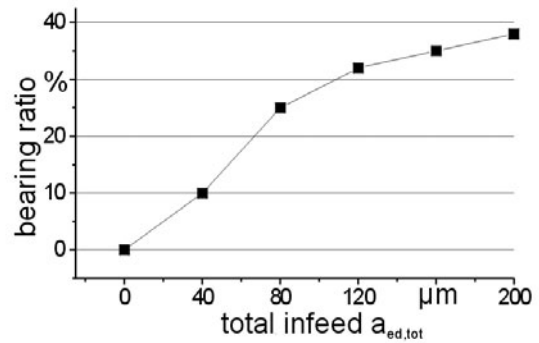


Fig. 3. Bearing ratio of the diamond grinding wheel during the conditioning process

The change of dressing forces in terms of normal force  $F_{nd}$  and tangential force  $F_{td}$ , as well as the dressing force ratio  $\mu_d = F_{td}/F_{nd}$  as a function of infeed in Z direction is shown in figure 4. As the infeed increases both,  $F_{nd}$  and  $F_{td}$ , increase accordingly in different slope

The dressing force ratio  $\mu_d = F_{td}/F_{nd}$  decreases from 0.35 to 0.25 when the conditioning was finished. This was caused by the increasing of grain surface bearing ratio. More flattened grain surfaces were generated on the grinding wheel and thereby the contacting area between diamond grains was increased, resulting in larger normal forces and tangential forces. However, the tangential force did not increase in the same slope as the normal force.

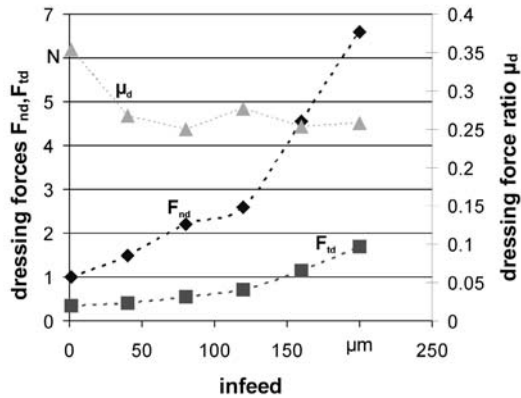


Fig. 4. Dressing forces  $F_{nd}$  and  $F_{td}$  and resulting force ratio  $\mu_d$

Generally, the wear mechanisms of abrasive particles are classified into the following 3 patterns: attrition, fracture and pullout. It can be seen from SEM photos (figure 2, right) that all diamond grains were smoothly flattened which can be associated with attrition wear mechanism. However, there are still some small fractures and cleavages present at the sides and edges of the diamond grains which are mainly attributed to the unique truncating process among super abrasives, as well as the anisotropic characteristics of the diamond grains. No grain pullout occurred.

Grinding BK7 glass in ductile mode is possible applying these conditioned coarse grained wheels, which is verified by regular grinding marks imprinted from the wheels profile, whereas the extreme brittle PVD-TiNiN hard coating could only be machined partially in ductile mode, see figure 5.

The grinding wheel with a grain size of  $91 \mu\text{m}$  can generate a surface roughness of about  $18 \text{ nm Ra}$  on BK7, measured with a white light interferometer. The grinding mark features low frequency with a small amplitude value in normal direction and no wheel wear could be detected in this investigation.

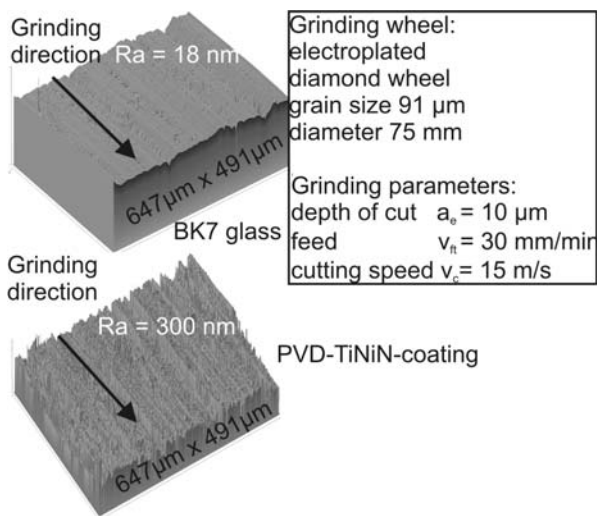


Fig. 5. Surface measurement of ground BK7 glass (WLI)

## 5. Conclusion

The newly developed conditioning technique applying ELID to dress the conditioning wheel is practical to generate minimized wheel run-out errors as well as constant grain protrusion heights and consequently a uniform peripheral envelope. This technique was proved to be applicable and feasible in conditioning electroplated monolayer coarse-grained diamond grinding wheels. It is also shown that the optical measurement system is also feasible to monitor and evaluate the improvement of the conditioning process. With such dressed grinding wheels it is possible to grind optical glass in ductile mode without high wheel wear.

## Acknowledgement

The results presented in this paper were partially achieved within the transregional collaborative research center SFB/TR4 "Process chains for replication of complex optical components", funded by the Deutsche Forschungsgemeinschaft (DFG). The authors express their sincere thanks to the DFG.

## References

- [1] H. Ohmori, T. Nakagawa: Mirror Surface Grinding of Silicon Wafers with Electrolytic In-Process Dressing Annals of the CIRP, 1990, Vol. 39/1:329-332.
- [2] A. Kanai, M. Miyashita, M. Sato, M. Daito: "Proposal of High Productivity in Ductile Mode Grinding of Brittle Materials". Proceedings of ASPE 10th Annual Meeting, Austin, Texas, Oct. 1995, pp. 167-170.
- [3] E. Brinksmeier, R. Malz, W. Preuss "Investigation of a novel tool concept for ductile grinding of optical glass". Proceedings of ASPE (2000) Annual Meeting, Scottsdale, Arizona, Oct. 2000, pp. 74-77.
- [4] Q. Zhao, E. Brinksmeier, O. Riemer, S. Dong: "Ultraprecision Grinding of Optical Glass Using Super Abrasive Diamond Wheel", ASPEN 2005, pp. 710-714.
- [5] M. Wakuda, T. Nakayama, K. Takashima and M. Ota, (2003), "Ultra High Speed and High Efficiency Grinding for Mirror-Like Surface Finish", (2003), International Conference on Leading Edge Manufacturing in 21st Century, Nov. 3-6, Niigata, Japan, pp. 285-290.
- [6] T.W. Hwang, C. J. Evans, S. Malkin. "An Investigation of High Speed Grinding with Electroplated Diamond Wheels". Annals of the CIRP 49/1: 245-248, 2000.
- [7] T.W. Hwang, C.J. Evans, E.P. Whinton, S. Malkin. "High speed grinding of silicon nitride with electroplated diamond wheels, I. Wear and wheel life". ASME J. Manuf. Sci. Eng. Vol. 122, February 2000: pp. 32-41.
- [8] T.W. Hwang, C.J. Evans and S. Malkin. "High speed grinding of silicon nitride with electroplated diamond wheels, II. Wheel topography and grinding mechanisms". ASME J. Manuf. Sci. Eng. Vol. 122, February 2000: pp. 42-50.

# Study on Subsurface Damage Generated in Ground Si Wafer

Bahman Soltani Hosseini<sup>1</sup>, Libo Zhou<sup>1</sup>, Tatsuya Tsuruga<sup>1</sup>, Jun Shimizu<sup>1</sup>, Hiroshi Eda<sup>1</sup>, Sumio Kamiya<sup>2</sup>, Hisao Iwase<sup>2</sup>  
<sup>1</sup>Ibaraki University, <sup>2</sup>Toyota Motor Corporation

Keywords: Backgrinding, Subsurface damage, Warpage height, Damaged layer, Residual stress, Grit size

## Abstract

In this paper, we study and evaluate the subsurface damage of the ground wafers to understand the effect of residual stress on the wafer deflection. The experimental results show that two indexes of depth of the damaged layer and degree of the residual stress are directly associated with the warpage of wafer. The degree of the damage decreases with an increasing in grit size of diamond wheel. The theoretical analysis suggests that the minimally achievable thickness of wafer is proportional to the degree of the damage introduced by respective process.

## 1 Interoduction

The miniaturization and integration of IC chips are increasingly demanded by mobile devices. As a cost effective solution, low-profile-package containing multi layers chips is a new trend for the applications like IC card, mobile phone and digital music player. The Si wafers for those applications have to be thinned down to less than 100 μm before being diced into individual chips. The conventional process for reducing thickness of Si wafers is back-grinding by diamond wheels. The most critical problem encountered is the subsurface damage generated in grinding process, because it's the reason of wafer breakage which directly lowers the yield rate.

In this paper, we study and evaluate the subsurface damage of the ground wafers to understand the effect of residual stress on the wafer deflection. The experimental results show that two indexes of depth of the damaged layer and degree of the residual stress are directly associated with the warpage of wafer. A theoretical analysis has then been made to establish a quantitative relationship between the warpage and the degree of subsurface damage, so that the quality of ground surface is able to be easily evaluated via the warpage. It is also shown that an amorphous layer, a polycrystalline zone and a strained crystalline zone are generated during grinding, subject to the property of diamond wheels and process parameters used. As the result, the minimally achievable thickness of Si wafer by different process is determinable via the parameters indexing the depth of damaged layer and the residual stress.



Fig. 1. Grinding machine

Table 1. Grinding conditions

Machine tool	Horizontal type precision grinder	
Wheel	SD400,SD800, SD2000,SD3000, SD5000	CMG
Workpiece	φ200mm Si wafer (100)	
Wheel revolution	1500 [rpm]	500 [rpm]
Work revolution	50 [rpm]	50 [rpm]
Feed rate	100, 70, 40, 30, 20, 10 [μm/min]	45 ~ 100 [kPa]
Coolant	40 [l/min]	Dry

## 2 Experiments and results

8 inch Si wafers (no protective tape applied) are used for the field test. Fig. 1 is photograph of the grinding machine. The wafers are ground by SD400, SD800, SD2000, SD3000 and SD5000 diamond wheels. The SD400 and SD800 diamond wheels remove Si materials rapidly but greatly damages the wafer surface, while the SD2000~SD5000 wheels is configured to minimize the damage layer and often used for

final process of backgrinding. For comparison, damage free surface achieved by a newly developed Chemo-mechanical-grinding (CMG) wheel are also discussed. The rest grinding conditions are listed in Table 1.

Shown in Fig. 2 (a)~(d) are wafers ground by SD400 wheel in different thickness, and (e)~(f) are wafers ground by CMG wheel in different thickness. The surface of each wafers ground by SD400 have grinding marks and some cracks left. But the surface of each wafer ground by CMG is mirror finished, without any crack left.

In addition, a radically swirl pattern of light reflection is seen from the ground surface by diamond wheels, and its distortion indicates the warpage of the wafer. Whereas, wafers produced by CMG are clean and flat. The comparison in Fig. 2 suggests a difference in ground surface between the diamond wheels and CMG wheel.

According to the mechanics of Si material, the internal stress of a bending wafer is roughly given as:

$$\sigma \approx k \cdot E \cdot \frac{t \cdot h}{D^2} \quad (1.1)$$

Where,  $E$  is the Young's modulus,  $D$  is the diameter of wafer,  $t$  is the thickness,  $h$  is the height of warpage, whereas,  $k$  is the constant containing the effect of the material geometry. The stress  $\sigma$  is supposed to remain same as long as the grinding conditions are unchanged. Therefore, the warpage height  $h$  is inversely proportional to the thickness  $t$ . As shown in Fig. 2 (c), the wafer bends as large as 20mm when it is 70 $\mu$ m thin. When the warpage exceeds the limit of deflective strength of Si, the wafer is broken as Fig. 2 (d).

All this kind of occurrence is resulted from the damage layer introduced by grinding. Fig. 3 is a TEM photo showing a typical cross-section of diamond ground wafer along the [110] crystal orientation. From the top there is an a-Si about 30~50 nm thick, and followed a quasi-polycrystalline zone (or mosaic structure) about 100 ~ 200 nm thick. Also dislocation is develop along [111] crystal orientation. This fact motivates us to further understand the subsurface damage after backgrinding operation.

### 3 Subsurface damage analysis

The damaged layer generated by backgrinding contains large stress. As a result, the wafer will bend in order to release some stress. Fig. 4 schematically shows a diagram of this phenomenon. The degree of wafere damage can therefore be expressed by two parameters: the depth of damaged layer  $\Delta_{\#}$  and its residual stress  $\sigma_{\#}$ .

In order to calculate the stress from the warpage of the wafer, Stoney's formula is used. This equation is, in general, use for calculating the stress of thin films. Although the damaged layer is not a real thin film, it acts as a thin film and its stress can be calculated by

$$\sigma_{\#} \Delta_{\#} = \frac{E}{1-\nu} \frac{t^2}{6\rho} \quad (1.2)$$

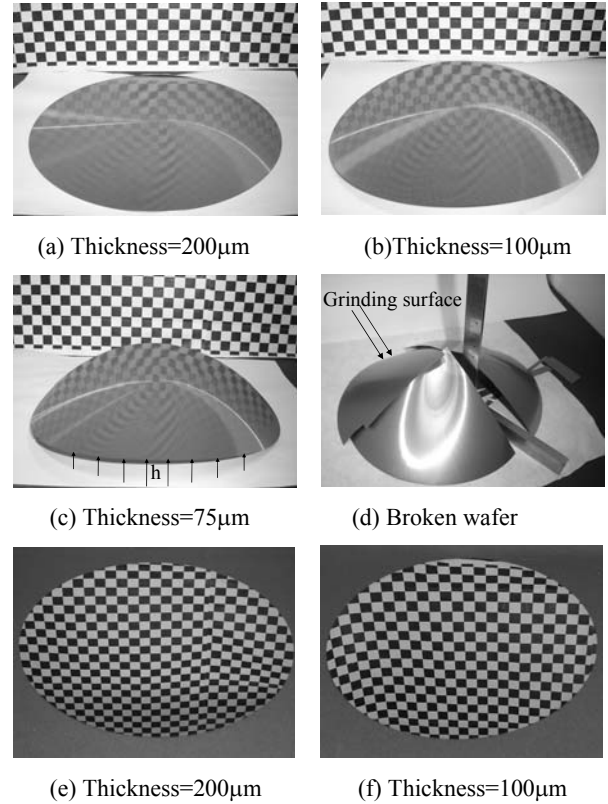


Fig. 2. External view of ground Si wafers

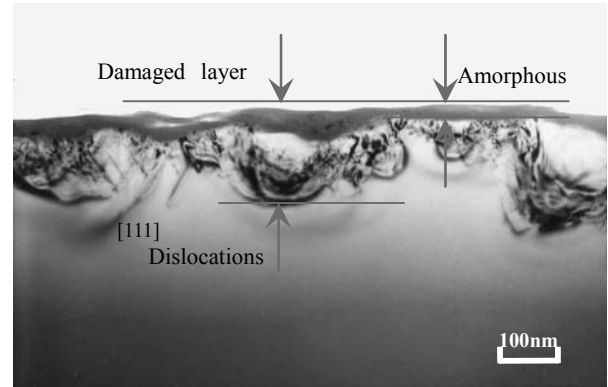


Fig. 3. Cross-section of ground Si wafer

Where,  $E/(1-\nu)$  is the biaxial modulus of the Si wafer,  $t$  is wafer thickness and  $\rho$  is the radius of wafer curvature which is caused by the  $\sigma_{\#}$ .

Assuming the warped wafer takes a part of circular arc, its radius can be obtain geometrically as follows.

$$\rho\theta = D \quad (1.3)$$

$$\cos \frac{\theta}{2} = \frac{\rho - h}{\rho} \quad (1.4)$$

Putting equation (1.4) into equation (1.3), since  $h \ll \rho$ ,  $h^2$  can be omitted, therefore we get;

$$\rho = \frac{D^2}{8h} \quad (1.5)$$

Equation (1.2) can be written as;

$$\sigma_{\#} \Delta_{\#} = \frac{4E}{3(1-\nu)} \frac{ht^2}{D^2} \quad (1.6)$$

The product of  $\Delta_{\#}$  and  $\sigma_{\#}$  means the specific internal force existing in an unit width of damaged layer, can thus be used as an index for the degree of the damage. Equation (1.6) derives the product of two important parameters from the wafer geometry. In another word, when the wafer thickness  $t$  and warpage height  $h$  are properly measured, the product of  $\Delta_{\#}$  and  $\sigma_{\#}$  or the degree of subsurface damage can be evaluated.

As shown in Fig. 5 (a) for measuring wafer thickness, Hamamatsu Photonics K.K. optical micro gauge 8125-55 is used. Fig. 5 (b) shows Kyence laser displacement gauge LK-G35 which use for measuring warpage height. As shown in Fig. 4 for measuring warpage height, the laser displacement gauge takes about 700 point across the wafer diameter. Fig. 6 shows an example of profile measured on a wafer after ground by SD400 where  $t = 250\mu\text{m}$  and  $h = 900\mu\text{m}$ .

In order to understand the effect of the process on the warpage height, the wafers are purposely ground into the same thickness of  $t = 100\mu\text{m}$  by different diamond wheels. The warpage height of each wafer after grinding is measured and shown in Fig. 7, which suggests that the warpage decreases with an increasing in the mesh number (or, decreasing in the grit size) of the diamond wheels.

To further improve the accuracy of measured warpage height, the wafer bending by its own weight should also be taken into account. According to the mechanics of material, the maximum deflection  $\xi_{\max}$  of a both ends supported beam occurs in its center and equals to;

$$\xi_{\max} = -\frac{5wD^4}{384EI} \quad (1.7)$$

The actual warpage height caused by surface damage is  $h + \xi_{\max}$ . Therefore, the equation (1.5) is rewritten as:

$$\rho = \frac{D^2}{8(h + \xi_{\max})} \quad (1.8)$$

Table 2 shows an example of the result for wafers ground by SD400 wheel in different thickness. In the same way, we obtain the results for other wafers ground by SD800, SD2000, SD3000, SD5000 and CMG wheels. Fig. 8 shows the relationship between the wafer thickness  $t$  and the radius of curvature  $\rho$ . It is found that the wafer takes larger radius when it is ground by a finer grit diamond wheel. Obviously, the largest radius is given to a damage free wafer which is slightly deflected by its own weight. It should also be noted that the CMG produces wafers almost free from residual stress (or damage). From these results, the relation

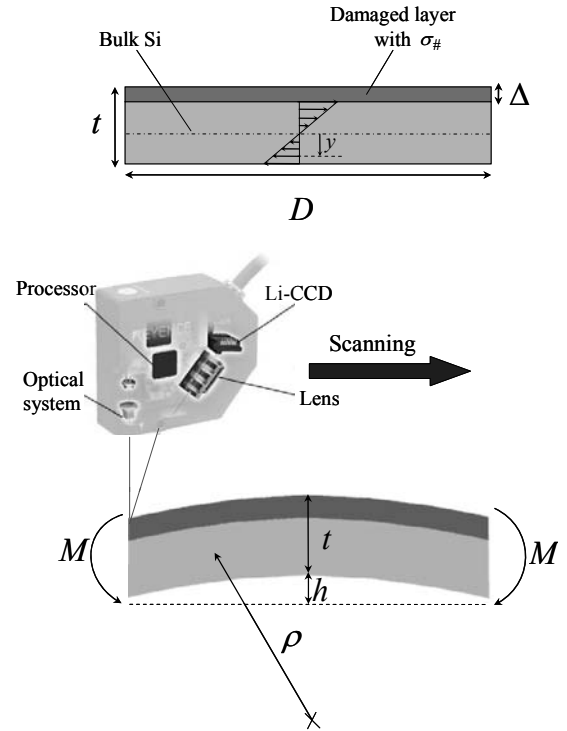
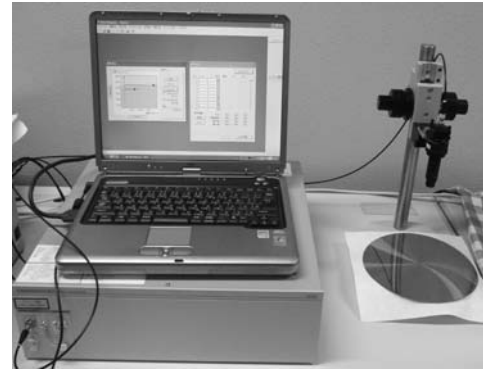
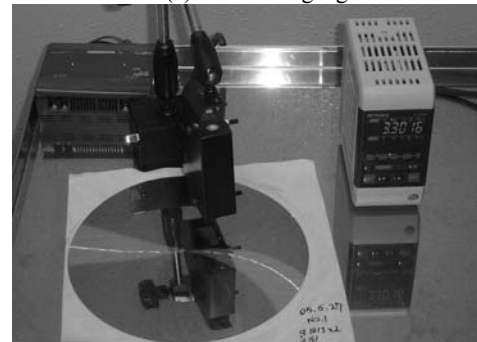


Fig. 4. Schematic diagram of subsurface damage



(a) Thickness gauge



(b) Laser displacement gauge

Fig. 5. Instruments

between the wafer thickness and the radius of warpage can be established for each different process (wheel).

Substituting the wafer thickness and the radius of warpage into the equation (1.2), the degree of subsurface damage  $\sigma_{\#}\Delta_{\#}$  for each process can be obtained. The average product  $\sigma_{\#}\Delta_{\#}$  is shown in Fig. 9. The results suggest that the grinding wheel with smaller grit abrasive produces less damage, and CMG produces near zero damage.

#### 4 Minimumly achievable thickness

The critical thickness of wafer which can bear the product of  $\sigma_{\#}\Delta_{\#}$  is the minimum thickness achievable by corresponding process. In a  $t$  thick beam shown in Fig. 4, the maximum stress are given as:

$$\sigma_{\max} = \frac{Et}{2\rho} \quad (1.9)$$

And  $\sigma_{\max}$  should be smaller than yield stress  $\sigma_y$ ,

( $\sigma_y = E\varepsilon_y$ , where  $\varepsilon_y$  is yield strain), thus:

$$\frac{Et}{2\rho} \leq E\varepsilon_y \quad (1.10)$$

$$t \leq 2\rho\varepsilon_y \quad (1.11)$$

Using equation (1.2) to eliminate the radius  $\rho$ , the minimum thickness is given as;

$$t_{\min} = \frac{3(1-\nu)}{E\varepsilon_y} \sigma_{\#}\Delta_{\#} \quad (1.12)$$

Since the  $\varepsilon_y$  for Si is about 0.02% ~ 0.03%, the minimum thickness is then proportional to the average product  $\sigma_{\#}\Delta_{\#}$ . The result for each process is shown in Fig.10 together with the minimum thickness achieved in our field tests. The experimental results vary in the same tendency of the theoretical analysis, but three times thicker than the minimally achievable thickness. This is mainly because the damaged layer contains not only the residual stress but also the other defects such as cracks, dislocations.

#### 5 Summary

In this study, the effects of grinding wheel and grinding conditions on the subsurface damages of Si wafer have been investigated to understand the effects of grinding damage on the wafer warpage and its deflective strength. The obtained results are summarized as follows;

- (1) The degree of the subsurface damaged layer can be expressed by the product of the depth of damaged layer  $\Delta_{\#}$  and the residual stress  $\sigma_{\#}$ .
- (2) Due to the stress after backgrinding, wafers are bent. The degree of the damage is quantitatively evaluated by

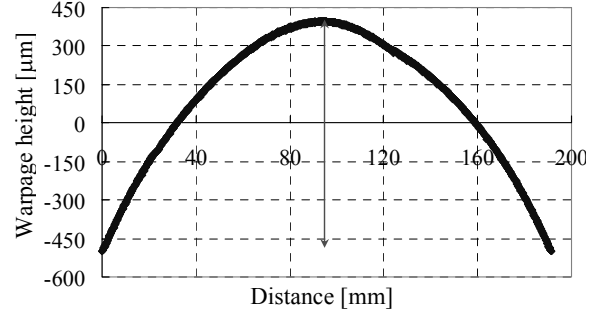


Fig. 6. Wafer bending profile after backgrinding

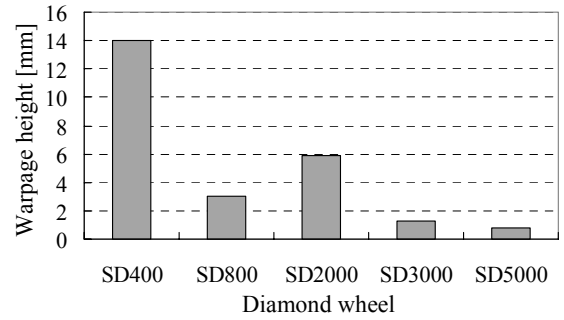


Fig. 7. Relation between warpage height and grit size of diamond wheel

Table 2 Result of grinding by SD400

$t$ [μm]	$h$ [mm]	$\xi_{\max}$ [mm]	$h + \xi_{\max}$ [mm]	$\rho$ [mm]
352	0.50	0.069	0.5669	8819.99
316	0.58	0.086	0.670	7463.04
285	0.67	0.106	0.771	6482.80
256	0.94	0.129	1.073	4659.63
200	1.70	0.210	1.910	2617.17
148	5.35	0.383	5.735	871.78
95	14.00	1.070	15.070	331.79

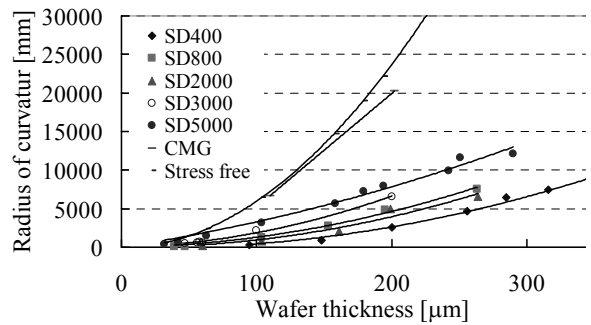


Fig. 8. Relation between wafer thickness and radius

the wafer geometry, or the wafer thickness and the warpage height.

- (3) The surface of the Si wafers is damaged after backgrinding. The degree of the damage decreases with an increasing in grit size of diamond wheel.
- (4) The theoretical analysis suggests that the minimally achievable thickness of wafer is proportional to the degree of the damage introduced by respective process.
- (5) The thickness achieved by diamond wheel grinding process demonstrates the same tendency of the theoretical analysis, but three times thicker than the minimally achievable thickness. The reason is due to other defects such as cracks, dislocations in addition to the residual stress.
- (6) A novel fixed abrasive process of CMG has been proposed to achieve damage-free Si surface, by introducing chemical effect into the grinding process.

### 6 Acknowledgement

This research was partially sponsored by the Grand-in-Aid for Scientific Research (No. 16360061) from the Ministry of Education Science and Culture of Japan, and other industrial joint research. The authors extend their appreciations to the contributions by all CMG project staff.

### 7 References

- [1] T.G.Bifano, T.A.Dow and R. O Scattergood: Ductile-Regime Grinding: A New Technology for Machining Brittle Materials, ASME J. Eng'g for Industry, Vol.113/2(1991), pp.184-189.
- [2] L.Zhang and I. Zarudi: Towards a Deeper Understanding of Plastic Deformation in Single crystal Silicon, Int'l J. of Mechanical Sciences, Vol. 43 (2001), pp.1985-1996.
- [3] Stoney G G 1909 Proc.R.Soc. A 82 172
- [4] P. Halahan and T. Schraub: Backgrinding technologies for thin-wafer production webpage, [http://www.chipscalereview.com/issues/0102/f6\\_01.html](http://www.chipscalereview.com/issues/0102/f6_01.html).
- [5] J. Chen and I. D. Wolf: Study of damage and stress induced by backgrinding in Si wafers, Semiconductor Science and Technology, Vol.18(2003), pp.261-268.
- [6] L. Zhou, J. Shimizu and H. Eda: A novel fixed abrasive process: chemo-mechanical grinding technology, Int. J. Manufacturing Tech. and Management, Vol.7, No.5/6(2005), pp.441-454.
- [7] L. Zhou, M. Yamaguchi, J. Shimizu and H. Eda: Study on Structure Transformation of Si Wafer in Grinding Process,

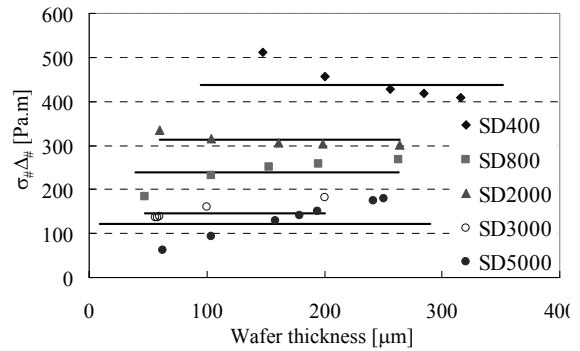


Fig. 9. Subsurface damage stress

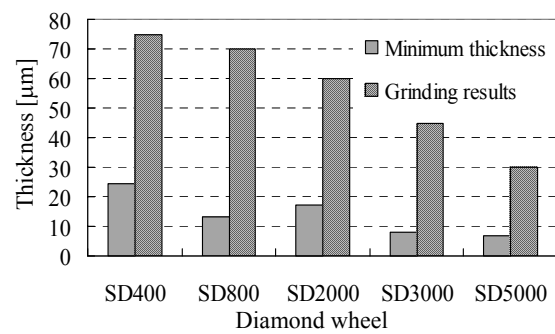


Fig. 10. Relation between wafer thickness and grit size of diamond wheel

---

# Fabrication of High-quality Surfaces on Precise Lens Mold Materials by a new ELID Grinding Wheel

Tomoyuki Saito<sup>1</sup>, Kazutoshi Katahira<sup>2</sup>, Hitoshi Ohmori<sup>2</sup>, Jun Komotori<sup>1</sup>, Masayoshi Mizutani<sup>2</sup>, Akihiko Nemoto<sup>3</sup>  
<sup>1</sup>KEIO University, <sup>2</sup>RIKEN, <sup>3</sup>NIPPON INSTITUTE of TECHNOLOGY

Keywords: ELID grinding, surface modification, cemented carbide alloys

## Abstract

In this study, we have performed efficient and high-precision grinding of cemented carbide alloys with a newly developed grinding wheel, and investigated the ground surface characteristics in detail. The processing results showed that final finishing using the Chromium bonding #8000 wheel produced an extremely smooth ground surface roughness  $R_a$  of 4 nm. And, a very interesting finding is that use of Chromium as a bonding material further promoted the diffusion of oxygen to the surface of a workpiece.

## 1. Introduction

In recent years, the rapid decrease in size and improved performance of digital image capturing devices and large capacity optical storage devices have required advances in the manufacturing technologies for micro aspheric optical elements that have shape accuracies on the nano-scale level and high quality surfaces. Materials with high hardnesses, viscosities, and glass transition temperatures are used in order to obtain higher refractivities for the micro aspheric lenses.

Mass production of optical components, especially the molding of glass lenses, demands a very high quality of lens mold surfaces. Cemented carbide alloys, because of their wear and chemical resistance, are very suitable mold materials for the glass molding process. However, advanced cemented carbide alloys are extremely hard to machine using conventional methods. That's why research on efficient, ultra-precision grinding techniques for cemented carbide alloys is essential. Until now, reproducible mirror surface machining of cemented carbide material parts has been performed primarily by polishing or lapping. Grinding in particular, compared with lapping and polishing, efficiently produces the necessary geometric form. New grinding techniques for cemented carbide alloys employ fine-bonded superabrasive wheels and high-stiffness grinding machines, and have been designed to achieve high grinding efficiency and high-quality cemented carbide parts. The ELID (Electrolytic In-Process Dressing) [1-6] is a specific grinding technique using a rigid metallic bond with the assistance of a special, pulse-electrolytic in-process method. In this study, we have performed efficient and high-precision grinding of cemented carbide alloys with a newly developed grinding

wheel, and investigated the ground surface characteristics in detail.

## 2. Experimental Procedure

The ELID grinding technique is a relatively new process, in which the abrasive characteristics of a metal-bond grinding wheel are maintained by an electrolytic process. Figure 1 shows a schematic of ELID grinding system. The electrically conductive, metal-bonded grinding wheel is connected to the positive outlet of the DC-pulse power supply. The fixed electrode is linked to the negative power source. An appropriate gap size of approximately 0.1–0.3 mm is preset between the grinding wheel and the dressing electrode. During grinding, electrolysis occurs with the supply of suitable grinding fluid, and a certain amount of electric current flows between the grinding wheel and the fixed electrode; this maintains the grinding wheel in a sharpened state. The dynamic and adoptive dressing process is schematically explained in Figure 2. Nonlinear electrolytic agents and high-frequency DC-pulse power supplies are recommended here to obtain the ideal wheel surface layer. The in-process dressing enables a stable grinding process, which in turn produces extremely good results, even with an ultra-fine abrasive wheel of micron or submicron grit.

Table 1 lists the experimental conditions for ELID grinding. A precision rotational grinder (NACHI Co., HSG-10A2) was used for external grinding. Metal-resinoid hybrid bond grinding wheels (#8000, abrasives of approximately 2  $\mu\text{m}$  in diameter) with two different bonding materials were used for finishing: Copper (Cu) and Chromium (Cr). For simplicity, these specimens are referred to as Cu-series and Cr-series, respectively. For comparison, another workpiece was polished with #4000 emery paper and then buffed with alumina abrasives prior to processing with the proposed apparatus. This procedure is hereafter referred to as the P-series.

Contact type surface profilometer, Energy Dispersive X-ray spectrometry (EDX) and X-ray Photoelectron Spectroscopy (XPS) were used to analyze the surfaces of the ground workpieces.



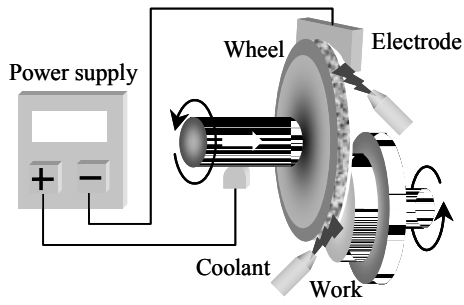


Fig. 1. Schematic illustration of ELID grinding system

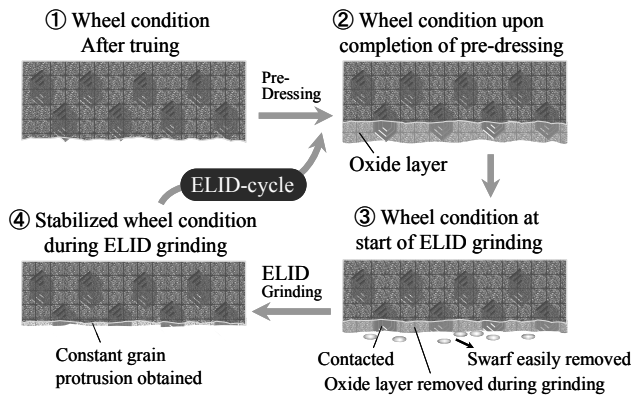


Fig.2. Dynamic and adoptive dressing

Table 1. Experimental condition for ELID grinding

Workpiece	Cemented carbide alloys (WC+TiC)
Grinding machine	HSG-10A2 [Nachi-Fujikoshi corp.]
Grinding wheel	#8000 metal (Copper, Chromium) and resinoid hybrid bond diamond wheels [FUJI DIE Co.]
ELID power source	ED-910 [FUJI DIE Co.]
Grinding condition	Grinding wheel rotating speed; 2000rpm Workpiece rotating speed; 300rpm Feed rate; 1µm/min

### 3. Experimental Results

The ELID grinding machining process was performed with two different types of #8000 grinding wheels, followed by surface roughness measurement, the results of which are shown in Figure 3. The figure reveals that the surface roughness value is sufficiently small for all abrasives. Also, as compared with the P-series specimens that had been finished by polishing, ELID grinding yielded better values across the board. This demonstrates that either of the two types of finishing grinding wheel abrasives could be used to finish the cemented carbide alloy without compromising the finished surface quality.

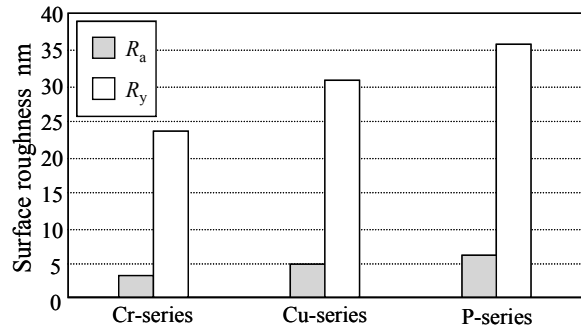


Fig.3. Comparison of the surface roughness  $R_a$

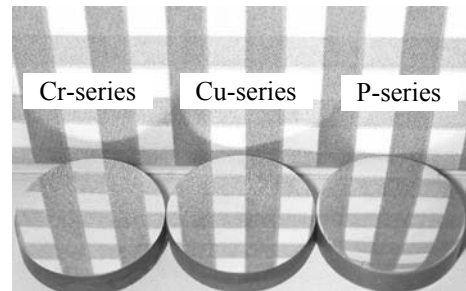


Fig.4. Comparison of the surface roughness  $R_a$

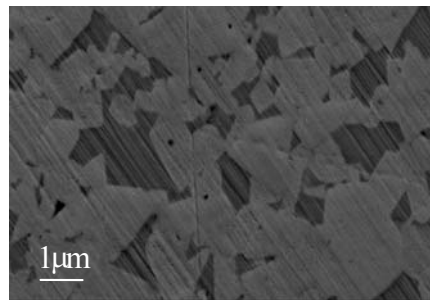


Fig.5. Surface appearance of the Cr-series

Finished examples are shown in Figure 4. In comparison with the Cu-series and Cr-series specimens, the P-series specimen which had been finished with a soft polishing pad appears to have a slightly distorted surface geometry.

Figure 5 shows the surface appearance of the Cr-series specimens observed with SEM. The Cr-series specimen has some grinding marks; however, no grain unevenness can be recognized. These results indicate that composite material can also be safely processed with ELID grinding.

### 4. Discussion

The results described in the preceding sections confirm that improved surface appearance can be achieved when ELID grinding is used instead of polishing as finish machining. In addition, a higher quality surface can be obtained when Cr rather than Cu is used as bonding material.

In this section, in order to clarify the causes for these results, electrolytic properties of the Cr bond grinding wheel are investigated, and elemental analysis of the surface after machining is conducted.

First, SEM observation and EDX analysis were conducted for the surface of the Cr bond grinding wheel before electrolysis; the results are shown in Figure 6. We can verify that diamond abrasive grains measuring a few microns in diameter have sharp edges.

Figure 7 shows the relationship between initial electrolytic dressing time and current for the Cr-series and Cu-series specimens. In the case of the Cu-series, current gradually decreases with time, indicating that the surface of the grinding wheel is becoming nonconducting. Meanwhile, in the case of the Cr-series, the current is constantly high; this indicates that the surface of the grinding wheel of the Cr-series does not become nonconducting, and that only constant dissolution of the bonding material may be taking place.

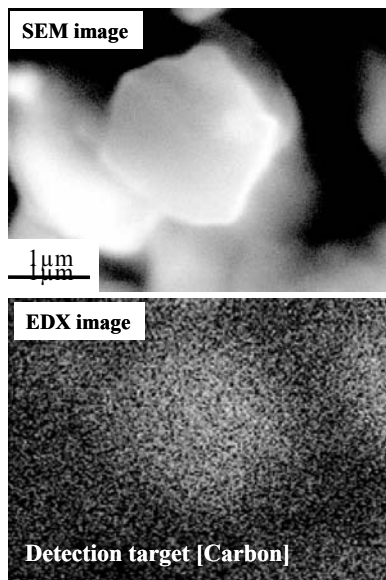


Fig.6. SEM observation and EDX analysis of Cr bond grinding wheel surface

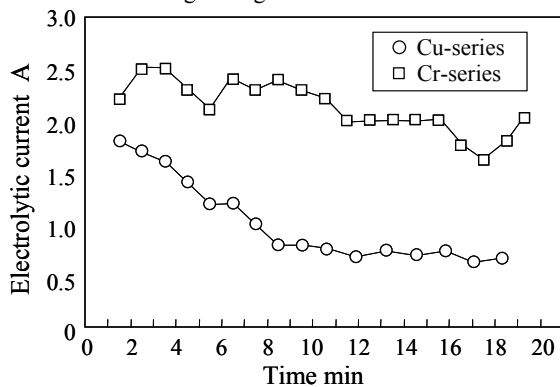


Fig.7. Behavior of the initial electrolytic current

Figure 8 shows the SEM observation results for the surface of the grinding wheel after the initial electrolytic dressing. After the electrolytic dressing, the entire surface of the grinding wheel used with the Cu-series is covered with a film that is considered to be copper oxide. In the case of the Cr-series, abrasive grains measuring a few microns in diameter can be recognized even after the electrolytic dressing. Figure 9 shows the results of EDX elemental analysis for the grinding wheel surface before and after electrolytic dressing. In the Cu-series, dressing reverses the ratio between carbon and oxygen. That is, as shown in Figure 8, the entire surface is covered with an oxide layer after the electrolytic dressing. In contrast, in the case of the Cr-series the high peak of carbon is maintained even after the electrolytic dressing, indicating the presence of diamond abrasive grains on the grinding wheel surface.

High quality surface machining is considered to be achieved in the Cr-series specimen by the action of the diamond abrasive grains exposed on the grinding wheel surface. However, a nonconducting film is not formed in the Cr-series during the electrolytic dressing. Thus, the abrasion of the grinding wheel may be fast. In the future, this point must be investigated further.

Figure 10 shows the results of elemental analysis in the depth direction conducted on various test material surfaces using X-ray photoelectron spectroscopy (XPS). With respect to the state of diffusion in the depth direction of the oxygen element, Cr-series maintains a peak higher than that of Cu-series [4-9].

During the ELID grinding process, a high electric potential difference is generated between the conductive grinding wheel and the electrode for dressing. As a result, the electrolysis of water takes place in the grinding fluid, which has been supplied to the gap, and the concentrations of hydroxide ions and dissolved oxygen are considered to increase significantly. Thus, the hydroxide ions and dissolved oxygen are presumed to have penetrated and diffused into the activated surface of the workpiece. A very interesting finding is that use of Chromium as a bonding material further promoted the diffusion of oxygen to the surface of a workpiece [4-6].

Further experiments are planned in order to clarify the modifying mechanism for the ground substrate surface in order to determine the optimum processing conditions including grinding conditions, type of abrasives, and grinding fluid.

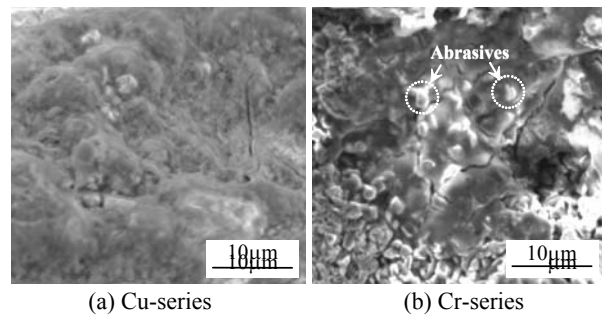


Fig.8. SEM observation results for the surface of the grinding wheel after the initial electrolytic dressing

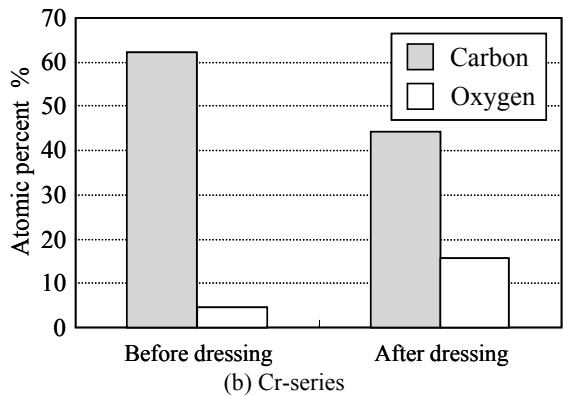
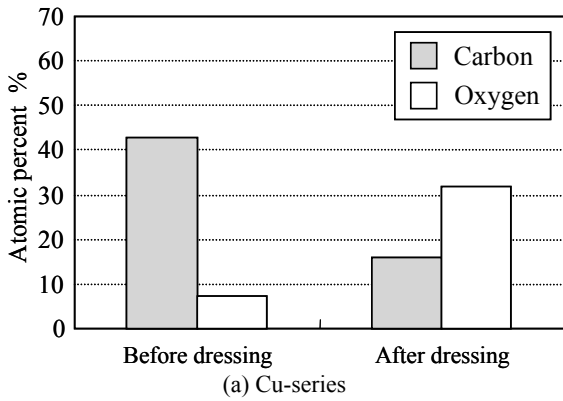
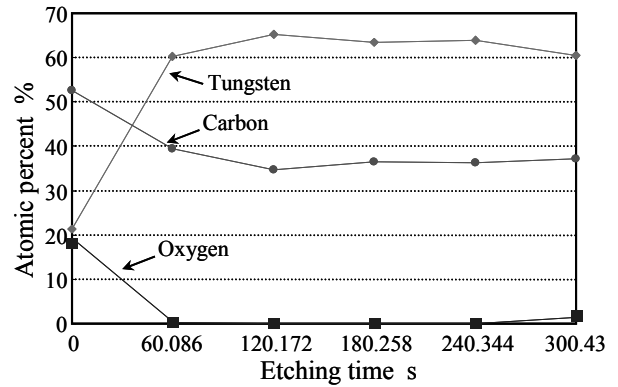
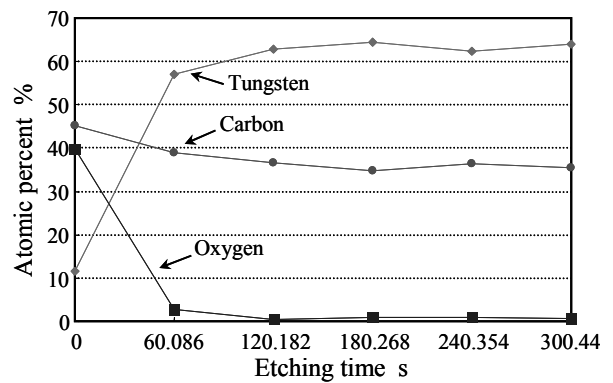


Fig.9. Results of EDX elemental analysis for the grinding wheel surface before and after electrolytic dressing



(a) Cu-series



(b) Cr-series

Fig.10. Results of XPS elemental analysis in the depth direction

## 5. Conclusions

In this study, we have performed efficient and high-precision grinding of cemented carbide alloys with a newly developed grinding wheel, and investigated the ground surface characteristics in detail. The processing results showed that final finishing using the Chromium bonding #8000 wheel produced an extremely smooth ground surface roughness  $R_a$  of 4 nm. And, a very interesting finding is that use of Chromium as a bonding material further promoted the diffusion of oxygen to the surface of a workpiece.

## Acknowledgments

The authors would like to express their appreciation to NEXSYS Corp. and AD&S center, RIKEN in testing

## References

- [1] Ohmori, H., Nakagawa, T., 1995, Analysis of Mirror Surface Generation of Hard and Brittle Materials by ELID (Electrolytic In-Process Dressing) Grinding with Superfine Grain Metallic Bond Wheels, *Annals of the CIRP*, 44/1: 287-290.
- [2] Ohmori, H., and Nakagawa, T., 1997, Utilization of Nonlinear Conditions in Precision Grinding with ELID (Electrolytic In-Process Dressing) for Fabrication of Hard Material Components, *Annals of the CIRP*, 46/1: 261-264.
- [3] Zhang, C., Ohmori, H., Kato, T., and Morita, N., 2001, Evaluation of Surface Characteristics of Ground CVD-SiC using Cast Iron Bond Diamond Wheels, *Precision Engineering*, 25: 56-62.
- [4] Ohmori H., Katahira K., Nagata J., Mizutani M., Komotori J., 2002, Improvement of Corrosion Resistance in Metallic Biomaterials by a New Electrical Grinding Technique, *Annals of the CIRP*, 51/1: 491-494.
- [5] Katahira K., Watanabe Y., Ohmori H., Kato T., 2002, ELID grinding and tribological characteristics of TiAlN film, *Int. J. Machine Tools & Manufacture*, 42:1307-1312.

# A GA-based Optimization of Compliant Micro-manipulator

G. Benu Madhab

## 1.1 Introduction

In recent years, the continuing rapid growth of miniaturization technology has brought many attractive solutions for the development of micromanipulators. Each type of the developed micromanipulator has its own advantages, disadvantages and appropriate set of applications. One of the earliest microgripper was developed by Ando et al. [1] in 1992 by etching beryllium copper plates actuated by piezoelectric stack actuators. In 1997 Ballandras et al. [2] proposed the microgripper design with the piezo actuator driven source and analyzed the working efficiency by FEA and fabricated using LIGA process. A successful attempt for manipulating mechanical micro-objects using various fabrication processes like laser-machined, photo-etched and LIGA fabricated microgripper was made by Carrozza et al. [3] in 2000.

This paper describes the working principle and design of a simple, two-fingered micro robot end-effector actuated by a piezoelectric multilayer stack actuator. A kinematic model is proposed and equivalent flexure-based mechanism is analyzed using Pseudo-Rigid-Body-Model (PRBM). A computer code written in C-language is developed for the optimization of design parameters of a circular flexure hinge and link lengths of micromanipulator. Here, Genetic Algorithms (GA) based approach is utilized to obtain the optimal combination of these values.

## 1.2 Pseudo-Rigid-Body-Model

The flexure-based mechanism is analytically studied using a method called pseudo-rigid-body-model which was developed by Howell and Midha [4] for analyzing compliant mechanisms. A miniature manipulator topology with two linear piezo actuators (one for opening and another for closing) is studied and designed. Fig.1.1a shows the flexure-based compliant manipulator mechanism with piezo 1 for closing and piezo 2 for opening the finger. A pseudo-rigid-body-model (PRBM) for the mechanism is developed as shown in Fig.1.1b.

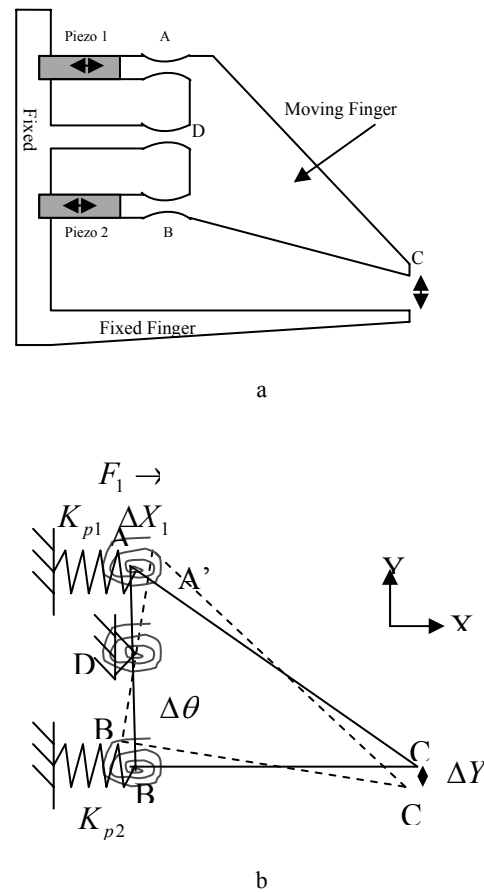


Fig 1.1. a. Flexure-based mechanism; b. PRBM

The output tip displacement is given by,

$$\Delta Y = \frac{2 \times F_1 \times BC \times AD}{2(K_{p1} \times AD^2 + K_{p2} \times BD^2) + (K_{A,\theta} + K_{D,\theta} + K_{B,\theta})} \quad (1.1)$$

where,  $K_{p1}, K_{p2}$  are the stiffness of the piezoelectric stack actuator 1 and 2 respectively,  $K_{A,\theta}, K_{D,\theta}, K_{B,\theta}$  are the rotational stiffness of flexure hinges A, D and B respectively.

As shown in Fig.1.2, a circular flexure hinge was adopted in our design.

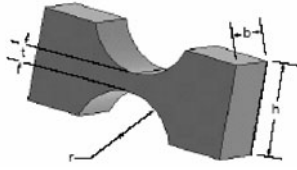


**Fig 1.2.** A circular flexure hinge

For identical circular flexure hinge dimensions, the rotational stiffness is given by [5],

$$K_{A,\theta} = K_{D,\theta} = K_{B,\theta} = \frac{2Ebt^{2.5}}{9\pi r^{0.5}} \quad (1.2)$$

Therefore the output displacement is given by the following expression,

$$\Delta Y = \frac{3 \times F_1 \times BC \times AD \times r^{0.5} \times \pi}{3\pi r^{0.5} (K_{p1} \times AD^2 + K_{p2} \times BD^2) + Ebt^{2.5}} \quad (1.3)$$

The maximum stress in a circular flexure hinge is given by [5],

$$\sigma_{\max} = \frac{4E\Delta\theta}{3\pi} \sqrt{\frac{t}{r}} \quad (1.4)$$

$$\text{i.e. } \sigma_{\max} = \frac{4 \times E \times F_1 \times AD \times t^{0.5}}{3\pi r^{0.5} (K_{p1} \times AD^2 + K_{p2} \times BD^2) + Ebt^{2.5}} \quad (1.5)$$

### 1.3 Optimization

A computer code ‘optgrip.c’ written in C-language is developed for the GA optimization of design parameters ( $r, b, t$ ) of a circular flexure hinge and link lengths ( $BC, AD, BD$ ) of miniature gripper main body.

*Objective function:*

Since piezoelectric stack actuators can give only small displacement (few microns), the main objective is to maximize the gripper jaw output displacement ( $\Delta Y$ ) of the gripper for a given input force ( $F_1$ ) as given by Eq.(1.1)

*Constraints:*

- The maximum stress at any point on the gripper should not exceed the maximum allowable stress i.e. yield stress.
- Due to manufacturing constraints, no dimension should be less than 0.1 mm.

Constraints can be formulated as:

*Constraint1:*  $\sigma_{\max} \leq \sigma_y$  (stress constraint)

The maximum stress in the gripper is given by Eq.(1.5) and  $\sigma_y$  is the yield strength of the material of gripper.

*Constraint2:*  $0.1 \leq r, b, t, BC, AD, BD$  (manufacturing constraint)

The code gives the following outputs at the end of each iteration (i.e. generation):

1.  $r, b, t, BC, AD, BD$  fitness values of each member of population.
2. Optimum combination of  $r, b, t, BC, AD, BD$  values and also the corresponding value of optimum displacement.
3. Sum of fitness values of all the members and also the maximum fitness value among the members of population.

A graph showing how the population converged to give the optimal solution is shown in Fig.1.3.

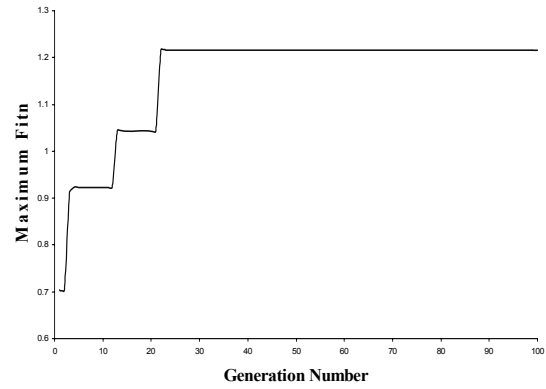


**Fig 1.3.** Convergence of optimization solution

### 1.4 Conclusions

A pseud-body-rigid-model for a micromanipulator mechanism is developed and its motion characteristics are studied. Based on this model and imposing manufacturing and stress constraints, a genetic algorithm based optimization technique is used to determine the best possible dimensions for the mechanism.

### 1.5 References

- [1] Ando Y., Sawada H., Okazaki Y., Ishikawa Y., Kitahara T., Tatsue Y., Furuta K., (1992) Development of micro grippers. Journal of Robotics and Mechatronics 2:214-217
- [2] Ballandras S., Basrou S., Robert L., Megtert S., Blind P., Rouillay M., Bernede P., Daniau W., (1997) Micro grippers fabricated by the LIGA technique. Sensors and Actuators A 58:265-272
- [3] Carrozza M.C., Eisinberg A., Menciassi A., Campolo D., Micera S., Dario P., (2000) Towards a force-controlled microgripper for assembling biomedical microdevices. Journal of Micromechanics and Microengineering 10:271-276
- [4] Howell L. L., (2001) Compliant Mechanisms. John Wiley & Sons
- [5] Paros J. M., Weisbord L., (1965) How to design flexure hinges. Machine Design 25:151-156

---

## Path Control Scheme for Vision Guided Micro Manipulation System

Hiroyuki Asano<sup>1</sup>, Zhoujun Qiu<sup>1</sup>, Libo Zhou<sup>1</sup>, Hirota Ojima<sup>1</sup>, Jun Shimizu<sup>1</sup>, Tomohiko Ishikawa<sup>1</sup>, Hiroshi Eda<sup>1</sup>  
<sup>1</sup>Ibaraki University

Keywords: Micro manipulation, Path control, Potential approach

### Abstract

Cloning is new and growing industry. However, the cell manipulation like enucleating and injection are manually done by skilled operators with the aid of a microscope, and thus tedious and time consuming. Thus, the objective of this research is to develop a manipulation system which is capable to automatically implement necessary operations, with high accuracy, reliability and repeatability, on the multiple targeted cells. In this paper, the path control scheme developed for vision guided micro manipulation system is proposed.

### 1 Introduction

Cloning is new and growing industry. The multiplied cell nucleuses are transplanted into pre-enucleated eggs and then the eggs are again transplanted into foster parent for giving the birth of second generation. Obviously, there are a lot of cell manipulations involved in this workflow. A typical arrangement of cell manipulation is shown in Fig. 1 seated in the center is the egg cell which is normally sized about 100 $\mu$ m in diameter, and distributed aside are the tools necessary for manipulation. For this arrangement, the right tool is used for holding, while the left tool is used for penetration. Currently, the manipulation like enucleating and injection are manually done by skilled operators with the aid of a microscope, and thus tedious and time consuming. The cell manipulation is highly expected to be automated. However, most of commercialized tools are manual of semi-automated, fail to meet the requirements.

The objective of this research is to develop a manipulation system which is capable to automatically implement necessary operations, with high accuracy, reliability and repeatability, on the multiple targeted cells. Described in this paper is the path control scheme developed for vision guided micro manipulation system.

### 2 System description

Fig. 2 shows the developed manipulation system, which consists of three main modules; the manipulation mechanism, the controller and the man-machine interface. Each module is responsible for different function. The mechanism module is the core element where the cell manipulations are carried out. The interface module provides the information to and

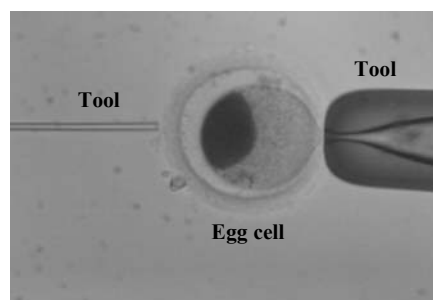


Fig. 1 Typical arrangement for egg cell operation

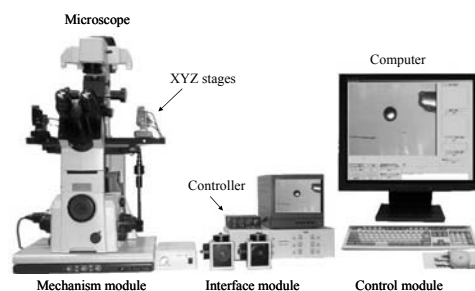


Fig. 2 External view of developed manipulation system

retrieves the instruction from the operator. The other tasks necessary for automation including the measurement, image processing and feedback controls are executed by the control module.

### 3 Tool path determination and control

In the actual manipulation, as shown in Fig. 3, there are multiple cells in the field of view. When implementing the visual control scheme into manipulator, the problem encountered is the conflict with other cells while the tool approaches to the targeted cell. It is therefore necessary to pre-determine the moving path according to the tool/cell configuration, and control the tool move exactly along the determined path. In this study, a potential approach is used for the path generation.

The potential approach assumes that target cell has an attractive potential, and other cells have repulsive potentials to tools. Each potential is considered as a function of the

distance from respective cell. When the tool is positioned at  $(x, y)$ , the targeted cell position at  $(x_g, y_g)$  and the obstacle position at  $(x_s, y_s)$ , the respective distances are given as;

$$d_g = \sqrt{(x-x_g)^2 + (y-y_g)^2} \quad (1.1)$$

$$d_s = \sqrt{(x-x_s)^2 + (y-y_s)^2} \quad (1.2)$$

The resultant potential  $U$  can therefore be written as:

$$U = K_g d_g^n + K_s d_s^m \quad (1.3)$$

Where  $K_g$  is the coefficient of the attracting potential and  $K_s$  is the coefficient of repulsive potential. The force acting on the tool is expressed as a vector  $\mathbf{f}$ .

$$\mathbf{f} = -\text{grad}(U) \quad (1.4)$$

The vector  $\mathbf{f}$  contains two important elements; the direction and the magnitude. By associating the moving direction with the direction of the vector  $\mathbf{f}$ , it is able to generate a path for the tool to approach the targeted cell while not conflict with others, if both potentials are properly defined. Fig. 4 shows some examples of potentials in 3D and their gradients in 2D, where (a)  $n=1, m=-2$  and (b)  $n=2, m=-2$ . In each cases, the path properly leads the tool to the targeted cell while avoids the obstacle cells. By associate the moving speed with the magnitude  $|\mathbf{f}|$  in addition, the tool moving speed can change proportionally to the distance between the tool and targeted cell. This makes it possible to chase a moving target, and is very useful when manipulation of a live spermatozoon is required.

Fig. 5 is snapshots of a field test showing a holding tool approaching to the cell (2), controlled under the potential approach with  $n=1, m=-2$ . (a) is the starting arrangement of the tool and cells where a obstacle cell (1) is allocated between the tool and targeted cell (2). The potential field and tool path are imposed on the image. (b), (c) and (d) show the tool moving sequence. The tool is automatically and precisely guided to the targeted cell without conflict with other cells.

## 4 Conclusion

In order to automate the bio-cell manipulation, this study has proposed and developed a visual control scheme to guide the movements of the tool arms for the micromanipulation system.

The core technology of the visual control scheme is the shape based pattern matching technique. Comparison with the conventional gray-scale based pattern matching.

The potential approach is applied to the path control, which is able to;

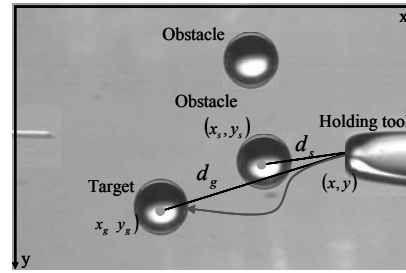
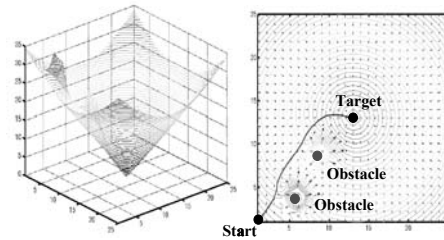
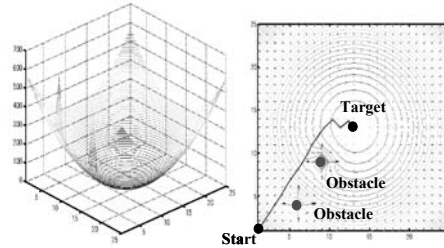


Fig. 3 Tool path to avoid confliction



(a)  $n=1, m=-2$



(b)  $n=2, m=-2$

Fig. 4 Potential approach

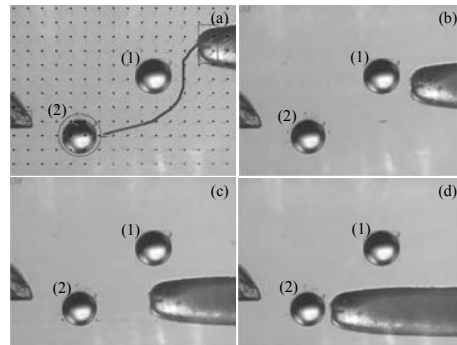


Fig. 5 Automatic cell manipulation by potential approach

1. properly guide to the target while to avoid unnecessary conflicts during the tool movements.
2. chase a moving target such as a live spermatozoon.

## Machined Surface Analysis for 5-axis Machine Tools

Makoto YAMADA,<sup>1</sup> Fumiki TANAKA<sup>2</sup>, Tsukasa KONDO<sup>3</sup>, and Takeshi KISHINAMI<sup>4</sup>  
<sup>1,3</sup> Hakodate National College of Technology, <sup>2,4</sup> Hokkaido University

Keywords: Machined surface analysis, 5-axis machine tools, Tilted tool axis machining, Ball end mill

### Abstract

Most of the mold and die machining by milling machine tools are manufactured by using a ball end mill. To realize a high precision machining, it is important to analyze the machined surface by ball end mill. The purpose of this research is to examine the characteristics of machined surfaces by using ball end mill on 5-axis machine tools. In this research, we propose the machined surface analysis method and the results of experimental results and computer simulation results. And, we show the results of machining experiments and computer simulations of the machining.

### 1 Introduction

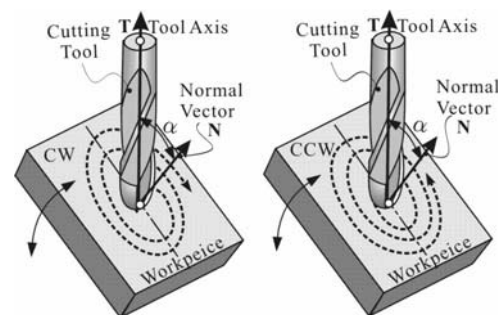
Nowadays the machining technology is required to manufacture complex shapes which are needed multiple orientation of tool axis. The use of 5-axis controlled machine tool is being necessary in the manufacturing of industrial products to deal with various requirements. There are three machining methods on the 5-axis machine tools, which are "5-axis simultaneously controlled machining", "Tilted Tool Axis Machining" and "3 axis control machining". In these machining, ball end mill cutting tools are widely used for the mold and die machining. Therefore, to analyze the machined surface by the ball end mill is important to realize a high precision machining. In this research, we investigate the characteristics of the machined surfaces by tilted tool axis machining and by 5-axis simultaneously controlled machining. Specially, we describe the following two things.

- 1) Ball end mill cutting tools have various machining performance by cutting edge parts, machining direction, cutting speed, and so on. We should know the characteristics of cutting tools ability for high precision machining. And so, We examine the machining performance to vary the tilting angle, direction of feed motion, and, direction of pick feed motion on tilted tool axis cutting.
- 2) We evaluate the comparison of 3-axis control machining and the 5-axis simultaneously controlled machining by using an equivalent machined plane. The equivalent machined plane is the plane which is formed by the 5-axis simultaneously controlled machining, and the contact point of the cutting tool edge becomes equivalent with the contact point which a curved surface is machined by the 3 axis control.

### 2 Experiment to Examine the Machining Performance by Ball end mill

We investigated the influence which an tilting angle and a feed direction exerted on the machined surface to find effective tilted tool angles by the machining experiment using 5-axis machine tools. There are three parameters to exert on the machined surface, 1) tilting angle, 2) tilting direction to the machining feed direction, 3) cross feed direction to machining feed.

As shown in the figure 1, we propose the machining method to tilt the cutting tool axis against the workpiece, and, to move the cutting tool circular motion. In this experiment, the angle  $\alpha$  to form with the cutting tool axis and normal vector of the machined surface is set up. All tilted directions to the machining feed motion can be investigated due to the circular motion by the tilted cutting tool.



(a) Clock-Wise motion (b) Counter Clock-Wise motion

Fig. 1. Machining experiment of circular feed motion

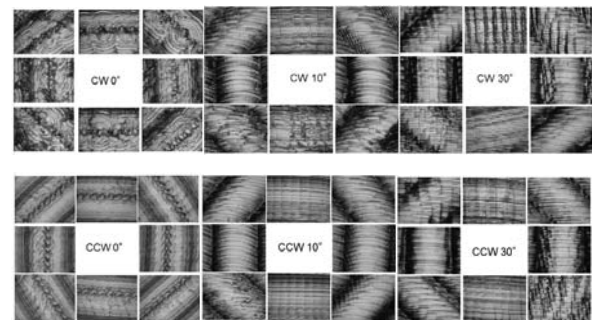


Fig. 2. Machined surface examples in circular feed motion



And then, a difference in the pick feed direction, which is the right and left to the feed motion, can be investigated by the machining of the clockwise direction and the counterclockwise direction, too. A microphotograph is about the circle feed motion result about the typical machining part in case of an inclination of inclination  $\alpha= 0^\circ 10^\circ 30^\circ$  in the figure 2. We confirmed that the surface profiles became stable by tilting at more than  $8^\circ$  in the back or the front to the feed motion and being machined process as that result.

### 3 The analysis of the machined surface in the simultaneous 5 axis control machining

In the experiment for the machined surface analysis, the posture of cutting tool is decided by A-axis rotational motion, and positioned by Y and Z axis. As for 3-axis machining, the relationship between the cutting tool and the workpiece in that machining point are decided by the required machining shape.

Now, we presume the case that a cylindrical surface in 3-axis machining is machined. And, we presume a plane machining by the simultaneous 5-axis control that a cutting tool in the machining point, a cutting tool posture, and machining conditions become equivalent to this 3-axis control machining, too. As shown in the figure 3, the cutting tool starts at the position of a cylindrical convex surface  $45^\circ$ , and a chain of movement are carried out till the end position of a cylindrical concave surface  $45^\circ$ . A cutting tool radius was set at 4mm, and, the radius of the cylindrical surface which is a machining target shape was set at 20mm. A use machine tool is the 5-axis control machining center of the table tilting type. This machine tool has A-axis rotational motion around the X-axis and C-axis rotational motion around the Z-axis in addition to 3-axis translational motion of X, Y and Z.

A plane was machined by 3-axis control and the cylindrical surface was machined by the simultaneous 5-axis control, in the 5-axis machining center of the table tilting type. The Y and Z axis were used for position control, the A axis was used for rotation control as well as the simulation.

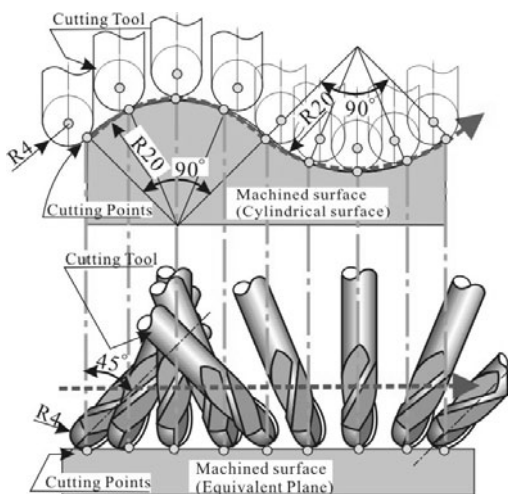


Fig. 3. Equivalent machining for tool posture and machining condition. between 3-axis and 5-axis control

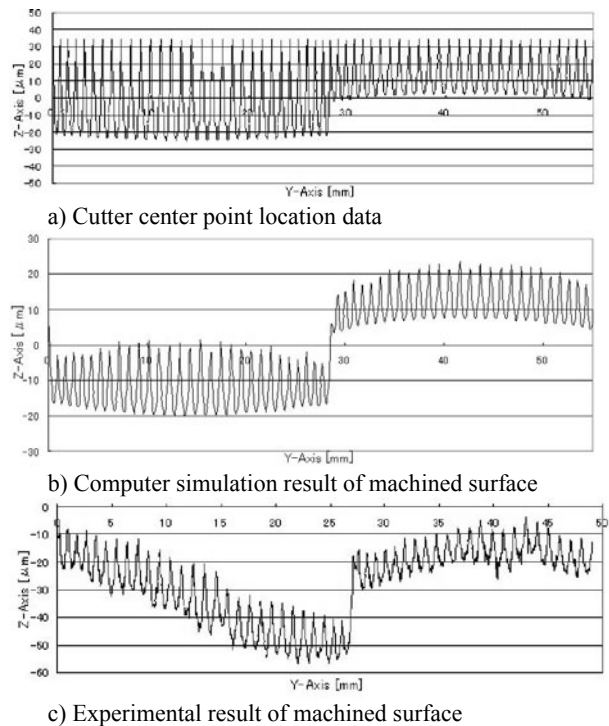


Fig. 4. Results of cutter location and machined surfaces by computer simulation and experimental results

Then, the cross section of the machined surface was measured by using the surface roughness measuring device along the feed direction. That result is shown in the figure 4. A serious change have occurred in opposite rotating direction as well as a computer simulation.

### 4 Conclusions

Following things were showed about machining method and machined surface on the 5-axis machine tools,

1. We proposed the evaluation method of effective cutting edge of ball end mill in tilted tool axis machining.
2. We define the equivalent machining, and showed the problem on simultaneous 5-axis control machining by equivalent plane machining which equivalent to the cylindrical surface machining.

### 5 References

- [1] T. Altan, B.Lilly, Y.C.Yen, Manufacturing of Dies and Molds: Annals of the CIRP, vol.50 no.2, pp. 405-423, 2001.
- [2] Andrew Warkentin, Fathy Ismail, Sanjeev Bedi, Comparison between multi-point and other 5-axis tool positioning strategied; International Journal of Machine Tools & Manufacture, 40, 185-208, (2000),
- [3] Makoto Yamada, Fumiki Tanaka, Tsukasa Kondo, Takeshi Kishinami, Akio Kohmura: Sculpture Surface Machining by Automatically Indexing Tilted ToolAxis on 5-axis Machine Tools (1streport) , Journal of the Japan Society for Precision Engineering, vol.70 no.1, pp. 65-69, 2004.

# A New Approach Manufacturing Cell Scheduling based on Skill-based Manufacturing Integrated to Genetic Algorithm

Bandit SUKSAWAT<sup>1</sup>, Hiroyuki HIRAOKA<sup>1</sup> and Tohru IHARA<sup>1</sup>

<sup>1</sup>Department of Precision Mechanics, Faculty of Science and Engineering, Chuo University, Tokyo, 112-8551, Japan

Keywords: Manufacturing Cell Scheduling, Skilled Workers-based Scheduling, Skill-based Manufacturing, Genetic Algorithm

## Abstract

The skilled workers-based scheduling method was developed using the evaluation of workers skill levels and the application of genetic algorithm. The scheduling method was presented through the workers gantt-chart. The scheduling performance indexes were evaluated by a free time index (FTI), a skill level index (SLI), and a working time index (TWI). The results showed that the maximum of FTI and the SLI indicated significant improvement in production efficiency. Additionally, the lowest of a TWI indicated the minimum differences among man-hour of workers.

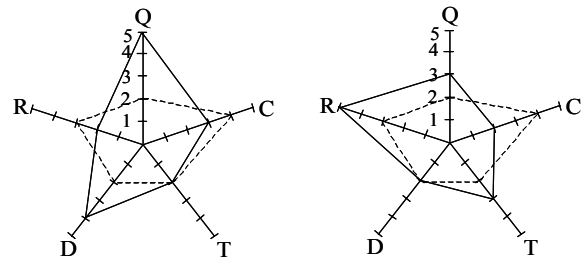
## 1 Introduction

Good scheduling strategies help modern manufacturing enterprises to respond to marketing demands quickly and to run plants more efficiently. Although, advanced manufacturing technology does not improve productivity unless accompanied with a coherent strategy and operated by a skilled or capable technician. However, allocation of skilled technicians on the suitable jobs is difficult and complicated due to varieties of technicians, job characteristics, machine types and machine models. This problem limits the manufacturing cell scheduling for flexible manufacturing operational efficiency. Furthermore, the increasing requirements in developing countries for flexible manufacturing technologies also require skilled technicians to ensure that the technologies will function successfully and efficiently. In this paper, we proposed to develop a skilled technicians-based scheduling method using the evaluation of skill levels of technicians and the application of genetic algorithm (GA).

## 2 Skill –based Manufacturing Thought Model

The skill-based manufacturing thought model<sup>(1)</sup> (mental model<sup>(2)</sup>) was extracted in order to determine the degree of job characteristics in one lot of jobbing productions and technician characteristics. All factors underlying jobs and technician characteristics, used in the proposed skill-based model were adapted from small and medium size enterprises survey data of our laboratory. The job balance in manufacturing cell was estimated before distribution all jobs to a suitable production process and machine tools by using

this model. The model's construction consists of five main-nodes for job balance, representing experience and proficiency on the job; a due date-specifying expected finish time, cost, available capacity of facilities and quantity that under the powerful influence by Japanese manufacturing culture. Besides the main-nodes, there are five sub-nodes for job distribution including quickness (Q), difficulty (D), complexity (C), thoroughness (T) and reliability (R) of job and technician characteristics. The drawing and details of job production as size, shape, material, processing method, capacity requirement, and accuracy that are important factors in process planning and design, were matched to job characteristics. The technicians were motivated by production process and using machine tools of each job. The technicians were interviewed and observed to evaluate their experiences, performances and learning skill in order to match the technician characteristics of each technician in all jobs. Both job and technician characteristics were evaluated by experienced cell leader based on facets of cognitive psychology for the leader decision making<sup>(2)</sup>.

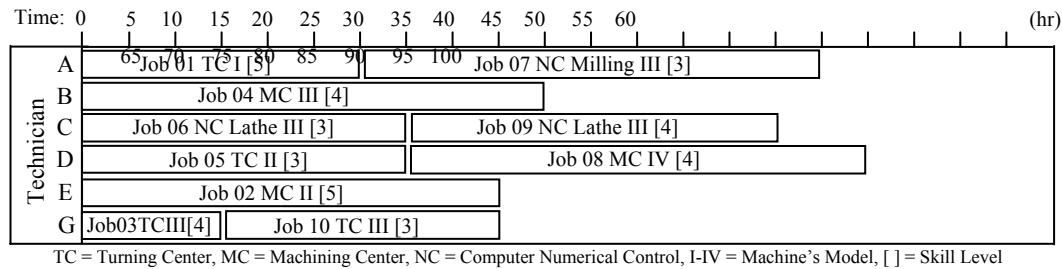


(a) An example of skill level 3 (b) An example of skill level 4

Fig. 1. Skill level evaluation of two technicians on a job

## 3 Skill Level Evaluation Adapted to GA

Figure 1 shows an investigation of compatibility of job characteristics and technician characteristics (Q, D, C, T, R) for each job, used radar-chart with five axes representing five sub-nodes of job characteristics indicated by the broken line and technician characteristics illustrated through the solid line. The skill level evaluation technique, however, was practically constructed through the algorithm and then integrated into initial populations selection process of GA. The high skilled technicians ranging from skill levels 3 to 5 were randomly selected and put on a sub-bit string of chromosome of initial populations. A bit string consists of



TC = Turning Center, MC = Machining Center, NC = Computer Numerical Control, I-IV = Machine's Model, [ ] = Skill Level

Fig. 2. Illustration of scheduling results in technician-work gantt-chart

three sub-bit strings including the machine type, machine model and skilled technician (skill level 3-5). One chromosome of initial populations had  $n$  (number of jobs) bit strings. The standard GA operation<sup>(3)</sup> as one point crossover and mutation was used in this approach with optimize  $p_c$  (crossover probability) = 0.7 and  $p_m$  (mutation probability) = 0.1.

#### 4 Scheduling Method and Illustration of an Example

One lot of jobs consisting of ten jobs and six technicians were used to illustrate the scheduling of the proposed method. The main contribution of this proposed scheduling method is described as follows. Firstly, all drawings of jobs were considered based on experience of leader to determine the suitable machining process and working time, however, job characteristics were considered by the skill-based thought model. Secondly, both machining process and machine tools usages were implemented to motivated a group of technicians in order to determine technician characteristics. Thirdly, the compatibilities between job and technician characteristics were evaluated to define technician's skill levels using the algorithm, and then the evaluated results were accumulated in the database. The technicians skill levels evaluation was integrated as a part of selection process in GA. The application of GA on skill-based manufacturing of technician was constrained by the convergence of GA in non-delay scheduling. The scheduling simulation consists of nine sets of different initial populations with sixteen replications on each set. Each set of initial population would randomly select skilled technicians and their operable machines. The results of scheduling simulation were further analyzed to achieve optimum scheduling.

#### 5 Results and Discussion

The skill level evaluation revealed that the technician skill level had a difference on the same job and the skill level of a technician was also different among the jobs. The result of scheduling was represented by the technician-work gantt-chart concerning job handlings, machine tool usages, skill levels and working time of each technician. However, the best one among the scheduling answers can not be selected from the same make-span. Therefore, to obtain the best scheduling analysis, the alternative method to evaluate scheduling performance was developed based on SLI, FTI, and TWI. Since each job requires operable machine tools,

the SLI will be useful to indicate the gross skill level. The summation of free time on each job is called FTI. Being last important index, TWI concept is applied to optimize the scheduling which is the difference between maximum man-hour and minimum man-hour of technicians.

In an attempt to apply GA to scheduling, the 144 scheduling results were classified into four groups as group  $\alpha$ ,  $\beta$ ,  $\kappa$  and  $\pi$  show a FIT of 250, 240, 235, and 205, respectively. The best answer of scheduling showed the minimum TWI = 40, the maximum FIT = 250 and SLI = 38 as shown in Figure 2. However, group  $\beta$  showed the highest possible occurrence (84.722%) among the others. Nevertheless, an implementation of the skill-based manufacturing thought model to other varying lots may result in different number of classified groups and value of each index depending on job characteristics, technician characteristics, a due-date and working time of each job.

#### 6 Conclusion

The technician skill level is different in each job and the technician-work gantt-chart shows jobs, skill levels and machine tools that will be involved directly in the production for each technician. The best scheduling results show maximum FTI and SLI value but a TWI value is minimum. Thus allocations of technicians to suitable jobs that have minimum working time are required for high efficiency productions. The minimum TWI value in a group of technicians ease of the next scheduling using this method and this satisfies engineers. The skill-based manufacturing thought model proposed to the scheduling method affects directly to productivity of manufacturing cell because it allocates the technician and an operable machine tool on a suitable job.

#### 7 References

- [1] Ihara T., Matsumura T. and Ito Y., (1998) Computer aided determination system for engineer's thought model regarding process planning – case of operation planning. Journal of the Japan Society for Precision Engineering, Vol. 60 No.8 : 111-115
- [2] Coppin G. and Skrzyniar A., (2001) Human-centered processes: individual and distributed decision support. IEEE Intelligent System, Vol. 18 No.4:27-33
- [3] Haupt R.L. and Haupt S.E., (2004) Practical genetic algorithms 2<sup>nd</sup> ed. John Wiley & Sons.

---

## Slide-bending Formation of Thin Metal Sheet by Using an Industrial Robot

Hiroshi HARADA, Ya Zhuo SUN, Yasuo MARUMO, Takeharu MATSUNO and Liqun RUAN

### 1.1 Introduction

This paper describes slide-bending formation of thin metal sheet by using an industrial robot. The formation of parts made of very thin sheets has become increasingly important following the miniaturization of industrial products, including electrical and mechanical devices [1]. The thinning of sheet thickness causes several problems on the formability and accuracy of the products. In order to solve such problems in bending, a new process where a foil work-piece was bent by a sliding tool was proposed. The method was called a slide bending formation and the bending formation of metal foil with 0.01mm-0.05mm thickness was bent by a sliding tool. Various bent products with complex shapes could be formed easily and precisely under optimum conditions using this method.

However, in order to form more precise products, it is necessary to construct a system which can be controlled more precisely. The authors have made an automatic slide-bending formation system which consists of a force sensor, a CCD camera and an industrial robot, which has five degrees of freedom. The slide-bending forming tool was mounted on the top of the robot. The force sensor was attached on the wrist of the robot. The bending formation of metal sheet with 0.03mm thickness made by stainless steel was investigated systematically. The reactive forces in the normal and the horizontal direction were measured by the force sensor. The trajectory of the robot was controlled so that the reactive force was kept constant. The bending angle of the sheet was measured by the CCD camera. From the results of the experiment, it is shown that the larger the applied load, the larger the bending angle of the thin metal sheet.

### 1.2 Slide-bending formation

The principle of slide bending formation is shown in Fig.1.1. One edge of a foil work-piece is fixed on the lower tool. Then, the upper tool is held to the surface of the metallic sheet and vertical load is applied to the surface by the upper tool. Then, by sliding the tool to horizontal direction, the metallic sheet is deformed slightly. Then the upper tool is detached from the metallic sheet and returned to the initial position. Again, the upper tool applies the vertical load to the foil work-piece and slides to horizontal direction. By repeating this procedure, a bending deformation is generated in the metallic sheet.

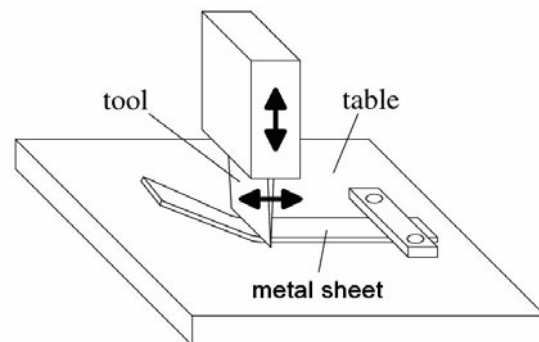


Fig. 1.1. Schematic illustration of bending a metallic sheet by tool slide

In order to perform basic experiments, the authors made an experimental system which consists of an electrically-driven micrometer head and a translation stage. The applied load was measured by a load cell which was built in a tool holder. A copper foil specimen with 0.02mm thickness was bent by the proposed method and the relation between the applied load and the bending angle was investigated.

### 1.3 Automatic slide-bending formation system

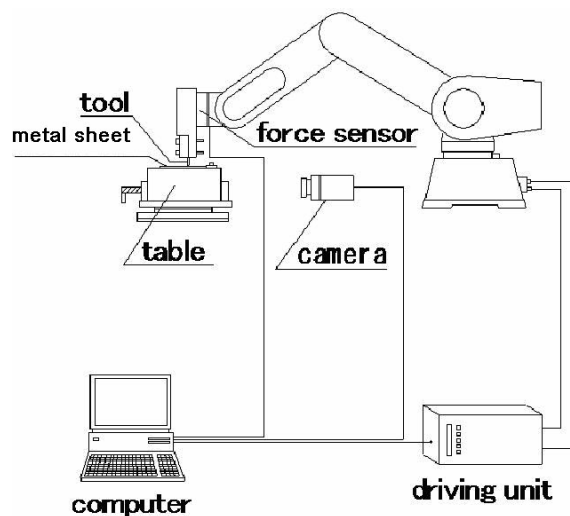


Fig. 1.2. Schematic configuration of the automatic slide-bending formation system

In order to construct a system for the more practical use, we made a new system that used an industrial robot. The automatic slide-bending formation system consists of a force sensor, a CCD camera and an industrial robot, which has five degrees of freedom. Fig.1.2 is a schematic configuration of the automatic slide-bending formation system. The Vickers hardness of the sliding bending tool was 830HV. The force sensor was attached on the wrist of the robot. The force sensor can measure forces in the direction of the  $x,y,z$  axes and a moment of force around the  $x,y,z$  axes. The coefficient of friction can also be evaluated by using the measured normal and horizontal reactive force.

The image of the deformed metallic sheet was taken by a CCD camera and the bending angle of the sheet was measured by using the image. The method was as follows. First, the part of the sheet was cut out from the image. Then, outline of the sheet was extracted by taking difference between the two adjacent pixels. Since the thickness of the sheet was constant, the outline of the sheet became two parallel lines. The bending angle of the metallic sheet was determined by using the inclination angle of these lines.

### 1.4 Experimental results

In order to confirm that the metallic sheet can be formed by the system, some experiments were carried out. The procedure of experiment was as follows. First, A metallic sheet with 0.03-0.04mm thickness made by stainless steel was fixed on a table. Then, the robot moved to the vertical direction and the tool mounted on the robot was applied the vertical load to the specimen. In this case, the vertical load was set to be constant. When the reactive force measured by the force sensor reached to the set load, the robot was moved horizontally to the constant distance. This procedure was repeated until the moving distance became a set value. The reactive force in the normal and the horizontal direction were measured during bending process.

The bending angle was measured by using a CCD camera. Fig.1.3 is a captured image of a deformed metallic sheet and the lower tool. In order to estimate the bending angle of the sheet, the image processing procedure mentioned above was carried out.

The relation between the vertical load and the bending angle is shown in Fig.1.4. In this experiment, metallic sheet with 0.03mm and 0.04mm thickness made by stainless steel was used. From the results of the experiment, it is shown that thin metal sheet can be bent stably by the proposed system. The thinner the metallic sheet, the larger the bending angle of the metal sheet. Since the larger the vertical load, the larger the bending angle of the thin metal sheet, the bending angle can be controlled by the vertical load.

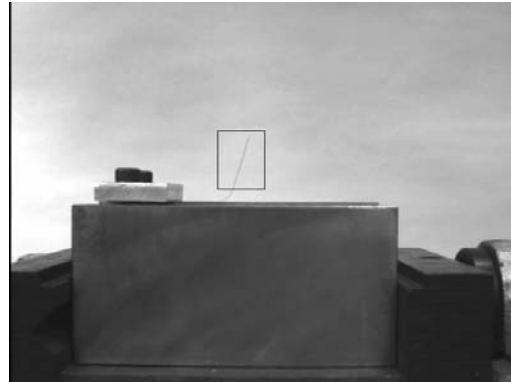


Fig. 1.3. An image of a deformed metallic sheet and the lower tool

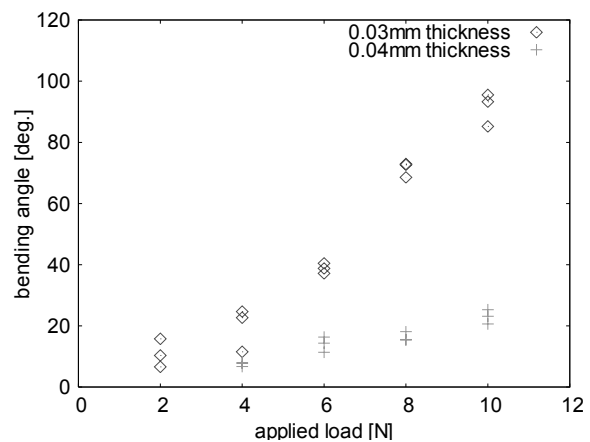


Fig. 1.4. Relation between the vertical load and the bending angle

### 1.5 Conclusion

In this paper we describes slide-bending formation of thin metal sheet by using an industrial robot which has five degrees of freedom. The reactive force were measured by a force sensor mounted on the robot and the bending angle og the metal sheet was measured by a CCD camera. The trajectory of the robot was controlled so that the reactive force was kept constant. From the results of the experiment, it is shown that The trajectory of the robot was controlled so that the reactive force was kept constant. The bending angle of the sheet was measured by the CCD camera. From the results of the experiment, it is shown that the bending angle of the thin metal sheet can be controlled by the applied load.

### 1.6 References

- [1] Vollersten F, Komel I, Kals R, (1995), The Laser Bending of Steel Foils for Micropars by Buckling Mechanism – A Model, Modelling Simulation. Mater. Sci. Eng, 3:107–119.

---

# High Accuracy and High Capacity Motor Cooling System Using Phase Change of Refrigerant for Semiconductor Lithography Apparatus

Alex Ka Tim Poon<sup>1</sup>, Fukunosuke Nishimatsu<sup>2</sup>, Masahiro Totsu<sup>2</sup>, Leonard Kho<sup>1</sup>, Gaurav Keswani<sup>1</sup>  
<sup>1</sup>Nikon Research Corporation of America, <sup>2</sup>Nikon Corporation

Keywords: motor cooling, phase change cooling, two-phase cooling, temperature control

## Abstract

As the requirement for the line width of semiconductor devices shrinks and the requirement for throughput of lithography exposure apparatus increases, a cooling system having higher accuracy as well as larger capacity is required in lithography exposure apparatuses. For this reason, the removal of heat generated by a linear motor, which is the major heat source in a lithography exposure apparatus, has become an important subject. This paper presents a method to accurately control the temperature of the motor using phase change of a refrigerant. Tests were conducted on a prototype motor using two-phase cooling system for uniform and varying heat loads upto 460 Watts. Results show that this system has the capability to remove a large amount of heat from the coils while maintaining uniform temperature across the motor with high accuracy.

## 1 Introduction

Accurate temperature control is vital for several precision engineering processes. Lithography exposure apparatuses, in particular, have highly challenging temperature control requirements. The process of lithography involves transferring images from a reticle to semiconductor wafers. Linear motors are employed for relative positioning of reticle and wafers. Since the critical dimensions in these images are in nanometer scale, precision in positioning of the stages is critical to this manufacturing process. Changes in dimensions of the motor structure caused by variations in temperature, adversely affect the precision in positioning. Additionally, temperature fluctuations within the system cause loss in accuracy of the measurement system which is used as feedback for position control. The present trend is to use single-phase forced convective cooling to remove heat generated in linear motors. The variation in temperature within the lithography exposure apparatus is typically maintained within 1°C. To meet stringent temperature control requirements of future devices, techniques beyond conventional cooling will have to be employed.

Two-phase heat transfer has been used in wide range of engineering systems like power plants, nuclear reactors and in refrigeration systems. Its fundamental qualities are well known and make it a highly attractive alternative over

single-phase convective cooling systems for this application. High heat capacity and high heat transfer coefficients associated with phase change facilitate using much smaller flow rates while simultaneously allowing higher current to flow through the motor coils without raising their temperature substantially. The most important feature of two-phase heat transfer that makes it an ideal choice, is the isothermal heat acquisition. This allows, in principle, a uniform temperature on the surface of motor by precisely controlling the saturation pressure. Although a well-known phenomenon, to our knowledge, this quality has not been practicably utilized in an application involving precise temperature control. Fujii and his group [1] have reported investigations on an experimental two-phase thermal control system targeted for space station and the Space Solar Power System. However, the requirement for this system was for a temperature control within  $\pm 5^\circ\text{C}$ . A two phase cooling system also been investigated to limit the maximum temperatures of power electronic devices [2].

The objective of our work is to utilize the advantages offered by two phase cooling to remove heat generated by coils inside a linear motor and to simultaneously provide a uniform temperature on the surface of the motor. A prototype system (schematic shown in figure 1), was designed wherein the refrigerant is pumped into one end of the motor so that the coils are immersed in fluid flow. The temperature of fluid entering the motor is controlled to be just under its saturation temperature using a Temperature Control Unit (TCU). A sub atmospheric pressure is maintained inside the motor to allow the refrigerant to boil at desired temperature. The system is capable of providing a thermal load of up to 460Watts using joule heating in the coils inside the motor. As the refrigerant moves over the heated coils, its temperature rises and reaches the saturation temperature. Beyond this region, boiling is initiated and the refrigerant absorbs a large amount of latent heat. As further generation of vapor takes place, a fully developed boiling flow is established. The flow exiting the motor is drawn into the separator where the vapor and liquid phase are separated. The vapor is condensed and the sub-cooled liquid thus obtained is returned to a reservoir. The liquid obtained from the separator is also pumped back into the reservoir, forming a closed loop circuit. A pressure control unit (PCU) controls the pressure inside the motor using feedback from a temperature sensor located at the outlet of motor.

Temperature sensors,  $T_s1$ - $T_s6$ , were mounted at six different locations on the bottom surface of the motor.

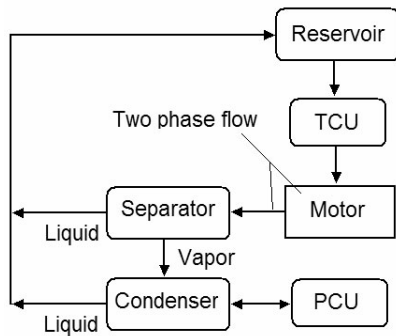


Fig. 1. Schematic of prototype system

## 2 Results

A series of tests were conducted to observe the capability of the system to maintain a uniform temperature of  $22.0^{\circ}\text{C}$  on the bottom surface of the motor under conditions of uniform and varying heat loads. Figure 2 shows the surface temperature data for a test where uniform heat loads of upto 460W were applied consecutively to the system. In this test first a single-phase flow at a very small flowrate was first established in the system with the pressure maintained close to the saturation pressure at  $22.0^{\circ}\text{C}$ . The inlet temperature was controlled to  $22.0^{\circ}\text{C}$  using the TCU. A heat load of 50Watts was then applied to the coils and the PCU was controlled to maintain outlet fluid temperature to  $22.0^{\circ}\text{C}$ . The system was allowed to stabilize and later in this test, the heat loads were varied to 100, 200, 300, 400 and 460Watts.

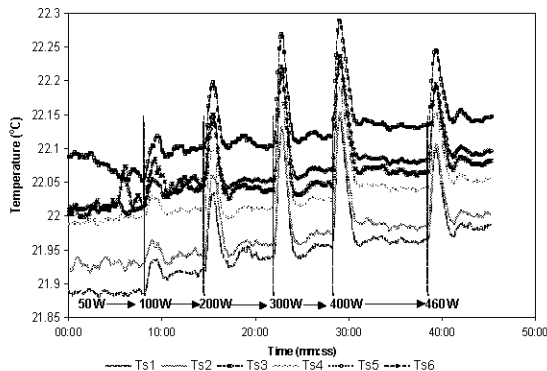


Fig. 2. Surface temperatures for constant heat load test

Changes in thermal load lead to increased boiling inside the motor. The sudden increase in the volume of vapor caused the pressure (and therefore the temperature of the two-phase flow) inside the motor to rise and this change in pressure was corrected by the PCU.

The variation in temperature at the measured locations on the surface was found to be within  $\pm 0.1^{\circ}\text{C}$  at all heat

loads, the minimum being at the inlet and maximum at the outlet. The average surface temperature at 460Watts heat load is higher than that at 50Watts by merely  $0.1^{\circ}\text{C}$ .

Another category of tests was aimed at obtaining the performance for system with heat load similar to that imposed on the motor cooling system during the actual operation of lithography exposure system. During these tests, the system was first allowed to stabilize with a heat load of 460 Watts in the motor. Power to the motor coils was then cut off for a duration of 10 seconds. The coils were then powered again with 460Watts heat load in the motor for a duration of 20 seconds. This process of alternating heat load was then performed repeatedly. Figure 3 shows the temperature data of the bottom surface for the first 10 cycles in one such operation mode test. The region in the figure before point a is of constant 460Watts heat load. At point a, the power was cut off to the coils for the first cycle. The pressure in the motor dropped rapidly because of decreased boiling and the average surface temperature reaches a minimum value of  $21.7^{\circ}\text{C}$ . It took about three complete cycles, between points a and b, for the response of the system to stabilize for the operation mode conditions. Beyond point b, all the surface temperatures fluctuated within a value slightly less than  $0.15^{\circ}\text{C}$  in coherence with the imposed heat load fluctuation. The difference between minimum and maximum temperatures on the surface at a given time remained at less than  $0.2^{\circ}\text{C}$ , as from the constant heat load test.

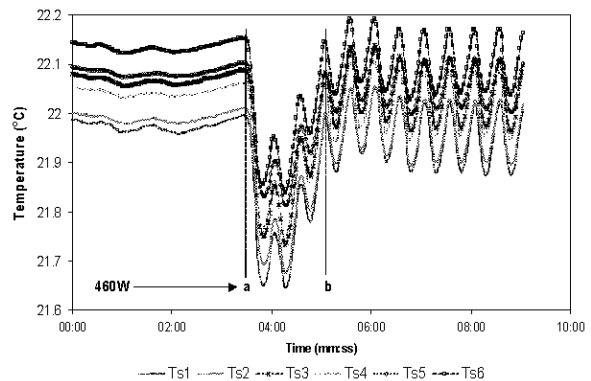


Fig. 3. Surface temperatures during operation mode test

## 3 References

- [1] Terushige FUJII, Katsumi SUGIMOTO, Eiji NISHITA, Masanobu WADA, Shinichi TOYAMA and Haruo KAWASAKI, (2003) An experiment of dynamic characteristics of a two-phase flow thermal control system. Journal of JSME. vol 69 series B
- [2] Jeremy B. Campbell, L. M. Tolbert, C. W. Ayers, and B. Ozpineci, (2005) Two-phase cooling method using R134a refrigerant to cool power electronics devices. Applied Power Electronics Conference. pp 141-147

# Development of the Earthworm Robot using a Shape Memory Alloy

Tomoyuki Saito, Tadao Kagiwada, Hiroyuki Harada, Yusuke Kawamura  
Hokkaido University, Hokkaido University, Hokkaido University, Hokkaido University

Keywords: Earthworm Robot, SMA, BioMetal

## Abstract

This paper describes the earthworm robot composed of commercial shape memory alloy, called BioMetal. Our mechanism has the unique structure with SF tubing for extension force. This robot aims at not only moving by changing length, but also changing thickness like real earthworm. The mechanism makes difference of a friction coefficient to the ground is produced, and the robot can move more smoothly. Finally, our robot realized a motion like earthworm by connecting units and controlling timing by the microcomputer. The robot has four units. The total length is 475[mm], and promotion speed is 3.4[mm/s].

## 1 The Background of Research

Human beings are extending a world of activity from the seabed to the universe today. However, the action range in which we can work actually is narrow. Therefore, it is very important to develop robots that becomes instead of man at place, which cannot be touched directly by human's hand, like a inside of a pipe, a dangerous place, or a small space. Many researchers are developing the earthworm robot, but the practical robot is not yet developed. Almost all of their robots are the type, which needs a big drive and cables, such as an air actuator. Therefore, the range that can move is restricted. Then, this research aims to develop an independent type robot which carries all of actuators and batteries.

## 2 About the movement of an earthworm

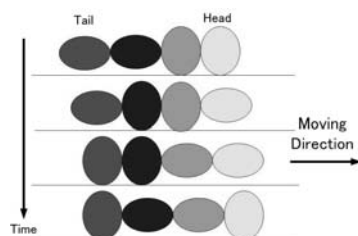


Fig.1. The model of an earthworm robot

We modeled earthworm movement as depicted in Figure.1. First, Section 1 and Section 2 become short and thick, and

they come to contact with the ground. Next, Section 1 becomes long and thin, and Section 3 becomes short and thick at the same time. Since Section 2 does not change at this time, a robot continues support in the position of Section 2. The whole robot move forward by the expansion of Section 1. By repeating this cycle, robot can move .

## 3 Actuator

In this research, We used the "BioMetal (a trademark of TOKI CORPORATION), which is a kind of a shape memory alloy. BioMetal is a fiber-like actuator which is anisotropically structured by special fabrication method from a Ti-Ni shape-memory alloy so as to deliver its superb performance characteristics in a specific direction. Since it is made of a metal and looks like a living thing because of its smooth movement, it is designated as BioMetal. Although soft and pliable like a nylon thread under normal conditions, it becomes stiff like a piano wire and sharply contracts, when a current is fed through it. If the passage of a current is stopped, it will soften and extend to its original length. TOKI CORPORATION provides two types of BioMetal. One product is called BioMetal Fiber(BMF), another is called BioMetal Helix(BMX)<sup>(1)</sup>.

Our first prototype used BMF, but we chose BMX as the second prototype. Although BMF makes strong shrinkage force(180gf), BMF's contraction length is 4.5%. BMX is small force(30gf), but, its stroke is 100%-200%.

Fundamentally, BMX is used, as shown in Figure.2. When a current fed through in BMX, it contracts. If the passage of current is stopped, it will move by spring's force.

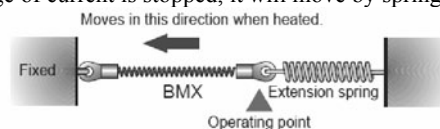


Fig.2. Basic use of the BMX<sup>(1)</sup>

But we use other material instead of extension spring. It is called SF tubing(SHINAGAWA SHOKO CO.,LTD) , that is A polyester braided tube for protecting wiring. The woven construction of the tube gives excellent elasticity and flexibility. It spreads to between 1.5 and 4 times its width under pressure.



### 4 Making of the robot

We designed earthworm mechanism as shown in Figure.3. When a current fed through in 4 BMX, the unit will contract and rubber will touch on the ground. At the time, the unit is fixed to the ground. If the passage of current is stopped, the unit will move by SF Tubing's force. At the time, 4 ball caster will touch to the ground instead of rubber. So unit can move freely. The unit we made is shown in Figure.4.

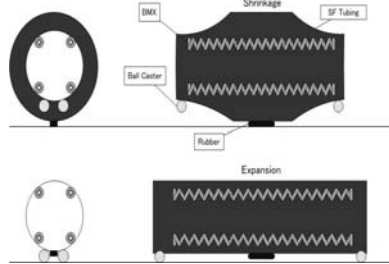


Fig.3. Design of one unit



Fig.4. Figure of one unit

#### 4.1 Results

We measured locomotion pattern of earthworm robot at each points (shown in Figure.5). The results are shown in Figure.6.

According to research of Ueda, the details of movement of an earthworm can be known by measuring propulsion time ( $T_p$ ), stopping time ( $T_s$ ), and promotion distance ( $L$ )<sup>(2)</sup>.

As in Figure.7, the value of point5 are,  $T_p=4.6s$ ,  $T_s=4.0s$ ,  $L=29mm$ . So we can calculate, Speed, Duty factor, Protrusion rate, Stride frequency.

$$speed = \frac{L}{T_p + T_s} = 3.4 [mm/s] \quad (1)$$

$$duty \ factor = \frac{T_s}{T_p + T_s} \times 100 = 47 [\%] \quad (2)$$

$$protrusion \ rate = \frac{L}{T_p} = 6.3 [mm/s] \quad (3)$$

$$stride \ frequency = \frac{1}{T_p + T_s} = 0.12 [Hz] \quad (4)$$

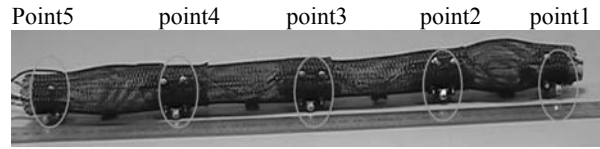


Fig.5. Measured points

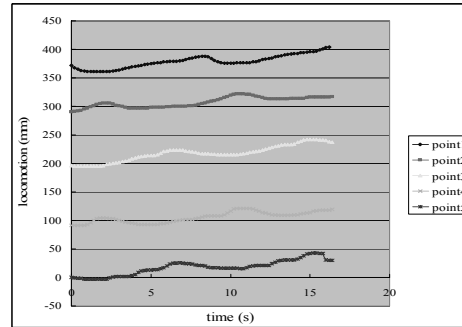


Fig.6. Locomotion patterns of the earthworm robot

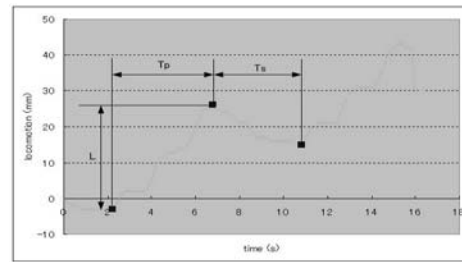


Fig.7. Locomotion pattern of point5

#### 4.2. Consideration

The unit is slipping back about 10mm. This affects the whole promotion distance. As the cause, the unit shrinkage timing doesn't suit enough. And friction force isn't enough too.

### 5 Conclusion

We developed the earthworm robot using BMX and made run experiment. It was showed that the robot can move like real earthworm.

### 7 References

[1] <http://www.toki.co.jp/BioMetal/>  
 [2] S, Ueda, N, Saga, & T, Nakamura, (2003.7) Study on Peristaltic Crawling Robot Using Artificial Muscle Actuator. SICE Tohoku Chapter the 210th research meeting data pp.1-7.

# Improvement of Propulsion Mechanism based on the Inertial Force

Hiroshi YOSHIKAWA, Tadao KAGIWADA, Hiroyuki HARADA, Masaki MIMURA  
 Hokkaido University, Hokkaido University, Hokkaido University, Hokkaido University

Keywords: Design, Transportation, Propulsion mechanism, Inertial force, Simulation, Robot

## Abstract

The present study develops a new propulsion mechanism based on the inertial force. This mechanism is based on a pulsating lateral inertial force arising from by a shaking mass, and through the difference between the friction coefficient equivalent according to the direction on the ground surface. On this report the promotion mechanism was simulated to study relation between the shaking mass and the direction of ground elements. This result of simulation is compared with result of locomotion tests using the advanced prototype robot. More efficient settings of the propulsion mechanism are given to use.

## 1 Introduction

The present study develops a new propulsion mechanism based on the inertial force. This mechanism is not a pushing away of the land surface but is based on a pulsating lateral inertial force arising from by a shaking mass, and through the difference between the friction coefficient equivalent according to the direction on the ground surface. The ground elements are freewheels, skates, skis, or similar that have no driving force but have very small friction coefficient equivalents in the direction of the own motion and large friction coefficient equivalents in the direction normal to the own motion, and are able to change the direction of the own motion actively or passively in time to a pulsating lateral inertial force. The inclining ground element propels the device (robot) in the direction of the own motion by the lateral inertial force through the difference between the friction coefficient equivalents. When the friction coefficient is not sufficiently large to overcome the resistance in the direction of the own motion of the ground elements, which is, for example, caused by the roughness of the surface where wheel based locomotion does not function, the present mechanism functions by using a larger lateral inertial force.

On past study, the principle of the propulsion mechanism was analyzed theoretically and it was proven that continuous locomotion actually could be induced. And through locomotion tested using the produced prototype robot, it was proven that the present propulsion mechanism functions in practice(e.g., [1]).

## 2 Principles of the propulsion mechanism

The locomotion mechanism developed in the present study is actualized by two principal actions, a shaking of a mass lateral to the direction of locomotion and a change in the own motion direction of the ground element. The acceleration of the weight,  $\alpha_{bx}$  and  $\alpha_{by}$ , is given by

$$\alpha_{bx} = \frac{-M_w \alpha'_{wx} - f_s \cos \theta - f_t \sin \theta}{M_w + M_b} \quad (2.1)$$

$$\alpha_{by} = \frac{-M_w \alpha'_{wy} + f_s \sin \theta - f_t \cos \theta}{M_w + M_b} \quad (2.2)$$

where  $M_w$  is mass of the weight,  $M_b$  is mass of the body,  $\theta$  is the oblique angle of the ground element,  $f_t$  is the frictional force in the direction of the ground element,  $f_s$  is the frictional force in the normal direction of the ground element  $\mu_s$  is the friction coefficient equivalent in the normal direction and  $g$  is the acceleration of gravity. When the ground element doesn't slip sideways, the frictional force in the normal direction of the ground element,  $f_s$ , acts only to change the propulsion direction, then  $f_s$ ,  $\alpha$ , is given by

$$f_s = -(M_b + M_w)v_b \frac{d\theta}{dt} - M_w(\alpha'_{wx} \cos \theta - \alpha'_{wy} \sin \theta) \quad (2.3)$$

When the ground element slips sideways,  $f_s$ ,  $\alpha$ , is given by

$$f_s = \mu_s(M_w + M_b)g \quad (2.4)$$

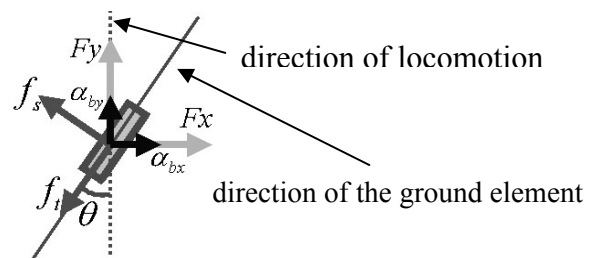


Fig. 2.1. The propulsion of a ground element by an Inertial force

### 3 simulation

#### 3.1 Function and constant used to simulation

On this report the dynamic characteristic of the promotion mechanism has been simulated to study relation between the shaking mass and the direction of ground elements. It are defined that two functions, the shaking mass and the ground elements, used for the simulation. Both are assumed to be a periodic function at same cycle T.

#### 3.2 Result of Simulation : the robot accelerates the most

The result of the simulation shows the robot accelerates the most when the oblique angle of the ground element is set to have the same phase as the relative displacement of the shaking mass in perpendicular to the direction of locomotion.

#### 3.3 Result of Simulation : equal velocity

It is an effective method for the speed adjustment of the body to move the phase of the weight and the phase of the oblique angle of the ground element. Because the result of the simulation shows the robot keep an equal velocity when the phase of the shaking mass shifts from the phase that accelerates most to the phase that added  $\pm 0.25T$  (1/4 cycles) : the absolute displacement of the shaking mass is a small shaking when this shifting phase is completed. This time Two methods of shifting the phase are considered here.

Case1 : the phase of the ground element delays 0.25T by slowly moving the ground element in a certain time.

Case2 : the phase of the ground element delays 0.25T by stopping the ground element in a certain time.

Fig.3.3.1. shows Both case1 and case2 calculation results. Fig.3.3.1. shows the absolute displacement of the weight and the body, and the oblique angle of the ground element every 0.1 seconds. both length and breadth has recorded lines at intervals of 0.1m.

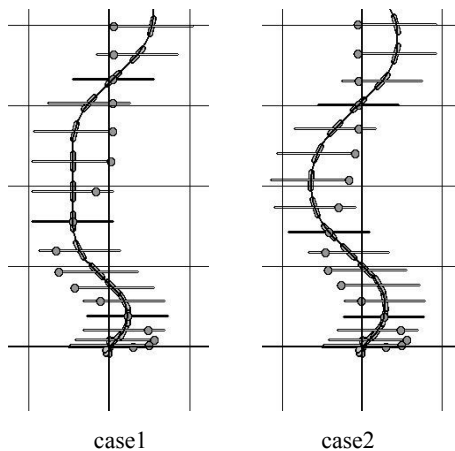


Fig.3.3.1 Locus of support unit (phase difference : 0.25T)

### 4 Tests using a new robot

It reports on the experiment by a new robot in this paper. the advanced prototype robot can set various movements of the shaking mass and the ground elements. the motion control of the wheel and the weight has gone by the microcomputer. In the experiment by a new robot, it is seemd that the acceleration efficiency of the weight's speed is better than that of increased weight. when the speed of the weight increases the number by 1.5, moved distance is doubled twice or four times near. Fig. 4.1 shows this robot using locomotion tested.

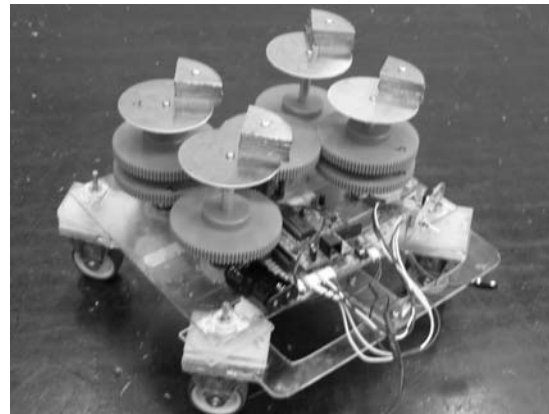


Fig. 4.1 Photograph of the prototype

### 5 Conclusions

A new propulsion mechanism based on the inertial force was developed. The principle of the propulsion mechanism is analyzed theoretically and it is proven that continuous locomotion actually can be induced. Through locomotion tests using the produced prototype robot, it is proven that the present propulsion mechanism functions in practice.

It is expressed to have converted a relative movement of the weight into the propulsion force by the simulation. And this result is shows effective method to move the phase of the weight and the phase of the oblique angle of the ground element for the speed adjustment in the body.

In the experiment by a new robot, it is seemd that the acceleration efficiency of the weight's speed is better than that of increased weight.

### 6 References

- [1] T.Kagiwada, H.Harada, H.Yoshikawa, (2003) "Propulsion Mechanism Based On The Inertial Force", Proc. of IASTED International Conference ROBOTICS AND APPLICATIONS, pp. 148-153

# A High-order Spline Filter for Surface Roughness Measurement

Munetoshi Numada<sup>1</sup>, Takashi Nomura<sup>2</sup>, Kazuhisa Yanagi<sup>3</sup>, Kazuhide Kamiya<sup>2</sup> and Hatsuzo Tashiro<sup>4</sup>

<sup>1</sup>Technology Corp., <sup>2</sup>Toyama Prefectural University, <sup>3</sup>Nagaoka University of Technology, <sup>4</sup>University of Toyama

Keywords: Roughness, Low-pass filter, Spline filter, Smoothing spline, Transmission characteristic

## Extended Abstract

A roughness profile is obtained by subtracting the mean line from the primary profile. In order to calculate this mean line a Gaussian filter (GF) is used.

However, the Gaussian filter has two problems: end effect and unsharp cut-off characteristic. To solve these two problems, a Gaussian regression (GR) filter and a spline filter are proposed. Ideally, a filter with sharper cut-off characteristic than that of these filters is preferable. However, it has not yet been realized. In this research, attention is focused on the fact that increasing the order of the spline filter makes the mean line smoother, which is useful in sharpening the cut-off characteristic of the spline filter.

However, since the high-order spline filter is an extension of the spline filter, there is a problem of long processing time. This is because the computational complexity of the Gaussian filter is in the order of  $N^2$ , whereas that of the spline filter is in the order of  $N^3$ . Therefore, the Gaussian filter can reliably calculate even several thousand data points within one second, but the spline filter will require a maximum of one hour. Naturally, the processing time of the high-order spline filter will never be shorter than that of this spline filter.

High-order spline function  $s(x)$  that minimizes the evaluation quantity  $\varepsilon$  in Eq. (1.1) below. Then, assume  $s_i = s(x_i)$ , and  $\mu$  is a smoothing parameter.

$$\varepsilon = \sum_{i=0}^{N-1} (s_i - f_i)^2 + \frac{\mu}{\Delta x^{2m-1}} \sum_{i=0}^{N-1} (\nabla^m s_i)^2 \rightarrow \min \quad (1.1)$$

Thus, when the high-order spline filter performs computation in the spatial domain, a problem of long processing time arises. However, it is predicted that carrying out computation in the frequency domain will shorten the processing time. The reason for this is that although convolution operation that occupies most of the filter operation in the spatial domain is high in computational complexity, it can be replaced with multiplication in the frequency domain, making the computational complexity lower. However, a frequency-type, namely, wavelength-type, low-pass filter has a problem of vibration occurring in the boundary region of filtering output, because ringing occurs when there is a difference in height or inclination at both

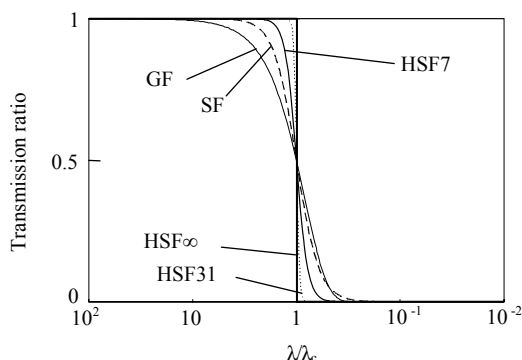


Fig. 1. Transmission characteristics of low-pass filters.

ends of data although the wavelength-type low-pass filter uses discrete Fourier transform (DFT) that presupposes periodicity of limited-length data. However, such a problem of vibration at data ends can be solved by adapting natural boundary conditions of a smoothing spline that fixes the higher-order differential coefficient at 0, at the data ends.

For this filter, the transmission characteristic can be changed by selecting the order of the smoothing spline. Eq. (1.2) shows the transmission ratio of the high-order spline filter. Here,  $u_c$  is a frequency variable corresponding to cut-off wavelength  $\lambda_c$  and there is the relationship of  $u_c = \Delta x / \lambda_c$ .

$$\Phi(u) = \left( 1 + \frac{\sin^{2m} \pi u}{\sin^{2m} \pi u_c} \right)^{-1} \quad (1.2)$$

Figure 1 shows the transmission ratio of each low-pass filter. As seen from this figure, the spline filter (SF) has a more step-edge-like cut-off characteristic than the Gaussian filter. As the order is increased in the order of the 7th-order spline filter (HSF7) and the 31st-order spline filter (HSF31), the cut-off characteristic becomes more step-like. A smoothing spline used in the spline filter, the 7th-order spline filter or the 31st-order spline filter has the order  $m$  in Eq. (1.1) of 2, 4, or 16, respectively. If  $m \rightarrow \infty$ , a  $\infty$ -th-order spline filter (HSF $\infty$ ) will be obtained, with the form of the transmission ratio being a step edge. As the order limit of the high-order spline filter, the ideal low-pass filter with a step-edge-type cut-off characteristic is realized.

Figure 2 shows the results obtained for the high-order spline filter (HSF) applied to the primary profile with wavelength  $\lambda$  of  $\lambda_c/0.9$ . The evaluation length is  $L=0.4\text{mm}$ , the number of data points is 201, the sampling interval is  $\Delta x=0.002\text{mm}$ , the cut-off wavelength is  $\lambda_c=L/5=0.08\text{mm}$ , and the amplitude is  $1.0\ \mu\text{m}$ . Since the wavelength of the primary profile is slightly longer than the cut-off wavelength value  $\lambda_c$ , the filtering output should be equal to the primary profile if the ideal low-pass filter is used. As a result of the experiments, the filtering output of the  $\infty$ th-order HSF (HSF $\infty$ ) was found to be equal to the primary profile. It was also confirmed that the filtering output of the HSF $\infty$  agreed with the primary profile not only in the center region of the primary profile but also in the boundary region  $\lambda_c/2$  from the ends where the end effect occurs. From this, it can be seen that the HSF $\infty$  is an ideal low-pass filter. In contrast to this, as the HSF order decreases, the amplitude of output attenuates. From these results, we confirmed that the higher the HSF order is, the more step-edge-like the cut-off characteristic will be.

Figure 3 shows the deviation of the output value in Figure 2, from the theoretical output value for each filter. The theoretical output value is obtained by multiplying the transmission ratio for  $\lambda=\lambda_c/0.9$  determined from the transmission characteristic in Figure 1, by the primary profile in Figure 2. In the boundary region  $\lambda_c/2$  from the ends, the end effect is large. The end effect decreases as the order increases as in SF, 7th-order HSF (HSF7), 11th-order HSF (HSF11), and 31st-order HSF (HSF31), resulting in 0 for HSF $\infty$ . Thus, it can be understood that the end effect increases more when the transmission ratio is attenuated.

DFT and inverse DFT can be sped up by using Chirp-Z transform. Their computational complexity is the same as that of fast Fourier transform (FFT), and using  $O$  notation it can be expressed as  $O(M\log_2 N)$ . Since the computational complexity for other processes is  $O(N)$ , the computational complexity for the proposed method will be expressed as  $O(M\log_2 N)$ . On the other hand, for the spline filter, a simultaneous linear equation must be solved, and even if either the Gauss-Jordan method or a faster Cholesky method is used, the computational complexity becomes  $O(N^3)$ .

Each type of filter (GF, GR0, GR2, SF, and HSF7) was examined for processing time using the primary profile in Figure 2 while varying the number of data points  $N$  from 101 to 501. For this purpose, a P4-2.4 GHz CPU was used for the PC, and Visual C/C++ used as the programming language. In addition, the linear simultaneous equation for computation of the spline filter was solved by the Cholesky method. As shown in Figure 4, it was confirmed that the computation time is proportional to  $N^2$  for each of GF, GR0, and GR2,  $N^3$  for SF, and  $M\log_2 N$  for HSF. Furthermore, the HSF had the same processing time at all the orders of 3, 7, 11, 31 and  $\infty$ . On the basis of the results of the number of data points  $N$  (101-501), the computation time for  $N=8001$  would be 0.90 seconds, 0.95 seconds, 7.2 seconds, 15.4 seconds, and 1.2 hours, respectively, for GF, HSF, GR0, GR2, and SF. The computation time for HSF is 0.95 seconds, making it faster by 4,500 times compared with SF.

In this research, attention was paid to the fact that increasing the order of the spline filter makes the mean line smoother, which made the cut-off characteristic of the spline filter more step-edge-like. Adopting the natural boundary

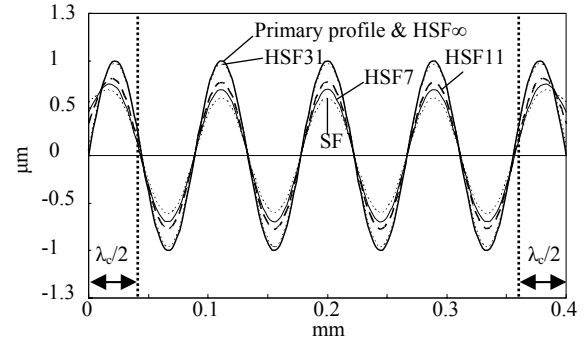


Fig. 2. Output of high-order spline filters ( $\lambda_c = 0.08\text{mm}$ ,  $\lambda=\lambda_c/0.9$ ).

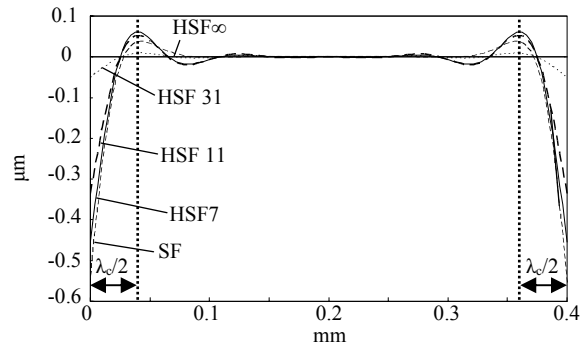


Fig. 3. Deviation of output of filters.

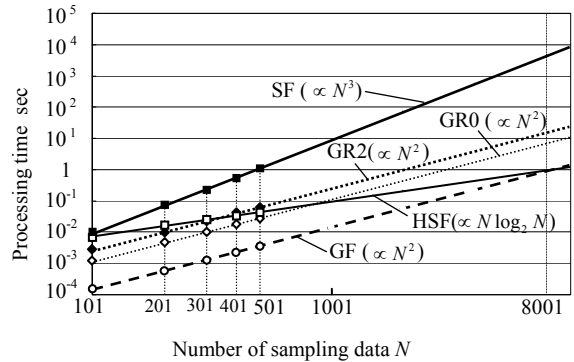


Fig. 4. Processing time.

condition of a smoothing spline, a wavelength-type high-order spline filter was realized. For this filter, the transmission characteristic can be changed by selecting the order of the smoothing spline. As the order limit of the high-order spline filter, the ideal low-pass filter with a step-edge-type cut-off characteristic was realized. The results of experiments confirmed that high-order spline filters have a smaller end effect than conventional low-pass filters. It was also confirmed that when several thousand data points are used, the spline filter requires a maximum of one hour for computation, whereas with the proposed method, it is possible within 1 second.

---

# Surface structure of monocrystalline silicon anisotropically etched with the help of microwaves

T. Krah, S. Büttgenbach  
Technische Universität Braunschweig, Institute for Microtechnology  
Alte Salzdahlumer Str. 203, 38124 Braunschweig, Germany  
E-mail: t.krah@tu-bs.de

Key words: microwave enhanced etching, monocrystalline silicon, roughness, comparison to thermal etching

## Abstract

This article deals with the surface structure of (100) oriented monocrystalline silicon wafers anisotropically etched under microwave irradiation in 10% and 33% KOH. Measurements have shown that with low and medium power those wafers etched in 33% KOH are clearly less rough and apart from that show much less variation with regard to the roughness than those etched in 10% KOH. Compared to etching silicon wafers thermally in 80°C KOH the roughness can be reduced by up to 25% with this new technique.

## 1 Introduction

In microtechnology it is a necessity to have precise structures for the calibration of the most diverse measurement devices at one's disposal, as well as the production of cavities with fixed depths and length scales with precise distances is demanded. However, producing that kind of calibration structures by means of traditional machining processes soon comes up against limiting factors. Monocrystalline silicon offers ideal qualities for the production of structures defined as mentioned above. Of particular importance is its anisotropical wet chemical reaction when etched. Depending on the orientation of the wafers' surface and its structure hollows of different profiles can be realised. The more or less rough structure of the surfaces etched must however be deemed negative when considering the use of silicon for calibration structures as the rough surface increases the measurement insecurities when the structures etched are used for the calibration of coordinate measurement devices. Reducing the roughness will simultaneously mean reducing the insecurity in measurement. Numerous tests have been performed with respect to the surface structure of anisotropically etched monocrystalline silicon so far. Source [1] states that the roughness increases the longer the etching process takes. [2] describes processes carried out to examine the etch rate of microwave-supported, anisotropically etched monocrystalline silicon in KOH.

Conclusively a number of tests has been performed which aim at a reduction of the surface roughness by limiting the time of etching to the highest extent possible. The tech-

nique of microwave-supported anisotropical etching in KOH was used in order to keep up the required high etch rate.

## 2 Set-up

An ordinary microwave with a magnetron frequency of 2450 MHz and  $P_{\text{eff}} = 700$  W was used for the tests. Moreover standard (100) n-type silicon wafers were used, and an  $\text{Si}_3\text{N}_4$  layer served as a masking layer. In order to see what roughnesses result from the microwave irradiation on the surfaces etched, the etch media were neither mixed nor were further substances added. The etching process was carried out as follows:

1. warming up the etch medium at 100% of the microwave's power for one minute
2. etching the wafers at varying microwave power (power chopped)
3. immediately cleaning the wafers with DI-water as well as drying them with an  $\text{N}_2$  stream

## 3 Results and discussion

An aqueous KOH solution with a concentration of 10% and 33% respectively was used as an etch medium. For every etching process the etch medium was replaced by new KOH. Following the etching process the roughness, etch depths, and etch rates  $V_{(100)}$  of the (100) surfaces were determined by means of a surface profiler.

First of all the etch rate  $V_{(100)}$  was determined. With an increase of microwave power the etch rate rises to 9,8  $\mu\text{m}/\text{min}$ , which means that the etch rate is about 12 times as high as that of the thermal etching process. It is also the case that in the range of higher power used the etch rate rises with the KOH concentration. These results correspond clearly with the results presented in [2].

Considering the roughnesses  $R_a$  of the (100) surfaces etched one must distinguish between different ranges of power (figure 1.).

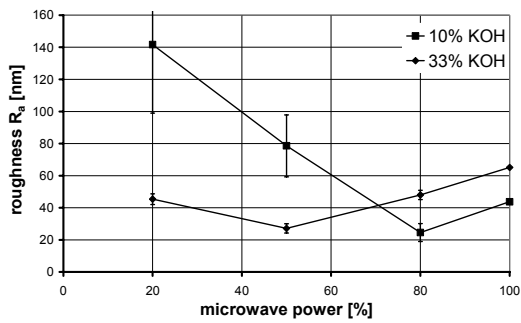


**Fig. 1.** average roughness  $R_a$  of the (100) surfaces etched under microwave irradiation with varying power

When using up to 60% microwave power those surfaces etched with 33% KOH show a roughness reduced to a clearly higher degree compared to those etched with 10% KOH. Using 70% or more microwave power however results in rougher etched surfaces both with 33% and 10% KOH. Furthermore, the variation in roughness is much lesser with the surfaces etched with 33% KOH than with those etched with 10% KOH. A minimal roughness of 24.6 nm with 10% KOH and 27.1 nm with 33% KOH could be reached, meaning that they range basically on the same level.

*Comparison with thermally etched wafers*

In order to be able to judge wafers etched under microwave irradiation their surfaces have been compared to thermally etched wafers. The wafers in question were etched in a standard process with 80°C KOH without additional substances. Figure 2. demonstrates the results.

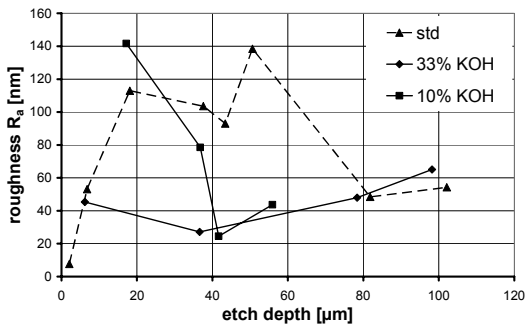


**Fig. 2.** Comparison of roughnesses  $R_a$  of (100) surfaces etched thermally and with the help of microwaves

The thermally etched wafers were etched until they reached the same depth that the wafers etched with the help of microwaves had shown respectively after 10 minutes. It can be seen that generally the roughness can be reduced by up to 25%, but that with high etch rates 33% KOH no longer holds advantages compared to thermal etching. Using 10% KOH results in exactly the opposite: here distinctively lower roughnesses can be obtained with high etch rates only.

Figure 3. compares thermally (figure 3. a) and microwave-supported (figure 3. b) etched surfaces, both cavities having the same etch depths. It is obvious that the surface

etched with the help of microwaves is significantly more even, and shows only few circular hollows. Furthermore, irregular spherical elevations of different size can be found on the thermally etched surface.

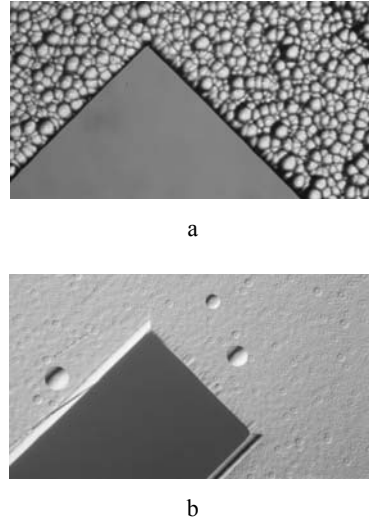


**Fig. 3.** monocrystalline silicon anisotropically etched in KOH a. thermally etched; b. etched with the help of microwaves

**4 Summary**

The tests have shown that a suitable choice of microwave energy as well as the right KOH concentration results not only in a considerable rise of the etch rate but also in a significantly reduced roughness of the surfaces etched in contrast to thermal anisotropical etching with KOH. Microwave-supported anisotropical etching could e.g. be used in the production of silicon calibration structures. With deviations as to form, shape, and position blurring in micro technology the reduction of roughness of the surfaces etched can contribute distinctively to a lower insecurity in the measuring process, especially with tactile measurement devices.

**5 Acknowledgement**

This project has been supported by the German research community Deutsche Forschungsgemeinschaft (DFG).

**6 Souces consulted/References**

[1] Shikida M.; Surface roughness of single-crystal silicon etched by TMAH solution; Sensors and Actuators A, Vol. 90, 2001: 223 – 231  
 [2] Dziuban J. A.; Microwave enhanced fast anisotropic etching of monocrystalline silicon; Sensors and Actuators, Vol. 85, 2000: 133 – 138

# Development of an Ultra-Thin 100 $\mu\text{m}$ Diametrical Coaxial Cable using a Coating Technique

Hayato Miyagawa<sup>1</sup>, Hidenori Ishihara<sup>1</sup>, Shigeru Kobayashi<sup>2</sup>, Kazuo Hira<sup>2</sup>, Yumi Horibe<sup>2</sup>, Yoshifumi Suzuki<sup>1</sup>  
<sup>1</sup>Faculty of Engineering, Kagawa University, <sup>2</sup>Yoshinogawa Electric Wire & Cable Co., Ltd

Keywords: Coaxial Cable, Cold Plasma under Atmospheric Pressure, AFM, XPS, Surface treatment

## Abstract

We report the method of developing an ultra-thin coaxial cable with a diameter of only 100 micron, in which a coating technique is used to make a shield layer. The key process is the surface treatment of the Fluoroplastic insulator core before coating the shield layer. Cold Plasma under Atmospheric Pressure (CPAP) is applied to modify the surface condition of Fluoroplastic. CPAP reduces the hydrophobicity by making surface roughness on Fluoroplastic and changing the state of chemical bonding. In this report, an overview of the process of development and details of the coating process are presented. The effects of CPAP on the surface process are investigated using Atomic Force Microscopy (AFM) and Scanning Electron Microscopy (SEM). X-ray Photoemission Spectroscopy (XPS) measurement is performed to obtain information on the chemical states. In addition, the characteristic features of the developed cable are discussed through the results of experiments which reveal its mechanical and electromagnetic properties.

## 1. 100 $\mu\text{m}$ Diametrical Coaxial Cable

A coaxial cable is a cable which contains the shield around the signal line and is advantageous for transmission of a high-quality signal over distance. A coaxial cable has been used in various applications because of its flexibility. Figure 1.1a indicates the basic architecture of a conventional coaxial cable, where the shield is made by knitted copper wires. The shield made by the knitted metal wires has the advantage of flexibility and durability, however, there is the limitation of downsizing. Figure 1.1b shows the 100  $\mu\text{m}$  diametrical coaxial cable with a metal-coated shield developed for this report. The developed cable consists of four parts as shown in Figure 1.1b: 1) the core metal, a copper line with a diameter of 30 micron; 2) an insulator of Fluoroplastic formed around the core metal, (its diameter containing the core metal is 82 micron;) 3) the shield layer, a metal layer with a 3 micron-thickness mounted around the insulator by coating; 4) the jacket, a Polyurethane covering of the shield layer.

The core metal is made of the In Situ Metal Fiber-Reinforced Copper Alloy. This alloy is a kind of copper

alloy containing the fine Cr ribbon [1]. When a thin cable is designed, we have to consider both resistance and stiffness. As for these two points, this alloy is very suitable for making the thin cable. Another subject is the method of forming the shield. We have paid attention to the way of the deposition of thin film as a new means of forming the shield. We introduced CPAP technique for pre-treatment before coating the shield, and it was successful to develop the thin coaxial cable.

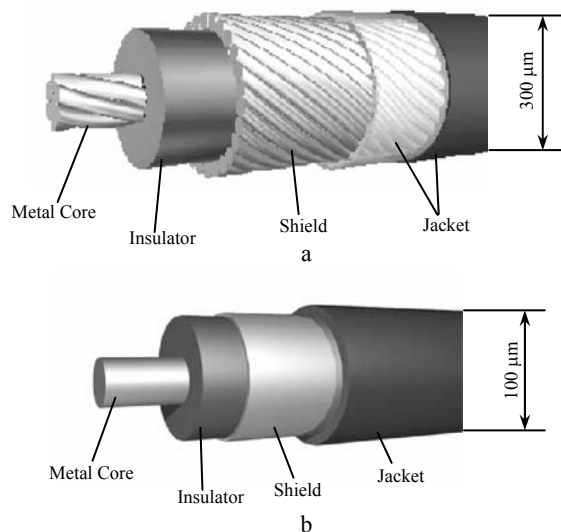


**Fig. 1.1.** a. Conventional coaxial cable, which contains the shield with knitted metal wires. b. Developed coaxial cable, which contains the shield of a metal film.

## 2. Surface Modification by CPAP

Fluoroplastic is so hydrophobic that it is difficult to deposit a substance on it. Therefore, it is very important to modify the surface properties from hydrophobicity to hydrophilicity before coating the metallic film.

Cold plasma under low pressure has been used as a common means of the deposition of thin metal film and surface modification. However, its reaction appears in the closed chamber, and therefore it is difficult to apply it to the



manufacturing line of a long cable such as our coaxial cable. Recently, cold plasma can be generated under atmospheric pressure, and its application has been expanded rapidly. Figure 2.1 illustrates a layout of the CPAP machine which was used to make the proposed coaxial cable. The plasma is generated in the space between the electrodes which are applied with the RF input. The basic method of cold plasma treatment utilizes the plasma generated in a space between two glass plates which are placed between the electrodes as shown in Figure 2.1. The optimized conditions of CPAP are as follows: the carrier gas is N<sub>2</sub> and the gas flow rate is 10000 ccm, the applied voltage is 7.5 kV and the frequency is 20kHz.

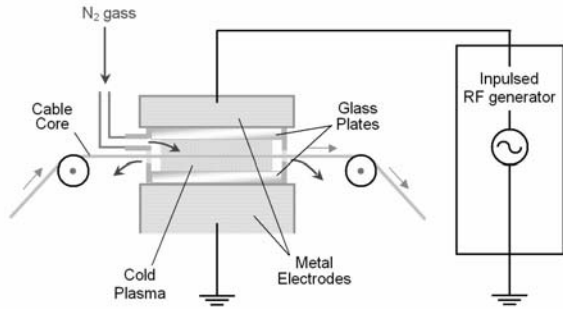


**Fig. 2.1.** Layout of the surface modification of the insulator core using CPAP.

The effectiveness of surface modification is evaluated by the angle of water around the boundary of the cable. As a result of this test, this angle after surface modification by CPAP was 76 degrees. The angle before treatment was 43 degrees. This result confirms the significant effect of CPAP on surface modification.

In order to investigate the effect of CPAP on the surface structure of the core insulator, Atomic Force Microscopy (AFM) measurements were performed. The AFM image obtained after CPAP treatment clearly shows that the surface has many sharp projections. It is thought that the cold plasma etched the surface of the insulator and the projections were formed. This etching mechanism is recognized as the same one reported in [2], which generates ‘quencher’ from the surface. With many projections, the surface area was increased. As a consequence, the hydrophilicity was improved.

Spectra of X-ray Photoemission Spectroscopy (XPS) are shown in Figure 2.2. Dashed and continuous lines represent spectra of the Fluoroplastic insulator before and after CPAP treatment, respectively. These spectra were normalized by the integral intensity of the C 1s spectra, which were supposed to be equal before and after CPAP treatment. In the C 1s spectra, two peaks are clearly observed; the peak in lower energy region originates from the C-C binding states and the one in higher energy region originates from C-F<sub>2</sub> binding states. A decrease of the peak intensities of both the F 1s peak and the peak of the C 1s in higher energy is interpreted to mean that a number of the F atoms at the surface is reduced by CPAP treatment. In addition, peaks of N 1s and O 1s in the spectra measured after CPAP means that CPAP treatment generated the C-O and C-N bindings at

the surface. The decrease of the C-F bindings and the increase of the C-O and C-N bindings are thought to cause the hydrophilicity at the surface of the core insulator.

The results of AFM and XPS measurements indicate that there are two types of effects of CPAP treatment: one is an increase of the surface area by forming the fine sharp projections, and another is a change of chemical bonding states at the surface. These two effects cause the reduction of hydrophobicity of the insulator core. Consequently, the adhesion of the shield layer coated on the insulator is reinforced, and the durability and the electric properties of the developed coaxial cable are improved. CPAP treatment is very useful for manufacturing a long thin cable. Both the properties of the transmission signal and the flexibility of the developed coaxial cable show sufficient values for practical use.

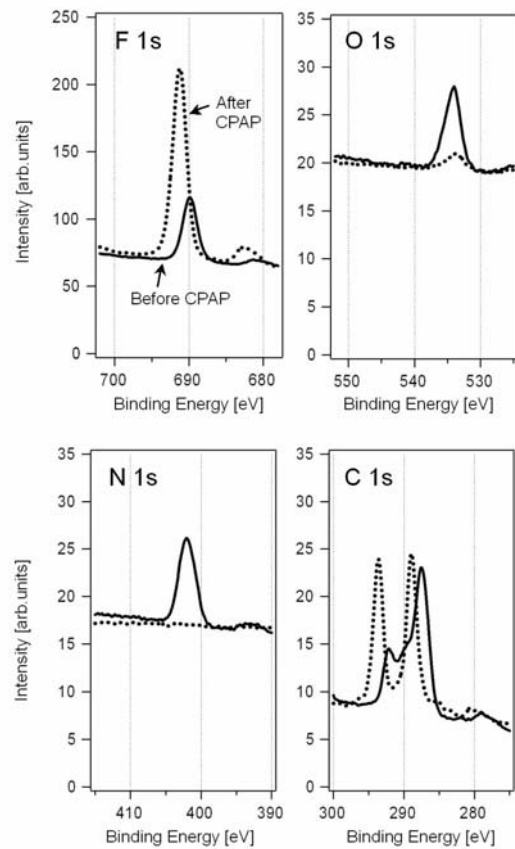


**Fig. 2.2.** XPS spectra of a surface of the Fluoroplastic insulator cores. Dashed and continuous lines are the spectra measured before and after CPAP treatment, respectively.

**References**

[1] S. Kobayashi, et al, (2001) Application of in-situ-formed Metallic Reinforced Copper to Cables used for Robots: *Materia Japan* 40: 70-72  
 [2] N. Gherardi and F. Massines, (2001) Mechanisms Controlling the Transition from Glow Silent Discharge to Streamer Discharge in Nitrogen: *IEEE Trans. Plasma Science* 29:536-544

# Study on Si Wafer Cooling by Low Pressure Argon Gas in Vacuum Eenvironment

Shinsuke Udagawa<sup>1</sup>, Satoshi Takahashi<sup>2</sup>, Daisuke Nakamura<sup>3</sup>, Kazuo Maeno<sup>1</sup>  
<sup>1</sup>Chiba University, <sup>2</sup>Nikon Corporation, <sup>3</sup>Dai Nippon Printing Corporation, Ltd

Keywords: heat transfer, low pressure gas, finite element method, wafer heating, next generation lithography

## Abstract

The circuit line width of DRAM has been matched 45nm design rule at half pitch in 2010 by the ITRS 2005<sup>[1]</sup>. The laser or low energy electron beam as next generation lithography exposure beam source has high energy, and the local and thermal deformation by the energy causes the pattern placement error. Therefore, decreasing the deformation is key issue. In this paper, we have performed the experiment with silicon wafer and argon gas by using experimental apparatus<sup>[2]</sup>. We also calculate the thermal accommodation coefficient between argon gas and silicon wafer by using our experimental results and FEM solutions.

## 1 Heat transfer characteristics by rarefied gas molecule

Heat transfer coefficient  $h$  at a regime of the low pressure gas is represented as a follows<sup>[3]</sup>.

$$h = \frac{(9\gamma - 5)}{4(L + 2g)} \eta c_v, \quad g = \frac{2 - \alpha}{\alpha} \frac{9\gamma - 5}{4(\gamma + 1)} \lambda, \quad (1.1)$$

where  $\eta$  is the viscosity coefficient,  $c_v$  is the specific heat at constant volume, and  $\gamma$  is specific heat ratio at constant pressure to that at constant volume. In these equation  $\alpha$  has the value

$$\alpha = \frac{\alpha_1 \alpha_2}{\alpha_1 + \alpha_2 - \alpha_1 \alpha_2}, \quad (1.2)$$

where  $\alpha_1$  and  $\alpha_2$  which are the thermal accommodation coefficient between solid material surface or cooling plate and low pressure argon gas respectively. The mean free path  $\lambda$  of molecules under Maxwell-Boltzmann distribution laws for molecular velocities is given by

$$\lambda = \frac{1}{\sqrt{2} \pi n \delta^2}, \quad (1.3)$$

## 2 Experimental apparatus and conditions

The experimental apparatus, which was developed in our previous study<sup>[2]</sup>, is shown Fig.2.1. The gap length  $L$  is taken from 200 to 900 $\mu\text{m}$ . The gas pressure  $p$  is set up 0, 133, 399 and 665Pa. The UV light is used as a heat source, and backside of the solid surfaces is cooled by the low pressure argon gas. The heat flux imposed by the UV light is approximately 800W/m<sup>2</sup> and 2600W/m<sup>2</sup> on to the exposure area for the aluminum disc and silicon wafer respectively. The apparatus is placed in a vacuum chamber, whose pressure is less than 1.3 $\times 10^{-2}$ Pa.

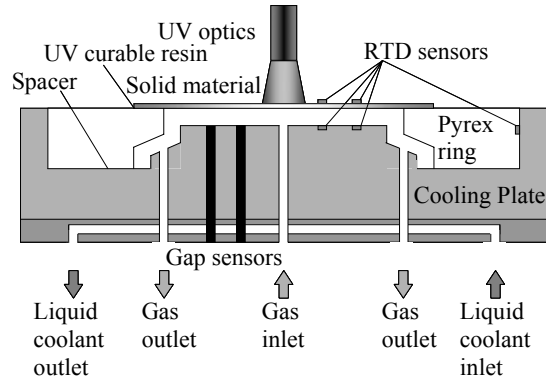


Fig. 2.1. Schematic of experimental apparatus

The gap length displacement caused by the pressure between the solid materials and the cooling plate is expressed theoretically as the following equations (2.1),

$$w = \frac{pa^4}{64D} \left(1 - \frac{r^2}{a^2}\right)^2, \quad D = \frac{Et^3}{12(1-\nu^2)}, \quad (2.1)$$

where  $w$ ,  $p$ ,  $a$ , and  $D$  are the quantity of flexure, uniform pressure, radius of disc, bending stiffness respectively. Considering the gap length displacement, hence we must define the effective gap length  $L'$  which is defined as the integral average.

### 3 Heat transfer by FEM analysis

A transient, thermal, and numerical model shown in Fig. 3.1 has been used to obtain the heat transfer coefficients of low pressure argon gas by curve fitting for experimental results. Firstly, we have performed simulate using our FEM model for the case without folling argon gas. After that, boundary conditions and material properties, the uniform heat transfer conditions between the solid materials and the cooling plate are imposed for the case of several argon gas pressures. The heat transfer coefficients of the low pressure argon gas are determined by curve fitting method using simulated solution for experimental results. Insulated conditions are given on the symmetrical surfaces for all models.

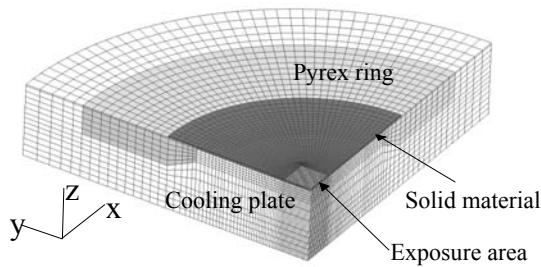


Fig. 3.1. Heat transfer FEM model

### 4 Experimental results and FEM solutions

Fig. 4.1 shows the curve fitting result for experimental temperature rise data on silicon wafer using our numerical analysis for  $p=0$ . From Fig. 4.1 the good agreement between the experiment and simulation data can be obtained. Similarly, the curve fitting result on aluminum disc for  $p=0$  shows also good agreement. From these results, we had confirmed the consistency of our FEM model.

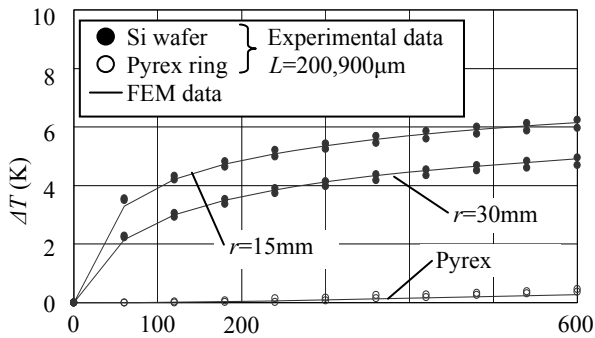


Fig. 4.1. Curve fitting for experimental temperature rise data on silicon wafer using simulation analysis for  $p=0$

For the case of aluminum disc, the heattransfer coefficients at the several pressures are obtained respectively. Similarly, the heat transfer coefficients are also obtained for the case of silicon wafer respectively. We have calculated the heat transfer coefficient using the same model at the gap length of

$L=900\mu\text{m}$ . Figure 4.2 shows the heat transfer coefficient between argon gas and aluminum disc, and the theoretical data, where the value of thermal accommodation coefficient is assumed to  $\alpha_1=\alpha_2=0.5$ . Additionally, we have calculated the case of silicon wafer by using the value of  $\alpha_2=0.5$ . As a concequence, we have obtained that the thermal accommodation coefficient between silicon wafer and argon gas is  $\alpha_1=3.0$ .

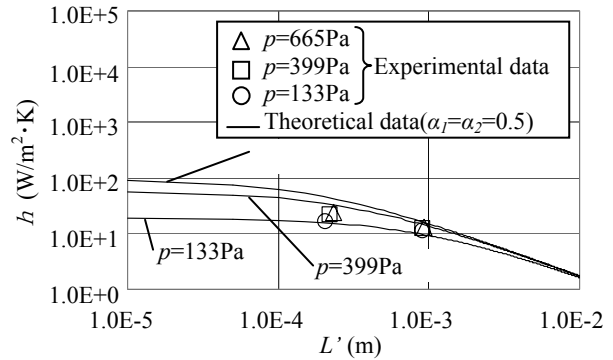


Fig. 4.2. Relation between heat transfer coefficient of aluminum disc and effective gap length  $L'$  for various argon gas pressures

### 5 Conclusion

From our results and discussion, the following points have been concluded.

1. The heat transfer coefficient between solid materials and low pressure argon gas has been obtained by curve fitting for experimental data using FEM.
2. These obtained heat transfer coefficients of aluminum disc show good agreement with theoretical data, which is represented by heat transfer equation (1.1) and (1.2) at  $\alpha_1=\alpha_2=0.5$ , except for high pressure conditions ( $p=399, 665\text{Pa}$ ) and short effective gap length ( $L'=211\sim 218\mu\text{m}$ ).
3. These obtained heat transfer coefficients of silicon wafer also show good agreement with theoretical data at  $\alpha_1=3.0$ . The obtained value of thermal accommodation coefficient  $\alpha_1$  is greater than unity. Accordingly, optimization of boundary conditions at FEM may be necessary for further investigation.

### 6 References

[1] International Technology Roadmap for Semiconductors 2005 edition, organized by International SEMATEC, <http://www.itrs.net/Common/2005ITRS/Litho2005.pdf>.  
 [2] S Takahashi, S Udagawa, K Maeno, N Hirayanagi, and I Shirahama, (2005) Heat Transfer Characteristics on Solid Cooling by Low-pressure Gas of Normal Temperature: Proceedings of The 20<sup>th</sup> Annual Meeting ASPE Vol.37:174-177.  
 [3] S.Dushman : Scientific Foundation of Vacuum Technique, 2nd edition, John Wiley & Sons, New York, (1962)

# Research on Development of Advanced Analyzer Components with Ultraprecision

H. Ohmori, K. Katahira, W. Lin, Y. Uehara, Y. Watanabe, A. Nakao, F. Yatagai, M. Iwaki, M. Mizutani  
Discovery Research Institute, RIKEN (The Institute of Physical and Chemical Research)

## 1. Introduction

Emerging necessities on advanced research in the fields of biology, material science, and engineering, require unique and original analyzing devices and instruments. For example, phenomena during specific treatment of biological specimens are to be analyzed under discussion of their mechanisms. On engineering fields such as materials fabrication, processing mechanisms are to be analyzed during experimental procedures. Those necessities show that several physical parameters are to be detected with in-situ and realtime, and to be processed efficiently with specific digital data structures for analysis. On the other hands, we have been studying material processing principles and mechanisms, analysis methodologies, and their systemization. Under these background, we introduce approaches on development of advanced analyzer components with ultraprecision.

## 2. Analyzer Components

Analyzer components can be roughly classified in **Table 1**. Many types of analyzers need ultraprecision components. Analyzing resolution, for example, strongly depends on optical and detecting resolution together with positioning resolution. Tools for specimens, also are to be prepared with high precision and down-sizing. Thus, we are concentrating on development of ultraprecision components such as optics, sensors, stages, tools, and chambers by applying our ultra/nano-precision micro-mechanical fabrication.

**Table 1** Analyzer Components

Component	Function
Optics	Optical system for beam control
Detector	Electric/optical signal detection
Beam source	Generator of beams for analyzer
Stage	Positioning device for analyzer
Tool	Fine tool for treatment/handling
Chamber	Clean chamber for analyzer
Monitor	Monitoring system for specimen
Specimen	Preparation of specimen
Loader/unloader	Loading/unloading of specimen
Imaging device	Imaging of analyzed signal
Software	Processing of digital imaging data

## 3. Ultraprecision Fabrication Processes and Systems

For fabricate optical elements, some processes such as mirror surface grinding process, mirror surface cutting process, micro-grinding process, micro-cutting process, surface modification process, etc. have been developed.

Optical elements and detecting device substrates mainly made of hard and brittle functional materials such as glass, ceramics, and semiconductors. Some optical elements are composed of hybrid materials. Those are, in general, difficult-to-machine materials. So, efficient ultraprecision processing method is expected to be applied. A ELID grinding was developed. In this process the dressing is continued even during grinding a work in order to prevent reduced wheel sharpness from wear, thereby realizing highly efficient mirror surfaces achieving nano level in roughness.

Optical materials which can be smoothly cut by diamond turning, are finished only by cutting. Single point diamond byte is used for this process. This process is good to be applied to machining of ductile materials. Several nanometric level in roughness of Ra can be achieved.

Micro-grinding process can be applied to fabricate micro-tools for treatment and handling of specimens. Tough materials such as ceramics, and carbide, can be ground to micro-meter level of diameter as micro-tools.

To produce special optical elements such as grating, sharp and fine diamond cutter is applied to generate micro-grooves. By using micro-cutting process, micro-grooves with optical diffractive function can be produced. Not only flat diffractive pattern, but also curved diffractive pattern can be produced by multi-axes numerical control.

During ELID, water is dissolved at the same time. So, if OH<sup>-</sup> ions can be trapped to ground metallic material surface by adding positive potential, surface modification of mirror-finished one is realized efficiently. Thick amorphous

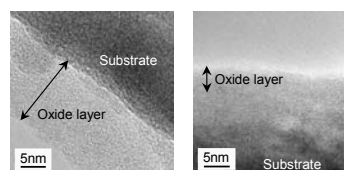


**Fig. 1** Surface modification process

oxidation layer on the work surface is observed after this process as **Figure 1**.

#### 4. Proposal of Advanced Analyzers applying with Ultraprecision Fabrication

Under the above-described backgrounds and through unification of experiences and new idea to create unique analyzing devices and instruments, we propose new concepts targeting at “only-one” analyzers: our concepts provide multiple function of “processing”, “monitoring”, and “analysis” by “all-in-one” analyzers, and “multi-beam” technology. Mechanical processes are inclusive as “multi-beam”. Three prototypes are introduced below.

**Figure 2** shows concept model of advanced hybrid profilometric fabricator: this is a kind of fabrication system which can cope with machining ultraprecision components under hybridization between machining and measurement, of which profilometer has multi-function to analyze profile and roughness, and to monitor machining forces.

**Figure 3** shows an illustration of the advanced XPS (X-ray Photo-electron Spectroscopy) analyzer. In the latest situation, XPS analysis for organic materials is required for advanced scientific fields. For example, structural analysis detecting and imaging chemical bonding conditions of inorganic materials/elements even inside the organic specimens. The proposed advanced XPS system is installed with X-ray source which can cope with low vacuum conditions, clean chamber, and micro-tool and micro-machining for slicing of specimens. Ultraprecision technology are to be well applied.

**Figure 4** shows the advanced cell analyzer. This system analyzes dynamisms on cells and organelles by multi-beams and multi-functions with real-time in one analyzer. X-ray or laser can damage cells in specific parts, for example, and laser can also trace the dynamic behaviors on the damages cells with fluorescent probes. The monitoring system can observe cells which are to be tagged by X-ray or laser. Ultraprecision technology by the advanced hybridized fabricator can produce X-ray/laser optics, stages, and micro-tools for cell manipulation for experiments and analysis.

Each technology development can be connected like a loop through ultraprecision components installation and its module-up. The advanced profilometric fabricator produces optical devices, micro-tools, stages for the Advanced Cell Analyzer. Through the module-up of those devices/components, the upgraded technology is transferred to the Advanced XPS Analyzer which requires also clean chamber development. Specimens can be micro-cut besides the chamber for multi-layer analysis. This new XPS system can analyze machining mechanisms again for the fabricator. **Figure 5** shows the integrated advanced analyzing system.

#### 5. Conclusions

This paper describes current technological seeds and backgrounds for development of advanced analyzer components, and proposed development approaches for prototypes of advanced analyzers. Integrated advanced analyzing system is also proposed for practical applications.

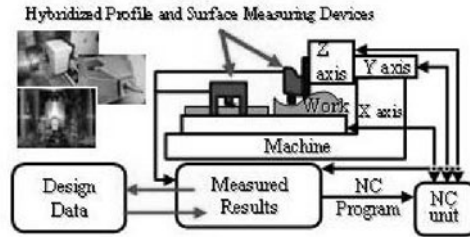


Fig. 2 Concept of Advanced Hybrid Profilometer

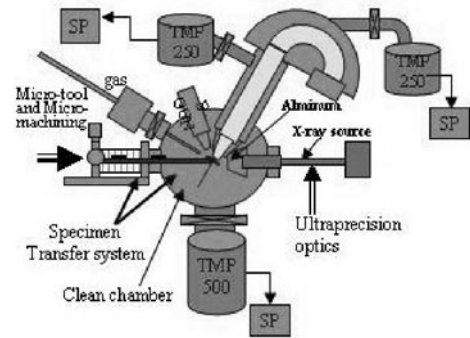


Fig. 3 Advanced XPS Analyzer

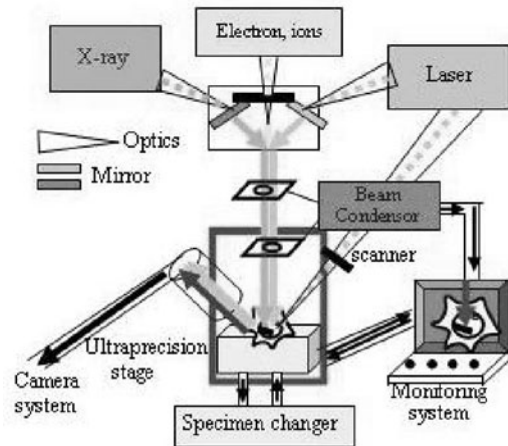


Fig. 4 Advanced Cell Analyzer

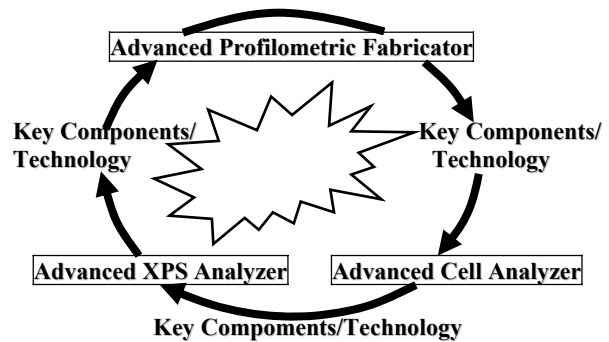


Fig. 5 Integrated Advanced Analyzing System

# Effects of Wear of Single Crystal Diamond Tool with Large Nose Radius on Work Hardening and Residual Stress

Eiji KONDO<sup>1</sup>, Ryuichi IWAMOTO<sup>2</sup>, Ippei TANAKA<sup>3</sup>, Norio KAWAGOISHI<sup>1</sup>  
<sup>1</sup>Kagoshima University, <sup>2</sup>Kagoshima Prefectural Institute of Industrial Technology, <sup>3</sup>Komatsu Electronic Co., Ltd.

Keywords: single crystal diamond tool, tool wear, ultra-precision cutting, aluminum alloy, surface integrity

## 1 Introduction

Because of improvement of quality of finished surface with progress of ultra-precision machining technology, quality of subsurface material like affected layer also becomes important lately [1]. Workpieces are actually machined with a worn diamond tool in machining shops. The purpose of this study is to find out the quantitative relation between the tool wear and the work hardening and residual stress of a machined surface in ultra-precision cutting process.

## 2 Experimental Method

Table 1 shows experimental conditions. End face of a cylindrical workpiece was machined by face turning with a single crystal diamond tool with large nose radius on a ultra-precision lathe in cutting tests.

Table 1. Experimental conditions

Tool	Material	Single crystal diamond		
	Corner radius	mm	2	
	Rake angle	deg.	0	
	Clearance angle	deg.	4	
Crystal face	Rake face	(110)		
	Flank face	(100)		
Workpiece	Material	JIS A5056		
	Diameter	mm	197 (, 30)	
	Heat treatment	Annealed		
	Hardness	Hv	63	
Feed rate	$f$ $\mu\text{m}/\text{rev}$	40	40	10 ~ 80
Depth of cut	$d$ $\mu\text{m}$	30	5 ~ 50	10
Cutting distance	$L$ km	0~2415	New, 2415	
Spindle speed	rpm	1000		
Cutting fluid		Kerosene		

Photographs of cutting edge wear were taken by using a scanning electro microscope of 300 magnifications. Widths of flank and rake wear lands were read off the photographs. Workpieces of 197 mm in diameter were used for extending cutting distance and small cylindrical workpiece of 30 mm in diameter were used for measurement. Effects of feed rate and depth of cut on machined surface integrity was investigated by machining the small cylindrical workpieces

with a new tool and a worn tool at cutting distance of about 2415 km. Hardness of machined surface was measured with a micro-Vickers hardness tester. Residual stress was measured in cutting direction and feed direction by X-ray.

## 3 Experimental Results and Considerations

Figure 1a shows conceptual figure of cutting process where shaded area is cutting cross section,  $l_w$  is distance from the right edge of a contact arc, and  $h$  is undeformed chip thickness. Variables  $w_f$  and  $w_r$  in Fig. 1b are widths of flank and rake wear lands, respectively. Shape of rake wear is flat land at a pseudo rake angle of about  $-11^\circ$  and flank wear land was at an angle of  $-6^\circ$  inclined to cutting direction.

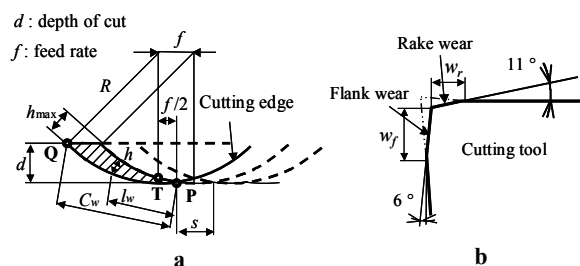
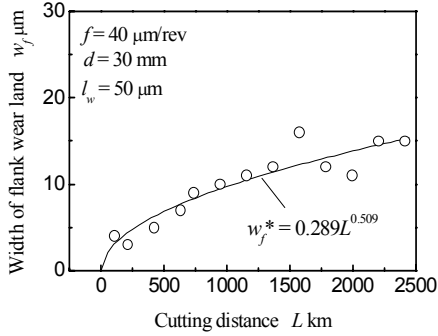


Fig. 1. Tool wear (a)conceptual figure of cutting process (b)conceptual figure of cross section of cutting edge

Figure 2 shows measured width of flank wear land  $w_f$  at a distance  $l_w$  of 50  $\mu\text{m}$  and estimated width of flank wear land  $w_f^*$  obtained by experimental equation is represented by the curve. The experimental equation of  $w_f^*$  is obtained by using the least-square method on the assumption that width of flank wear land  $w_f$  increases exponentially with increase of cutting distance  $L$ . On the other hand, width of flank wear land  $w_f$  at a cutting distance  $L$  of 2415 km was measured along with cutting edge. Estimated width  $w_f^*$  was obtained in the similar way and formulated in  $w_f^* = 3.16(l_w)^{0.409}$ .

Vickers hardness of machined surface obtained with a measuring force of 0.49 N with increase of cutting distance  $L$  is shown in Fig. 3 which shows increase tendency similar to increase tendency of flank wear land width  $w_f$  shown in Fig. 2. New surface close to right edge of a contact arc generated

within the range  $s$  shown in Fig. 1a was left as a machined surface. Consequently, the hardness of machined surface was fairly affected by the flank wear within the range  $l_w$  of 0 and 40  $\mu\text{m}$  since the feed rate  $f$  is 40  $\mu\text{m}/\text{rev}$ .



**Fig. 2.** Width of flank wear land with increase in cutting distance

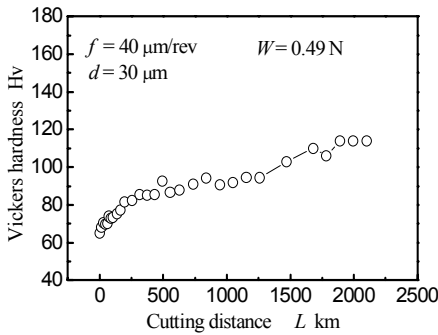


**Fig. 3.** Vickers hardness with increase in cutting distance

Figure 4 shows relationship between normalized Vickers hardness  $(Hv-Hv_0)/h_T$  and normalized width of flank wear land  $w_{fT}^*/h_T$ . The width  $w_{fT}^*$  and the thickness  $h_T$  are width of flank wear land and undeformed chip thickness at the center of cutting edge generating machined surface, respectively. The hardness  $Hv_0$  is Vickers hardness of machined surface in the early stage of cutting. Normalized hardness represented by symbols  $\circ$  was calculated from the values of Vickers hardness shown in Fig. 3 and estimated width  $w_{fT}^*$  was calculated by the equation  $w_{fT}^* = 0.199L^{0.509}$ . Coefficient of the equation  $w_{fT}^* = 0.199L^{0.509}$  at  $l_w$  of 20  $\mu\text{m}$  was modified from coefficient of the equation  $w_{fT}^* = 0.289L^{0.509}$  at  $l_w$  of 50  $\mu\text{m}$  shown in Fig. 2 since the ratio of  $w_{fT}^*$  at  $l_w$  of 20  $\mu\text{m}$  to  $w_{fT}^*$  at  $l_w$  of 50  $\mu\text{m}$  is 0.688 which is calculated by the equation  $w_f^* = 3.16(l_w)^{0.409}$ . Normalized hardness with increase of feed rate is represented by symbol  $\square$ . Solid line in Fig. 4 represents estimated normalized Vickers hardness  $(Hv-Hv_0)/h_T$ . Increment of Vickers hardness  $(Hv-Hv_0)$  is almost proportional to width of flank wear land  $w_{fT}^*$  since the obtained equation can be changed for equation  $(Hv-Hv_0) = (w_{fT}^*)^{1.06} (h_T)^{-0.06}$ .

It has been reported in previous study that residual stress of metal linearly increases with increase of hardness in plastic deformation of metal [2]. Consequently, it can be

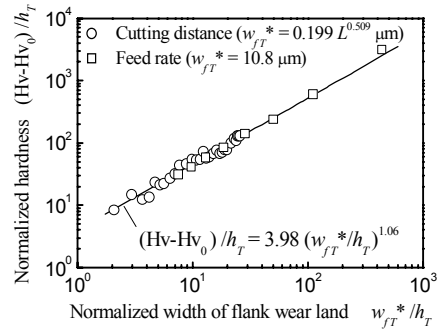


**Fig. 4.** Normalized hardness with increase in flank wear land

considered that residual stress  $\sigma_y$  has the same relation with width of flank wear land  $w_{fT}^*$  as the normalized Vickers hardness of machined surface shown in Fig. 4. Figure 5 shows absolute increment of residual stress  $|\sigma_y - \sigma_{y0}|$  with increase of width of flank wear land  $w_{fT}^*$ . Stress  $\sigma_{y0}$  is the residual stress generated with a new tool. Straight solid line represents estimated absolute increment of residual stress  $|\sigma_y - \sigma_{y0}|$  in the similar way used for the experimental equation  $(Hv-Hv_0)/h_T = 3.96(w_{fT}^*/h_T)^{1.06}$  shown in Fig. 4.

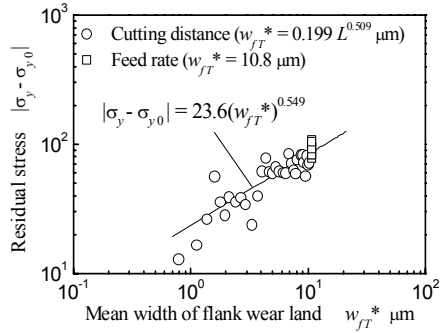


**Fig. 5.** Absolute increment of residual stress in cutting direction with increase in width of flank wear land

## 4 Conclusions

Increment of hardness and residual stress in cutting direction of machined surface with increase of tool wear exponentially increased with increase of width of flank wear land at the center of cutting edge generating machined surface.

## 5 References

- [1] Yoshida Y, (1992) Survey of research on surface integrity. Journal of the Society of Grinding Engineers (in Japanese) 36: 132-140
- [2] Ramarekers JAH, Veensta PC, (1970) The relation between effective deformation and micro-hardness in a state of large plastic deformation. Annals of the CIRP 18: 541-545

---

## Experimental Analysis and Optimization of Cutting Parameters for End Milling Aluminium Alloy

Nafis Ahmad<sup>1</sup>, Ryo Wakabayashi<sup>2</sup>, Tanaka Tomohisa<sup>3</sup>, Yoshio Saito<sup>4</sup>

<sup>1,2,3,4</sup>Department of Mechanical and Control Engineering, Tokyo Institute of Technology, Tokyo 152-8552, Japan

Keywords: End Milling, Optimization, Aluminium Alloy

### Abstract

There have been many works for optimization of cutting parameters for end milling by Genetic Algorithms (GAs) and other Artificial Intelligent (AI) techniques based on theoretical relationships. However these works do not reflect the actual shop floor situation where experimental result is more important than theoretical result. In this work we investigated cutting parameters for end milling Aluminium Alloy by experiment, compared with theoretical results from optimization point of view.

### 1 Introduction

As the cutting conditions play an important role in the efficient use of a machine tool and the high cost of NC/CNC machines tools, there is also an economic need to operate these machines as efficiently as possible. As end milling operation is highly complex, the relationship between cutting parameters and different constraints are very difficult to explain. However, we need these relationships to find the optimum cutting parameters to finish a job at the minimum time or cost. Optimization works for end milling operation using mathematical model for one specific situation is not suitable for other situation specially when the machine tool, workpiece material or cutting tool is changed. In this work, we have conducted this work to find the relationships of cutting parameters and different constraints on machining center for end milling Duralumin (Aluminium Alloy 7075-T6), which has been used extensively for complex high strength, thin wall components in aerospace industries by machining operation. We also compared the result obtained by the experiment with that of GA where mathematical models for determining the optimum cutting parameters [2] are used.

### 2 End Milling Operation

In case of end milling operation, metal is usually removed from a workpiece by a single or multiple point cutting tool. The independent variables for optimal cutting parameters are tool diameter, tool length, number of passes, depth of cut (radial and axial), spindle speed or cutting speed and feed

rate (mm per tooth, per revolution or per unit time). As in this work a four flutes end mill cutter is used for a single pass end milling operation optimization, feed rate and cutting speed are considered to be the two cutting parameters, that effect the success of such machining conditions

#### 2.1 Machining Time

In a single pass end milling the machining time  $T_m$  can be determined by Eqn.2.1, where the workpiece length, feed per tooth, number of flutes of the cutting tool, cutting speed and tool diameter are  $L$ ,  $t_x$ ,  $N_f$   $V$  and  $D$  respectively.

$$T_m = \frac{\pi DL}{1000Vt_x N_f} \quad (2.1)$$

#### 2.2 Constraints for Cutting Process

Here surface finish, maximum allowable cutting force and cutting power of the machine tool are the constraints. The cutting force,  $F$  applied to the cutting tool in a milling operation can be calculated from the force components in X, Y and Z direction of the dynamometer. The theoretical cutting force is calculated by the mathematical model developed by Zheng et. al. [1]. The theoretical surface roughness  $R_a$ , is calculated from the feed rate and tool diameter by Eqn.2.2[2]. The surface roughness value  $R_a$ , must not exceed surface roughness limit  $R_{req}$ .

$$R_a = 318 \frac{t_x^2}{4D} \quad (2.2)$$

This work is performed using machining center (PV5, Toyoda heavy industries) which has power limit of 7.5kW, rotational speed of 25-5500rpm, cutting speed upto 5400mm/min. 4 flutes HSS end mill cutter of 10mm diameter, 34mm length and 30° helix angle is used here. Feed per tooth and cutting speed are varied within the rang of 0.02-0.12mm/tooth and 47-113m/min respectively. Radial and axial depth of cut are 50% of the tool diameter.



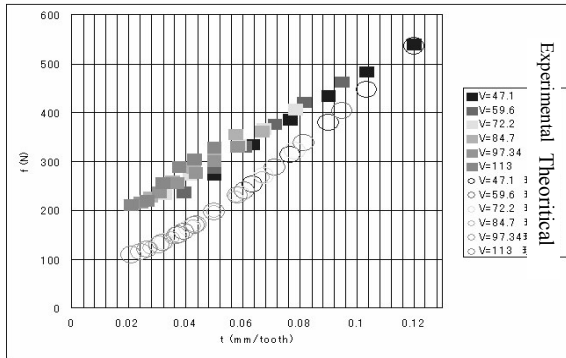


Fig. 3.1. Theoretical and experimental cutting force

Force components in X, Y and Z direction are measured by a dynamometer (KISTLER, 9257BU) connected with digital oscilloscope through a charge amplifier. A clamp-on power meter (CW120, Yokogawa Electric) is used to measure the cutting power. Though the force and the power are measured online, the roughness of the machined surface is measured offline using digital surface measuring device nanofocus.

### 3 Result and Discussion

In Fig 3.1 experimental result cutting force follows similar pattern with the theoretical one. Cutting force increases gradually as feed/tooth increases. As cutting force does not depend on cutting speed, when only a force constraint exist we can increase feed/tooth until force limit is violated. We can also increase cutting speed to minimize the cutting time without violating other constraints. In Fig. 3.2, cutting power does not maintain a similar pattern to theoretical cutting power like cutting force. As cutting power depends both on feed/tooth and cutting speed, when we increase feed/tooth and cutting speed to minimize cutting time we have to check power constraint also. In case of surface finish theoretical surface finish and surface finish obtained by the experiment are significantly different from each other. The main reason may be the chatter vibration. Though theoretically surface finish does not depend on cutting speed, in the experiment surface finish depends on both feed per tooth and cutting speed. As a result when surface finish is an active constraint we have to be careful about using a suitable feed/tooth and cutting speed so that surface finish constraint is not violated.

In Table 3.1. we have presented some typical situation with different constraint limits and their respective optimum cutting parameters obtained by the experiment and by using GA as discussed in [2]. The optimum cutting parameters by experiments are determined by selecting the cutting parameter combination which can finish the machining work at the minimum possible time without violating constraints.

In the first case force limit is the active constraint while power and surface finish are redundant because cutting power and surface roughness are well inside their own limits. Cutting force is close to the limit at the optimum condition. In the second case, the power constraint is active and at the optimum condition machining time is 8.333sec. In the third case surface finish constraint is active and the optimum time

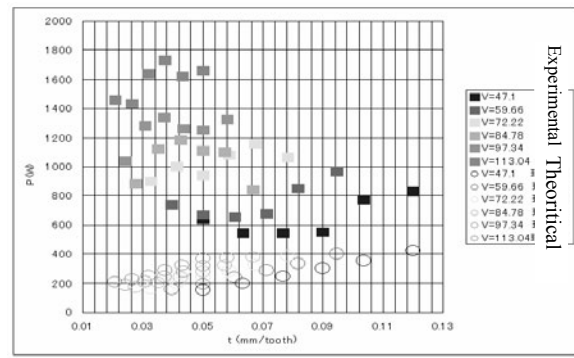


Fig. 3.2. Theoretical and experimental cutting power

to finish machining is again 8.333sec but feed rate and cutting speed are different from the previous condition. As many factors influence the actual machining operation which are not considered in of GA, optimum condition in GA is better than experimental result.

Table 3.1. Optimum condition at different constraint limits

	Constraint limits			Optimum condition		
	Force (N)	Power (W)	Ra ( $\mu$ m)	Feed mm/tooth	Cutting speed (m/min)	Time (Sec)
Experimental	300	1000	10	0.043	113.04	9.6774
	1000	400	10	0.05	113.04	8.3333
	1000	1000	2	0.12	47.1	8.3333
GA	300	1000	10	0.0736	112.9446	3.966
	1000	400	10	0.0559	108.5396	5.43
	1000	1000	2	0.125	112.994	2.334

### 4 Conclusion

Relationships of cutting parameters with different constraints for end milling Duralumin are discussed. As the theoretical and experimental results of power and surface finish are different, it is necessary to study factors also. To use the mathematical model for optimization purpose we need to check the model for specific optimization condition. Further work can be conducted by changing axial/radial depth of cut.

### 5 References

- [1] Zheng, H., Chiou, Y.S., Liang, S.Y., "Three dimensional cutting force analysis in end milling", Int. J. Mech. Sci. Vol.38, No.3, pp.259-269, 1996
- [2] Ahmad, N., Tanaka, T. and Saito, Y., "Optimization Of Cutting Parameters For End Milling Operation By SOAP based Genetic Algorithm", Proceeding of Int. Conf. on Mech. Engg. Dhaka, Bangladesh, AM-08, pp.1-5, 2005.

---

## Study on the ELID Grinding Forces of Ceramics and Steels

Jianqiang GUO, Hitoshi OHMORI, Yoshihiro UEHARA, Yutaka WATANABE, Muneaki ASAMI  
The Institute of Physical and Chemical Research, 2-1 Hirosawa, Wako, Saitama, 351-0198, Japan

Keywords: ELID grinding, ceramics, grinding force, material removal mechanism

### Abstract

Grinding forces are very important phenomenon of grinding process. The higher grinding forces show more difficult removing material from workpiece surface. Ceramics is typical brittle material and metal is important ductile materials. These materials have different use due to their physical and mechanical properties. Through the comparative study of ELID (ELECTROLYTIC In-process Dressing) grinding on ceramics and metals, a more thorough knowledge about grinding mechanism may be acquired. But there are few researchers to study on the ELID grinding forces of ceramics and metals on the same experiment. The present experiment was carried out on a surface grinder. Four kinds of material were selected, such as SiC, ZrO<sub>2</sub>, SKD11 and STAVAX. In grinding process, grinding forces were measured by a three-component forces dynamometer. F<sub>x</sub>, F<sub>y</sub>, and F<sub>z</sub> were respectively in the direction of longitudinal feed, traverse feed and grinding depth of abrasive wheel. On the same conditions, grinding forces of SKD11 and STAVAX were greater than that of SiC and ZrO<sub>2</sub>.

### 1 Introduction

Various materials have different use because of its own physical and mechanical properties. Ceramics has many advantages, such as lightweight, high hardness, high wear resistance, high corrosion resistance, and low thermal expansion coefficient. However, steel has a lower hardness than ceramics, but the reliability of the high strength steel is higher than that of ceramic. Thus, today steel is still the most widely used material in engineering and ceramics is the potential one in the specific field.

Many researchers took their effort to study the material removal mode of ceramics in order to improve the machined surface quality in the last twenty years. As known, grinding force is a very important phenomenon of a grinding process. If the grinding force is higher, it shows that removing material from workpiece surface is more difficult. Thus the effect of grinding parameters on grinding forces was investigated in this experiment.

ELID (ELECTROLYTIC In-process Dressing) grinding is a novel technique, which was proposed by one of the authors in 1987[1-2]. ELID grinding makes it possible using super-

fine abrasive wheel to grind workpiece stably for a long time. It is easy to get a mirror surface of the high hardness materials by ELID grinding. Since this method was proposed, some researchers have respectively done the ELID grinding experiment of ceramics or steels. However, there is no one done a comparative study on the ELID grinding of ceramics and steel at the same experimental conditions. Through doing this kind of experiment, it may be acquired a thorough knowledge of the removal mechanism of various materials.

It is easy to construct an ELID system on a conventional grinder. This system includes a metal bonding abrasive wheel, electrolytic power supply, electrode and electrolyte (also used as grinding coolant). The metal bonding abrasive wheel is connected to the positive pole of the electrolytic power supply by an electric brush and the electrode is connected to the negative one. There is a gap about 0.2mm between the grinding wheel and electrode. Electrolysis occurs in this gap under the presence of voltage and grinding coolant. As a result, the bonding material is electrolyzed and a stable oxide layer is formed on the grinding wheel surface.

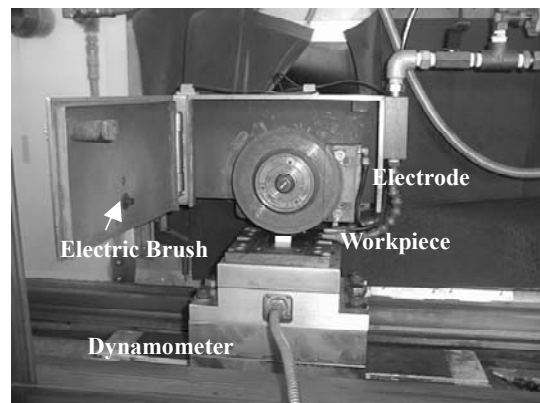


Fig. 1 Photo of experimental setup

### 2 Experimental procedures and results

This experiment was carried out on a surface grinder using ELID grinding method. Fig. 1 shows the experimental setup. Table 1 shows the experimental conditions. Four kinds of material, such as ZrO<sub>2</sub>, SiC, STAVAX and SKD11, were selected. The size of specimens was 20×20×10mm. Specimens were ground by #325, #1200, and #4000 abrasive

wheels respectively. A three-component forces dynamometer MC6-3-1000 made by AMTI was used in this experiment. In order to obtain the correct result, grinding forces were measured in the process of continuous six infeeds of the abrasive wheel.

**Table 1** Experiment conditions

<b>Grinding wheels</b>	SD325N100FA, SD1200N75FA SD4000N50FA Size: $\phi 150 \times w 10 \text{mm}$
<b>Workpiece</b>	SiC, ZrO <sub>2</sub> , SKD11, STAVAX Size: $20 \times 20 \times 10 \text{mm}$
<b>Coolant</b>	CEM diluted to 5% with water
<b>Electric conditions</b>	V <sub>p</sub> =60V, I <sub>p</sub> =8A Pulse interval: $\tau_{\text{on}}=2\mu\text{s}$ , $\tau_{\text{off}}=2\mu\text{s}$
<b>Dynamometer</b>	MC6-3-1000 (AMTI)

**Table 2** Grinding parameters

Wheels	vs (rpm)	a ( $\mu\text{m}$ )	f <sub>t</sub> (m/min)	f <sub>s</sub> (m/min)
#325	2548	1, 2, 3, 4, 5,	6.5	0.12
#1200	2548	1, 2, 3,4	4.5	0.1
#4000	2548	1	1	0.05

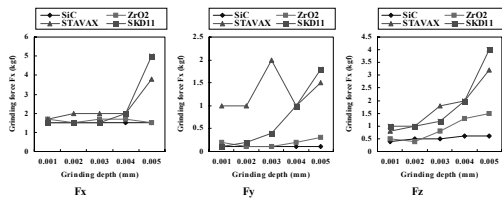


**Fig. 2** Grinding forces using #325 abrasive wheel

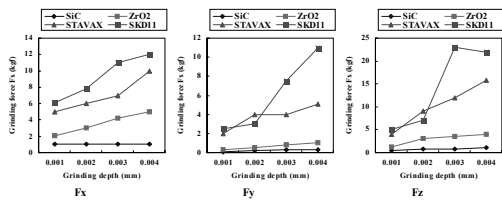


**Fig. 3** Grinding forces using #1200 abrasive wheel

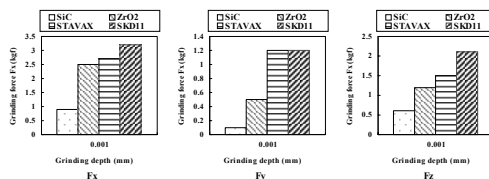


**Fig. 4** Grinding forces using #4000 abrasive wheel

The method of scanning surface grinding was used in this experiment. Grinding force F<sub>x</sub> was at the longitudinal feed direction of work table, F<sub>y</sub> at the traverse feed, and F<sub>z</sub> at the grinding depth of the abrasive wheel. In this experiment, F<sub>x</sub>, F<sub>y</sub> and F<sub>z</sub> were measured using a three-component forces dynamometer at same time. Grinding parameters used in this experiment are shown in Table 2. Where V<sub>s</sub>, a, f<sub>t</sub> and f<sub>s</sub> are the rotary speed of the abrasive wheel, the grinding depth of the abrasive wheel, the longitudinal feed speed and the traverse feed speed of the work table respectively.

Fig.2, Fig.3 and Fig.4 show the relationship of the grinding forces with the grinding parameters using #325, #1200 and #4000 abrasive wheel respectively.

### 3 Discussions

In this experiment, grinding forces of steel STAVAX and SKD11 are higher than these of ceramic SiC and ZrO<sub>2</sub> no matter what mesh size grinding wheel was used. These phenomena are explained as follows.

First, the force needed to initialize a chip of steel SKD11 or STAVAX is higher than that of ceramic SiC or ZrO<sub>2</sub> in the primary deformation zone.

Secondly, the friction force of steel SKD11 or STAVAX chip with the diamond grain is higher than that of ceramic SiC or ZrO<sub>2</sub> debris.

Thirdly, the sliding and plowing force of the diamond grain with the ground surface of steel SKD11 and STAVAX is higher than that of ceramic SiC and ZrO<sub>2</sub>.

### 4 Conclusions

In this comparative experiment, grinding forces of four kinds of material, such as ceramics of ZrO<sub>2</sub> and SiC, steels of STAVAX and SKD11, were investigated at the same grinding conditions. On the basis of the chip formation theory, the grinding force phenomenon was explained. The main conclusions are as follows.

The grinding force of steel is higher than that of ceramics at the same grinding condition. The decisive factor of this phenomenon is the material mechanical properties and the chip formation mode. The impact value of ceramics is the most important factor affecting grinding force of ceramics. According to this experiment, it can be concluded that removing material from high strength steel is more difficult than from ceramics.

### Reference

[1] Ohmori, H., Nakagawa, T., 1990, Mirror Surface Grinding of Silicon Wafers with Electrolytic In-Process Dressing, *Annals of the CIRP*, Vol.39, p.329-332  
 [2] Ohmori, H., Nakagawa, T., 1995, Analysis of Mirror Surface Generation of Hard and Brittle Materials by ELID (Electrolytic In-Process Dressing) Grinding with Superfine Grain Metallic Bond Wheels, *Annals of the CIRP*, Vol.44, p.287-290

## Grinding of C/C-SiC Composite in Dry Method

Tetsuya Tashiro<sup>1</sup>, Junsuke Fujiwara<sup>2</sup>, Yasuhiro Takenaka<sup>2</sup>

<sup>1</sup>Osaka Prefectural College of Technology, <sup>2</sup>Osaka University

Keywords: C/C-SiC, Grinding, Difficult-to-cut material

### Abstract

C/C-SiC composite which has recently been developed is the C/C composite impregnated silicon. This material was used as a workpiece for the machining. In order to get the good machining conditions for this material, some experiments were carried out. The machined surface and the tool surface were observed. And the grinding forces were also measured. The main results obtained are as follows: 1) The cemented carbide K10 endmill was not suitable because of the severe wear. 2) The ground surface with a diamond wheel was better than that with a WA wheel.

### 1 Introduction

Carbon/Carbon (C/C) composite which is one of the advanced materials is widely used for high performance brake systems of aircraft and racing cars, bolt, nut in the furnace and etc. The high tensile and bending strength is maintained even in high temperature above 1,000 °C. However, the C/C composite has the characteristics of high wear rates and an instable coefficient of friction under high humidity and temperature. New C/C-SiC composite which is impregnated silicon has been developed recently. It has the characteristic of oxide-resistance maintaining the strength in high temperature. This C/C-SiC composite has the high coefficient of friction and low wear rates even the temperatures above 1000 °C, too. This material will be more widely used for the brake systems, precision parts and etc. in many fields. Recently it is researched for the emergency brake system of the elevator[1]. These parts are necessary to be finished with cutting and grinding process. But there were few reports about the grinding of this new material. In order to get the good machining conditions, some experiments were carried out. Then the machined surface of the C/C-SiC composite and the tool surface were observed with a microscope.

### 2 Workpiece

Fig. 1 shows the production method of the C/C-SiC composite. At first a yarn is made from 12,000 carbon fibers.

The preformed yarns are arranged side-by-side and a yarn sheet is formed. These yarn sheets are piled up alternately. By sintering the piled-up sheet at 2,000 °C, the C/C composite is made. This C/C composite has a lot of pores. Then, melted Si is impregnated into these pores and the C/C-SiC composite is made. The SEM microphotographs of the cross section of these materials are also shown in Fig. 1. The melted Si is combined with the carbon in the matrix and changed to SiC.

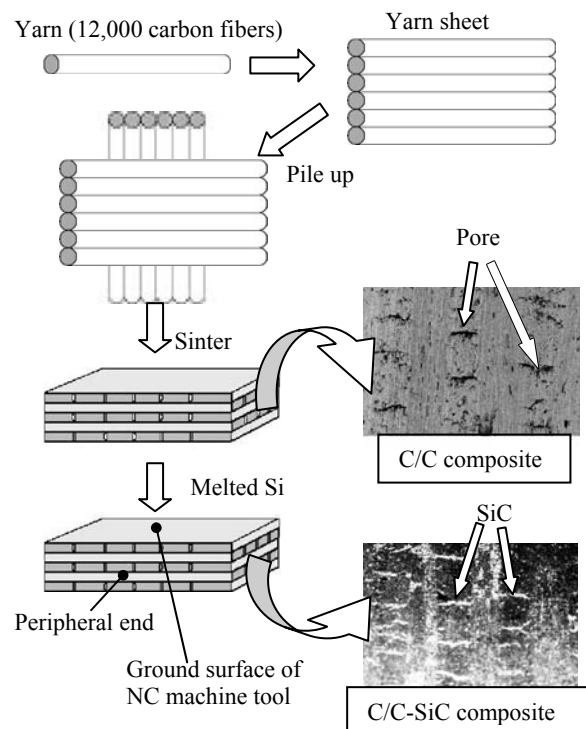


Fig. 1. Preformed yarn production method of C/C and C/C-SiC composite

### 3 Experiments and Results

Fig. 2 shows the experimental apparatus on the Machining Center (PCV 40 Osaka-Kikoh). An air grinder was attached

to the main shaft. The air was compressed by the compressor and was conducted to the rotor through a dry filter. The rotational speed of the air grinder was 60,000 rpm when the air pressure was 0.4 MPa. A lubricator was only used for the lubrication of the air grinder and not used for the coolant. If a coolant is used in the machining of the C/C-SiC composite, it soaks into the pores of the workpiece by the capillary action. And it is difficult to clear the coolant. So the use of the coolant is undesirable for the brake disk parts. Hence, the cutting and the grinding experiments were carried out without the coolant. Machining forces were measured with the dynamometer (Kistler 9257A). The force axis were also shown in Fig. 2. The feed direction was X axis in this figure. The surface of the workpiece was machined as shown in Fig. 1. Table 1 shows the experimental conditions in this experiment.

At first, cemented carbide end mill (K10) was used. Cutting speed was 12.6 m/s. A turbine sound rapidly decreased in very short time from the cutting start. The tool's rotational speed was slowly in a few seconds and finally

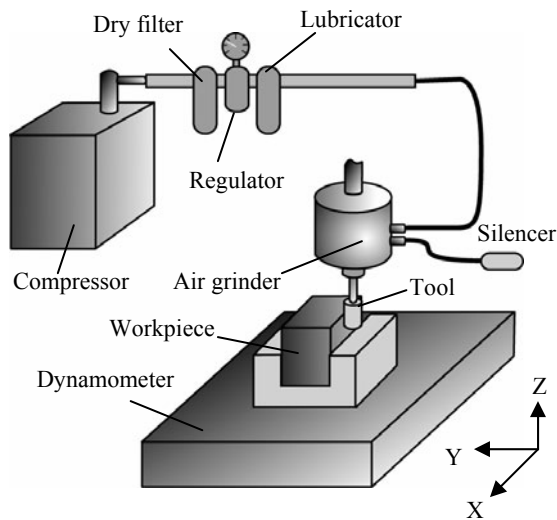


Fig. 2. Experimental apparatus

Table 1 Experimental conditions

Tool	Cemented carbide K10 ( $\phi 6$ ) WA120 wheel ( $\phi 8$ ) SD180V (Porus vitrified bonded diamond wheel : $\phi 9$ )
Grinding method	Down cut
Grinding fluid	Dry
Depth of cut	10 $\mu\text{m}$ : K10 cemented carbide tool 20 $\mu\text{m}$ : WA wheel, Diamond wheel
Hight of cut	5 mm
Feed rate	20 mm/min

stopped. Figure 3 shows the cutting edge of this tool before and after cutting. The wear of the tool face was very severe. The cutting edge was flat and scraped in the rotational direction at many places.

Next, the C/C-SiC composite was ground with a WA wheel and a porous vitrified bonded diamond wheel. Figure 4 shows the ground surface. White things in the white circles in Fig. 4(a) were uncut SiC regions of the workpiece. The SiC was not cut and unremoved from the ground surface. But in case of diamond wheel, there were few grooves and uncut SiC areas as shown in Fig. 4(b).

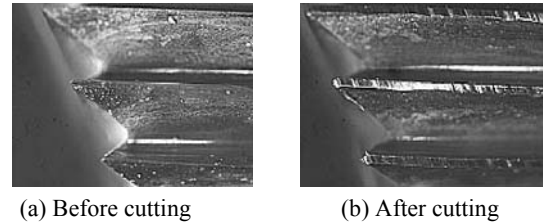


Fig. 3. Microphotograph of tool wear of K10

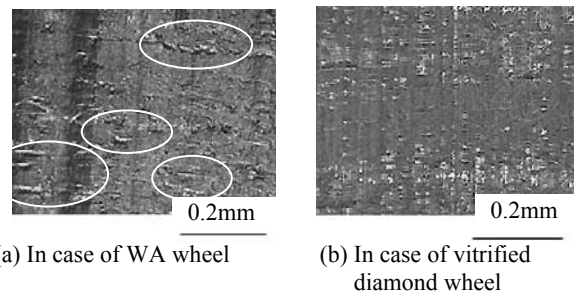


Fig. 4. Microphotograph of ground surface

## 4 Conclusions

The main results were obtained as follows in machining of C/C-SiC composite.

- (1) It was very difficult to cut C/C-SiC composite.
- (2) The porous vitrified bonded diamond wheel was the best tool in this experiment.

## Acknowledgement

This research was supported in part by a grant from SUZUKI FOUNDATION. And the workpiece was offered from ACROSS CORPORATION. I wish to thank to them.

## 5 References

- [1] Renz, R., Krenkel W., (2000) C/C-SiC Composites For High Performance Emergency Brake Systems, ECCM - 9, 9th European Conference on Composite Materials. Design and Applications, Brighton, UK, June 4 - 7

# Micromachining Characteristics of Sapphire Surface with Fifth Harmonic Nd:YAG Lasers

Toshiyuki Noji<sup>1</sup>, Kazuo Nakamura<sup>1</sup>, Hideyuki Horisawa<sup>1</sup> and Nobuo Yasunaga<sup>1</sup>  
<sup>1</sup>Tokai University

Keywords: 5<sup>th</sup> HG wave, Nd-YAG laser, Micromachining, Sapphire.

## Abstract

In order to reduce the thermal influences in laser machining of sapphire surface, effects of a short-pulse ultra-violet laser were investigated. For the UV laser, the Fifth harmonic generation (Fifth HG) wave of an Nd:YAG laser (wavelength:213nm) was utilized. Significant reduction of thermal damages on the surface was demonstrated with the Fifth HG pulses compared to longer wavelengths of the Nd:YAG laser. It was shown that the control of depth of bottom surface with reduced thermal influences was possible in lower fluence cases (less than 4J/cm<sup>2</sup>) with a homogenized beam and smooth surface roughness Ra < 300nm was obtainable.

## 1. Introduction

Sapphire is one of desirable sensor materials which are usable in strong acid and/or alkaline environments. Since sapphire is one of mechanically and chemically difficult-to-machine materials because of its high hardness and chemical stability, laser processing is expected to be a suitable method for precision machining of sapphire. However, infrared lasers like CO<sub>2</sub> laser and YAG laser are not fit for machining thermally friable materials like sapphire[1]. It is expected that the shorter wavelength and pulse laser is more useful for micromachining of a sapphire[2].

The purpose of this paper is to clarify the possibility of thermal-damage-free shape machining of sapphire using a 5th harmonic generation YAG laser which has UV wave length of 213nm.

## 2. Experimental Procedure

In this study, a YAG laser having maximum output energy of 200 mJ/pulse (Tempest-10, New-wave Research corporation) was used. The experimental setup is shown in Fig. 1.

This laser device can generate 4th and 5th harmonic wave (wave length  $\lambda$  of 266nm and 213nm, respectively) having the pulse width of 4ns and the repetition pulse number of 10 pulses/s through a non-linear optical crystal.

As this laser oscillator has an unstable resonator, the output beam has a ring-shape mode of 4mm diameter. After this beam was expanded to twice as large as the original beam, a comparatively uniform part is cut out through a pin-hole aperture of 2mm diameter as shown in Fig.2 which shows a burned pattern on a thermal paper with energy 3mJ and this cut-out beam is focused on a polished sapphire wafer (R-face, 0.55mm thick) with a focusing lens of  $f=50$ mm.

The wafer is scanned on a PC-controlled X-Y stage with the movement speed of 1.7 $\mu$ m/pulse. The formed shapes are observed with a surface roughness meter ET-30HK (Kosaka Laboratory), 3D profile meter New View6000 (Zygo Corporation), Nomarski differential interference microscope (Nikon Corporation) and SEM (JEOL).

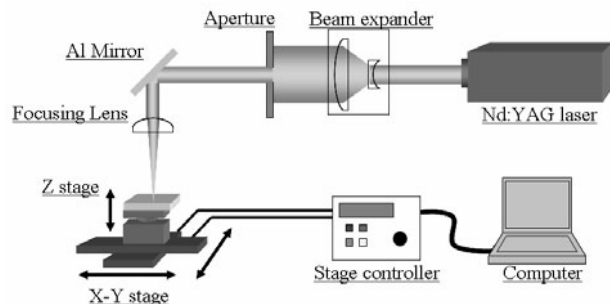


Fig. 1. Schematic diagram of the experimental setup

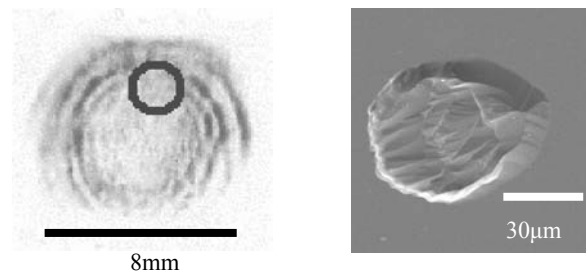
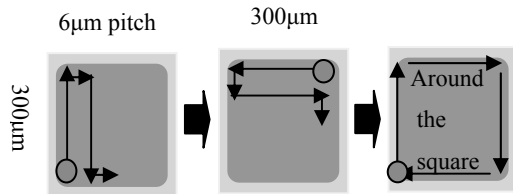


Fig. 2. A burn pattern of the expanded laser beam(left) and SEM photo of an evaporated pattern on a polished sapphire plate at the focusing spot of the cut-out beam marked in red(right)

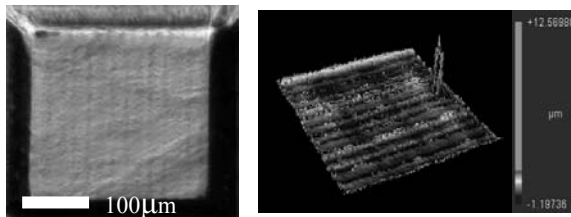
### 3. Results and Discussion

Square shape grooves are machined by the laser beam scanning on the tracks as described in Fig.8. The x-y stage first moves 300 $\mu\text{m}$ , then turns at right angle moving 6 $\mu\text{m}$ , returns further 300 $\mu\text{m}$  and repeats this movement until a square 300 $\mu\text{m}$  groove is formed. The beam finally runs once around the square. This operation is 1 cycle of square shape machining.

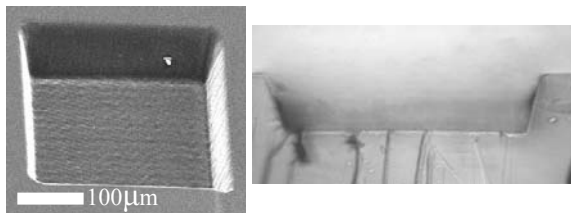


**Fig.8.** A beam operation procedure for square machining.

Figure 9 shows shape observations of square grooves formed after 5 and 10 cycles of operation with the same irradiation condition of the beam energy of 0.05mJ and the beam spot size of 50 $\mu\text{m}$ . In the case of 5 cycles of operation, the removed depth is 40 $\mu\text{m}$ , no crack is observed and the surface roughness is Ra:0.268 $\mu\text{m}$  on the bottom. In the case of 10 cycles of operation, the removed depth is 70 $\mu\text{m}$  having the slope angle about 70°.



General view of the groove after 5 cycles of operation with Nomarski microscope (left) and 3D profile meter (right).



General view of the groove after 10 cycles of operation with SEM(left) and cross-sectional view with Nomarski microscope(right).

**Fig.9.** Observations of the laser machined square groove

Figure 10 shows a relationship between number of operation cycles and removed depth formed by different 3 beam conditions, namely 0.13mJ with spot size of 65 $\mu\text{m}$ , 0.09mJ with 40 $\mu\text{m}$  and 0.03mJ with 30 $\mu\text{m}$ . This figure indicates that

the removed depth approximately proportionally increases as the operation cycles and irradiation energy increase and fluence (energy density) does not affect the removed depth.

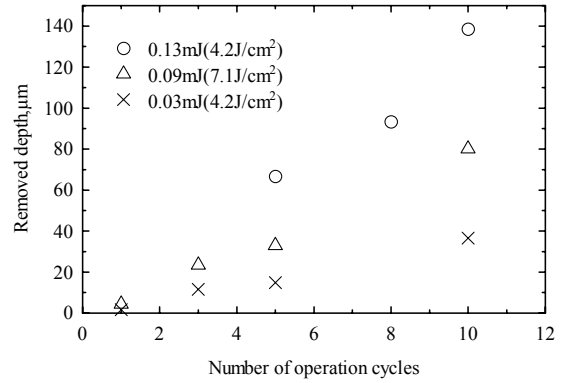


**Fig. 10.** Relationship between the number of operation cycles and removed depth.

### 4. Conclusion

Performance of UV 5<sup>th</sup> HG YAG laser in forming fine square groove on mechanically-difficult-to-machine sapphire was investigated. Main results were obtained as follows.

1. Thermal melting is not avoidable even in so-called non-thermal ablation processing by UV 5<sup>th</sup> HG laser.
2. Generation of thermal cracks is avoidable in UV 5<sup>th</sup> HG laser processing.
3. Removed depth proportionally increases as the operation cycles and irradiation energy increase and the fluence (energy density) does not affect the removed depth.

### 5. Acknowledgement

Authors thanks Zygo Corporation for their cooperation in measuring groove shapes with NewView6000.

### 6. References

- [1] Tamura S. et al.: Laser Ablation of Sapphire with a Pulsed Ultra-Violet Laser Beam, Initiatives of Precision Engineering at the Beginning of a Millennium, p.224, 2001
- [2] Horisawa, H, Emura, H and Yasunaga, N, Surface machining characteristics of sapphire with fifth harmonic YAG laser pulses: Proc 4th Int Symp Appl Plasma Sci 2003, pp. 349-354, 2004.

# Development of an Automatic Scraping Machine with Recognition for Bearing of Scraped Surfaces - Construction of Automatic Scraping Machine -

Hiroataka TSUTSUMI<sup>1</sup>, Ryuta YAMADA<sup>2</sup>, Akira KYUSOJIN<sup>3</sup>, Teruyuki NAKAMURA<sup>3</sup>

<sup>1</sup>Tokyo National College of Technology, <sup>2</sup>Janome Sewing Machine Co., Ltd., <sup>3</sup>Nagaoka University of Technology, <sup>4</sup>Kyowa Co. Ltd.,

Keywords: Image Processing, Scraping, Skilled Worker,

## Abstract

Scraping was only method of sculpting flat, strait surfaces in cast iron slide way that make contact evenly across the whole length and width of their machining surfaces[3].

It is necessary to highly experienced skill, so skilled worker must practice for a long time to acquisition the hand scraping technique. Furtuermore, in some cases, workers trow out their back due to heavy load to their body in the work. Also, scraping will be one of skilled work that people worry about the skill scession in our country.

For these reasons, several studies have been made on automatic scraping machine. They have been reported that pioneer scraping machines with a CCD camera and a scraping tool [1][2], however followings are still unknown: measuring performansece for points of black bearing (black bearings : target points to scrape), tool positioning precision using the CCD imaging system and automation procedure of scraping work.

The purpose of this study is to find out realiziable

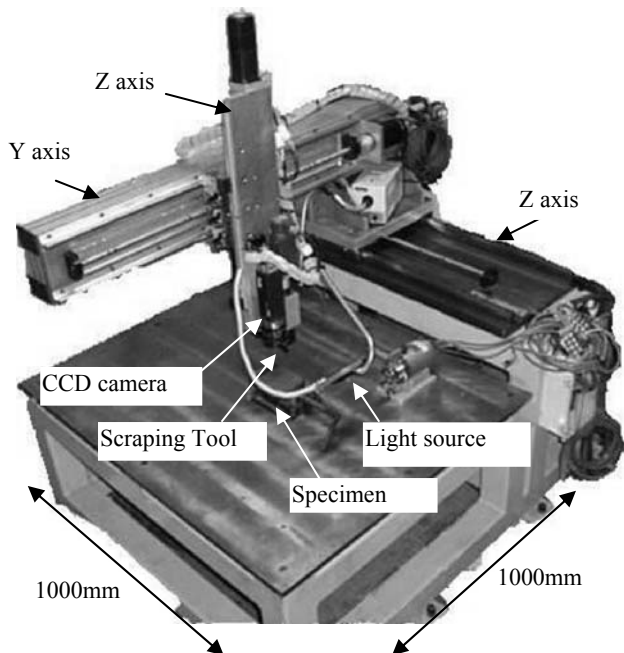


Fig. 1. Scheme of automatic scraping machine

possibility of intelligent automation for the scraping work.

Automatic scraping machine with a CCD camera and a scraper type tool was manufactured. Image processing method and image cordinate system were considered to identify points of bearings on the specimen, and to position the tool on them, precisely. Depth of scraping was decided from size of bearings to be possible to efficiently finish. The working procedure in automatic scraping was considered experimentally to finish surface plate.

## 1 Automatic Scraping Machine and the Method of the Automation

Automatic scraping machine is shown in figure 1.

The Linear motion positioning stage of 3 degrees of freedom is equipped with scraper type tool and CCD camera, which enable to find out scraping points and to scrape just like human scraping. CCD imaging system identify points to scrape by applying thin coats of marking compounds to specimen surface. After sliding the surface against each other, CCD imaging system examines the bearing (black bearing) points left in the making compound. Next, The scraper tool is positioned on each bearing points, and scrape the black bearings individually. This work is repeatedly carried out over the work plane, as a result, the points of bearing to scrape are spread evenly across the whole bearing(specimen) face.

Positioning stages were composed of high-precise ball screws and servomotors. The working area covers 1000×1000mm. Positioning precision of each axis is less than 10 μm. Maximum moving velocity is 100mm/sec. The stage has a simple scraper type tool as illustrated in Fig. 2. The tool which skilled worker used was applied for the machining. The machine operates the tool at triangular

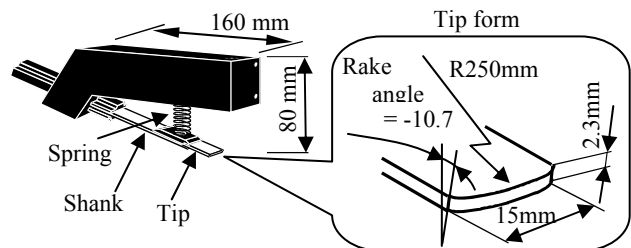


Fig. 2. Scheme of scraper



motion, and scrapes the specimen surface such as Fig. 4.(b).

The flow of image processing is shown in Fig. 3. The optical density of making compound is depend on it's applied depth, and points with low optical density are identified as bearing points to be scraped. Space coordinate of each points were calculated after a series of image processing are performed.

## 2 Tool Positioning Using the CCD Imaging System and Automatic Scraping Work

The result of scraping the surface plate is shown in figures 4..

Scraping depth was decided correspond to size of target marker recognized. The specimen surface was ground, and the marker (white paint) of three arbitrary shapes was prepared. (a) is shown marker before scraping and, (b) is shown after scraping. Both picture were taken at same position. The size of scraping mark were adjusted correspond to the marker size. The error between bearing area and scraper mark area was 11.7% in average. And tool positioning error was less than 0.58mm.

Bearing plane before and after scraping are shown in Fig. 5. (a) is before scraping, (b) is after scraping. Black bearings are black color, and making compound is red color. It is proven that the position of scraping marks and black bearings agrees well. Averages of recognized black bearings

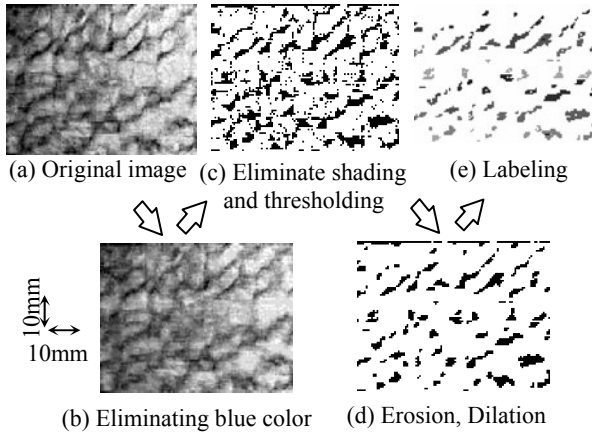


Fig. 3. The flow of the image processing

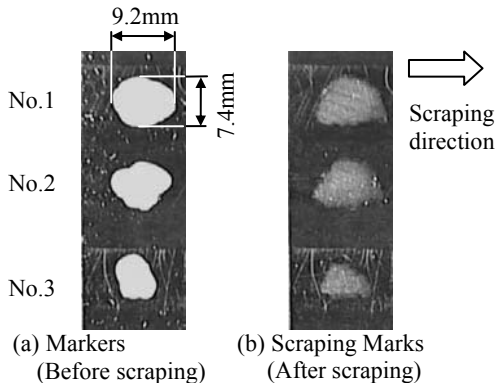


Fig. 4. Markers ( before scraping ) and scraping marks ( after scraping ).

width and length were 3.2mm and 2.3mm respectively.

Scraping failure that imaging system takes a couple of for single bearing appear in Fig.5. (b) A,B,C. There are about five failure for 106 black bearings in one working.

Finished plain made by automatic scraping machine is shown in Fig.6.. Surface flatness was 11.6 μm, and surface roughness was 25.42 μm (maximum height).

## 3 Conclusion

Automatic scraping machine equipped large size positioning stage with a CCD camera and scraper tool was manufactured.

CCD camera detected the area of black bearings with 11.7% error in the average. Scraper tool was positioned with 0.58 mm error. As a result, surface flatness of finished plain was 11.6 μm, and surface roughness was 25.42 μm (maximum height).

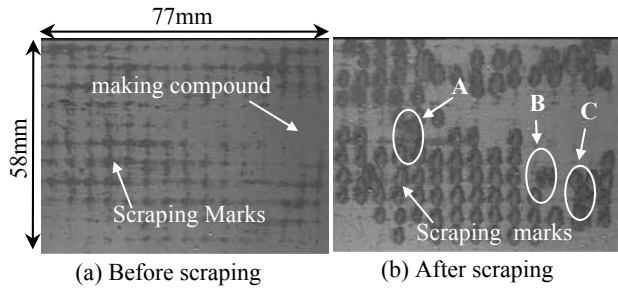


Fig. 5. Bearing plane which applied the making compound (1-st time scraping)

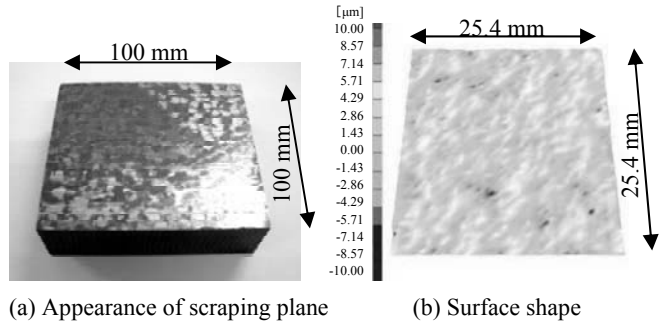


Fig. 6. Scraped plane (Recognizing and scraping )

## 4 References

- H TSUTSUMI, A KYUSOJIN, T NAKAMURA, Development of an Automatic Scraping Machine with Recognition for Bearing of Scraped Surfaces (1st report), (2005): JSPE Proceedings 71,3:358-343
- [1] Y TAKEUCHI et al., (1986): The recognition of bearings by means of a CCD line sensor and the automation of scraping works, JSPE 52,12:2087-2092
  - [2] Y YAMANE et al., (1989), Application of Multi-Joint Type Industrial Robot to Scraping of Surface: JSPE 55,10:55-60
  - [3] Andrew.J.Devitt, (1998), Sliding-Way Design Primer: Feb. 1998-Manufacturing Engineering: 68-74